RHEOLOGY OF COHESIVE SEDIMENTS

by

SUSAN JILL PARTRIDGE

A thesis submitted in partial fulfilment of the requirements for the Degree of Doctor of Philosophy.

Department of Physical Chemistry.
Bristol University.

July 1985.

MEMORANDUM

The work described in this thesis was carried out in the Department of Physical Chemistry of Bristol University and at ICI Corporate Bioscience and Colloid Laboratory under the joint supervision of Dr. J.W. Goodwin and Dr. R. Buscall between November 1982 and December 1984. The work is original unless otherwise stated in the text. No part of this work has been submitted for a degree at this or any other university.

Acknowledgements

First, and most importantly, I extend my sincere thanks to my supervisors, Dr. J.W. Goodwin and Dr. R. Buscall, for their considerable guidance and advice throughout the duration of this project.

I am deeply indebted to Professor C.F. Zukoski for his stimulating introduction to statistical mechanics and to Mr. R.W. Hughes for helpful discussions. I also thank Miss G.E. Barratt for mathematical advice.

I acknowledge the cooperation of the technical staff at Bristol University and at ICI Corporate Bioscience and Colloid Laboratory with the provision of laboratory services.

My thanks to my mother, Mrs. P. Partridge, for typing my manuscript efficiently and accurately and to Dr. D.R. Skuse for his invaluable help with the diagrams. Thanks also to Mr. A.R. Partridge and Miss I.P. MacDonald for their help with thesis compilation.

I acknowledge the financial support of the Science and Engineering Research Council and ICI Corporate Bioscience and Colloid Laboratory who made this work possible.

I would like to thank all members of the Ottewill-Goodwin research group for many interesting discussions and for making my stay in Bristol so enjoyable.

Finally, my special thanks to my parents for their continued support, both financial and otherwise, throughout my education.

To My Parents, Alan and David.

Abstract

Polystyrene latices of particle diameter 0.97 μm, 1.41 μm and 1.92 μm, at an electrolyte concentration of 0.5 mol dm^{-3} sodium chloride, were sterically stabilised by the adsorption of a monolayer of a monodisperse nonionic surface active agent, $C_{12}E_6$. Optical microscopy showed that the resultant systems were weakly flocculated, with only slight agitation required to destroy the flocs. Calculations showed that the van der Waals attractive potential dominated the highly screened electrostatic repulsive potential; the particles were prevented from coagulating into the primary minimum through the presence of the steric barrier. Potential energy well depths of 7 - 15 kT were obtained. Rapid sedimentation of the systems occurred by consolidation of the aggregated structure after an induction period which increased with increasing volume fraction to give a final sediment volume fraction of approximately 0.4 - 0.45. Constant stress viscometry demonstrated that the suspensions were shear thinning with a limiting Newtonian viscosity at low stresses. At high stresses the viscosity was similar to that expected for a dispersion of hard spheres as calculated from Krieger's equation.[82] Shear wave propagation experiments were performed to measure the high frequency limit of the shear modulus as a function of volume fraction. The values obtained were compared with a theoretical model due to Zwanzig and Mountain[79] and based on a statistical mechanical description of the microstructure combined with the pair interaction potential of the particles. Parameters required for the model were the suspension volume fraction, the Stern potential, the Hamaker constant and the extent of the adsorbed layer, all of which were determined independently of the rheological measurements. Good agreement was obtained between theoretical and experimental data when using a Barker Henderson perturbed hard sphere potential model to calculate the pair distribution

function. The model thus provided a strong test of the use of liquid state theory for the prediction of the transport properties of colloidal suspensions. Predictions of the zero shear viscosity were made using a similar model.

RHEOLOGY OF COHESIVE SEDIMENTS

Chapter Seven Preparation of Systems

Chapter Eight Characterisation of Systems

Chapter Nine Sedimentation

Chapter One

Introduction

Chapter One Introduction

Many industrial processes result in the formation of colloidal dispersions, i.e. suspensions of particles with at least one dimension of the order of 1 nm - 1 μm. To facilitate easier and cheaper transportation and distribution of the products the solid matter must be separated from the dispersion medium, either completely or partially. Such products include plastics, pigments, dyes, ceramics, fertilisers, pesticides and pharmaceuticals. As a result the dewatering of slurries of fine chemicals is an important operation in the chemical industry. Likewise in the treatment of sewage, where vast quantities of sludge have to be concentrated from a voluminous sediment, the economics can be critically dependent on the handling properties.

At present isolation of the solid product is usually accomplished in two stages, by an initial mechanical dewatering, such as filter pressing, followed by a drying step. The effectiveness of the dewatering process, and the cost incurred, depends not only on the mechanical equipment but very much on the properties of the suspension itself. Hence the ability to control the structure of a suspension and its derivative properties such as sedimentation and rheological behaviour is of great importance. The rheological behaviour of a system of course comprises both its flow and deformation properties.

In the case of fine suspensions, where the particle size is less than 10 μm, coagulation or flocculation of the particles is usually employed to enhance the rate of dewatering by increasing the sedimentation rate. However, coagulation can adversely affect the final efficiency of the dewatering process by the formation of a space filling open-network after sedimentation which contains a high water content of up to 75% so that extensive drying is required and this becomes expensive.

A useful solution to this problem is to only weakly flocculate the system, i.e. to produce aggregation that is easily reversible, so that consolidation of the sediment by centrifugation or filtration can be readily accomplished. Some preliminary work at Corporate Bioscience and Colloid Laboratory, ICI[1-3] has indicated a strong correlation between the behaviour of flocculated dispersions in model and actual dewatering processes and their behaviour in well-defined rheological tests. It is clearly important to study the structure and flow properties of flocculated systems with this correlation in mind. Equally important is the ability to theoretically predict the flow properties of such systems.

A directly analogous problem to that of dewatering occurs in the long term storage of suspensions. These are often weakly flocculated in order to prevent the formation of a dense sediment in favour of one which, if formed, can be readily redispersed.

This work is concerned with an experimental study of the rheological and sedimentation properties of weakly flocculated model colloidal systems and with the theoretical prediction of the rheological properties based on a knowledge of interparticle interaction energies.

A simple model colloidal system is a suspension of monodisperse spheres of colloidal size.Synthetic polymer latices can be utilised in this context as they may be prepared to a high specificity of monodispersity and particle size and have easily characterisable surface properties.

The properties of a colloidal system are controlled by the forces that exist between the particles, a combination of electrostatic repulsive forces and van der Waals attractive forces, of similar magnitude to Brownian forces. Dominant repulsive forces ensure that a system is stable in the colloidal sense whereas dominant attractive forces cause the

particles to aggregate. It is possible to screen electrostatic repulsive interactions to such an extent that the particle interaction forces are dominated by the van der Waals forces of attraction. This may be achieved by the presence of high concentration electrolyte.

It is also possible to sterically stabilise colloidal particles by the adsorption of a layer of soluble molecules onto the particle surfaces which limit the extent of the attractive forces by restricting the closest distance of approach to give values of attractive energies of a similar order of magnitude to the thermal energy. This controls the particle aggregation and ensures that weak flocculation rather than coagulation occurs.

The weakly flocculated, model colloidal systems utilised in this work were polystyrene latices of various particle size and volume fraction, coated with a monolayer of nonionic surface active agent, n-dodecyl hexaoxyethylene monoether, $C_{12}E_6$. The coated particles were suspended in a 0.5 mol dm^{-3} sodium chloride solution.

The sedimentation behaviour of the systems was examined, both at 1 g and at higher g values by means of slow speed centrifugation.

The rheological properties were studied by two types of experiment: continuous shear and oscillatory rheometry. Rotational viscometry was utilised to measure the flow properties of the systems over a wide range of shear rates and stress whereas shear wave propagation measurements were used to quantify the viscoelastic properties of the systems by measurement of the shear wave rigidity modulus. All measurements were made as a function of volume fraction.

A prediction of the experimentally obtained properties of high frequency shear modulus and zero shear viscosity was made from a statistical mechanical description of the system and a knowledge of the particle

interaction forces. The theoretical and experimental results were compared and a good correlation obtained.

Chapter Two

Basic Rheological Theory

Chapter Two Basic Rheological Theory

2.1. Introduction.

Rheology is defined as 'the study of the deformation of materials, including flow'[4]. It has important applications industrially as information gleaned on the heat and mass transfer properties of a system gives insight to its applicability for a particular purpose.

When a stress τ, that is a force per unit area, is applied to a material it will deform, so that there will be no change in position of points of the material relative to each other. The extent of the deformation relative to the original dimensions of the material is known as the strain, γ. A mathematical description of the general deformation of a material as a result of an arbitrarily applied stress is complicated.[5,6] As an illustration of the problem consider the stress tensors acting on a cube of material under applied stress. The stress can be expressed in terms of its three components using a Cartesian coordinate system. Each of these component forces can be expressed in terms of their components giving a matrix of nine components, see Figure 2.1. Hence in order to describe a general deformation it is necessary to know all nine component values. An identical situation occurs with the strain, γ.

In the laboratory it is possible to select simple geometries for applying stress, setting as many components as possible to zero, to simplify the mathematics. Two examples of this are simple shear and uniaxial extension, shown in Figures 2.2 and 2.3.

Throughout this work only simple deformations will be considered but it is important to remember that the stress distribution may not be simple and it may be rash to approximate the complex flows that occur in chemical plants to viscometric flows used in the laboratory.

Figure 2.1.

Stress tensors on a cube of material

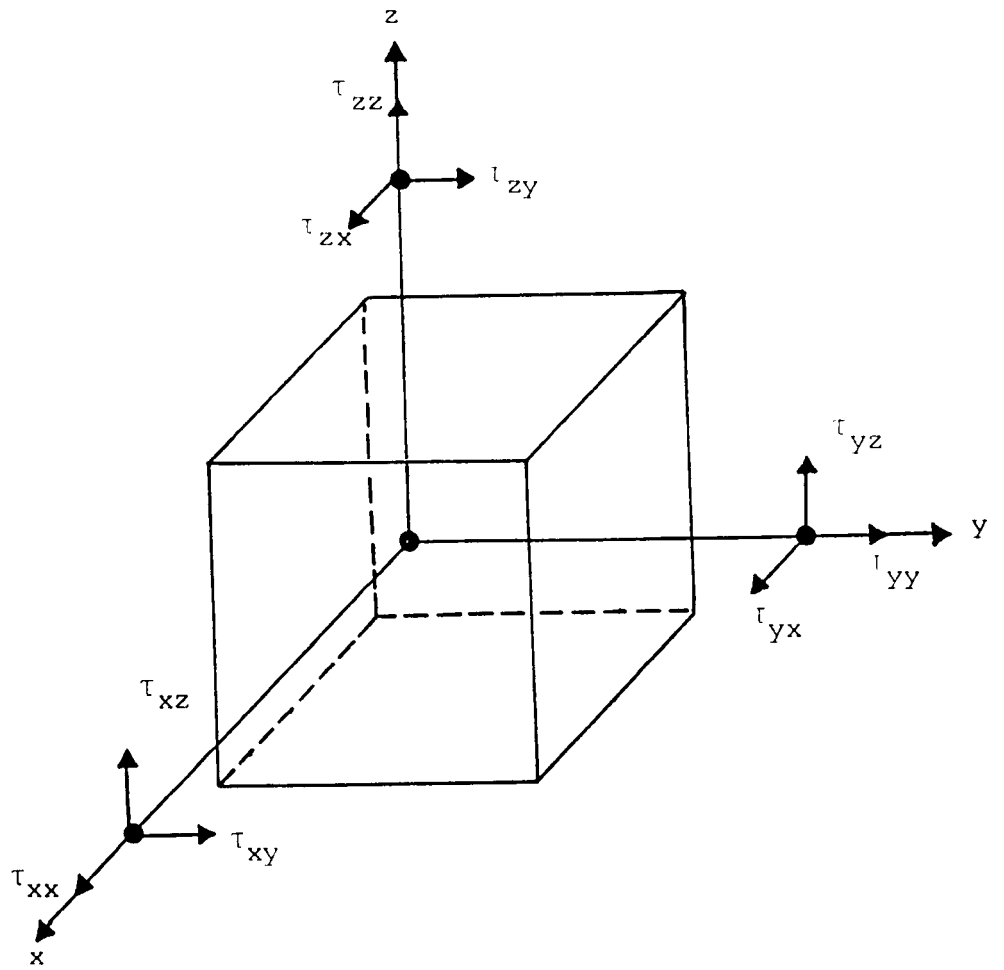

$$\tau = \begin{vmatrix} \tau_{xx} & \tau_{xy} & \tau_{xz} \\ \tau_{yx} & \tau_{yy} & \tau_{yz} \\ \tau_{zx} & \tau_{zy} & \tau_{zz} \end{vmatrix}$$

Similarly strain, γ:

$$\gamma = \begin{vmatrix} \gamma_{xx} & \gamma_{xy} & \gamma_{xz} \\ \gamma_{yx} & \gamma_{yy} & \gamma_{yz} \\ \gamma_{zx} & \gamma_{zy} & \gamma_{zz} \end{vmatrix}$$

Figure 2.2.

Simple shear stress for a Hookean material.

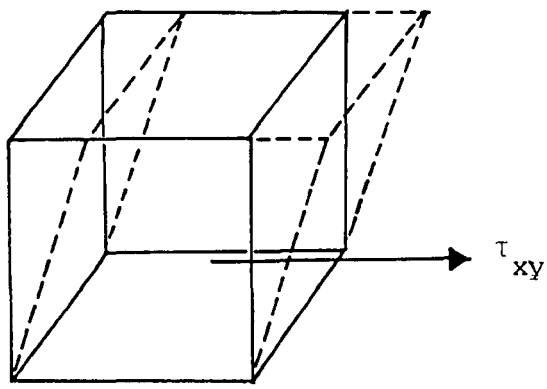

$$\tau = \begin{vmatrix} 0 & \tau_{xy} & 0 \\ \tau_{yx} & 0 & 0 \\ 0 & 0 & 0 \end{vmatrix} \qquad \gamma = \begin{vmatrix} 0 & \frac{\gamma_{xy}}{2} & 0 \\ \frac{\gamma_{yx}}{2} & 0 & 0 \\ 0 & 0 & 0 \end{vmatrix}$$

Figure 2.3.

Uniaxial extension for a Hookean material

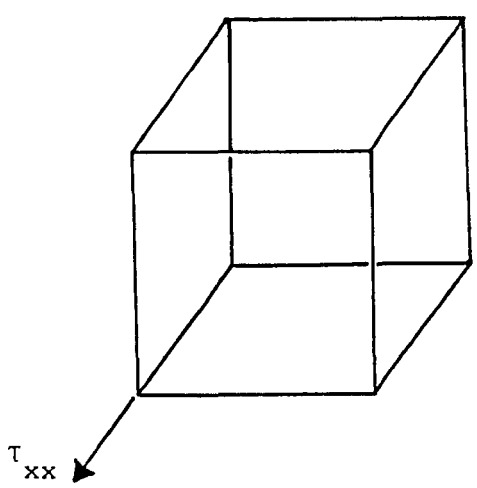

$$\tau = \begin{vmatrix} \tau_{xx} & 0 & 0 \\ 0 & 0 & 0 \\ 0 & 0 & 0 \end{vmatrix} \qquad \gamma = \begin{vmatrix} \gamma_{xx} & 0 & 0 \\ 0 & -\frac{\gamma_{yy}}{2} & 0 \\ 0 & 0 & -\frac{\gamma_{zz}}{2} \end{vmatrix}$$

There are three basic types of behaviour observed in response to an applied stress. If the deformation is reversible on removal of the stress the material stores energy and is said to be elastic. If the components of the material diffuse a sufficient distance during the experiment to relieve the applied stress a viscous flow is said to have occurred resulting in an irreversible deformation and energy dissipated as heat. In reality the response of many materials to an applied stress lies between these two extremes and such materials are termed viscoelastic, exhibiting both viscous and elastic properties.

The classification of material properties is therefore governed by the decay of elastically stored energy.[7] If the time scale for a significant amount of decay is short compared to the duration of the experiment the material is said to respond as a viscous fluid, and conversely for insignificant relaxation, the material is taken to be an elastic solid. This classification is defined in terms of the Deborah number, De:

$$De = \frac{t_r}{t_e} \qquad (2.1)$$

where t_r is the stress relaxation time of the material and t_e is the experimental time, so that:

$De \gg 1$ elastic response, solid

$De \ll 1$ viscous response, fluid

$De \simeq 1$ viscoelastic response

The laboratory time scale is generally of the order of $10^{-3} < t_e < 10^{3}$s, which is suitable for most experiments. In very rapid experiments equipment becomes expensive and difficult to design and in very slow experiments temperature control and stability of recording equipment becomes a problem.

Stress relaxation times for dilute dispersions of colloidal particles

are shorter than the above t_e range due to the rapid diffusive motion of both the solvent molecules and the particles and hence the systems are taken to be viscous fluids. However, in concentrated colloidal dispersions the particle diffusivity can be markedly reduced due to strong interactions between the particles and viscoelastic behaviour is observed.

The three types of behaviour, elastic, viscous and viscoelastic, observed in response to an applied stress are illustrated in Figure 2.4.

In order to describe viscous, elastic and viscoelastic behaviour it is necessary to find suitable equations relating stress, strain and time, i.e. it is necessary to find satisfactory constitutive equations.[5-7] A useful technique is to set up the equations by means of mechanical analogues which show the same type of stress-strain-time behaviour as the materials under consideration.

The simplest elastic behaviour exhibited by an elastic solid is that in accordance with Hookes law[5]:

$$\tau = G\gamma \qquad (2.2)$$

in which there is a linear relationship between the applied stress, τ, and the resultant strain, γ, with no dependence on the rate of strain, $\dot{\gamma}$. (Newtons dot signifies the time derivative). The proportionality constant, G, is termed the shear modulus. The mechanical analogue used to represent an elastic solid is a spring which obeys Hooke's law with the correct stress-strain proportionality constant, i.e. the shear modulus. This is illustrated in Figure 2.5(a).

A common simple hydrodynamic behaviour of viscous liquids is that in accordance with Newtons law:

$$\tau = \eta\dot{\gamma} \qquad (2.3)$$

in which the stress is directly proportional to the rate of strain but

Figure 2.4.

Elastic, viscous and viscoelastic behaviour observed in response to an applied stress.

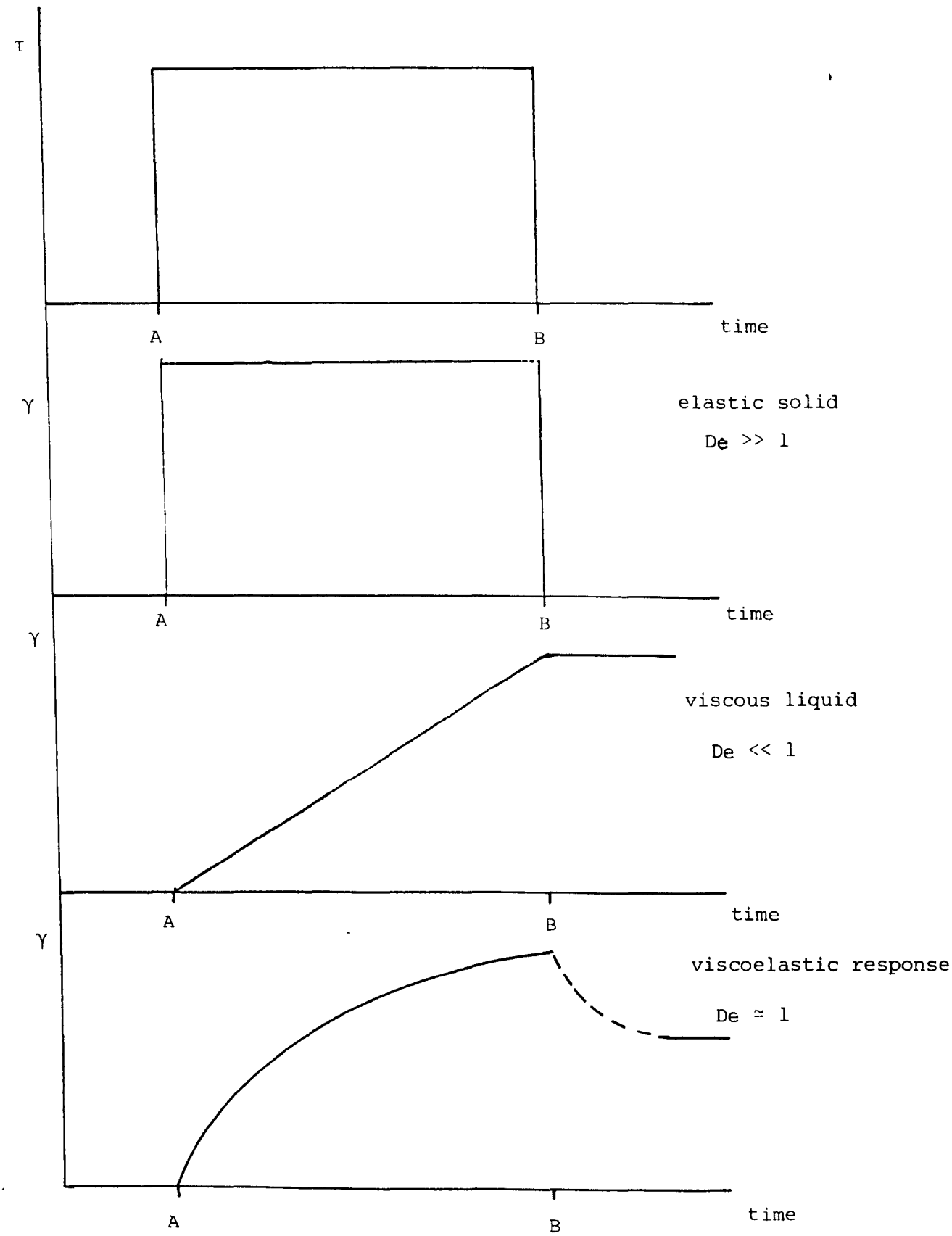

Figure 2.5.

Mechanical analogues and constitutive equations for a Hookean solid and a Newtonian fluid.

(a) Hookean solid

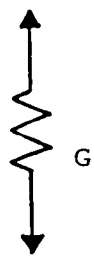

$$\tau = G\gamma$$

(b) Newtonian fluid

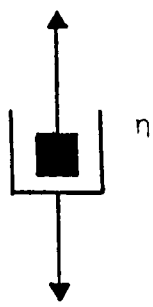

$$\tau = \eta\dot{\gamma}$$

Figure 2.6.

Mechanical analogue and constitutive equations for a viscoelastic fluid. Maxwell model.

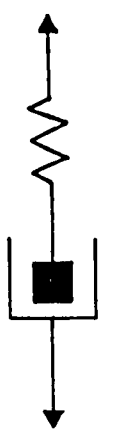

$$G \leftarrow \dot{\gamma} = \frac{\dot{\tau}}{G}$$

$$\eta \leftarrow \dot{\gamma} = \frac{\tau}{\eta}$$

$$\dot{\gamma} = \frac{\tau}{\eta} + \frac{\dot{\tau}}{G}$$

$$\tau = \eta\dot{\gamma} - \dot{\tau}\,\frac{\eta}{G}$$

$$\frac{\eta}{G} = t_M$$

= Maxwell relaxation time

Stress same in both elements

Strains additive

independent of the strain itself. The proportionality constant, η, is termed the viscosity. The mechanical analogue used to represent a Newtonian fluid is a dashpot filled with a Newtonian liquid of the appropriate viscosity to generate the correct stress-shear rate relationship. This is illustrated in Figure 2.5(b).

The two simple models for elastic solids and viscous liquids may be used as building blocks for more sophisticated responses. The Maxwell model, as illustrated in Figure 2.6, represents a viscoelastic fluid and is represented by a dashpot and spring in series. The spring provides the driving force for the relaxation of the stress while the dashpot governs the rate. The stress is the same in both elements whilst the strains are additive. The model is characterised by the following constitutive equations:

$$\dot{\gamma} = \frac{\tau}{\eta} + \frac{\dot{\tau}}{G} \qquad (2.4)$$

i.e.
$$\tau = \eta\dot{\gamma} - \frac{\dot{\tau}\eta}{G} \qquad (2.5)$$

$$\frac{\eta}{G} = t_M \qquad (2.6)$$

where $\dot{\tau}$ is the time differential of the stress and t_M is the Maxwell relaxation time, characteristic of a given system.

In practice such a simple system with a single relaxation time is rarely found.[6] A much more likely situation involves a wide range of characteristic times which could be associated with a range of microstructural changes. This situation is represented by the generalised Maxwell model which has an infinite series of Maxwell units connected in parallel, see Figure 2.7. The concept leads to a spectrum of relaxation times or 'relaxation spectra'. The model can be used to describe most viscoelastic materials; viscoelastic solid type responses can be simulated if the viscosity in the final dashpot is set to infinity.

Figure 2.7.

Generalised Maxwell body

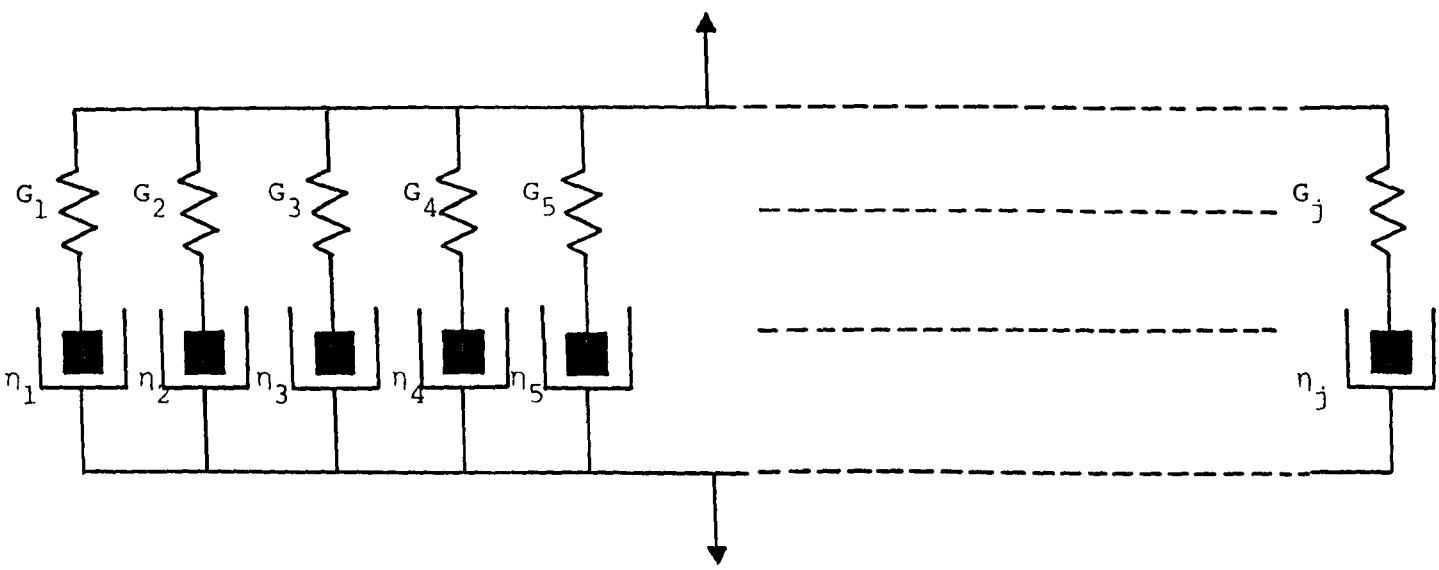

In the study of rheology the broad experimental objective is to define how much energy is stored elastically when a material is deformed and how much is lost by diffusive relaxation resulting in viscous flow. Continuous shear viscometry gives an estimate of the latter while oscillatory testing, of which shear wave propagation is one technique, also measures elastic response.

2.2. Continuous Shear Viscometry.

There are three types of geometrical arrangements available for continuous shear viscometry measurements: capillary tubes, concentric cylinders and cones and plates.[6] Concentric cylinder and cone and plate measuring elements are used in rotational viscometers where for a constant angular rotation shear stress is constant across the sample and can be measured as a function of both shear rate and time.

Consider first the couette or concentric cylinder viscometer, as illustrated schematically in Figure 2.8 with inner cylinder radius R_{ccl}, outer cylinder radius R_{cc2} and arbitrary radius r_{cc} such that $R_{ccl} < r_{cc} < R_{cc2}$. The height of the outer cylinder is l_{cc} and the angular rotation Ω_{cc2}. The torque of the spring on the inner cylinder is taken to be T_{cc} with a Newtonian fluid in the gap:

$$\dot{\gamma} = \frac{r_{cc} d\Omega_{cc}}{dr_{cc}} \tag{2.7}$$

$$T_{cc} = \tau A^{*}_{cc} r_{cc} = \eta r_{cc} \frac{d\Omega_{cc}}{dr_{cc}} 2\pi r^{2}_{cc} l_{cc} \tag{2.8}$$

Boundary conditions:

$$\left.\begin{aligned} \Omega_{cc} &= 0 \text{ when } r_{cc} = R_{ccl} \\ \Omega_{cc} &= \Omega_{cc2} \text{ when } r_{cc} = R_{cc2} \end{aligned}\right\} \text{ No slip assumption}$$

Figure 2.8.

A couette (concentric cylinder) viscometer

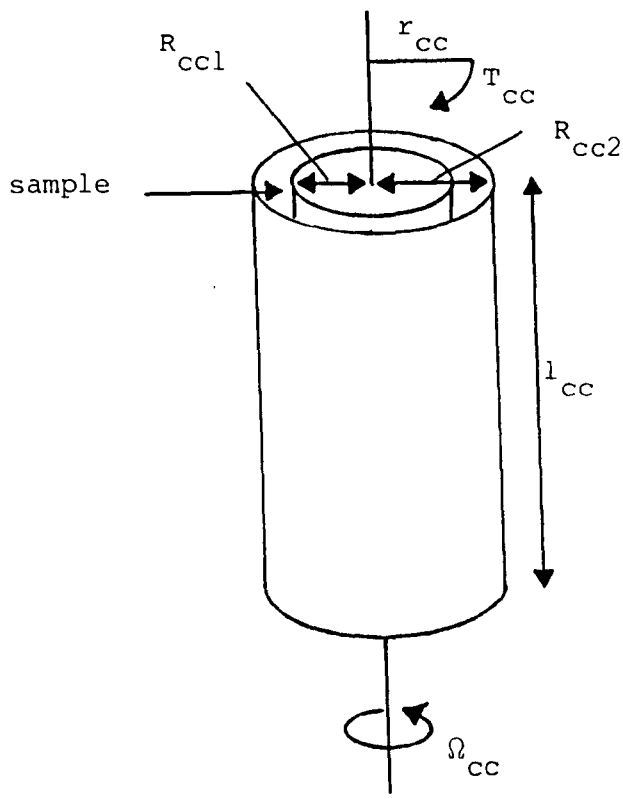

Therefore from (2.8)

$$\int_{o}^{\Omega_{cc2}} d\Omega_{cc} = \frac{T_{cc}}{2\pi l_{cc}\eta} \int_{R_{cc1}}^{R_{cc2}} \frac{dr_{cc}}{r^3_{cc}} \qquad (2.9)$$

$$\Omega_{cc2} = \frac{T_{cc}}{4\pi l_{cc}\eta} \left[\frac{1}{R^2_{cc1}} - \frac{1}{R^2_{cc2}} \right] \qquad (2.10)$$

$$T_{cc} = \eta 4\pi \Omega_{cc2} l_{cc} \left[\frac{R^2_{cc1} R^2_{cc2}}{R^2_{cc2} - R^2_{cc1}} \right] \qquad \underline{\text{Margules Equation}} \quad (2.11)$$

At any point, r_{cc}, in the fluid:

$$\tau(r_{cc}) = \frac{T_{cc}}{2\pi l_{cc} r^2_{cc}} \qquad (2.12)$$

Therefore combining (2.11) and (2.12) for a Newtonian fluid

$$\dot{\gamma}(r_{cc}) = \frac{2\Omega_{cc2}}{r^2_{cc}} \left[\frac{R^2_{cc1} R^2_{cc2}}{R^2_{cc2} - R^2_{cc1}} \right] \qquad (2.13)$$

For the condition of small gaps between the cylinders and large cylinder radii equation (2.13) reduces to:

$$\dot{\gamma} \simeq \frac{\Omega_{cc2} R_{cc2}}{R_{cc2} - R_{cc1}} \qquad (2.14)$$

Most industrial couette viscometers are designed for this relationship to hold. The Margules equation then reduces to:

$$T_{cc} = \frac{2\pi l_{cc} \Omega_{cc} R_{cc2} R^2_{cc1} \eta}{R_{cc2} - R_{cc1}} \qquad \text{Approximate Margules Equation} \quad (2.15)$$

For non-Newtonian fluids the appropriate constitutive equation must be used in the derivation. An equation to take account of Bingham plastic flow in a couette viscometer has been derived by Riener

and Riwlin[8]:

$$T_{cc} = \frac{2\pi l_{cc}\eta_{pl}\Omega_{cc2}R_{cc2}R_{ccl}^2}{(R_{cc2} - R_{ccl})} + \frac{2\pi l_{cc}\tau_B R_{cc2}R_{ccl}^2}{(R_{cc2} - R_{ccl})\eta_{pl}} \ln\left(\frac{R_{cc2}}{R_{ccl}}\right)$$

Riener-Riwlin Equation (2.16)

where η_{pl} is the plastic viscosity and τ_B the Bingham yield stress, see later.

Cone and plate geometry can also be used in rotational viscometers.[6]

A cone and plate viscometer is illustrated schematically in Figure 2.9 with cone and plate radius R_{cp}, cone angle $\hat{\alpha}_{cp}$, torque T_{cp} and rotational angular velocity Ω_{cp}. At an arbitrary radius r_{cp}, the cone and plate separation is Z_{cp}.

$$\dot{\gamma} = \frac{r_{cp}\, d\Omega_{cp}}{dZ_{cp}} \qquad (2.17)$$

For small values of $\hat{\alpha}_{cp}$, $\hat{\alpha}_{cp} < 4\%$ the velocity gradient is linear and hence to a good approximation:

$$\dot{\gamma} = \frac{r_{cp}\Omega_{cp}}{Z_{cp}} \simeq \frac{\Omega_{cp}}{\hat{\alpha}_{cp}} \qquad (2.18)$$

The torque on the plate with a Newtonian fluid in the gap is:

$$T_{cp} = \int_0^{R_{cp}} \frac{\eta\Omega_{cp}}{\hat{\alpha}_{cp}} r_{cp} 2\pi r_{cp} dr_{cp} \qquad (2.19)$$

$$T_{cp} = \frac{2\pi\Omega_{cp}R_{cp}^3\eta}{3\hat{\alpha}_{cp}} \qquad (2.20)$$

Equation (2.20) is equivalent to Margules equation for concentric cylinder geometry.

Continuous shear viscometry measurements afford an estimation of the amount of energy lost by diffusive relaxation, resulting in viscous flow; it measures the viscous properties of a system. The data obtained are often plotted in the form of stress, τ, versus rate of strain, $\dot{\gamma}$, curves as illustrated in Figure 2.10.

Figure 2.9.

A cone and plate viscometer

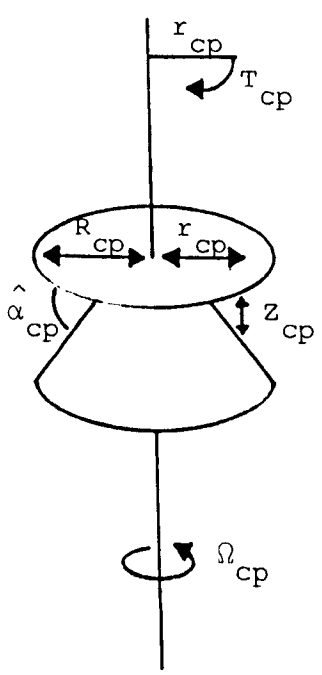

Figure 2.10.

Stress versus shear rate for Newtonian and non-Newtonian flow.

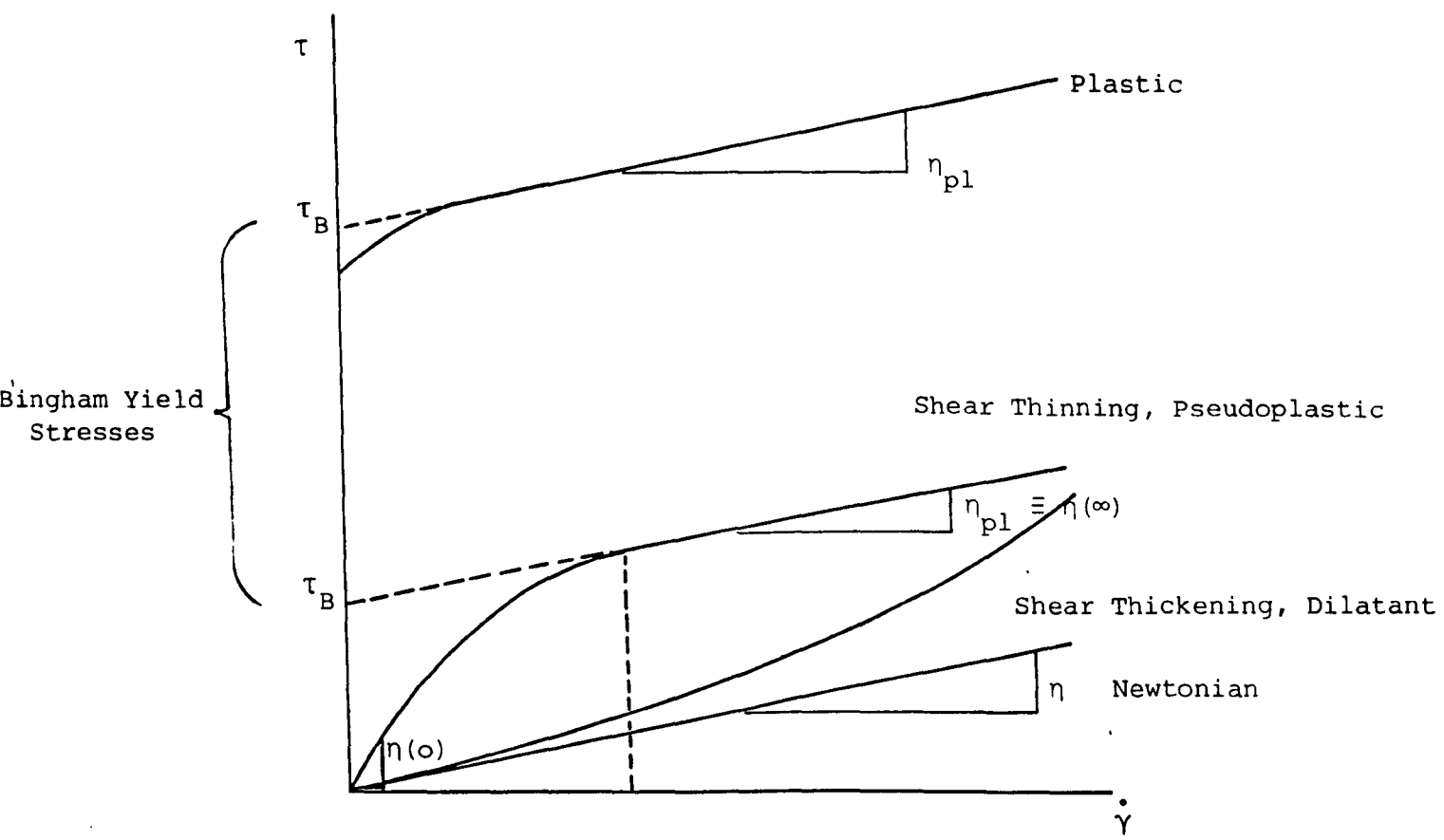

For a Newtonian fluid the stress is directly proportional to the rate of strain with a proportionality constant η, the viscosity. Non Newtonian behaviour in colloidal dispersions is frequently the result of interparticle interactions and the steady state flow may be characterised into various types.[4]

Pseudoplastic behaviour is exhibited by materials that show no yield value but whose viscosity falls progressively with rising stress such that the consistency curve approaches a straight line that has a finite intercept on the stress axis known as the Bingham yield stress, τ_B. Such shear thinning behaviour may be as a result of breakdown of particle aggregates which leads to a reduction in the amount of solvent immobilised by the particles, thus lowering the apparent viscosity of the system. The term shear thinning strictly applies to a decrease in viscosity with increasing shear rate.

Plastic behaviour is essentially similar to pseudoplastic behaviour except that a critical shear stress is required before the system will flow. At high shear rates pseudoplastic flow approximates to plastic flow and the flow may be characterised by the equation:

$$\tau = \eta_{pl}\dot{\gamma} + \tau_B \qquad (2.21)$$

where η_{pl} is the plastic viscosity. An important difference between plastic and pseudoplastic behaviour is that plastic materials may be moulded whereas pseudoplastic materials may not.

Shear thickening flow arises from an increase in viscosity with increasing rate of strain. As the shear rate is increased in a densely packed system, with only sufficient fluid to fill the voids, the dense packing must be expanded to allow the particles to flow past each other. The resulting expansion leaves insufficient liquid to fill the voids and is opposed by surface tension. Dilatancy, often confused with shear thickening, strictly applies to an increase in volume caused by shear.

A further complication is introduced in the form of thixotropy or time dependent behaviour. Thixotropy is the time dependent analogue of shear thinning and plastic behaviour and arises from somewhat similar causes. If a thixotropic system is allowed to stand and then sheared at a constant rate the viscosity decreases with time until a balance between structural breakdown and reformation is achieved. If the sheared system is then allowed to stand it eventually regains its original structure and a thixotropic hysteresis loop is set up, see Figures 2.11[6] and 2.12[5]. The opposite situation of antithixotropy occurs with shear thickening systems.

Continuous shear viscometry data are also often plotted in the form of the logarithm of suspension viscosity versus the logarithm of the shear stress. A typical rheogram for a concentrated dispersion is presented in Figure 2.13.[5] As the shear stress is progressively increased in a concentrated dispersion, a decrease in viscosity is usually observed due to a reversible change in the three dimensional structure of the system. This may be caused by the breakdown of aggregates present or of the symmetry of the distribution of particles.

At high shear stress a shear thickening behaviour can be observed caused by unsteady or turbulent flow which occurs when the inertial forces in the system under observation are of a comparable magnitude to the viscous forces. As the shear rate increases the inertia increases until, at a critical shear rate, onset of turbulent flow occurs in the form of eddys and vortices. These lead to increased energy dissipation which causes the apparent viscosity to increase, as illustrated schematically in Figure 2.14.

The Reynolds number, Re, is a dimensionless measure of the relative importance of inertial to viscous forces. For concentric cylinders, one

Figure 2.11.

Thixotropic Behaviour

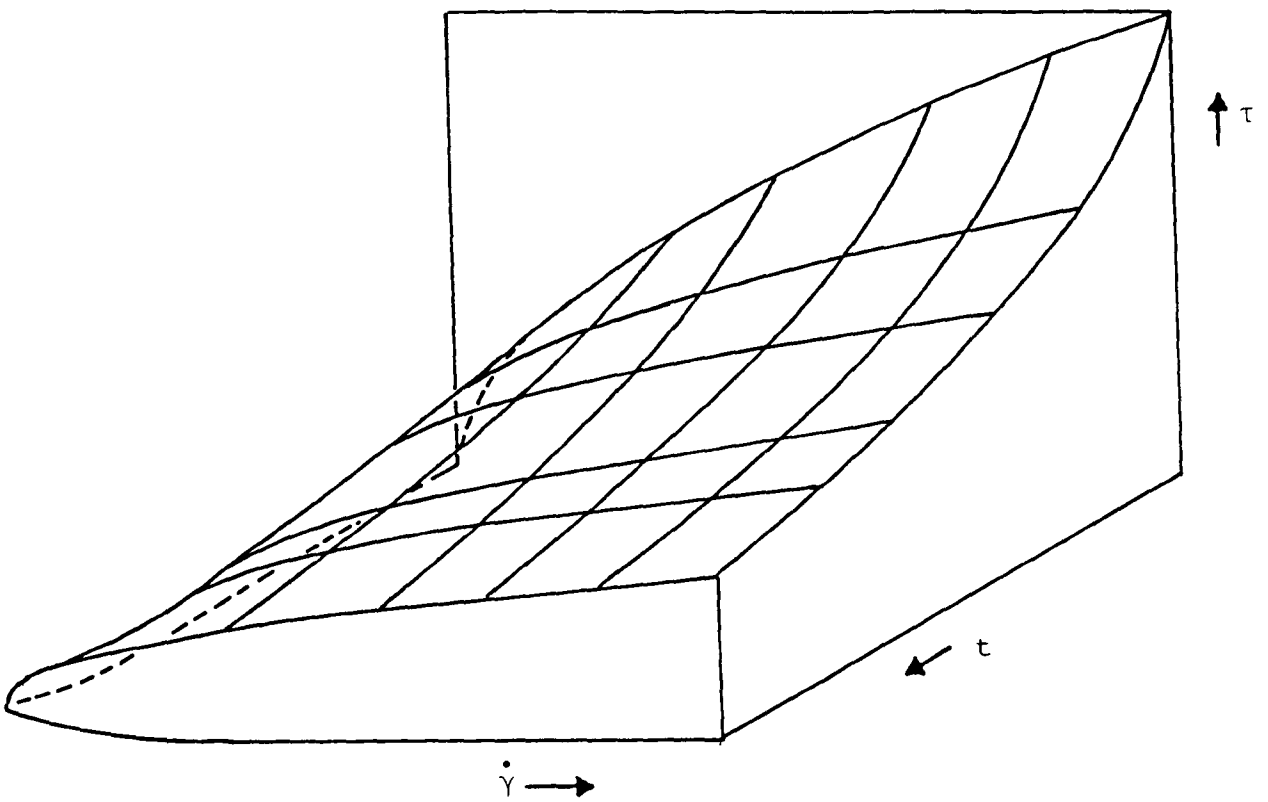

Figure 2.12.

Thixotropic Behaviour - Hysteresis Loop

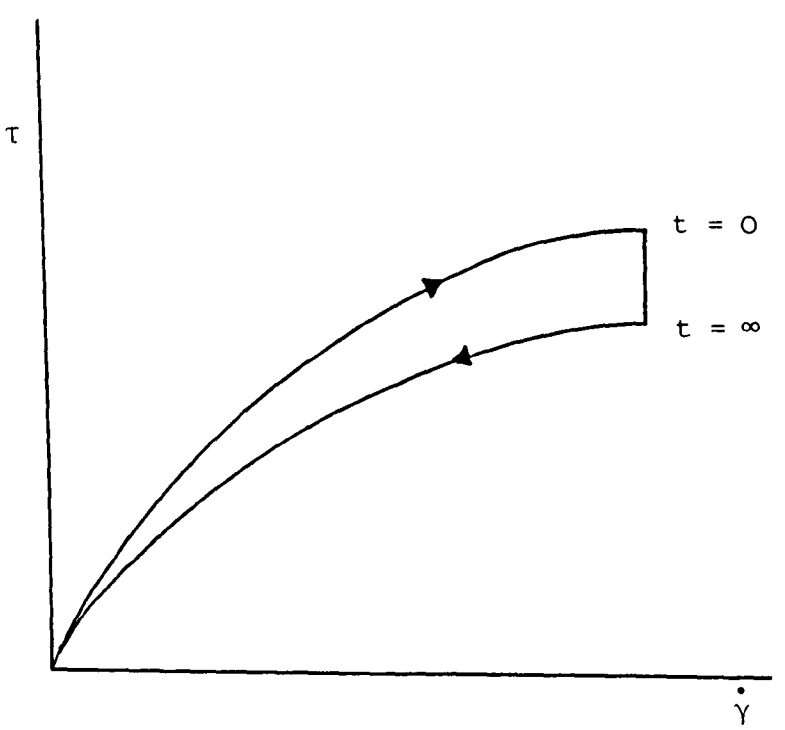

Figure 2.13

Typical rheogram for a concentrated dispersion

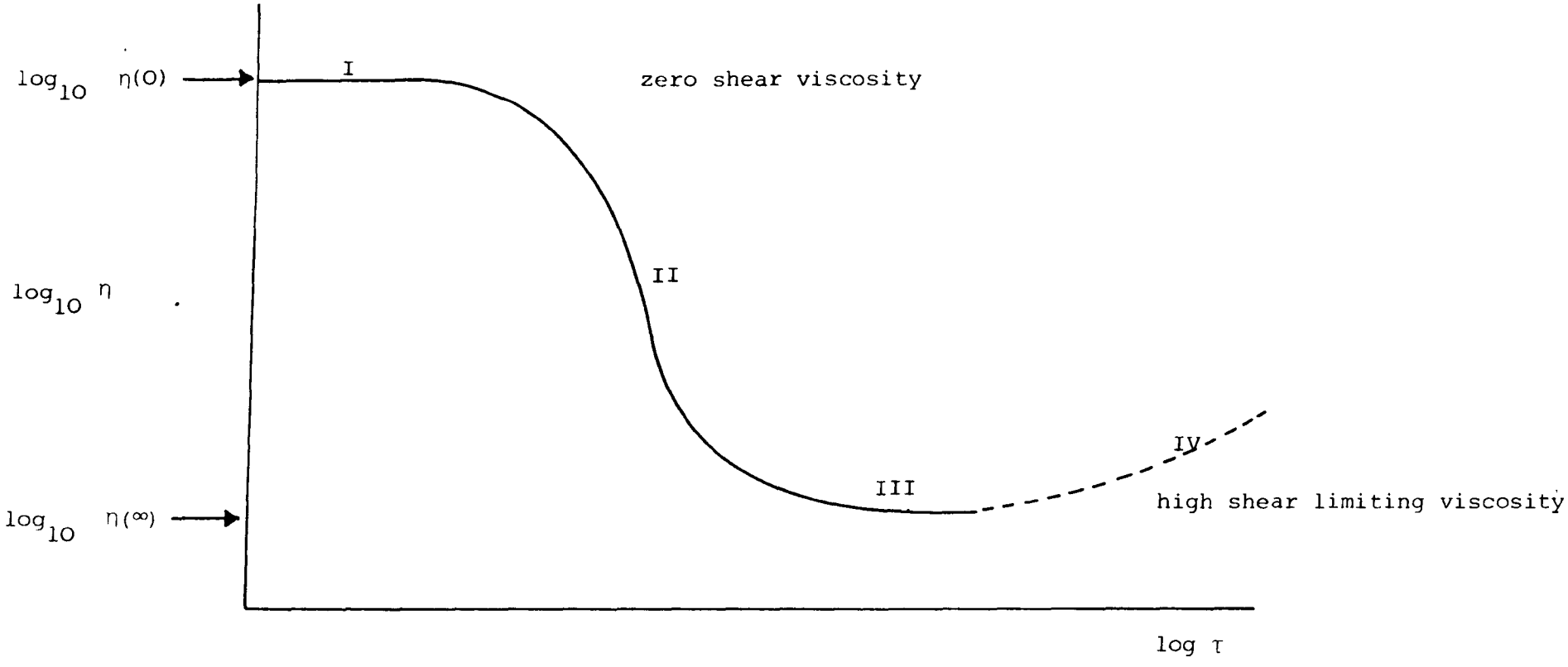

I Diffusive relaxation, 3-dimensional structure, Newtonian.

II Structural change, shear thinning.

III 2-dimensional structure, Newtonian

IV Turbulent flow, structural disruption and dilantancy, shear thickening

Figure 2.14

Rheogram showing onset of turbulent flow

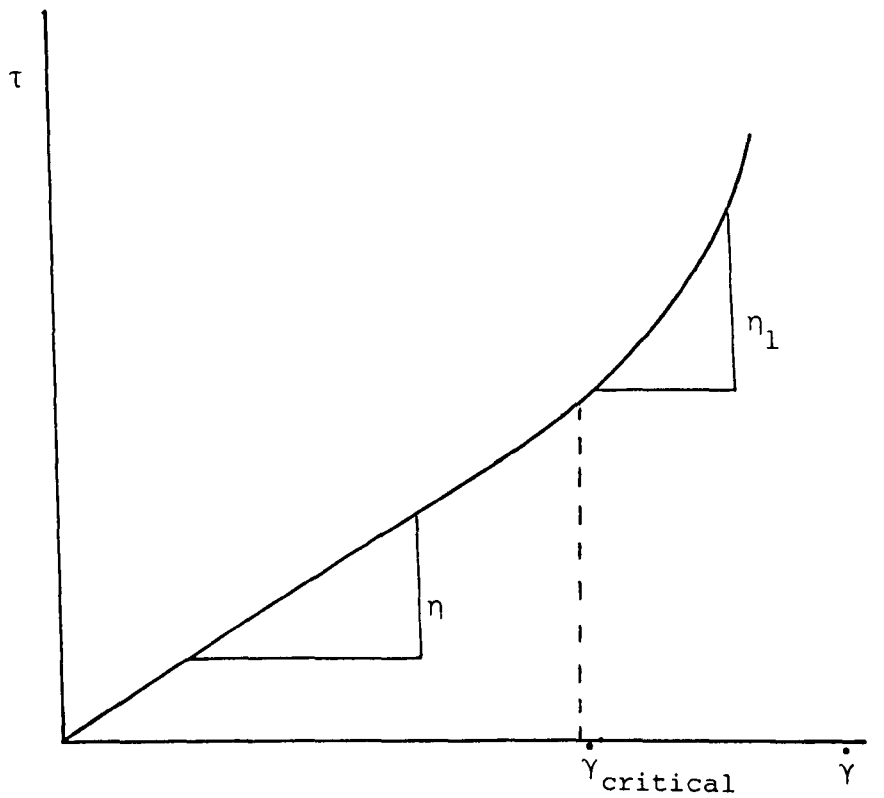

$\eta_1 > \eta$

of the geometrical arrangements used in continuous shear viscometry, the Reynolds number, Re_{cc}, is given by:

$$Re_{cc} = \frac{u^{*} (R_{cc2} - R_{cc1}) \rho\dagger}{\eta} \qquad (2.22)$$

where u^{*} is the fluid velocity and $\rho\dagger$ the density of the fluid.

The inertial force scales with the sample density and gap size, hence large gaps between cylinders or between cones and plates should be avoided.

For small gaps:

$$\dot{\gamma} = \frac{u^{*}}{R_{cc2} - R_{cc1}} \qquad (2.23)$$

Hence the Reynolds number at the onset of turbulent flow may be defined:

$$Re_{cc\ crit} = \frac{\dot{\gamma}_{crit} (R_{cc2} - R_{cc1})^{2} \rho\dagger}{\eta} \qquad (2.24)$$

Creep compliance measurements are the most convenient method available for characterising the low shear part of a rheogram. Creep measurements involve the application of a constant shear stress to a sample and the measurement of the resulting sample deformation with time. Figure 2.15 illustrates the creep compliance curve and mechanical analogue for a visco-elastic fluid[9] indicating the four regions: instantaneous elastic response, retarded elastic response and viscous compliance while the stress is applied and the relaxation on removal of the stress.

The creep compliance, J, resulting from the application of a constant shearing stress is defined as:[10]

$$J(t) = \frac{\gamma(t)}{\tau} \qquad (2.25)$$

where $\gamma(t)$ is the strain measured after a time t has elapsed.

Figure 2.15

Creep compliance curve and mechanical analogue for a viscoelastic fluid

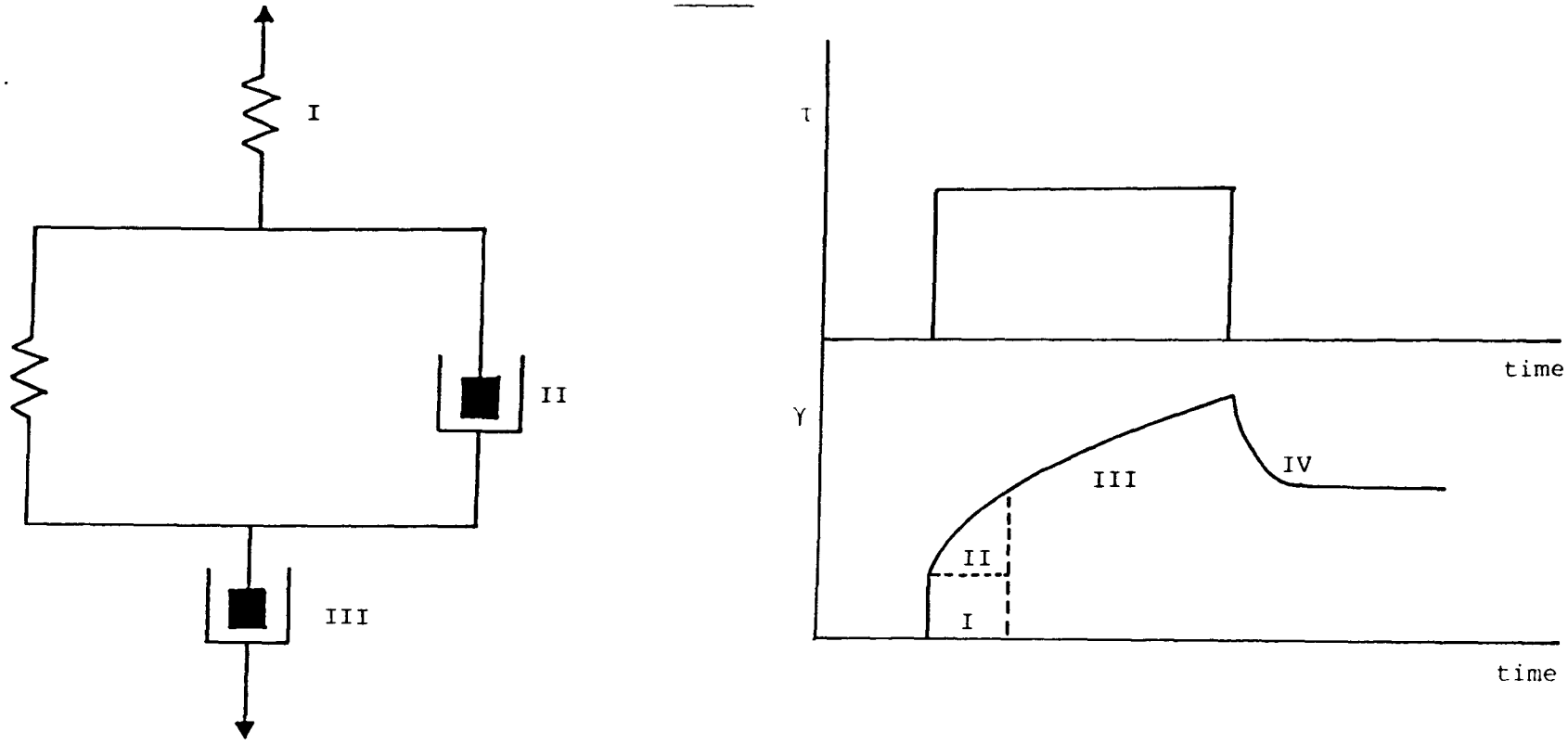

I	Instantaneous elastic response (→ G(∞))
II	Retarded elastic response
III	Viscous compliance (→ η(0))
IV	Stress relaxation

For a viscoelastic fluid the compliance has the general form:

$$J(t) = \frac{1}{G_o} + \Sigma_j \frac{1}{G_j}\left[1 - \exp\left(\frac{-tG_j}{\eta_j}\right)\right] + \frac{t}{\eta(0)} \qquad (2.26)$$

2.3. Oscillatory Testing.

Oscillatory or dynamic testing involves subjecting a material to a small amplitude oscillatory deformation and measuring the stress response of the material. The term small refers to strains of less than 5% and preferably less than 1% to ensure a linear viscoelastic response. Particulate systems are particularly intolerant of large strains as the interparticle forces that characterise colloidal interactions are highly non-linear and hence only small deformations can be expected to fit a linear approximation.[6]

The experimental system usually consists of the sample material held between two parallel discs with the upper disc spring mounted; concentric cylinder and cone and plate geometries may also be used. A small rotational oscillation with sinusoidal form, γ, is applied to the lower disc and the resultant stress, τ, on the upper disc measured by the spring. This is illustrated schematically in Figure 2.16.

The response varies depending on the viscous and elastic nature of the material under consideration. For a purely elastic solid the input deformation and output deformation are exactly in phase, see Figure 2.17(i), whereas for a purely viscous fluid the input and output deformations are 90° out of phase, see Figure 2.17(ii). The response for a viscoelastic material lies between these two extremes with the output deformation between 0° and 90° out of phase with the input deformation, see Figure 2.17(iii).

The time scale of the experiment is the inverse of the angular

Figure 2.16

Schematic representation of experimental oscillatory testing device.

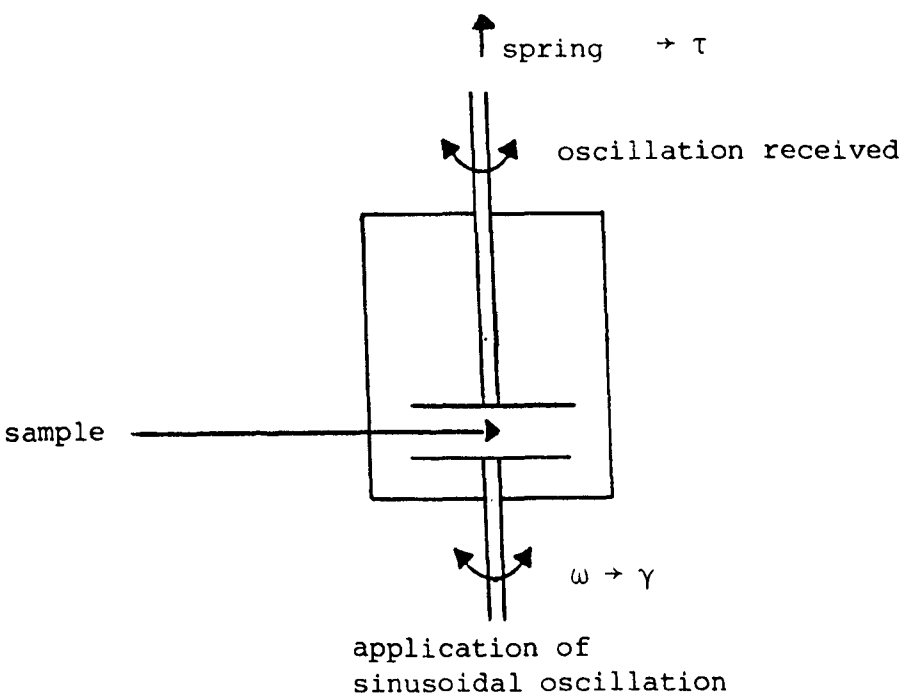

Figure 2.17

Elastic, viscous and viscoelastic responses to oscillatory testing

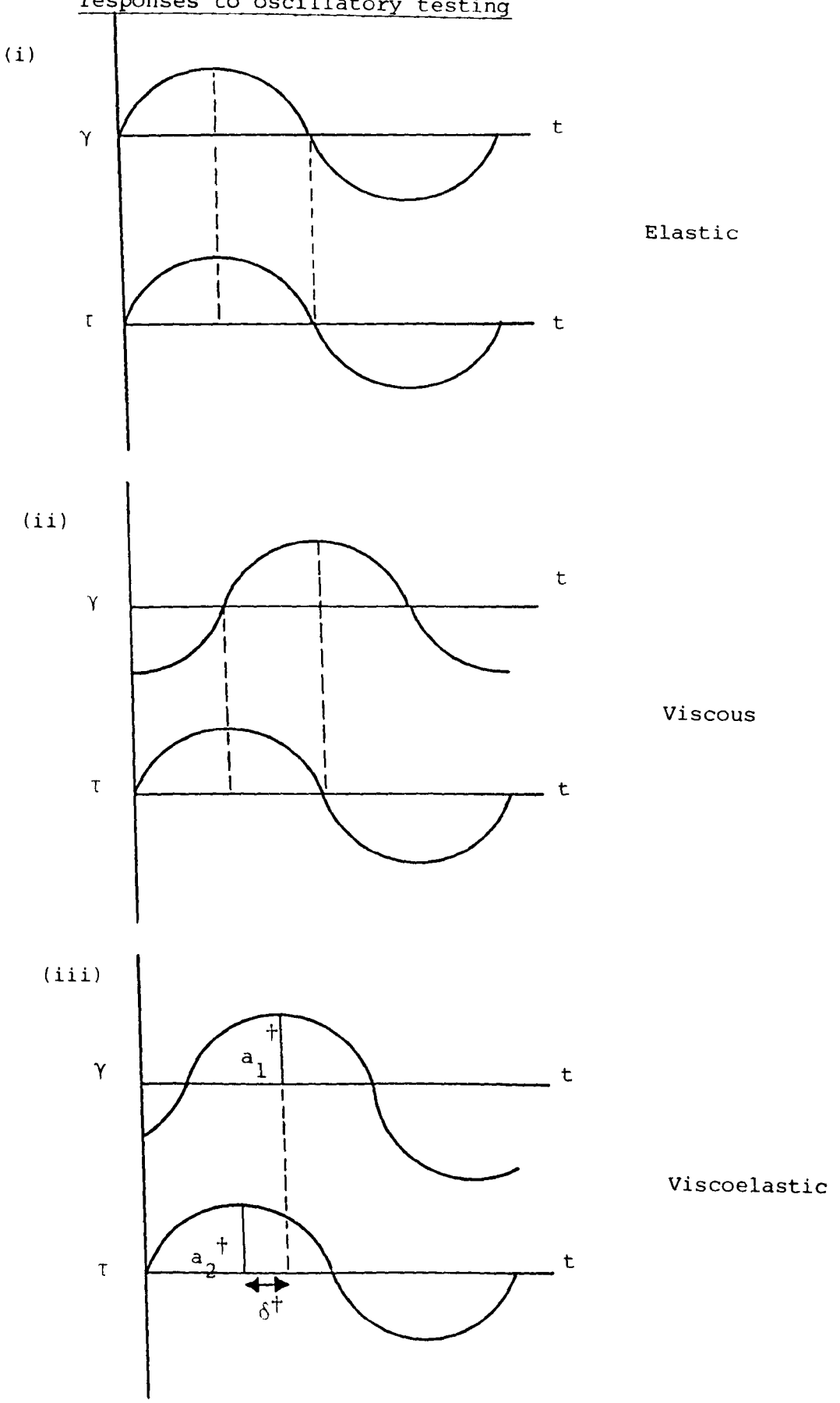

frequency, ω, of the sinusoidal wave where the frequency is given by:

$$\omega = 2\pi\nu \tag{2.27}$$

where ν is the Hertzian frequency. The frequency can be varied over a wide range to probe the change in the Deborah number.

The experimental parameters that are measured are the phase lag, $\delta^{\dagger}$, and the amplitude ratio, $a_1^{\dagger}/a_2^{\dagger}$, i.e. the ratio of the maximum stress to maximum strain which is the complex modulus, G^*. The complex modulus G^* is the sum of the elastic or storage component, G', and the viscous or loss component, G'':

$$G^* = G' + iG'' \tag{2.28}$$

The sinusoidal oscillations can conveniently be written in complex number notation:[11]

$$\tau = \tau_o \exp\left\{i(\omega t + \delta^{\dagger})\right\} \tag{2.29}$$

$$\gamma = \gamma_o \exp(i\omega t) \tag{2.30}$$

where the subscript zero denotes the maximum value.

Now,

$$G' = \frac{\tau_o}{\gamma_o} \cos\delta^{\dagger} \tag{2.31}$$

$$G'' = \frac{\tau_o}{\gamma_o} \sin\delta^{\dagger} \tag{2.32}$$

and therefore $$\frac{G''}{G'} = \tan\delta^{\dagger} \tag{2.33}$$

This corresponds to a vectoral resolution of the components in the complex plane as shown in Figure 2.18.

It is evident that G' is the ratio of the stress in phase with the strain to the strain and G'' is the ratio of the stress out of phase with the strain to the strain. Both G' and G'' are functions of the frequency of deformation, ω.

Figure 2.18

Vertical resolution of components of complex modulus in sinusoidal shear deformations

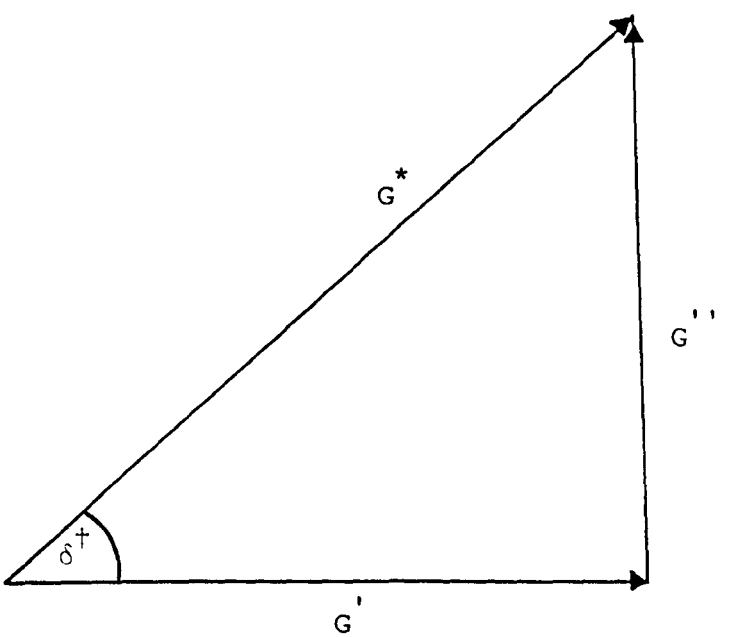

Under steady-flow conditions, $\omega \rightarrow 0$, purely viscous behaviour is observed and G', the dynamic rigidity modulus vanishes. The loss modulus G'' may be defined in terms of the dynamic viscosity, η':

$$G'' = \omega\eta' \tag{2.34}$$

Hence at the low frequency limit the steady state viscosity, $\eta(0)$ may be defined as:

$$\eta(0) = \lim_{\omega \rightarrow 0} \eta' \tag{2.35}$$

At the high frequency limit the elastic modulus, G', becomes the dominant function and approaches a limiting value, $G(\infty)$, given by:

$$G(\infty) = \lim_{\omega \rightarrow \infty} G' \tag{2.36}$$

Under non steady shear conditions, intermediate to these extremes both dissipation and storage occur in varying degrees and must both be considered.

Using the Maxwell model for a viscoelastic model and combining the constitutive equation, equation (2.5) with[7]:

$$G^* = \frac{\tau}{\gamma} \tag{2.37}$$

yields:

$$\frac{i\omega\tau_o \exp(i\omega t)}{G^*} = \frac{\tau_o \exp(i\omega t)}{Gt_m} + \frac{i\omega\tau_o \exp(i\omega t)}{G} \tag{2.38}$$

which rearranges to give:

$$\frac{Gi\omega t_m}{G^*} = 1+i\omega t_m \tag{2.39}$$

Inversion and multiplication of both sides by the factor $(1-i\omega t_m)$ yields:

$$\frac{G^*(1-i\omega t_m)}{Gi\omega t_m} = \frac{1-i\omega t_m}{1+i\omega t_m} \tag{2.40}$$

which can be rearranged to give the complex modulus in terms of both

real and imaginary parts:

$$\frac{\underline{G}^*}{G} = \frac{i\omega t_m + \omega^2 t_m^2}{1 + \omega^2 t_m^2} \qquad (2.41)$$

Hence:

$$\frac{\underline{G}'}{G} = \frac{\omega^2 t_m^2}{1+\omega^2 t_m^2} \qquad (2.42)$$

$$\frac{\underline{G}''}{G} = \frac{\omega t_m}{1+\omega^2 t_m^2} \qquad (2.43)$$

The response of this model is illustrated in Figure 2.19 from equations (2.42) and (2.43) for the storage and loss moduli. It is noted that when $\log \omega t_m = 0$, i.e. when the Deborah number = 1, G' and G'' are equal and that at high frequency the elastic modulus becomes equal to the spring constant used in the model.

To model real system behaviour, the generalised Maxwell model, see (2.1), is often used where each relaxation time corresponds to a particular spring-dashpot pair. The storage and loss moduli are now given by:[7]

$$G' = \int_{-\infty}^{\infty} \frac{H(t)\omega^2 t^2}{1+\omega^2 t^2} \, d\ln t \qquad (2.44)$$

$$G'' = \int_{-\infty}^{\infty} \frac{H(t)\omega t}{1+\omega^2 t^2} \, d\ln t \qquad (2.45)$$

where $H(t)$ is the spectrum of relaxation times.

Integration under the $H(t)$ versus t curve gives the sum of all spring constants, i.e. the high frequency limit of the storage modulus, $G(\infty)$, which is given by:

$$\mathrm{Lim}_{\omega\to\infty} G(\infty) = \int_{-\infty}^{\infty} H(t)\, d\ln t \qquad (2.46)$$

Figure 2.19

Relative storage and loss moduli as a function of reduced frequency calculated for a Maxwell body

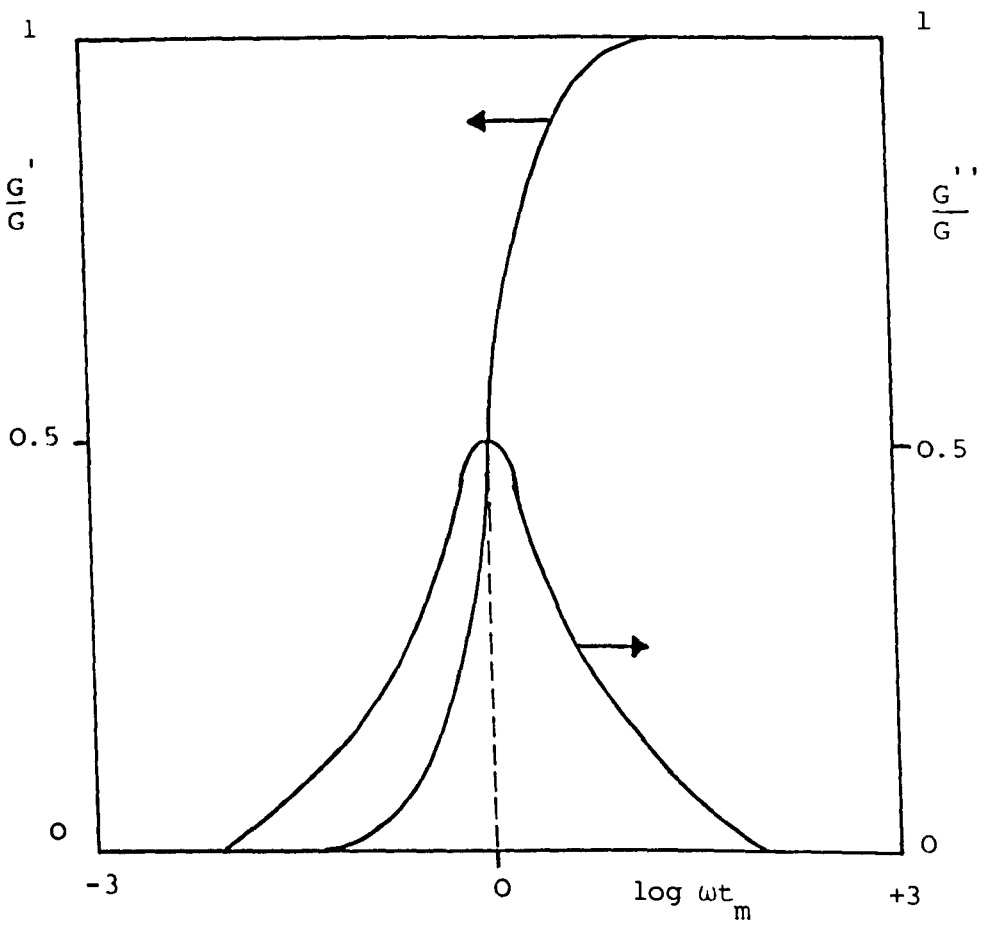

From equation (2.34) the loss modulus, G'', is defined in terms of the dynamic viscosity, η', which, from equation (2.35), is given by the zero shear viscosity, $\eta(0)$. Hence, combining equations (2.34), (2.35) and (2.45) at the low frequency limit yields:

$$\text{Lim}_{\omega \to 0} \eta(0) = \int_{-\infty}^{\infty} tH(t)d\ln t \qquad (2.47)$$

The value of $G(\infty)$ can be measured directly if an experiment is carried out at a sufficiently high frequency that none of the components are allowed to relax, i.e. $De >> 1$. High frequency techniques are available, one of these being shear wave propagation.[12,13,10]

Shear wave propagation involves the initiation of a high frequency pulse through a dispersion and the measurement of its propagation velocity through that dispersion.

The wave rigidity modulus, $\tilde{G}$, is related to the propagation velocity of the wave, u, and the density of the sample, ρ^*, by the expression:[10]

$$\tilde{G} = \rho^* u^2 \qquad (2.48)$$

The storage and loss moduli, G' and G'', may be expressed in terms of this wave rigidity modulus:

$$G' = \tilde{G} \frac{(1-r^{\dagger 2})}{(1+r^{\dagger 2})^2} \qquad (2.49)$$

$$G'' = \tilde{G} \frac{2r^{\dagger}}{(1+r^{\dagger 2})^2} \qquad (2.50)$$

with

$$r^{\dagger} = \frac{\Lambda}{2x_o} \qquad (2.51)$$

where Λ is the wavelength of the wave and x_o is the critical damping length. The wavelength of a wave is related to its frequency, ν, and velocity, u, by:

$$\Lambda = \frac{u}{\nu} = \frac{2\pi u}{\omega} \qquad (2.52)$$

At high frequencies $r^{\dagger}$ has a low value and for $r^{\dagger} < 0.1$:

$$\frac{(1-r^{\dagger 2})}{(1+r^{\dagger 2})^2} \rightarrow 1$$

and $G' \rightarrow \tilde{G}$

At high frequencies the storage modulus is much greater than the loss modulus and approaches a limiting value $G(\infty)$. Hence the high frequency limit of the shear modulus $G(\infty)$ may be given by the expression:

$$G(\infty) = u^2\rho^* \qquad (2.53)$$

At low frequencies the loss modulus is dominant and is related to the propagation velocity by the expression:

$$G'' = \frac{2\rho^* u^2 r^{\dagger}}{(1+r^{\dagger 2})^2} \qquad (2.54)$$

Combining equations (2.34) and (2.54) gives an expression for the dynamic viscosity, η', as a function of $r^{\dagger}$:

$$\eta' = \frac{2\rho^* u^2 r^{\dagger}}{\omega(1+r^{\dagger 2})^2} \qquad (2.55)$$

At low frequencies η' approaches the low frequency limit of the viscosity, $\eta(0)$ which may be independently determined from creep compliance measurements. In this way an independent determination of $r^{\dagger}$ may be achieved.

Chapter Three

Colloid Stability Theory

Chapter Three Colloid Stability Theory.

3.1. Introduction.

A colloidal system may be described as one in which one or more of the components has at least one dimension within the range ≈1 nm to≈1μm.[14] A dispersion of solid colloidal particles suspended in a liquid medium is known as a sol.[15] Colloidal dispersions may be categorised into two main classes, lyophilic and lyophobic, exhibiting quite different behaviour. Lyophilic systems are thermodynamically stable whereas lyophobic dispersions are not in thermodynamic equilibrium but may, if well prepared, exist for many years.[16]

The stability of a dispersion with respect to particle aggregation is determined by the net interaction force between particles. Colloid particles always attract one another by long range van der Waals, or dispersion, forces; this attraction may be countered by a repulsive interaction. Various types of repulsion are known, an electrostatic repulsion based on the charge of the particle and a steric repulsion caused by the presence of a layer of soluble species attached to the particle surface. In addition a very strong repulsion due to orbital overlap occurs at very short particle separations preventing the primary minimum from approaching infinity. At high electrolyte concentrations hydration forces are important. Summation of the interactions control a systems stability.

3.2. Electrostatic Repulsion.

3.2.1. Electrical Double Layer.

An electric charge at an interface causes an electrostatic potential, ψ_o, at the interface relative to a point in the bulk electrolyte system.

Close to the particle surface a higher concentration of counter ions than co-ions exists due to a combination of an electrostatic interaction and diffusive forces. This charged surface layer counterbalanced with a diffuse layer of counter ions is known as the electrical double layer.

The surface charge on a particle may be the result of:[17]

(i) the presence of ionogenic groups at the surface,

(ii) isomorphous substitution within the particle crystal lattice,

(iii) adsorption of surface active ions,

(iv) adsorption of potential determining ions.

The first quantitative treatment of the electrical double layer was advanced by Gouy[18,19] and Chapman[20] based on the theory of interionic interaction effects in electrolyte solutions proposed by Debye and Hückel.[21,22] They assumed that the surface was planar with a homogeneous potential, that the ions were point charges and that the distribution of counter ions in the region of the surface could be described by the Poisson-Boltzmann law.

Figure 3.1. shows a schematic representation of the Gouy-Chapman model with corresponding potential diagram.

Using this model the electrical potential, ψ, can be expressed as a function of the distance, $x^{\dagger}$, from the planar surface:[14]

$$\psi = \psi_o \exp (- \kappa x^{\dagger}) \qquad (3.1)$$

for the limiting case of low potentials such that

$$\frac{ze\psi_o}{2kT} \ll 1$$

where ψ_o = surface potential

κ = Debye-Hückel reciprocal length

z = ionic valency

Figure 3.1.

Schematic representation of the Gouy-Chapman model for the diffuse electrical double layer.

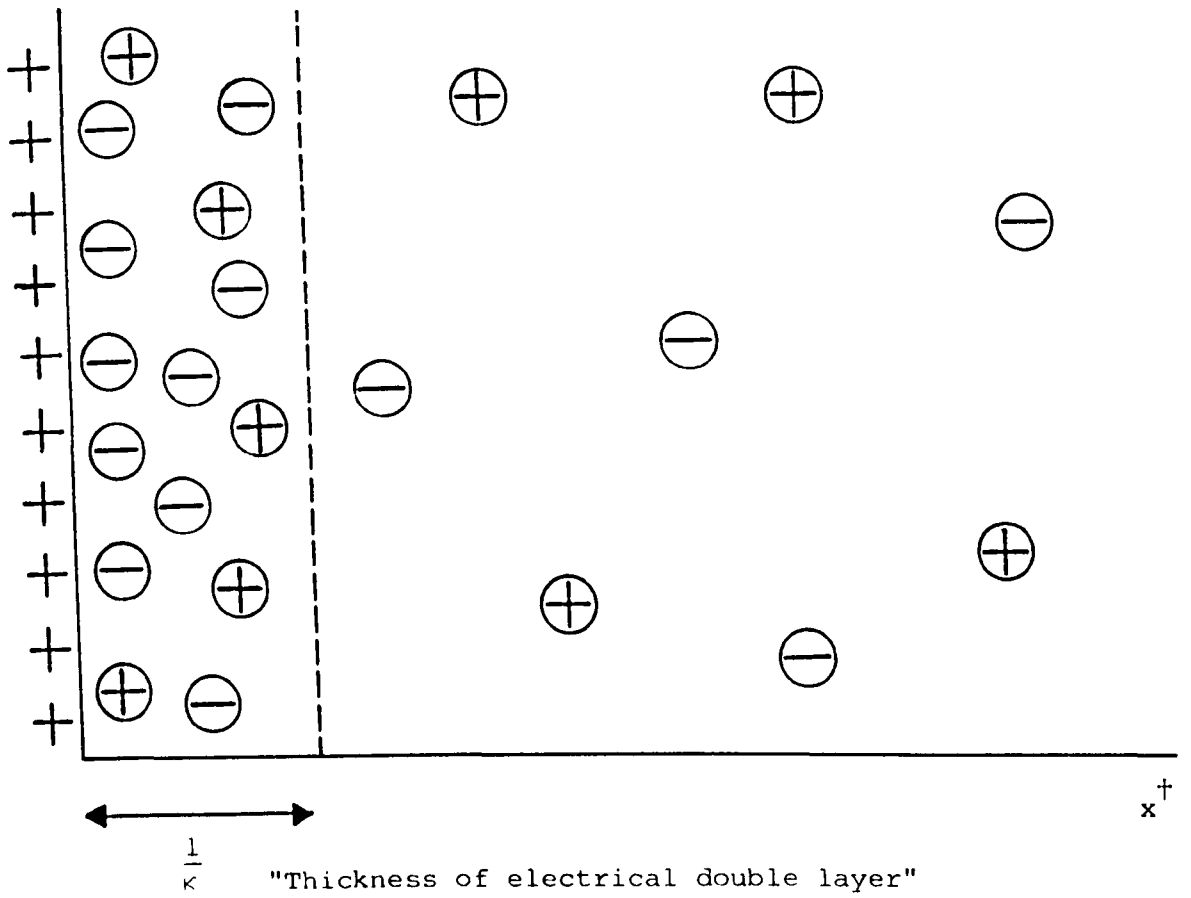

Schematic representation of the potential diagram corresponding to the Gouy-Chapman model for the diffuse electrical double layer.

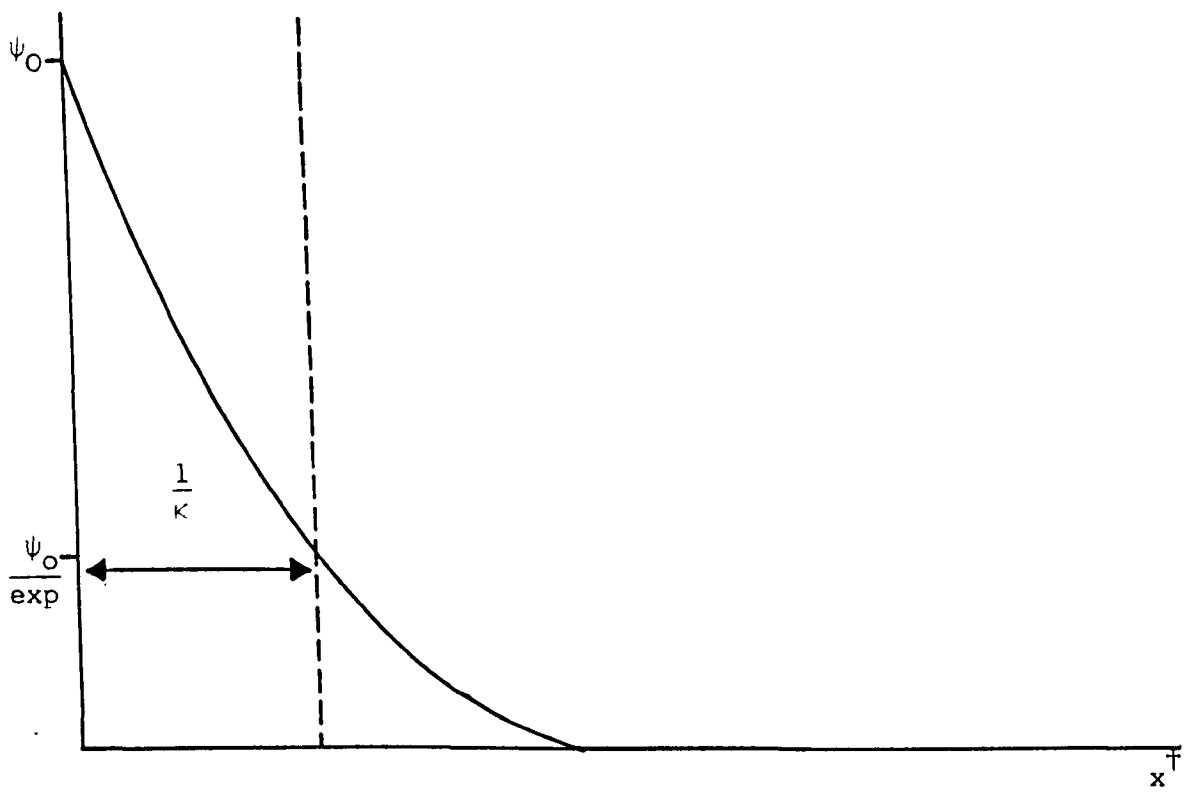

e = the fundamental unit charge

k = Boltzmann's constant

T = absolute temperature.

For a symmetrical electrolyte[23]

$$\kappa = \left(\frac{2e^2 n_o z^2}{\varepsilon_r \varepsilon_o kT} \right)^{\frac{1}{2}} \qquad (3.2)$$

where n_o = number of cations or anions per unit volume.

ε_r = relative permittivity of the medium

ε_o = permittivity of free space.

The quantity $1/\kappa$ describes the distance at which the surface potential has fallen to ψ_o/exp; it is often referred to as the "thickness of the electrical double layer".[24]

As the electrolyte concentration is increased, κ increases and hence the double layer thickness is reduced.[25] This is illustrated in Figure 3.2.

The Gouy-Chapman approach was modified by Stern[26] who took into account the finite dimensions of the ions. Stern divided the double layer into two parts. The inner part consisted of a compact layer of ions specifically adsorbed at the surface, known as the Stern layer, and the outer part a diffuse or Gouy layer. The Stern plane is located at a distance d_s from the surface, approximately an adsorbed ion radius, and is therefore the position where the charge is equal to the total charge in the diffuse layer. The potential is taken to change linearly from ψ_o to ψ_d, the Stern potential, across the Stern layer and to decay exponentially from ψ_d to zero in the diffuse layer. The Stern model is illustrated in Figure 3.3.

The Stern equation is expressed in terms of the surface charge

Figure 3.2.

Schematic representation of potential diagrams showing the effect on the double layer of the electrolyte concentration.

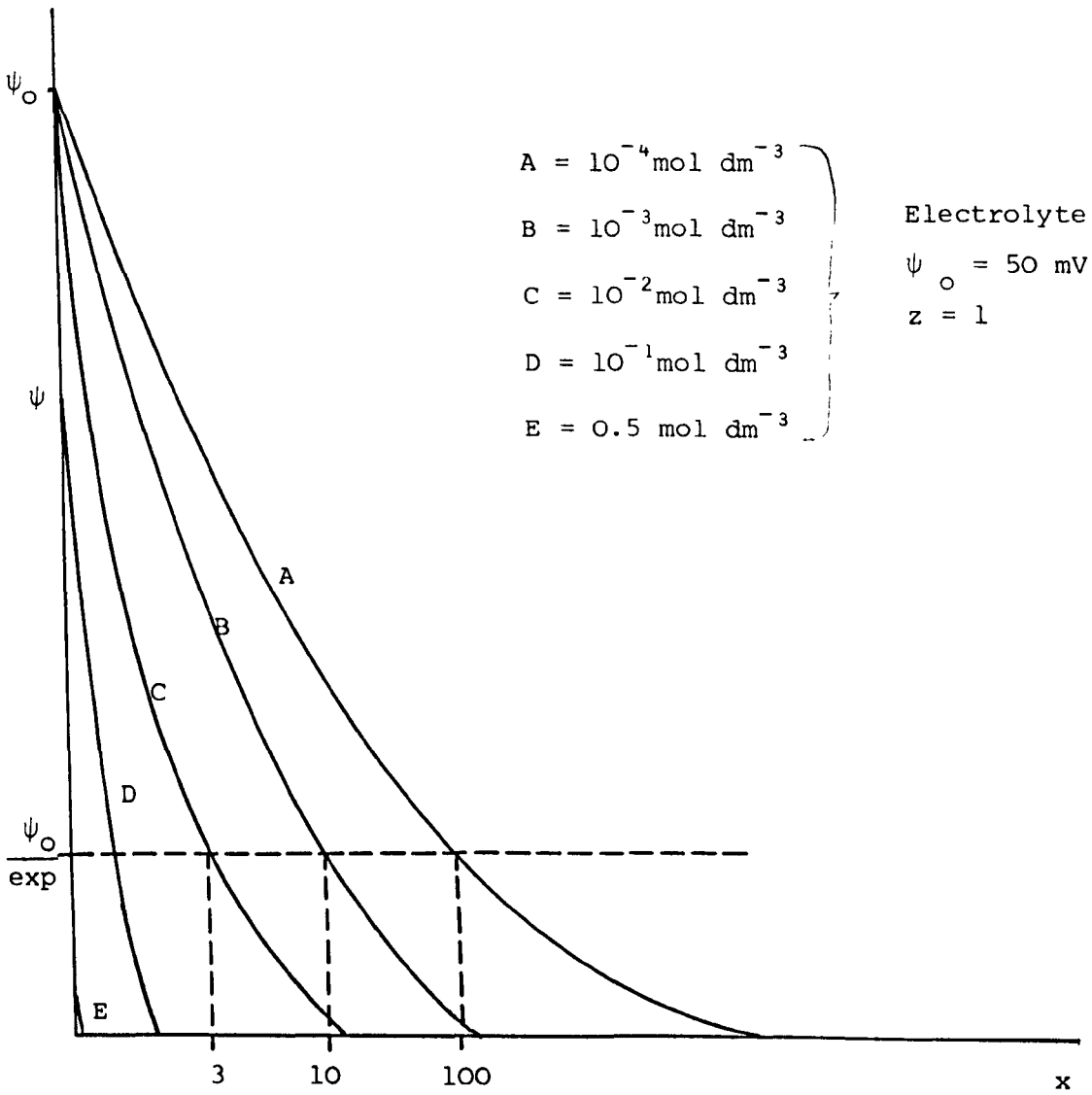

Figure 3.3.

Schematic representation of the structure of the electrical double layer according to Stern's theory and corresponding potential diagram.

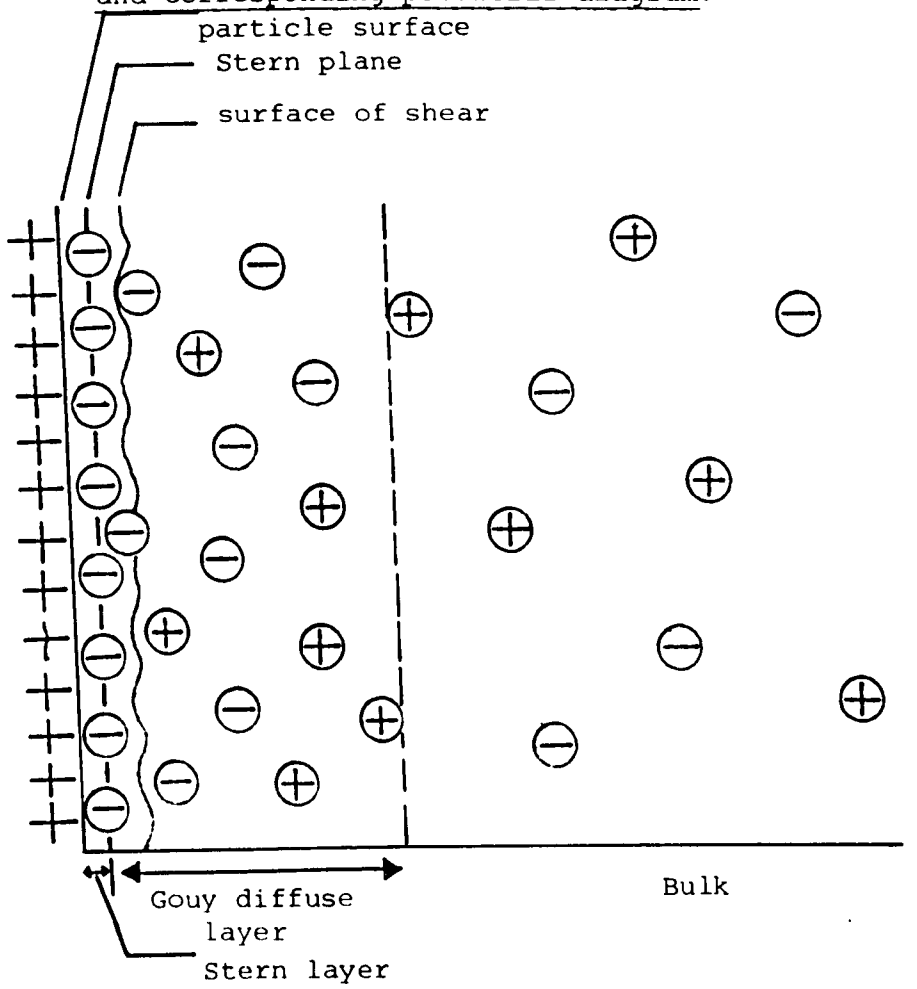

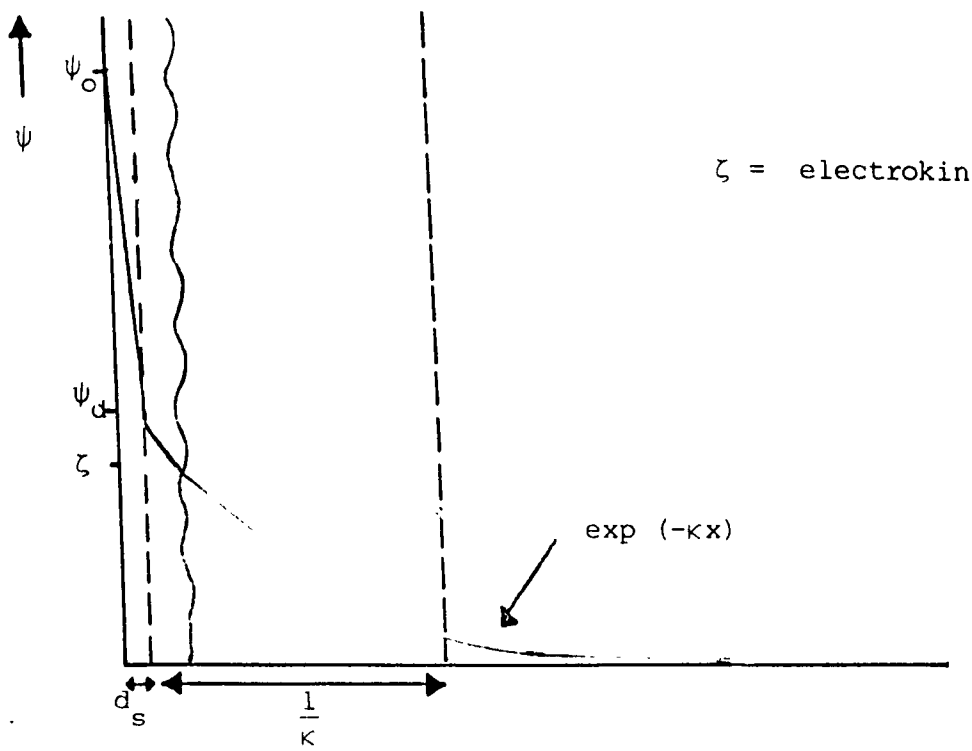

ζ = electrokinetic potential

density of the Stern layer, $\sigma_1^{\dagger}$:

$$\sigma_1^{\dagger} = \frac{\sigma^{\dagger}}{1 + \frac{N_A}{n_o v_m} \exp\left(\frac{ze\,\psi_d + \Phi}{kT}\right)} \qquad (3.3.)$$

where $\sigma^{\dagger}$ = surface charge density

N_A = Avogadro's number

v_m = molar volume of the solvent

Φ = specific adsorption potential

When charged particles are subjected to an electric field the particles plus the layer of bound ions will migrate towards the electrode of opposite charge. The separation of bound ions and those moving with the field occurs at the "plane of the shear" and the potential at this plane known as the electrokinetic or zeta-potential, ζ. The shear plane is a region of discontinuity where viscous properties and permittivity change from bulk continuum values to atomic values in the bound layer. The exact location of the shear plane is ill-defined but is assumed to be located at a small distance further from the surface than the Stern plane. At high electrolyte concentrations ζ is closer to ψ_d than to ψ_o.

3.2.2. Diffuse Layer Overlap.

Forces of repulsion in charged colloidal systems are a direct result of the overlap of the diffuse layers around each particle. As the particles approach closely their diffuse double layers interpenetrate so that the counter ion concentration between the particles is greater than that in the bulk medium.

Langmuir [27] derived an expression for the repulsive force, based on the Gouy-Chapman model of diffuse double layers, by considering the osmotic pressure developed in the mid-plane between two approaching flat

plates. Linear superposition of potential was assumed in the calculation of the ion concentration. Langmuir's expression, for flat plates with equal surface potentials and weak interactions, ($\kappa H_o^\dagger > 2$) is given by:

$$P_E = 64\, n_o kT\hat{\gamma}^2 \exp(-\kappa H_o^\dagger) \qquad (3.4)$$

where P_E = excess osmotic pressure due to double layer overlap

$H_o^\dagger$ = surface to surface separation of the planes

$$\hat{\gamma} = \frac{\exp\left(\frac{ze\psi_d}{2kT}\right) - 1}{\exp\left(\frac{ze\psi_d}{2kT}\right) + 1} \qquad (3.5)$$

Verwey and Overbeek[15] determined the potential energy of repulsive interaction, V_R, by integration of equation (3.4):

$$V_R = \frac{64\, n_o kT\hat{\gamma}^2}{\kappa} \exp(-\kappa H_o^\dagger) \qquad (3.6)$$

Interactions between spherical particles are more complicated due to the curvature of the diffuse layer. Derjaguin[28] and Verwey and Overbeek[15] obtained expressions for the potential energy of repulsion for spheres of equal radius, a, and equal, small potentials, $\psi_d < 25$mV, for the limiting cases of small and large particles:

small particles, $\kappa a < 3$:

$$V_R = \frac{4\pi\varepsilon_r\varepsilon_o a\psi_d^2}{H_o + 2a} \exp(-\kappa H_o) \qquad (3.7)$$

large particles, $\kappa a > 10$:

$$V_R = 2\pi\varepsilon_r\varepsilon_o a\psi_d^2 \ln(1 + \exp(-\kappa H_o)) \qquad (3.8)$$

where H_o is the separation of the spheres surfaces.

Reerink and Overbeek[29] developed an approximate expression for the intermediate κa region for particles of equal radius:

$$V_R = \frac{32\pi\varepsilon_r\varepsilon_o ak^2T^2\hat{\gamma}^2}{e^2z^2} \exp(-\kappa H_o) \qquad (3.9)$$

It can be seen that in all cases the electrostatic repulsion is

proportional to the particle radius and the square of the potential and also that the range of repulsion is determined by the Debye-Hückel reciprocal length. The repulsion becomes steeper and shorter range as the ionic strength of the medium is increased.

3.3. van der Waals Attraction.

The main source of attraction between colloidal particles are van der Waals forces of which there are three types: the Keesom[30,31] force due to permanent dipole-dipole interactions between the particles; the Debye[32,33] force, induction forces due to interaction between dipoles and dipole-induced-dipoles; and the London[34] dispersion force which is the result of the coupling of fluctuating dipole moments due to the electron motion that occurs in all atoms. The energies of attraction, V_A, are given for the three forces acting between two atoms,[35]:

Keesom:

$$V_A^K = \frac{-2\mu_1^{*2}\mu_2^{*2}}{3kTr^{*6}} \qquad (3.10)$$

Debye:

$$V_A^D = \frac{-(\alpha_1^*\mu_2^{*2} + \alpha_2^*\mu_1^{*2})}{r^{*6}} \qquad (3.11)$$

London dispersion:

$$V_A^L = \frac{-3h\nu_o\alpha^{*2}}{4r^{*6}} \qquad (3.12)$$

where μ^* = dipole moment

α^* = atomic polarisability

h = Planck's constant

ν_o = frequency of electronic fluctuation

r^* = distance between the atoms

Subscripts 1 and 2 refer to molecules of different types.

All these forces are short range but the additive effect of the London dispersion forces constitutes an effective long range force. The vector addition of the Keesom and Debye forces over a large number of atoms results in zero net force and hence only the London forces are important when considering interaction between colloidal particles.

Two methods have been employed to calculate the forces of attraction between surfaces,[36] a microscopic approach by de Boer[37] and Hamaker[38-41] and a macroscopic approach developed by Lifshitz.[42,43]

Hamaker split the van der Waals force into two parts, a purely geometrical part and a constant, A, called the Hamaker constant, dependent only on the material involved. The expression he derived for the potential energy of attraction between two spheres of the same material with equal radius is given by:

$$V_A = \frac{-A}{12}\left(\frac{1}{x^2+2x} + \frac{1}{x^2+2x+1} + 2\ln\frac{x^2+2x}{x^2+2x+1}\right) \qquad (3.13)$$

where A is the Hamaker constant and x given by:

$$x = \frac{H_o}{2a} \qquad (3.14)$$

When $x \ll 1$, for spheres of equal radius, equation (3.13) reduces to:

$$V_A = -\frac{Aa}{12H_o} \qquad (3.15)$$

The Hamaker constant for material in a vacuum is defined as:

$$A = \pi^2 q^2 \frac{3}{4} h\nu_o \alpha^{*2} \qquad (3.16)$$

where q is the number of atoms per unit volume (cm^3).

The presence of a liquid medium has the effect of weakening the attraction as the molecules in the medium are attracted to the molecules in the particles producing a smaller net effect. Hence for colloidal systems a net or composite Hamaker constant must be calculated:

$$A = (A_{11}^{\frac{1}{2}} - A_{22}^{\frac{1}{2}})^2 \quad (3.17)$$

where $A_{11} = \pi^2 q_1^2 \frac{3}{4} h\nu_o \alpha_1^{*2}$ (3.18)

= the Hamaker constant for material 1

$$A_{22} = \pi^2 q_2^2 \frac{3}{4} h\nu_o \alpha_2^{*2} \quad (3.19)$$

= the Hamaker constant for liquid medium 2.

The Hamaker constant is generally of the order $10^{-21} - 10^{-19}$ J depending on the nature of the particles and the medium.[36]

Lifshitz and coworkers developed a theory for the interaction between condensed bodies involving only bulk properties, namely the optical properties, of the material over the complete electromagnetic spectrum. Hence the Lifshitz theory is restricted to materials for which electromagnetic data are available. Some data are available for polystyrene latex systems.

When the distance of separation between particles approaches 20 nm[44-46] the retardation effect becomes significant and the attraction between particles is significantly less than indicated by Hamaker's equations. This retardation is as a result of the finite propagation time of electromagnetic radiation giving a poorer correlation between oscillating dipoles at large distances of separation. The energy dependence on distance then goes from $1/H_o$ to $1/H_o^2$. Lifshitz's theory takes account of the distinction between non-retarded and retarded forces and in general predicts the same force law dependence as the Hamaker theory.

At very short distances of separation the molecular orbitals of the particles overlap and a strong repulsion results. This is known as the Born repulsion and is illustrated in Figure 3.4.

It is noted that the concentration of electrolyte has no effect upon the range of attraction.

3.4. DLVO Theory.

Derjaguin and Landau[47] and Verwey and Overbeek[15] made the assumption that for lyophobic colloidal systems the total potential energy of interaction between particles, V_T, is the sum of the potential energies of repulsion and attraction:

$$V_T = V_R + V_A + V_B \qquad (3.20)$$

where V_B is the Born repulsion.

Schematic representations of two potential energy diagrams for colloidal systems are shown in Figure 3.4, the first for a system stable in the colloidal sense and the second for a system unstable in the colloidal sense, i.e. aggregated.

A necessary condition for the stability of a colloidal system is that there is a net repulsion keeping the particles separate. The total potential energy must be positive at some range of interparticle separation with an energy maximum present as illustrated in Figure 3.4(a). If the energy of repulsion decays rapidly at larger distances a secondary minimum occurs, as illustrated, and the particles undergo a reversible aggregation or flocculation. In this case the particles may be easily redispersed by imparting some energy to the system, for example by shaking.

For the case where attractive forces dominate, as illustrated in Figure 3.4(b) the net interaction is attractive with a deep potential energy well which results in an irreversible aggregation or coagulation. This situation is most likely to occur at high electrolyte concentrations, with large particles which have large Hamaker constants.

Figure 3.4.

Schematic representation of potential energy diagrams for colloidally stable and unstable systems.

(a) Colloidally stable system

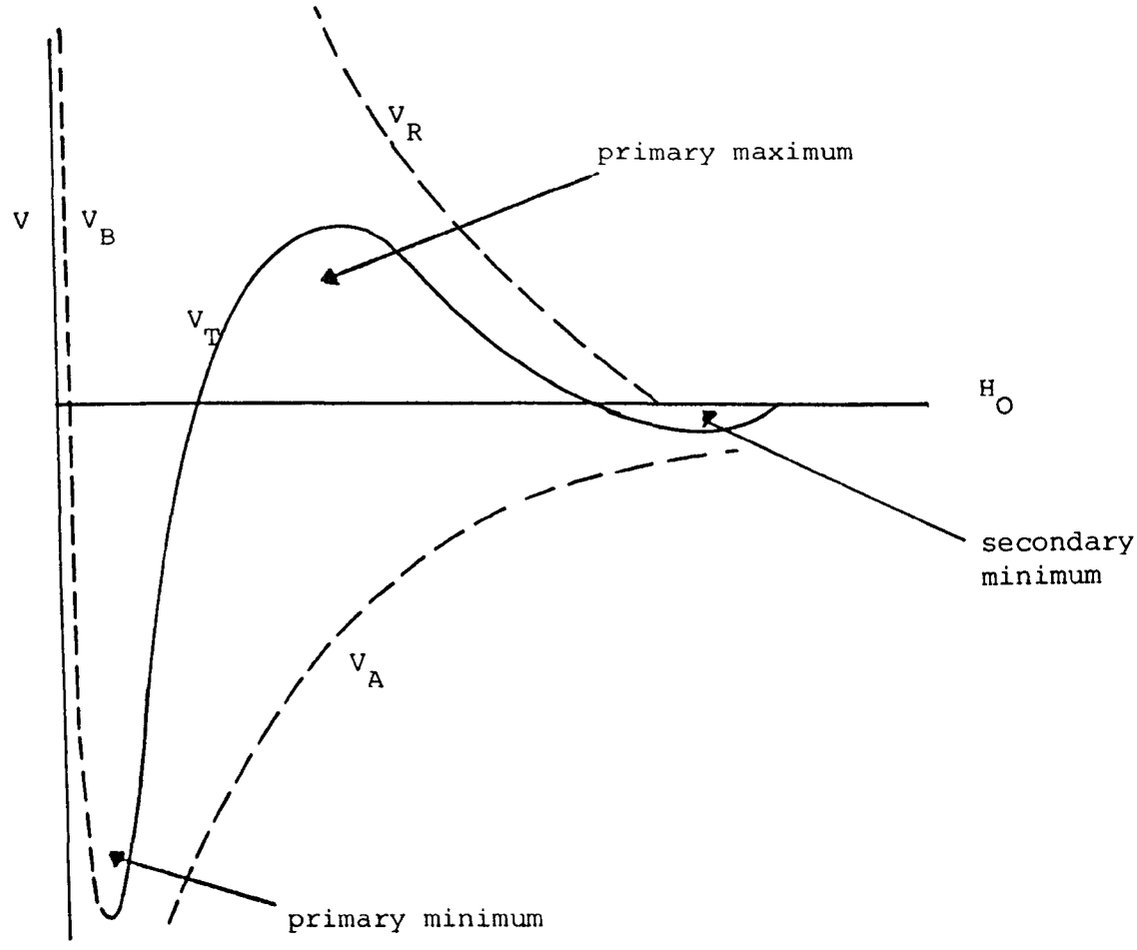

(b) Colloidally unstable system

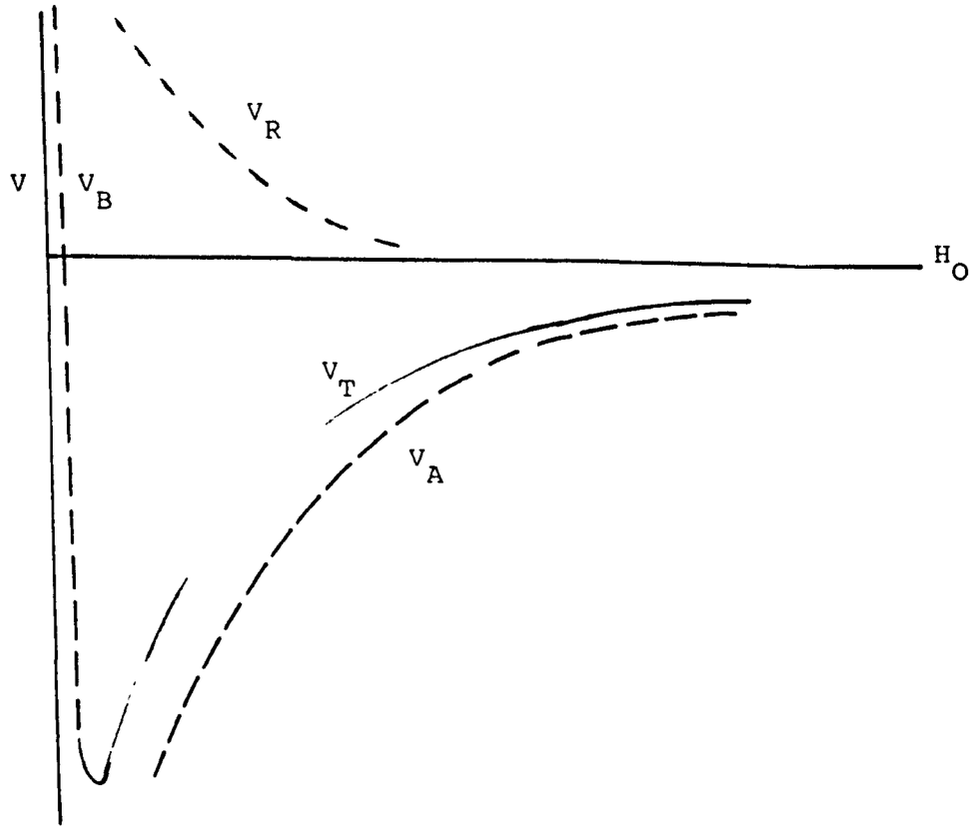

3.5. Steric Stabilisation.

3.5.1. Introduction.

Colloidal dispersions may be stabilised with respect to aggregation by protecting the particles by adsorption of a polymer or surface active agent onto the particles surfaces.[48] Stability may be imparted to a system in a number of ways, depending on the nature of the adsorbate. Ionic surface active agents as adsorbates give rise to an electrostatic repulsion, as described in (3.2), whereas with nonionic surface active agents and polymers repulsion between the particles is ensured by the steric interaction of the adsorbed layers on the particle surfaces. Polyelectrolytes impart a mixture of electrostatic and steric stabilisation.

The presence of an adsorbed layer may also have an effect on the net Hamaker constant of a system and hence on the forces of attraction.

3.5.2. Steric Repulsion.

Repulsive forces in a sterically stabilised system arise in two ways, from entropic and enthalpic effects.[49]

Consider the approach of two spherical particles, each of radius α with adsorbed layers of thickness δ, such that the total sphere radius, a, is given by

$$a = \alpha + \delta \qquad (3.21)$$

The centre to centre separation is taken as r, the surface separation of the particles as H_o and the adsorbed layer surface to surface separation as Δ. This is depicted schematically in Figure 3.5(a).

Four regions of particle interaction can be visualised depending

Figure 3.5.

Limiting interactions between sterically stabilised particles at a constant adsorption.

(a) No interaction between particles.

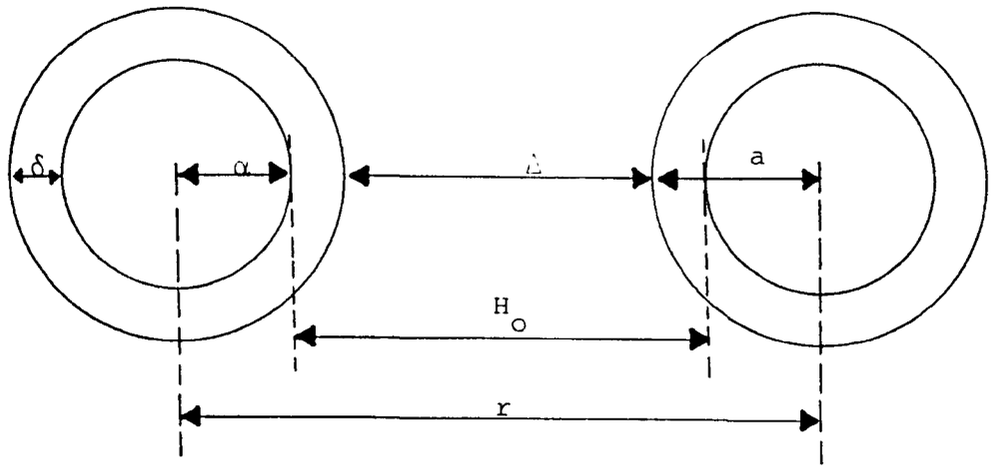

(b) Interpenetration without compression.

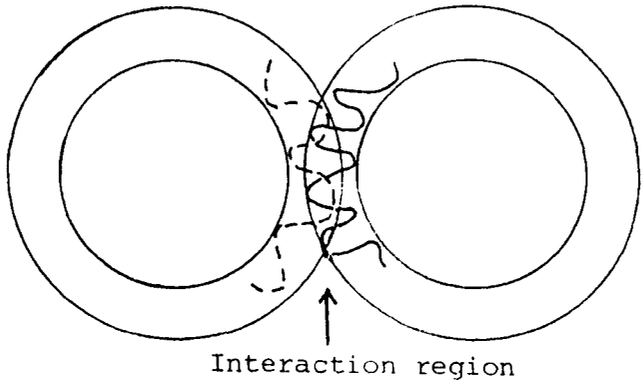

(c) Compression without interpenetration.

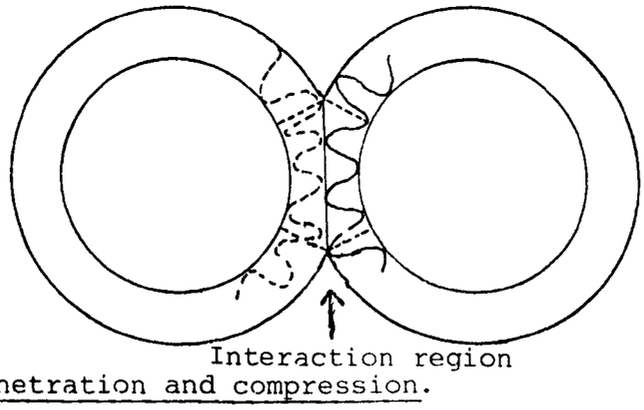

(d) Interpenetration and compression.

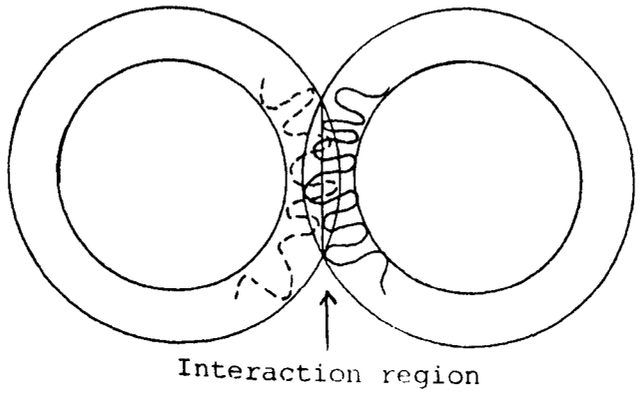

on the distance of particle separation:[50,51]

(i) $H_o > 2\delta$, where particles experience no interaction from one another, illustrated in Figure 3.5(a).

(ii) & (iii) $\delta < H_o < 2\delta$, where interpenetration and/or compression of the adsorbed layers occurs, possibly accompanied by desorption of some adsorbate, illustrated in Figure 3.5(b) and 3.5(c).

(iv) $H_o < \delta$, where compression of the adsorbed layers necessarily occurs, often resulting in some desorption, illustrated in Figure 3.5(d).

The onset of steric interaction occurs just as the two adsorbed layers begin to overlap and interpenetrate, i.e. at $H_o = 2\delta$. This results in an increase in local segment density and hence an increase in osmotic pressure. The effect is known as 'osmotic' or 'mixing' effect and is described by the free energy of mixing, ΔG_{mix}. In the fourth region of interaction, greater interpenetration results in compression of the layers and an additional effect, a decrease in entropy due to a loss of configurational freedom of the adsorbate molecules. This effect is known as the 'volume restriction' or 'entropic' effect. The loss of entropic energy of the stabilising moieties is balanced by a gain in elastic energy, hence this effect may be described by the elastic free energy change, ΔG_{VR}.

Simplistically the free energy of steric repulsion, ΔG_s, can be represented by the expression:

$$\Delta G_s = \Delta G_{mix} + \Delta G_{VR} \qquad (3.22)$$

where the relative importance of the terms varies as the adsorbed layer overlap varies.

Fischer[52] was the first to stress the importance of solvent molecules in steric stabilisation and considered the excess chemical potential of

the system, $\Delta\mu_E$, when the adsorbed layers overlapped. This is related to the excess osmotic pressure, π_E, by the relationship:

$$\Delta\mu_E = \pi_E \bar{v}_1 \qquad (3.23)$$

where $\bar{v}_1$ is the molar volume of the solvent. An expression was obtained for the free energy of mixing in terms of this:[49,53]

$$\Delta G_{mix} = 2 \int_0^V \pi_E dv_{ov} \qquad (3.24)$$

where v_{ov} is the overlap volume which may be defined as:

$$v_{ov} = \frac{2}{3}\pi\left(\delta - \frac{H}{2}^o\right)^2 \left(3\alpha + 2\delta + \frac{H}{2}^o\right) \qquad (3.25)$$

The excess osmotic pressure may be expressed in terms of the second virial coefficient, B_2:

$$\pi_E = RTB_2 c_s^2 \qquad (3.26)$$

where c_s is the concentration of material in the adsorbed layer and R is the Universal Gas Constant and hence, combining equations (3.24), (3.25) and (3.26) a relationship for the free energy of mixing may be obtained in terms of the second virial coefficient:

$$\Delta G_{mix} = \frac{4}{3}\pi RTB_2 c_s^2 \left(\delta - \frac{H}{2}^o\right)^2 \left(3\alpha + 2\delta + \frac{H}{2}^o\right) \qquad (3.27)$$

Ottewill and Walker[54,55] developed Fischer's model by application of the Flory-Huggins theory to calculate the second virial coefficient by means of the expression:

$$B_2 = \frac{\psi^* - \chi^*}{\bar{v}_1 \rho^{**2}} \qquad (3.28)$$

where ψ^* is the dimensionless entropy parameter which characterises the dilution, χ^* is the dimensionless enthalpy parameter which characterises the interaction energy of the adsorbate per solvent molecule and ρ^{**} is the density of the stabilising species. Under ideal conditions the entropy term, ψ^*, may be taken as ½.

This led to the Ottewill-Walker equation for the overlap of adsorbed

layers on spherical particles, assuming no desorption or migration of the stabilising species:

$$\Delta G_{mix} = \frac{4\pi c_s^2 kT}{3V_1 \rho^{**2}} (\psi^* - \chi^*) \left(\delta - \frac{H_o}{2} \right)^2 \left(3\alpha + 2\delta + \frac{H_o}{2} \right) \qquad (3.29)$$

where V_1 is the molecular volume of the dispersion.

The model for the Fischer-Ottewill-Walker model, depicted schematically in Figure 3.6, has two basic assumptions; that the concentration of adsorbate is uniform throughout the layer and falls off abruptly to zero at the outer edge and that the overlapping of two layers produces a lens-like volume in which the concentration of adsorbate is doubled.

Doroszkowski and Lambourne[56] attempted to correct for the abrupt step from a uniform adsorbate concentration to double that concentration in the overlap region by extending the lens-like overlap volume, as depicted in Figure 3.7 and assuming that the adsorbate molecules distribute themselves uniformly over this arbitrarily chosen volume. As this overlap volume is greater than assumed by Fischer and Ottewill and Walker this redistribution method predicts significantly weaker repulsions. For short chain adsorbate molecules there is little advantage in this model.

3.5.3. Modification of Attractive Forces by Adsorbed Layer.

Although the most marked effect on interaction caused by the presence of an adsorbed layer is that on the repulsive forces, the presence of adsorbed molecules also modifies the van der Waals interaction.

Vold[57] extended Hamaker's treatment for the attraction between spherical particles, see 3.3, to include the effect of homogeneous adsorbed layers She predicted that the presence of the adsorbed layers would lead to a

Figure 3.6.

Fischer-Ottewill-Walker model for interactions between particles with adsorbed layers.

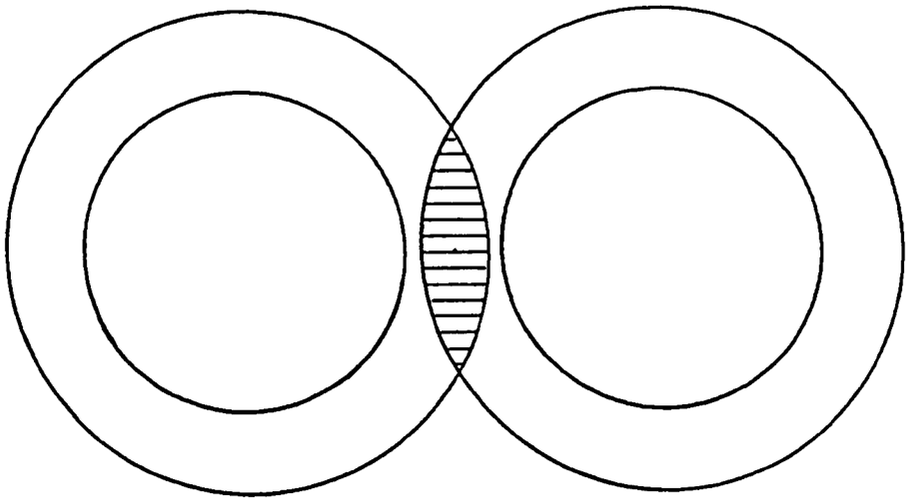

Figure 3.7.

Doroszkowski-Lambourne model for interactions between particles with adsorbed layers.

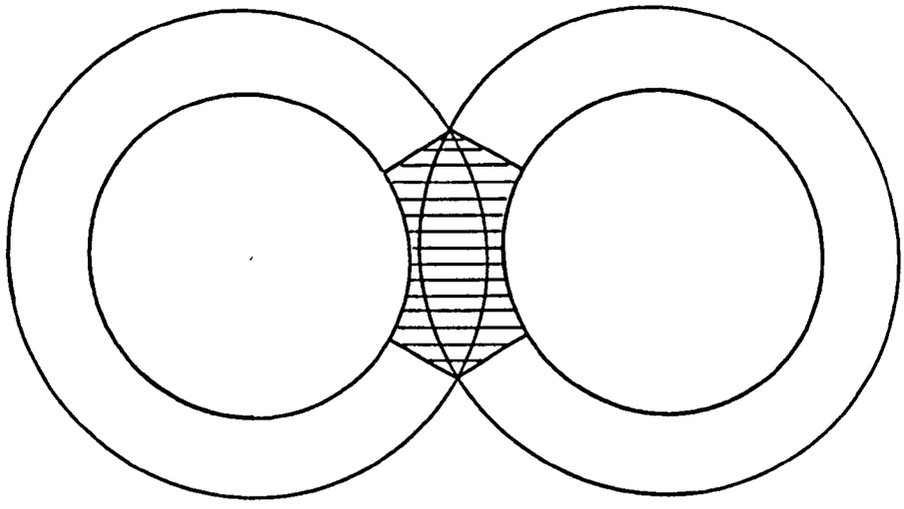

reduction in the attraction between the particles. This reduction is known as the 'Vold Effect'. Vold derived an expression for the energy of attraction, V_A, between two spheres of equal radius, α, each surrounded by an adsorbed layer of thickness δ and dispersed in a medium:

$$V_A = -\frac{1}{12}\left\{ (A_m^{\frac{1}{2}} - A_s^{\frac{1}{2}})^2 H_s + (A_s^{\frac{1}{2}} - A_p^{\frac{1}{2}})^2 H_p + 2 (A_m^{\frac{1}{2}} - A_s^{\frac{1}{2}}) (A_s^{\frac{1}{2}} - A_p^{\frac{1}{2}}) H_{ps} \right\} \qquad (3.30)$$

where A is the Hamaker constant and H a geometic function; subscripts p, s and m refer to the core particle, the adsorbed layer and the medium respectively.

The geometric function, H, is defined by the expression:

$$H(x,y) = \frac{y}{x^2+xy+x} + \frac{y}{x^2+xy+x+y} + 2 \ln\left(\frac{x^2+xy+x}{x^2+xy+x+y}\right) \qquad (3.31)$$

where x and y are defined in terms ofα,δ and Δ, the separation between the adsorbed layer surfaces ($\Delta = H_o - 2\delta$).

For H_s $\quad x = \frac{\Delta}{2(\alpha+\delta)}$ $\quad y = 1$

For H_p $\quad x = \frac{\Delta+2\delta}{2\alpha}$ $\quad y = 1$

For H_{ps} $\quad x = \frac{\Delta+\delta}{2\alpha}$ $\quad y = \frac{\alpha+\delta}{\alpha}$

Vold determined a sequence of Hamaker constants necessary for a net reduction in the free energy of attraction to occur but made an algebraic error in the derivation. Vincent and cpworkers[58] corrected the error and showed the necessary sequence to be:

$$A_s > A_m > A_p \qquad \text{or} \qquad A_s < A_m < A_p$$

The Vold effect becomes most significant at distances of separation greater than $\alpha+\delta$. However it can significantly decrease the force of attraction at short separations for particles with small radii and/or thick adsorbed layers.

3.6. Total Energy of Interaction.

The total energy of interaction, V_T, in a charged colloidal system, sterically stabilised by the presence of an adsorbed layer may be represented by the sum of the energy of attraction, V_A, the electrostatic energy of repulsion, V_R, and the steric energy of repulsion, V_S, which may be equated by the free energy of steric repulsion, ΔG_s:

$$V_T = V_A + V_R + V_S \qquad (3.32)$$

However, it is important to note that a fundamental problem arises in the linear superposition of potentials which have been evaluated separately rather than using a self-consistent model. This problem only arises when a steric layer is present and is due to the models used to take account of it.

Vold[57] calculated the attractive energy as a function of the distance between the adsorbed layer surfaces, Δ, and hence the model takes no account of any interpenetration of the adsorbed layers. As the adsorbed layer surfaces come into contact, from equation(3.30):

$$\Delta = 0, \quad H_o = 2\delta \quad \text{and} \quad V_A \rightarrow -\infty$$

Conversely, the steric repulsive energy is calculated as a function of the distance of separation of the core particles, H_o, and the equations are only valid for $H_o < 2\delta$. Once the adsorbed layers are no longer in contact, no steric repulsive energy is exerted.

Hence there is a discontinuity between the terms V_A and V_S. Various models may be adopted in order to circumvent this problem.[53]

The simplest approach is to use a hard-sphere model, see (4.1), for the steric repulsion. Then, as the adsorbed layer surfaces come into contact the energy of repulsion rises to infinity:

$$H_o = 2\delta \qquad V_S \rightarrow +\infty$$

However this is not consistent with Vold's model as at:

$$H_o = 2\delta \qquad V_A \rightarrow -\infty$$

However, if the Hamaker constant of the adsorbed layer, A_s, is taken to be equal to that of the medium, A_m, the original Hamaker expression is recovered. In this case it is possible to add on the hard sphere repulsion.

For the more general case, when the Hamaker constants of the adsorbed layer and medium may not be treated as equal, a solvation layer outside the adsorbed layer may be postulated. Then, taking the thickness of the solvation layer to be t_s, as the solvation layers come into contact the hard sphere potential may be taken to rise to infinity:

$$\Delta = 2t_s \qquad V_S = \infty$$

The problem with this model is the assignment of a value for t_s. Ottewill and Walker [55] took the value of t_s to be 3Å, representing a layer of water molecules surrounding a polystyrene latex particle stabilised by surface active agent $C_{12}E_6$.

In this model a rigid solvent sheath must be assumed, otherwise the same problem of discontinuity between V_A and V_S arises.

For the case of charged sterically stabilised systems, as previously stated the electrostatic repulsion energy, V_R, must be taken into account as well as the steric and attractive energies. The model used in this work was as follows.

The adsorbed layer was taken to be rigid and the steric repulsion to act as a step function and assume a hard sphere potential at the outside surface of the monodisperse adsorbed layer. The electrostatic repulsion was calculated from the outside of this layer with a potential equal to the electrokinetic potential. It was assumed that the van der Waals attraction is unaffected by the presence of the adsorbed layers.

The forms of the total energy of interaction, V_T, versus interparticle separation, H_o, curves for (a) a small electrostatic term and (b) a large electrostatic term in a sterically stabilised system, according to this model, are illustrated schematically in Figure 3.8. It is noted that the thickness of the adsorbed layer controls the depth of the potential energy minimum, the greater the extent of the adsorbed layer, the shallower the well.

Figure 3.8.

Total energies of interaction for identical, sterically stabilised colloidal particles.

(a) Small electrostatic term

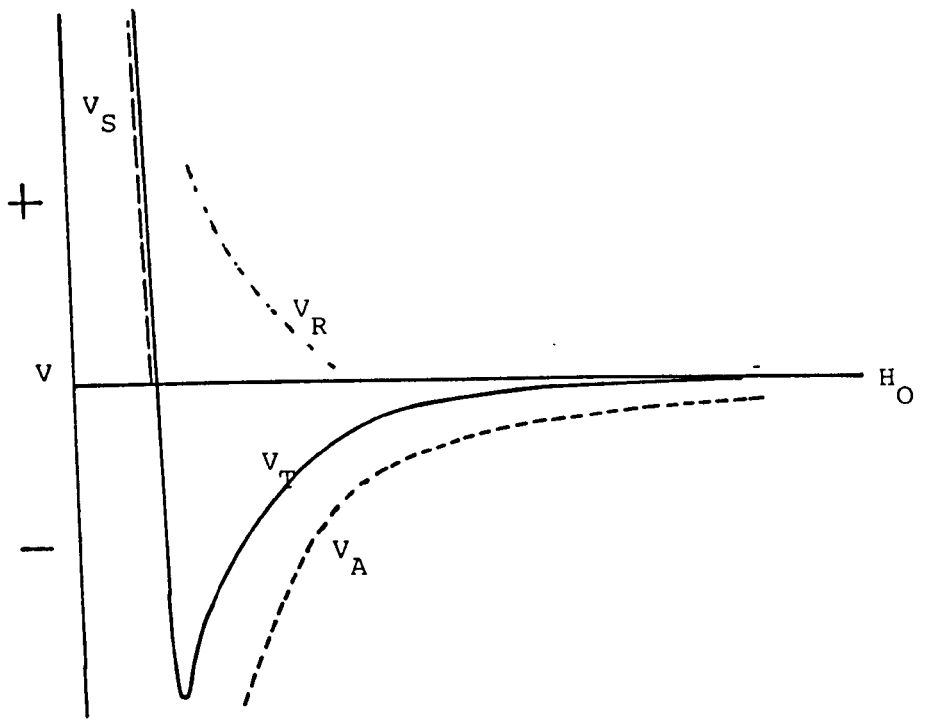

(b) Large electrostatic term

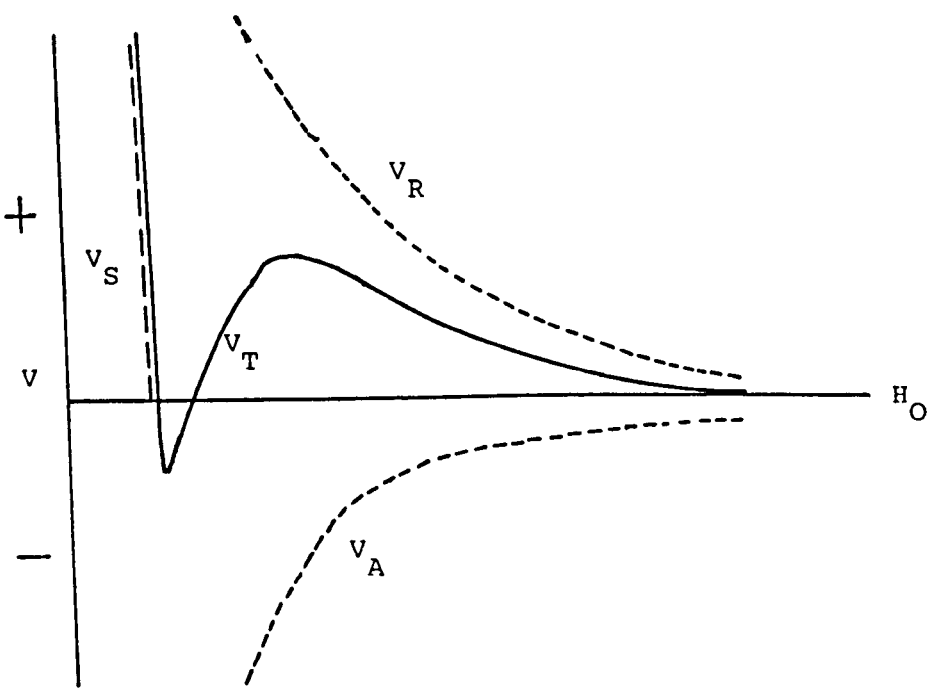

Chapter Four

Application of Statistical Mechanics to Concentrated Colloidal Systems

Chapter Four Application of Statistical Mechanics to Concentrated Colloidal Systems.

4.1. Introduction.

In Chapter Three the interactions between colloidal particles were described in terms of the repulsive and attractive forces acting between a pair of colloidal particles, and the stability of the particles with respect to aggregation was determined by the net energy of interaction.

The simplest possible description of particle interactions in a colloidal system is that the dispersion is a suspension of hard, mutually impenetrable spheres of diameter, σ. The hard sphere diameter is defined as the distance of particle centre separation at which a harsh repulsion occurs rising very steeply to plus infinity as a consequence of the impenetrable nature of the particles. This model can be extended to dispersions which are stabilised either by steric layers or by electrostatic interactions. In the former case the effective hard sphere diameter can be taken as the diameter of the particle including the adsorbed layer, whilst in the latter case the effective hard sphere diameter is less well defined and can be thought of as including a distance at which the interparticle forces become significant compared with the thermal energy of the system.

The hard sphere potential, V_{HS}, is illustrated in Figure 4.1[59] and taken to be:

$$V_{HS} = \begin{cases} \infty, & r < \sigma \\ 0, & r \geq \sigma \end{cases} \qquad (4.1)$$

A volume fraction of the hard sphere dispersion, ϕ_{HS}, must be defined as:[59]

$$\phi_{HS} = \frac{N_p 4\pi a_{HS}^3}{v\ 3} \qquad (4.2)$$

Figure 4.1.

Interaction between hard spheres

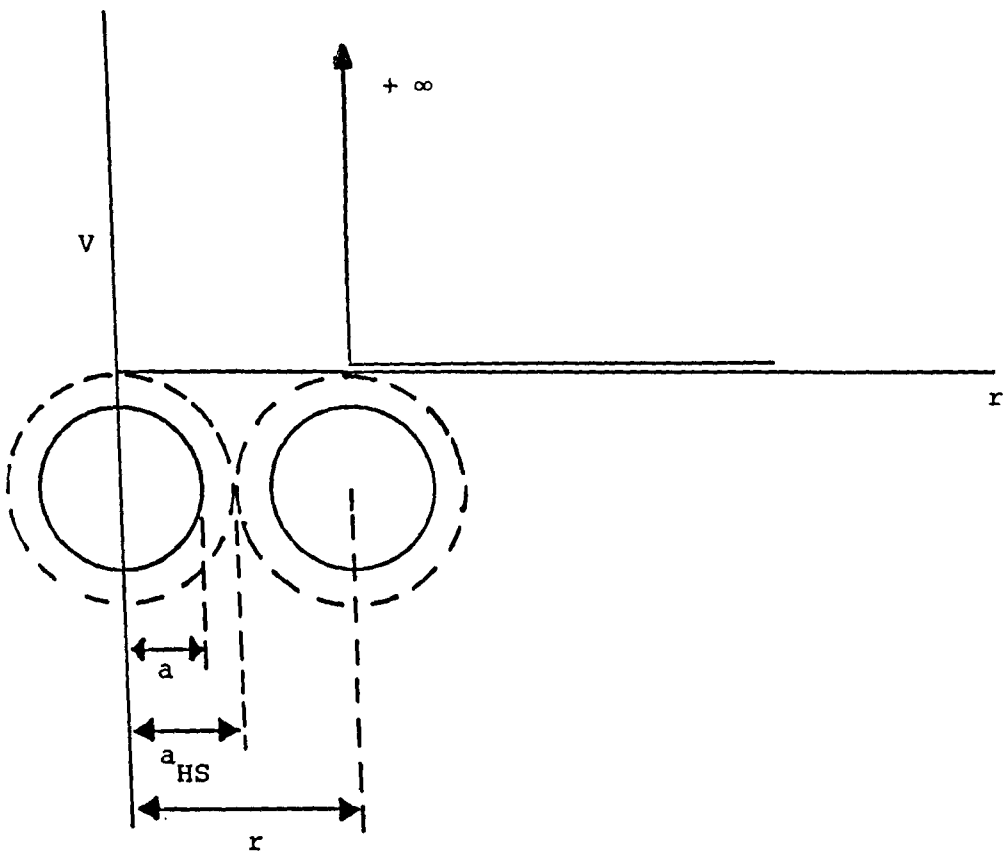

where the hard sphere particle radius, $a_{HS} > a$, the particle radius i.e.

$$\phi_{HS} = \frac{\rho\pi\sigma^3}{6} \qquad (4.3)$$

where N_p is the number of particles in the total dispersion volume, v, and ρ is the particle number density.

The hard sphere approximation frequently forms a good reference point for subsequent refinements to accommodate softer repulsions or attractive forces.

The structure of a colloidal system has an important influence on the macroscopic properties of the system and must be described in detail. If a very simplistic view is taken of concentrated systems there are two extreme cases of particle arrangement, illustrated schematically in Figure 4.2. In a situation where the repulsive forces are dominant as depicted in Figure 4.2(a) a dispersion of high order is obtained with a large effective radius and a high particle coordination number. Alternatively, when attractive interactions are dominant the particles "stick" on coming into an attractive energy well with the consequent formation of a highly disordered system of the type shown in Figure 4.2(b). In such a system the void volume is high and the particle coordination number low. In dispersions where the interparticle attractions are minimal the arrangement of particles is as random as the Brownian motion of individual particles allows.

Between these extremes of high stability/high order and strong aggregation/random distribution, a range of other possibilities exist. Hence methods are required to describe the state of a system in terms of both the spatial and temporal correlations between the particles so that a statistical description of the structure is achieved. With a sufficiently detailed statistical description and knowledge of the inter-

Figure 4.2.

Comparison of particle arrangements in concentrated colloidal dispersions.

(a) Stable Colloidal System.

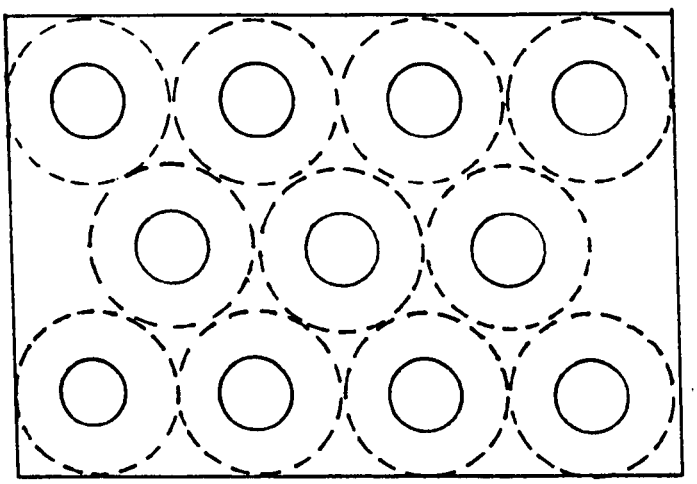

(b) Aggregated Colloidal System.

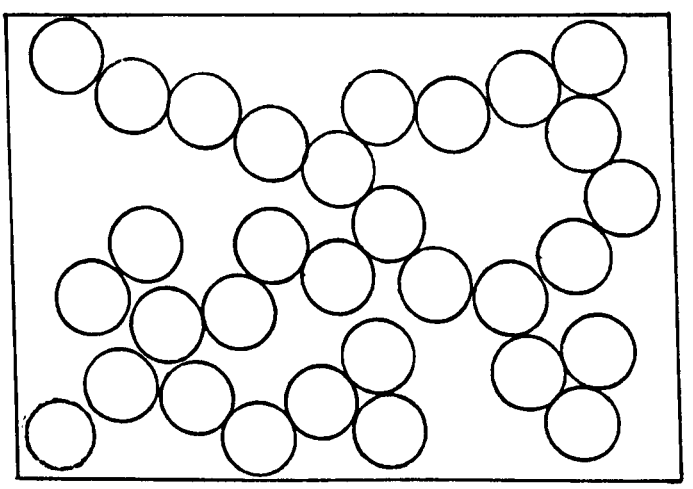

particle forces it should be possible to predict the macroscopic properties of the system. The goal of statistical mechanics is the understanding and prediction of macroscopic phenomena and the calculation of macroscopic properties from the properties of the individual molecules making up the system.[60]

The bulk of work in statistical mechanics is based upon atomic or molecular fluids, in particular liquid argon and liquid helium. Lennard-Jones and Devonshire[61,62] were the first to develop theoretical models to predict thermodynamic properties of dense gases and liquids in terms of interatomic forces. They considered the potential energy of an atom to be not only a function of volume but also a function of the position of the atom relative to its neighbours. They employed statistical methods to calculate the probability of an atom in any assigned position and deduced the average potential energy and available free volume.

When such a statistical mechanical approach is extended and applied to colloidal systems it is necessary to take account of the differences between colloidal suspensions and molecular condensed phases. Significant differences exist because of the softness and longer range of the interaction potentials in colloidal systems and because of the ionic and molecular association and dissociation phenomena that may make the interaction "dynamic". The continuous phase in colloidal suspensions has thermodynamic properties and hydrodynamic interactions of its own; these may also need to be taken into consideration. Such a consideration is not encountered with molecular liquids. Although when one is concerned with the transport aspects of colloidal dispersions, the long range hydrodynamic interactions among the suspended particles must also be taken into account, these do not, however, exert any influence on the equilibrium thermodynamic properties of the dispersion.

This chapter describes briefly how some basic concepts of a statistical description of the liquid state may be extended to represent concentrated colloidal dispersions. Also how a pairwise additive summation of pair potentials combined with a statistical description of dispersion structure may be used to theoretically predict macroscopic properties such as the zero shear rate viscosity and the high frequency limit of the shear modulus.

4.2. Radial Distribution Function.

The radial distribution function is a means by which the spatial distribution of particles in a colloidal dispersion may be described.[59]

Consider a colloidal dispersion in a container, volume v, such that there are N_p particles of radius a; the macroscopic number density, ρ_o may then be expressed as:

$$\rho_o = \frac{N_p}{v} \qquad (4.4)$$

If now the microscopic view of the system is considered as seen by one representative particle within the system, a radial distribution of neighbouring particles is observed as depicted schematically in Figure 4.3.[59] As the distance from the central particle, r, is increased, spherically symmetric successive shells of thickness dr are encountered, each containing more particles than the previous one but with increasing shell volumes. As r approaches infinity, the number density of particles in a shell must approach the macroscopic density, ρ_o. It is impossible for there to be a neighbouring particle at a closer distance of centre-centre separation than 2a. Hence it is possible to define the limiting values of the density distribution function, $\rho(r)$:

$$\rho(r) \to \rho_o \quad \text{as} \quad r \to \infty$$

$$\rho(r) \to 0 \quad \text{as} \quad r \to 2a$$

Figure 4.3.

Schematic illustration of the radial distribution of particles around a central particle.

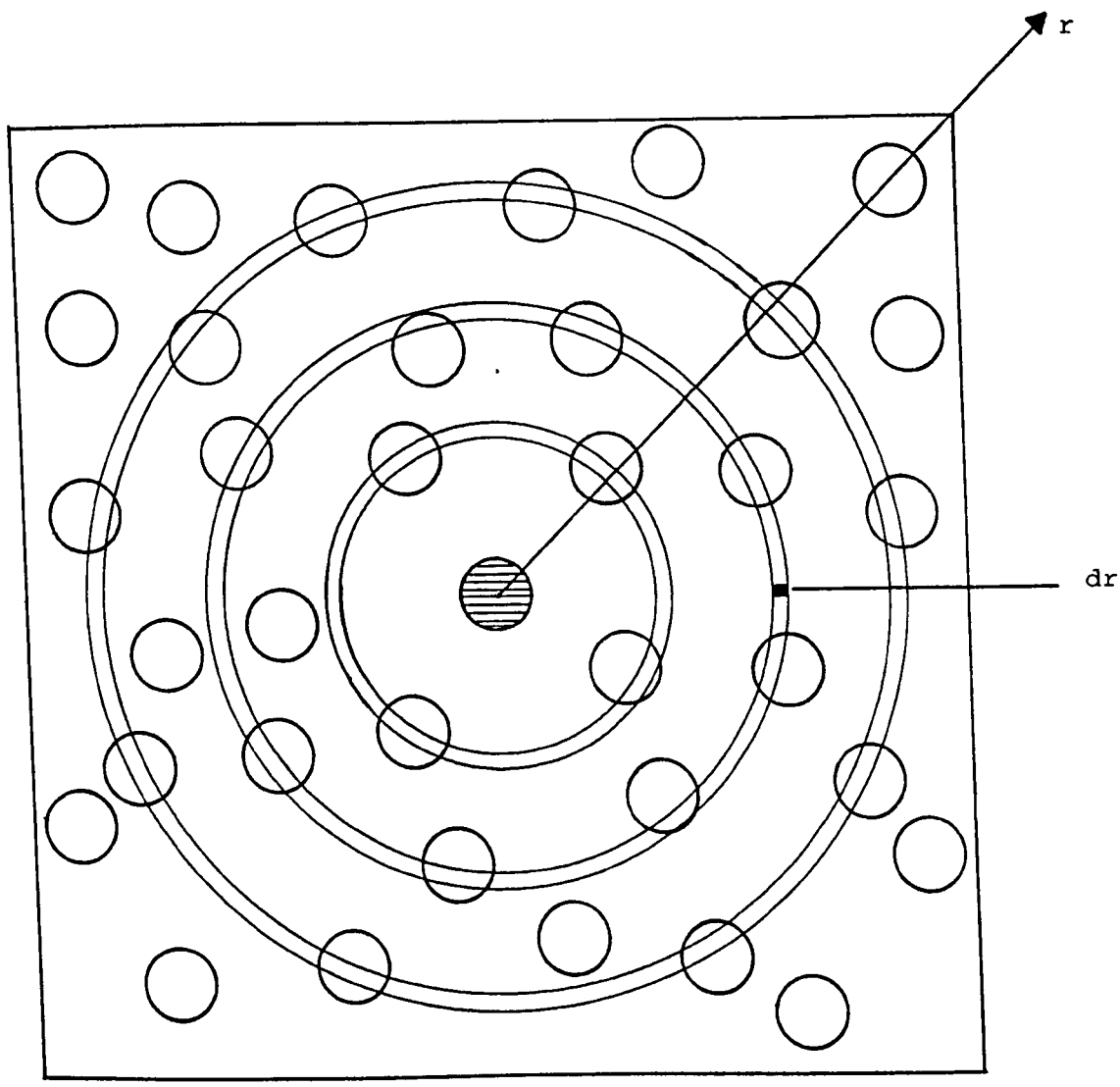

The term radial distribution function strictly applies to the quantity:

$$4\pi r^2 \rho(r)$$

but it is often used, as it is here, to represent the distribution function, g(r), which gives the probability of finding a particle at a distance r from the reference sphere and is defined:

$$g(r) = \frac{\rho(r)}{\rho_o} \qquad (4.5)$$

and has the limiting values:

$$g(r) \to 1 \text{ as } r \to \infty$$

$$g(r) \to 0 \text{ as } r \to 2a$$

The function g(r) provides an important means of characterising the system; Figure 4.4 shows schematically the g(r) versus r curves for three types of system.[63] For a highly ordered crystalline structure g(r) consists of a series of spikes, depicted in Figure 4.4(a), corresponding to the radial shells whereas for a very dilute system the structure is said to be "vapour-like" and there is no structure. In this case g(r) becomes unity as depicted in Figure 4.4(c). It is the intermediate "fluid-like" case which describes concentrated dispersions that is of most interest. In this case there is a pronounced first peak, corresponding to the first shell, followed by a number of subsidiary oscillations damping out to unity when the radial structure is uncorrelated to the presence of the central particle. This is depicted in Figure 4.4(b). Successive peaks are seen to become broader as the correlation decreases.

The probability may be related to a Boltzmann distribution calculated from a hypothetical net pair potential termed the 'potential of mean force' such that:[64]

Figure 4.4.

Radial distribution function, g(r), versus r for various states.

(a) Fixed Site, "Crystal"

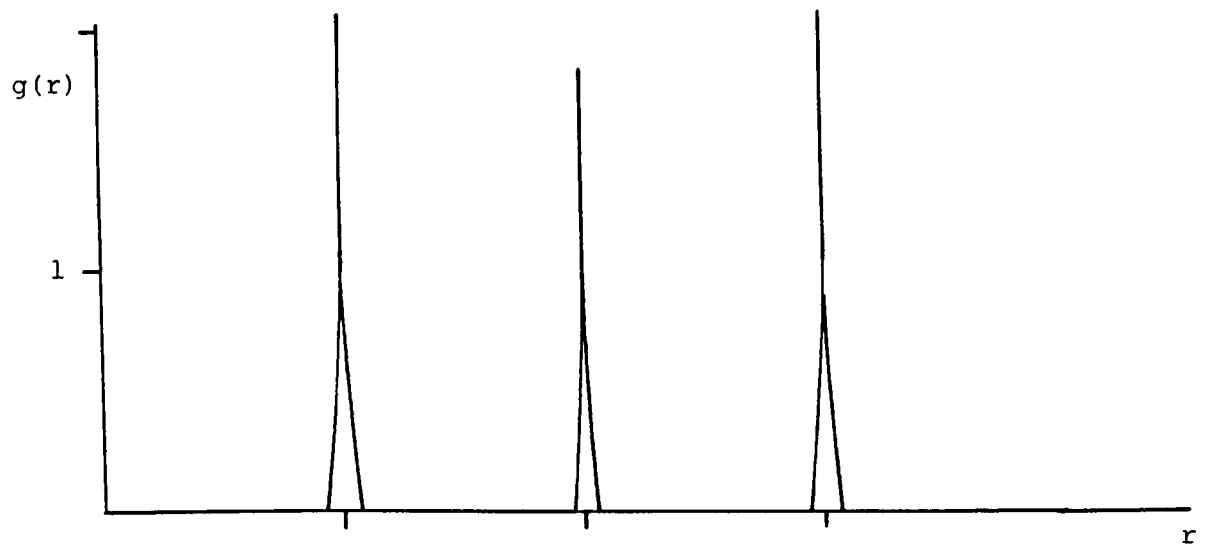

(b) ConcentratedDispersions, "Liquid-like".

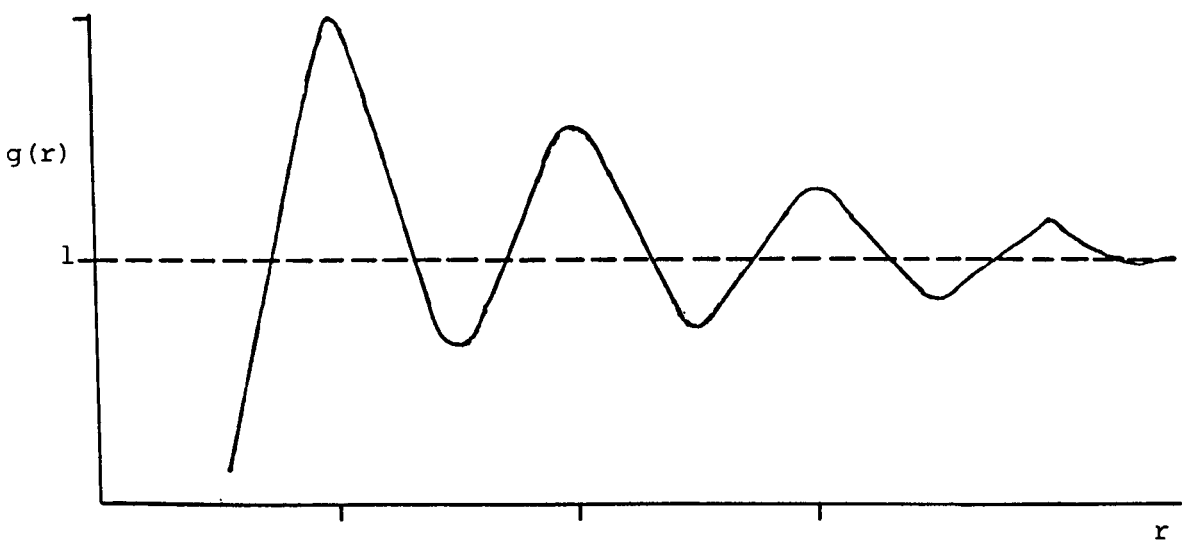

(c) Dilute Dispersions, "Vapour-like".

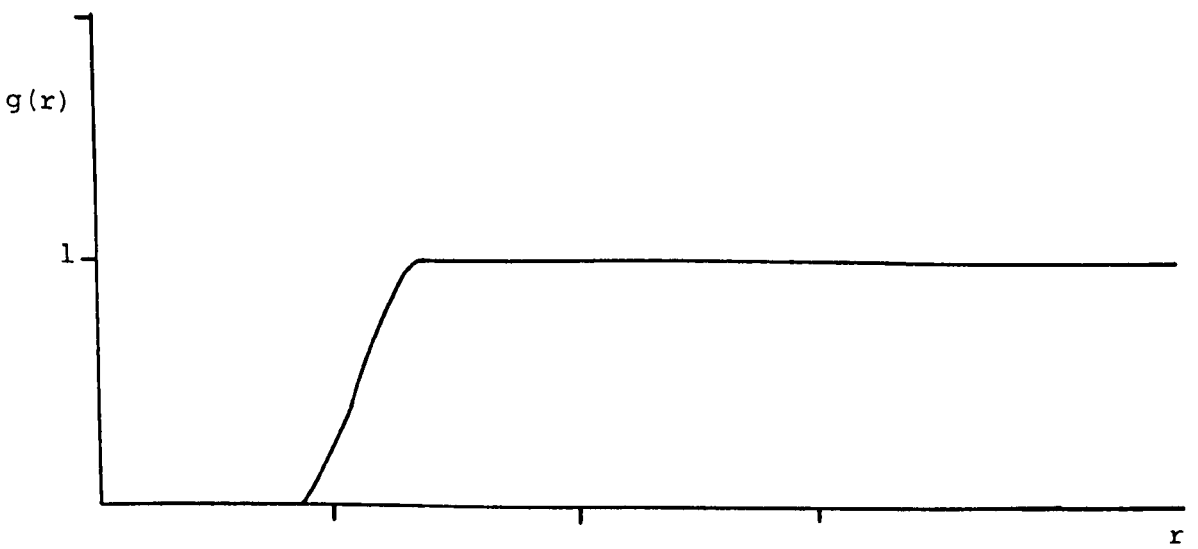

$$g(r_{12}) = \exp\left(- \frac{\Psi(r_{12})}{kT} \right) \quad (4.6)$$

with $g(r_{12}) = 0$ at $r_{12} < 2a$ (4.7)

where $\Psi(r_{12}) = V(r_{12}) + W(r_{12})$ (4.8)

and $W(r_{12})$ is the modifying potential due to the remaining (N-2) particles in the system were N is the total number of particles.

The radial distribution function is an extremely useful quantity in the description of a colloidal system in combination with the pair potential as it can provide the information necessary to obtain the equilibrium thermodynamic properties of the dispersion such as osmotic pressure and isothermal compressibilities.

There are two main ways of determining the radial distribution function, experimentally via the structure factor, S(Q), which can be measured from scattering techniques[59,63] and then converted to the radial distribution function by Fourier transformation; and theoretically from various models for dispersion structure and particle-particle interactions. These theoretical models are discussed briefly in the following sections.

Monte Carlo computer simulations of particle configurations are available for the 'exact' calculation of radial distribution functions; these being exact in so far as it may be assumed that the potential function is accurately known and that the potentials are pairwise additive. However, they may be shown to offer the closest fit to experimental data. Barker and Henderson[65] have tabulated accurate hard sphere radial distributions, computed using the Monte Carlo method, and these may be used to check the validity of other models.

4.3. Percus Yevick Approximation.

Fluid structure may be determined through the concepts of direct and indirect correlation. As was shown in (4.2), the potential of mean force, $\Psi(r)$, may be resolved into a direct component, $V(r)$, the straightforward pair potential and an indirect component, $W(r)$ which accounts for the modifying effect of the remaining particles. An analogous resolution may be made in terms of the correlation rather than the potential; this will of course affect the potential[64].

The total correlation, $h(r)$, is defined:

$$h(r) = g(r) - 1 \qquad (4.9)$$

and is the fluctuation about the uniform probability, $g(r) = 1$, of finding a second particle located at a distance r from another located at the origin. Ornstein and Zernicke[66], in 1914, defined the total correlation in terms of its direct and indirect components:

$$\underset{\text{total}}{h(r_{12})} = \underset{\text{direct}}{c(r_{12})} + \rho \int \underset{\text{indirect}}{c(r_{13})h(r_{23})dr_3} \qquad (4.10)$$

where $c(r)$ is the direct correlation function and r_{ij} is the distance between particles i and j. Figure 4.5 shows a qualitative breakdown of the total correlation into its direct and indirect components.[64]

A precise description of the system may be obtained by solving equation (4.10) for $h(r)$; however this requires all interactions between particles and all indirect interactions to be taken into account. Suitable approximations are therefore required.

At low densities, i.e. as $\rho \to 0$, the total correlation function equates to the direct correlation function:

$$h(r) \to c(r) \quad \text{as} \quad \rho \to 0$$

Figure 4.5.

Qualitative breakdown of the total correlation into its direct and indirect components.

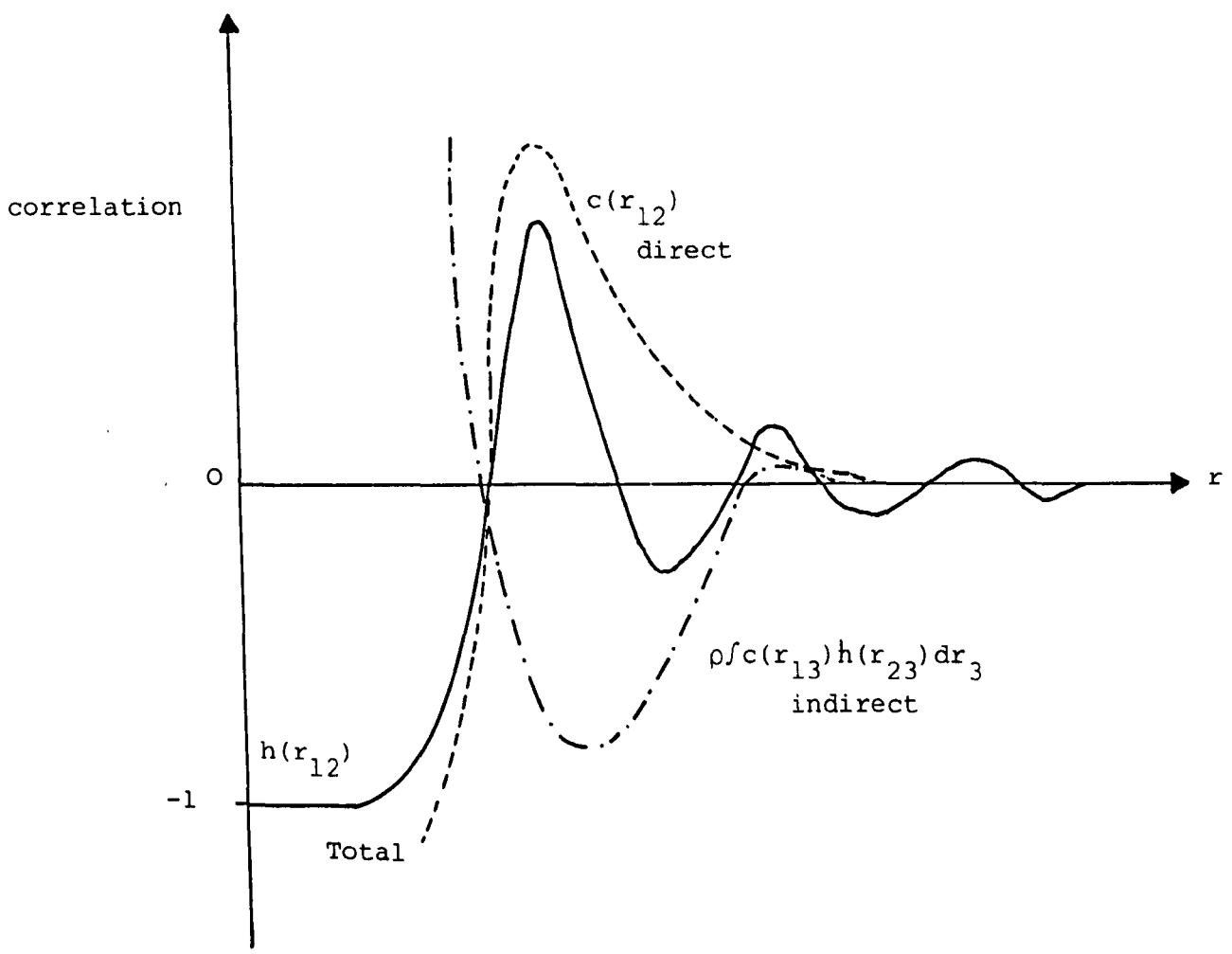

and from equation (4.9)

$$g(r) = c(r) + 1 \qquad (4.11)$$

Under these conditions:

$$g(r) = \exp\left(\frac{-\Psi(r)}{kT}\right) \rightarrow \exp\left(\frac{-V(r)}{kT}\right) \rightarrow c(r) + 1 \qquad (4.12)$$

and therefore the direct correlation function reduces to the Mayer f-function:

$$c(r) = \exp\left(\frac{-V(r)}{kT}\right) - 1 \qquad (4.13)$$

It is clear from equation (4.13) and from Figure 4.5 that the direct correlation function is responsible for short range structure. A knowledge of the direct correlation inserted in the Ornstein-Zernicke equation therefore enables the analytic description of the structure.

The Percus Yevick approximation for the direct correlation function consists of dropping the long range component but preserving the exact short range form. The approximation may be expressed:[64]

$$c_{PY}(r) = h(r) - \left\{ g(r) \exp\left(\frac{V(r)}{kT}\right) - 1 \right\} \qquad (4.14)$$

Insertion of the Percus-Yevick approximation for the direct correlation into the Ornstein-Zernicke equation yields the Percus-Yevick equation:

$$g(r_{12}) - c(r_{12}) = 1 - \rho \int c(r_{13}) dr_3 + \rho \int g(r_{23}) c(r_{13}) dr_3 \qquad (4.15)$$

This equation may be solved analytically for hard spheres. For short range interactions a reasonably good fit to Monte Carlo computer simulation results is obtained.[64]

The Percus-Yevick (PY) equation for the radial distribution function has been solved exactly for hard spheres by Wertheim[67] by inversion of the Laplace transformation of the PY equation. Throop and Bearman[68] performed the inversion numerically and evaluated the radial distribution function for a range of number densities. Henderson has written a program to

compute this hard sphere radial distribution function, based on Throop and Bearman's numerical inversion of the Laplace transform of the PY equation, using a correction due to Verlet and Weis[69] which was designed to take the radial distribution function into agreement with the Monte Carlo computer simulation solution.[65] The program is presented in McQuarrie.[60]

4.4. Perturbation Theories.

The hard sphere approximation, described in (4.1) provides an excellent basis for a perturbative extension to more realistic soft sphere schemes. The statistical mechanical theory for perturbations was developed by Zwanzig[70] who calculated the configurational integral in terms of unperturbed and perturbed components.

In the general scheme of perturbation theories the particle interaction energy, $V(r)$, is divided into two parts, a reference potential, $V_o(r)$, with a perturbation on that potential of $V_p(r)$:[71]

$$V(r) = V_o(r) + V_p(r) \qquad (4.16)$$

The reference potential is usually chosen to include the steep, short-range repulsive contribution, whereas V_p contains the smoothly-varying long-range attractive part. This form of the potential is then introduced into the statistical mechanical expression for the partition function from which the free energy is calculated. The free energy, A^*, is then expanded in terms of V_p[60] to obtain the series:

$$A^* = A_o^* + A_1^* + A_2^* + \ldots\ldots\ldots \qquad (4.17)$$

where A_o^* is the Helmholtz free energy of the reference system and A_1, A_2 etc. are the perturbation corrections. The first-order term in this expansion is given by:

$$A_1^* = 2\pi\rho N_o \int^{\infty} V_p(r) g_o(r) r^2 dr \qquad (4.18)$$

where $g_o(r)$ is the radial distribution function of the reference scheme and ρ is the number density.

The second step in the procedure is to relate the properties of the reference system to those of a well-understood system such as a system of hard spheres whose free energy and radial distribution function are available in the literature.

The energy expansion in the first step of the perturbation depends upon the point chosen for perturbation on the pair potential curves; this is the basis for the different perturbation methods. The two most used perturbation theories are those due to Barker and Henderson and to Weeks, Chandler and Anderson.

Barker-Henderson Perturbation Theory (BH)

The Barker-Henderson[71] model divides the pair potential on the basis of the sign of the interaction energy so that:

$$V_o(r) = V(r) \qquad r < \sigma$$

$$V_o(r) = 0 \qquad r > \sigma$$

$$V_p(r) = 0 \qquad r < \sigma$$

$$V_p(r) = V(r) \qquad r > \sigma$$

This is illustrated schematically in Figure 4.6(a).[72]

The reference system is related to a hard-sphere system through the definition of the Barker-Henderson diameter, d_E, given by:[72]

$$d_E = \int_0^{\sigma} \left\{ 1 - \exp\left(- \frac{V(r)}{kT} \right) \right\} dr \qquad (4.19)$$

To avoid carrying the integration over the primary minimum of the interaction potential a point is selected, d_o, where $\exp\left(- \frac{V(r)}{kT} \right)$ is negligible ($<10^{-6}$) and equation (4.19) is rewritten as:

$$d_E = d_o + \int_{d_o}^{\sigma} \left\{ 1 - \exp\left(- \frac{V(r)}{kT} \right) \right\} dr \qquad (4.20)$$

Figure 4.6.

Selection of the reference and perturbation potentials in the Barker-Henderson and Weeks-Chandler-Andersen perturbation theories.

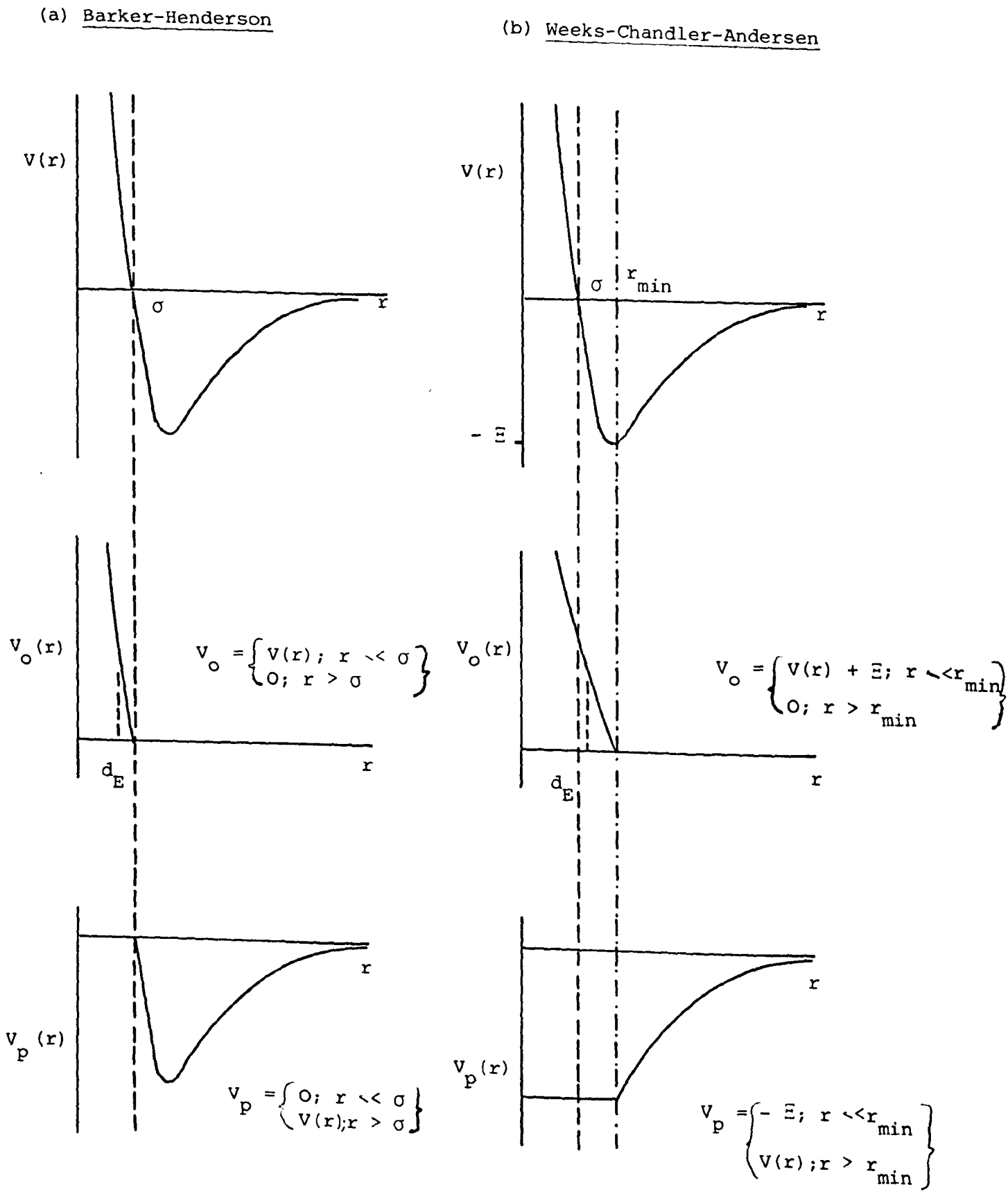

The effective volume fraction, ϕ_E, is then calculated from:

$$\phi_E = \phi\left(\frac{d}{a}E\right)^3 \qquad (4.21)$$

and the properties of the reference system taken to be equal to those of a hard sphere system with volume fraction, ϕ_E.

i.e. the radial distribution function is taken as:

$$g_o(r) = g_{HS}(r;\ \phi_E) \qquad (4.22)$$

Weeks-Chandler-Andersen Perturbation Theory (WCA)

The Weeks-Chandler-Andersen[73] model divides the pair potential at the point where the interparticle forces become zero, i.e. at the minimum of the potential, r_{min}, so that:

$$V_o(r) = V(r) + \Xi \qquad r \lesssim r_{min}$$

$$V_o(r) = 0 \qquad r > r_{min}$$

$$V_p(r) = -\Xi \qquad r \lesssim r_{min}$$

$$V_p(r) = V(r) \qquad r > r_{min}$$

where Ξ is the potential energy minimum. This is illustrated schematically in Figure 4.6(b).[72]

The radial distribution function is calculated in terms of the indirect correlation function, y(r), which is defined by:

$$y(r) = g(r)\ \exp\left(\frac{V(r)}{kT}\right) \qquad (4.23)$$

and is relatively insensitive to the pair potential. Hence:

$$y_o(r) = y_{HS}(r) \qquad (4.24)$$

Then, combining equations (4.23) and (4.24) yields:

$$g_o(r) = y_{HS}(r;d_E)\ \exp\left(\frac{-V_o(r)}{kT}\right) \qquad (4.25)$$

where $y_{HS}(r;d_\epsilon)$ is y(r) for a system of hard spheres of effective diameter, d_E. This value isobtained by an iterative solution of:

$$\int_{d_E}^{r_{min}} y_{HS}(r;\ d_E) r^2 dr \ = \ \int_{o}^{r_{min}} y_{HS}(r;\ d_E)\ \exp\left(\frac{-V_o(r)}{kT}\right) r^2 dr \qquad (4.26)$$

A Verlet-Weis[69] algorithm has been used to determine d_E and this procedure is summarised in Table 4.1.[71]

The radial distribution function can be calculated from perturbation theory using the expansion:

$$g(r) \ = \ g_o(r) + g_1(r) + ... \qquad (4.27)$$

Where $g_o(r)$ is the radial distribution function of the reference system and $g_1(r)$ is the first order perturbation correction.

An approximate method must be used to determine $g_1(r)$ which may be given by[72]:

$$g_1(r) \ = - kT \left(\frac{\partial \rho}{\partial p}\right) \frac{V_p(r)}{kT}\ g_o(r) \qquad (4.28)$$

Therefore:

$$g(r) \ = \ g_o(r) \left\{ 1 - \frac{V_p(r)}{kT}\ kT \left(\frac{\partial \rho}{\partial p}\right) \right\} \qquad (4.29)$$

where $\left(\frac{\partial \rho}{\partial p}\right)$ is the osmotic compressibility which may be determined from the Carnahan-Starling[74] equation of state:

$$\frac{PV}{NkT} \ = \ \frac{1 + \phi + \phi^2 - \phi^3}{(1-\phi)^3} \qquad (4.30)$$

The perturbed radial distribution function, calculated from equation (4.29), may then be used in conjunction with the perturbed potential energy, from equation (4.16) to calculate appropriate macroscopic properties such as the shear modulus and the viscosity.

Table 4.1.

Verlet-Weis algorithm for the WCA hard sphere diameter.

1. Use a BH-like HS diameter as initial guess.

$$d_E = d_{BH} = \int_0^{r_{min}} \left\{ 1 - \exp\left(\frac{-V_o(r)}{kT} \right) \right\} dr$$

2. Iterate as follows:

2.1. Calculate $\phi_E = \phi \left(\frac{d_E}{d_p} \right)^3$

2.2. Calculate ϕ_W as $\phi_W = \phi_E - \frac{\phi_E^2}{16}$

2.3. Evaluate α^{**} and δ^* from:

$$\alpha^{**} = \frac{1 - 4.25\ \phi_W + 1.362\ \phi_W^2 - 0.8751\ \phi_W^3}{(1 - \phi_W)^3}$$

$$\delta^* = \int_0^{\infty} \left(\frac{r}{d_{BH}} - 1 \right)^2 \frac{d}{dr} \left\{ \exp\left(- \frac{V_o(r)}{kT} \right) \right\} dr$$

2.4. Obtain a new estimate as

$$d_E' = d_E\ (1 + \alpha^{**} \delta^*)$$

3. Iteration is complete with $d_E' \simeq d_E$ in successive iterations.

4.5. Theoretical Calculations of Shear Modulus.

When a mechanical force is applied suddenly to a fluid, the fluid responds elastically at first as if it was a solid body. This initial response may be described by two quantities, the high frequency limit of the shear or rigidity modulus, $G(\infty)$, and the high frequency limit of the bulk modulus, or modulus of compression, $K(\infty)$.

Green[75] forwarded a theoretical description of the shear modulus of a fluid based on the general statistical mechanical formula for the stress tensor of a fluid in an arbitrary non equilibrium state. The expression contains the one- and two-body distribution functions of the field, and the pair interaction potential. When an external force is applied suddenly the fluid particles are moved to new positions so that the fluid is strained. The stress tensor is then expanded in powers of the strain tensor, and the coefficient of the linear term related to the shear modulus. Green[76] proposed a similar model for the determination of the bulk modulus. This approach yielded correct intermolecular force contributions but incorrect kinetic contributions.

Herzfeld[77] expanded the time-correlation theory of viscosity coefficients developed by Green[78] to express the coefficients in the Maxwell form, i.e. as a product of a modulus and a relaxation time, and made some rough estimates of the shear and bulk moduli.

Zwanzig and Mountain[79] investigated the approach of Herzfield more thoroughly and used a statistical mechanical treatment to calculate the elastic moduli of a monatomic fluid. They arrived at a final expression for the high frequency limit shear modulus given by:

$$G(\infty) = \rho kT + \frac{2\pi\rho^2}{15} \int_0^\infty g(r) \frac{d}{dr}\left[r^4 \frac{dV(r)}{dr}\right] dr \qquad (4.31)$$

The second term in the equation agrees exactly with Green's result, the first term, a kinetic term was not found by Green.

The authors obtained an expression for the bulk modulus at the high frequency limit given by:

$$K(\infty) = \frac{2}{3}\rho kT + P + \frac{2\pi\rho^2}{9}\int_0^\infty g(r)r^3\frac{d}{dr}\left[\frac{rdV(r)}{dr}\right] dr \qquad (4.32)$$

where P is the dynamic pressure of the fluid, expressed:

$$P = \rho kT - \frac{2\pi\rho^2}{3}\int_0^\infty g(r)\, r^3\, \frac{dV(r)}{dr}\, dr \qquad (4.33)$$

This result for the bulk modulus does not agree with that of Green; Zwanzig and Mountain[79] attributed this to Green's incorrect treatment of the kinetic term.

The high frequency bulk modulus may be related to the high frequency shear modulus and the pressure by the relationship:

$$K(\infty) = \frac{5}{3}\, G(\infty) + 2\,(P - \rho kT) \qquad (4.34)$$

Zukoski[80] developed an expression for the high frequency shear modulus adopting a similar approach to that of Zwanzig and Mountain but in a rather more transparent fashion. This is given in outline below.

A viscoelastic suspension of spherical particles of radius a, total volume, v, with two particles located in the coordinate system is illustrated in Figure 4.7. When the suspension is strained with a linear strain field in the $\underline{x}$ direction the restoring force $\underline{F}$ is given by the rate of change of the interparticle force, $\underline{F}_i$, and the displacement, i.e. infinitesimal strains are assumed so that only linear terms are included:

$$\underline{F} = \nabla.\underline{F}_i.\hat{x}\,(\gamma z) + O\,(\gamma z\hat{x})^2 \qquad (4.35)$$

and the stored energy for the interaction given by the product of the restoring force and the displacement:

$$V_i = \nabla.\underline{F}_i.\hat{x}.\hat{x}\,(\gamma z)^2 \qquad (4.36)$$

Figure 4.7.

The coordinate system for two particles in a viscoelastic fluid.

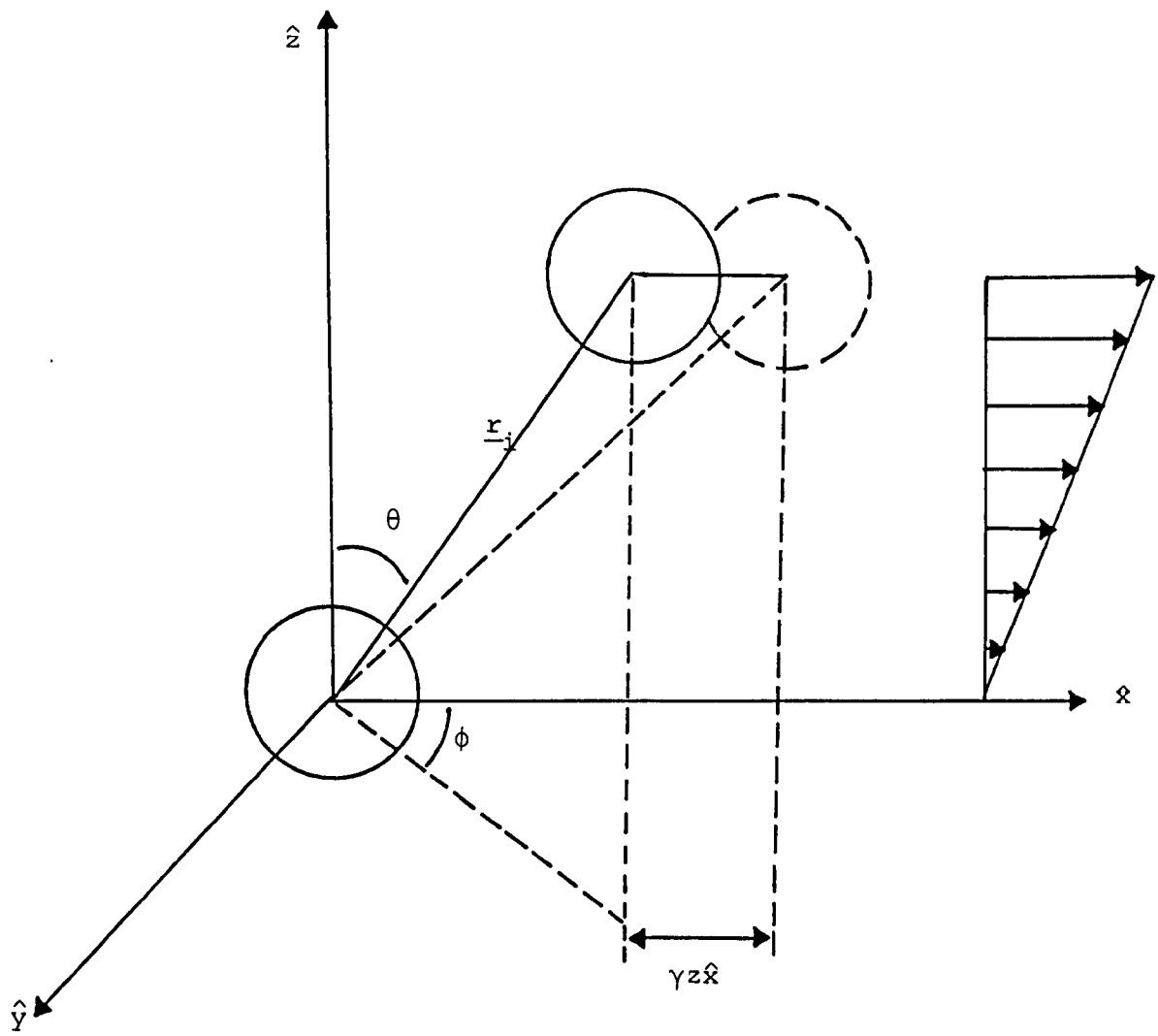

Assuming pairwise additivity the force per particle can be summed over the j neighbours:

$$\underline{F}_i = \sum_j \underline{F}_{ij} = \sum_j \nabla . V_{ij} \qquad (4.37)$$

where V_{ij} is the pair potential. The total energy stored as a result of the strain, V, may be obtained from half the sum over the i-particles in the volume v:

$$\frac{V}{v} = \frac{1}{2v} \left\langle \sum_i \sum_j \gamma^2 z_{ij}^2 \nabla .^2 V_{ij} . \hat{x} . \hat{x} \right\rangle \qquad (4.38)$$

The ensemble average above takes account of the spatial distribution of particle number density in the microstructure.

In the high frequency limit, the small perturbation limits the hydrodynamic contribution and structural relaxation is minimum. The shear modulus may then be obtained from the general model of a linearly viscoelastic material given by:

$$G(\infty) = \frac{2V}{v\gamma^2} \qquad (4.39)$$

Then, combining equations (4.38) and (4.39) an expression for the high frequency limit of the shear modulus may be written as:

$$G(\infty) = \frac{1}{v} \left\langle \sum_{ij} \sum z_{ij}^2 \nabla^2 . V_{ij} . \hat{x} . \hat{x} \right\rangle \qquad (4.40)$$

The ensemble average may be evaluated in terms of the probability of finding a particle at a given position, p(r), expressed in terms of the radial distribution function, g(r), and the number density of particles, ρ:

$$p(\underline{r}_{12}) = \rho^2 g(\underline{r}_{12}) \qquad (4.41)$$

Rewriting the ensemble average and including the probability term yields:

$$G(\infty) = \rho^2 \int_{\underline{r}_{12}} z_{12}^2 \nabla^2 . V_{12} . \hat{x} . \hat{x} \; g(\underline{r}_{12}) \; d\underline{r}_{12} \qquad (4.42)$$

It was convenient to transform the equation (4.42) into polar coordinates:

$$G(\infty) = \rho^2 \int_{\underline{r}} g(\underline{r}) r^2 \left\{ \frac{d^2 V}{dr} \sin^2\theta \cos^2\theta \cos^2\phi \right\} r^2 \sin\theta \, dr \, d\theta \, d\phi \qquad (4.43)$$

In order to make this evaluation of $G(\infty)$ as simple as possible it was assumed that only nearest neighbour interactions were important. This assumption will not introduce significant errors if the range of the interparticle forces is less than a particle radius. Averaging the energy over all the angles:

$$\int_0^{2\pi}\int_0^{\pi} \sin^3\theta \cos^2\theta \cos^2\phi \, d\theta \, d\phi = \frac{2\pi}{15} \tag{4.44}$$

Therefore the high frequency limit of the shear modulus expressed in terms of the spatial arrangement of the microstructure and the restoring force for each particle pair interaction summed over all pairs is given by:

$$G(\infty) = \frac{2\pi}{15} \rho^2 \int g(r) \, r^4 \frac{d^2V}{dr^2} \, dr \tag{4.45}$$

This result is the same as that obtained by Zwanzig and Mountain except that it is dependent only on the second differential of the energy acting between the particles and not on the force. On a physical basis, it is unsatisfactory for the modulus to be dependent on the force in addition to the rate of change of force with displacement as well. These differences have yet to be reconciled although the magnitude of the force makes the difference numerically unimportant. Zwanzig and Mountain also included the small entropic term, ρkT, which accounts for the thermal fluctuations in the system.

4.6. Theoretical Calculations of Viscosity.

For an interacting system of particles three contributions to the coefficient of shear viscosity, η, may be assumed, these contributions being kinetic, η_K, hydrodynamic, η_H, and potential, η_V such that:

$$\eta = \eta_K + \eta_H + \eta_V \tag{4.46}$$

At zero potential only kinetic and hydrodynamic effects contribute to the viscosity.

The viscosity contribution due to kinetic effects, η_K, is due to the Brownian motion of the particles and may be expressed in an analogous manner to the viscosity of gases. For a gas at low density, i.e. below the critical point, the viscosity has been expressed by Maxwell[81] as

$$\eta_K = \left(\frac{m}{kT} \right)^{\frac{1}{2}} \frac{1}{6\pi 3/2a^2} \tag{4.47}$$

where m is the mass of a particle given by:

$$m = \frac{4\pi}{3} a^3 (\rho_p^* - \rho_o^*) \tag{4.48}$$

i.e.

$$\eta_K = \left(\frac{\rho_p^* - \rho_o^*}{27kT\pi a} \right)^{\frac{1}{2}} \tag{4.49}$$

For a colloidal sol the contribution of η_K will be negligible due to the particle size dependence and hence to a good approximation:

$$\eta = \eta_H + \eta_V \tag{4.50}$$

The viscosity contribution due to hydrodynamic effects, η_H, must be included for colloidal systems and are largest at high shear stresses. Long range hydrodynamic interactions are important at high stress and analogies with molecular fluids, where just kinetic and potential contributions are considered, break down. The hydrodynamic contribution to the viscosity may be calculated from Kriegers equation[82] for rigid spherical particles, (see(5. 2)):

$$\eta_H = \eta_O \left(1 - \frac{\phi}{\phi_m} \right)^{-2.5\phi_m} \tag{4.51}$$

where η_O is the viscosity at infinite dilution, ϕ is the volume fraction and ϕ_m the maximum packing fraction. Since the volume fraction may be defined:

$$\phi = \frac{4\pi}{3} \rho a^3 \tag{4.52}$$

equation (4.51) may be rewritten as:

$$\eta_H = \eta_O \left(1 - \frac{4\pi\rho a^3}{3\phi_m} \right)^{-2.5\phi_m} \tag{4.53}$$

The potential contribution to the viscosity, η_V, has been derived from a statistical mechanical treatment by Kirkwood et al[83] and Eisenschitz et al[84] and described by Croxton[64]. An expression analogous to that of Zwanzig and Mountain[79] and Zukoski[80] for shear modulus has been obtained for the potential contribution to the viscosity given by[64]:

$$\eta_V = \frac{2\pi\rho^2}{15} \beta \int_0^\infty \frac{dV}{dr}(r)\, g(r)\, u(r)\, r^3 dr \qquad (4.54)$$

where β is the two body coefficient of friction of the particles and has units of time. The function $u(r)$ is a function of particle separation and represents the distortion of the equilibrium pair distribution function as a result of an applied shear. It is known as the radial distortion function and may be determined by the solution of the following second order equation[64]:

$$\frac{d^2u(r)}{dr^2} + \left(\frac{2}{r} - \frac{1}{kT}\frac{dV}{dr}\right)\frac{du(r)}{dr} - \frac{6}{r^2} = -\frac{m\beta\dot{\gamma}}{(kT)^2}\frac{dV}{dr}\, r \qquad (4.55)$$

for the case of laminar, Newtonian flow. The solution of this equation is not straight forward and there is some discussion in the literature[83,84] of the correct boundary conditions to use. However, for the limiting case of the zero shear viscosity, $\eta(0)$:

$$u(r) \to 1 \quad \text{as} \quad \dot{\gamma} \to 0$$

i.e. the equilibrium pair distribution function is retained undistorted. This will remain true until the structural relaxation time due to diffusive motion approaches $1/\dot{\gamma}$, the time characteristic of the deformation. At the zero limit of the shear rate equation (4.54) reduces to:

$$\eta(0) = \frac{2\pi\rho^2}{15} \beta \int_0^\infty \frac{dV(r)}{dr}\, g(r)\, r^3\, dr + \eta_H \qquad (4.56)$$

Direct comparison of this expression with that of Zwanzig and Mountain for the high frequency limit shear modulus:

$$G(\infty) = \frac{2\pi\rho^2}{15} \int_0^\infty \frac{d^2V}{dr^2}\, g(r)\, r^4\, dr + \rho kT$$

clearly illustrates the similarity of the potential contributions.

Substituting for η_H from equation (4.53) gives:

$$\eta(0) = \frac{2\pi\rho^2}{15} \beta \int_0^\infty \frac{dV(r)}{dr} g(r) r^3 dr + \eta_o \left(1 - \frac{4\pi\rho a^3}{3\phi_m}\right)^{-2.5\phi_m} \quad (4.57)$$

However, in many cases of colloidal systems showing significant particle interactions, the hydrodynamic contribution will be small compared to the potential contribution in the low stress limit.

Chapter Five

Rheological Properties of Colloidal Systems

Chapter Five. Rheological Properties of Colloidal Systems.

5.1. Introduction.

The rheological properties of colloidal dispersions are among their most important characteristics, rheological measurements serving to provide information on both the stability of dispersions and on the nature of the disperse phase. When considering the mechanical properties of colloidal dispersions it is important to understand how the hydrodynamic forces that occur during flow are modified by the presence of particles. The particle shape and charge, the extent of aggregation, the presence of adsorbed layers and the volume fraction all have an effect and must be taken into consideration.

Dilute systems are in many respects easier to deal with than concentrated dispersions where the problem of multibody interactions arises. Hence much work in the literature is concerned with volume fractions of less than 0.2. Many industrial suspensions are concentrated and there is thus the need to extend theories to systems of high volume fraction; this has been attempted by some workers.

Many colloidal dispersions are viscoelastic and can be characterised by a viscosity coefficient, η, which is defined as the ratio of shear stress, τ, to shear rate, $\dot{\gamma}$:

$$\eta = \frac{\tau}{\dot{\gamma}} \qquad (5.1)$$

The relative viscosity, η_r, is conveniently defined

$$\eta_r = \frac{\eta}{\eta_o} \qquad (5.2)$$

where η_o is the viscosity of the continuous phase. In addition, the rigidity of a colloidal dispersion is characterised by the shear modulus, G,

defined:

$$G = \frac{\tau}{\gamma} \qquad (5.3)$$

where γ is the strain.

Stability of colloidal systems is often achieved by the adsorption of a layer of molecules onto the surface of the particles to provide electrostatic or steric stabilisation. In this case the effective volume fraction, ϕ', must be used in the viscosity and elasticity calculations. For a densely packed, well defined layer the layer will not be free draining and any solvent in the layer can be considered to be trapped so that the hydrodynamic volume of each particle is increased by the volume of the adsorbed layer such that:

$$\phi' = \phi\left(1 + \frac{\delta}{\alpha}\right)^3 \qquad (5.4)$$

where δ is the thickness of the adsorbed layer and α is the core particle radius.

Aggregation is a common phenomenon in colloidal dispersions and this has a substantial effect upon the viscoelastic properties of a system, this must therefore be considered; also the effect of shear upon particle aggregation.

The presence of charge manifests itself in three ways, these are termed the three electroviscous effects and all increase the viscosity of a system. These effects are minimal for the type of system under consideration in this work, large, sterically stabilised particles and will only be briefly detailed in (5.4). The electroviscous effects are greatest for dispersions of small, highly charged particles.

Various models have been proposed to describe the viscosity of colloidal systems for both Newtonian and non-Newtonian behaviour. Pertinent models and, where applicable, the corresponding equations are described in

(5.2) and (5.5). The special case of zero shear rate viscosity is considered in (5.3) and the electroviscous effects outlined in (5.4). A model for the theoretical shear modulus and bulk modulus is presented in (5.6), together with the derivation of the theoretical expressions.

5.2. Viscosity of Newtonian Dispersions.

A colloidal suspension is characterised by a viscosity coefficient which is greater than the coefficient of the suspending fluid.[85] This is a consequence of an enhanced rate of energy dissipation during laminar shear flow and is due to the perturbation of the streamlines by the colloidal particles as illustrated in Figure 5.1.

Einstein[86,87] developed a theoretical expression to describe the viscosity of a colloidal suspension in terms of the system volume fraction. He took the simplest case of a system of rigid, uncharged spheres which exhibit no long range electrostatic or steric interactions and no aggregation and considered the particles to be small compared with the measuring apparatus, thus ignoring wall effects. He considered the particles to be at the limit of infinite dilution so that interparticle separations were large and the hydrodynamic interactions between particles could be ignored. In this way the increase in viscosity produced by one particle could be summed over the total number of particles. The other assumptions he made were that the flow rates were so slow that inertial effects were negligible, i.e. he assumed low Reynolds number hydrodynamics, and that there was no slip at the particle/medium interface. He derived the expression:

$$\eta_r = 1 + \frac{5}{2}\phi + 4\phi^2 + \frac{11}{2}\phi^3 + 7\phi^4 + \ldots\ldots\ldots \qquad (5.5)$$

which for low volume fraction dispersions reduces to:

$$\eta_r = 1 + \frac{5}{2}\phi \qquad (5.6)$$

Figure 5.1.

Dilation of the streamlines around one particle.

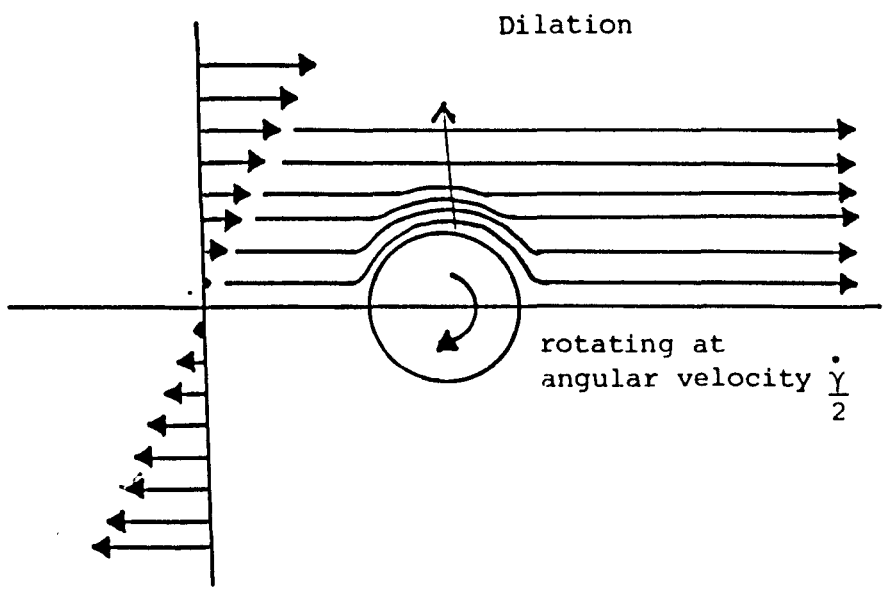

by neglecting all terms in ϕ of higher than order unity. This expression is the well known Einstein equation which is also expressed:

$$\eta_r = 1 + [\eta]\phi \qquad (5.7)$$

where $[\eta]$ is the intrinsic viscosity defined as

$$[\eta] = \text{Lim}_{\phi \to 0} \left(\frac{\eta_r - 1}{\phi} \right) \qquad (5.8)$$

and equal to 2.5 for dispersions of spheres regardless of the size or size distribution of the particles.[82] The Einstein equation can be used with a negligible error for $\phi < 0.01$ for suspensions of particles approximating to hard spheres.

At volume fractions of greater than $\phi = 0.01$ the viscosity of a suspension is increased due to the formation of temporary doublets, triplets and higher order multipletswhich enhance the rate of energy dissipation. Various models, both theoretical and empirical, have been proposed to describe the viscosity of disperse systems at volume fractions of $\phi > 0.01$. Some of the more prominent theories will be reviewed here.

One school of thought is the use of a general power series equation in volume fraction of the form of equation (5.5) given by:

$$\eta_r = 1 + k_1\phi + k_2\phi^2 + k_3\phi^3 + \ldots\ldots \qquad (5.9)$$

For suspensions of rigid, uncharged spherical particles equation (5.9) must approach equation (5.6) in the dilute limit and k_1 is taken as having a value of 2.5. The coefficient k_2 is calculated from the perturbation of the streamlines by collision doublets and k_3, k_4 etc. are used to describe higher order collisions. Various values have been obtained for k_2[85] from theoretical hydrodynamic approaches, for example Batchelor and Green[88,89] obtained a value of 7.6. A rigorous hydrodynamic solution for coefficients k_3, k_4 etc. is not available due to the difficulties inherent in handling three-body, and higher, collisions. Hence experimental

estimates have been made of k_s, these vary from 16 to 50.[85] At very high concentrations, a large number of terms in the power series would be required to describe the viscosity behaviour adequately; no satisfactory physical description has been developed to calculate these coefficients.

An exponential relationship has also been proposed for disperse systems which may also be expanded as a power series, this is given by:[85]

$$\eta_r = \exp(k_1\phi) \qquad (5.10)$$

where k_1 is a constant and would be equal to 2.5 if equation (5.10) is to reduce to equation (5.6) at infinite dilution. A more general case is given by:

$$\eta_r = \exp\left(\frac{k_1 h^\dagger \phi}{1 - h^\dagger \phi}\right) \qquad (5.11)$$

where the concentration is corrected by a solvation factor, $h^\dagger$.

As the volume fraction increases the relative viscosity increases rapidly up to a particular volume fraction when the dispersed particles lock into a rigid structure, flow ceases and the viscosity approaches infinity. This volume fraction is the maximum packing fraction, ϕ_m, which is dependent on the type of packing. For hexagonal close packing and face-centred cubic packing, both with coordination numbers of 12, $\phi_m = 0.74$; for body-centred cubic packing with a coordination number of 8, $\phi_m = 0.68$ and for random close packing with a coordination number of 6, $\phi_m = 0.62$. Figure 5.2 illustrates the effect volume fraction has on relative viscosity; in the dilute region the gradient is the intrinsic viscosity, $[\eta]$, while at high concentrations there is considerable deviation from this behaviour.

Mooney[90] has derived an equation of the exponential form from space filling considerations and taking into account the maximum packing

Figure 5.2.

Effect on viscosity of increasing volume fraction,

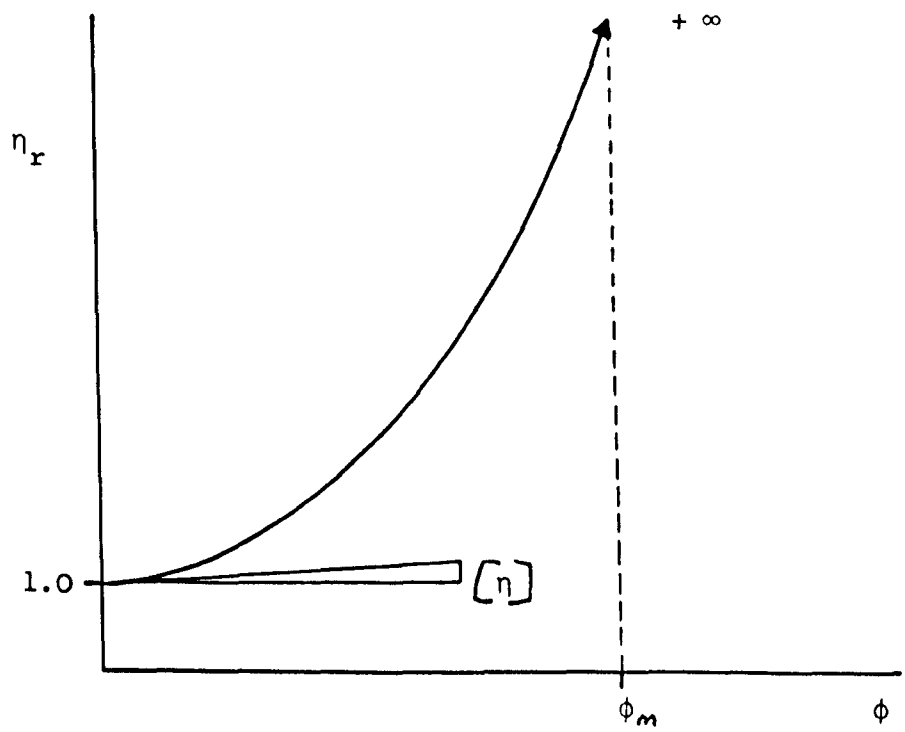

fraction:

$$\eta_r = \exp\left(\frac{[\eta]\,\phi}{1 - \frac{\phi}{\phi_m}}\right) \qquad (5.12)$$

Krieger and Dougherty[82] contended that Mooney had included the packing fraction twice and corrected his derivation to obtain the following expression:

$$\eta_r = \left(1 - \frac{\phi}{\phi_m}\right)^{-[\eta]\phi_m} \qquad (5.13)$$

where the intrinsic viscosity is equal to 2.5 for rigid uncharged spheres. The experimental data of Woods and Krieger[91] for polystyrene and polyvinyl toluene latices are presented in Figure 5.3. A good fit to equation (5.13) can be seen using a maximum volume fraction for flow of 0.68 which is in reasonable agreement with the value for random packing. To fit Mooney's equation, equation (5.12), to the data required a value for the packing fraction of 1.05 to be used which is clearly inconsistent with any packing model for monodisperse rigid spheres.

It is possible to derive Krieger's equation using a mean field argument as was shown by Ball and Richmond[92], starting with Einstein's equation, equation (5.7):

$$\eta_r = 1 + [\eta]\,\phi = \frac{\eta}{\eta_o}$$

Differentiating this gives the initial rate of change of viscosity:

$$\frac{d\eta}{d\phi} = [\eta]\,\eta_o \qquad (5.14)$$

The mean field argument predicts that the initial rate of change of viscosity is everywhere the same. Hence on addition of a small number of particles:

$$\frac{\delta\eta}{\delta\phi} = [\eta]\,\eta \qquad (5.15)$$

The volume occupied by the particles must be taken into account as this is unavailable volume. This is termed the excluded volume

Figure 5.3.

High shear rate relative viscosity as a function of volume fraction (open symbols) and as a function of the volume fraction of polymer plus adsorbed surface active agent (filled symbols). Triangles, squares and circles refer respectively to particles of 0.2, 0.66 and 1.1 μm diameter. Full line is fit to Krieger's equation (5.13).

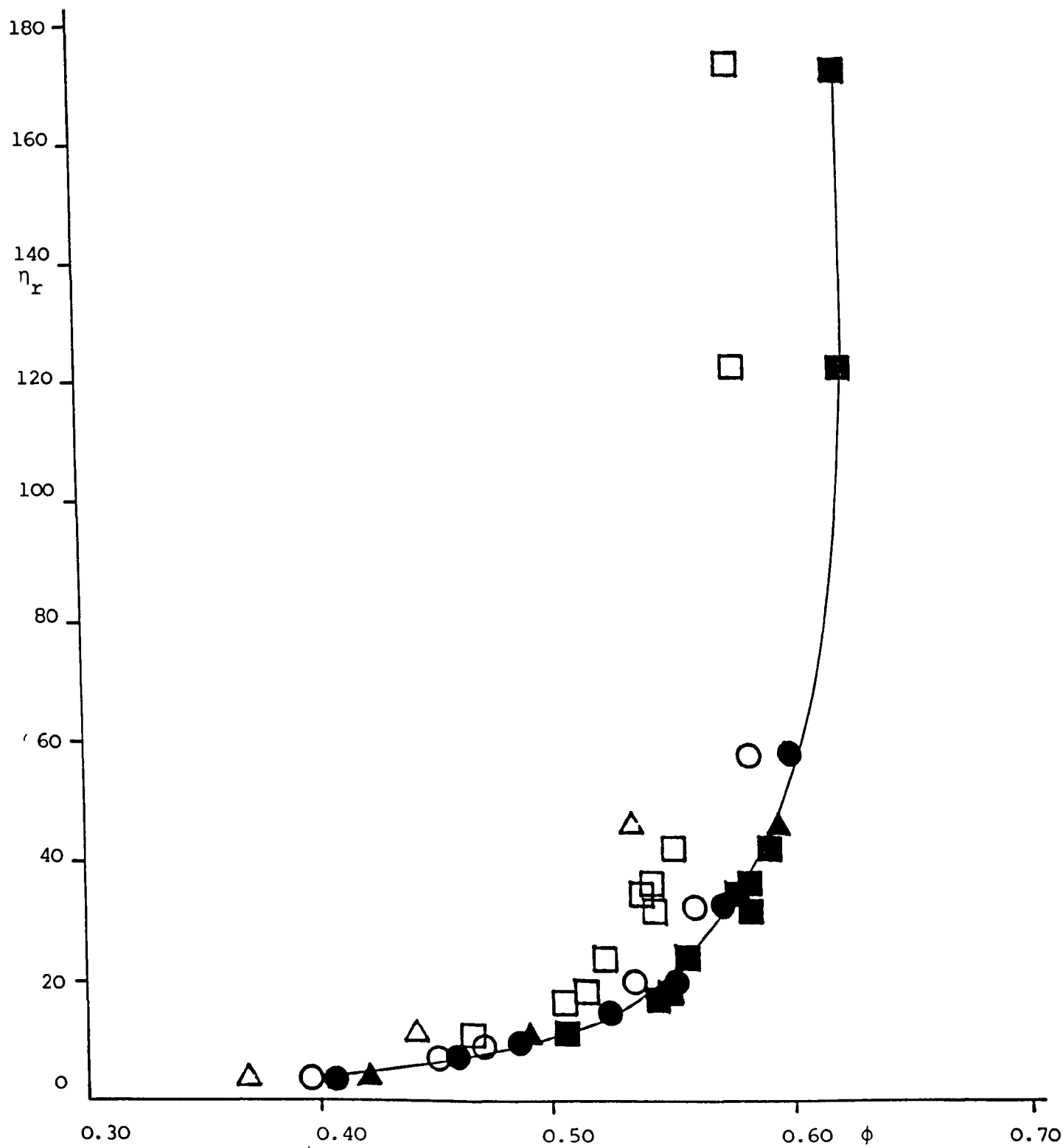

expressed:

$$\text{Excluded volume} = \frac{4\pi a^3}{3\phi_m} \tag{5.16}$$

Hence for N_p particles per unit volume of dispersion, the second addition of particles is to a reduced volume:

$$= 1 - \frac{N_p 4\pi a^3}{3\phi_m} \tag{5.17}$$

$$\text{Hence change in volume fraction} = \frac{\delta\phi}{1-\frac{\phi}{\phi_m}} \tag{5.18}$$

Then from equation (5.15):

$$\frac{d\eta}{\eta} = \frac{[\eta]d\phi}{1 - \frac{\phi}{\phi_m}} \tag{5.19}$$

Therefore:

$$\int \frac{d\eta}{\eta} = [\eta] \int \frac{d\phi}{1 - \frac{\phi}{\phi_m}} \tag{5.20}$$

Therefore:

$$\ln \eta = -[\eta]\phi_m \ln \left(1 - \frac{\phi}{\phi_m} \right) + \text{constant} \tag{5.21}$$

Boundary conditions are:

$$\eta \to \eta_o \quad \text{as} \quad \phi \to 0$$

Hence:

$$\ln \eta = -[\eta]\phi_m \ln \left(1 - \frac{\phi}{\phi_m} \right) + \ln \eta_o \tag{5.22}$$

So:

$$\eta_r = \left(1 - \frac{\phi}{\phi_m} \right)^{-[\eta]\phi_m} \tag{5.23}$$

which is Krieger's equation, equation (5.13).

Krieger's exponential equation may be expanded as a power series and compared with that obtained by hydrodynamic analysis:[85]

$$\eta_r = 1 + 2.5\phi + 5.1\phi^2 + 9.5\phi^3 + 15.5\phi^4 + \ldots\ldots \tag{5.24}$$

From this it can be expected that Krieger's equation should give the best fit at volume fractions of ϕ <0.25.

At volume fractions of greater than ϕ= 0.25 it is common for non-Newtonian behaviour to occur, this is discussed in (5.5).

Polydispersity may be taken account in an expression of the form of Krieger's equation:

$$\eta_r = \left(1 - \frac{\phi}{\phi_m \lambda_p}\right)^{-[\eta]\phi_m} \qquad (5.25)$$

where λ_p is the polydispersity factor where $\lambda_p = 1$ for monodisperse systems and $\lambda_p < 1$ for polydisperse systems.

It is clear that any model predicting viscous behaviour beyond the dilute limit must include ϕ_m and to match the dilute limit must contain $[\eta]$.[92a] It is notable that almost all physical and chemical features of a suspension are characterised through either $[\eta]$ or ϕ_m or both. The intrinsic viscosity reflects the particle shape as well as the primary electroviscous effect, which is discussed in (5.4), and a degree of shear dependence consistent with the former. For uncharged spheres there is no shear dependence in $[\eta]$ and in general the dependence is weak. There is no effect of particle size, polydispersity or particle surface chemistry except where aggregation takes place in which case $[\eta]$ characterises the aggregates with excluded liquid rather than the dispersed particles.

It is through ϕ_m that most system parameters are manifested and always more than through $[\eta]$. Particle shape is an obvious factor in the value of ϕ_m, different shapes having different packing efficiencies. For a given particle shape polydispersity enters by increasing ϕ_m since a polydisperse system has more packing faults and can therefore allow slip

at a higher concentration. The maximum packing fraction, ϕ_m, also reflects the state of aggregation and therefore indirectly represents the particle charge and surface chemistry that influence the tendency to form aggregates, their microstructure and their resistance to breakdown.

Another approach adopted by a number of workers to describe the viscosity of colloidal dispersions is the use of a cell model.[93] Frankel and Acrivos[94], Ackerman and Shen[95] and Graham[96] used cell models with simple cubic symmetry and calculated the total energy dissipated as the sum of that dissipated by fluid flow around a central sphere and that due to the interactions between the spheres calculated by means of lubrication theory.

In another approach to the problem Cross[97] also took a kinetic argument and described the experimental rheogram, omitting dilatancy by an equation of the form:

$$\frac{\eta - \eta(\infty)}{\eta(0) - \eta(\infty)} = \frac{1}{1+(k^{\dagger}\dot{\gamma})^{n}} \qquad (5.25)$$

which is useful for curve fitting exercises but sheds little insight into the mechanism taking place.

Pätzold[98], working with pseudo-Newtonian suspensions of monosized glass spheres in mineral oil and glucose/water solutions found that, after shear, the spheres were ordered in a two-dimensional hexagonal packing as a result of flow in the shear field, the two dimensional layers lying parallel to the planes of constant shear. The beads were large, 14 - 79 μm, and hence Brownian forces were minimal and the flow response obtained dependent upon the flow field superimposed upon the suspension and the hydrodynamics of flow about the particles. From this it was concluded that such conditions favour the formation of a two dimensional structure.

5.3. Zero Shear Viscosity.

In a colloidal dispersion particles move continuously with Brownian motion;[93] this motion may be usefully characterised in terms of the Péclet number which is given by:

$$\text{Péclet number} = \frac{6\pi\eta_o a^3}{kT} \qquad (5.27)$$

which gives the time taken for a particle to diffuse a distance equal to its radius. This characterises the time taken for the restoration of the equilibrium microstructure after a disturbance, e.g. convection, and is therefore the relaxation time of the microstructure. The time scale of shear flow is the reciprocal of the shear rate, $\dot{\gamma}$. The dimensionless group formed by the ratio of these times, the reduced shear rate, $\dot{\gamma}_r$, is given by:

$$\dot{\gamma}_r = \frac{6\pi\eta_o a^3\dot{\gamma}}{kT} \equiv De \qquad (5.28)$$

which gives the relative importance of diffusion and convection to the microstructure.

At low shear stresses:

$$\frac{6\pi\eta_o a^3\dot{\gamma}}{kT} << 1 \qquad (5.29)$$

and the particle distribution is only slightly altered by the flow, i.e. Brownian motion is dominant. In this case the structure of the system remains isotropic and the viscosity approximates to its zero shear limiting value, $\eta(0)$.

Batchelor[99-101] studied this case and extended it to Einstein's equation, equation (5.6), by solving the hydrodynamic equations for hard sphere suspensions for two flow fields:

$$\frac{\eta(0)}{\eta_o} = 1 + 2.5\phi + 6.2\phi^2 + O(\phi^3) \qquad (5.30)$$

and obtained an analogous expression for extensional flow;

$$\frac{\eta(0)}{\eta_o} = 1 + 2.5\phi + 7.6\phi^2 + O(\phi^3) \qquad (5.31)$$

He derived the coefficients of ϕ^2 from the combination of far field interactions and the rotation of temporary doublets formed during particle collisions.

5.4. Electroviscous Effects.

Stable colloidal dispersions in aqueous media frequently owe their stability, at least in part, to the forces of electrostatic repulsion between the particles, see Chapter Three. Three distinct electroviscous effects have been identified and the result of these can be a dramatic change in viscosity with changes in the electrolyte concentration or the pH of the suspending medium.

The primary electroviscous effect was first identified by von Smoluchowski and is an increment to the intrinsic viscosity due to the distortion under shear of the electrical double layer:

$$[\eta] = 2.5\ (1 + E_1) \qquad (5.32)$$

where E_1 is the primary electroviscous factor, von Smoluchowski obtained the following expression for the relative viscosity:

$$\eta_r = 1 + 2.5\phi \left\{ 1 + (2\varepsilon_r \varepsilon_o \zeta)^2 \frac{1}{\lambda_o \eta_o a^2} \right\} \qquad (5.33)$$

where ε_r is the relative permittivity, ε_o is the permittivity of free space, ζ is the zeta potential and λ_o is the specific conductivity of the continuous phase.

Booth[102] derived an equation for weak flows i.e. small double layer distortions and low zeta potentials, $\zeta < 25$mV:

$$\eta_r = 1 + 2.5\phi \left\{ 1 + (2\varepsilon_r \varepsilon_o \zeta)^2 \frac{(\kappa a)\ (1 + \kappa a)^2\ Z\ (\kappa a)}{\lambda_o \eta_o a^2} \right\} \qquad (5.34)$$

where κ is the reciprocal Debye length and $Z(\kappa a)$ is Booth's function, a

power series with two limiting forms for extended diffuse layers:[93]

$$\text{small } \kappa a \; : \; Z(\kappa a) = \frac{1}{200\,\pi\kappa a} + \frac{11\,\kappa a}{3200\pi} \qquad (5.35)$$

$$\text{large } \kappa a \; : \; Z(\kappa a) = \frac{3}{2\pi(\kappa a)^4} \qquad (5.36)$$

Watterson and White[103] considered the more general case, without restrictions on the zeta potential, and obtained a numerical solution for the intrinsic viscosity as a function of the zeta potential for given κa values. Russel[104] and Lever[105] extended the analysis to stronger flows and both predicted a shear thinning contribution and normal shear stresses.

The secondary electroviscous effect is an increase in the viscosity at finite concentrations due to Coulombic interactions between the double layers of different particles. In practice this is often larger than the primary electroviscous effect and more important. When the particles are uncharged they approach to a small distance of separation, rotate with the vorticity of the shear field and separate when the doublet reaches the mirror image of the collision configuration. However, when the particles are charged the double layer repulsion increases the minimum interparticle separation and prevents the particles from approaching closer than a surface-surface separation of d_o^*, and a centre-centre separation of L_o where:

$$L_o = 2a + d_o^* \qquad (5.37)$$

The minimum separation between particles and hence the pair distribution function is dependent on the ratio of the net interparticle repulsive forces to those due to Brownian motion given by Russel[106,107] to be the dimensionless group $\alpha^{*\dagger}$:

$$\alpha^{*\dagger} = \frac{16\pi^2\varepsilon_r\varepsilon_o\zeta^2a^4\kappa \exp(2\kappa a)}{kT} \qquad (5.38)$$

For the case of strong repulsive forces, $\alpha^{*\dagger} >> 1$, and L_o may be

defined as:

$$L_o = \frac{1}{\kappa} \ln \left(\frac{\alpha^{*\dagger}}{\ln \left(\frac{\alpha^{*\dagger}}{\ln \alpha^{*\dagger}} \right)} \right) \qquad (5.39)$$

Under the application of shear stress the value of d^* is reduced from d_o^* so that

$$\tau \to 0 \qquad L \to 2a + d_o^*$$

$$\tau \to \infty \qquad L \to 2a$$

This clearly indicates a shear thinning response with limiting values at high and low stress of the type found by Krieger.[82] Russel gives the expression for the zero shear limit of the relative viscosity:

$$\frac{\eta(0)}{\eta_o} = 1 + [\eta]\phi + \frac{2}{5}[\eta]^2\phi^2 + \frac{3}{40} \ln\left(\frac{\alpha^{*\dagger}}{\ln\alpha^{*\dagger}}\right) \left[\ln \frac{\alpha^{*\dagger}}{\ln \frac{\alpha^{*\dagger}}{\ln\alpha^{*\dagger}}} \right]^4 \frac{\phi^2}{(\kappa a)^5} \qquad (5.40)$$

hydrodynamic interaction term

electrostatic pair interaction term

The tertiary electroviscous effect is due to the distortion of the particle itself as a result of electrostatic forces arising from the presence of charges on the particles. For dispersions of particles stabilised by a layer of polyelectrolyte, adsorbed or chemically bound to the surface of the particles, the problem resolves to the calculation of the conformation of the stabiliser molecules and the use of equation (5.4) for the calculation of the effective volume fraction.

5.5. Viscosity of non-Newtonian Dispersions.

Probably the most common type of non-Newtonian flow that is found with suspensions is a decrease in viscosity with increasing shear rate, i.e. shear thinning behaviour.[85] Shear thinning, and shear thickening, behaviour is commonly observed in colloidal dispersions at volume fractions of $\phi > 0.25$

although under conditions where a suspension exhibits marked electroviscous effects the onset of non-Newtonian flow can occur at volume fractions considerably below 0.25.

At high shear stress the Péclet number is large:

$$\frac{6\pi\eta_o a^3\dot{\gamma}}{kT} \gg 1 \qquad (5.41)$$

and the microstructure is significantly affected by the flow giving rise to shear thinning behaviour in many viscoelastic systems. Various models have been proposed to explain this.

Krieger and Dougherty[82,108] have developed a theory to explain non-Newtonian flow in hard sphere dispersions in terms of particle doublet rotation and destruction, resulting in the equation:

$$\eta = \eta(\infty) + \frac{\eta(0) - \eta(\infty)}{1 + \frac{a^3\tau}{kT}} \qquad (5.42)$$

An isolated sphere, under a steady shear rate, $\dot{\gamma}$, rotates at a steady angular velocity of $\dot{\gamma}/2$ with the fluid velocity perturbed in the neighbourhood, see Figure 5.1. If a second sphere is introduced into this perturbed fluid region the two spheres no longer rotate independently but the velocity of the medium about one sphere will give rise to a stress on the other sphere and vice versa. As a consequence of this, claim the authors, the spheres take on a doublet rotation which, in high shear fields subsequently causes the particles to separate. This doublet rotation arises purely from hydrodynamic forces and causes more energy dissipation than would two single particles. Hence, the destruction of the doublet as a consequence of high shear causes the system to be shear thinning.

A more likely explanation of shear thinning behaviour is that forwarded by Hoffman[109] which involves the transition from a three-

dimensional structure to a two-dimensional structure. Particles randomly placed by the dominance of Brownian forces jam into one another as they are forced to move in a shear field. When hydrodynamic forces predominate at high shear rates, however, particles move in layers which glide over one another with essentially no jamming. Without particle jamming less energy is required to make the suspension flow and thus the high shear plateau viscosity is lower than the low shear plateau in shear thinning systems.

In flocculated systems the attractive force between the particles is the dominant colloidal interaction controlling their flow response. When there is no external shear applied to the system a flocculated network of particles is established throughout the sample. Under shear, however, this network is broken down into smaller units of flocculated spheres which can withstand the force of the shear field. The size of the units which generally survive will be determined by a balance between the forces of shear which tend to break the units down and the forces of attraction which hold the spheres together. The appropriate dimensionless group characterising this process is $\eta_o a^3 \dot{\gamma}/A$.

Hoffman[109] postulated that each flocculated unit rotates in the shear field and forms layers, much as individual spheres do in Newtonian systems, (see (5.2)). As the shear rate increases the unit size decreases, ultimately becoming an individual sphere and it is thus reasonable to presume that as this happens the spheres order in layers as with the pseudo-Newtonian cases and the relative viscosity approaches the constant value obtained with a pseudo-Newtonian system at high shear. This is what was found by Willey and Macosko[110] working with two flocculated, shear thinning suspensions and one Newtonian suspension. This is not proof that spheres order in a flocculated suspension at high shear but the results do support the concept.

The prediction of structural change in flocculated systems with a change in shear is compounded by the fact that these systems are thixotropic.[110] Once shear is initiated some finite time is required to break down the network of agglomerated particles into units of flocculated spheres which persist under the field of shear to which they are exposed. As smaller and smaller units are formed more fluid is liberated from the interstices within the flocculated units of particles, thereby reducing the effective volume of solids and causing a decrease in viscosity. Similar arguments involving the effective volume of solids can be invoked to explain the shear thinning response.

5.6. Shear Modulus of Colloidal Systems.

A quasi-static lattice model has been developed by Buscall and Goodwin and coworkers[13,111] for the theoretical calculation of the high frequency limit shear modulus, $G(\infty)$, as measured by pulse shearometry. The model is based on a concentrated dispersion assuming an ordered array of monodisperse colloidal particles, and on the energies of interaction acting between a pair of the particles. For a high frequency pulse the time period of the wave is small with respect to the relaxation time of the particles in the array and similarly the relaxation time of the electrical double layer is small compared with the relaxation time of the lattice. Under these conditions the authors assumed that the equations corresponding to the equilibrium condition of the electrical double layer could be used to calculate the restoring force of the lattice.

Consider a pair of particles initially separated by a distance $\hat{R}$, one at the origin of a coordinate system, the other at A, as illustrated in Figure 5.4. A small shearing strain ds^*/dz has the effect of displacing the second particle a distance s^* from A $(\hat{R},\hat{\theta},\hat{\Phi})$ to A^1 $(\hat{R}_1,\hat{\theta}_1,\hat{\Phi}_1)$ and the concomitant change in particle separation $\hat{R}$ may be

Figure 5.4.

Coordinate system for evaluating the effect of shear on pairwise particle interaction.[111]

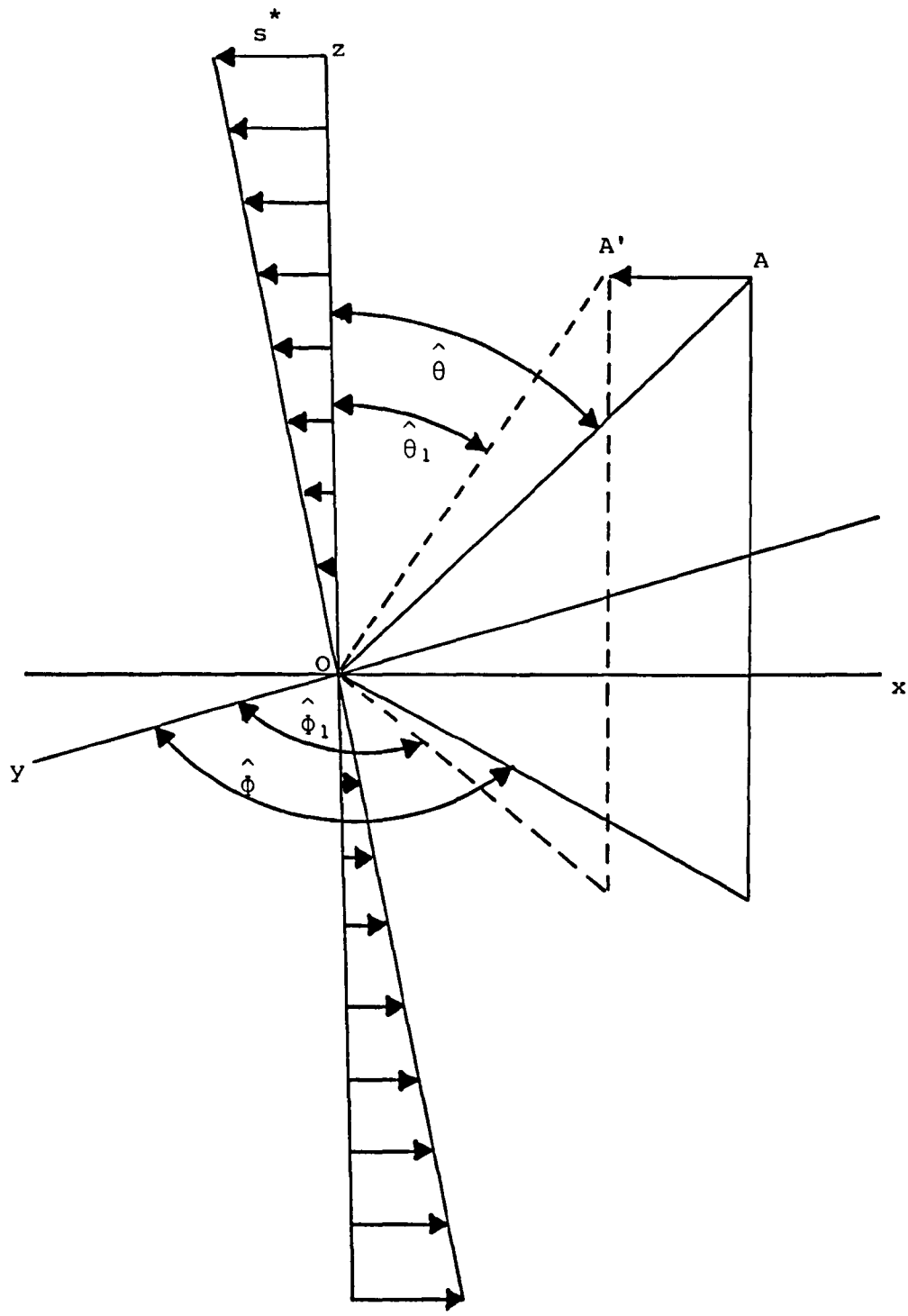

related to s^* by:

$$2\hat{R}\,\hat{dR} - (\hat{\delta R})^2 = 2\hat{R}\,\delta\sin\hat{\Phi} - s^{*2} \tag{5.43}$$

which for linear strains can be linearised to yield:

$$\hat{\delta R} = \hat{R}\,\frac{ds}{dz}\cos\hat{\theta}\sin\hat{\theta}\sin\hat{\Phi} \tag{5.44}$$

For small strains the force acting along $\hat{R}$ is given by:

$$F = \hat{\delta R}\,\frac{\partial^2 V_T}{\partial \hat{R}^2} \tag{5.45}$$

and the restoring force, the component of F in the x-direction given by:

$$F_x = \hat{\delta R}\,\frac{\partial^2 V_T}{\partial \hat{R}^2}\sin\hat{\theta}_1\sin\hat{\Phi}_1 \tag{5.46}$$

Then, substituting for $\hat{\delta R}$ from equation (5.44) into equation (5.46) for small strains yields:

$$F_x = \hat{R}\,\frac{\partial^2 V_T}{\partial \hat{R}^2}\,\frac{ds^*}{dz}\sin^2\hat{\theta}\cos\hat{\theta}\sin^2\hat{\Phi} \tag{5.47}$$

The contribution of F_x to the shear stress is given by F_x/A^*_{xy} where A^*_{xy} is the projected area of the particle pair in the xy-plane. The volume occupied by the two particles is $\frac{\pi\hat{R}^3}{3\phi_m}$ so that:

$$A_{xy}^* = \frac{\pi\hat{R}^2}{3\phi_m\cos\hat{\theta}} \tag{5.48}$$

and the contribution of F_x to the shear stress becomes:

$$\tau_1 = \frac{3\phi_m}{\pi\hat{R}}\,\frac{\partial^2 V_T}{\partial \hat{R}^2}\,\frac{ds^*}{dz}\cos^2\hat{\theta}\sin^2\hat{\Theta}\sin^2\hat{\Phi} \tag{5.49}$$

Averaging the pairwise contribution to the shear stress over all orientations gives an average shear stress expressed:

$$\bar{\tau}_1 = \frac{3\phi_m}{4\pi^2\hat{R}}\,\frac{\partial^2 V_T}{\partial \hat{R}^2}\,\frac{ds^*}{dz}\int_0^{2\pi}\int_0^{\pi}\cos^2\hat{\theta}\sin^2\hat{\theta}\sin^2\hat{\Phi}\,d\hat{\theta}\,d\hat{\Phi} \tag{5.50}$$

Since each particle has n nearest neighbours the total stress is given

by:

$$\tau = \sum_{i=1}^{n} \tau_i = n\bar{\tau}_1 \qquad (5.51)$$

or

$$\tau = \frac{3n\phi_m}{32\hat{R}} \frac{\partial^2 V_T}{\partial R^2} \frac{ds^*}{dz} \qquad (5.52)$$

Finally, the authors obtained an expression for the shear modulus at high frequency, ignoring relaxation, given by:

$$G_\infty^{th} = \frac{\tau}{ds/dz} = \frac{\alpha^{\dagger *}}{\hat{R}} \left(\frac{\partial^2 V_T}{\partial R^2} \right) \qquad (5.53)$$

with

$$\alpha^{\dagger *} = \frac{3}{32} \phi_m n \qquad (5.54)$$

and $\hat{R}$ may be expressed:

$$\hat{R} = 2a \left(\frac{\phi_m}{\phi} \right)^{1/3} \qquad (5.55)$$

For face-centred cubic (f.c.c.) and hexagonal close packed structures $\alpha^{\dagger *}$ reduces to 0.833 whereas for a body-centred cubic (b.c.c.) array $\alpha^{\dagger *} = 0.510$. The type of structure in a concentrated colloidal dispersion is still under debate, there is evidence from light scattering and electron microscopy for b.c.c. at low volume fractions and f.c.c. at high volume fractions.

The separation of particles in an ordered array, given by $\hat{R}$, is expressed as follows for the f.c.c. and b.c.c. cases:

$$\hat{R}_{f.c.c.} = 2a \left(\frac{0.74}{\phi} \right)^{1/3} \qquad (5.56)$$

$$\hat{R}_{b.c.c.} = 2a \left(\frac{0.68}{\phi} \right)^{1/3} \qquad (5.57)$$

The interaction energy, V_T, was defined by the sum of the van der Waals attractive energy, V_A, and the electrostatic repulsive energy, V_R. The second differential of the energy function with respect to the

distance was determined.[13,111]

For large particles, $\kappa a > 10$:

$$V_T = -\frac{A}{12}\left(\frac{1}{x^2+2x} + \frac{1}{x^2+2x+1} + 2\ln\frac{x^2+2x}{x^2+2x+1}\right) + 2\pi\varepsilon_r\varepsilon_o a\psi_d^2 \ln\left(1 + \exp\left(-\kappa H_o\right)\right) \quad (5.58)$$

where $x = \frac{H_o}{2a}$

$$\frac{dV_T}{dH_o} = -F = \frac{A}{24a}\left(\frac{-2x+2}{(x^2+2x)^2} - \frac{2x+2}{(x^2+2x+1)^2} + \frac{2(2x+2)}{(x^2+2x)(x^2+2x+1)}\right) - 2\pi\varepsilon_r\varepsilon_o a\psi_d^2 \frac{\kappa\exp\left(-\kappa H_o\right)}{\left(1 + \exp\left(-\kappa H_o\right)\right)} \quad (5.59)$$

$$\frac{d^2V_T}{dH_o^2} = \frac{A}{24a^2}\left[\frac{3(x^2+2x)+4}{(x^2+2x)^3} + \frac{3}{(x+1)^4} - \frac{6(x^2+2x)+4}{(x^2+2x)^2(x+1)^2}\right] + 2\pi\varepsilon_r\varepsilon_o a\psi_d^2\left(\frac{\kappa^2\exp\left(-\kappa H_o\right)}{\{1+\exp\left(-\kappa H_o\right)\}^2}\right) \quad (5.60)$$

For small particles, $\kappa a < 3$:

$$V_T = -\frac{A}{12}\left(\frac{1}{x^2+2x} + \frac{1}{x^2+2x+1} + 2\ln\frac{x^2+2x}{x^2+2x+1}\right) + \frac{4\pi\varepsilon_r\varepsilon_o a\psi_d^2}{H_o + 2a}\exp\left(-\kappa H_o\right) \quad (5.61)$$

$$\frac{dV_T}{dH_o} = -F = \frac{A}{24a}\left(\frac{-2x+2}{(x^2+2x)^2} - \frac{2x+2}{(x^2+2x+1)^2} + \frac{2(2x+2)}{(x^2+2x)(x^2+2x+1)}\right) - 4\pi\varepsilon_r\varepsilon_o a\psi_d^2 \frac{(\kappa H_o+2a\kappa+1)\exp\left(-\kappa H_o\right)}{(H_o+2a)^2} \quad (5.62)$$

$$\frac{d^2V_T}{dH_o^2} = \frac{-dF}{dH_o} = \frac{A}{24a^2}\left[\frac{3(x^2+2x)+4}{(x^2+2x)^3} + \frac{3}{(x+1)^4} - \frac{6(x^2+2x)+4}{(x^2+2x)^2(x+1)^2}\right] + 4\pi\varepsilon_r\varepsilon_o a\psi_d^2 \frac{\exp\left(-\kappa H_o\right)\left[\kappa^2(H_o+2a)^2 + 2\kappa(H_o+2a)+2\right]}{(H_o+2a)^3} \quad (5.63)$$

The shear modulus may then be expressed as:

$\kappa a > 10$

$$G_\infty^{th} = \frac{\alpha^{\dagger *}}{\hat{R}}\frac{A}{24a^2}\left[\frac{3(x^2+2x)+4}{(x^2+2x)^3} + \frac{3}{(x+1)^4} - \frac{6(x^2+2x)+4}{(x^2+2x)^2(x+1)^2}\right] + \frac{2\pi\alpha^{\dagger *}\varepsilon_r\varepsilon_o a\psi_d^2}{\hat{R}}\left(\frac{\kappa^2\exp\left(-\kappa H_o\right)}{\{1 + \exp\left(-\kappa H_o\right)\}^2}\right) \quad (5.64)$$

$\kappa a < 3$

$$G_{\infty}^{th} = \frac{\alpha^{\dagger *}}{\hat{R}} \frac{A}{24a^2} \left[\frac{3(x^2+2x)+4}{(x^2+2x)^3} + \frac{3}{(x+1)^4} - \frac{6(x^2+2x)+4}{(x^2+2x)^2(x+1)^2} \right] + \frac{4\pi\alpha^{\dagger *}\varepsilon_r\varepsilon_o a\,\psi_d^2 \exp(-\kappa H_o)[\kappa^2(H_o+2a)^2+2\kappa(H_o+2a)+2]}{\hat{R}\,(H_o+2a)^3} \quad (5.65)$$

At low electrolyte concentrations the electrostatic repulsion is dominant and the repulsive potential may be equated to the total potential.

Buscall et al[111] also developed an expression for the bulk modulus, K, using a similar lattice model:

$$K = \frac{3\phi^3 N_A n}{8\pi a^3} \frac{d^2 V_T}{d\phi^2} \quad (5.66)$$

Substitution of (5.55) into (5.66) for a f.c.c. array yields:

$$K = \frac{n\phi_m^{7/2}}{3\pi} \left(\frac{1}{\hat{R}} \frac{d^4 V_T}{\overset{\wedge}{dR^2}} \right) \quad (5.67)$$

Comparing equations (5.53) and (5.67) a relationship relating $G^{(\infty)}$ with K may be obtained:

$$G(\infty) = \frac{9\pi}{32\phi_m^{4/3}} K \quad (5.68)$$

For f.c.c. or h.c.p. arrays $G\infty/K = 1.317$ and for b.c.c. arrays $G\infty/K = 1.477$.

Bulk moduli and hence shear moduli may be obtained experimentally from compression cell or pressure filtration techniques[112] and theoretically from theoretically computed isothermal compressibilities by means of direct correlation functions.[64]

The isothermal compressibility, χ_T, is related to the bulk modulus K by the expression:[64]

$$\chi_T = -\frac{1}{v}\frac{dv}{dp} = \frac{1}{K} \quad (5.69)$$

where p is the pressure; and to the direct correlation function, c(r), by

the expression:

$$\frac{1}{kT\chi_T} = 1 - 4\pi\rho \int_0^\infty c(r)\ r^2\ dr \qquad (5.70)$$

The Percus-Yevick direct correlation function may be simplified for use in this equation.

Chapter Six

Sedimentation Theory

Chapter Six Sedimentation Theory

6.1. Introduction.

Closely allied to the problem of understanding and predicting the rheological properties of a suspension is that of understanding and predicting the sedimentation behaviour of particles in a viscous medium in the presence of other particles. This has important technological implications since in many industrial preparations it is essential that dispersed particles remain suspended for the lifetime of the product. Conversely there is great interest in the part sedimentation plays in solid/liquid separation operations.

The term sedimentation describes the process by which suspended solids settle under the influence of gravity or other external force. The way in which dispersions sediment depends on various factors, for example particle size, density etc. The structure of the system also plays an important role. Michaels and Bolger [113] classified suspensions into their various sedimentation profiles which are dependent on the particulate concentration and the degree of aggregation in the system; these are illustrated schematically in Figure 6.1.[114]

Curve B can be seen to have an induction period. This is often indicative of channelling. A vertical discontinuity mechanism has been proposed by Michaels[115], working with clays, to explain this phenomenon. He assumed that the interstitial spaces remaining after initial aggregation of the suspension into flocs are arranged by upward liquid flow giving a vertical "shell and tube" configuration. This mechanism appears to be widely accepted in the literature.

Slow speed centrifugation affords a means by which an enhanced acceleration field may be applied to a sedimenting suspension.

Figure 6.1.

Typical batch sedimentation curves.

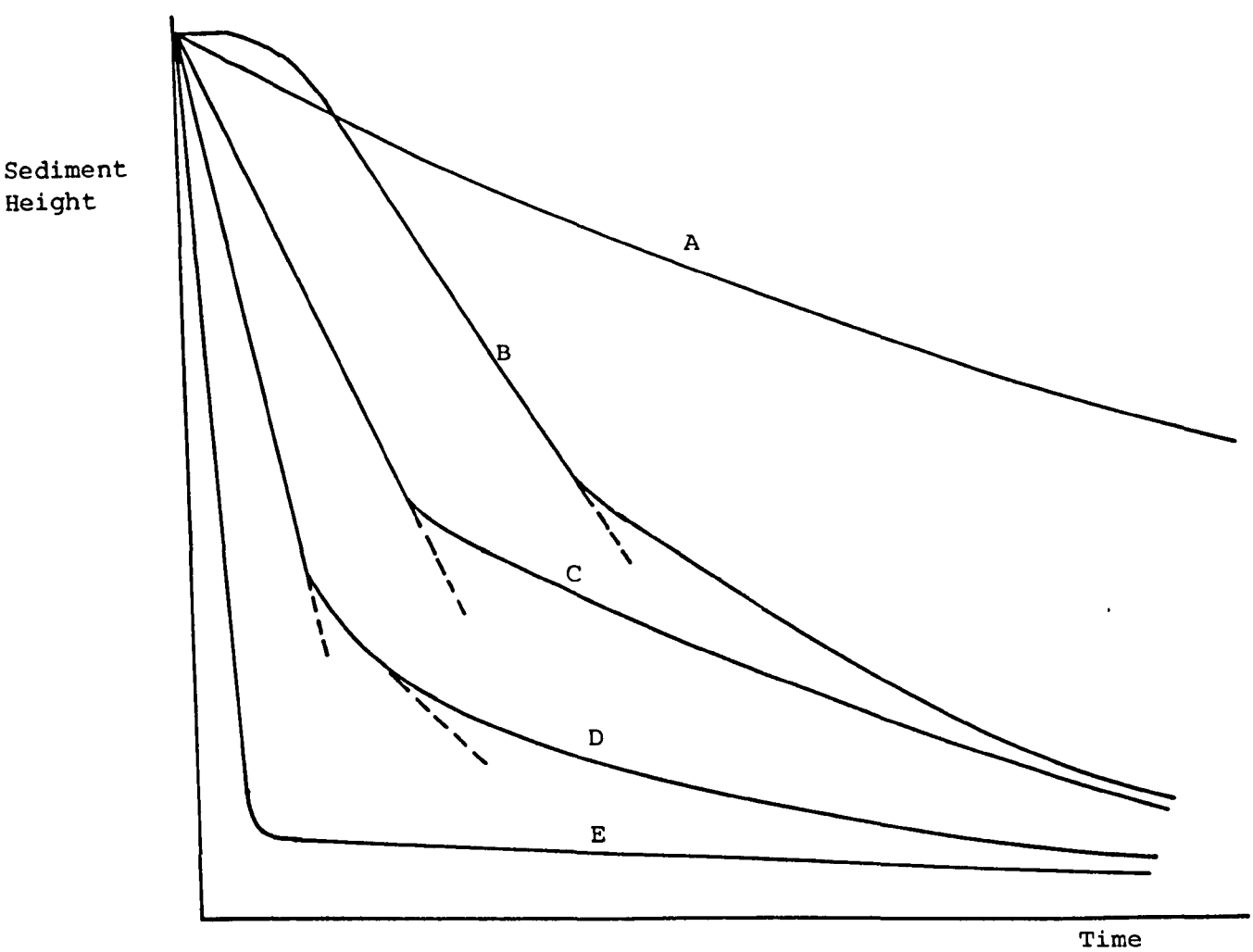

A Concentrated, flocculated or unflocculated, suspension.

B Intermediate flocculated or unflocculated suspension showing an induction time.

C As (B) but showing no induction time.

D Dilute, flocculated suspension.

E Dilute, unflocculated suspension.

Sedimentation velocities and mutual- and self-diffusion coefficients of colloidal particles in concentrated suspensions depend on the volume fraction, ϕ, because of both hydrodynamic and potential interactions. Due to the complexity of multiparticle hydrodynamics many attempts to calculate these properties have focussed primarily on the dilute limit, $\phi < 0.1$, where only pair interactions are important. The sedimentation behaviour of dilute systems is discussed in (6.2) and the behaviour at high concentrations discussed in (6.3). Sedimentation at high g is discussed in (6.4).

All the sedimentation theory is based on the systems obeying low Reynolds number hydrodynamics.[116] The Reynolds number, Re, which may be expressed:

$$Re = \frac{\rho_o^* Sa}{\eta_o} \qquad (6.1)$$

where S is the sedimentation rate and ρ_o^* and η_o are the density and viscosity of the medium respectively, is a measure of the relative importance of inertial and viscous forces acting in a system. Systems with low Reynolds number, $Re < 5$, undergo 'slow viscous flow' as viscous forces predominate over inertial forces.

6.2. Sedimentation at 1g - Dilute Limit.

Various factors affect the rate at which suspended particles settle in the earth's gravitational field, these being the size, shape, density, concentration, polydispersity and charge of the particles and the viscosity and density of the suspension medium.[117]

The simplest model on which to base a mathematical theory for sedimentation is the case of a single spherical particle settling in a gravitational field in an unbounded fluid. In 1851 Stokes developed an equation to describe the sedimentation rate of such a particle by equating

the viscous drag on the sedimenting sphere, F_V, with the effective gravitational field acting, F_G:

$$F_V = F_G \tag{6.2}$$

He derived an equation for the viscous drag, known as Stokes' Law, expressed as:

$$F_V = 6\pi\eta_o \, a \, S_o \tag{6.3}$$

where S_o is the velocity of sedimentation of a sphere at infinite dilution. The effective gravitational force may be given by the equation:

$$F_G = \frac{4\pi a^3}{3} (\rho_p^* - \rho_o^*) \, g \tag{6.4}$$

where ρ_p^* is the density of the particle and g is the acceleration due to the earth's gravitational field. Equating the expressions for F_V and F_G yields the sedimentation velocity of a sphere at infinite dilution:

$$S_o = \frac{2a^2 (\rho_p^* - \rho_o^*) \, g}{9\eta_o} \tag{6.5}$$

or

$$S_o = \frac{2a^2 (\rho_p^* - \rho_o^*) \, g \hat{A}}{9\eta_o} \tag{6.6}$$

where $\hat{A}$ is the acceleration in units of g, for sedimentation enhanced acceleration.

When more than one particle is settling in a system there is a deviation from this ideal behaviour due to the interactions between particles as a result of the velocity distribution generated in the fluid surrounding each particle. Account must be taken of multibody interactions, also of the bounded nature of fluids, irregularly shaped particles, polydispersity and flocculated systems.

Much work has been carried out on the effect of volume fraction on particle sedimentation rate. These theoretical investigations fell into three main groups depending on the assumptions made on the arrangement of the spherical particles in the dispersion and the nature of their interaction.

The first group treated the particle centres as occupying the sites of a regular geometric array. The calculations yielded a dependence on sedimentation rate of $\phi^{1/3}$, for dilute dispersions ($\phi < 0.1$), with a constant of proportionality of order unity and which varies with the type of arrangement assumed.

The second train of thought was the use of a cell model of the interaction effects, assuming that the hydrodynamic effect on one sphere of the presence of all the other spheres in the dispersion is equivalent to that of a spherical boundary around the sphere under consideration. Using this model the sedimentation rate was also calculated to be proportional to $\phi^{1/3}$, with a constant of proportionality again of order unity but different to that obtained from the regular array model.

Investigators in the third group employed a statistical analytical approach in order to determine the hindered settling of a homogeneous or random distribution of spheres in a dilute dispersion. A difficulty is encountered in such an approach due to the lack of absolute convergence of the sum of the separate effects of an indefinitely large number of falling spheres on a given sphere, both for a random distribution and a regular distribution. Burgers[118] overcame this problem for low concentrations and obtained an expression for the sedimentation rate with a dependence of ϕ. He obtained an equation of the form:

$$\frac{S}{S_o} = \frac{1}{1 + k_s\phi} \qquad (6.7)$$

which approximates to:

$$\frac{S}{S_o} \simeq 1 - k_s\phi + O(\phi^2) \qquad (6.8)$$

where k_s is the sedimentation coefficient. He obtained a value of 6.88 for k_s.

Pyun and Fixman[119] employed a generally similar statistical approach and obtained a ϕ dependence on sedimentation rate. They obtained a value for the sedimentation coefficient for hard spheres of 7.16 and a lower dependence for soft spheres.

In 1972 Batchelor[117] produced his classical paper on sedimentation in dilute dispersions of spheres. He considered a dilute suspension of rigid spherical particles with uniform probability of all accessible sphere configurations and rigorously overcame the previous difficulty of non-convergent integrals in the summation of hydrodynamic interactions by specification of parameter $\underline{V}$. Parameter $\underline{V}$ was selected such that its mean value could be exactly determined and such that it had the same long range dependence on a second sphere as the sedimentation rate S. Then the mean of $(S - \underline{V})$ could be expressed in terms of an absolutely convergent integral.

To calculate the sedimentation coefficient Batchelor took into account the effects of multiparticle flow in the system which modifies the rate from that at infinite dilution. The downward flux of volume of solid material in the dispersion is accompanied by a corresponding net upward flux of fluid volume, causing the mean settling speed of a single particle to differ from the value it would have in an infinite clear fluid by an amount of $-\phi S_o$. The sedimenting spheres drag with them some adjoining fluid which is again accompanied by an equal upward flux; the contribution to the change in mean settling rate of this is $-\frac{9}{2} \phi S_o$. The motion of the spheres generates collectively a velocity distribution in the fluid, changing the mean velocity by $+ \frac{1}{2} \phi S_o$. Finally, the interaction between one sphere and a neighbouring suspended sphere leads to a change in the translational velocity of the test sphere; this affords a change in the mean settling velocity of $- 1.55 \phi S_o$.

Batchelor summed these effects:

$$S = S_o + \phi S_o (-1 - 4.5 + 0.5 - 1.55) \qquad (6.9)$$

to arrive at his well known equation for the sedimentation of spheres in a dilute dispersion, expressed:

$$\frac{S}{S_o} = 1 - 6.55\phi \qquad (6.10)$$

A full analysis and the derivation of the various contributions is presented in Batchelor's paper.[117]

It is noted that the largest contribution to the modification of the sedimentation rate as a result of multibody sedimentation is that from the diffuse upward current compensating for the downward flux of fluid surrounding the sedimenting particles.

Batchelor also pointed out the sensitivity of the value of the sedimentation coefficient to the precise spatial arrangement and that a tendency for the particles to cluster would result in an increase in sedimentation rate and a decrease in the sedimentation coefficient.

Reed and Anderson[120,121] extended Batchelor's theory to include the force of repulsive interaction between the particles, taking into consideration Batchelor's near-field and far-field effects. A test particle close to a neighbouring sedimenting particle experiences the down flow of the neighbour, enhancing its sedimentation velocity whereas a test particle far from a neighbour experiences the reverse fluid flow of the neighbour, thus retarding its settling rate. Reed and Anderson determined that the inclusion of repulsive forces leads to a greater particle separation, hence reducing the near-field effect and thus leading to a net enhanced hindrance of settling. For a suspension of particles interacting by the hard sphere potential a value for the sedimentation coefficient of 5.80 was obtained.

Batchelor[122,123] has developed a comprehensive theory to take account of polydispersity in dilute systems of interacting spheres in terms of the pair distribution function which is determined by the motion of the particles through the fluid.

Dickinson and Parker[124] have also considered sedimentation in polydisperse systems and have used Brownian dynamics to simulate the motion of hydrodynamically interacting doublets of DLVO-type colloidal particles in a sedimenting field.

Much experimental analysis has been reported in the literature. Maude and Whitmore[125] analysed some early experimental data and discovered that, over a wide range of volume fractions, the sedimentation behaviour may be represented by the expression:

$$\frac{S}{S_o} = (1-\phi)^{\beta^*} \qquad (6.11)$$

where β^* was found to be approximately 5 for spheres in creeping flow, 2 - 4 for spheres in turbulent flow and 7 - 10 for rough particles in creeping flow. For a dilute system of spheres equation (6.11) approximates to an equation of the same form as predicted theoretically:

$$\frac{S}{S_o} = 1 - 5\phi + \ldots\ldots \qquad (6.12)$$

Cheng and Schachman[126] obtained a value for the sedimentation coefficient of 5.1 from their ultracentrifugation studies on polystyrene latices.

Richardson and Zaki[127] obtained a similar relationship to equation (6.11) with a value for β^* of 4.65.

Buscall et al[128] carried out an experimental investigation into the settling rate of polystyrene latex dispersions with particles of radius 1.55 μm in sodium chloride solution over a volume fraction range of

ca. 0.01 to 0.5. At low volume fractions a value for the sedimentation coefficient of 5.4 ± 0.1 was obtained. Buscall et al explained the difference between this value and that obtained by Batchelor by Batchelor's neglection of diffusion effects during sedimentation and the consequent effect of transient clusters.

The author[129] studied the sedimentation behaviour of polyvinylchloride latex, particle radius 0.25 μm, in sodium chloride concentrations 1×10^{-2} mol dm^{-3} and 1×10^{-3} mol dm^{-3}, at low volume fractions. Values for the sedimentation coefficient of 6.55 and 6.6 were obtained, in very good agreement with Batchelor's predictions.

6.3. Sedimentation at 1g - Concentrated Systems.

To model sedimentation behaviour and predict sedimentation rates of concentrated systems multiparticle hydrodynamics must be taken into account which greatly increases the complexity of the calculations. Since moderate to high volume fractions are frequently encountered in real systems this is an important topic.

Glendinning and Russel[130] extended the theories for sedimentation of particles in the dilute limit to sedimentation of concentrated particle dispersions, taking into account the critical role of the suspension microstructure. They recognised four problems to be overcome: approximation of many-body hydrodynamics, description of the suspension microstructure, renormalisation of non-convergent integrals arising from hydrodynamic interactions and incorporation of thermodynamic effects in mutual diffusion.

A variety of methods exist for approximating multiparticle hydrodynamics; cell models, self-consistent field models, method of reflections and numerical solutions based on multipole expansions. Glendinning and

Russel assumed the interactions to be pairwise additive to preserve the $O(\phi)$ limit and minimise the information needed about the microstructure.

For sedimentation at low Péclet numbers microscopic perturbations from equilibrium are unimportant and for pairwise additive interactions the equilibrium radial distribution function, g(r), may be used to fully characterise the suspension microstructure. As described in Chapter Four g(r) may be calculated from a variety of interaction potentials; in this piece of work a Percus-Yevick hard sphere potential was assumed.

O'Briens[131] scheme for deducing the bulk properties of dilute suspensions from local interactions and the microstructure by means of an integral representation of the solution to the governing equation was employed and extended to higher concentrations. The problem of non-convergent integrals was overcome using Batchelor's[117] method. Finally the authors used a statistical mechanical treatment to describe the thermodynamic aspects of the mutual diffusion process. An expression was obtained for the sedimentation velocity in a concentrated suspension of monodisperse rigid spheres, given by:

$$S = \frac{\overset{I}{S_o} + \rho \int_v S_o \, c(r) \, dV + \overset{II}{\frac{1}{2}\phi S_o} + \overset{III}{\phi \int H(r) \, g(r) \, dr} - \overset{IV}{\phi^2 S_o}}{1 + \phi} \qquad (6.13)$$

where ρ is the number density of the particles, V is the interaction potential, S_o is the fluid velocity due to an isolated sphere, c(r) is the direct correlation function, v is the volume of the fluid and H(r) is a hydrodynamic function which must be determined numerically. H(r) is given by Batchelor[122] to be:

$$H(r) = S_o \left(A_{11}^{\dagger} + A_{12}^{\dagger} + 2B_{11}^{\dagger} + 2B_{12}^{\dagger} - 3\left(1 + \frac{a}{r}\right) \right) \frac{r^2}{a^3} \qquad (6.14)$$

where $A_{ij}^{\dagger}$ and $B_{ij}^{\dagger}$ are hydrodynamic coefficients dependent only upon interparticle separation, see later.

The individual terms of equation (6.13) may be physically identified. Term I determines the effect of backflow, the reverse flow of fluid necessary to compensate for the volume flux of particles and associated fluid and therefore has a retarding effect. Term II causes a slight enhancement in settling rate due to a pressure gradient in the suspension whereas Term III represents the slight hindrance due to nearfield hydrodynamic interactions. Term IV has a backflow enhancement effect and therefore has a retarding effect upon the sedimentation velocity. In the dilute limit equation (6.13) reduces to Batchelor's result, equation (6.10):

$$S = S_o \ (1 - 6.55 \ \phi)$$

As the volume fraction increases, the particles become crowded closer together leading to increased hydrodynamic near-field interactions and therefore a slight increase in sedimentation hindrance. The effect of particle crowding also results in screening of the particles from far-field effects and hence in a substantial decrease in retardation due to backflow.

Although this theory extends predictions of sedimentation behaviour beyond the dilute limit the hydrodynamic approximation of pairwise additivity becomes inadequare at $\simeq \phi = 0.2$. Glendinning and Russel proposed a correction factor originally suggested by Anderson and Reed[121] but this too fails at high volume fractions.

Batchelor[122] has derived an expression to describe the sedimentation of idential spheres in terms of a pair distribution function given by:

$$S = - 6.55 + \int_{\lambda}^{\infty} (A_{11}^{\dagger} + 2B_{11}^{\dagger} - 3 + A_{12}^{\dagger} + 2B_{12}^{\dagger}) \left\{ \exp\left(\frac{-V}{kT}\right) - 1 \right\} \hat{r}^2 \, d\hat{r} \qquad (6.15)$$

where $\hat{r}$ is the rescaled particle centre-centre separation given by:

$$\hat{r} = \frac{r}{a} \qquad (6.16)$$

The value of - 6.55 is Batchelor's value for the sedimentation coefficient.

The hydrodynamic mobility functions $A_{ij}^{\dagger}$ and $B_{ij}^{\dagger}$ for identical particles may be expressed:

$$A_{11}^{\dagger} = 1 - \frac{60}{\hat{r}^4} + \frac{480}{\hat{r}^6} - \frac{960}{\hat{r}^8} \tag{6.17}$$

$$B_{11}^{\dagger} = 1 - \frac{320}{\hat{r}^8} \tag{6.18}$$

$$A_{12}^{\dagger} = \frac{3}{2\hat{r}} - \frac{6}{\hat{r}^3} \tag{6.19}$$

$$B_{12}^{\dagger} = \frac{3}{4\hat{r}} + \frac{3}{\hat{r}^3} \tag{6.20}$$

Often the interparticle interaction potential is only significant at close interparticle separations, i.e. at small values for $(\hat{r} - 2)$ and an approximation to (6.15) may be made. According to Batchelor[117] the hydrodynamic contribution: $(A_{11}^{\dagger} + 2B_{11}^{\dagger} - 3 + A_{12}^{\dagger} + 2B_{12}^{\dagger})$ varies by only 6% over the range $2 < \hat{r} < 2.2$ and as an approximation it may be considered to be constant and equal to 1.32 over that range. Equation (6.15) then reduces to:

$$S = - 6.55 + 0.44\ \alpha^{\dagger} \tag{6.21}$$

where

$$\alpha^{\dagger} = 3 \int_2^{\infty} \left\{ \exp\left(-\frac{V}{kT}\right) - 1 \right\} \hat{r}^4\ d\hat{r} \tag{6.22}$$

To a first approximation the exponential term $\left\{ \exp\left(\frac{-V}{kT}\right) \right\}$ may be approximated to the radial distribution function, g(r):

$$\exp\left(-\frac{V}{kT}\right) = g(r) \tag{6.23}$$

Therefore equation (6.15) may be rewritten:

$$S = - 6.55 + \int_2^{\infty} H(\hat{r}) \left[g(\hat{r}) - 1 \right] \hat{r}^4\ d\hat{r} \tag{6.24}$$

where $H(\hat{r})$ is a hydrodynamic function given by:

$$H(\hat{r}) = A_{11}^{\dagger} + 2B_{11}^{\dagger} - 3 + A_{12}^{\dagger} + 2B_{12}^{\dagger} \tag{6.25}$$

The function $\left[g(\hat{r}) - 1 \right]$ is also known as the direct correlation function, c(r) and the equation (6.24) may be expressed:

$$S = - 6.55 + \int_2^{\infty} H(\hat{r})\ c(\hat{r})\ \hat{r}^2\ d\hat{r} \tag{6.26}$$

This is the result obtained by Dickinson[132] for the sedimentation of colloidal particles.

Buscall et al[128] evaluated the sedimentation rates for polystyrene latex dispersions in sodium chloride solution over a wide range of volume fractions, ϕ = 0.01 - 0.5. At volume fractions greater than 0.085 they found that the plot of S/S_o versus ϕ became non-linear as shown in Figure 6.2.[128] At the highest volume fraction examined the value of S/S_o tended to zero as the particles approached the region of close packing, i.e. as $\phi \rightarrow \phi_m$ where ϕ_m is the maximum packing fraction.

Dougherty amd Krieger [82] have obtained an expression relating the viscosity of a suspension with the maximum packing fraction given by equation (5.13):

$$\eta = \eta_o \left(1 - \frac{\phi}{\phi_m}\right)^{-[\eta]\phi_m}$$

Buscall et al[128] reasoned that as a first approximation that:

$$\frac{S}{S_o} = \left(\frac{\eta_o}{\eta}\right)^{\alpha^{\dagger\dagger}} \qquad (6.27)$$

where $\alpha^{\dagger\dagger}$ was an empirical constant and then combined equations (5.13) and (6.27) to yield:

$$\frac{S}{S_o} = \left(1 - \frac{\phi}{\phi_m}\right)^{\alpha^{\dagger\dagger}[\eta]\phi_m} \qquad (6.28)$$

Differentiating the relative sedimentation rate with respect to the volume fraction at the dilute limit gives:

$$\left[\frac{d(S/S_o)}{d\phi}\right]_{\phi \rightarrow 0} = -\alpha^{\dagger\dagger}[\eta] \qquad (6.29)$$

The general equation for sedimentation in a dilute system is given by equation (6.8):

$$\frac{S}{S_o} = 1 - k_s\phi$$

where k_s is the sedimentation coefficient. Buscall et al differentiated this

Figure 6.2.

Relative settling rates of polystyrene latex in 1 x 10^{-3} mol dm^{-3} sodium chloride solution as a function of volume fraction as obtained by Buscall et al[128].

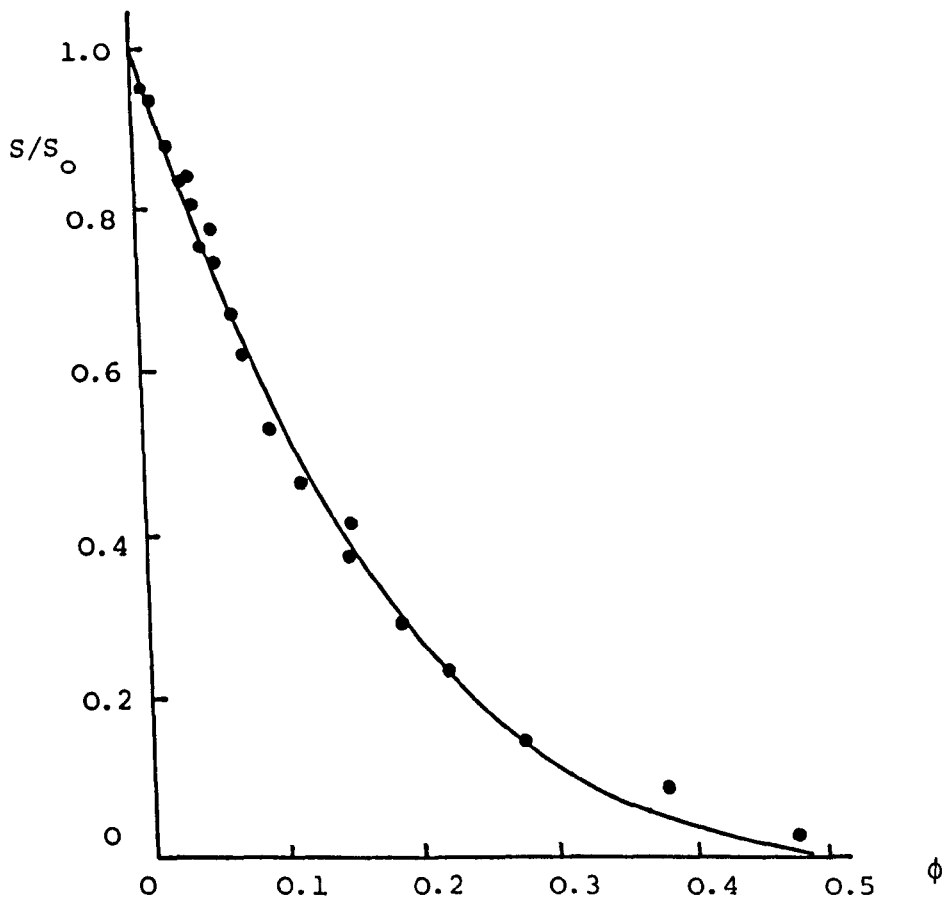

Points: experimental.

Continuous line: theoretical.

with respect to volume fraction at the low volume fraction limit:

$$\left[\frac{d(S/S_o)}{d\phi}\right]_{\phi \to 0} = -k_s \qquad (6.30)$$

and combined equations (6.29) and (6.30) to obtain:

$$k_s = \alpha^{\dagger\dagger}[\eta] \qquad (6.31)$$

The authors then substituted equation (6.31) into equation (6.28) to give the empirical equation:

$$\frac{S}{S_o} = \left(1 - \frac{\phi}{\phi_m}\right)^{k_s \phi_m} \qquad (6.32)$$

i.e. at $\phi = 0$ $S = S_o$

$\phi = \phi_m$ $S = 0$

Buscall et al experimentally obtained a value for ϕ_m of 0.58 and took the sedimentation coefficient to be 5.4, the value they determined at low volume fraction. Calculation of S/S_o as a function of ϕ using equation (6.32) gave the full line shown in Figure 6.2. which is in reasonable agreement with the experimental data.

Note that the quantity $\left(1 - \frac{\phi}{\phi_m}\right)$ is an available free volume term. To a good approximation the various transport coefficients appear to be power law functions of this quantity for colloidally stable spheres.[3]

6.4. Sedimentation Enhanced by Slow Speed Centrifugation.

In addition to the study of the sedimentation behaviour of particles settling in a gravitational field, i.e. at 1g, it is possible, by a simple centrifugation technique to apply a field of greater than 1g and study the accelerated sedimentation behaviour.

Centrifugation has been used as a means of carrying out accelerated storage testing in particulate dispersions but relating the sedimentation rates at high stress with those at low stress unambiguously has received much criticsm.[133] It is considered that any application of medium or high

speeds may change the properties of a system in a manner that bears no relationship to the changes that occur under normal gravitational forces. For example a weakly flocculated system may be broken up or a gel structure destroyed.

However, slow speed centrifugation has important implications and can be used to investigate the elastic properties of a dispersion and to determine a network modulus, K, which is closely related to the shear modulus, G, previously considered. Much work in this area has been pioneered by Buscall [1 - 3] working with colloidally stable systems and with strongly and weakly flocculated systems.

Flocculated dispersions display an interesting feature in that the application of a small acceleration in a centrifuge rarely causes complete densification of the solid phase but a limited amount of consolidation occurs initially giving thereafter a stable sediment only a little more concentrated than the original dispersion. Application of further acceleration again causes consolidation until the new pressure can again be supported elastically.

A slow speed centrifugation experiment, as used by Buscall, is illustrated schematically in Figure 6.3.[1] Consider an initially homogeneous particulate dispersion of volume fraction ϕ_o occupying a centrifuge tube to a height h_o^*. After centrifugation the sediment height reaches an equilibrium value h_e^*. The excess pressure, P_{EX}, due to the presence of the disperse phase at any point h^* below the sediment boundary may then be expressed:

$$P_{EX}(h^*) = \omega_r^2 \Delta\rho^* \int_0^{h^*} (R^* + h^1)\ \phi(h^1)\ dh^1 \qquad (6.33)$$

with $R^* = R^1 - h_e^*$ (6.34)

where ω_r is the angular velocity of the rotor, $\Delta\rho^*$ is the density difference between the disperse and continuous phases, $\phi(h^1)$ is the

Figure 6.3.

Schematic illustration of a slow speed centrifuge experiment.

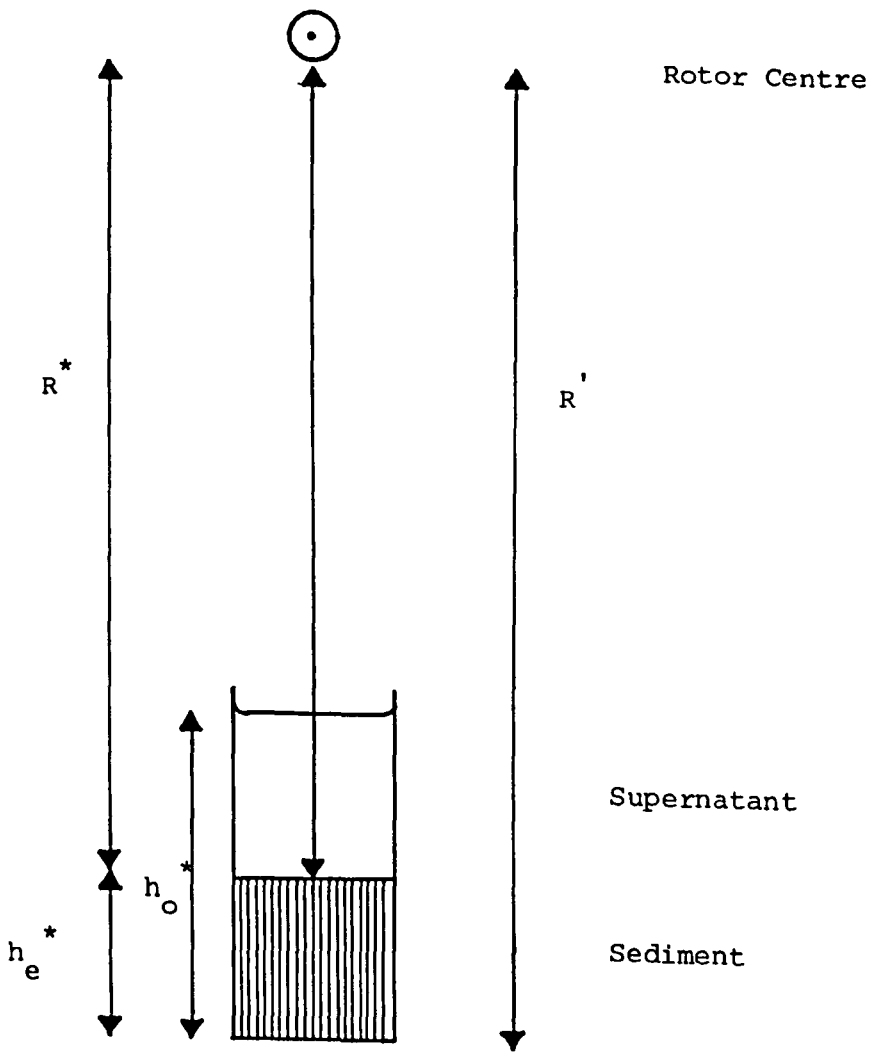

volume fraction of solids at any level h^1 and R^1 is the distance between the rotor centre and the bottom of the centrifuge tube.

From his pressure filtration studies on flocculated latices and attapulgite clay Buscall,[1] in the same paper, determined that the pressure, P_{EX}, appeared to be related to the network modulus, K^*, by the expression:

$$K^*(\phi) = \frac{dP_{EX}}{d\ln\phi} \qquad (6.35)$$

Since the system volume, v, is related to the volume fraction by the relationship:

$$v \propto \frac{1}{\phi} \qquad (6.36)$$

the network modulus may be expressed in terms of volume:

$$K^*(v) = \frac{-dP_{EX}}{d\ln v} \qquad (6.37)$$

Then, combining equations (6.33) and (6.35) yields:

$$\omega_r^2 \Delta\rho^* \int_0^{h^*} (R^* + h^1)\, \phi\,(h^1)\, dh^1 - \int_{\phi_o}^{\phi h^*} \frac{K^*(\phi)}{\phi}\, d\phi = 0 \qquad (6.38)$$

To avoid the need for the measurement of the complete concentration profile in the sediment Buscall considered the mean excess pressure, $\bar{P}_{EX}$, in the sediment given from the equation (6.33) by:

$$\bar{P}_{EX} = \frac{\omega_r^2 \Delta\rho^*}{2h_e^*} \int_0^{h_e^*} \int_0^{h^*} \phi\,(h^1)\,(R^* + h^1)\, dh^1\, dh^* \qquad (6.39)$$

Assuming that the difference in solids content between the top and bottom of the sediment is small, for $h_e^* << R^1$ the mean pressure may be approximated to $\bar{P}'_{EX}$ given by:

$$\bar{P}'_{EX} = \omega_r^2 \left(R^1 - \frac{h_e^*}{2} \right) \Delta\rho^* \phi_o \frac{h_o^*}{2} \qquad (6.40)$$

An approximate modulus, $K^{*'}$, from equation (6.35) may be defined in terms of the mean volume fraction in the sediment, $\bar{\phi}$:

$$K^{*'} = \frac{\bar{\phi}\, dP_{EX}}{d\bar{\phi}'} \qquad (6.41)$$

with $\bar{\phi} = \frac{\phi_o h_o^*}{h_e^*}$ (6.42)

Therefore, combination of equations (6.41) and (6.42) gives:

$$K^{*'}(\phi) = \frac{h_e^* dP'_{EX}}{dh_e^*} \tag{6.43}$$

and combination of equations (6.40) and (6.43) yields:

$$K^{*'}(\phi) = \frac{\Delta\rho^* \phi_o h_o^* h_e^*}{2} \left[\left(R^1 - \frac{h_e^*}{2} \right) \frac{d(\omega_r')}{dh_e^*} - \frac{\omega_r^2}{2} \right] \tag{6.44}$$

or equivalently

$$K^*_{approx}(\bar{\phi}) = \Delta\rho^* \phi_o h_o^* h_e^* \left[\left(R - \frac{h_e^*}{2} \right) \frac{d\omega_r}{dh_e^*} - \frac{\omega_r}{4} \right] \omega_r \tag{6.45}$$

Thus the approximate modulus at any volume fraction can be obtained from the slope of a curve of sediment height versus centrifuge speed. In the limit $h_o^* \to 0$ the true modulus is related to the approximate modulus by the relationship:

$$K^*(\bar{\phi}) = \lim_{h_o^* \to 0} K^*_{approx}(\bar{\phi}) \tag{6.46}$$

and therefore extrapolation techniques may be employed to determine the true modulus.

Hence a compressional modulus may be obtained from slow speed centrifugation methods under circumstances where a sedimentation equilibrium is set up. In rheological terms, $K^*(\phi)$ is thus measurable when the Deborah number appropriate to irreversible consolidation is large.

The other simple type of deformation that can be achieved experimentally with fluid dispersions is shear, the shear modulus being an easily measured dynamic modulus. In a dynamic shear experiment, the relevant Deborah number is given by the product of the driving frequency, $\tilde{\omega}$ and the stress relaxation time, t_r. Thus the shear modulus analogous to the network modulus measured by slow speed centrifugation is the high frequency shear modulus, $G(\infty)$, measured from pulse shearometry, see (2.3).

Comparisons of $G(\infty)$ and K^* have been made by Buscall[1] for three disparate colloidal systems; flocculated latex, flocculated clay and montmorillonite sols, consisting of flocculated spheres, flocculated rods and aligned platelets respectively and in each case the shear modulus and compression modulus were found to be identical.

With weakly flocculated systems steady and continued consolidation is observed rather than the yield type behaviour observed with the strongly flocculated systems discussed above.

Buscall et al[2,3] studied weakly flocculated systems of polystyrene latex flocculated with sodium carboxymethylcellulose and obtained an interesting correlation between their sedimentation data and their viscosity data. They plotted their sedimentation data in the form of a dimensionless collective friction coefficient, f_c, given by

$$f_c = \frac{S_1 \hat{A}}{S} \qquad (6.47)$$

where S_1 is the sedimentation rate, i.e. the rate of fall of the sediment boundary, at 1g, S is the sedimentation rate at acceleration $\hat{A}$ and $\hat{A}$ is given in units of g, the normal acceleration due to gravity. The plot obtained by Buscall and McGowan[2] for f_c versus $\hat{A}$ is presented in Figure 6.4. It can be seen that the dependence of the collective friction coefficient on gravitational acceleration is very similar to the typical dependence of viscosity on shear stress, see (2.4) with a limiting value approached at low and high g.

Buscall[3] claimed that the two types of non-linear behaviour are related and proposed the relationship:

$$\frac{f_c \alpha^{**} \hat{A}}{f_c(0)} = \frac{\eta}{\eta(0)} \qquad (6.48)$$

where α^{**} is some scaling constant and η is the viscosity. He also thought that at low stresses and accelerations where the dynamics is dominated by cohesive forces that the concentration dependencies of

Figure 6.4.

Normalised collective friction coefficient versus centrifugal acceleration as obtained by Buscall and McGowan[2] for weakly flocculated polystyrene latex dispersions at $\phi = 0.225$.

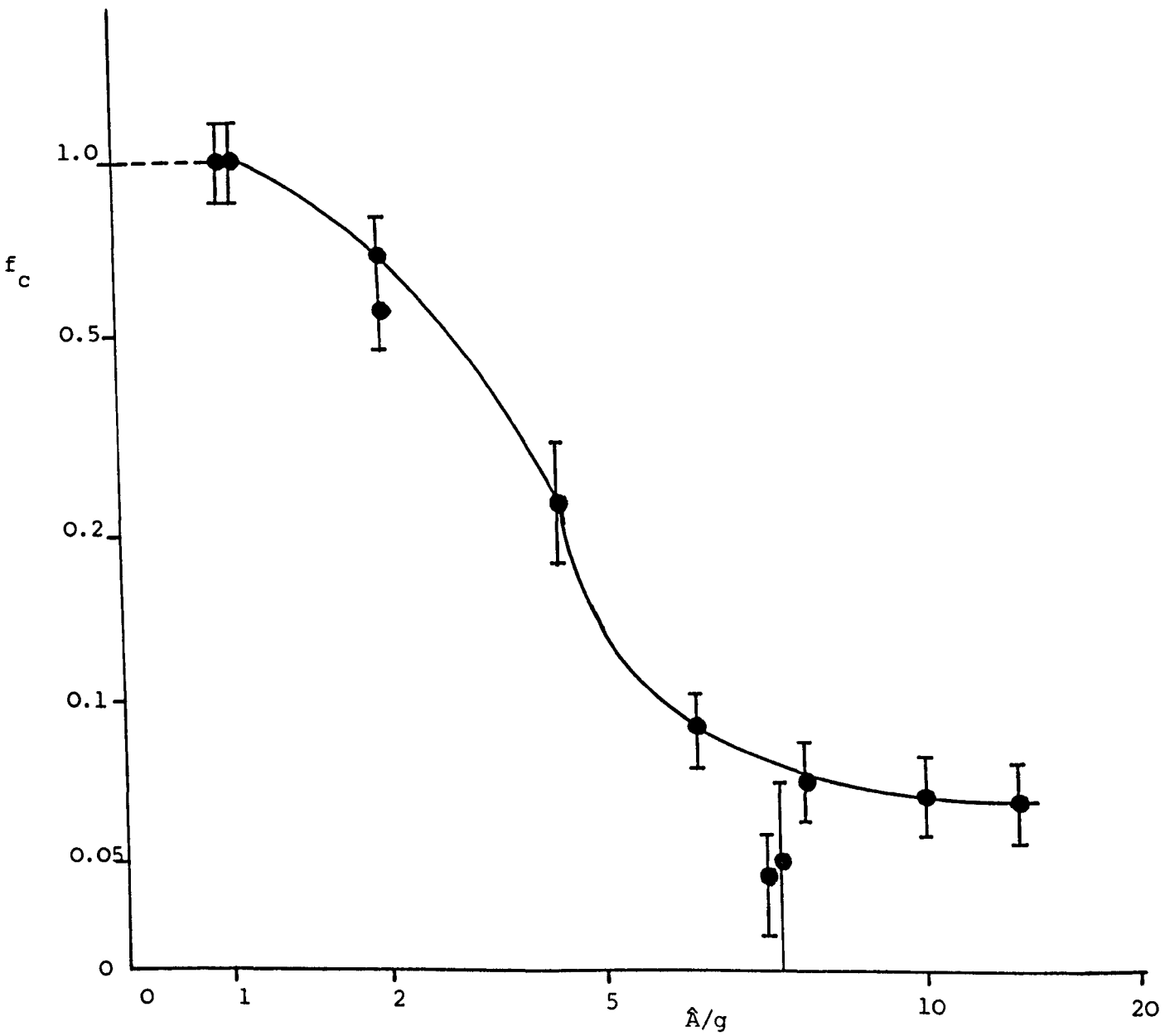

the collective friction coefficient and the viscosity might be similar and proposed the relationship:

$$f_c(\phi) \simeq \eta(\phi) \qquad (\hat{A}.\tau \to 0) \tag{6.49}$$

As it was not practicable to measure f_c over a wide range of concentrations Buscall attempted to predict the sedimentation behaviour of a weakly flocculated polystyrene latex dispersion at different g values using a model for the sedimentation rate which embodied as assumptions the relationships given in equations (6.48) and (6.49). He used Stokes' model for the sedimentation velocity given previously in equation (6.6):

$$S_o = \frac{2a^2 \Delta\rho^* g \hat{A}}{9\eta_o}$$

and used this together with Kynch's continuity equations.[134] A value was assigned to the scaling constant α^{**} from equation (6.48) by fitting the model to the curve for lg and from this the remaining curves predicted. The experimental and predicted data of Buscall are presented in Figure 6.5 and the agreement found to be good. Buscall concluded that this may have been, in part, fortuitous but that it demonstrated similar concentration dependencies of the dimensionless frictional coefficient and the viscosity.

Figure 6.5.

Sediment height versus time at various accelerations as determined by Buscall and McGowan[2] for weakly flocculated polystyrene latex dispersions at $\phi = 0.225$

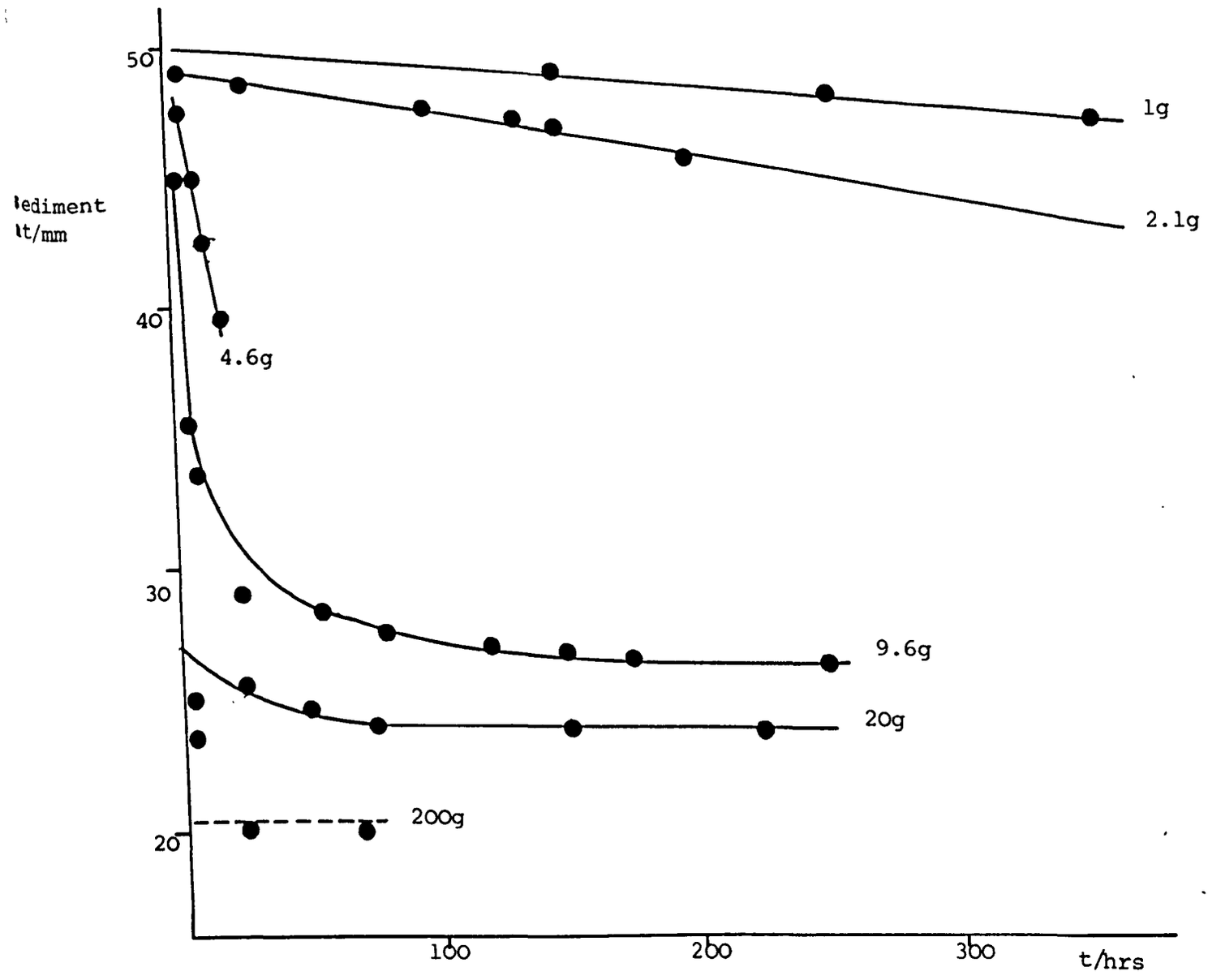

Points: experimental

Continuous curves: theoretical

Chapter Seven

Preparation of Systems.

Chapter Seven. Preparation of Systems.

7.1. Introduction.

Theoretically the interaction between colloidal particles can be treated most easily when the model for mathematical analysis is based upon interaction between flat plates or between spherical particles of equal size. Hence, in order for experimental studies to be correlated with theory it is useful if the experimental systems fall into one of these categories.

Weak flocculation may be achieved in a colloidal system of spherical particles by balancing two interparticle forces, van der Waals attraction and steric stabilisation. High electrolyte concentration increases attractive interparticle forces which leads to aggregation of the particles. To ensure that it is flocculation (reversible aggregation) that occurs and not coagulation (irreversible aggregation) it is necessary to sterically stabilise the colloidal particles. This involves adsorption or attachment of polymeric material on to the particle surfaces.

Polymer latices are suitable model systems of spherical colloidal particles that have been widely used, consisting of dispersions of high molecular weight polymer. Latices often have a high degree of monodispersity, can be well characterised and the mean particle size varied from ca. 30 nm to 5 μm according to requirements. Polystyrene latices were selected for the work here due to their readily controllable monodispersity and size.

The process of polymer adsorption onto colloidal particles is relatively complex as in addition to the usual adsorption considerations there is the conformation of the polymer molecule on the surface to be

considered. A given adsorbed polymer molecule may be in the form of "loops", "trains" and "tails". Polymer solutions have relatively broad size distributions which is disadvantageous in theoretical modelling.

The same sort of stabilising action may be produced by long chain nonionic surface active agents which are better defined and have less complex adsorption mechanisms than polymers.[133] A commonly used nonionic surface active agent as adsorbate from aqueous solutions has polyoxyethylene chains attached to alkyl chains with the general formula:

$$C_{\hat{n}}H_{2\hat{n}+1} - O(CH_2CH_2O)_{\hat{x}}H$$

This formula is usually abbreviated to:

$$C_{\hat{n}}E_{\hat{x}}$$

with $\hat{n}$ denoting the number of carbon atoms in the alkyl chain and $\hat{x}$ the number of oxyethylene units in the polyoxyethylene chain. Most commercially available nonionic surface active agents of this type have an average value of $8 < \hat{n} < 18$ and $3 < \hat{x} < 30$. It is, however, possible to obtain pure, monodisperse surface active agent and in this work monodisperse $C_{12}E_6$ was used.

7.2. Preparation of Polystyrene Latices.

7.2.1. Mechanistic Background.

The preparation of monodisperse polymer latices by means of emulsion polymerisation is a well-known procedure,[135-137] pioneered from work by Vanderhoff et al[138] and followed by many others.[139-151] The principles of the theory were originally advanced by Harkins[152-154] and Yurzhenko[155] and the consequences of their theory of particle formation by micellar capture was elaborated in kinetic terms by

Smith and Ewart.[156]

Conventional emulsion polymerisation involves emulsification of a water-immiscible monomer in a continuous water medium using a surface active agent as emulsifier, and polymerisation using a water soluble initiator, to give a colloidal dispersion of polymer particles in water. The term "emulsion polymerisation" comes from the original supposition that the polymerisation actually takes place within the emulsion droplets. This is now known not to be the case. The presence of the emulsifier has various drawbacks: considerable difficulty may be encountered in its removal and the extent of removal is not easy to ascertain.[157] Also the removal of the surface active agent, which often stabilises the suspension by adsorption onto the particles surfaces, can lead to destabilisation of the latex causing it to flocculate or coagulate.

Much work has been carried out by Ottewill and co-workers[140,143,144] and others[142] into the possibility of emulsifier-free polymerisation involving a free-radical initiator. This has been very successful and monodisperse latices can be readily prepared in the absence of surface active agents. The three requisites for emulsifier-free polymerisation are monomer, free-radical initiator and salt, these usually being styrene, potassium persulphate and sodium chloride in the case of polystyrene latex preparation.

The persulphate is thermally decomposed and forms sulphate ion-radicals which attack the styrene to form styryl sulphate radicals. These in turn can react with further monomer to form growing surface active oligomers which rapidly become insoluble in the aqueous phase and associate or micellise. These nascent particles then grow, by a combination of coalescence and swelling by monomer, into the final latex particles.

This process is illustrated schematically in Figure 7.1.[150]

The resultant latex particles are electrostatically stabilised by repulsive forces acting between the charged surface sulphate groups which are an integral part of the particles and may not be removed by dialysis.

The surface groups and hence the nature of the surface properties of the latex may be varied by using initiators with different functional groups. It is possible to prepare latices with cationic[146,149] and zwitterionic[158] surface groups as well as anionic.

The diameter of the latex particles may be controlled by suitable adjustment of reaction conditions. Goodwin et al[144,148] have developed an equation, based on experimental data, by which the final latex particle diameter, D^* may be expressed as a function of the total initial ionic strength of the aqueous phase, $[I]$, the initiator concentration in the aqueous phase, $[P]$, the monomer concentration, $[M]$, based on the total volume and the absolute temperature, T:

$$\log D^* = 0.238 \left[\log \frac{[I][M]^{1.723}}{[P]} + \frac{4929}{T} \right] - 0.827 \quad (7.1)$$

The equation may be usefully used to determine reaction conditions required to produce a polystyrene latex of a required diameter within the range 100 nm to 1 μm.

From equation (7.1) it is evident that the ionic strength, and hence the electrolyte concentration, has an important effect on the particle diameter. There is, however, a limit. If the total ionic strength, electrolyte plus initiator, becomes too high gross coagulation of the latex will result. Using a styrene, potassium persulphate and sodium chloride system latices have been successfully prepared at an ionic strength of up to 5.4×10^{-2}.[148] The lower limit of ionic strength is determined by the amount of initiator required to produce

Figure 7.1.

Schematic representation of emulsifier-free preparation of polystyrene latex.

Reactants:

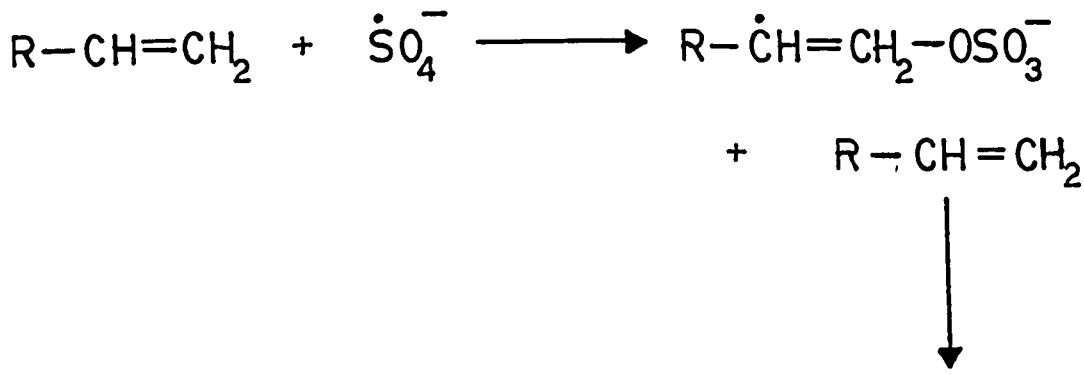

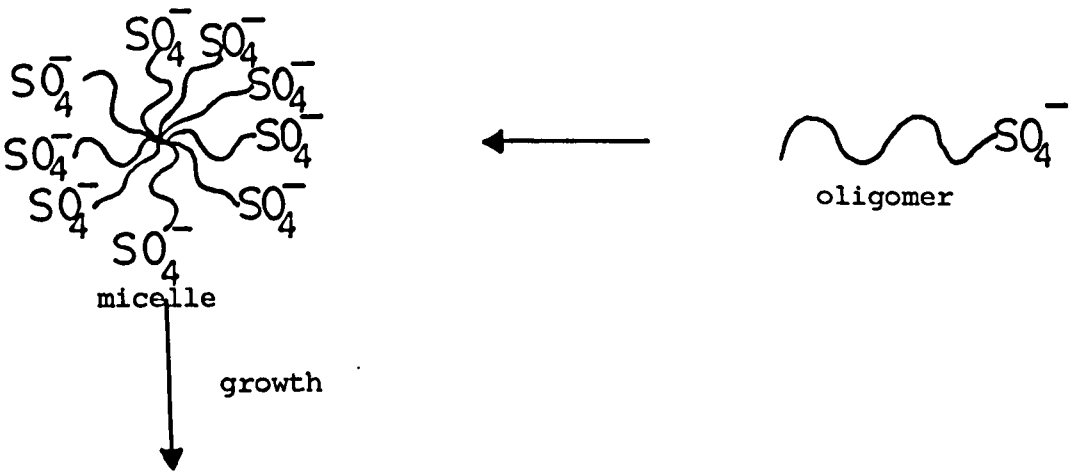

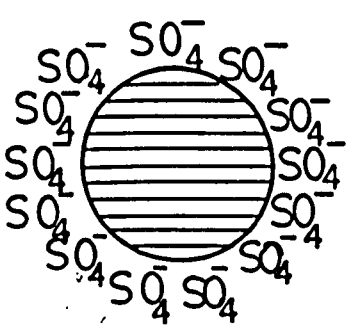

latex particle

sufficient radical generation. For potassium persulphate the lower limit has been found to be ca. 5×10^{-4} mol dm^{-3} at $70^{o}C$.[148]

There is a limit to the size of latex that can be obtained directly by polymerisation. For large particles, greater than ca. 500 nm in diameter for preparations involving a surface active agent emulsifier[141] and greater than ca. 1 μm in diameter for emulsifier free preparations,[147] a seeded-growth technique is employed. A smaller "seed" latex is prepared and then this further swelled by more monomer. To prevent new nucleation and hence a bimodal product it is essential that the growth is carried out with electrolyte present in the emulsifier-free case. With surface active agent present the concentration must be kept below the critical micelle concentration, c.m.c., for the same reason.[140] This procedure is more successful in the emulsifier-free case; monodisperse latices have been prepared with particle diameters of up to 5 μm.

A simple model was originally assumed for the mechanism of seeded growth involving the diffusion of more monomer into the seed latex particles where it subsequently polymerised. However, work by Chung-li, Goodwin and Ottewill[147] showed that the rate of polymerisation was too great for this to occur. The alternative mechanism proposed assumes that the main locus of polymerisation is in the aqueous phase where small particles form (secondary growth) and become swollen by monomer. These then migrate to the surface of the seed particles where aggregation occurs to complete the polymerisation.

Appendix I gives the method of calculating the conditions required for the growth of a seed latex to a particular particle diameter. Homola and co-workers[145] have shown that the yield and polymerisation rate may be improved by the addition of an alcohol to the reactants. Methanol is an obvious choice for polystyrene latex preparation due to its

infinite miscibility with both water and styrene and its lack of solvency for the polymer. Methanol may also be easily removed from the resultant latex by dialysis. The presence of an alcohol has various effects on the polymerisation, not least to vary the surface properties, i.e. the contact angle, of the forming latex particles. This is of particular importance in the case of latices with a final particle diameter of greater than ca. 750 nm as reduction of the contact angle prevents frothing from occuring which has a catastrophic effect on the preparation.

Table 7.1. gives a summary of methods of polymer latex preparation, with and without surface active agent emulsifier, and the size of particles these are most suited to.[148]

7.2.2. Materials.

All the distilled water used was doubly distilled, the second distillation carried out using a borosilicate glass still fitted with a quartz fractionating column.

The styrene was B.D.H. reagent grade material. This was purified by distillation at 40 - 50°C in an atmosphere of nitrogen at a pressure of ca. 5 mm Hg to remove any initiator or polymerised material. The purified styrene was stored at 5°C. The methanol was B.D.H. reagent grade material. The potassium persulphate, sodium chloride and sodium hydrogen carbonate were B.D.H. 'AnalaR' materials. The surface active agent used was Aerosol M.A. from Cyanamid, Netherlands. All nitrogen used was British Oxygen Company white spot gas.

Table 7.1.

Methods for the preparation of polymer latices in the size range 20 nm to 5μm with and without surface active agent (SAA) present.

	Approximate Particle Diameter Range	Methods	Comments
With surface active agent:			
	20 nm - 90 nm	Emulsion Polymerisation	SAA above cmc. Easy. Rapid. SAA must be removed after preparation.
	90 nm - 500 nm	Seeded Emulsion Polymerisation	SAA below cmc. Not easy to control. Secondary growth frequent.
Without surface active agent:			
	50 nm - 150 nm	High Temperature and Pressure	Very rapid decomposition of initiator Can work well.
	100 nm - 1 μm	Variable Ionic Strength Well stirred	Longer reaction than emulsion polymerisation. Reproducible. Excellent control of particle size.
	1μm - 5μm	Seeded Growth. Variable Ionic Strength Careful control of stirring to avoid orthokinetic effects	Needs careful control to avoid secondary growth. Can be subject to surface coagulation.

7.2.3. Experimental.

The polymerisation reactions were carried out in round-bottomed three-necked flasks of varying capacity depending on the reaction volume. The contents of the flask were stirred using a PTFE paddle stirrer (1 x 5.2 cm, type Q-ST 7/2 and 1 x 7.3 cm, type Q-ST 7/3), the size again depending on the reaction volume, which was inserted into the central neck of the flask. The stirrer speed was maintained at a constant rate of 350 r.p.m. or 450 r.p.m.; a faster rate was required for the larger volume preparations to ensure sufficient agitation. The rate was checked at frequent intervals with a tachometer (Smiths Industrial division). The two remaining outlets of the flask housed a water-cooled condenser and a nitrogen inlet. In order to flush oxygen from the system nitrogen was bubbled continuously through the system throughout the reaction, at a low rate to minimise evaporation. It is essential that the polymerisation is carried out in the absence of oxygen as it is a radical scavenger. To prevent back-diffusion of oxygen into the system, the condenser was connected to the atmosphere via a dreschel bottle containing water. The flask was maintained at a constant temperature of 70°C (± 0.5°C) by immersion to the neck in a water-thermostat bath.

All the reactants, except the initiator and most of the water were added to the flask and left under nitrogen to attain temperature equilibrium and expel the oxygen. The potassium persulphate, dissolved in the remaining water, was then added. The reaction time was generally about 18 hours.

After this the latex was cooled and filtered through glass wool (lead-free B.D.H. material) into well boiled Visking dialysis tubing.

The latex was dialysed against distilled water to remove any unreacted monomer and any short chain reaction products that were present.

The ratio of dialysate to latex was ca. 7:1 and the dialysate was changed daily for thirty changes, the last two changes being twice distilled water.

In the case of preparations with methanol present the first dialysate was water : methanol in the same proportion as in the polymerisation reaction and then the methanol content reduced to zero within the next four dialysate changes. This was to prevent bursting of the dialysis tubes due to a build up of osmotic pressure.

The latex was finally stored in steam-cleaned polypropylene bottles.

7.2.4. Recipes.

The recipes for the latices prepared: SJP4 - SJP12 are given in Tables 7.2 and 7.3.

7.2.5. Results and Discussion.

All the latices prepared were opaque and white in colour. Latex SJP12 exhibited an opalescent effect on dialysis which increased in intensity throughout the dialysis and remained on storage. This effect was not observed to any extent in any of the other, larger particle sized, latices.

One latex was prepared following the recipe for SJP5, but with no methanol present. Extensive frothing occurred due to the surface coagulation of the large growing particles and the nitrogen flow. When 15% methanol was included in the reactants this problem did not occur.

Another latex was prepared following the seeded growth recipe for SJP8 with the omission of the sodium chloride. A bimodal latex

Table 7.2.

Recipes and Conditions used for Polystyrene Latex Preparations I.

	SJP4	SJP5	SJP6	SJP7
Temperature	70°C	70°C	70°C	70°C
Reaction time	21 hours	18 hours	18 hours	18 hours
Stirrer speed	350 rpm	350 rpm	350 rpm	450 rpm
Reaction vessel volume	2000 cm^3	2000 cm^3	2000 cm^3	10000 cm^3
Total reaction volume	1600 cm^3	1600 cm^3	1400 cm^3	8000 cm^3
Water	1440 cm^3 90% of total volume	1200 cm^3 75% of total volume	609 cm^3 43.5% of total volume	6000 cm^3 75% of total volume
Styrene	160 cm^3 10% of total volume	160 cm^3 10% of total volume	41 cm^3 2.9% of total volume	800 cm^3 10% of total volume
Potassium persulphate	1.17 g $3x10^{-3}$ mol dm^{-3} in aqueous phase	1.17 g $3x10^{-3}$ mol dm^{-3} in aqueous phase	1.06 g $3x10^{-3}$ mol dm^{-3} in aqueous phase	5.84 g $3x10^{-3}$ mol dm^{-3} in agueous phase
Methanol	-	240 cm^3 15% of total volume	-	1200 cm^3 15% of total volume
Sodium chloride	-	2.53 g $3x10^{-2}$ mol dm^{-3} in aqueous phase	-	12.62 g $3x10^{-2}$ mol dm^{-3} in aqueous phase
Seed Latex	-	-	SJP5 750 cm 53.6% of total volume	-

Table 7.3.

Recipes and Conditions used for Polystyrene Latex Preparations II.

	SJP8	SJP9	SJP10	SJP11	SJP12
Temperature	70°C	70°C	70°C	70°C	70°C
Reaction time	18 hours	18 hours	18 hours	18 hours	18 hours
Stirrer speed	450 rpm	450 rpm	450 rpm	450 rpm	450 rpm
Reaction vessel volume	12500 cm^3	12500 cm^3	12500 cm^3	12500 cm^3	5000 cm^3
Total reaction volume	11000 cm^3	11000 cm^3	11000 cm^3	11000 cm^3	4000 cm^3
Water	5500 cm^3 50% of total volume	5500 cm^3 50% of total volume	4671 cm^3 42.5% of total volume	7057 cm^3 64.1% of total volume	3200 cm^3 80% of total volume
Styrene	2200 cm^3 20% of total volume	2200 cm^3 20% of total volume	1594 cm^3 14.5% of total volume	1944 cm^3 17.7% of total volume	800 cm^3 20% of total volume
Potassium persulphate	7.14 g $3x10^{-3}moldm^{-3}$ in aqueous phase	7.14 g $3x10^{-3}moldm^{-3}$ in aqueous phase	7.14 g $3x10^{-3}moldm^{-3}$ in aqueous phase	7.14 g $3x10^{-3}moldm^{-3}$ in aqueous phase	5.7 g $6.5x10^{-3}moldm^{-3}$ in aqueous phase
Ethanol	3300 cm^3 30% of total volume	3300 cm^3 30% of total volume	-	-	-
Sodium chloride	15.43 g $3x10^{-3}moldm^{-3}$ in aqueous phase	15.43 g $3x10^{-2}$mol dm^{-3} in aqueous phase	15.43 g $3x10^{-2}moldm^{-3}$ in aqueous phase	15.43 g $3x10^{-2}moldm^{-3}$ in aqueous phase	-
Seed Latex	-	-	SJP9 4735 cm^3 43% of total volume	SJP9 1999 cm^3 18.2% of total volume	-
Sodium hydrogen carbonate	-	-	-	-	5.7 g $2x10^{-2}moldm^{-3}$ in aqueous phase
Aerosol M.A. (80% solution in ethanol)	-	-	-	-	41.07 g

resulted with large particles similar in size to the seed latex and many new smaller particles formed by new nucleation. When sodium chloride was included a monodisperse latex was formed.

7.3. Characterisation of Polystyrene Latices.

7.3.1. Electron Microscopy.

Samples of dialysed polystyrene latices were diluted with doubly distilled water and examined in a Joel JEM-100CX transmission electron microscope.* A low beam current was used to avoid shrinkage of the particles. Photomicrographs were taken of the latices at intervals across the grid and of a diffraction grating, all at the same magnification. The grating had a mean spacing of 472 ± 5 nm, previously calibrated using an optical microscope.

The micrographs were enlarged, printed onto Kodak P84 paper and analysed using a Carl Zeiss TGZ3 Particle Size Analyser. For each sample approximately 1000 particles were measured.

The results were considered to be accurate within ± 5%.

Plates 7.1 - 7.9 are micrographs of the latices SJP4 - SJP12. The results obtained from the particle size analysis are presented in Table 7.4.

All the latices were found, under observation in the electron microscope, to contain spherical particles of approximately equal size. All coefficients of variation were less than 5% on the mean particle diameter and may be considered to be monodisperse. Wachtel and La Mer[139]

---

* The author gratefully acknowledges the help of Dr. D.W. Thompson of Bristol University.

Electron Micrographs of Polystyrene Latices.

Plate 7.1. SJP4

diameter = 5.51×10^{-7}m
coefficient of variation = 2.5%

Plate 7.2. SJP5

diameter = 9.05×10^{-7}m
coefficient of variation = 2.3%

Plate 7.3. SJP6

diameter = 1.092×10^{-6}m
coefficient of variation = 2.6%

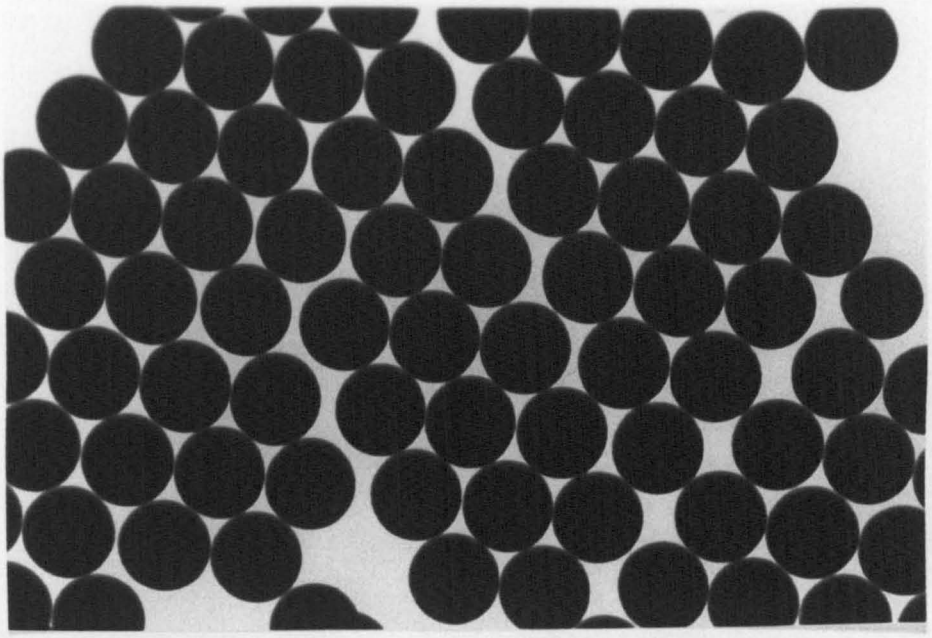

Plate 7.1.

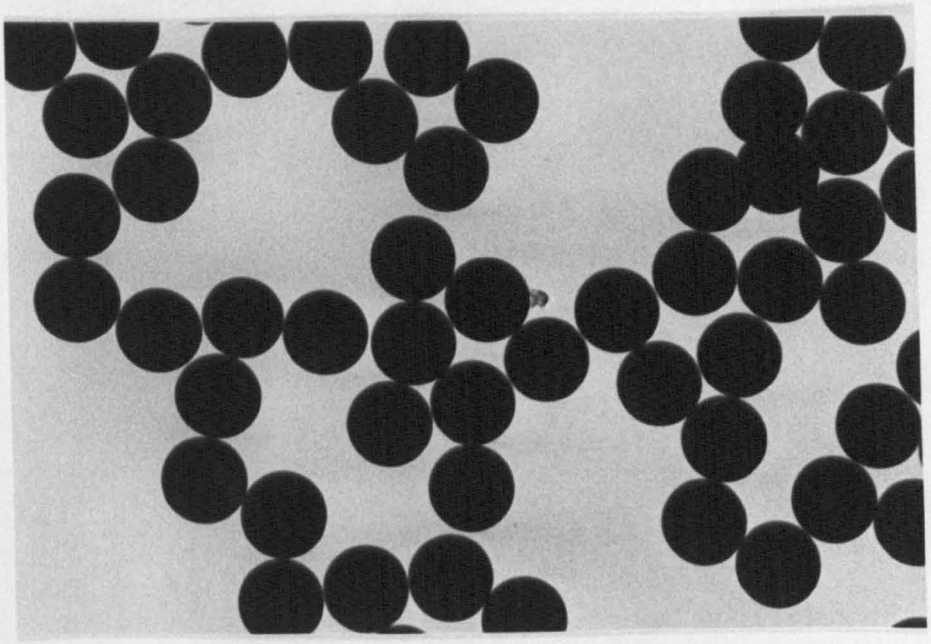

Plate 7.2.

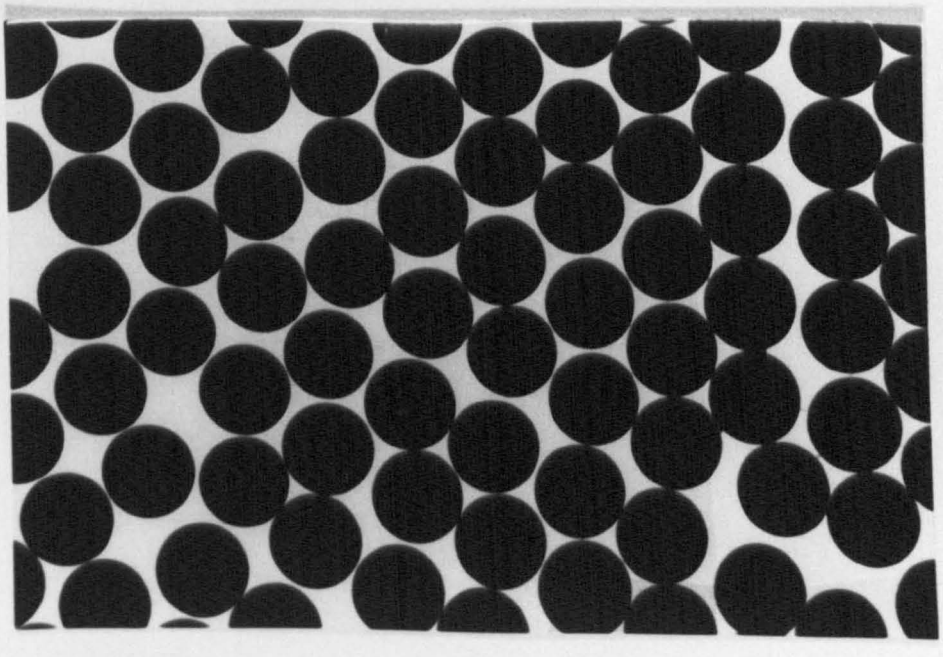

Plate 7.3.

Electron Micrographs of Polystyrene Latices

Plate 7.4. SJP7

diameter = 7.30×10^{-7}m
coefficient of variation = 3.1%

Plate 7.5. SJP9

diameter = 9.76×10^{-7} m
coefficient of variation = 2.6%

Plate 7.6. SJP12

diameter = 1.44×10^{-7} m
coefficient of variation = 3.7%

Plate 7.4.

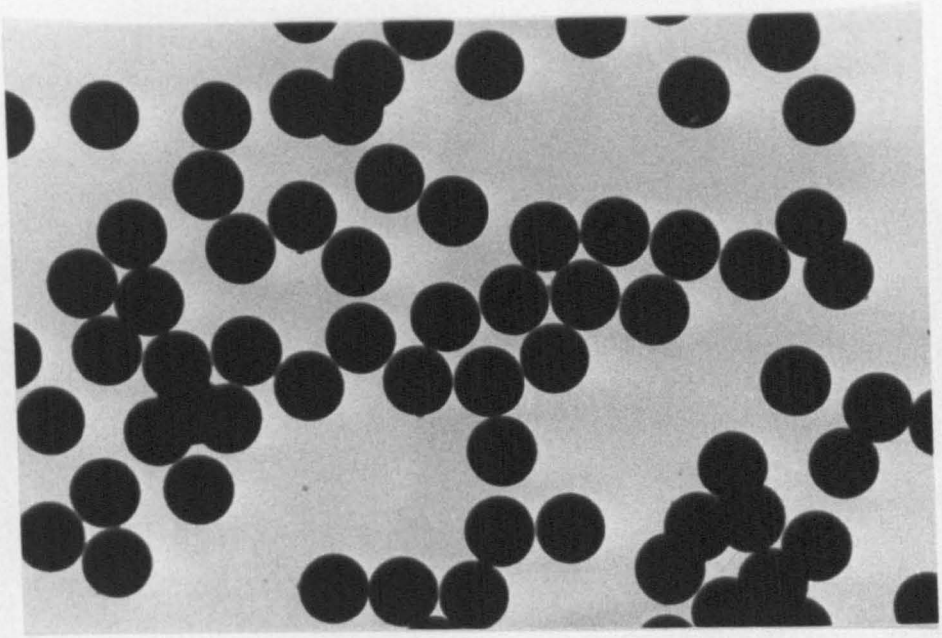

Plate 7.5.

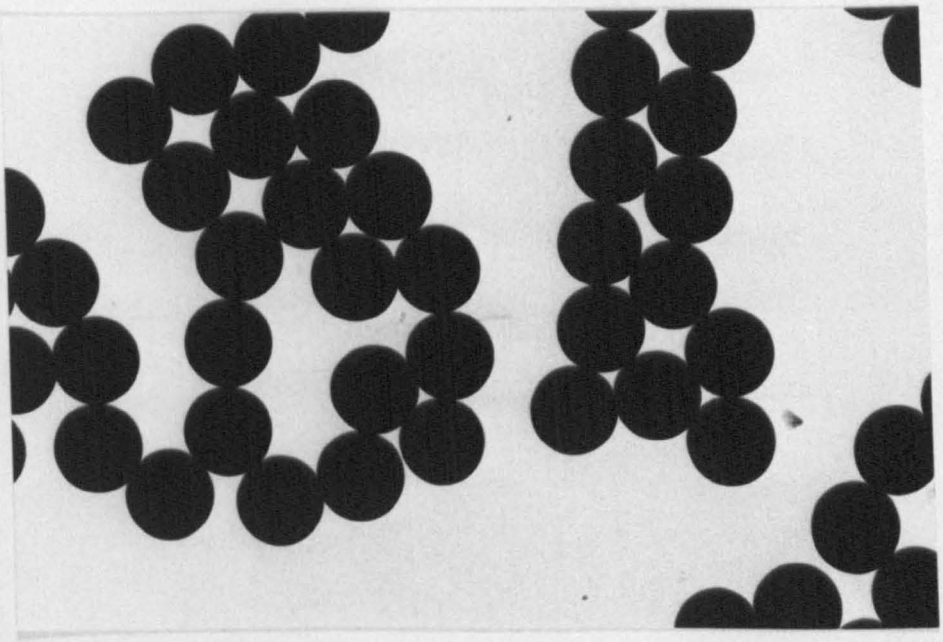

Plate 7.6.

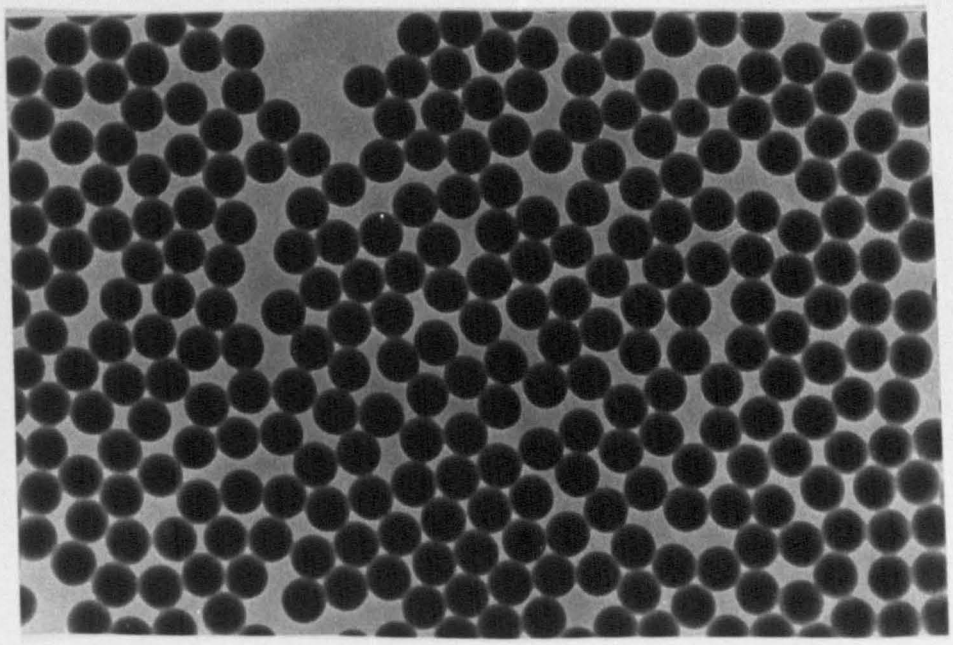

Electron Micrographs of Polystyrene Latices.

Plate 7.7. SJP8

diameter = 9.74×10^{-7} m
coefficient of variation = 2.3%

Plate 7.8. SJP10

diameter = 1.411×10^{-6} m
coefficient of variation = 4.4%

Plate 7.9. SJP11

diameter = 1.916×10^{-6} m
coefficient of variation = 4.9%

Plate 7.7.

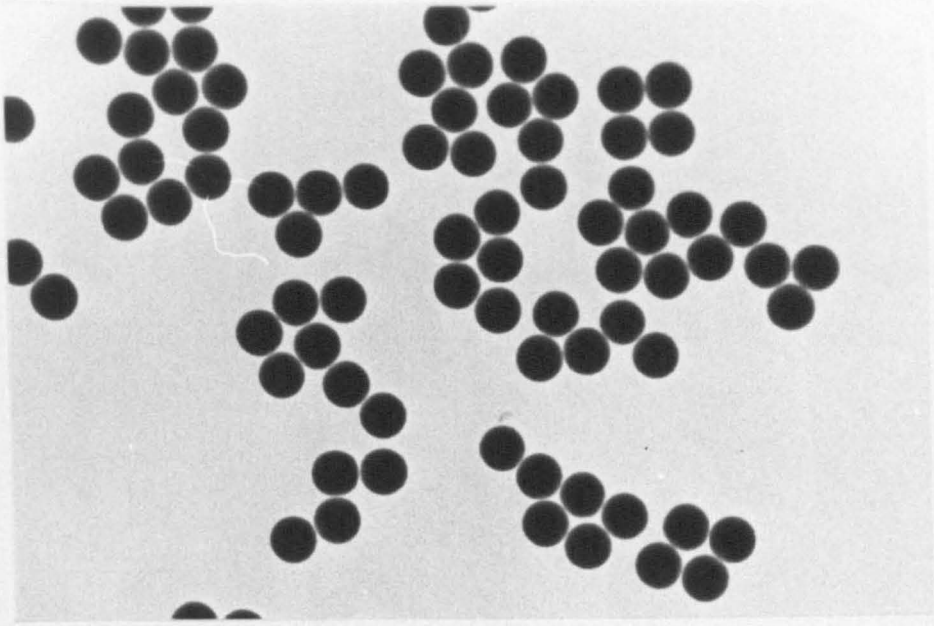

Plate 7.8.

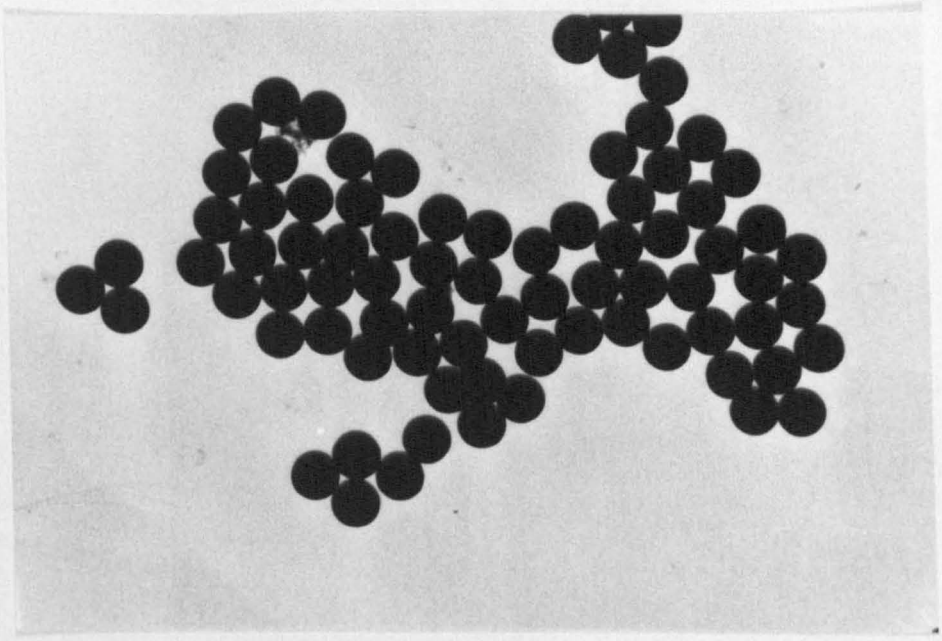

Plate 7.9.

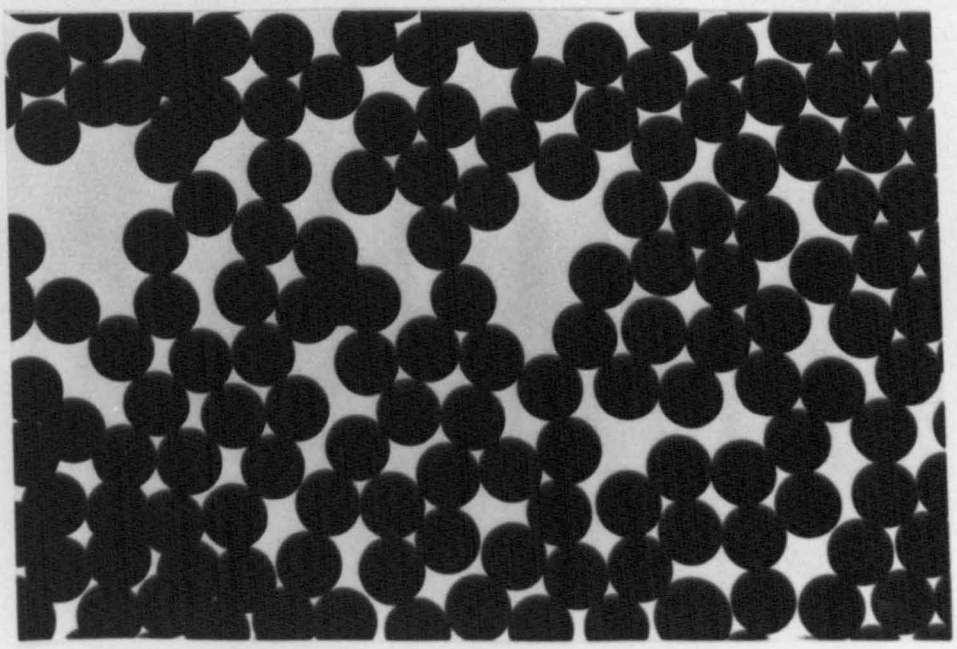

Table 7.4.

Particle size determination of polystyrene latices.

	SJP4	SJP5	SJP6	SJP7	SJP8	SJP9	SJP10	SJP11	SJP12
Number average particle diameter/m	5.51×10^{-7}	9.05×10^{-7}	1.092×10^{-6}	7.30×10^{-7}	9.74×10^{-7}	9.76×10^{-7}	1.411×10^{-6}	1.916×10^{-6}	1.44×10^{-7}
Coefficient of variation/%	2.5	2.3	2.6	3.1	2.3	2.6	4.4	4.9	3.7
Area per unit volume/m^2cm^{-3}	10.91	6.68	5.50	8.25	6.16	6.15	4.27	3.15	41.80
Specific surface area/m^2g^{-1}	10.35	6.33	5.22	7.83	5.84	5.83	4.05	2.99	39.66
Number average particle diameter before dialysis/m	5.20×10^{-7}	8.35×10^{-7}	1.07×10^{-6}	-	9.45×10^{-7}	-	1.22×10^{-6}	1.71×10^{-6}	1.39×10^{-7}

suggested that any dispersion of particles with a coefficient of variation of less than 10% be considered monodisperse.

In all cases the particle diameter was found to be lower prior to dialysis. This can be attributed to the fact that the spheres were softer before dialysis and were therefore susceptible to shrinkage under the electron beam. Dialysis, as well as purifying latices, tended to harden the latex particles.

Latices SJP8 and SJP9 were prepared following exactly the same recipe. Their resultant latex particle diameters were 9.74×10^{-7}m and 9.76×10^{-7}m respectively which was the same within the experimental error of ± 5%. This shows that latex preparation was extremely reproducible.

Latices SJP5 and SJP7 were prepared using the same proportions of reactants but in different quantities. Their resultant particle diameters were 9.05×10^{-7}m and 7.30×10^{-7}m respectively. This showed that increasing the reaction volume five-fold had an effect on the resultant latex particle size.

Latices SJP10 and SJP11, prepared by seeded growth of SJP9 were intended, by calculation (see Appendix I),to have particle diameters of 1.5×10^{-6}m and 2.0×10^{-6}m. They were found to have particle diameters of 1.41×10^{-6}m and 1.92×10^{-6}m, values within 6% of the calculated values, the experimental error being ± 5%. Hence the seeded growth method can be considered to be controllable.

Latex SJP5 was prepared in the same way as SJP4, but with methanol and sodium chloride present. Their substantially different diameters, 9.05×10^{-7}m and 5.51×10^{-7}m showed that the ionic strength had an effect on particle diameter as predicted in equation (4.1).

7.3.2. Higher Order Tyndall Spectra, HOTS.

Another test for the polydispersity of latices is the observation of a higher order Tyndall spectrum (HOTS). When a beam of white light is passed through a suspension of particles, of radius of the same order of magnitude as the wavelength of the light, the colour of the scattered light at a given angular position depends on the radius of the particles illuminated.[139,159] Thus, if a latex is monodisperse the scattered light will be observed as bands of colour; if there is a broad distribution of particle sizes the light will be of the usual white colour and HOTS will not be observed.

Testing a latex for HOTS is a useful, quick way to test for monodispersity and to check that a latex preparation has been successful.

All the latices prepared exhibited HOTS.

7.3.3. Iridescence.

Iridescence is a light diffraction phenomenon exhibited by regular arrays of monodisperse particles.[160,161] It is due to the Bragg reflection of visible light by ordered arrays of particles when the centre to centre separation between the particles is comparable with the wavelength of the light. As it is the centre to centre separation that is important, the particle diameter, the surface charge, the electrolyte concentration and the volume fraction all contribute as they control the particle interaction forces.

All the latices were found to be opaque and white with only SJP12 displaying iridescence. This is evidence that the particle diameter of the SJP12 latex particles was substantially smaller than the diameters of the other latex particles and that it was monodisperse. The

iridescence developed with time as the latex particles formed an ordered structure.

The other latices did not display any iridescence as their diameters were too large for the particle centre to centre separation to be comparable with the wavelength of visible light.

7.4. Selection of the Adsorbate.

Ideally the adsorbate must be as monodisperse and as well characterised as possible as this simplifies the mathematical modelling of the experimental system. Flocculation may be brought about by a number of mechanisms including bridging flocculation and flocculation induced by the addition of electrolyte to a sterically stabilised system. The latter type of mechanism is simpler to model in theoretical terms and is likely to be weaker and so more easily reversible.

Preliminary work on weakly flocculated systems was carried out by Buscall and McGowan[2] at Corporate Bioscience and Colloid Division, ICI, using a modified cellulosic material, sodium carboxymethylcellulose, Cellofas B200 (M.W. $\simeq 2 \times 10^5$), as the adsorbate. Being polymeric theoretical analysis was difficult due to the polydispersity of the molecules. It was also likely that some form of "sticky" interaction took place between the coated particle surfaces due to long-chain molecules. Hence, although the system was intended to be sterically stabilised there was undoubtedly some effect due to bridging flocculation.

Pure nonionic surface active agents in monodisperse form are available from Nikko Chemicals Co., Tokyo, Japan. Some n-dodecyl hexaoxyethylene monoether, $C_{12}E_6$ was obtained. Its monodispersity

was ascertained by gas-liquid chromatography, glc. A narrow single peak was obtained, evidence that only one fraction was present. The chromatograph is presented in Figure 7.2.

The phase diagram for $C_{12}E_6$ - H_2O was determined by Clunie and coworkers[162] and is given in Figure 7.3. It can be seen that at low composition, at temperatures in the range to be considered in this work, the $C_{12}E_6$ - H_2O system exists as an isotropic solution.

7.5. Adsorption Isotherms.

7.5.1. Theory.

Surface active agents behave in two very distinctive ways in water; by adsorption they significantly modify interfacial properties at low bulk concentrations and by co-operative self-association they aggregate over a very narrow concentration range to form micelles. The concentration at which micellesform is known as the critical micelle concentration, c.m.c., and is characteristic of a particular surface active agent.

The effect surface active agents have upon interfacial properties may be utilised to calculate the extent of adsorption and the c.m.c. of a particular surface active agent by means of surface tension measurements. The typical form of a surface tension, γ, versus $\log_{10}$ surface active agent concentration, $\hat{c}$, plot is illustrated schematically in Figure 7.4. In region I only individual surface active agent molecules exist whereas in region II, above the c.m.c., both individual molecules and micelles coexist in dynamic equilibrium.

The extent of adsorption may be calculated from the Gibbs adsorption

Figure 7.2.

Gas liquid chromomatogram of $C_{12}E_6$

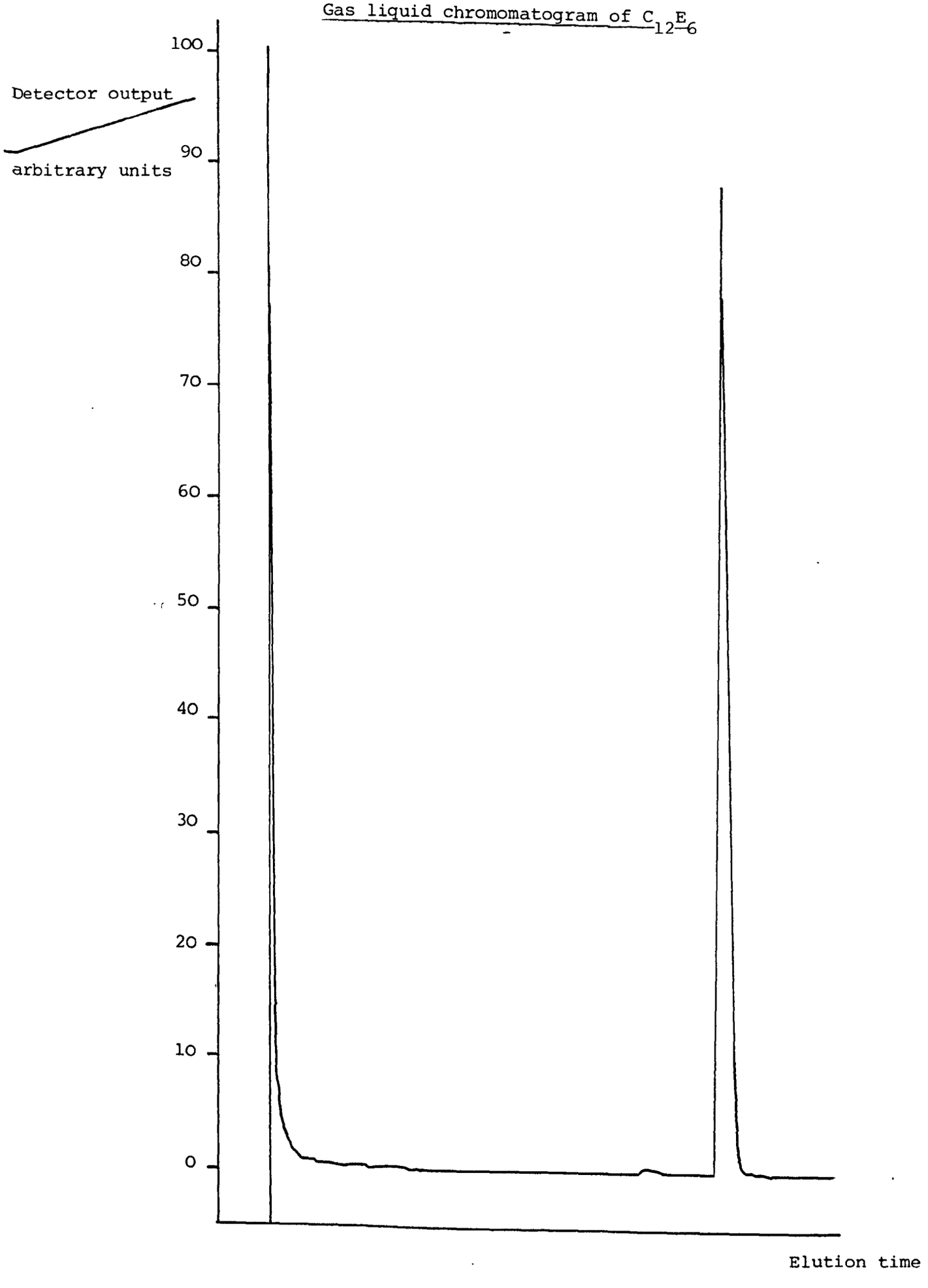

Figure 7.3.

Phase Diagram for $C_{12}E_6 + H_2O$.

2L = co-existing isotropic liquids, S = isotropic solution, M = middle phase, N = neat phase, I = ice, C = crystals.

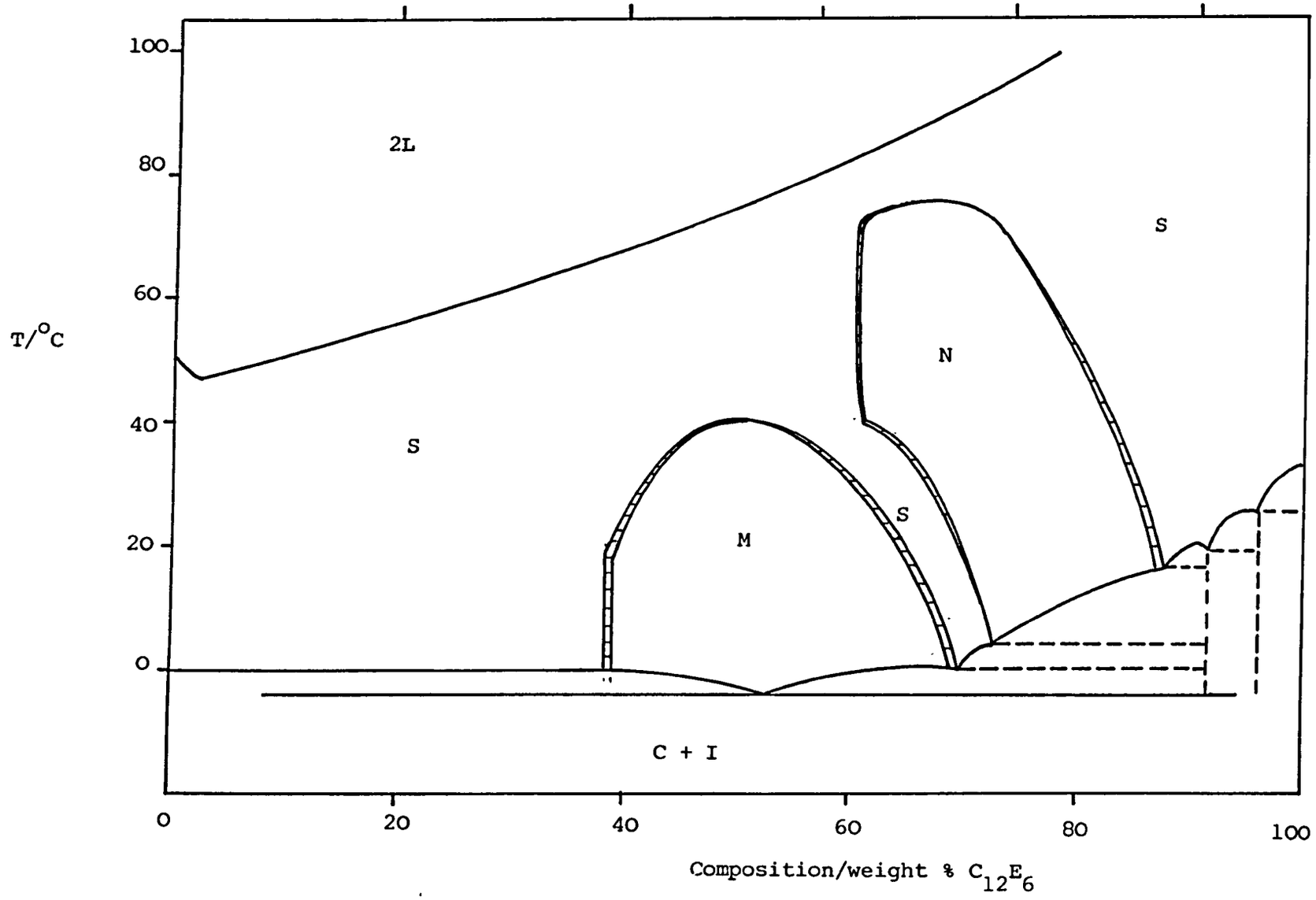

Figure 7.4.

Typical surface tension, $\hat{\gamma}$, versus $\log_{10}$ concentration, $\hat{c}$, plot for nonionic surface active agents.

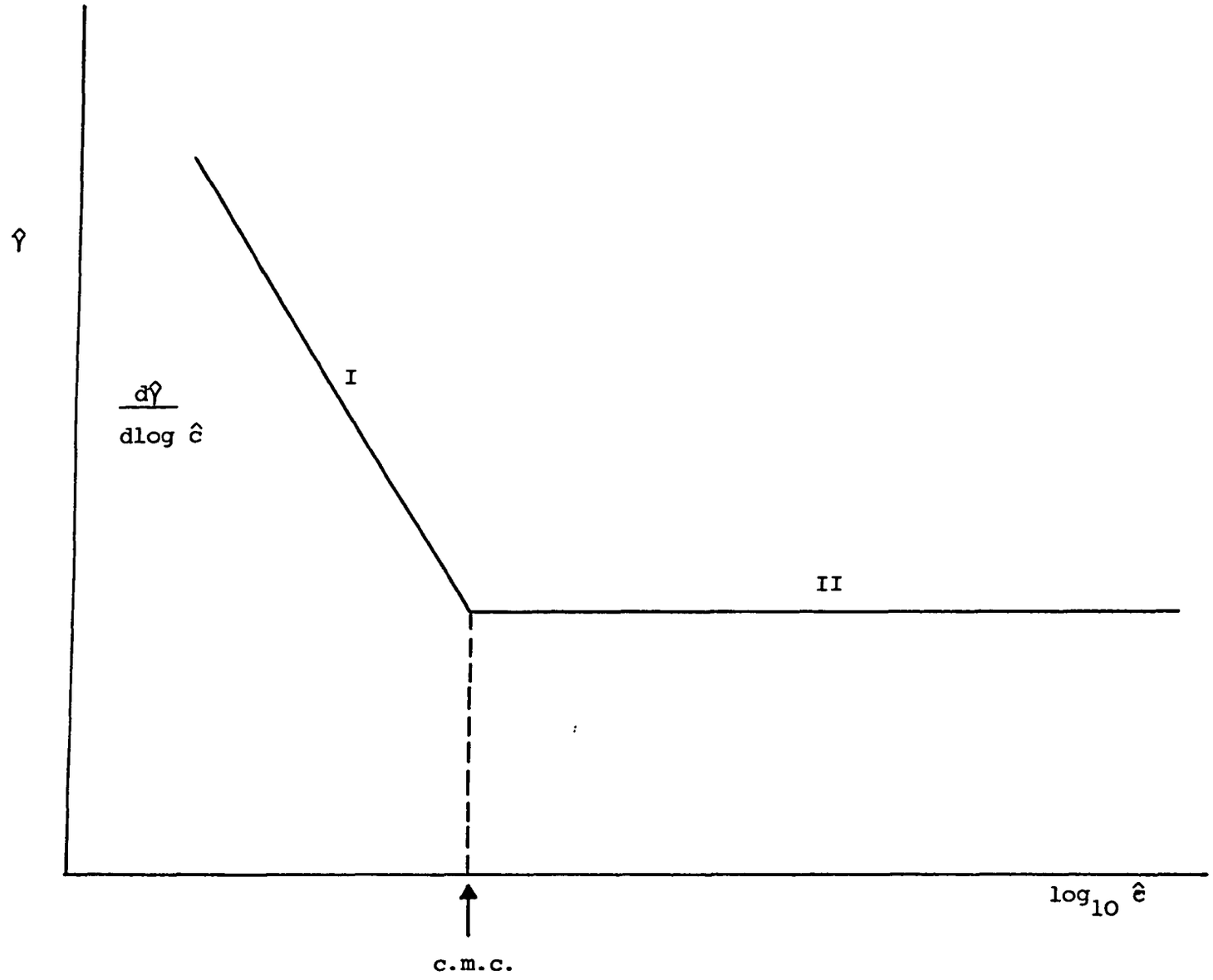

equation given below:

$$\Gamma = -\frac{1}{RT}\left[\frac{d\hat{\gamma}}{d\ln\hat{c}}\right]_T = -\frac{1}{2.303\ RT}\left[\frac{d\hat{\gamma}}{d\log\hat{c}}\right]_T \qquad (7.2)$$

where Γ is the surface excess concentration, a measure of the adsorption and inversely related to the area occupied by one molecule at the surface, A_s.

Nonionic surface active agents are physically adsorbed rather than chemisorbed at the solid-liquid interface; the adsorption is very sensitive to small changes in temperature and concentration.

Three models for the adsorption of nonionic surface active agent are illustrated in Figure 7.5,[163] showing the orientation of the adsorbate molecules at the surface in terms of increasing surface active agent concentration. Three situations are shown, illustrating the relatively weak, intermediate and strong interactions between the adsorbent and the hydrophilic moiety of the surface active agent. The corresponding adsorption isotherms (Γ versus $\hat{c}$) are given in Figure 7.6.

At very low concentrations (I) the adsorbate molecule adsorbs onto a surface where there are very few other adsorbate molecules present and where, consequently adsorbate-adsorbate interactions are negligible. The adsorption is due to van der Waals attraction and it is therefore the hydrophobic moiety of the surface active agent that is dominant in aqueous media. The hydrophilic ethylene oxide groups do, however, undergo some interaction with the surface and hence the molecules tend to lie flat on the particle surface.

As the surface active agent concentration increases monolayer saturation of molecules lying flat is approached (II). At this point it is the adsorbate-adsorbent interaction that determines how the adsorption progresses. In the case of weak hydrophilic adsorption the hydrophilic ethylene oxide groups are displaced from the surface by the

Figure 7.5.

Models for the adsorption of nonionic surface active agent, showing the orientation of molecules at the surface with increasing surface active agent concentration.

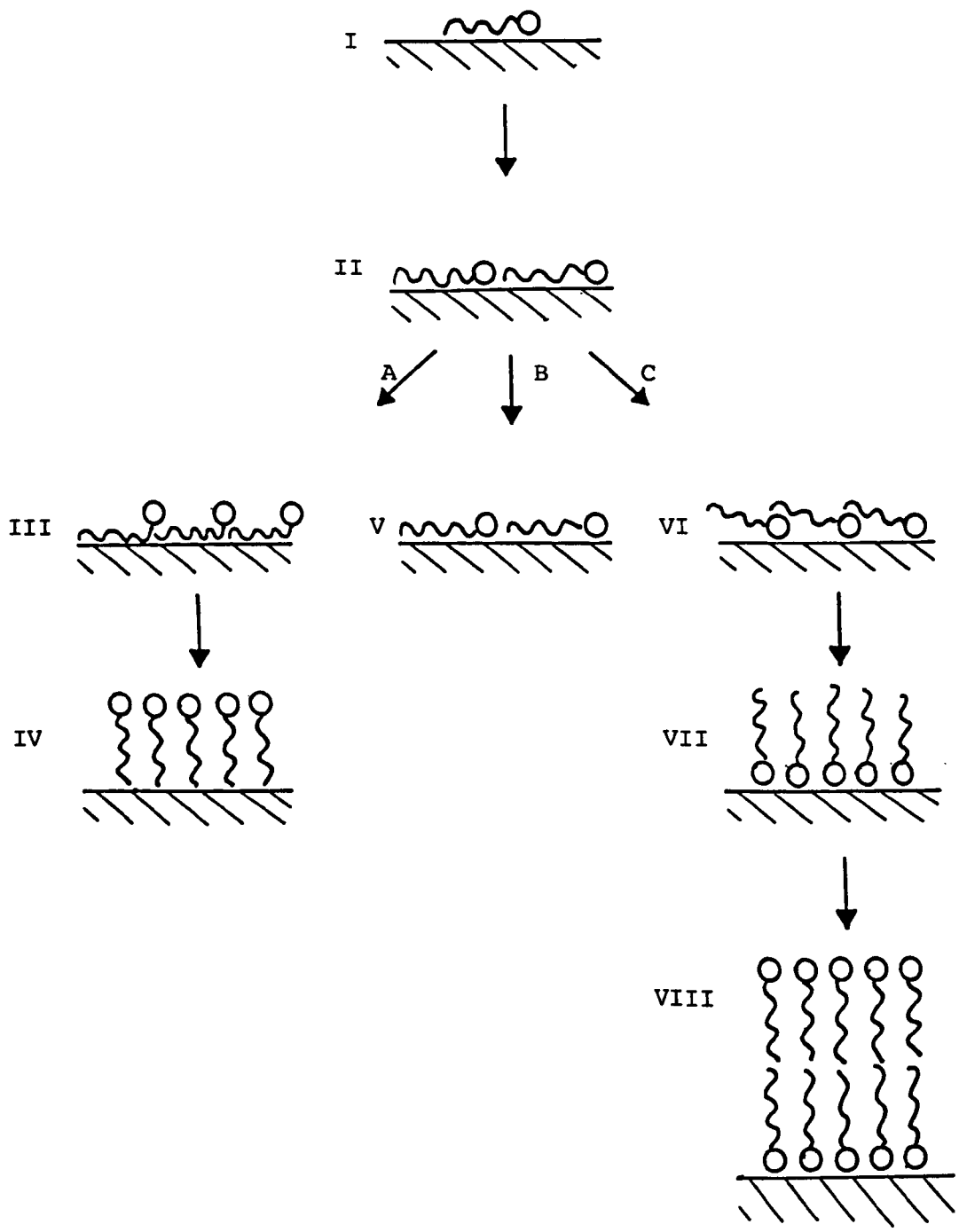

Sequences A - C correspond to situations where there are respectively weak, intermediate and strong interactions between the adsorbent and the hydrophilic moiety of the surface active agent.

Figure 7.6.

Adsorption isotherms corresponding to the three adsorption sequences shown in Figure 7.5. indicating the different orientations of adsorbed molecules.

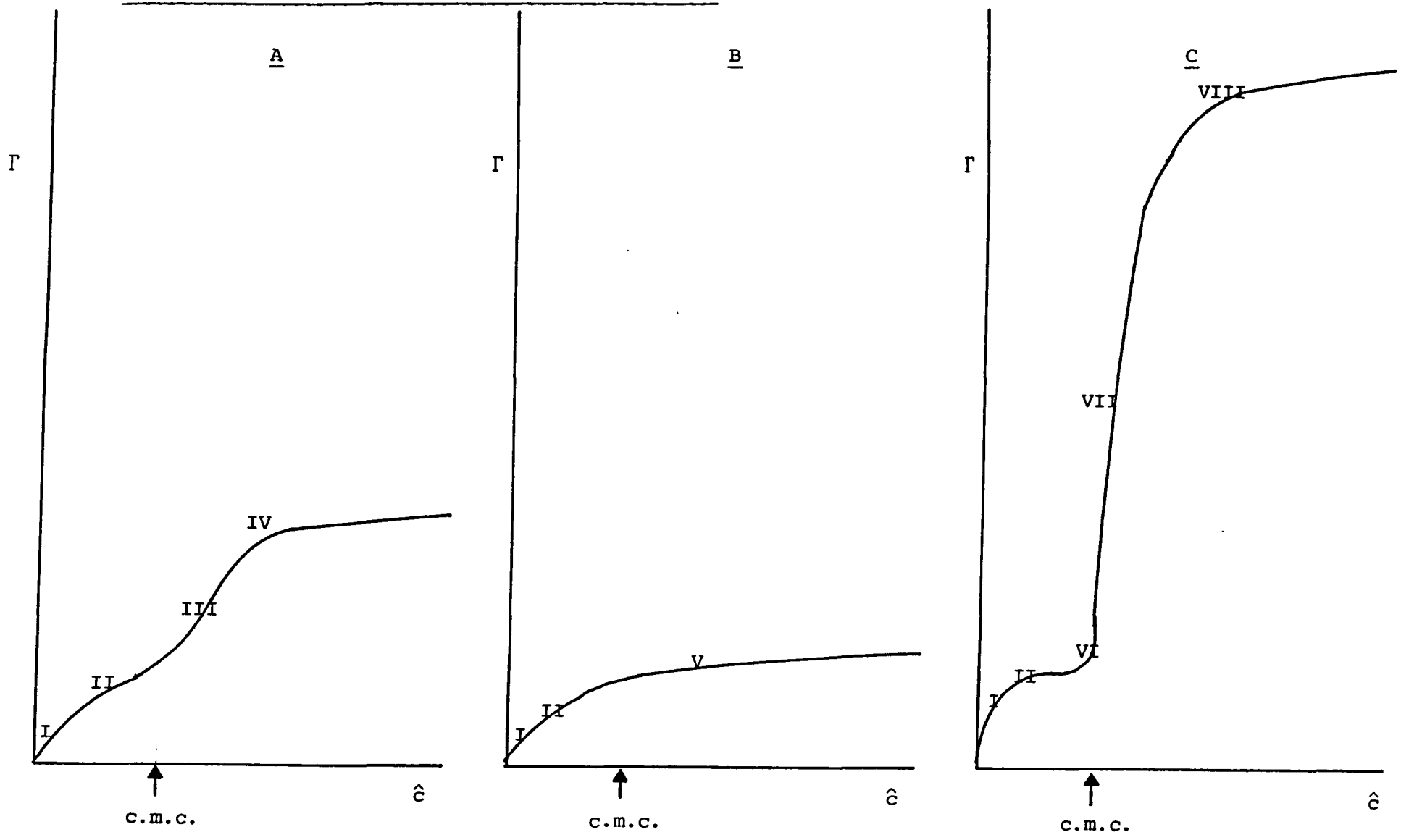

alkyl chains of adjacent molecules (III) as illustrated in sequence A. As the concentration increases further a monolayer is formed of vertically orientated surface active agent molecules, anchored on the particle surface by the alkyl chains (IV).

If there is a strong interaction between the hydrophilic group and the surface, such as may occur with polar adsorbents like silicates and oxides, the alkyl chain is displaced (VI) and sequence C is followed. As the concentration increases a monolayer analogous to (IV) is formed, anchored by the hydrophilic group (VII). As the concentration increases further a bi-molecular leaflet is formed (VIII).

The intermediate situation, sequence B, occurs when neither type of displacement is favoured and the adsorbate then remains flat on the surface (V).

Giles et al[164,165] have classified adsorption isotherms into four main classes according to the nature of the slope of the initial part of the curve; subgroups relate to the behaviour at higher concentrations. The various isotherm shapes considered are illustrated in Figure 7.7.

The L (Langmuir) class is the most common and is characterised by an initial region which is concave to the concentration axis. For the S class the initial slope is convex to the concentration axis; this is frequently followed by a point of inflection leading to an S-shaped isotherm. The H (high affinity) class results from extremely strong adsorption at very low concentrations giving an apparent intercept on the ordinate. The C (constant partition) class has an individual linear portion which indicates constant partition of the solute between solution and adsorbent.

Figure 7.7.

Classification of isotherm shapes according to Giles et al[164,165]

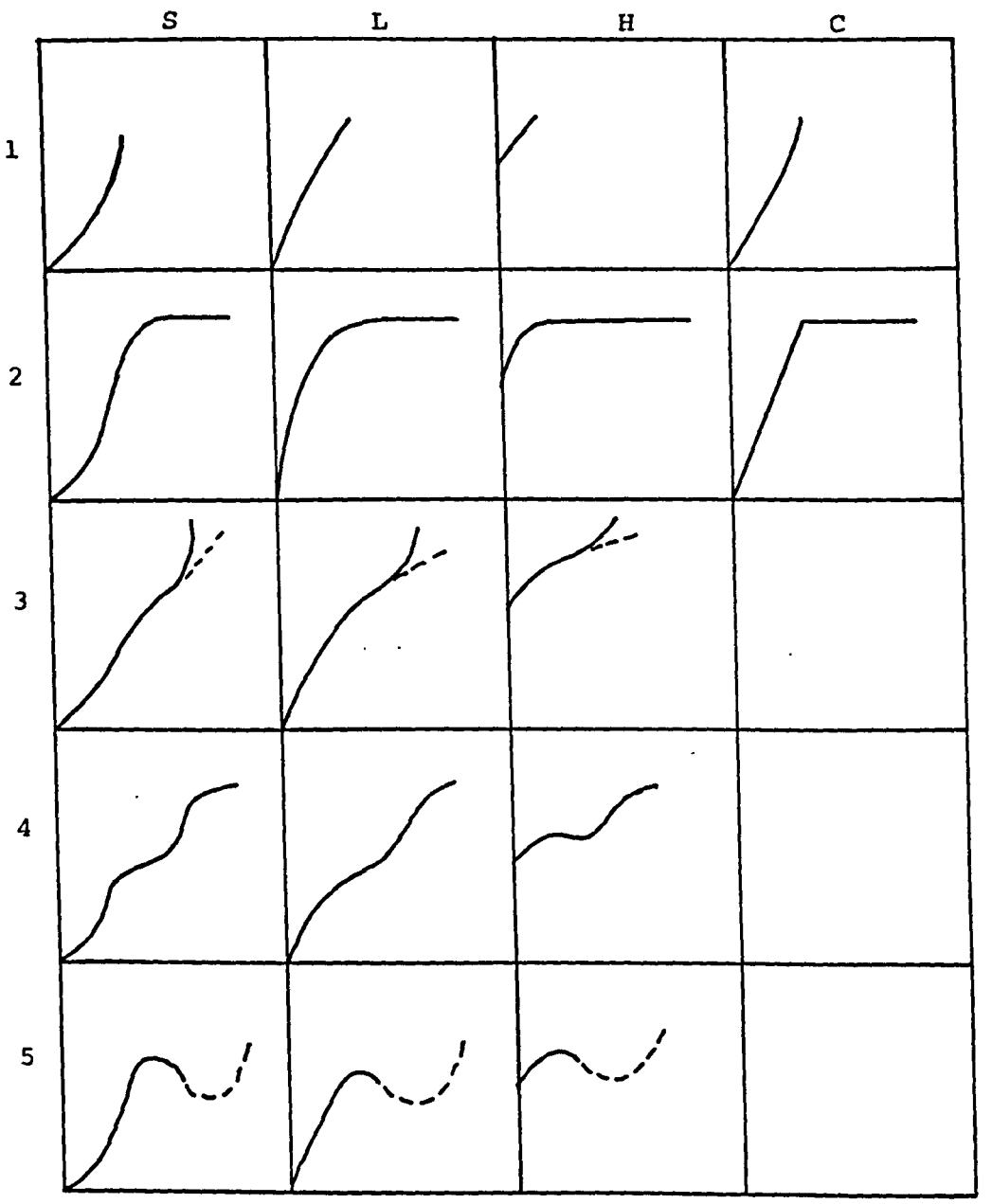

The construction of an adsorption isotherm for a given adsorption process at the solid-liquid interface is very useful as from it information may be obtained as to the type of adsorption, the monolayer coverage and the equilibrium concentration of the adsorption medium after adsorption has occurred.

The usual way of determining an adsorption isotherm is to stir together known amounts of adsorbent particles with a series of adsorbate solutions of varying concentration at constant temperature until adsorption equilibrium is attained.[166] The coated adsorbent particles are removed and the concentration of adsorbate in the supernatant determined. The surface excess concentration, Γ, may be deduced as follows:

$$\Gamma = \frac{(n_i - n_{eqm})N_A}{m_L A_L^*} \qquad (7.3)$$

where n_i and n_{eqm} are the initial and equilibrium number of moles of adsorbate in the sample, N_A is Avogadro's number, m_L is the mass of adsorbent particles in the sample and A_L the specific surface area of the adsorbent particles.

A calibration measurement is required for the determination of the concentration of adsorbate in the supernatant. In the case of surface active agent adsorbates it is convenient for this calibration method to be surface tension measurements.

Surface tension measurements may be made using the du Noüy ring method. A horizontal ring is dipped into the surface of a liquid and gradually raised. As the ring is slowly pulled out of the surface, the force exerted on it, measured by a balance, increases steadily until the point is reached when the ring detaches itself from the liquid surface. This point of instability of the meniscus corresponds to the maximum force exerted which is a measure of the surface tension of the

liquid.

To obtain absolute values of surface tension a correction factor based on the ring dimensions and the volume of the raised liquid[168] is required. This is not necessary in the case of an adsorption isotherm calibration as the error will remain constant.

7.5.2. Surface Tension Measurements.

The surface tension measurements were carried out using a Krüss du Noüy tensiometer which is illustrated in Figure 7.8.[169] The sample cell was maintained at a temperature of 25 ± 0.1°C by means of a thermostatted jacket. The glass sample cell was cleaned by immersion overnight in concentrated nitric acid and thoroughly rinsed in tap water and finally in twice distilled water. The platinum ring was cleaned between each reading by flaming to red heat in a blue Bunsen flame.

The glass cell was filled with surface active agent solution of concentration above the c.m.c. and the zero set by means of the torsion wire. The cell platform was gradually raised until the ring touched the liquid surface. The platform was then very slowly lowered as the torsion wire was simultaneously tightened to maintain the horizontal position of the torsion balance. At a given tension the ring was pulled from the liquid surface, this was the surface tension.

Because of surface aging effects, after a first test measurement was made the tension was slowly raised to a value ≃ 15m Nm^{-1} below the actual surface tension and held for five minutes. This was repeated after a further ≃ 7 m Nm^{-1} before the final reading was taken. This procedure was repeated three times or until concordant results were obtained. A repeatability of ± 0.1 m Nm^{-1} was obtained.

The surface active agent was systematically diluted with twice

Figure 7.8.

Krüss du Noüy Tensiometer

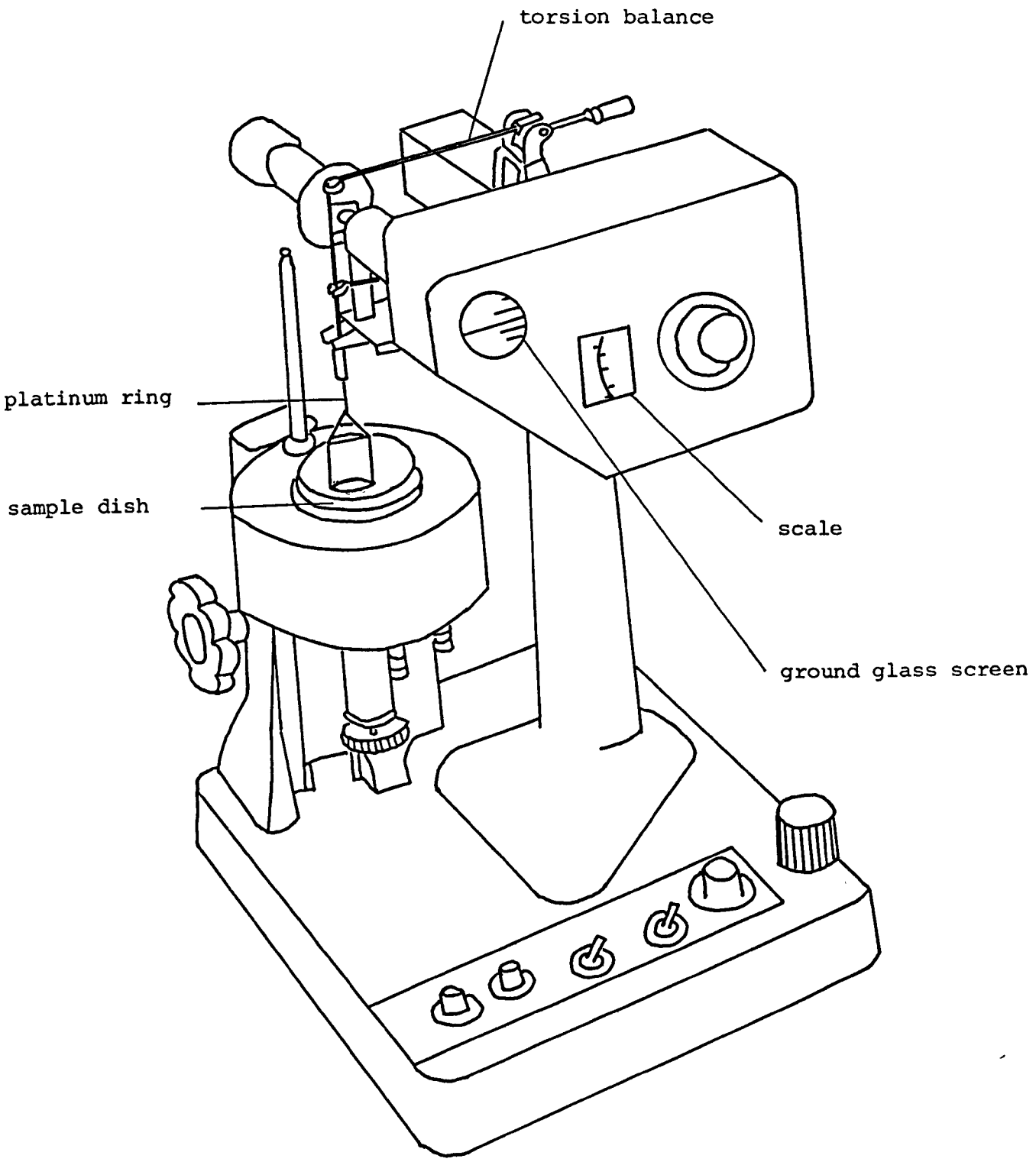

distilled water, well stirred and the procedure repeated. In the very dilute solutions, as the system approached pure water, the readings became more difficult to take.

The whole procedure was repeated in 1 x 10^{-1} mol dm^{-3} sodium chloride solution.

The surface tension versus $\log_{10}$ concentration plot for $C_{12}E_6$ in water at 25°C is presented in Figure 7.9. A sharp turning point was obtained giving a value of 8 x 10^{-5} mol dm^{-3} for the c.m.c. The sharpness of the turning point indicated that the surface active agent was pure as if an impurity was present a dip would have been observed around the c.m.c. The gradient of the plot was - 17.9 m Nm^{-1}.

A similar plot was obtained for $C_{12}E_6$ in 1 x 10^{-1} mol dm^{-3} sodium chloride solution again with a sharp turning point. The c.m.c. value was 6.7 x 10^{-5} mol dm^{-3} and the gradient was - 20.7 m Nm^{-1}.

7.5.3. Construction of Adsorption Isotherms.

A stock solution of 5 x 10^{-4} mol dm^{-3} $C_{12}E_6$ was placed in increasing quantities from 0.79 cm^3 to 14.67 cm^3 into 40 25 cm^3 clean glass sample bottles. To each sample 0.32 cm^3 of polystyrene latex SJP4, with a volume fraction of 0.094, was added so that each sample contained 0.03 g of polystyrene latex particles. Latex SJP4 was selected having a high surface area : volume fraction ratio, important for adsorption studies; each sample was made up to a total volume of 15 cm^3 with twice distilled water, to give a $C_{12}E_6$ concentration range of 2.63 x 10^{-5} mol dm^{-3} to 4.90 x 10^{-4} mol dm^{-3}.

The samples were stirred by end-over-end inversion overnight to allow adsorption equilibrium to be attained. The stirred samples were transferred to clean polypropylene centrifuge tubes and centrifuged for 30 minutes at ≃ 10,000 r.p.m. in an M.S.E. High Speed 18 centrifuge.

Figure 7.9.

Surface tension, $\hat{\gamma}/mNm^{-1}$ versus $\log_{10}$ concentration, $\log_{10}\hat{c}$, for $C_{12}E_6$ solution in twice distilled water and in 1 x 10^{-1} mol dm^{-3} NaCl, at 25°C.

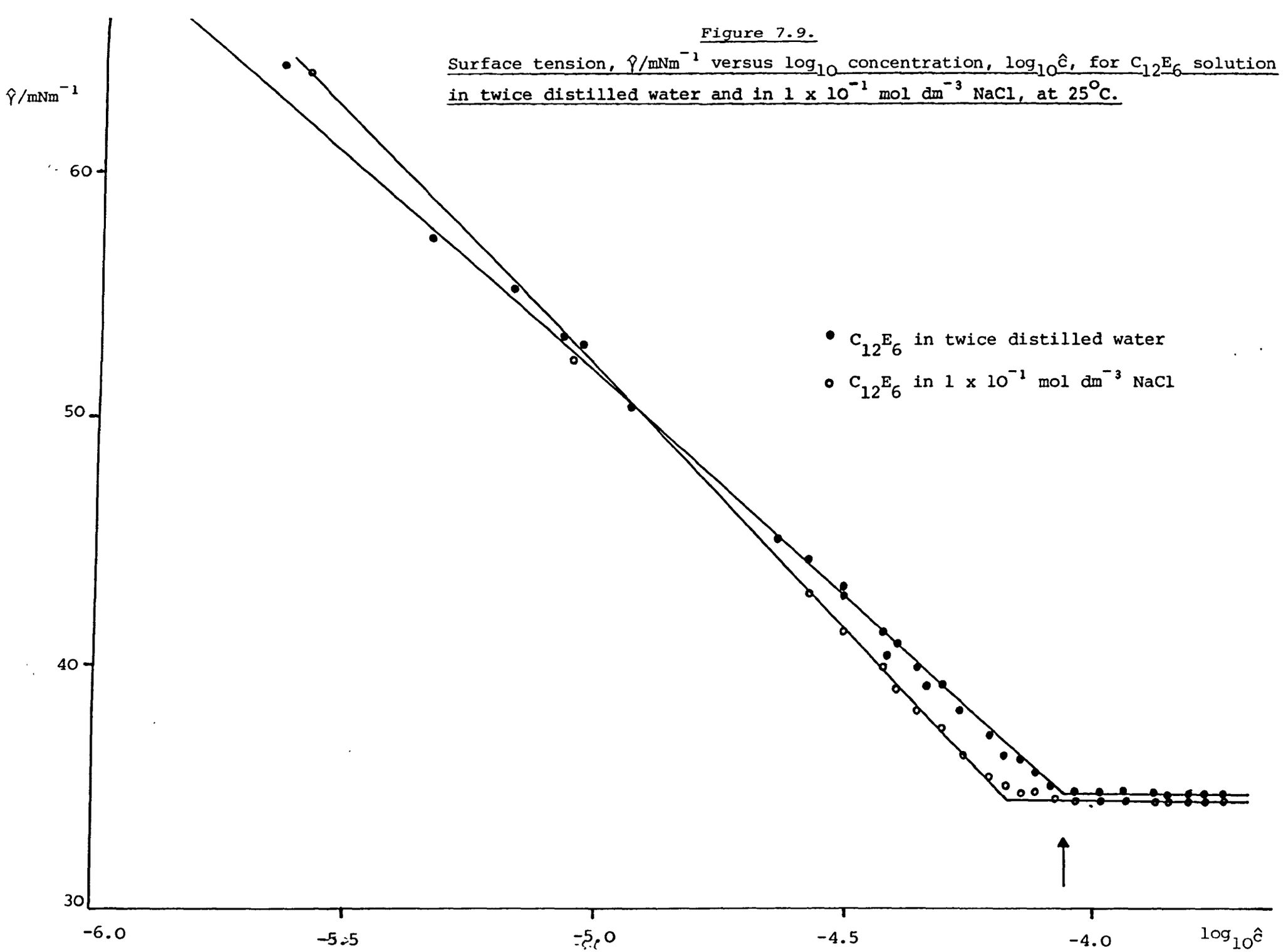

All the latex particles sedimented leaving clear supernatants which were pipetted into further clean glass sample tubes.

The surface tension of each sample was measured using a du Noüy tensiometer and the equilibrium supernatant concentration of each sample deduced from the $C_{12}E_6$ $\hat{\gamma}$ versus $\log_{10}$ $\hat{c}$ plot previously obtained and shown in Figure 7.9.

Concentrations of $C_{12}E_6$ above the c.m.c. gave the plateau surface tension value, so these had to be diluted to a concentration below the c.m.c. with twice distilled water, the surface tension measured and the equilibrium concentration scaled accordingly.

To discover the effect of an added electrolyte on the adsorption process several measurements were made in 1×10^{-1} mol dm^{-3} sodium chloride solution and calibrated against the $\hat{\gamma}$ versus $\log_{10}$ $\hat{c}$ plot for $C_{12}E_6$ in 1×10^{-1}mol dm^{-3}sodium chloride solution.

The adsorption isotherm obtained is presented in Figure 7.10. A well defined plateau was found at equilibrium concentrations in excess of the c.m.c. of 8×10^{-5} mol dm^{-3} with a surface excess concentration of 3.75×10^{18} molecules m^{-2}. A small step was observed at approximately half the equilibrium concentration with a surface excess concentration of 3.75×10^{18} molecules m^{-2}. The adsorption isotherm was broadly Langmuirian, type L4[164,165], see Figure 7.7.

The surface excess concentration versus equilibrium concentration values for the adsorption in the presence of 1×10^{-1} mol dm^{-3} sodium chloride solution are presented in Figure 7.10. A plateau was found at a surface excess concentration of 2.6×10^{18} molecules m^{-2}, at equilibrium concentration in excess of the c.m.c. A step was not defined from the limited data and the isotherm was taken to be Langmuirian of the L2 type.

Adsorption isotherm for the adsorption of $C_{12}E_6$ onto polystyrene latex SJP4.

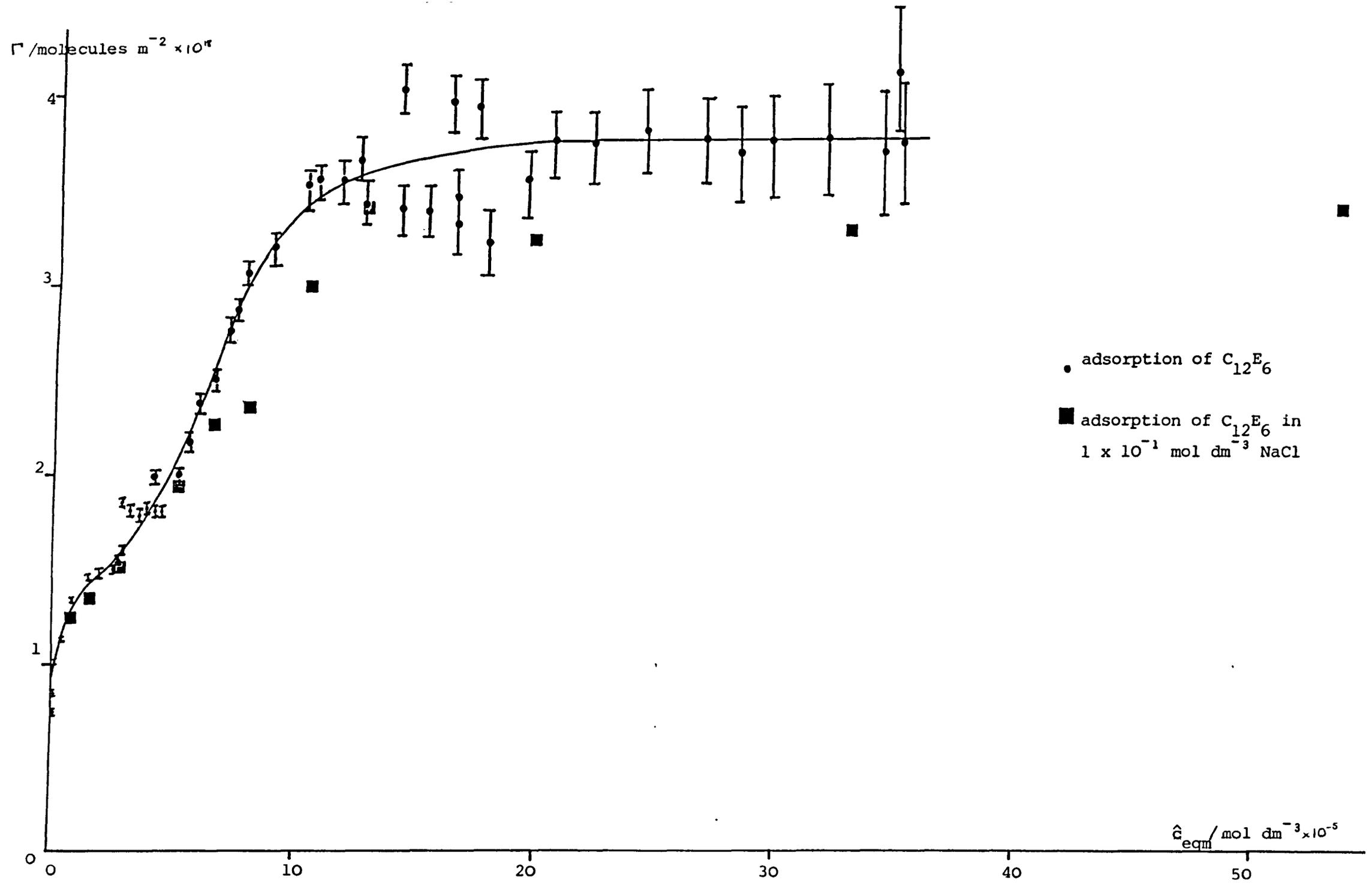

7.5.4. Discussion.

The value of the c.m.c. obtained from the $\hat{\gamma}$ versus $\log_{10} \hat{c}$ plot for $C_{12}E_6$, Figure 7.9, was found to be 8×10^{-5} mol dm^{-3}. This is in good agreement with literature values of 8.7×10^{-5} mol dm^{-3} found by Corkill, Goodman and Harrold[170]; 7.8×10^{-5} mol dm^{-3} obtained by Ottewill and Walker[54]; and 8×10^{-5} mol dm^{-3} found by Hough.[171]

The gradient of the same $\hat{\gamma}$ versus $\log_{10} \hat{c}$ plot was - 17.9 m Nm^{-1}.

From equation (7.2):

$$\Gamma = - \frac{1}{2.303RT} \left[\frac{d\hat{\gamma}}{d\log_{10}\hat{c}} \right]_T$$

the surface excess concentration, Γ, was calculated to be 3.13×10^{-6} mole m^{-2} and the area per molecule at the interface, A_s, 0.53 nm^2 $molecule^{-1}$.

The plateau region of the adsorption isotherm occurred at a value of 3.75×10^{18} molecules m^{-2} or 6.23×10^{-6} moles m^{-2} which corresponded to an area per molecule of $C_{12}E_6$ adsorbed at the particle surface of 0.27 nm^2 $molecule^{-1}$. The step occurred at 1.75×10^{18} molecules m^{-2} or 2.91×10^{-6} moles m^{-2}, corresponding to an area per molecule of 0.57 nm^2 $molecule^{-1}$.

Values have been reported by a number of workers for the coverage of $C_{12}E_6$ when adsorbed at a surface. Lange[172] theoretically calculated a value of 0.60 nm^2 $molecule^{-1}$ for a close-packed monolayer at the air-water interface. Corkill and co-workers[173] reported a value of 0.55 nm^2 $molecule^{-1}$ for $C_{12}E_6$ adsorption onto graphon while Hough[171] obtained monolayer coverage at 0.43 nm^2 $molecule^{-1}$ for his work with silver iodide. Ottewill and Walker[54,174] and Barclay and Ottewill[175,176], working with polystyrene latices obtained values of 0.40 and 0.32 nm^2 $molecule^{-1}$ respectively.

The value obtained for the area occupied per $C_{12}E_6$ molecule at the air-water interface, 0.53 nm^2 $molecule^{-1}$, was in good agreement with Lange's

predicted value of 0.60 nm^2 $molecule^{-1}$ at that interface.

The value of area per molecule obtained on the plateau for the adsorption of $C_{12}E_6$ onto polystyrene latex, 0.27 nm^2 $molecule^{-1}$ was slightly lower than the value obtained by Ottewill and Walker, 0.40 nm^2 $molecule^{-1}$ but was similar to Barclay and Ottewill's value of 0.32 nm^2 $molecule^{-1}$.

A step has not previously been reported in the adsorption isotherms of $C_{12}E_6$ adsorbing onto polystyrene latex.[54,174-176] This can be attributed to the fact that previously fewer points were taken at low equilibrium concentrations and the step, being fairly small, could easily have been missed. The adsorption isotherm here was repeated four times, and in each case a step was observed in the same position.

The possibility of the step indicating monolayer coverage and the plateau a bimolecular leaflet, as depicted in pathway C in Figures 7.5 and 7.6, was discounted. It is highly improbable that the hydrophilic ethylene oxide group would adsorb onto the latex particle surface in preference to the hydrophobic alkyl tail group.

The step was taken to indicate a change in conformation of the adsorbed molecules from a relatively flat configuration at low concentrations to a radially oriented close packed arrangement at high concentrations. This is illustrated in pathway A in Figure 7.5 and the corresponding isotherm, isotherm A in Figure 7.6 is of the form obtained experimentally.

Adsorption is a dynamic process and an equilibrium is set up between adsorbed molecules and molecules in solution. This must be considered in the construction of an adsorbate-adsorbent system and sufficient surface active agent added to a system to account for the equilibrium process. The excess concentration of surface active agent required is the equilibrium concentration at which the plateau is established. In this case the equilibrium concentration was taken to be 2×10^{-4} mol dm^{-3}.

The presence of the added electrolyte, 1×10^{-1} mol dm^{-3} sodium chloride solution, was found to lower the c.m.c. from 8×10^{-5} mol dm^{-3} to 6.7×10^{-5} mol dm^{-3}, a substantial difference. The gradient of the $\hat{\gamma}$ versus $\log_{10} \hat{c}$ plot was found to increase from - 17.9 m Nm^{-1} to - 20.7 n Nm^{-1}. From equation (4.2) this gradient gave a value of 3.63×10^{-6} moles m^{-2} for the surface excess concentration, Γ, and 0.46 nm^2 $molecule^{-1}$ for the area per molecule at the interface.

The plateau region of the isotherm occurred at a value of 2.6×10^{18} molecules m^{-2} or 4.32×10^{-6} moles m^{-2} corresponding to an area per molecule of $C_{12}E_6$ adsorbed at the particle surface of 0.39 nm^2 $molecule^{-1}$.

No step was observed; this could be due to the fact that less extensive data was obtained than in the absence of added electrolyte, hence overlooking the step. However, the adsorption isotherm was repeated twice and in neither case was a step detected.

Throughout this study, in the preparation of systems of particles with full coverage of $C_{12}E_6$, the monolayer coverage was taken to occur at 3.75×10^{18} molecules m^{-2} and the equilibrium concentration taken to be 2×10^{-4} mol dm^{-3} $C_{12}E_6$.

7.6. Selection of the Electrolyte Type and Concentration.

7.6.1. Introduction.

Weak flocculation may be achieved in a sterically stabilised system by the addition of electrolyte which tends to increase interparticle attraction by screening the electrostatic repulsion.

The sedimentation behaviour at low volume fractions is a good indication of whether a system is flocculated or not, as flocculated particles settle far more rapidly than single ones. Hence if a system is found to sediment

far more rapidly at one electrolyte concentration than another at another concentration, and is found to be redispersible, it may be taken to be flocculated.

7.6.2. Experimental.

A series of straight-walled flat bottomed glass tubes ≃ 13 cm by 1.5 cm diameter fitted with Quickfit Q14/23 sockets was set up in a draught-free cabinet. Into each tube the required quantities of polystyrene latex SJP9 coated with $C_{12}E_6$, salt solution and water was added. An equilibrium concentration of 2×10^{-4} mol dm^{-3} $C_{12}E_6$ was maintained in each sample. The tubes were stoppered, sealed with paraffin wax film to prevent evaporation and thoroughly shaken. The sedimentation behaviour was studied by following the descent of the solids boundary at known time intervals after agitation of the systems.

Four salts were selected: sodium chloride (1:1), barium nitrate (2:1), magnesium nitrate (2:1) and magnesium sulphate (2:2) and studied at concentrations of 1×10^{-3}, 1×10^{-2}, 1×10^{-1} and 5×10^{-1} mol dm^{-3} in the case of the 1:1 electrolyte and at 1×10^{-3}, 1×10^{-2}, 5×10^{-2} and 1×10^{-1} mol dm^{-3} for the other systems.

Initial tests were carried out on two systems: polystyrene latex SJP9 uncoated, and coated with $C_{12}E_6$, both at volume fractions of $\phi = 0.05$ to determine the effect of surface active agent on the sedimentation.

A series of systems was prepared with polystyrene latex coated with $C_{12}E_6$ at a solids content of $\phi = 0.05$ at the electrolyte concentrations listed above and the sedimentation followed.

Irreversibility of the sedimentation process was tested for by shaking the systems well when sedimentation was complete.

In all cases plots were made of the distance of boundary descent versus time after agitation of the system. The sedimentation rates were calculated from the gradients of these plots.

7.6.3. Results and Discussion.

In all cases good straight lines were obtained, passing through the origin showing linear sedimentation behaviour.

In the case of the two initial tests with latex particles with and without adsorbed layers, and with no added electrolyte present, the values for the sedimentation rates obtained were $1.08 \times 10^{-8} ms^{-1}$ and $1.36 \times 10^{-8} ms^{-1}$ respectively.

The results of the series of tests at constant SJP9/$C_{12}E_6$ solids content and variable electrolyte and electrolyte concentration are tabulated in Table 7.5 and are illustrated in Figure 7.11.

The sedimentation rates for the coated and uncoated latex in the absence of added electrolyte were found to be substantially different, 1.38×10^{-8} and $1.08 \times 10^{-8} ms^{-1}$ respectively showing that the surface active agent caused an increase in sedimentation velocity and therefore must have had some effect on the physical properties of the system.

The results of the series of tests at SJP9/$C_{12}E_6$ $\phi = 0.05$ in variable electrolyte and electrolyte concentration showed quite conclusively that electrolyte above a certain concentration had a pronounced effect on the system. Up to a critical concentration, in the case of all the electrolytes, the sedimentation rate was of the order of 10^{-8} ms^{-1} whereas above a critical concentration the rate increased a hundredfold.

The highest electrolyte concentration required to induce rapid sedimentation was with the 1:1 electrolyte, the sodium chloride had to be 5×10^{-1} mol dm^{-3}, while the 2:2 electrolyte, magnesium sulphate, induced

TABLE 7.5.

Sedimentation Rates / ms^{-1} for the sedimentation of Polystyrene Latex SJP9/$C_{12}E_6$ at ϕ= 0.05 in varying electrolyte solutions.

electrolyte / [electrolyte] / mol dm^{-3}	NaCl(1:1)	$Ba(NO_3)_2$ (2:1)	$Mg(NO_3)_2$ (2:1)	$MgSO_4$ (2:2)
1×10^{-3}	1.60×10^{-8}	1.52×10^{-8}	1.55×10^{-8}	1.60×10^{-8}
1×10^{-2}	1.63×10^{-8}	1.45×10^{-8}	1.57×10^{-8}	1.60×10^{-8}
5×10^{-2}	-	2.22×10^{-6}	2.38×10^{-6}	1.88×10^{-8}
1×10^{-1}	1.65×10^{-8}	2.12×10^{-6}	3.38×10^{-6}	2.05×10^{-6}
5×10^{-1}	2.55×10^{-6}	-	-	-

Figure 7.11.

Sedimentation at 1g of SJP9/$C_{12}E_6$, ϕ = 0.05 in varying electrolyte and electrolyte concentrations.

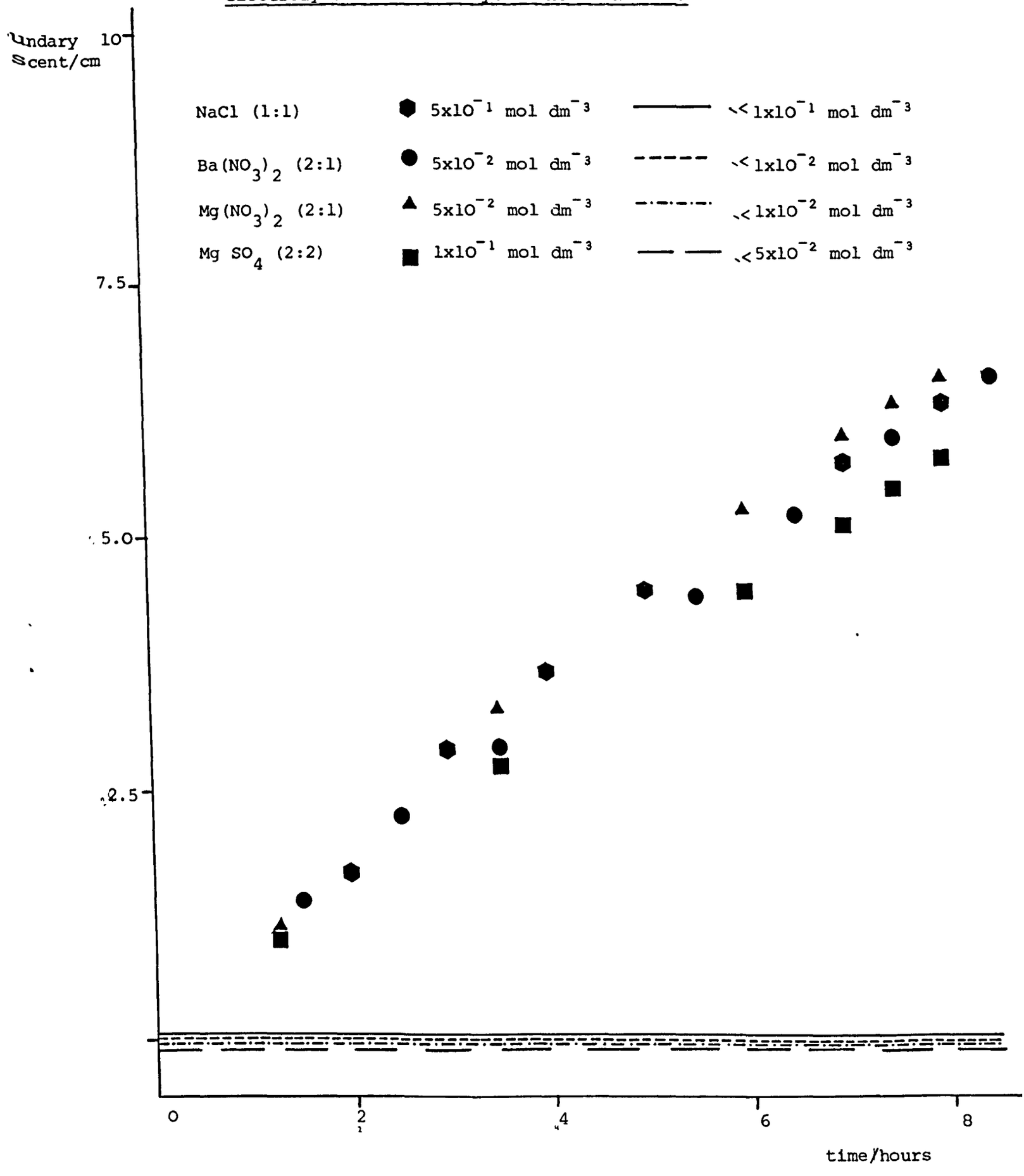

rapid sedimentation at 1×10^{-1} mol dm^{-3} and both the 2:1 electrolytes, barium nitrate and magnesium nitrate, needed to be at a concentration of 5×10^{-2} mol dm^{-3} for the same effect.

This showed that the type of electrolyte played a role in the sedimentation, the 2:1 electrolytes induced rapid sedimentation at lower concentrations than the 2:2 which in turn needed to be lower than the 1:1.

At electrolyte concentrations below the critical concentration the rates of sedimentation were found to be constant for all the salt types, and approximately the same rate as the coated particles in the absence of added salt.

The results showed that the rate of sedimentation was very dependent upon the electrolyte concentration. As the electrolyte concentration increased the interparticle attraction increased as explained previously. Rapid sedimentation was observed in the presence of critically high electrolyte concentrations, i.e. at critically high interparticle forces of attraction. This suggested that it was the interparticle attractive forces that brought about the rapid sedimentation which can be explained by the onset of particle aggregation.

When shaken the systems were readily redispersed showing that the aggregation was flocculation rather than coagulation. This was due to the particles being sterically stabilised by the adsorbed surface active agent. Uncoated latex at the critical electrolyte concentrations considered here rapidly coagulated.

All the salts chosen appeared to be suitable for the purpose required here, to induce flocculation in the system. As salt concentrations become high in a system bouyancy effects become important and particles float. This was obviously undesirable for the purpose here and so it had to be ensured that this did not occur with the electrolyte system selected.

Although the sodium chloride system needed to be at a higher concentration than the other salts its critical concentration was below that where bouyancy became a problem ($\simeq$ 1 mol dm^{-3}). It also had the advantage of being a 1:1 electrolyte and its behaviour was easiest to model of the four. Hence sodium chloride was selected as the electrolyte to be used throughout the experiments at a concentration of 0.5 mol dm^{-3}.

7.7. Preparation of Systems.

The system has now been fully defined: monodisperse polystyrene latex particles coated with a monolayer of monodisperse nonionic surface active agent $C_{12}E_6$ in an equilibrium background of 2×10^{-4} mol dm^{-3} $C_{12}E_6$ in 0.5 mol dm^{-3} sodium chloride solution.

Three polystyrene latex particle sizes were selected for the work: $\simeq$ 1 μm, $\simeq$ 1.5 μm and $\simeq$ 2 μm diameter. Latices of these sizes were prepared in 11 litre batches so that there was sufficient latex for all measurements on one particle size to be made from the same batch for direct comparisons. The systems were prepared with volume fractions of $\phi = 0.2$ to $\phi = 0.6$.

The volume fraction of a stock of latex was calculated from dry weight determination. The amount of surface active agent, $C_{12}E_6$, required for monolayer coverage of the particles (6.23×10^{-6} moles m^{-2}) plus the amount required for the equilibrium background (2×10^{-4} mol dm^{-3}) plus 10% was calculated and added dropwise to the latex. The melting point of $C_{12}E_6$ is $25.2^{o}C$[177] and so the mixture was warmed under a flow of warm water to melt the $C_{12}E_6$ and allow it to be dispersed. The latex/$C_{12}E_6$ mixture was shaken well and stirred using a magnetic follower.

The sodium chloride was added at a concentration of 0.5 mol dm^{-3} in the aqueous phase after adsorption of $C_{12}E_6$ was complete and the system shaken and stirred again. The electrolyte was added after the surface active agent to prevent coagulation.

To concentrate the system up to $\simeq \phi = 0.35 - 0.4$ the particles were allowed to sediment overnight and the supernatant removed by pipette.

The method of ultrafiltration was used to increase the concentration further. The system was contained in well-boiled Visking dialysis tubing and tightly sealed and placed in a fused quartz cylinder $\simeq$ 40 cm by 5.1 cm diameter containing a dialysate of 0.5 mol dm^{-3} NaCl, 2 x 10^{-4} mol dm^{-3} $C_{12}E_6$, the background solution of the system. This was to prevent any osmotic effect. A sealed fused quartz cylinder 20 cm by 4.9 cm diameter containing mercury to increase the mass was lowered onto the dilute system and left overnight. The dialysis tubing allowed the solution, but not the particles, to be forced out by the weight of the mercury thus concentrating the system. The dialysis tubing was tightened after removal of pressure and dialysed against the same dialysate.

The processwas repeated until the system was sufficiently concentrated. The limit appeared to be $\simeq \phi = 0.63$ when the system solidified. The volume fractions of the systems were determined from dry weight measurements.

The resultant systems of variable volume fraction were stored in steam-cleaned polypropylene bottles. These systems were used soon after preparation as they tend to deteriorate after several months.

The three latices used were SJP8, diameter 0.97 μm, SJP10, diameter 1.41 μm and SJP11, diameter 1.92 μm.

Chapter Eight

Characterisation of Systems

Chapter Eight. Characterisation of Systems.

8.1. Introduction.

The selection and preparation of the systems to be used throughout this work has been described in Chapter Seven. The systems were polystyrene latices of various size coated with a monolayer of $C_{12}E_6$ in 0.5 mol dm^{-3} sodium chloride solution. For use in theoretical calculations various parameters were required to describe the system such as the extent of the adsorbed layer, the zeta potential and so on. The determination of the length of a $C_{12}E_6$ molecule and hence the adsorbed layer thickness is described in (8.2); also the adsorbed layer packing density. Microelectrophoresis data are presented in (8.3) and the values subsequently obtained for the zeta potentials of the latices with and without $C_{12}E_6$ monolayer coverage. The data are presented as a function of electrolyte concentration and pH for latices SJP8, SJP10 and SJP11.

The morphology of the systems was also examined using two microscope techniques. A freeze etch microscopy technique is described in (8.4), together with micrographs obtained. The dynamic morphology of the systems was qualitatively examined using an optical microscope and the observations and relevant micrographs are presented in(8.5).

8.2. Extent of the Adsorbed Layer.

The adsorbed layer, taken to be a monolayer of $C_{12}E_6$ molecules, must be defined in terms of its extent, δ, into the solution for theoretical purposes.

Two experimental methods were attempted in this piece of work to define δ: photon correlation spectroscopy (p.c.s.) and transmission electron microscopy (T.E.M.) In both cases particle size determinations were made on polystyrene latex SJP12, with and without the addition of $C_{12}E_6$.

SJP12 has a particle radius of 72nm which is near the lower size limit that it is possible to prepare monodisperse latices. However, with an adsorbed layer of ≃ 4 - 5 nm, this is within the experimental error of the latex particle size and neither p.c.s. nor T.E.M. was sensitive enough to detect a definable difference between coated and uncoated particles.

The structure of the $C_{12}E_6$ molecule is given in Figure 8.1. It consists of a 12 carbon alkyl chain attached to a six ethylene oxide chain. From geometry, using typical bond angles and bond lengths[178], the extended molecule length was found to be ≃ 3.5 nm.

From Catalin models the fully extended length of a $C_{12}E_6$ molecule is taken to be 3.85 nm.[174]

Ottewill and Walker[54,174] obtained a value of 5.0 ± 5 nm for the saturated adsorbed layer thickness of $C_{12}E_6$ from ultracentrifugation studies. This is in reasonable agreement with the value obtained by Corkill and co-workers [179] of 8.1 nm for the thickness of a stable black aqueous soap film of $C_{12}E_6$ which corresponds to two molecule lengths.

The Catalin model value for the extended length of a $C_{12}E_6$ molecule was considered the most accurate value available; furthermore it agrees well with experimental and geometric data. Hence the $C_{12}E_6$ molecule length was taken to be 3.85 nm. Since the adsorbed layer is a monolayer of close packed $C_{12}E_6$ molecules it is assumed that the molecules are standing on end and hence the adsorbed layer thickness, δ, is taken to be 3.85 nm throughout this piece of work.

The packing density of the adsorbed layer, ϕ_p, was also determined. The molecular volume of one $C_{12}E_6$ molecule, as illustrated in Figure 8.2, was determined assuming cylindrical geometry and assuming a monolayer of bound water molecules around the ethylene oxide head group. The volume

Figure 8.1.

Structure of a $C_{12}E_6$ molecule.

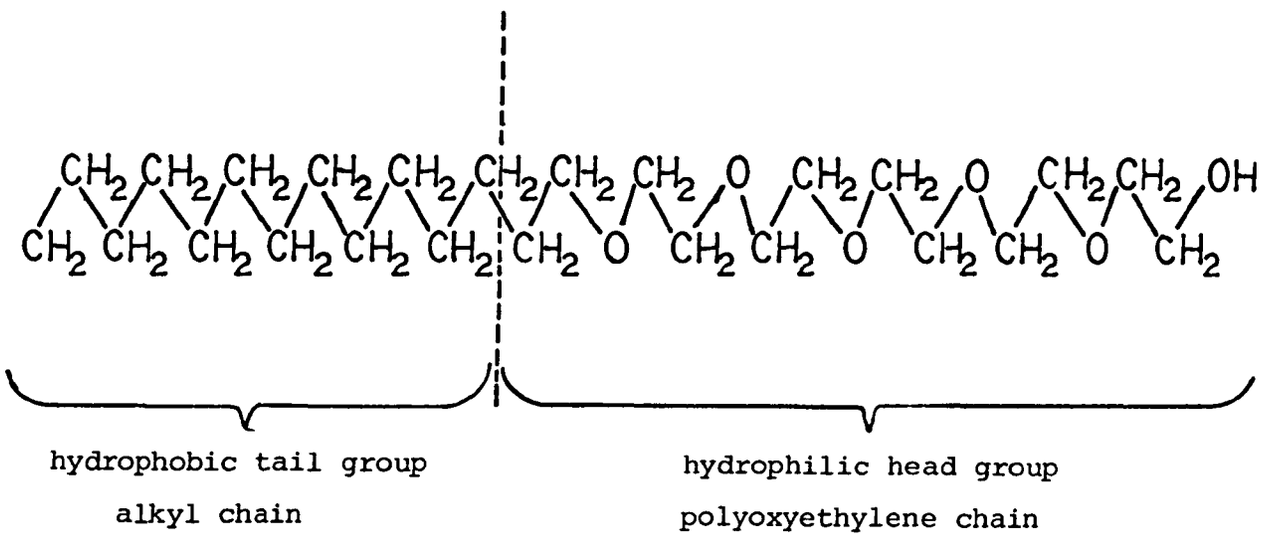

Figure 8.2.

Determination of Molecular Volume of a $C_{12}E_6$ molecule.

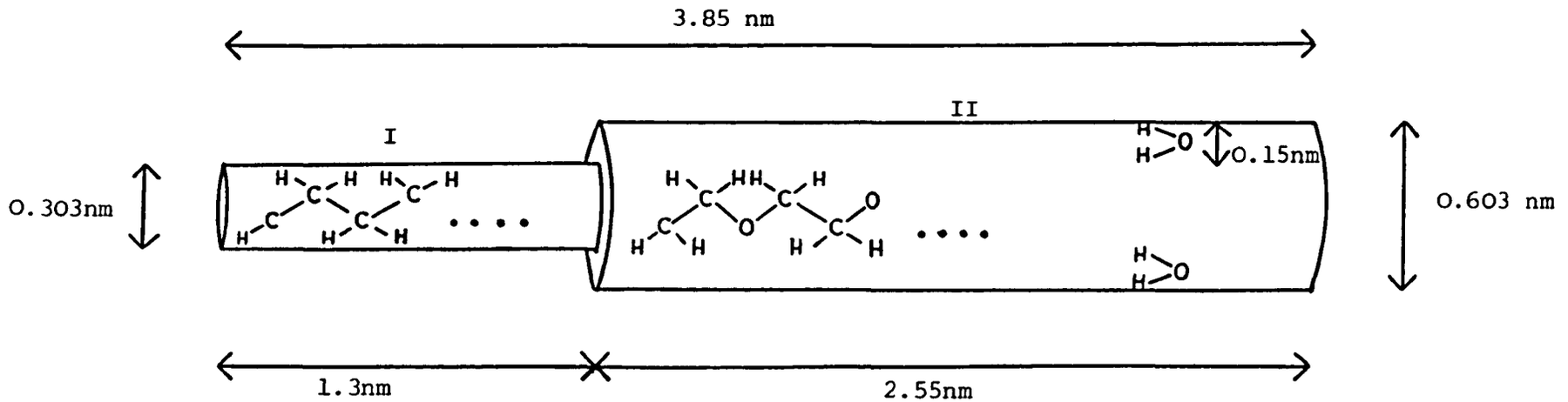

Volume I = $\pi(0.152)^2 . 1.3$

= $0.094\ nm^3$

Volume II = $\pi(0.302)^2 . 2.55$

= $0.731\ nm^3$

Total volume = $0.825\ nm^3$

of one molecule was found to be 8.25×10^{-28} m^3 and the packing density of the adsorbed layer 0.8.

8.3. Microelectrophoresis.

8.3.1. Theory.

Electrophoresis may be defined as the movement of a charged surface relative to stationary liquid caused by an applied electric field.[180,14] If the material under question is in the form of a suspension of microscopically visible particles the electrophoretic behaviour can be observed and measured directly. This process, termed microelectrophoresis, involves the observation of the motion of suspension particles at the stationary level of a capillary tube as an electric field is applied.

The electrophoretic behaviour of a suspension of particles is important in that it gives information on the charged nature of a particle surface and the surface at the plane of shear.

When a potential gradient is applied across a suspension of particles, the particles tend to move towards the electrode of charge opposite in sign to that of the particle surface. A steady velocity is attained by the particles as a result of balance between opposing electrical and viscous forces. This velocity, v^*, is proportional to the electrophoretic mobility, U_E, given by:

$$U_E = \frac{v^* l}{E} \qquad (8.1)$$

where l is the distance between the electrodes and E is the applied potential. The potential gradient, E, at the point of observation is usually calculated from the current, I, the cross sectional area of the channel, A_c^*, and the separately determined conductivity of the dispersion, k_o:

$$E = \frac{I}{k_o A_c^*} \qquad (8.2)$$

The potential at the surface of shear between the charged surface of a particle and the electrolyte solution is known as the electrokinetic or zeta potential, ζ. The exact location of the shear plane is unknown but it is assumed to be a little further away from the particle surface than the Stern plane (See 2.2.) The zeta potential may not be directly measured but can be deduced from the electrophoretic mobility.

The first equations for the conversion of electrophoretic mobility to zeta potential are attributed to Hückel[181] and Smoluchowski.[182] The Hückel equation applies for small κa[14] ($\kappa a < 1$) where the particle is sufficiently small to be treated as a point charge but large enough for Stoke's law to apply. The Hückel equation is given by:

$$U_E = \frac{\zeta \varepsilon_r \varepsilon_o}{1.5\eta} \qquad (8.3)$$

It is not generally suitable for aqueous systems but can be applicable to electrophoresis in non-aqueous media.

The Smoluchowski equation applies at high κa[14] ($\kappa a > 10$), where the particle is sufficiently large that the double layer may be treated as flat. The Smoluchowski equation is given by:

$$U_E = \frac{\zeta \varepsilon_r \varepsilon_o}{\eta} \qquad (8.4)$$

The ions in the mobile part of the double layer show a net movement in a direction opposite to that of the particle under the influence of the applied electric field.[180] This creates a local movement of the liquid which opposes the motion of the particle, and is known as electrophoretic retardation. It is allowed for in Henry's equation for non-conducting spheres given by:

$$U_E = \frac{\zeta \varepsilon_r \varepsilon_o f(\kappa a)}{1.5\eta} \qquad (8.5)$$

where f (κa) varies between 1.0 for small κa (Hückel equation) and 1.5 for large κa (Smoluchowski equation).

The movement of the particle relative to the mobile part of the double layer results in the double layer being distorted because a finite time is required for the original symmetry to be restored by diffusion and relaxation.[180] The resulting asymmetric ionic atmosphere exerts an additional retarding force on the particle, known as the relaxation effect, not accounted for in the Henry equation.

Overbeek[184] and Booth[185] derived expressions for the electrophoretic mobility as a power series in $e\zeta/kT$ for zeta potentials of less than 25mV, including retardation, relaxation and surface conductance effects. Wiersama and co-workers[186] subsequently obtained a numerical solution of the problem giving mobility as a complete power series in zeta potential. Their solutions are presented in dimensional form by Ottewill and Shaw[187] for systems of positively or negatively charged spheres in the presence of a 1:1 electrolyte at 25°C. These solutions are shown in Figure 8.3 which gives theoretical values of electrophoretic mobility as a function of zeta potential and κa. Hence for a known mobility and κa the zeta potential may be deduced. The iterative scheme employed by Wiersama failed to converge at high zeta potentials; for a 1:1 electrolyte system results could only be obtained for a zeta potential of less than 150 mV. O'Brien and White[186a] extended their analysis to high zeta potentials using a numerical method.

Levine et al[188], working with human erythrocytes, have analysed the situation of particles with polyelectrolyte layers on the surface. The electrophoretic mobilities predicted from this analysis were significantly smaller than those from the Smoluchowski equation. In the classical treatment the charge is assumed to be spread uniformly over the hydrodynamic surface. However, erythrocytes have a low packing density ($\phi_p \simeq 0.04$) in

Figure 8.3.

Theoretical values of electrophoretic mobility, U_E, as a function of zeta potential, ζ, and κa for a positively or negatively charged sphere in the presence of a 1:1 electrolyte at 25°C.

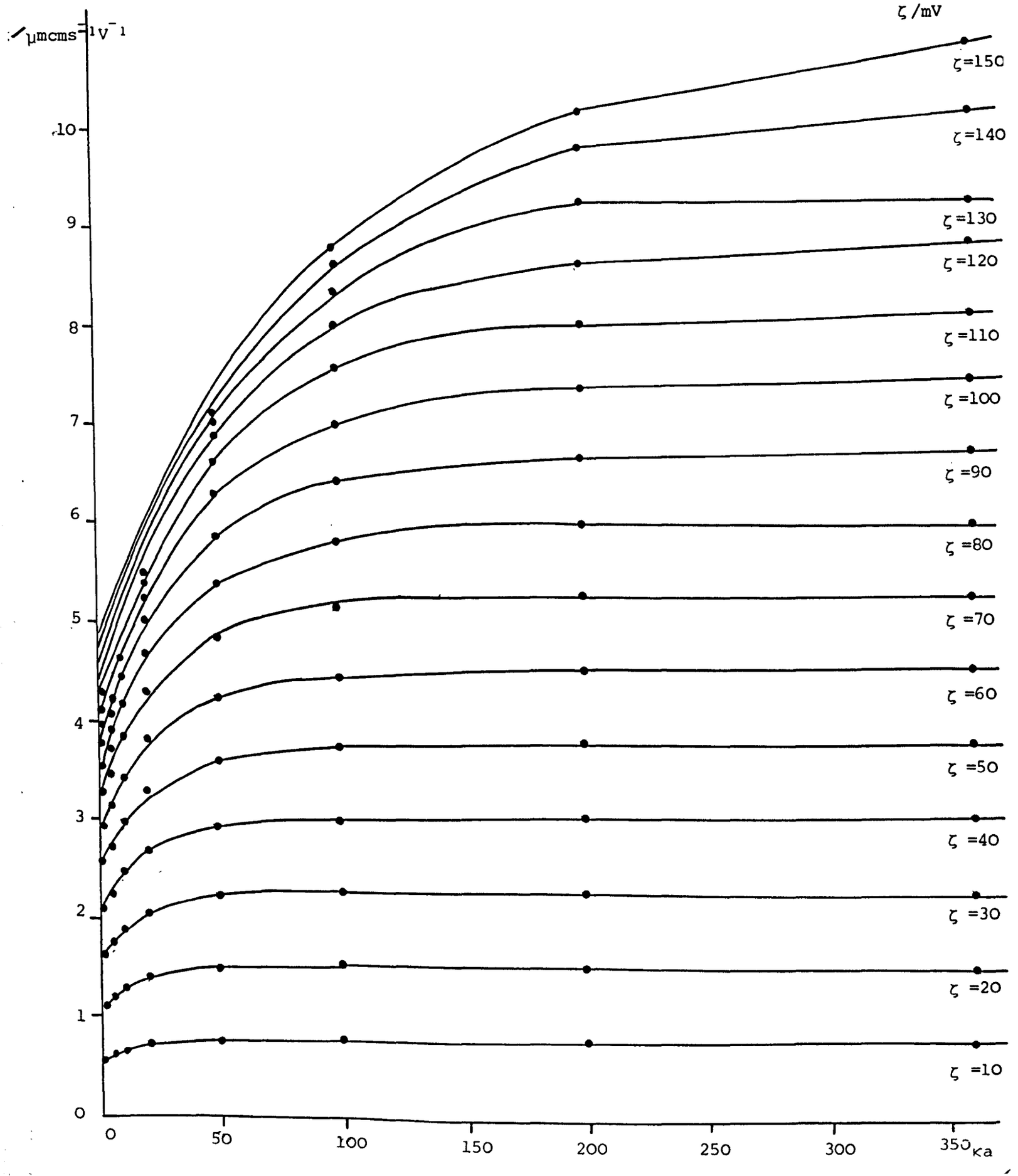

their well drained adsorbed layer of glycoprotein. The authors assumed that the charge was uniformly distributed throughout this layer and that fluid flow in the layer was dominated by Stokes' friction arising from idealised bead string polymer segments. They obtained an expression for the electrophoretic mobility which was dependent on the thickness of the adsorbed layer and the mean polymer segment radius.

For systems of the type considered in this work which have high adsorbed layer packing densities ($\phi_p \simeq 0.8$, see (8.2)), i.e. closely packed head groups, little penetration should have occurred and the layers may be considered rigid. In this case flow within the adsorbed layer may be discounted and Smoluchowski's relation should be a good approximation.

8.3.2. Experimental.

The instrument used was a Penkem system 3000 Automated Electrokinetic Analyser* which comprised of a fully automated system to characterise such properties as electrophoretic mobility, diffusion coefficient, sedimentation velocity, specific conductance, pH amd turbidity. The electrophoresis chamber, a cylindrical silica tube with permanently bonded palladium electrodes, was illuminated normally with a 2 mW helium-neon laser with a chopped beam. This illuminated particles at the focal plane of a microscope system. The velocity of the particles was then calculated from the change in frequency signal as the particles moved compared to a reference. This gave a doppler type of signal.

A circulatory flow was set up inside the cylinder due to the phenomenon of electro-osmosis at the walls and its counter-flow in the centre of the tube, which can be described by the Poiseuille equations. Two stationary levels exist in a given plane and it was at one of these stationary levels that the microscope system was focussed and the distribution of particle

* The technical assistance of Mr. J.W. Dimery is gratefully acknowledged.

velocities measured when an electric field was applied between the electrodes. The direction of the field was switched alternately and sixteen measurements of particles' velocity made in each direction. The velocity of many particles was measured in each case.

A fast Fourier transformation was made of the doppler signal obtained to compute a frequency spectrum. Successive spectra were averaged to obtain a distribution function of the electrophoretic mobilities. The frequency of the distribution curve was based on the scattering power of the particles and so a mean value was a higher moment than a number average value.

Values for some electrophoretic mobilities obtained from the Penkem Automated Electrokinetic Analyser were checked against values from the Rank microelectrophoresis apparatus and the results found to tally well.

The electrophoretic mobility and hence the zeta potential was measured of all the latices prepared both uncoated and with full coverage of $C_{12}E_6$, all at 5×10^{-4} mol dm^{-3} sodium chloride solution using the Penkem System 3000.

In the cases of the latices SJP8, SJP10 and SJP11 the electrophoretic mobility was determined as a function of pH at sodium chloride concentrations varying from 1×10^{-4} mol dm^{-3} to 5×10^{-1} mol dm^{-3}, for the latices with and without full coverage of $C_{12}E_6$. The pH was varied using sodium hydroxide solution and hydrochloric acid solution. Extremely low volume fractions were used in every case. The very low volume fractions and the fact that all solutions were freshly made up immediately before use prevented coagulation of uncoated latex particles at high salt concentration from being a problem.

8.3.3. Results and Discussion.

The values of κ for the systems at a sodium chloride concentration of 0.5 mol dm^{-3} were determined from equation (3.2) and are summarised in Table 8.1. The fundamental charge was taken to be 1.61 x 10^{-19} C,[189] the Avogadro number 6.023 x 10^{23},[189] the relative permittivity 78.54[190], the permittivity of free space 8.854 x 10^{-12} Fm^{-1}[189] and Boltzmann's constant 1.38 x 10^{-23} JK^{-1}.[189] It can be seen that in all cases κa was large and hence the zeta potentials were calculated from Smoluchowski's equation, equation (8.4). The viscosity and the relative permittivity were taken to be the same as that of water at 25°C with values of 8.904 x 10^{-4} Nsm^{-2}[190] and 78.54[190] respectively. The results obtained from the electrophoretic measurements of all the latices with and without adsorbed $C_{12}E_6$ at 0.5 mol dm^{-3} sodium chloride solution are tabulated in Table 8.2. The data for latices SJP8, SJP10 and SJP11 with and without adsorbed $C_{12}E_6$, as a function of pH and sodium chloride concentration, are illustrated in Figures 8.4 - 8.9. and the results summarised in Table 8.3 and Figure 8.10.

The electrokinetic or zeta potential is a measure of the potential at the surface of shear between the charged particle surface and the electrolyte solution. For uncoated latex particles, the surface of shear is situated just beyond the Stern plane and the zeta potential may be approximated to ψ_d, the potential at the Stern plane. Adsorption of a nonionic surface active agent onto the particle surface results in the surface of shear being located at a relatively large distance from the Stern plane and a zeta potential subsequently lower than ψ_d.

This was clearly observed in the values obtained for the electrophoretic mobilities and zeta potentials of all the latices, with and without a monolayer coverage of $C_{12}E_6$, in 0.5 mol dm^{-3} sodium chloride solution. The values obtained for the zeta potentials of the coated latices were substantially lower

Table 8.1.

Calculated Ka values for the polystyrene latices with full coverage $C_{12}E_6$ in 5 x 10 mol dm^{-3} NaCl.

Latex	a/m	Ka
SJP4	2.79×10^{-7}	649.0
SJP5	4.56×10^{-7}	1060.0
SJP6	5.50×10^{-7}	1277.6
SJP7	3.69×10^{-7}	857.0
SJP9	4.92×10^{-7}	1142.8
SJP12	7.58×10^{-8}	176.0
SJP8	4.91×10^{-7}	1140.5
SJP10	7.09×10^{-7}	1648.3
SJP11	9.62×10^{-7}	2235.1

Table 8.2.

Values for the electrophoretic mobility/ms^{-1}/Vm^{-1} and zeta potential/mV of all the latices, with and without full coverage of $C_{12}E_6$, in 5 x 10^{-1} mol dm^{-3} NaCl.

system	diameter /m	ph	U_E x 10^{-8}/ms^{-1}/Vm^{-1}	ζ /mV
SJP4	5.51 x 10^{-7}	5.0	1.95	25.0
SJP4/$C_{12}E_6$	5.59 x 10^{-7}	5.0	0.51	6.5
SJP5	9.05 x 10^{-7}	4.9	2.00	25.6
SJP5/$C_{12}E_6$	9.13 x 10^{-7}	5.1	0.71	9.1
SJP6	1.092 x 10^{-6}	4.9	2.23	28.6
SJP6/$C_{12}E_6$	1.100 x 10^{-6}	5.0	0.79	10.1
SJP7	7.30 x 10^{-7}	5.1	2.45	31.4
SJP7/$C_{12}E_6$	7.38 x 10^{-7}	4.9	0.75	9.6
SJP9	9.76 x 10^{-7}	5.0	2.30	29.4
SJP9/$C_{12}E_6$	9.84 x 10^{-7}	5.0	0.48	6.1
SJP12	1.44 x 10^{-7}		system coagulated	
SJP12/$C_{12}E_6$	1.52 x 10^{-7}	5.3	0.48	6.1
SJP8	9.74 x 10^{-7}	5.1	2.34	30.0
SJP8/$C_{12}E_6$	9.82 x 10^{-7}	5.4	0.78	10.0
SJP10	1.411 x 10^{-6}	5.2	1.82	23.3
SJP10/$C_{12}E_6$	1.419 x 10^{-6}	5.3	0.84	10.8
SJP11	1.916 x 10^{-6}	5.2	1.79	22.9
SJP11/$C_{12}E_6$	1.924 x 10^{-6}	5.4	0.76	9.7

Figure 8.4.

Electrophoretic mobility of polystyrene latex SJP8 particles (diameter 0.97 μm) as a function of pH and sodium chloride concentration

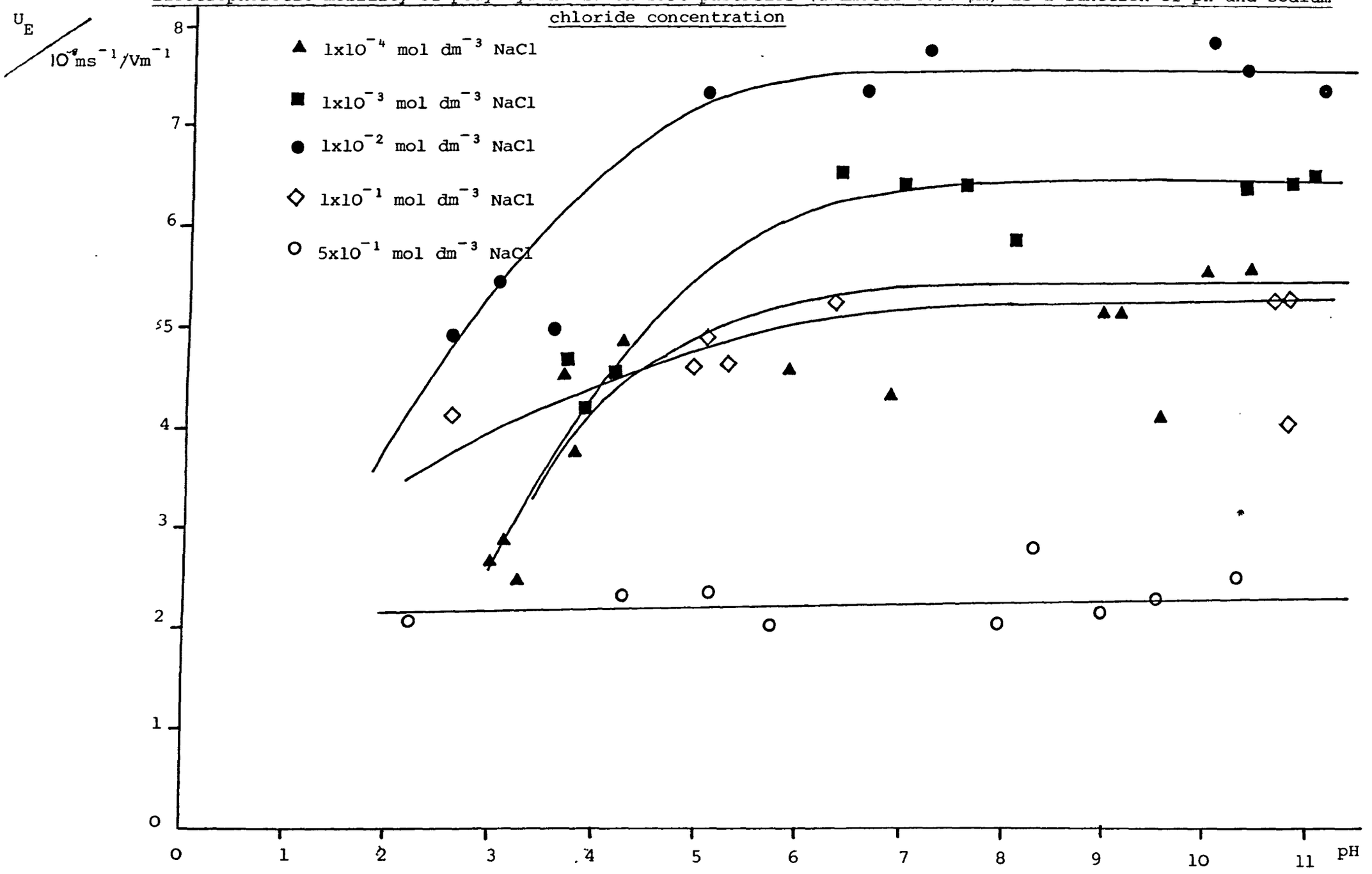

Figure 6.44

Electrophoretic mobility of polystyrene latex SJP8 particles (diameter 0.97 μm) with full coverage of $C_{12}E_6$ as a function of pH and sodium chloride concentration.

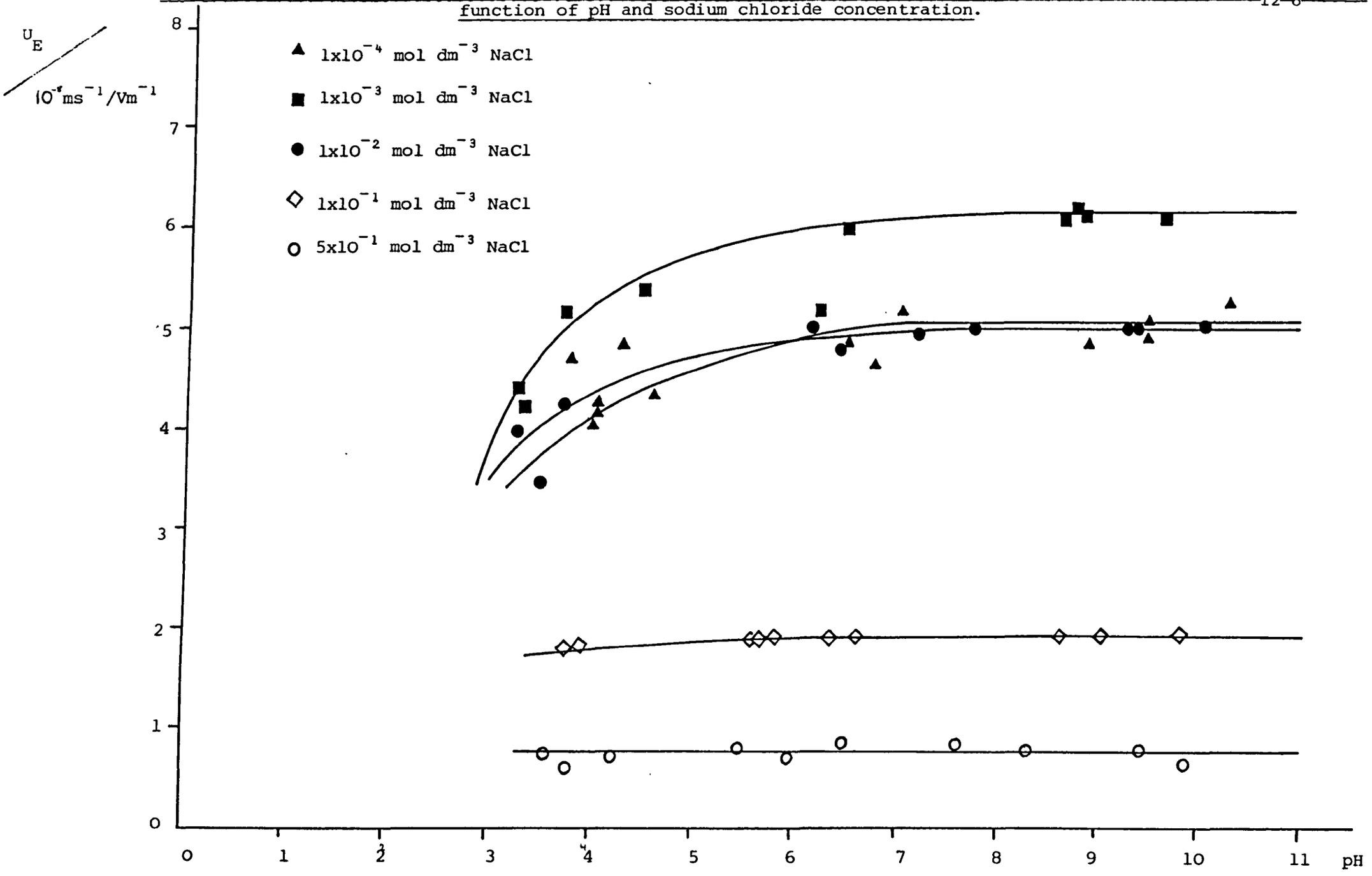

Electrophoretic mobility of polystyrene latex SJP10 particles (diameter 1.41 μm) as a function of pH and sodium chloride concentration.

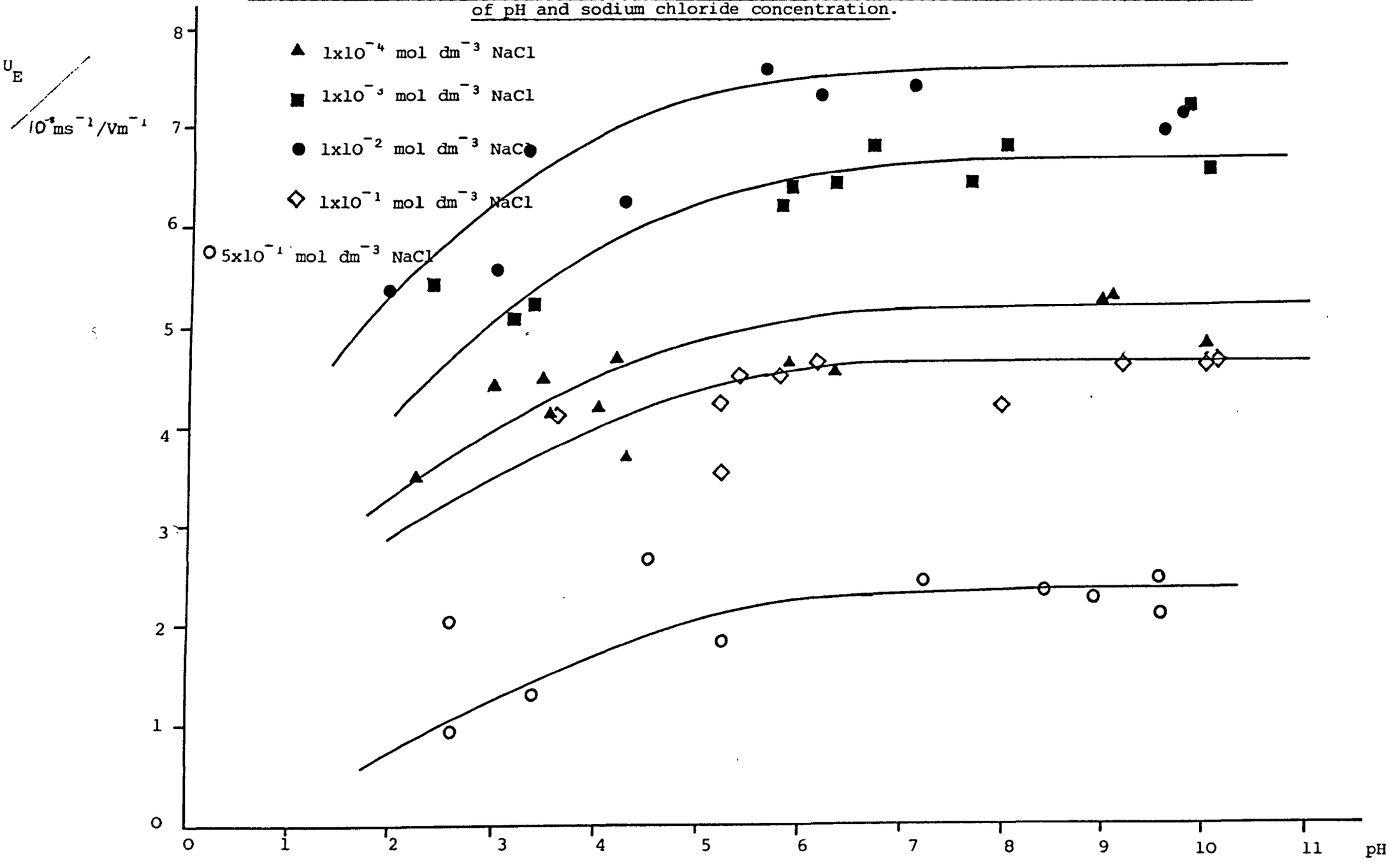

Electrophoretic mobility of polystyrene latex SJP10 particles (diameter 1.41 μm) with full coverage of $C_{12}E_6$ as a function of pH and sodium chloride concentration

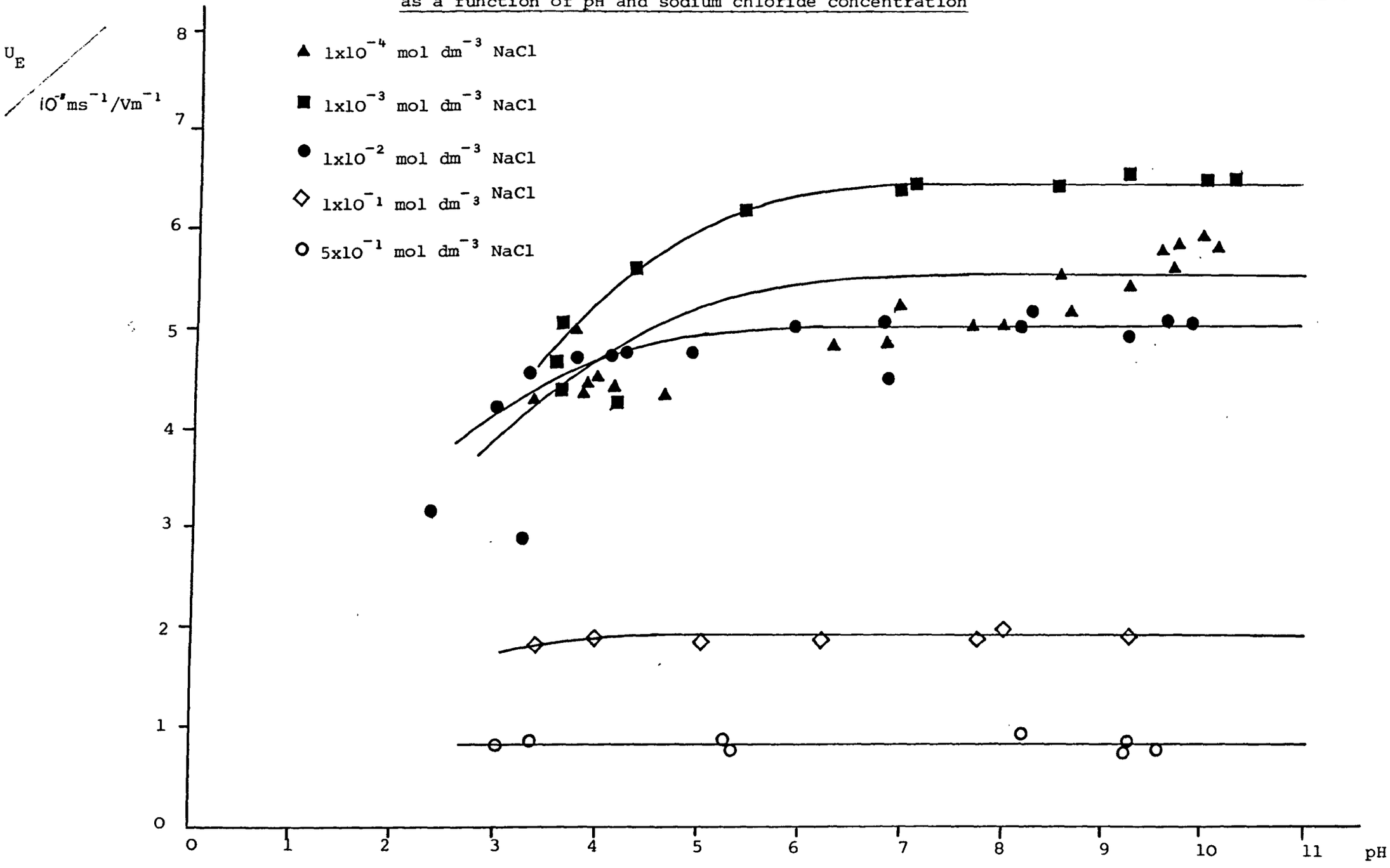

Figure 8.8.

Electrophoretic mobility of polystyrene latex SJP11 particles (diameter 1.92 μm) as a function of pH and sodium chloride concentration.

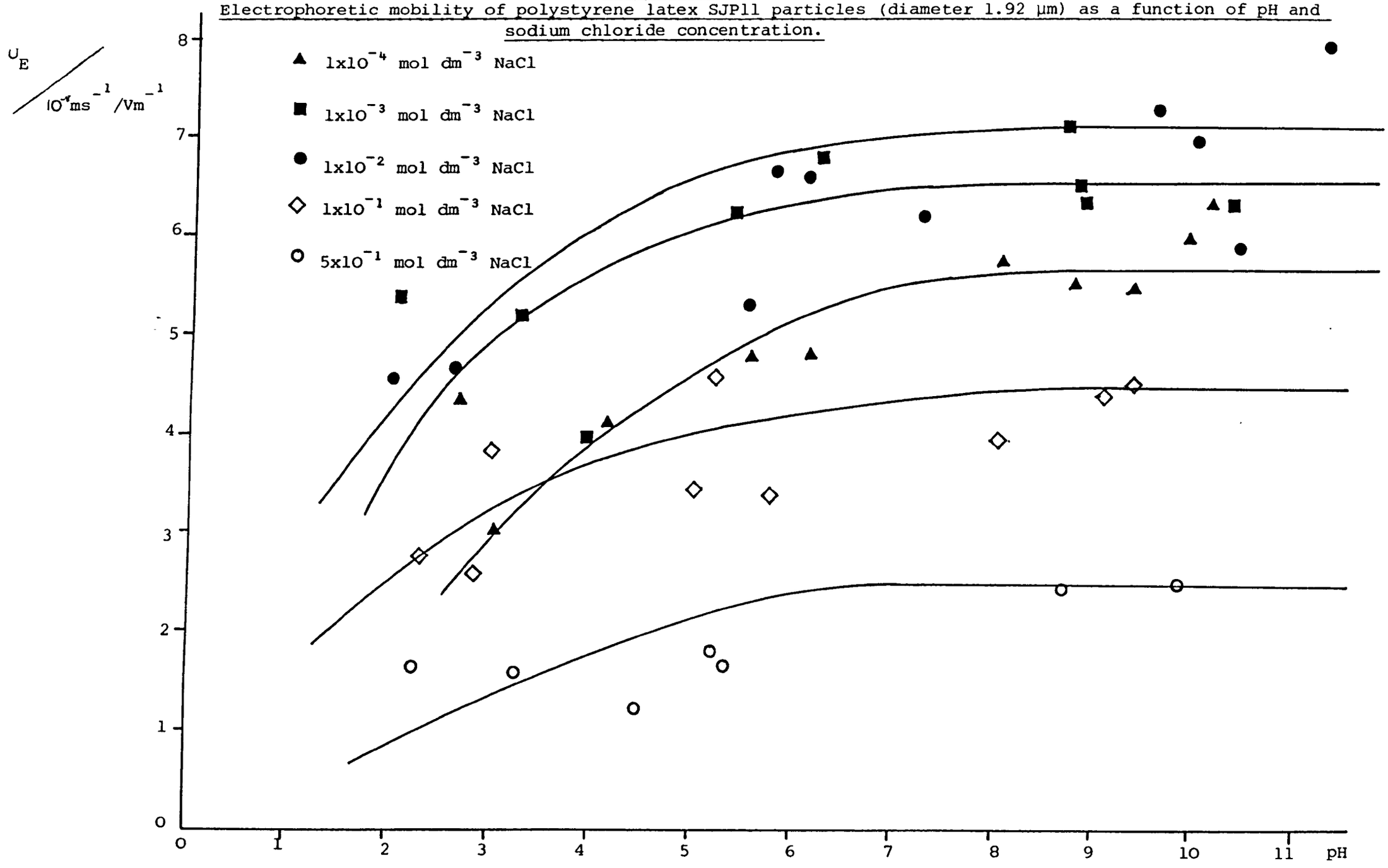

Electrophoretic mobility of polystyrene latex SJP11 particles (diameter 1.92 μm) with full coverage of $C_{12}E_6$ as a function of pH and sodium chloride concentration.

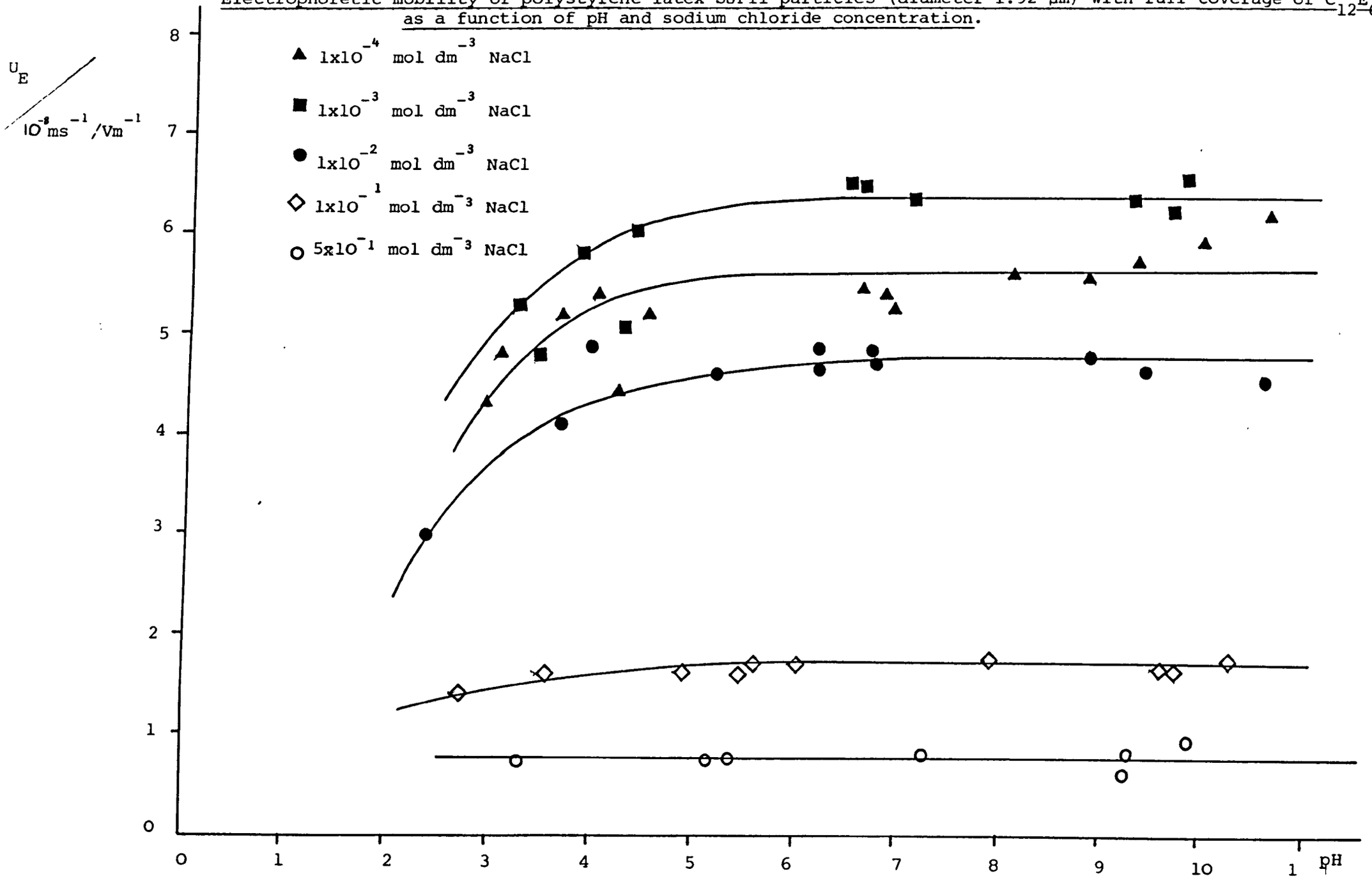

Table 8.3.

Zeta potentials/mV of polystyrene latex particles with and without full coverage of $C_{12}E_6$ at plateau pH in varying sodium chloride concentration.

System \ [NaCl] /mol dm^{-3}	1×10^{-4}	1×10^{-3}	1×10^{-2}	1×10^{-1}	5×10^{-1}
SJP8	69.1	81.9	96.0	66.6	28.8
SJP8/$C_{12}E_6$	64.0	78.1	63.4	24.3	9.7
SJP10	65.9	84.5	96.0	58.9	30.1
SJP10/$C_{12}E_6$	70.4	81.9	64.0	24.3	10.2
SJP11	72.3	83.9	90.9	57.0	32.0
SJP11/$C_{12}E_6$	71.1	80.7	60.2	21.8	9.7

Figure 6.10.

Zeta potentials of polystyrene latex particles with and without full coverage of $C_{12}E_6$ at plateau pH as a function of $\log_{10}$ sodium chloride concentration.

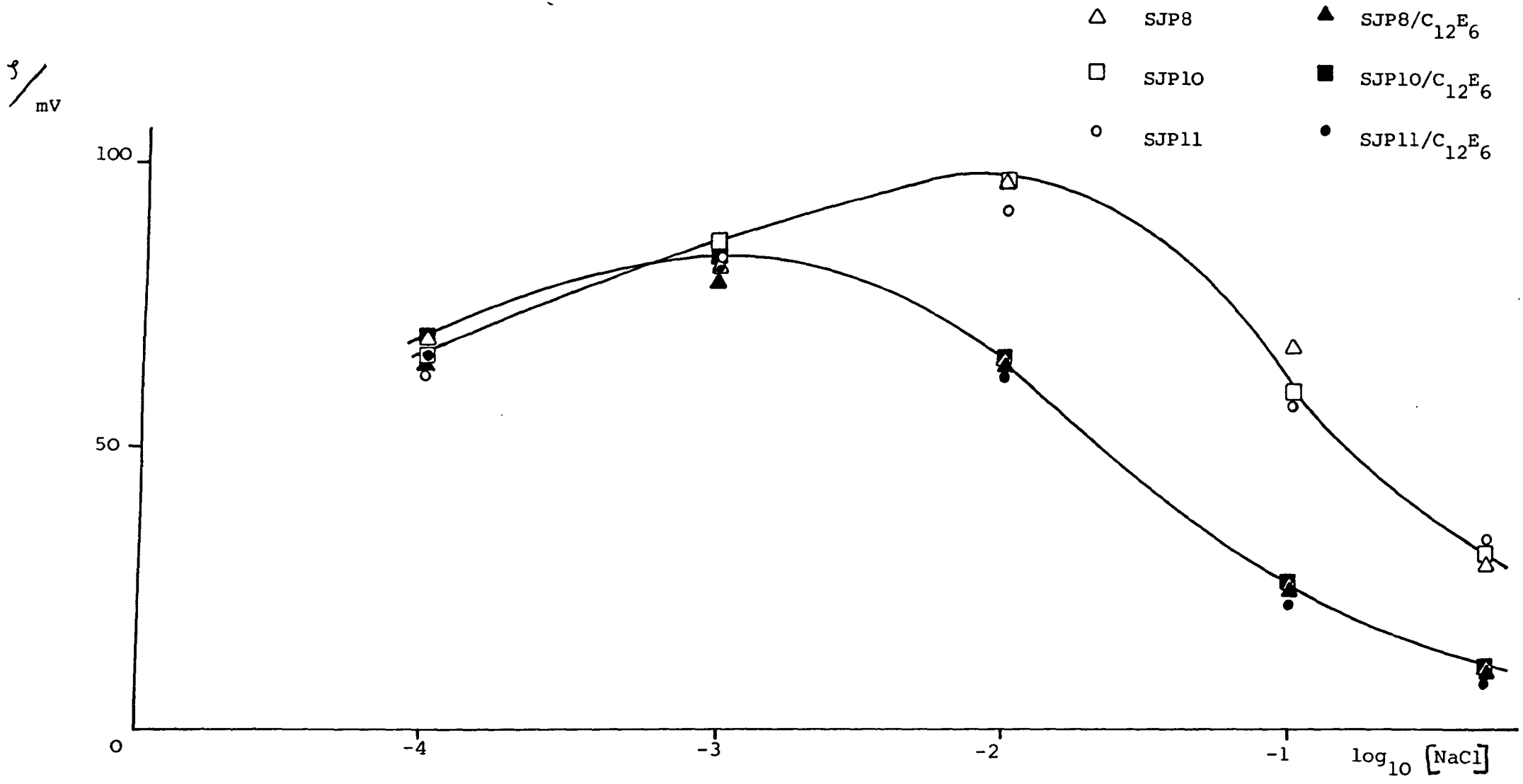

than the values obtained for the zeta potentials of the uncoated latices. The variation was a factor of 2 - 4.

The pH values of all the latices, coated and uncoated, with no additional acid or base at 0.5 mol dm^{-3} sodium chloride solution was pH5 ± 0.4. No significant difference in pH was reported due to the presence of added surface active agent.

The electrophoretic behaviour of latices SJP8, SJP10 and SJP11 was studied at four other sodium chloride concentrations: 10^{-4}, 10^{-3}, 10^{-2} and 10^{-1} mol dm^{-3}. The pH values of the naked latices at these concentrations, with no added acid or base, was found to be pH 5.6 ± 0.6. The presence of surface active agent at the lower concentrations served to increase the pH and at 10^{-4} and 10^{-3} sodium chloride concentration the pH range was found to be pH 6.7 ± 0.2.

The electrophoretic mobilities of the latices SJP8, SJP10 and SJP11, with and without $C_{12}E_6$, measured at the five salt concentrations cited previously were plotted as a function of pH, see Figures 8.4 - 8.9. In each case the electrophoretic mobility increased with the pH to a plateau value which commenced at approximately pH5. This was important to note as it was essential that experiments were carried out at the plateau mobility to enable accurate characterisation of the system. The natural pH of the systems was above pH5 and hence no extra base was required throughout the experiments performed in this piece of work.

Plots were made of the plateau zeta potential versus electrolyte concentration for the six systems studied, SJP8, SJP10 amd SJP11, with and without $C_{12}E_6$, see Figure 8.10. The results of the three bare latices may be represented by one line with a peak at 1 x 10^{-2} mol dm^{-3} electrolyte concentration and the results for the three coated latices by one line with a peak at 1 x 10^{-3} mol dm^{-3} sodium chloride concentration. The presence of the

adsorbed layers on the particle surfaces clearly affected the trend of electrophoretic behaviour.

The systems that were of most interest were the three latices coated with monolayer $C_{12}E_6$ in 0.5 mol dm^{-3} sodium chloride solution as these were the systems used in the bulk of the work in this thesis. The plateau zeta potentials for these were 9.7 mV for the SJP8/$C_{12}E_6$ (particle diameter 9.74 x 10^{-7}m) and the SJP11/$C_{12}E_6$ (particle diameter 1.92 x 10^{-6}m) cases and 10.2 mV for the SJP10/$C_{12}E_6$ (particle diameter 1.41 x 10^{-6}m) system. These values were low but still significant and must be included in calculations of interparticle interactions, an electrostatic repulsion term must be included.

8.4. Freeze Etch Microscopy.

8.4.1. Introduction.

The technique of freeze-etch microscopy as applied to floc morphology has been developed by Stewart and Sutton at the Corporate Bioscience and Colloid Division of ICI.[191,192] The process involves five basic steps: freezing, fracturing, etching, replication and observation and has application in a great number of aqueous and volatile non-aqueous suspensions.

It is necessary to cool a sample in such a way that disturbance of the internal microstructure by the formation of ice crystals is minimal. This may be achieved by very rapid cooling of a small sample in a suitable coolant. "Arcton 12", dichlorodifluoromethane, melting point -156°C is used as coolant in preference to liquid nitrogen, melting point -210°C, as its boiling point is sufficiently high to prevent the formation of a heat-insulating gas layer.

8.4.2. Experimental.

The work was carried out at ICI Corporate Bioscience and Colloid Laboratory, Runcorn, under the supervision of Mr. C.C. Donaldson (freeze etch)

and Mrs. K. Schofield (electron microscope).

The apparatus used in the freeze etch experiments was a Cressington S30 freeze etch module seated on a dedicated Edwards E 306 vacuum coater. The sample holder consists of two copper tubes, 2 mm and 3mm in length, 1 mm internal diameter,which are placed on top of each other such that after freezing the sample may be fractured at the junction between the two tubes.

The sample holder was filled with sample, frozen by immersion in "Arcton 12" and stored under liquid nitrogen before being placed onto a pre-cooled specimen table ($-130^{\circ}C$) in the freeze etch apparatus and clamped into position under a backflow of dry nitrogen gas.[193] The whole apparatus was then evacuated to a pressure of 5×10^{-7} torr and the cutting knife, precooled to $-196^{\circ}C$, rapidly sliced through the sample leaving an exposed freshly cut surface.

To obtain information on the three-dimensional structure of the system $\simeq 1\mu m$ depth of the dispersion medium at the surface was removed by vacuum sublimation. This was achieved by raising the temperature to $-100^{\circ}C$ for two minutes.

To replicate the fractured surface it was coated first with platinum at an angle of 45° and then the thin film strengthened by carbon evaporation at an angle of 90° to the fractured face.

The sample was placed under liquid nitrogen after removal from the specimen tube. The replica was then floated off onto the surface of freshly distilled water where it remained for 30 minutes to remove any attached particles. The replica was picked up on a 400 mesh, hexagonal electron microscope grid and allowed to dry. Xylene was washed over the grid to remove any remaining organic material and again left to dry.

The fractured surface replica was studied using a Philips 300 transmission electron microscope with a High Resolution Stage.

Seven systems were studied - all SJP8/$C_{12}E_6$ particles, 0.97 μm diameter, in 0.5 mol dm^{-3}NaCl with a volume fraction range of ϕ = 0.1 to ϕ = 0.6.

8.4.3. Results and Discussion.

Some electron micrographs are presented in Plates 8.1 to 8.4.

To fill the sample holder a large amount of shearing of the system was required which tends to disperse the particles and break up flocs. The system was then rapidly frozen, in its disturbed state, before the particles had time to reflocculate.

To overcome this problem the systems were left to stand for about ten minutes in the sample holder before being frozen in "Arcton 12". This improved the results and a greater degree of particle flocculation could be observed when the systems were allowed to settle before freezing than when they were immediately frozen. There was, however, a limit to the time that the filled sample holder could be left to stand before freezing as the systems, being low in volume, tended to dry out. Also, sedimentation had to be considered.

Hence freeze etch microscopy has limited value in the study of weakly flocculated systems such as these, although some information may be gleaned.

Plates 8.1 and 8.2 show that some form of aggregation of the particles definitely took place, clusters of particles and areas with no particles can be observed. The higher magnification electron micrographs, given in Plates 8.3 and 8.4 show that some form of ordered arrangement of the particles occurred.

Freeze-Etch Micrographs of Polystyrene Latex SJP8 (diameter 0.97 μm) with full coverage of $C_{12}E_6$ in 5×10^{-1} mol dm^{-3} NaCl.

Plate 8.1.

ϕ = 0.24

magnification = 10K

Plate 8.2.

ϕ = 0.24

magnification = 12K

Plate 8.1.

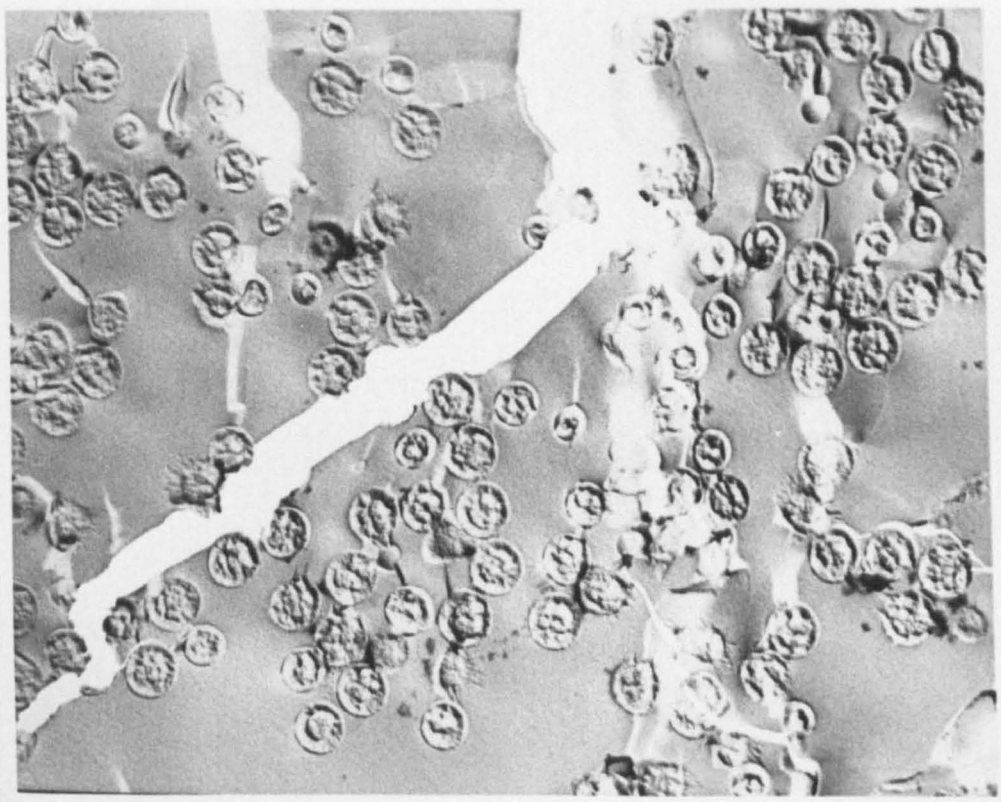

Plate 8.2.

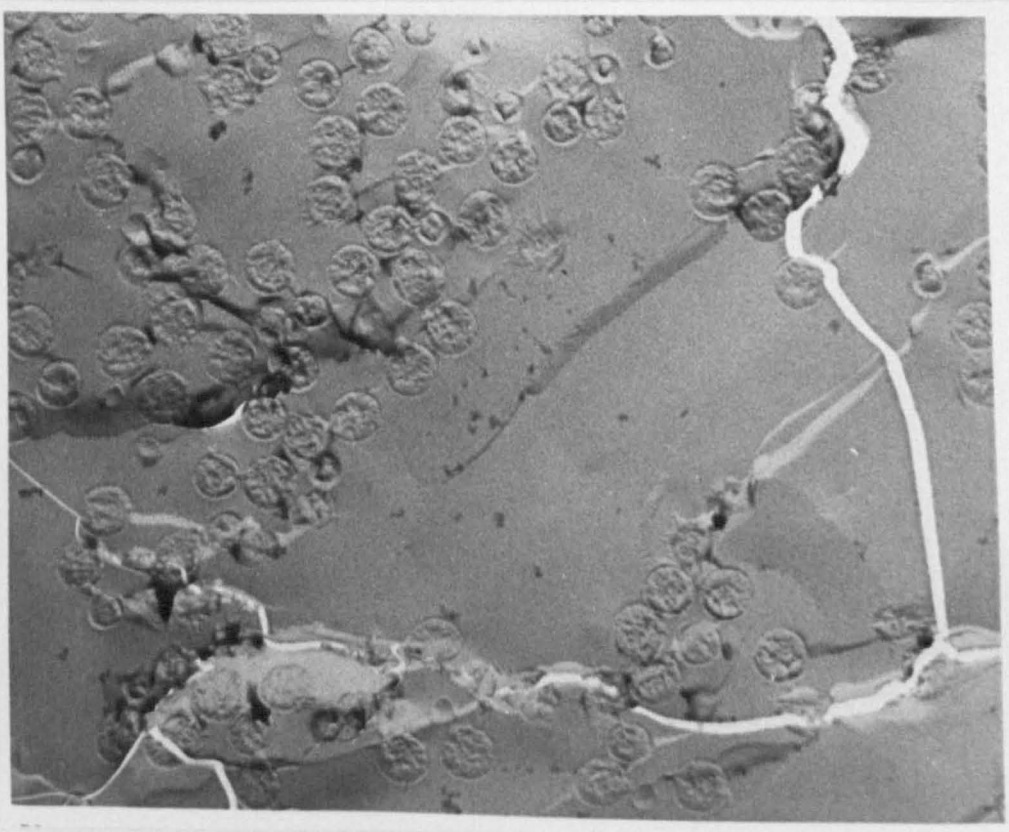

Freeze-Etch Micrographs of Polystyrene Latex SJP8 (diameter 0.97 μm) with full coverage of $C_{12}E_6$ in 5×10^{-1} mol dm^{-3} NaCl.

Plate 8.3.

ϕ = 0.10

magnification = 50K

Plate 8.4.

ϕ = 0.24

magnification = 50K

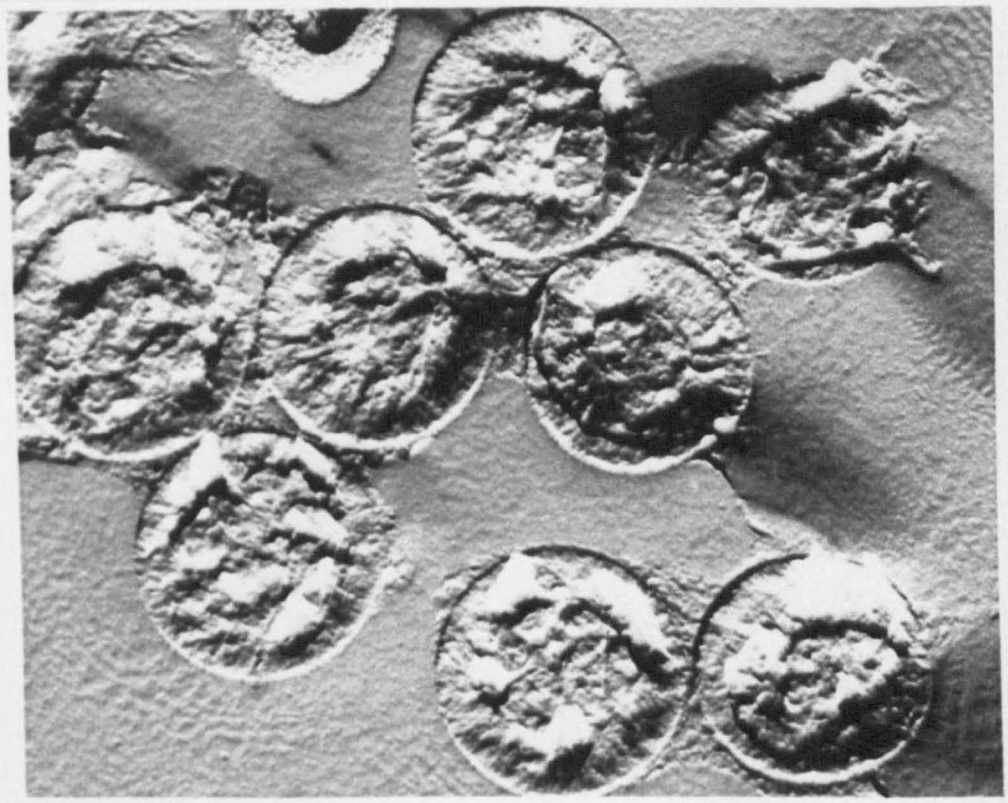

Plate 8.3.

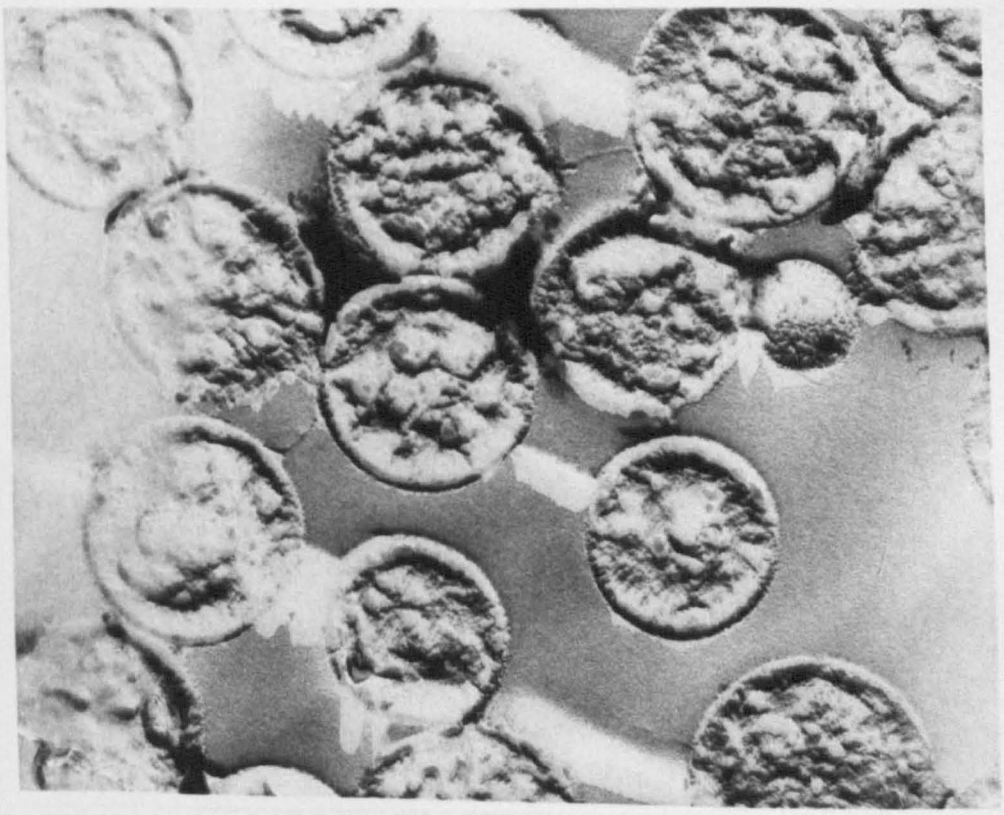

Plate 8.4.

8.5. Optical Microscopy.

8.5.1. Introduction.

Optical microscopy affords a means by which a system may be directly observed without the artefacts that could be introduced when freezing, drying or coating is involved. It also allows a dynamic rather than purely static picture of the system. The disadvantage with optical microscopy is its resolution - many colloidal particles are too small to be readily observed. The particles used in this work: 0.97 μm, 1.41 μm and 1.92 μm are easily resolvable by optical microscopy and therefore the technique is very useful.

8.5.2. Experimental.

The experimental work was carried out at ICI Corporate Bioscience and Colloid Laboratory with the help of Mr. J. McMahon and Mrs. K. Schofield.

The apparatus used was an Olympus research optical microscope, model BH2 fitted with a photomicrographic camera attachment. The magnification range was from 10x to 100x.

A drop of sample was placed on a clean glass slide, covered with a cover slip and observed directly. A given slide could be studied for about 20 minutes before the samples dried out.

The systems studied were polystyrene latices SJP8 (diameter 0.97 μm), SJP10 (diameter 1.41 μm) and SJP11 (diameter 1.92 μm), all with full coverage of $C_{12}E_6$ in 0.5 mol dm^{-3} sodium chloride solution.

The systems were observed at low volume fractions, $\phi \simeq 0.001 - 0.01$, for a clear picture of the flocs and the floc formation. At high volume fractions, $\phi > 0.1$, individual flocs could not be clearly distinguished.

The kinetics of the flocculation of the particles was estimated qualitatively by lightly jarring the microscope slide and observing the reformation of the flocs as a function of time.

8.5.3. Results and Discussion.

Some optical micrographs are presented in Plates 8.5 to 8.16. Almost all the particles at any one time were found to be associated with others, the size of the aggregation depending on the volume fraction of the system under observation. The systems were found to be extremely weakly flocculated - a slight jarring of the microscope slide resulted in the complete break up of the aggregations or flocs and flow lines in the direction of the applied force were observed. This is illustrated in Plate 8.5.

After agitation of the systems the particles could be seen to re-flocculate, the rate depending on the volume fraction of the system, i.e. on the proximity of other particles. In the very dilute systems small flocs were seen to form and then scavenge other individual particles as they came across them. In all cases reflocculation occurred after about 15 minutes. The flocs themselves were dynamic structures with the particles constantly shifting relative positions but remaining associated. In the very low volume fraction systems an individual particle could be seen to be shifting its position in a floc until it settled. Once the particles were in flocs they never left them unless some external force was applied. This is in contradiction to the model of Vincent and coworkers[194] of dynamic flocculation. Cornell et al[195] examined the aggregation of polystyrene latices in the presence of added electrolyte and obtained evidence for a reversible aggregation process with a finite lifetime in the associated state for doublets before dissociation into single particles. They also found evidence for the mobility of particles within floccules.

Optical Micrographs of Polystyrene Latices with full coverage of $C_{12}E_6$ in 5×10^{-1} mol dm^{-3} NaCl.

Plate 8.5.

latex = SJP8 (diameter 0.97 μm)

magnification = 100 x

Plate 8.6.

latex = SJP10 (diameter 1.41 μm)

magnification = 40 x

Plate 8.5.

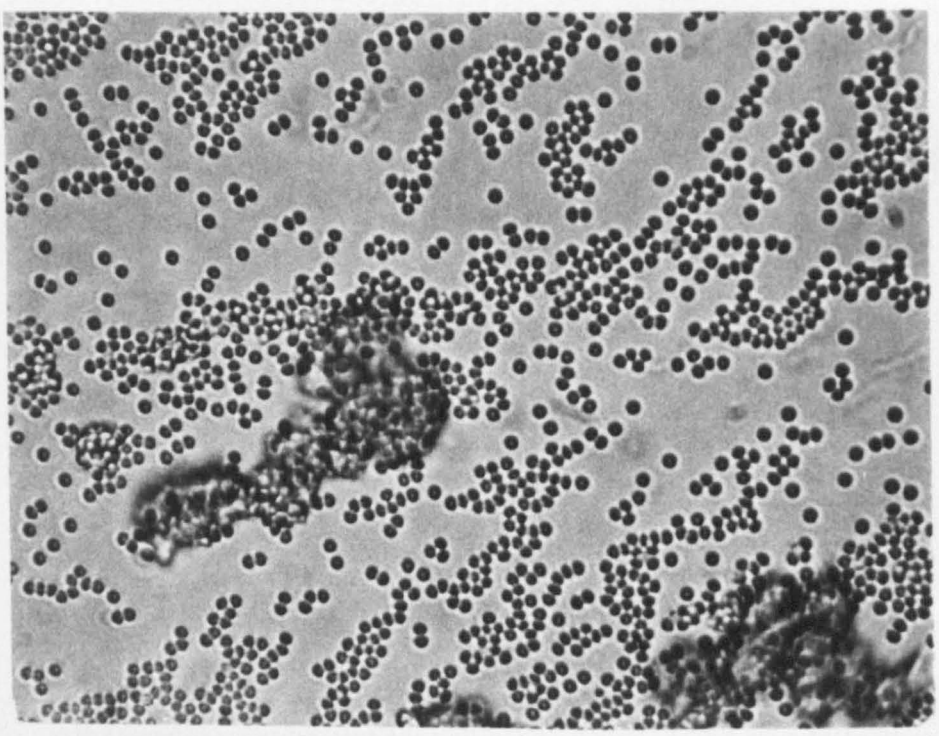

Plate 8.6.

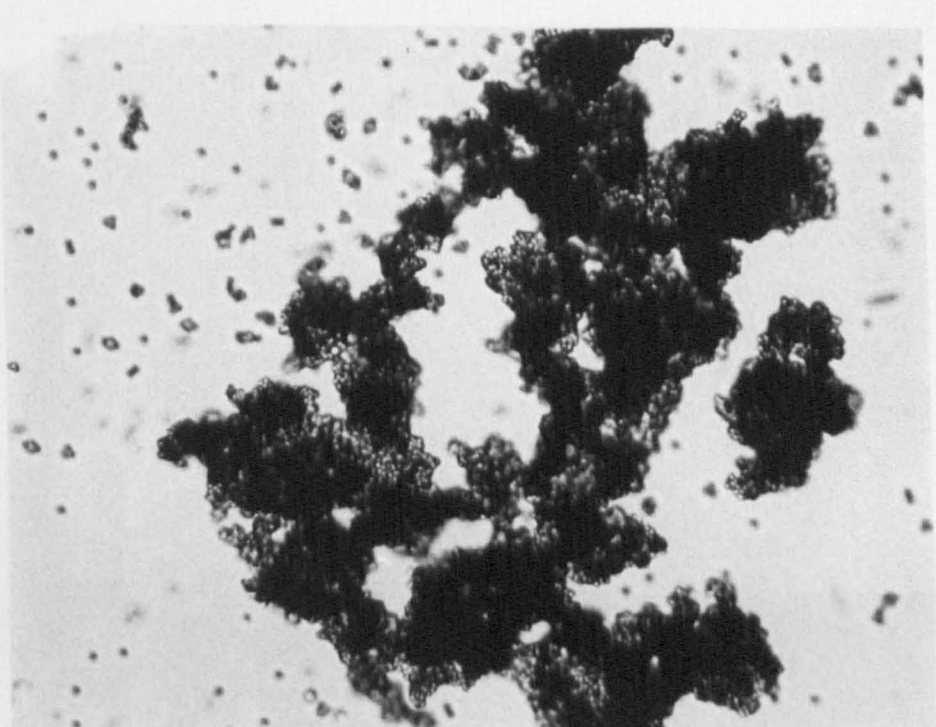

Optical Micrographs of Polystyrene Latices with full coverage of $C_{12}E_6$ in 5×10^{-1} mol dm^{-3} NaCl.

Plate 8.7.

latex = SJP8 (diameter 0.97 μm)
magnification = 10 x

Plate 8.8.

latex = SJP11 (diameter 1.92 μm)

magnification = 40 x

Plate 8.7.

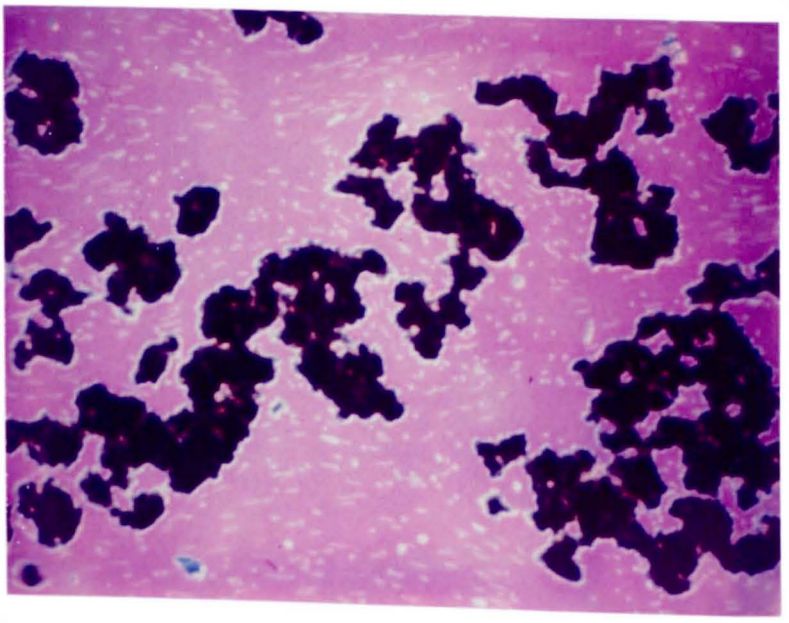

Plate 8.8.

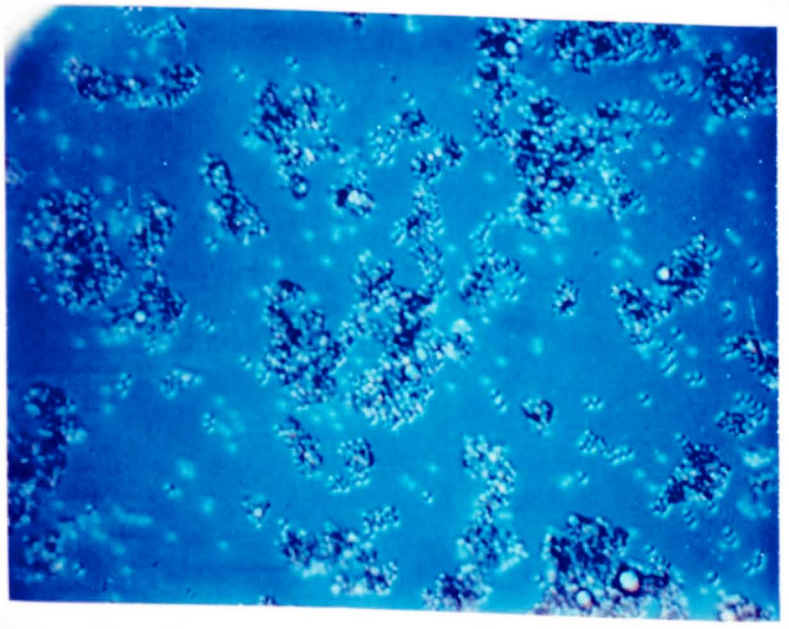

Optical Micrographs of Polystyrene Latices with full coverage of $C_{12}E_6$ in 5×10^{-1} mol dm^{-3} NaCl.

Plate 8.9.

latex = SJP8 (diameter 0.97 μm)
magnification = 100 x

Plate 8.10.

latex = SJP8 (diameter 0.97 μm)
magnification = 40 x

Plate 8.9.

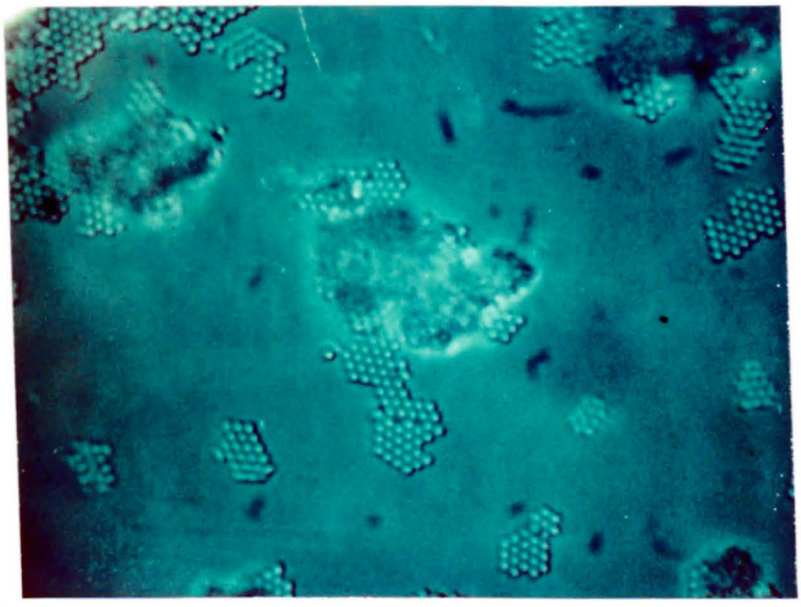

Plate 8.10.

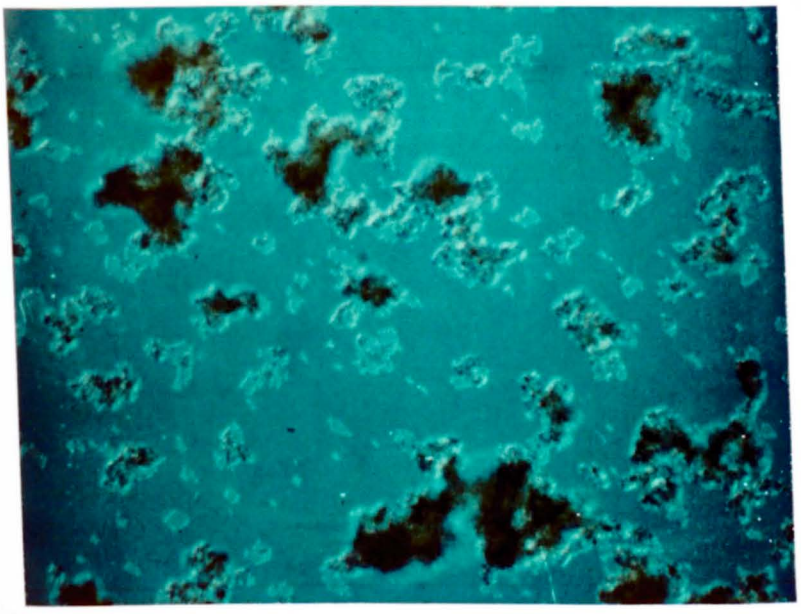

Optical Micrographs of Polystyrene Latices with full coverage of $C_{12}E_6$ in 5 x 10^{-1} mol dm^{-3} NaCl.

Plate 8.11.

latex = SJP10 (diameter 1.41 μm)
magnification = 100 x

Plate 8.12.

latex = SJP10 (diameter 1.41 μm)
magnification = 100 x

Plate 8.11.

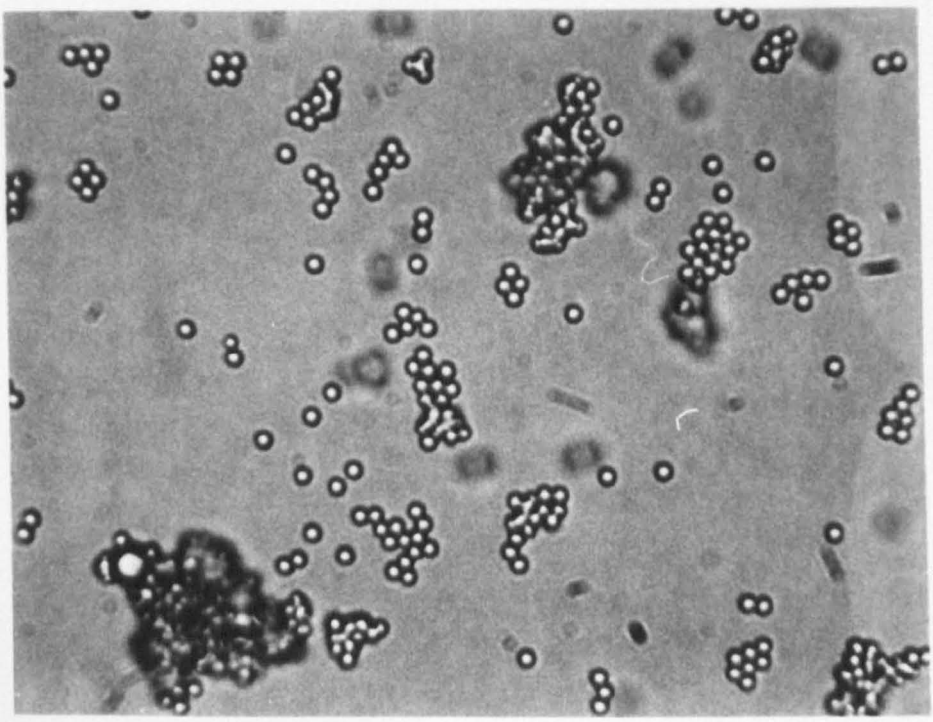

Plate 8.12.

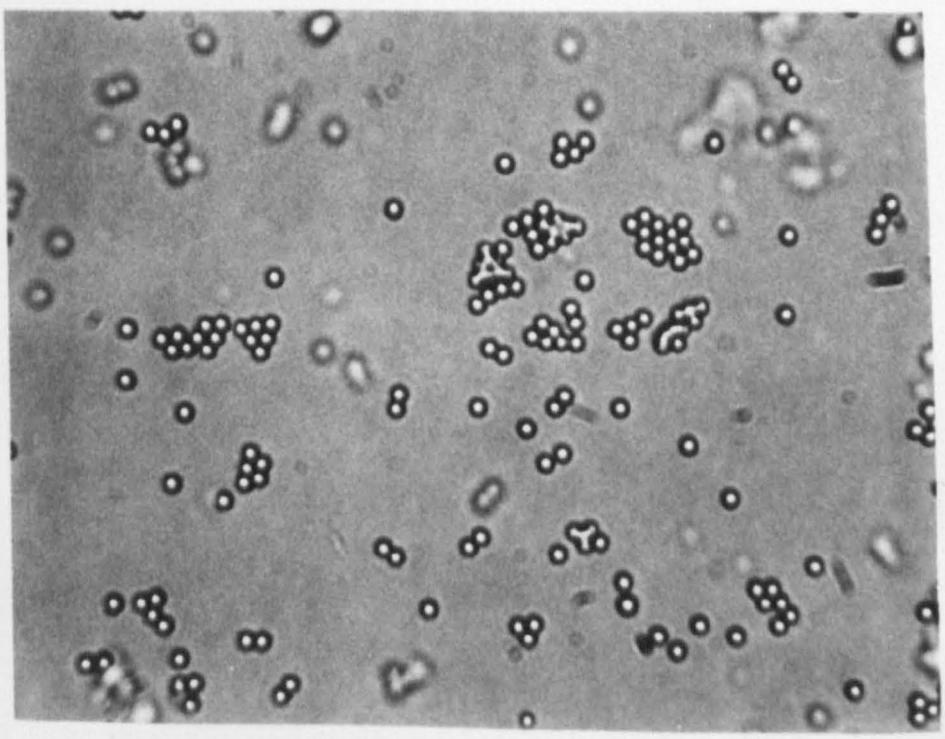

Optical Micrographs of Polystyrene Latices with full coverage of $C_{12}E_6$ in 5 x 10^{-1} mol dm^{-3} NaCl.

Plate 8.13.

latex = SJP11 (diameter 1.92 μm)

magnification = 100 x

Plate 8.14.

latex = SJP11 (diameter 1.92 μm)
magnification = 100 x

Plate 8.13.

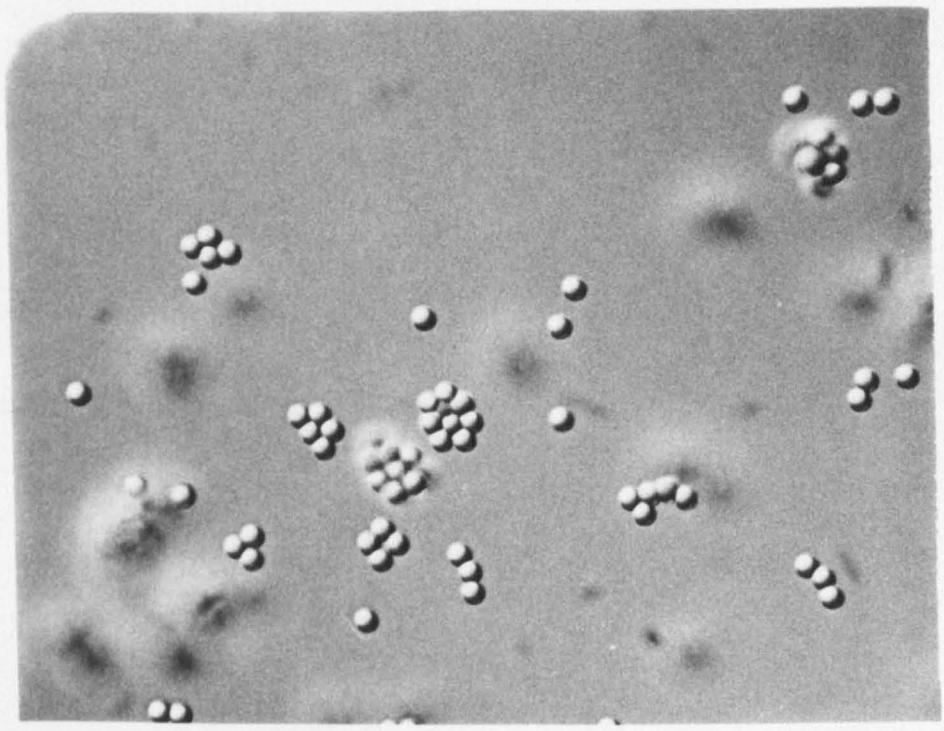

Plate 8.14.

Optical Micrographs of Polystyrene Latices with full coverage of $C_{12}E_6$ in 5×10^{-1} mol dm^{-3} NaCl.

Plate 8.15.

latex = SJP11 (diameter 1.92 μm)
magnification = 100 x

Plate 8.16.

latex = SJP11 (diameter 1.92 μm)
magnification = 100 x

Plate 8.15.

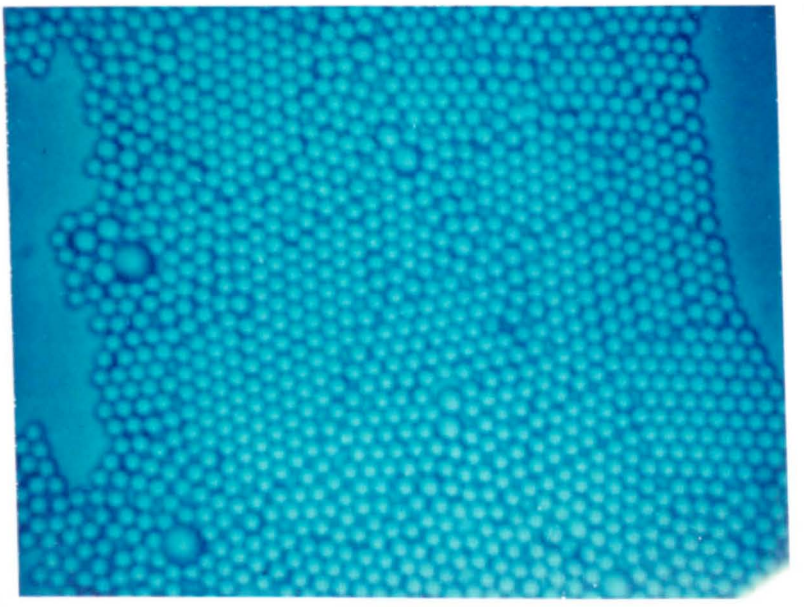

Plate 8.16.

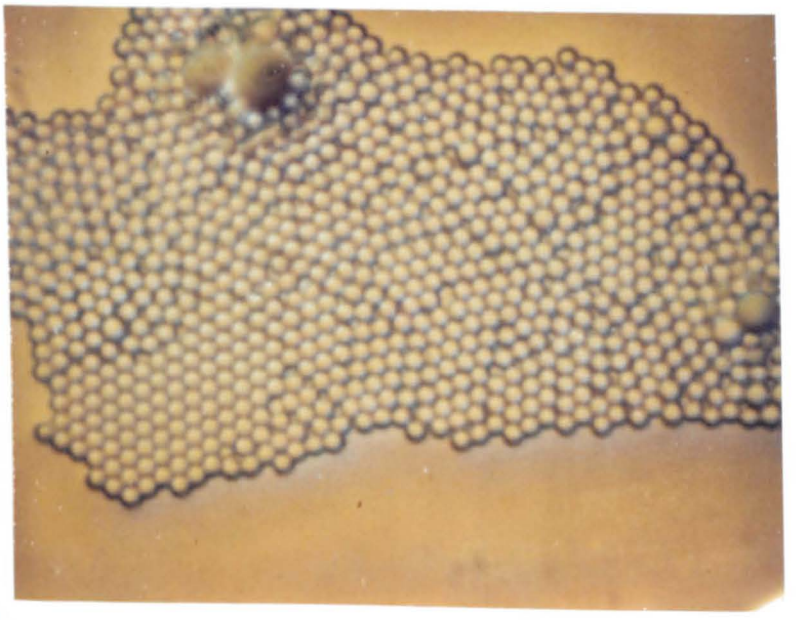

The structure within the flocs themselves was discovered to be highly ordered hexagonal close packing. This is clearly illustrated in the high magnification micrographs Plates 8.11 - 8.14 and especially clearly in Plates 8.9 and 8.10.

In the low volume fraction systems individual particles could be seen to move into an ordered position after association with a floc. This was nicely shown with a five particle floc consisting of one central particle and four hexagonally arranged about it leaving two adjacent spaces. A particle joined the floc and moved about it into the space where it shifted from one particle space to the other before settling.

Ordered structures in flocculated systems have been obtained by Kose and Hachisu[196] who worked with monodisperse polystyrene latices flocculated with sodium polyacrylate. This type of flocculation, involving a polymeric flocculant, will involve bridging flocculation and be stronger than the very weak flocculation in the systems in this piece of work.

The particles on sedimentation formed highly ordered arrays, this is shown in Plates 8.15 and 8.16.

Chapter Nine

Sedimentation

Chapter Nine. Sedimentation.

9.1. Introduction.

Sedimentation measurements were carried out at normal gravitational acceleration, i.e. at 1g, in a thermostatted cabinet and at accelerations greater than this by means of a slow speed centrifugation technique. In all cases the sedimentation behaviour was monitored by following the descent of the sediment boundary with time.

Preliminary sedimentation measurements were performed using polystyrene latex SJP9 (particle diameter 0.96 μm) at low volume fractions in various electrolytes; sodium chloride, barium nitrate, magnesium nitrate and magnesium sulphate. All the electrolytes were at concentrations sufficiently high so as to achieve weak flocculation, (see 7.6). The systems studied in the bulk of the work, at 1g and at various higher g-values, were the weakly flocculated polystyrene latex dispersions as described in (7. 7); polystyrene latices SJP8 (diameter 0.97 μm), SJP10 (diameter 1.41 μm) and SJP11 (diameter 1.92 μm) coated with a monolayer coverage of $C_{12}E_6$ in 0.5 mol dm^{-3} sodium chloride solution. For each latex system the sedimentation behaviour was investigated over a volume fraction range of ϕ = 0.05 - 0.6.

The measurements made at 1g are described first followed by the measurements at > 1g. The results are presented and initial observations discussed. The results are considered in relation to theoretical predictions in (9.4) and comparisons made with rheological behaviour in Chapter Twelve.

9.2. Experimental.

9.2.1. Sedimentation at 1g.

The sedimentation rate studies were performed in cylindrical flat-bottomed glass tubes c.a. 10 cm long x 1 cm diameter. These were made from Quickfit B14/23 sockets with the bottoms sealed and flattened. This ensured straight parallel sides for the tubes and a diameter large enough for wall effects to be considered negligible. On filling the ground glass joints were fitted with polypropylene stoppers, Quickfit C14/15, and further sealed with 'parafilm' to avoid evaporation of the sample.

A reference level was fired onto each tube using 'Decal' transfers at a filled volume of 15 cm^3. This provided a reference level from which to measure the sediment boundary descent.

The tubes were vertically positioned in metal stands fixed in a constant temperature cabinet fitted with a double glazed 'Perspex' front so that each tube was clearly visible. The air temperature, within the cabinet, was maintained at $25^{\circ}C \pm 0.5^{\circ}C$ by means of a heater working against a heat sink provided by a cold water circulation system. The cabinet also served to eliminate convection currents which can affect sedimentation behaviour.

The descent of the sediment boundary was measured to an accuracy of ± 0.5 mm by means of a rule as when measuring the settling velocity of particles using a centrifugation technique, use of a more accurate method of determination such as a cathetometer was not practicable. Therefore since the results of the two types of experiment were to be compared a similar method of rate determination was sensible.

All the glassware used was thoroughly cleaned in concentrated nitric acid, extensively rinsed in distilled water, steamed and dried in an oven.

The tubes were filled to the reference level with the samples under investigation, labelled, well shaken and placed in the constant temperature cabinet. Readings were taken of the descent of the sediment boundary as a function of time.

9.2.2. Sedimentation at > 1g.

To study the sedimentation behaviour at enhanced gravitational acceleration an M.S.E. Centaur II Bench Top Centrifuge was employed with an operation range of 0 - 3600 r.p.m. which corresponds to 0 - 2000 g. To convert the angular velocity into g-values the following expression was used:

$$x^{\dagger} = \frac{N^{\dagger 2} 4\pi^2 r^{\dagger}}{3600\ g} \qquad (9.1)$$

where $x^{\dagger}$ is the number of g-value, $N^{\dagger}$ is the number of revolutions per minute, $r^{\dagger}$ is the radius of the rotation, i.e. the distance from the centre of the rotor to the bottom of the spinning tube (0.14m). A plot was made of the r.p.m. values versus the g-values for simple reference; this is presented in Figure 9.1.

To monitor the angular velocity of the rotor, the centrifuge had a digital read out of r.p.m. correct to ± 50 r.p.m. This was not considered to be accurate enough as in a 100 r.p.m. range there is a substantial variation in g-values. Hence the centrifuge was modified by means of an optical tachometer.* The instrumentational set up is illustrated in Figure 9.2.

A low speed optical tachometer was obtained from Ducklin Instruments, Havant, Model: LO-REV 290 with a detection range of 0 - 20,000 r.p.m.

---

* The author gratefully acknowledges the assistance of Mr. J. Cunningham of the School of Chemistry Engineering Workshop in the modification of the instrument.

Figure 9.1.

Calibration plot for Centaur 2 centrifuge for conversion of r.p.m. to g.

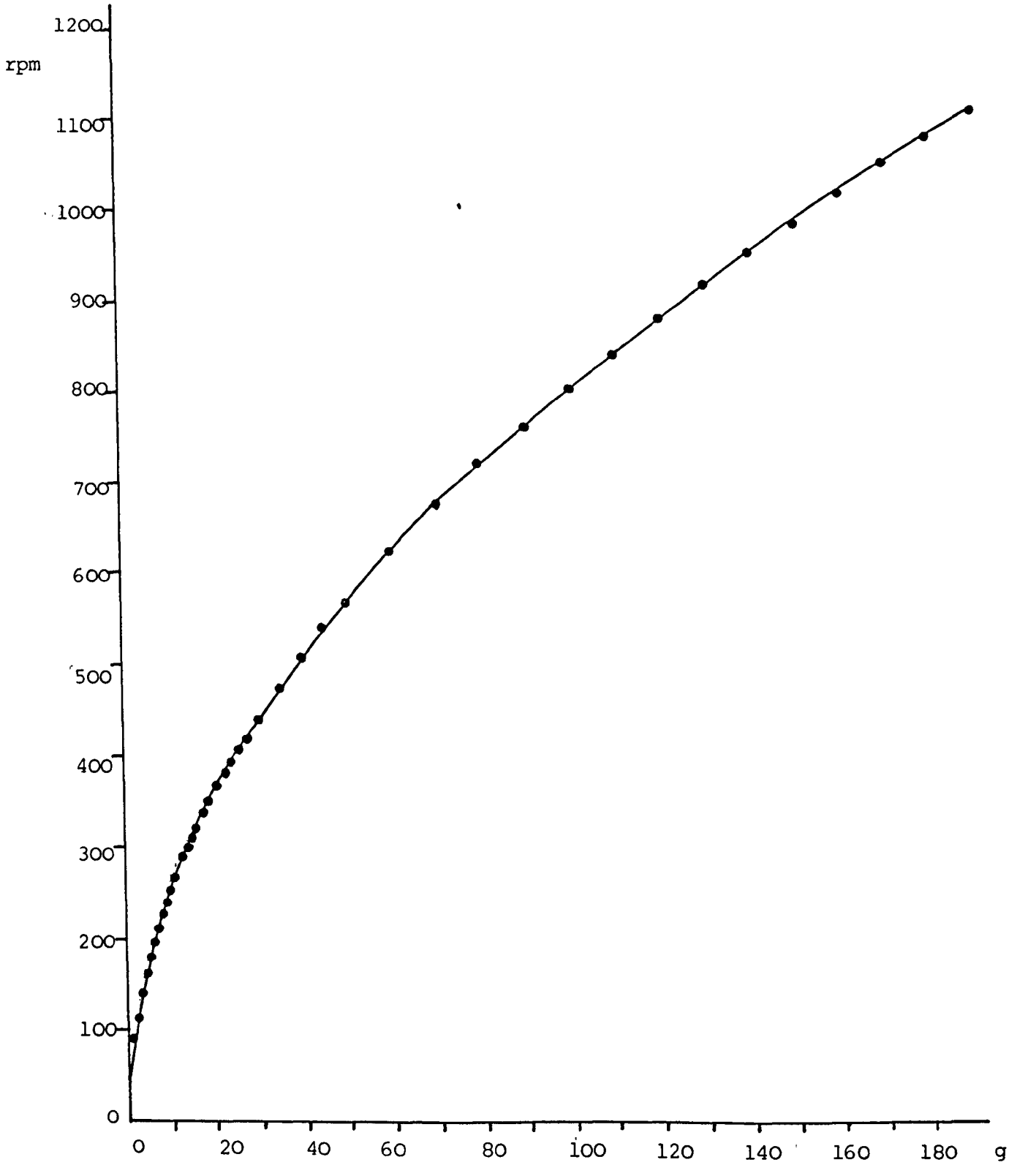

Figure 9.2.

Schematic illustration of section view of a modified slow speed centrifuge.

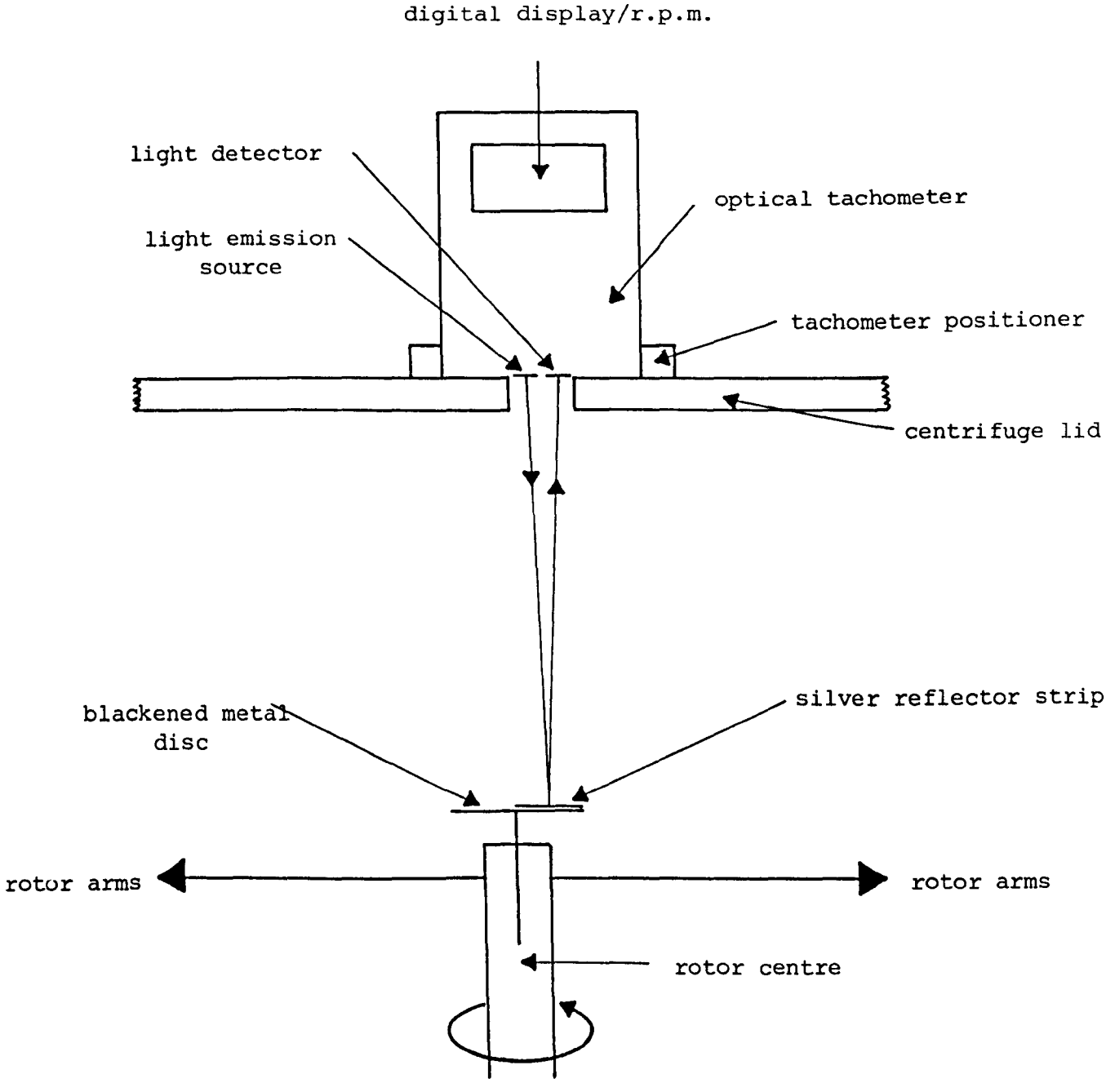

angular velocity. An optical tachometer consists of a small light emission source positioned adjacent to a detector so that when the light beam shines upon a reflector it is reflected back to the tachometer and received by the detector which monitors the frequency of light reflections.

A small hole, 1.5 cm x 0.5 cm was drilled into the lid of the Centaur II centrifuge above, but just offset from the rotor centre and the tachometer positioned above this hole such that the light emitter and detector were directly above the hole. An attachment was fitted to the lid to allow simple repositioning of the tachometer after removal e.g. to open the centrifuge. A metal disc, 3 cm in diameter was blackened, fixed to a screw and screwed into the rotor centre. A silver reflector strip, 1.5 cm x 0.5 cm was glued onto the disc positioned as a radius such that when the strip passed beneath the light emitter a signal was recorded and when anywhere else on the disc passed beneath the emitter no signal was recorded. Thus the rate of rotation of the centrifuge could be recorded. Care was taken to ensure that no surplus reflection was detected by careful positioning of the reflector strip and the tachometer.

A four-bucket rotor was used, each bucket accommodating seven centrifuge tubes of 12 cm x 1.6 cm diameter. This had two advantages, many samples could be studied together allowing direct comparisons between different systems, and the heavy rotor afforded a more constant angular velocity.

Glass tubes of height $\simeq$ 11 cm by 1.3 cm diameter with a reference level etched at a filled volume of 12 cm^3 were prepared in the same way as for gravitational acceleration. On filling, the tubes were stoppered with corks and sealed with 'parafilm'. The tubes were numbered and placed into the centrifuge. The sediment boundary descent was monitored

as before, with a rule, as a function of time. To take the readings the centrifuge was stopped and the tubes lifted very carefully from the buckets to avoid agitation.

9.3. Results.

In every sedimentation system considered in this work the sediment boundary was clearly definable and the measurement of boundary descent straightforward. In all the systems a clear supernatant was formed.

To analyse sedimentation behaviour plots were made of the descent of the sediment boundary versus the time taken for the sedimentation. The gradients of such plots then yielded values for the sedimentation rates of the systems in question.

Initially the sedimentation of low volume fraction dispersions of latex SJP9, particle diameter 0.96 μm, coated with $C_{12}E_6$ in various electrolyte solutions was followed. Volume fractions of 0.01, 0.02, 0.05, 0.07 and 0.1 were considered in 0.5 mol dm^{-3} NaCl, 5 x 10^{-2} mol dm^{-3} $Ba(NO_3)_2$, 5 x 10^{-2} mol dm^{-3} $Mg(NO_3)_2$ and 1 x 10^{-1}mol dm^{-3} $MgSO_4$. In every case good straight line plots, passing through the origin, were obtained for plots of sediment boundary descent versus time. The results for dispersions at ϕ = 0.05 in the various electrolyte solutions are presented in Figure 9.3 and for dispersions in 0.5 mol dm^{-3} sodium chloride solution at various volume fractions in Figure 9.4. A summary of the sedimentation rates for all the systems is presented in Table 9.1.

The sedimentation behaviour was also followed of latices SJP8/$C_{12}E_6$, SJP10/$C_{12}E_6$ and SJP11/$C_{12}E_6$, all in 0.5 mol dm^{-3} sodium chloride solution over a volume fraction range of ϕ = 0.05 - 0.5. The results obtained are presented in Figures 9.5 - 9.10 in the form of plots of sediment boundary descent versus sedimentation time.

Figure 9.3.

Sediment boundary descent versus time for SJP9/$C_{12}E_6$ at ϕ = 0.05 in various electrolyte solutions at 1g.

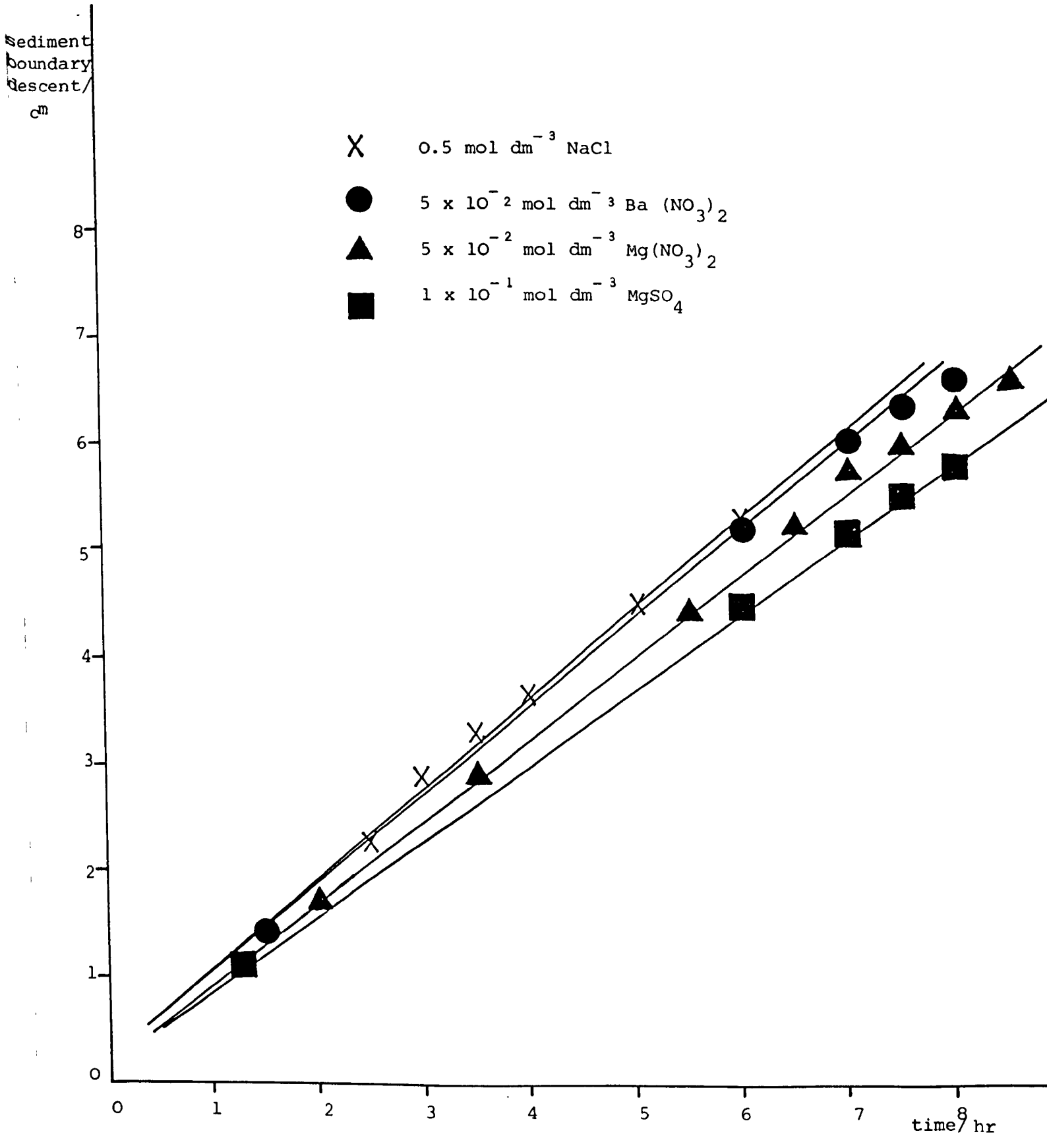

Figure 9.4.

Sediment boundary descent versus time for SJP9/$C_{12}E_6$ in 0.5 mol dm^{-3} NaCl solution at various volume fractions at 1g.

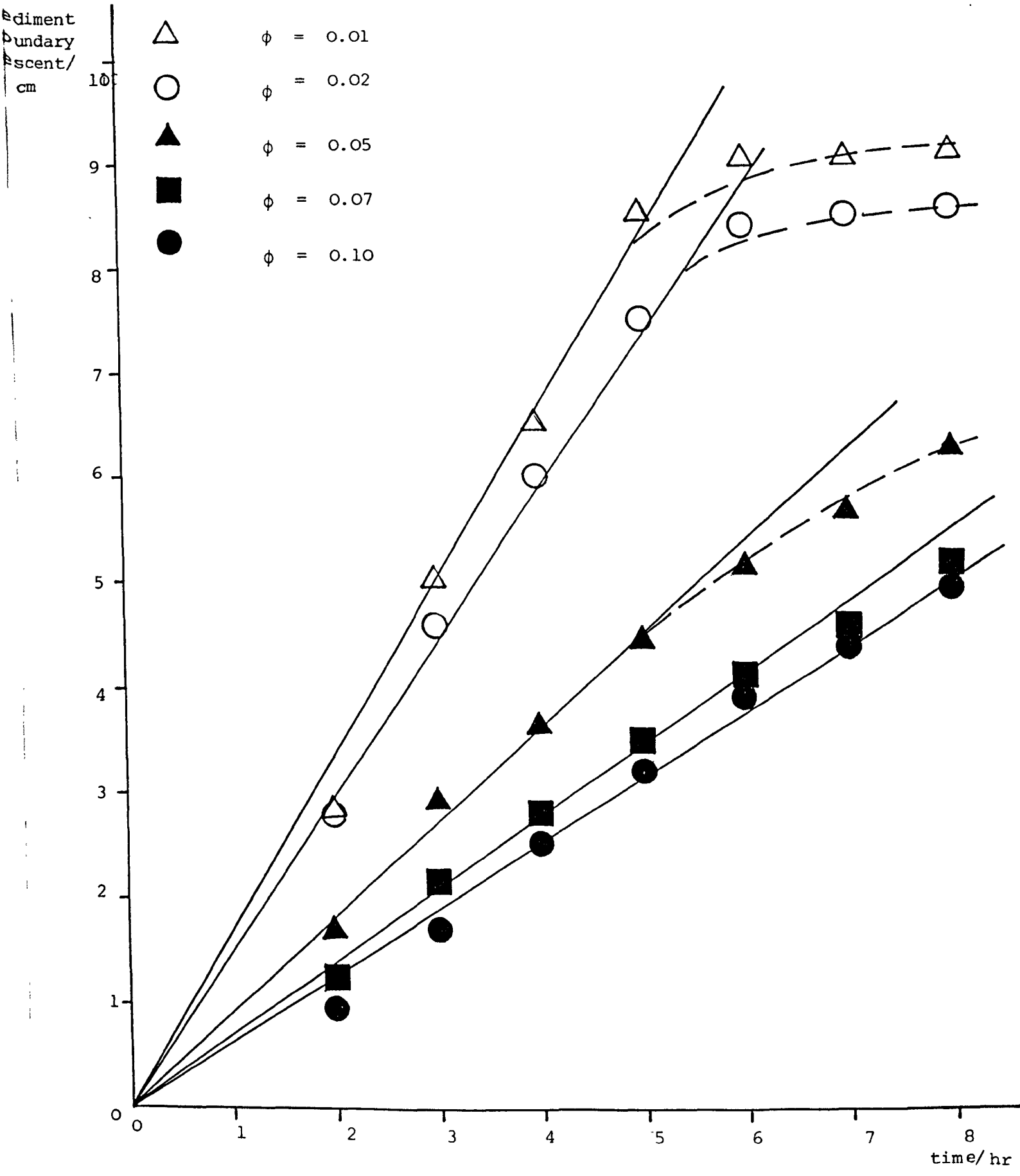

Table 9.1.

Sedimentation rates/ms^{-1} for SJP9/$C_{12}E_6$ at low volume fractions in various electrolytes at 1g.

electrolyte / ϕ	NaCl 0.5 mol dm^{-3}	$Ba(NO_3)_2$ 5×10^{-2} mol dm^{-3}	$Mg(NO_3)_2$ 5×10^{-2} mol dm^{-3}	$MgSO_4$ 0.1 mol dm^{-3}
0.01	4.86×10^{-6}	3.96×10^{-6}	3.85×10^{-6}	3.44×10^{-6}
0.02	4.12×10^{-6}	3.78×10^{-6}	3.63×10^{-6}	3.24×10^{-6}
0.05	2.55×10^{-6}	2.22×10^{-6}	2.38×10^{-6}	2.05×10^{-6}
0.07	1.94×10^{-6}	1.71×10^{-6}	1.75×10^{-6}	1.57×10^{-6}
0.10	1.67×10^{-6}	1.35×10^{-6}	1.55×10^{-6}	1.22×10^{-6}

Figure 9.5.

Sediment boundary descent versus time for SJP8/$C_{12}E_6$ in 0.5 mol dm^{-3} sodium chloride solution at various volume fractions at 1g.

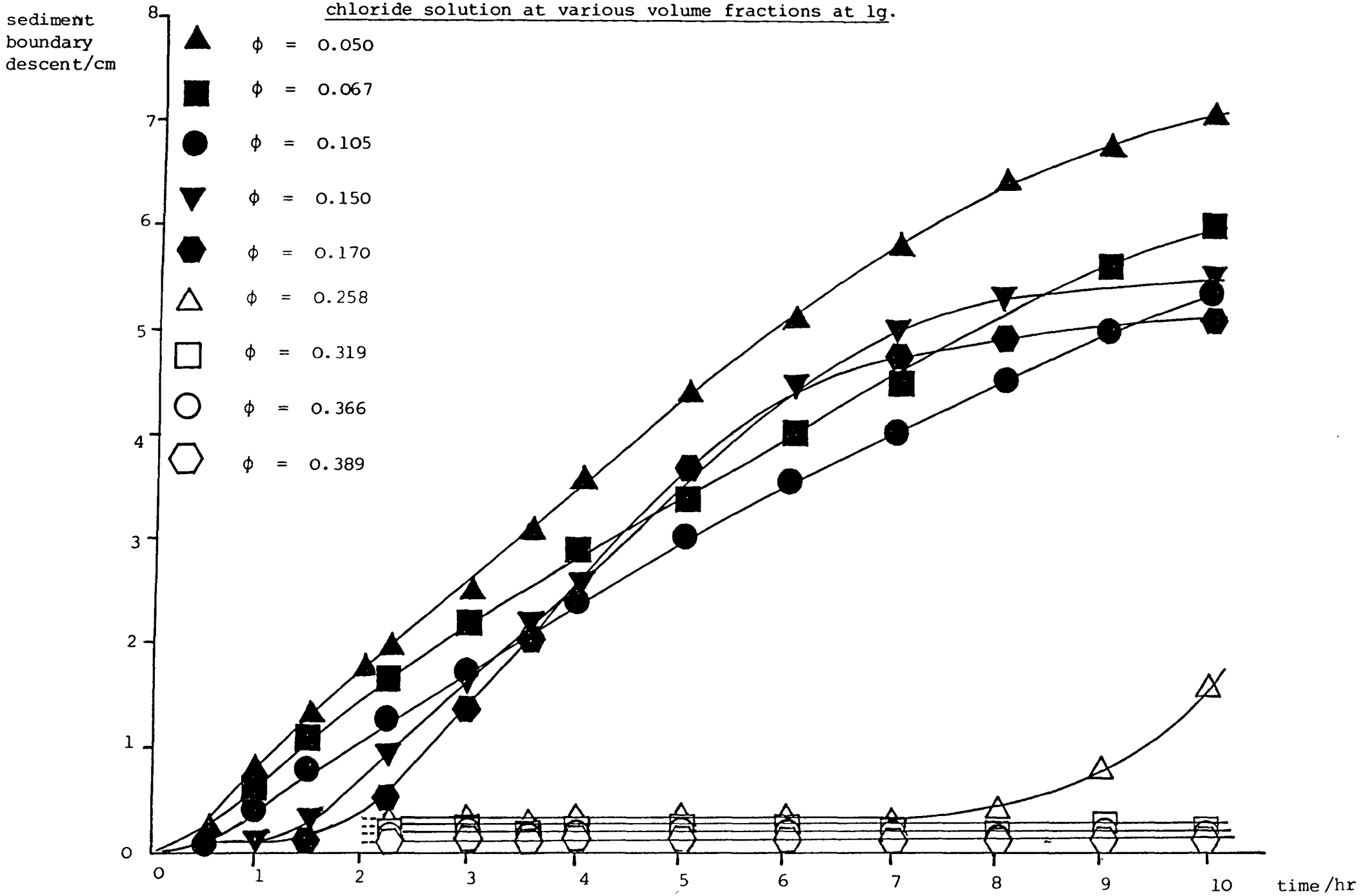

Figure 9.6.

Sediment boundary descent versus time for SJP8/$C_{12}E_6$ in 0.5 mol dm^{-3} sodium chloride solution at various volume fractions at 1g.

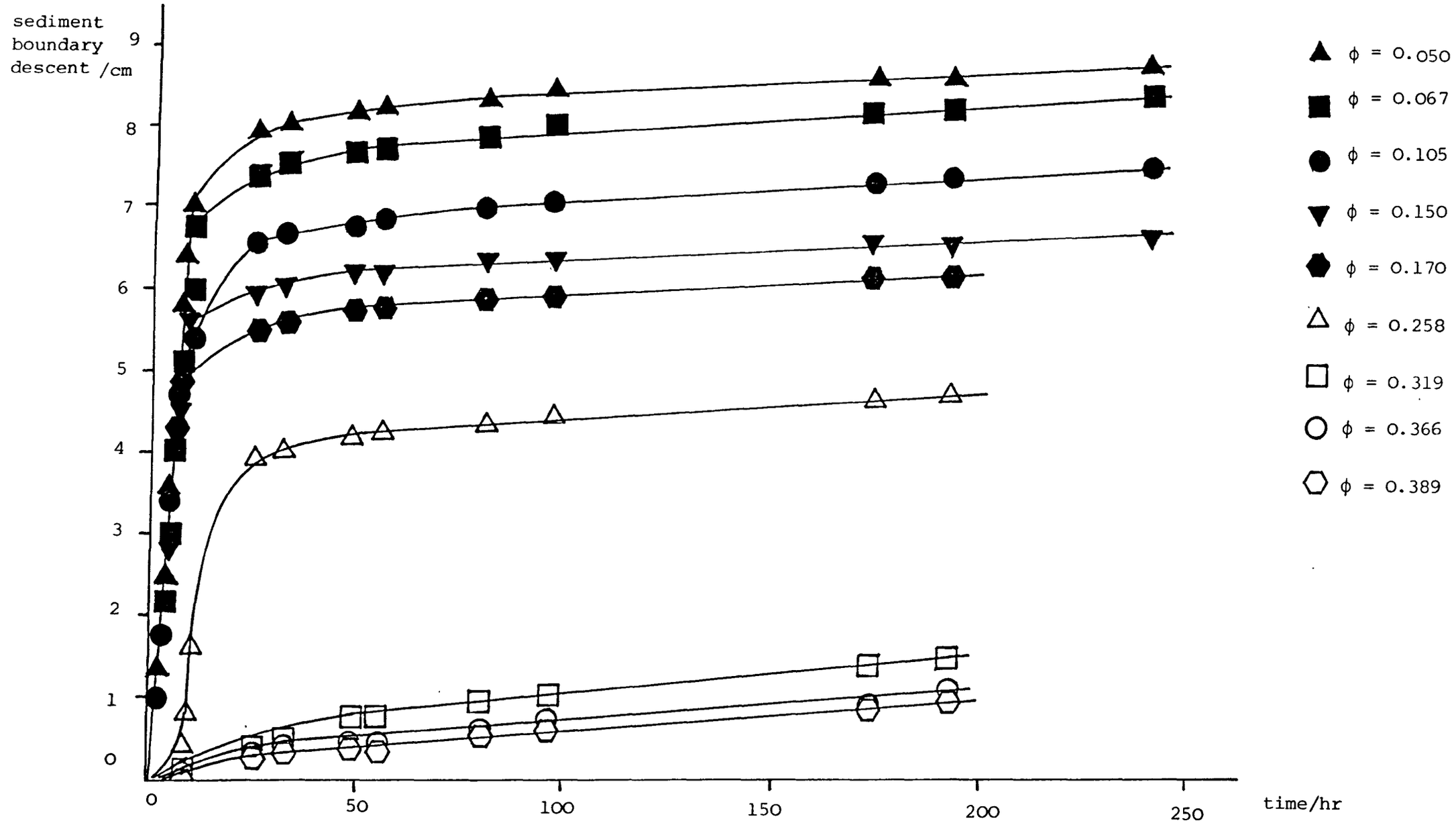

Figure 9.7.

Sediment boundary descent versus time for SJP10/$C_{12}E_6$ in 0.5 mol dm^{-3} sodium chloride solution at various volume fractions, at 1g.

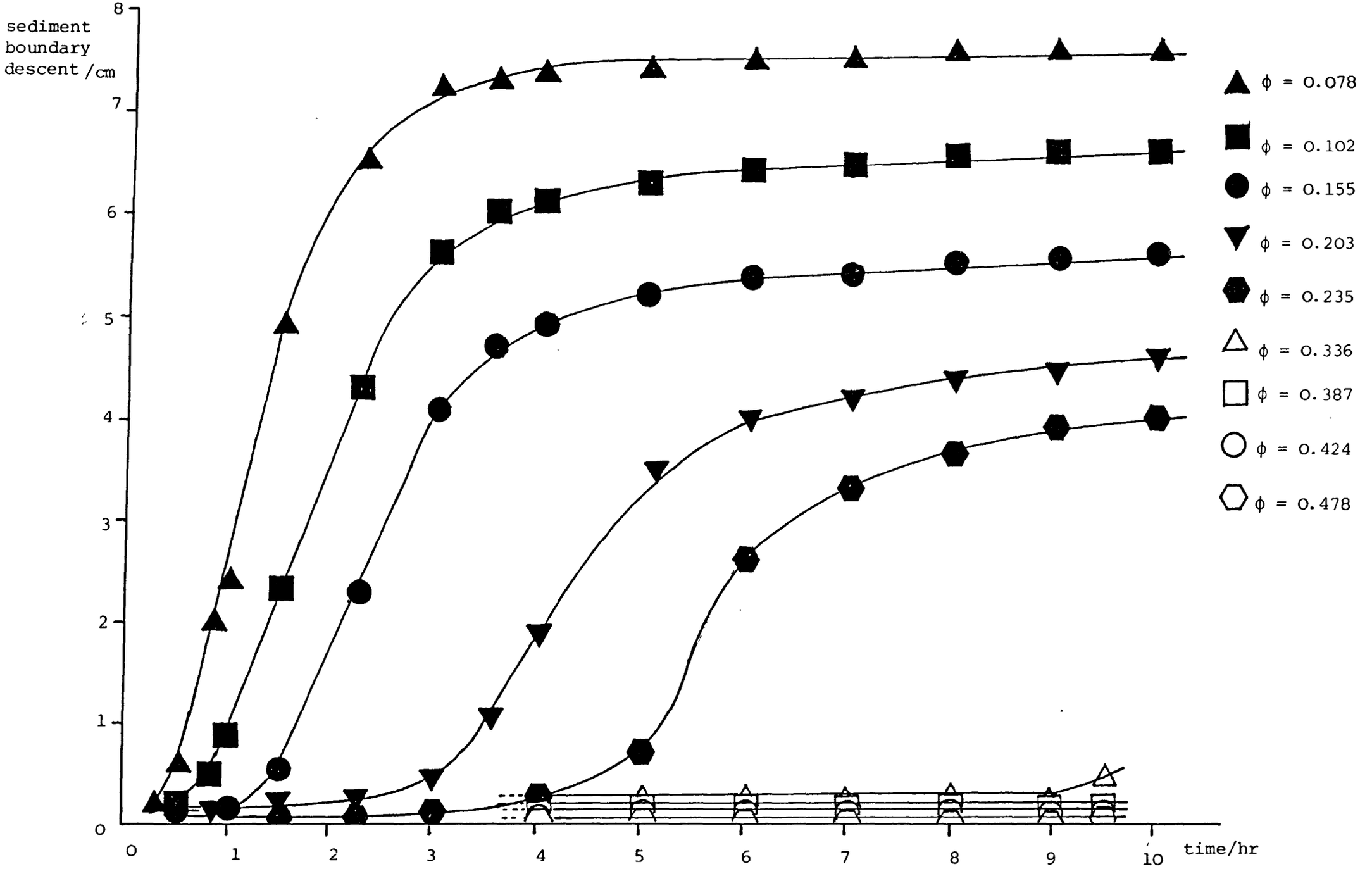

Sediment boundary descent versus time for SJP10/$C_{12}E_6$ in 0.5 mol dm^{-3} sodium chloride solution at various volume fractions at lg.

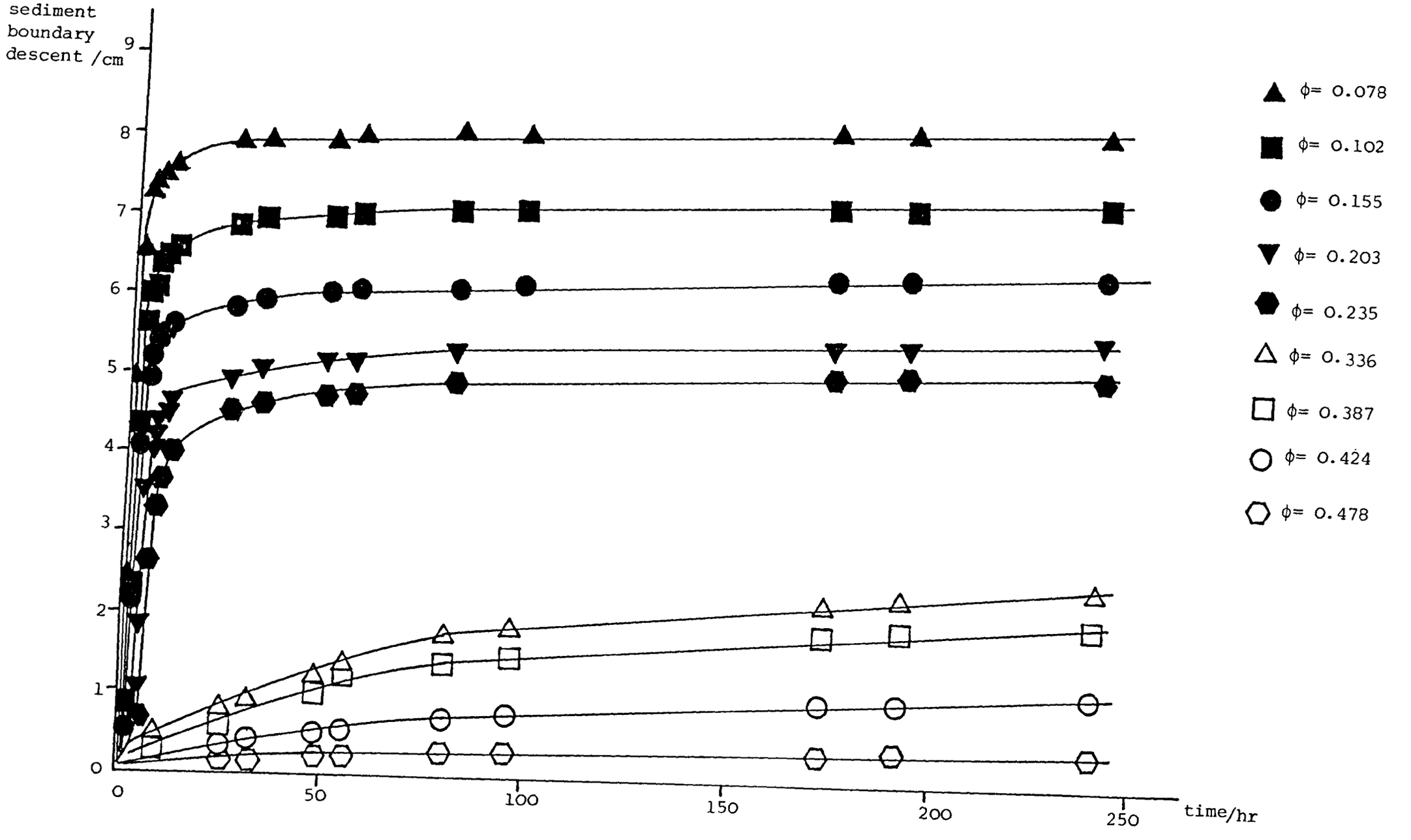

Figure 9.9.

Sediment boundary descent versus time for SJP11/$C_{12}E_6$ in 0.5 mol dm^{-3} sodium chloride solution at various volume fractions at lg.

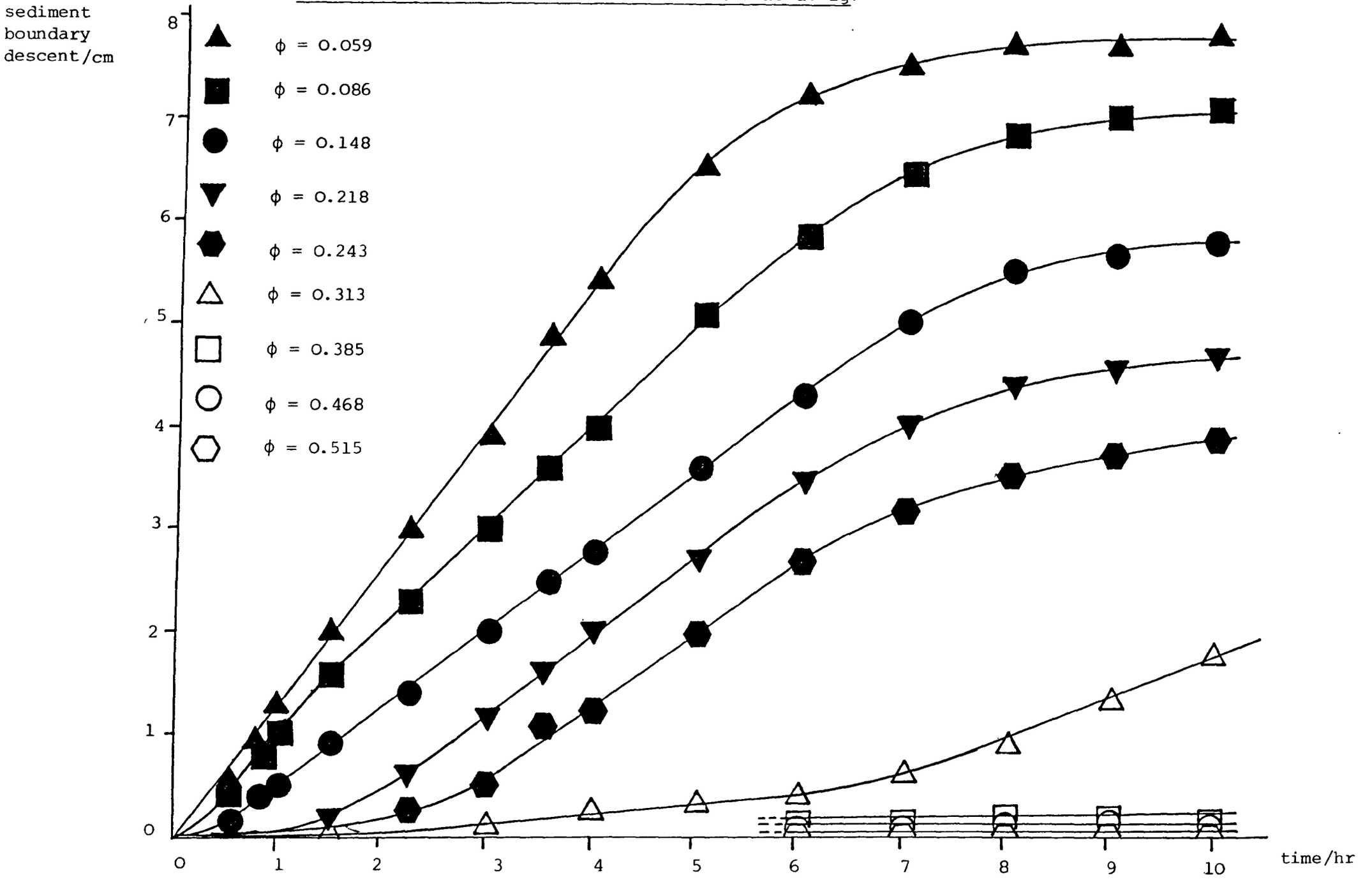

Figure 9.10.

Sediment boundary descent versus time for SJP11/$C_{12}E_6$ in 0.5 mol dm^{-3} sodium chloride solution at various volume fractions at 1g.

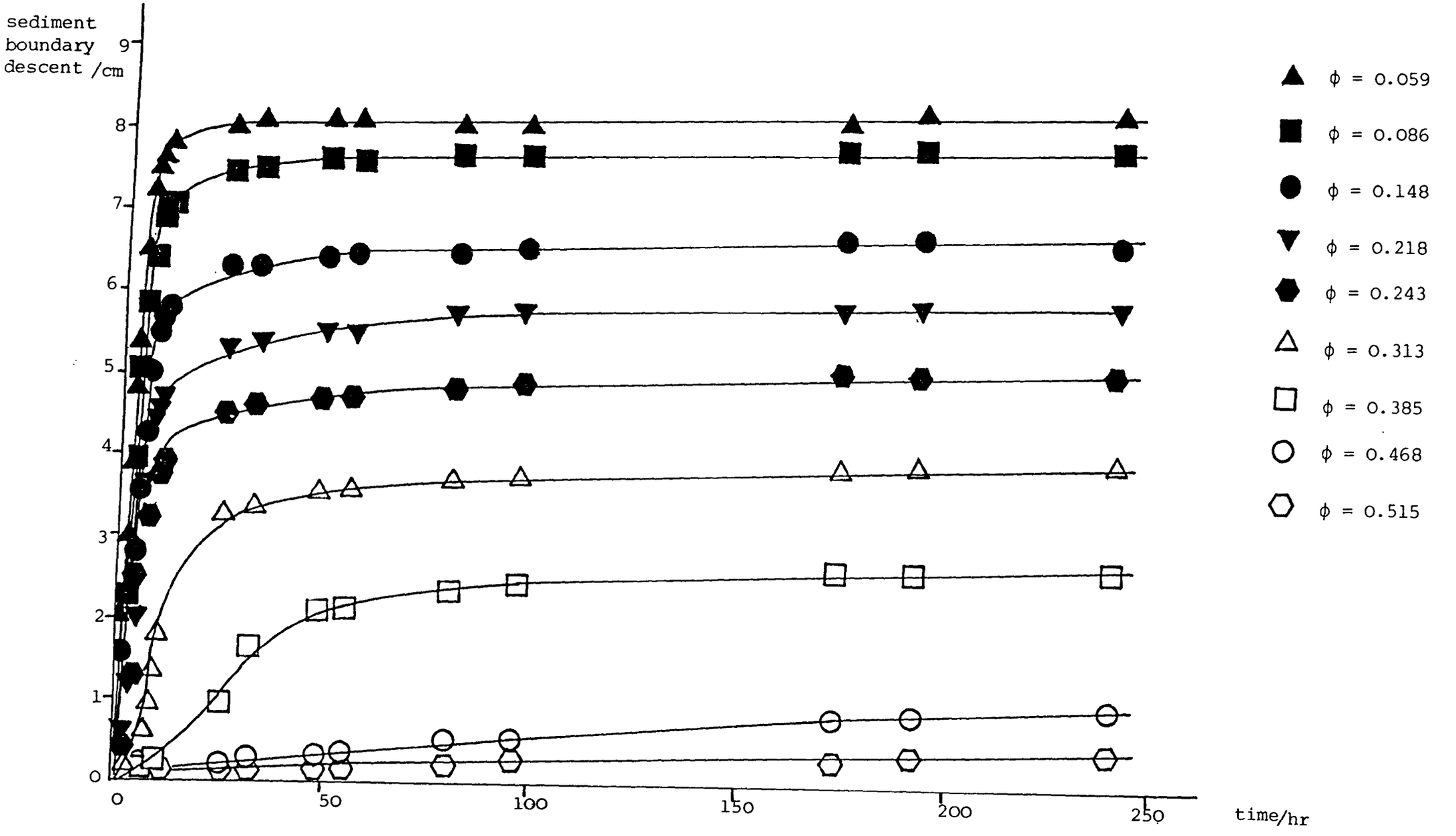

Figures 9.5, 9.7 and 9.9 show sedimentation behaviour at short settling times, of 0 - 12 hours for the three latex systems SJP8/$C_{12}E_6$, SJP10/$C_{12}E_6$ and SJP11/$C_{12}E_6$ respectively. Figures 9.6, 9.8 and 9.10 are sedimentation curves over a much longer observation time, of 0 - 240 hours.

Induction periods were observed which increased with increasing volume fraction. The induction times obtained for the three latex systems at the various volume fractions are tabulated in Table 9.2. Table 9.3. presents values for the sedimentation rates of the systems after the initial induction period.

The flocculated systems were found to sediment rapidly to a particle volume fraction of approximately 0.4 - 0.45 after which only very slow consolidation of the sedimented bed occurred.

Latices SJP8, SJP10 and SJP11 coated with $C_{12}E_6$ in 0.5 mol dm^{-3} sodium chloride solution at various volume fractions were also studied at enhanced acceleration by means of slow speed centrifugation. The sedimentation behaviour of the systems was investigated at a variety of accelerations and the results at 1.5g and 7g compared with behaviour at 1g.

The results obtained at 1.5g and 7g for the three latex systems at various volume fraction are presented in Figures 9.11 - 9.16 as plots of sediment boundary versus sedimentation time for the various systems. The sedimentation rates obtained are presented in Tables 9.4 - 9.6.

As with sedimentation at 1g, induction periods were observed, increasing in magnitude with increasing volume fraction; the induction periods obtained are listed in Tables 9.7 - 9.9.

Table 9.2.

Induction Periods, t_I/s, for the sedimentation of SJP8/$C_{12}E_6$, SJP10/$C_{12}E_6$ and SJP11/$C_{12}E_6$ in 0.5 mol dm^{-3} sodium chloride solution at various volume fractions at 1g.

SJP8/$C_{12}E_6$		SJP10/$C_{12}E_6$		SJP11/$C_{12}E_6$	
ϕ	t_I/s	ϕ	t_I/s	ϕ	t_I/s
0.10	1.8×10^3	0.08	9×10^2	0.09	1.08×10^3
0.15	4.5×10^3	0.10	2.7×10^3	0.15	1.8×10^3
0.17	7.2×10^3	0.155	4.9×10^3	0.22	7.2×10^3
0.26	2.7×10^4	0.20	1.04×10^4	0.24	9.9×10^3
		0.235	1.71×10^4	0.31	2.43×10^4

Table 9.3.

Sedimentation Rates S/ms^{-1}, for the sedimentation of SJP8/$C_{12}E_6$, SJP10/$C_{12}E_6$ and SJP11/$C_{12}E_6$ in 0.5 mol dm^{-3} sodium chloride solution at various volume fractions at 1g.

SJP8/$C_{12}E_6$		SJP10/$C_{12}E_6$		SJP11/$C_{12}E_6$	
ϕ	S/ms^{-1}	ϕ	S/ms^{-1}	ϕ	S/ms^{-1}
0.01	4.86×10^{-6}	0.078	1.23×10^{-5}	0.059	3.8×10^{-6}
0.02	4.12×10^{-6}	0.102	7.48×10^{-6}	0.086	2.69×10^{-6}
0.05	2.55×10^{-6}	0.155	6.41×10^{-6}	0.148	2.16×10^{-6}
0.51	2.44×10^{-6}	0.203	4.63×10^{-6}	0.218	2.18×10^{-6}
0.067	1.91×10^{-6}	0.235	5.4×10^{-6}	0.243	1.10×10^{-6}
0.07	1.94×10^{-6}				
0.01	1.67×10^{-6}				
0.105	1.79×10^{-6}				
0.150	2.63×10^{-6}				
0.170	1.71×10^{-6}				

Figure 9.11.

Sediment boundary descent versus time for SJP8/$C_{12}E_6$ in 0.5 mol dm^{-3} sodium chloride solution at various volume fractions at 1.5g.

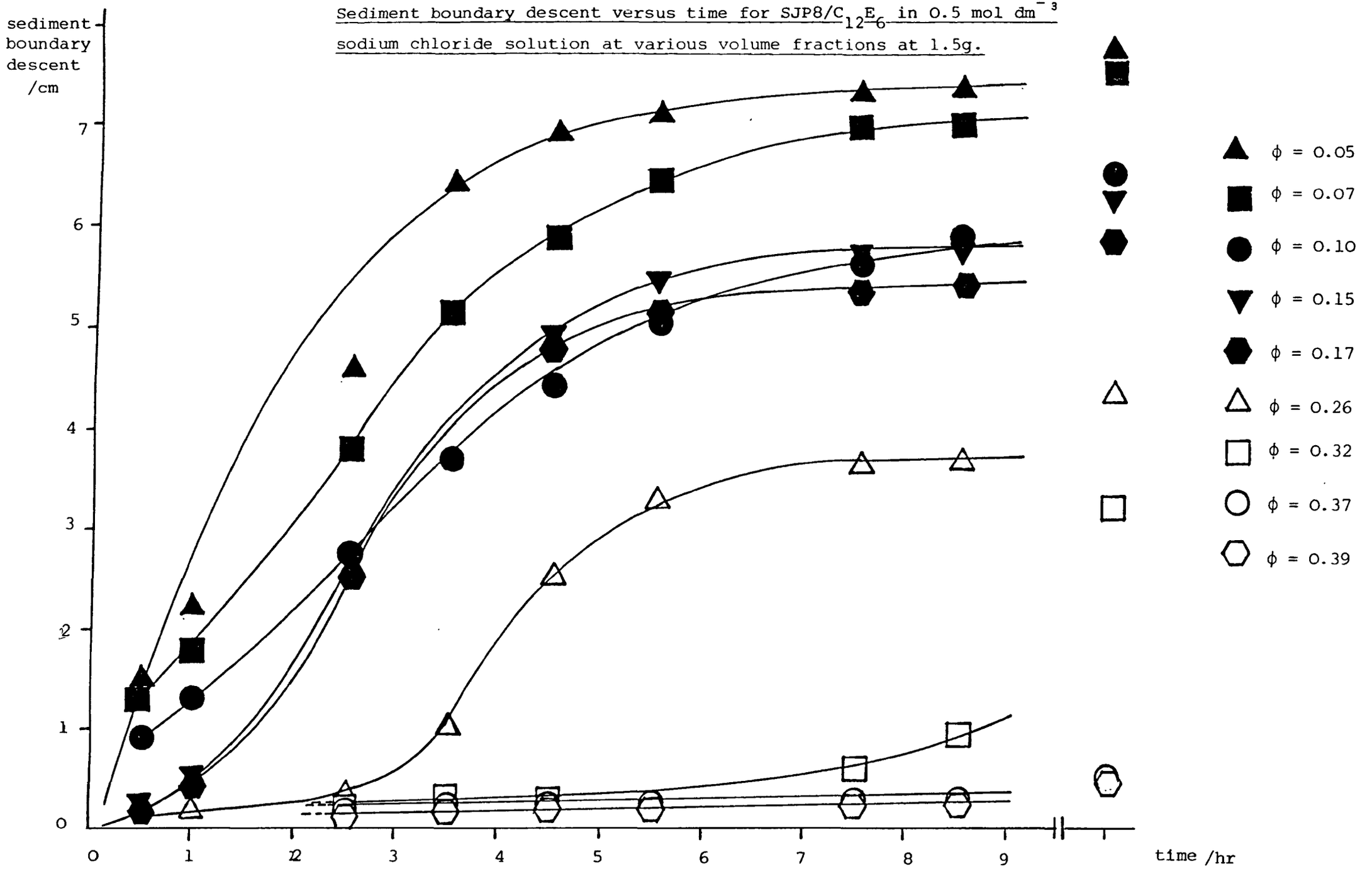

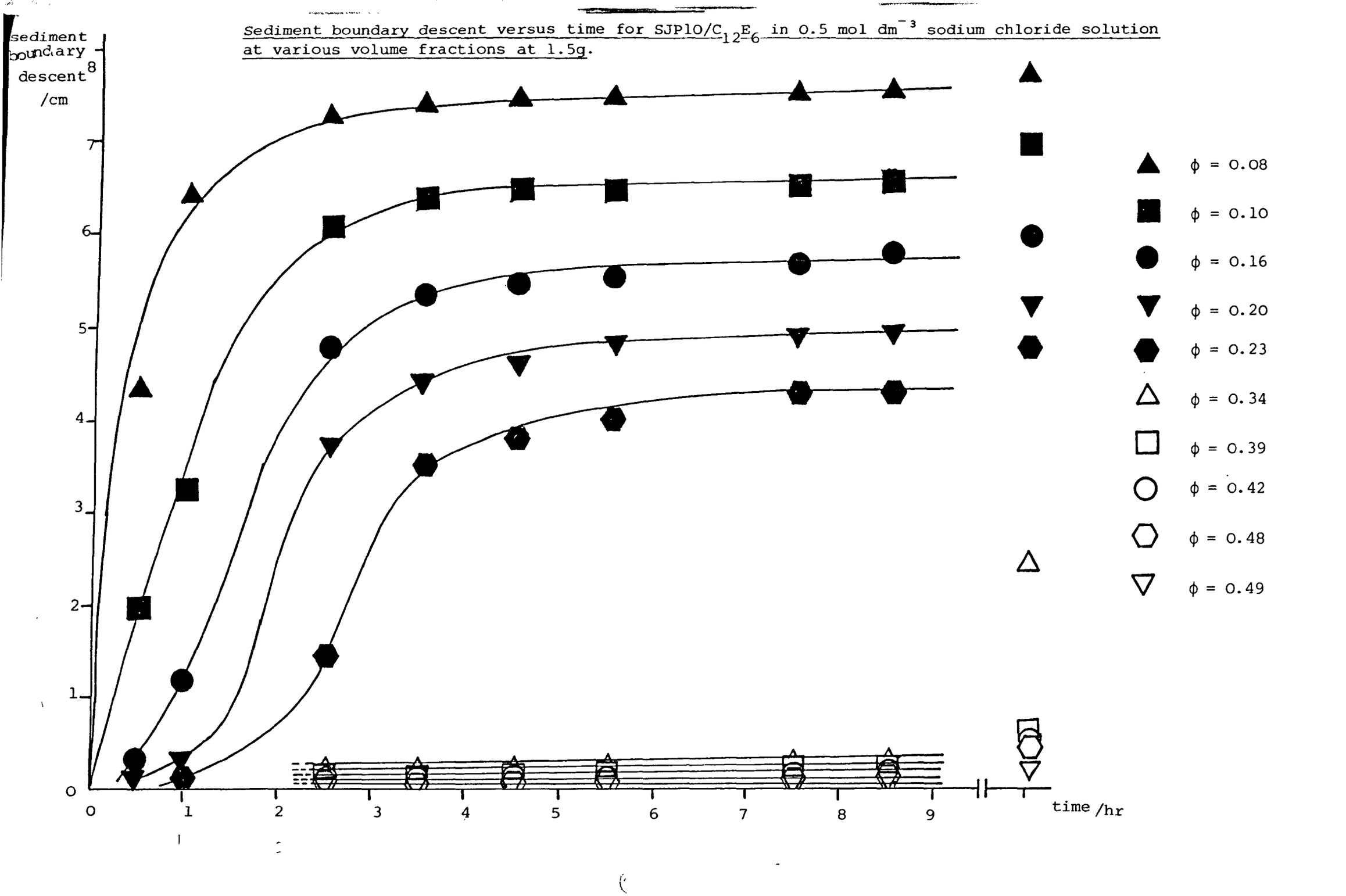
Sediment boundary descent versus time for SJP10/$C_{12}E_6$ in 0.5 mol dm^{-3} sodium chloride solution at various volume fractions at 1.5g.
sediment boundary descent /cm
time /hr
0
1
2
3
4
5
6
7
8
9
ϕ = 0.08
ϕ = 0.10
ϕ = 0.16
ϕ = 0.20
ϕ = 0.23
ϕ = 0.34
ϕ = 0.39
ϕ = 0.42
ϕ = 0.48
ϕ = 0.49

Sediment boundary descent versus time for SJP11/$C_{12}E_6$ in 0.5 mol dm^{-3} sodium chloride solution at various volume fractions at 1.5g.

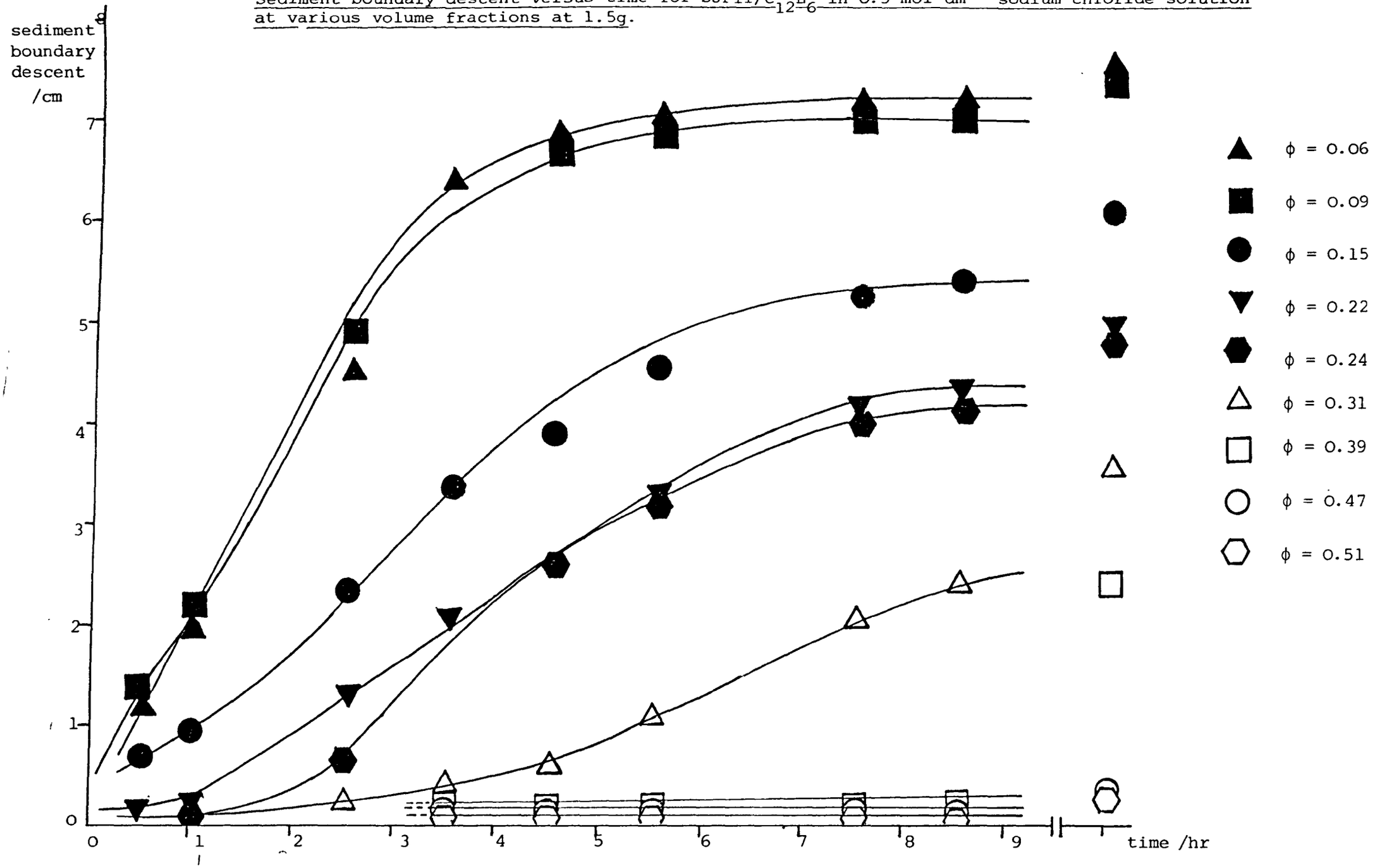

Sediment boundary descent versus time for SJP8/$C_{12}E_6$ in 0.5 mol dm^{-3} sodium chloride solution at various volume fractions at 7g.

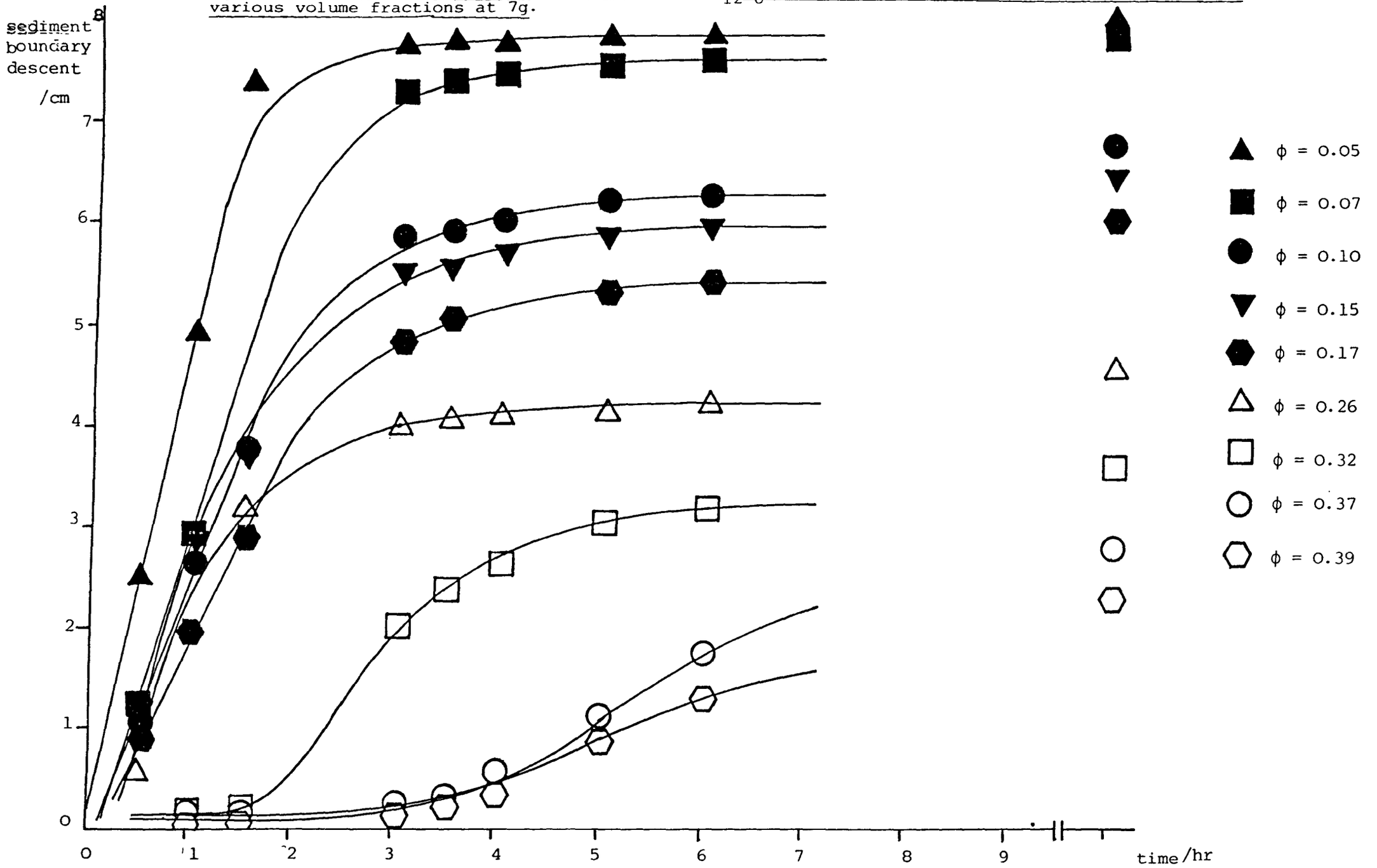

Sediment boundary descent versus time for SJP10/$C_{12}E_6$ in 0.5 mol dm^{-3} sodium chloride solution at various volume fractions at 7g.

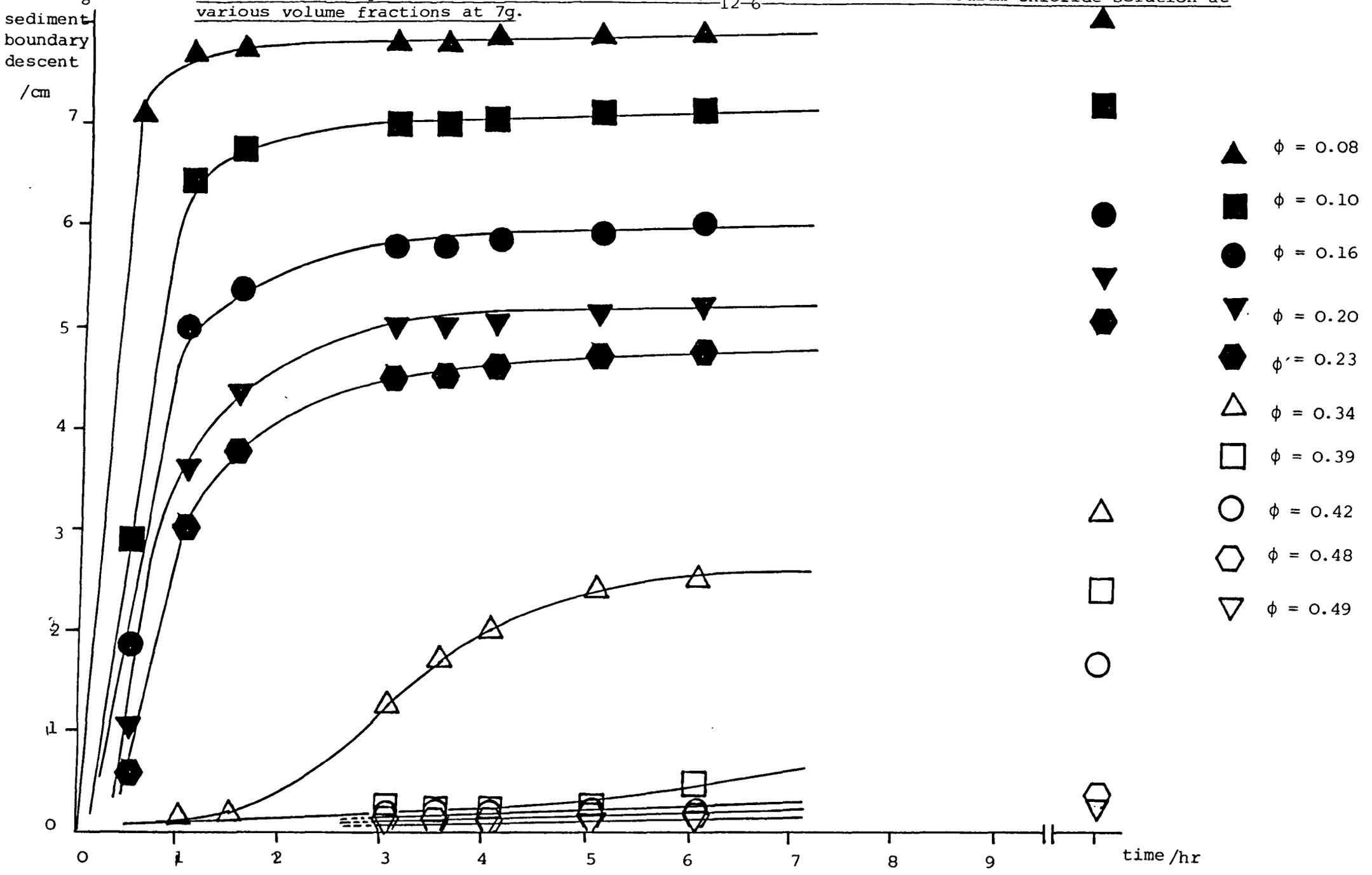

Figure 9.16.

Sediment boundary descent versus time for SJP11/$C_{12}E_6$ in 0.5 mol dm^{-3} sodium chloride solution at various volume fractions at 7g.

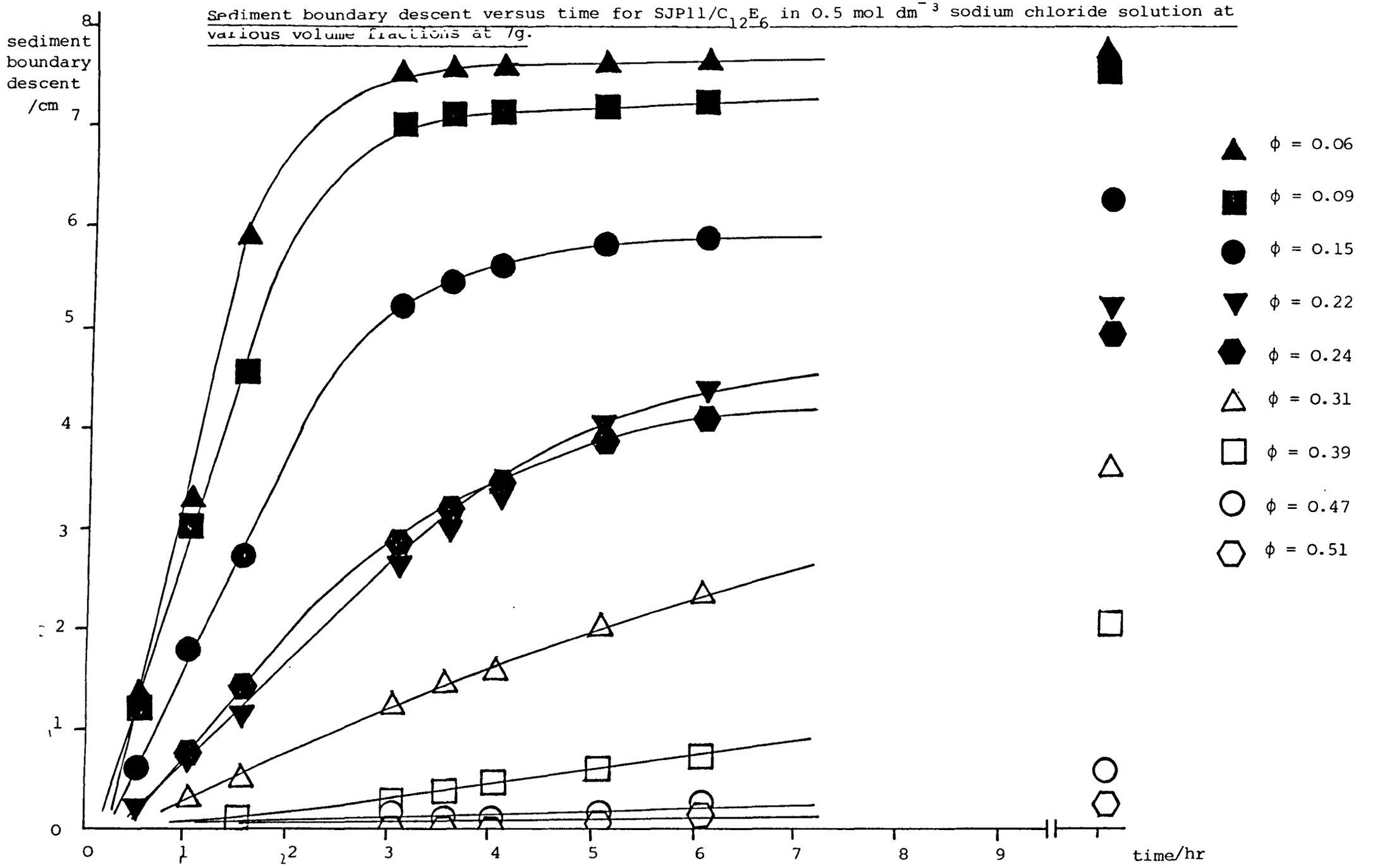

Table 9.4.

Sedimentation rates, S/ms^{-1}, for the sedimentation of SJP8/$C_{12}E_6$ in 0.5 mol dm^{-3} sodium chloride solution at various volume fractions and accelerations.

1g		1.5g		7g	
ϕ	S/ms^{-1}	ϕ	S/ms^{-1}	ϕ	S/ms^{-1}
0.01	4.86×10^{-6}	0.051	6.15×10^{-6}	0.051	1.39×10^{-5}
0.02	4.12×10^{-6}	0.067	3.97×10^{-6}	0.067	9.26×10^{-6}
0.05	2.55×10^{-6}	0.105	2.47×10^{-6}	0.105	7.47×10^{-6}
0.05	2.44×10^{-6}	0.170	5.02×10^{-6}	0.170	8.47×10^{-6}
0.07	1.91×10^{-6}	0.258	5.56×10^{-6}	0.258	6.17×10^{-6}
0.07	1.94×10^{-6}	0.319	4.17×10^{-6}	0.319	6.54×10^{-6}
0.1	1.67×10^{-6}	0.366	1.04×10^{-6}	0.366	4.08×10^{-6}
0.1	1.79×10^{-6}			0.389	1.74×10^{-6}
0.17	2.63×10^{-6}				
0.26	1.71×10^{-6}				

Table 9.5.

Sedimentation rates, S/ms^{-1}, for the sedimentation of SJP10/$C_{12}E_6$ in 0.5 mol dm^{-3} sodium chloride solution at various volume fractions and accelerations.

1g		1.5g		7g	
ϕ	S/ms^{-1}	ϕ	S/ms^{-1}	ϕ	S/ms^{-1}
0.08	1.23×10^{-5}	0.08	2.77×10^{-5}	0.08	4.16×10^{-5}
0.10	7.48×10^{-6}	0.10	9.26×10^{-6}	0.10	2.31×10^{-5}
0.16	6.41×10^{-6}	0.16	7.72×10^{-6}	0.16	1.63×10^{-5}
0.20	4.63×10^{-6}	0.20	7.25×10^{-6}	0.20	1.45×10^{-5}
0.24	5.4×10^{-6}	0.24	5.55×10^{-6}	0.24	9.92×10^{-6}
				0.34	2.37×10^{-6}

Table 9.6.

Sedimentation rates, S/ms^{-1}, for the sedimentation of SJP11/$C_{12}E_6$ in mol dm^{-3} sodium chloride solution at various volume fractions and accelerations.

1g		1.5g		7g	
ϕ	S/ms^{-1}	ϕ	S/ms^{-1}	ϕ	s/ms^{-1}
0.06	3.8×10^{-6}	0.06	5.75×10^{-6}	0.06	1.31×10^{-5}
0.09	2.69×10^{-6}	0.09	5.11×10^{-6}	0.09	9.44×10^{-6}
0.15	2.16×10^{-6}	0.15	2.98×10^{-6}	0.15	6.08×10^{-6}
0.22	2.18×10^{-6}	0.22	1.98×10^{-6}	0.22	2.78×10^{-6}
0.24	1.10×10^{-6}	0.24	2.87×10^{-6}	0.24	3.47×10^{-6}
		0.31	1.29×10^{-6}	0.31	1.17×10^{-6}
				0.39	3.96×10^{-7}

Table 9.7.

Induction periods, t_I/s, for the sedimentation of SJP8/$C_{12}E_6$ in 0.5 mol dm^{-3} sodium chloride solution at various volume fractions and accelerations.

1g		1.5g		7g	
ϕ	t_I/s	ϕ	t_I/s	ϕ	t_I/s
0.10	1.8×10^3	0.15	2.7×10^3	0.26	9×10^2
0.15	4.5×10^3	0.17	2.9×10^3	0.32	5.4×10^3
0.17	7.2×10^3	0.26	1.15×10^4	0.37	1.08×10^4
0.26	2.7×10^4	0.32	2.52×10^4	0.39	1.08×10^4

Table 9.8.

Induction periods, t_I/s, for the sedimentation of SJP10/$C_{12}E_6$ in 0.5 mol dm^{-3} sodium chloride solution at various volume fractions and accelerations.

1g		1.5g		7g	
ϕ	t_I/s	ϕ	t_I/s	ϕ	t_I/s
0.08	9×10^2	0.155	9×10^2	0.20	1.08×10^3
0.10	2.7×10^3	0.20	2.7×10^3	0.235	1.44×10^3
0.155	4.9×10^3	0.235	7.2×10^3	0.34	7.2×10^3
0.20	1.04×10^4			0.39	1.62×10^4
0.235	1.71×10^4				

Table 9.9.

Induction periods, t_I/s, for the sedimentation of SJP11/$C_{12}E_6$ in 0.5 mol dm^{-3} sodium chloride solution at various volume fractions and accelerations.

1g		1.5 g		7g	
ϕ	t_I/s	ϕ	t_I/s	ϕ	t_I/s
0.09	1.08×10^3	0.22	3.6×10^3	0.22	1.8×10^3
0.15	1.8×10^3	0.24	6.3×10^3	0.24	1.8×10^3
0.22	7.2×10^3	0.31	1.44×10^4	0.31	2.7×10^3
0.24	9.9×10^3			0.39	9×10^3
0.31	2.43×10^4				

9.4. Discussion.

The sedimentation behaviour of a particulate system is often considered in terms of the sedimentation rate relative to the sedimentation rate of an isolated particle, S/S_o. The sedimentation rate at infinite dilution may be determined by extrapolation to zero volume fraction of sedimentation rate versus volume fraction plots and from Stokes' Law, equation (6. 5):

$$S_o = \frac{2a^2 (\rho_p^* - \rho_o^*) g}{9 \eta_o}$$

The S_o values were calculated from the above equation to be 3.24×10^{-8} ms^{-1} for SJP8, 3.25×10^{-8} ms^{-1} for SJP9, 6.77×10^{-8} ms^{-1} for SJP10 and 1.25×10^{-7} ms^{-1} for SJP11.

The sedimentation behaviour of polystyrene latex SJP9 coated with $C_{12}E_6$ in 0.5 mol dm^{-3} sodium chloride solution was initially determined at low volume fractions. Linear plots of sedimentation distance versus time were obtained which passed through the origin as illustrated in Figure 9.2.

A plot of the sedimentation rate versus volume fraction was constructed, presented in 9.17, which was linear at low volume fractions with an intercept on the y-axis of 5.38×10^{-6} ms^{-1}, corresponding to S_o. This was markedly faster than the Stokes' law value of 3.24×10^{-8} ms^{-1}. The sedimentation rates were a hundredfold greater for these flocculated systems than for the unflocculated systems at lower electrolyte concentrations as shown in (7. 6). This suggested that the flocculation process dominated the sedimentation of the systems at all concentrations and that flocs of particles rather than individual particles were the settling units. The values obtained from Stokes' law were of the same magnitude as the experimentally obtained values for the unflocculated system, presented in (7. 6).

Figure 9.17.

Sedimentation rate/ms^{-1} versus volume fraction for polystyrene latex SJP9/$C_{12}E_6$ in 0.5 mol dm^{-3} sodium chloride solution.

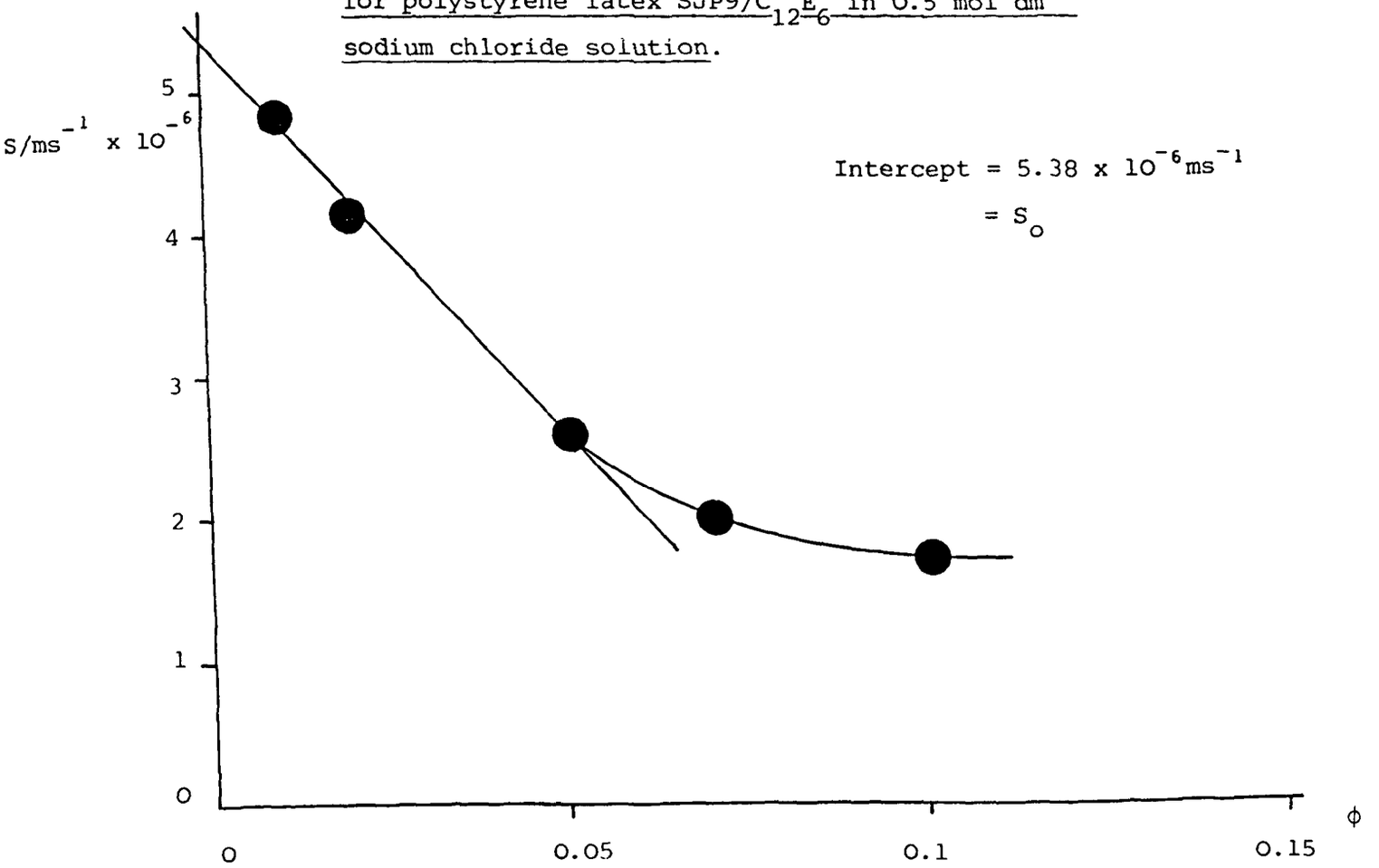

Figure 9.18.

Relative sedimentation rate versus volume fraction for polystyrene latex SJP9/$C_{12}E_6$ in 0.5 mol dm^{-3} sodium chloride solution — — calculated from Batchelor's equation with $k_s = -6.55$

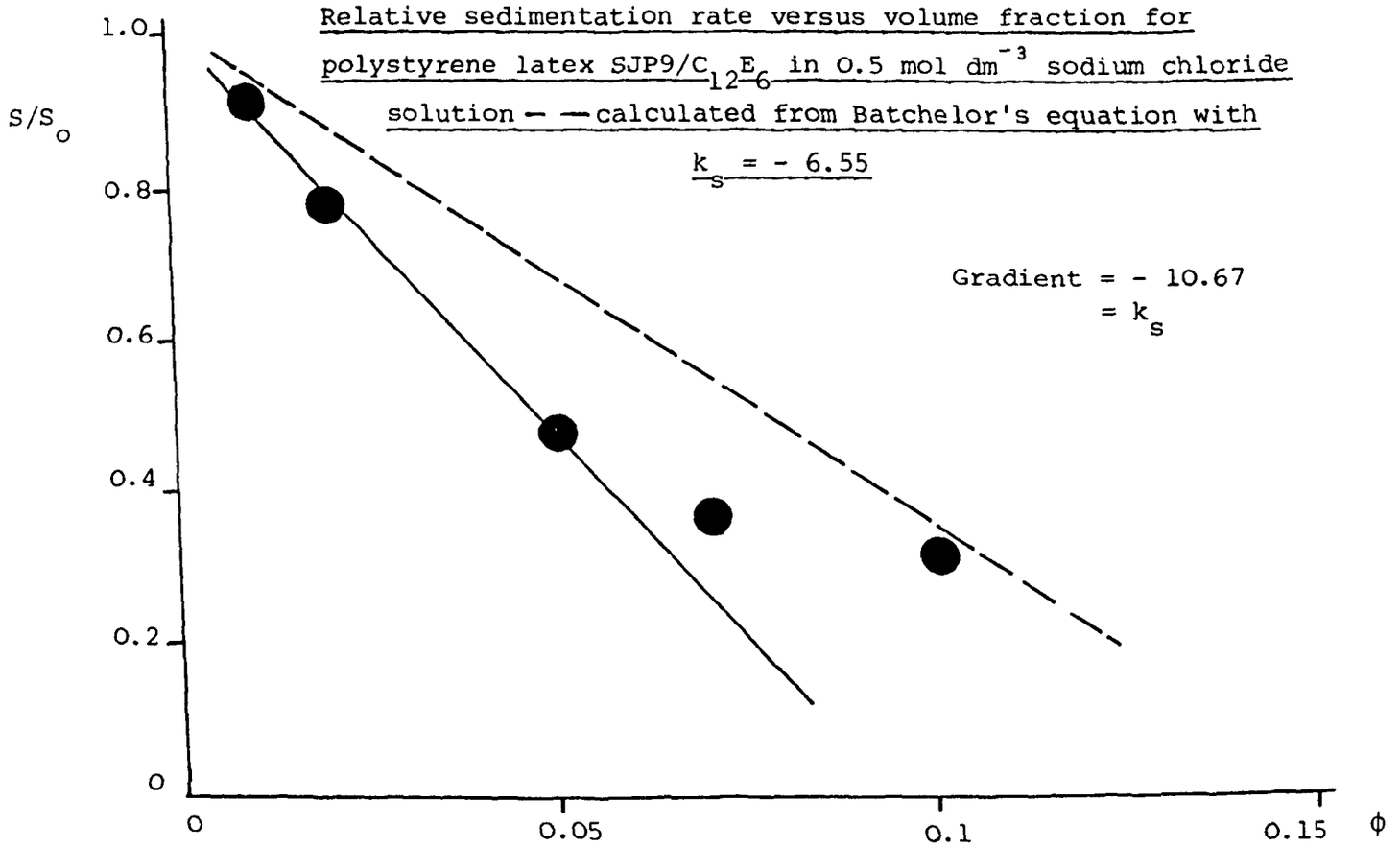

The low volume fraction sedimentation data was plotted as the relative sedimentation rate versus volume fraction, taking the extrapolated S_o value, as shown in Figure 9.18 and the gradient, corresponding to the sedimentation coefficient was found to be - 10.67. The value calculated from a rigorous hydrodynamic analysis by Batchelor[117] is - 6.55. A theoretical plot is also presented in Figure 9.18, calculated from Batchelor's equation, equation (6.10):

$$\frac{S}{S_o} = 1 - 6.55\,\phi$$

and agreement with experiment seen to be poor. This may be explained in the same way as the poor correlation between calculated and extrapolated S_o values and attributed to the aggregation of the particles. The volume fraction under consideration was not the volume fraction of the individual particles, as in the Batchelor analysis, but an effective volume fraction, taking account of the occluded liquid within the flocs. The effective volume fraction of the particles within the flocs was then determined as the ratio of the Batchelorsedimentation coefficient to the sedimentation coefficient experimentally obtained. A value of 0.63 was obtained. This corresponded to the maximum packing fraction value that could be experimentally obtained, when concentrating the systems under pressure, of 0.63. The flocs themselves, in the absence of excess pressure, were considered to settle to a random packed state, corresponding to a volume fraction of 0.62. Hence the total packing fraction of the sedimented bed was calculated to be 0.63 x 0.62 which equals 0.39, very close to the value experimentally obtained for spontaneous sedimentation of 0.4. These values suggested that a packing fraction within the flocs of 0.63 was sensible. From this the floc size was determined from Stokes' equation rearranged:

$$a = \left(\frac{S_o . 9 . \eta_o}{2(\rho_p^* - \rho_o^*)g} \right)^{\frac{1}{2}}$$

$$= \left(\frac{5.38 \times 10^{-6} . 9 . 8.904 \times 10^{-4}}{2 \quad (1035 - 1000) \quad 9.8} \right)^{\frac{1}{2}}$$

$$= 7.93 \times 10^{-6} \text{ m}$$

Hence the floc radius was calculated to be 7.93×10^{-6} m for the SJP9/$C_{12}E_6$ system, corresponding to a floc volume of 2.09×10^{-15} m^3. One particle occupies 4.96×10^{-19} m^3 and therefore, at a packing fraction of 0.63, the number of particles per floc was determined to be 2,655.

As the volume fraction was increased beyond the dilute limit deviations from simple linear sedimentation behaviour were observed. Plots of the height sedimented versus the time show that an induction period passed in every case, apart from the very dilute cases, before sedimentation of the systems occurred. This is particularly well shown in Figure 9.7 with the SJP10/$C_{12}E_6$ system. At enhanced acceleration this effect was also observed, though to a lesser extent with increased acceleration. Plots have been constructed of the induction periods at different g-values as functions of particle volume fraction. These are presented in Figures 9.19 - 9.21 for gravitational acceleration values of 1g, 1.5g and 7g respectively. The induction periods are compared at the different accelerations for the three systems in Figures 9.22 - 9.24.

It was seen that as the volume fraction increased the induction period increased. This was in contradiction of the initial reaction to expect the reverse situation; an increase in volume fraction indicates an increase in particle proximity and therefore an increase in the rate of floc formation and in the sedimentation velocity. The situation that actually occurred may be attributed to the phenomenon of channelling whereby channels of liquid form through a solid network enabling the suspension medium to rise to the network surface as it is displaced by the settling particles. As the solids content of the network increases the network

Figure 9.19.

Induction period/s versus volume fraction for sedimentation at 1g for SJP8/$C_{12}E_6$, SJP10/$C_{12}E_6$ and SJP11/$C_{12}E_6$, all in 0.5 mol dm^{-3} sodium chloride solution.

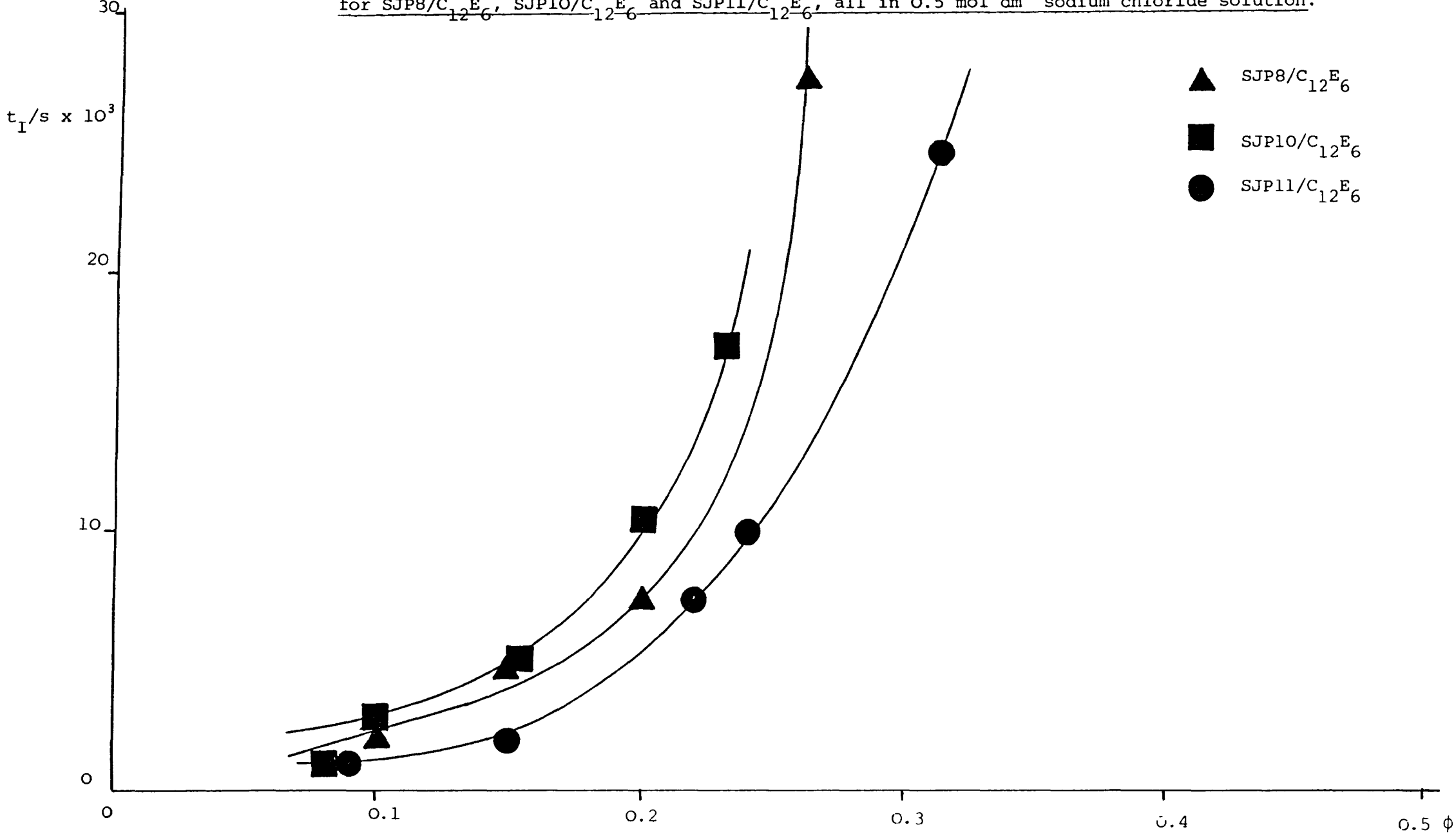

Figure 9.20.

Induction period/s versus volume fraction for sedimentation at 1.5g for SJP8/$C_{12}E_6$, SJP10/$C_{12}E_6$ and SJP11/$C_{12}E_6$, all in 0.5 mol dm^{-3} sodium chloride solution.

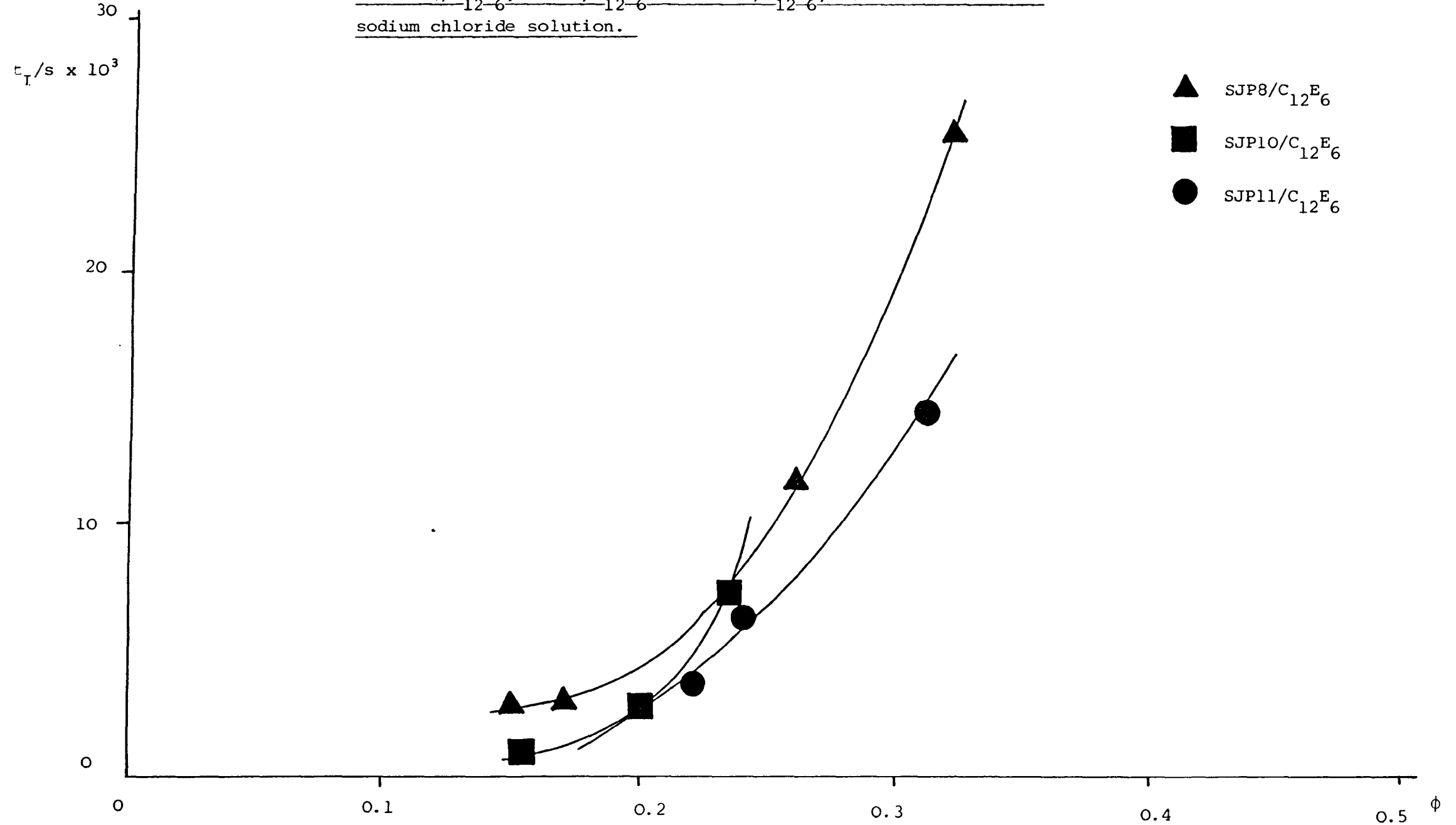

Figure 9.21

Induction period/s versus volume fraction for sedimentation at 7g for SJP8/$C_{12}E_6$, SJP10/$C_{12}E_6$ and SJP11/$C_{12}E_6$, all in 0.5 mol dm^{-3} sodium chloride solution.

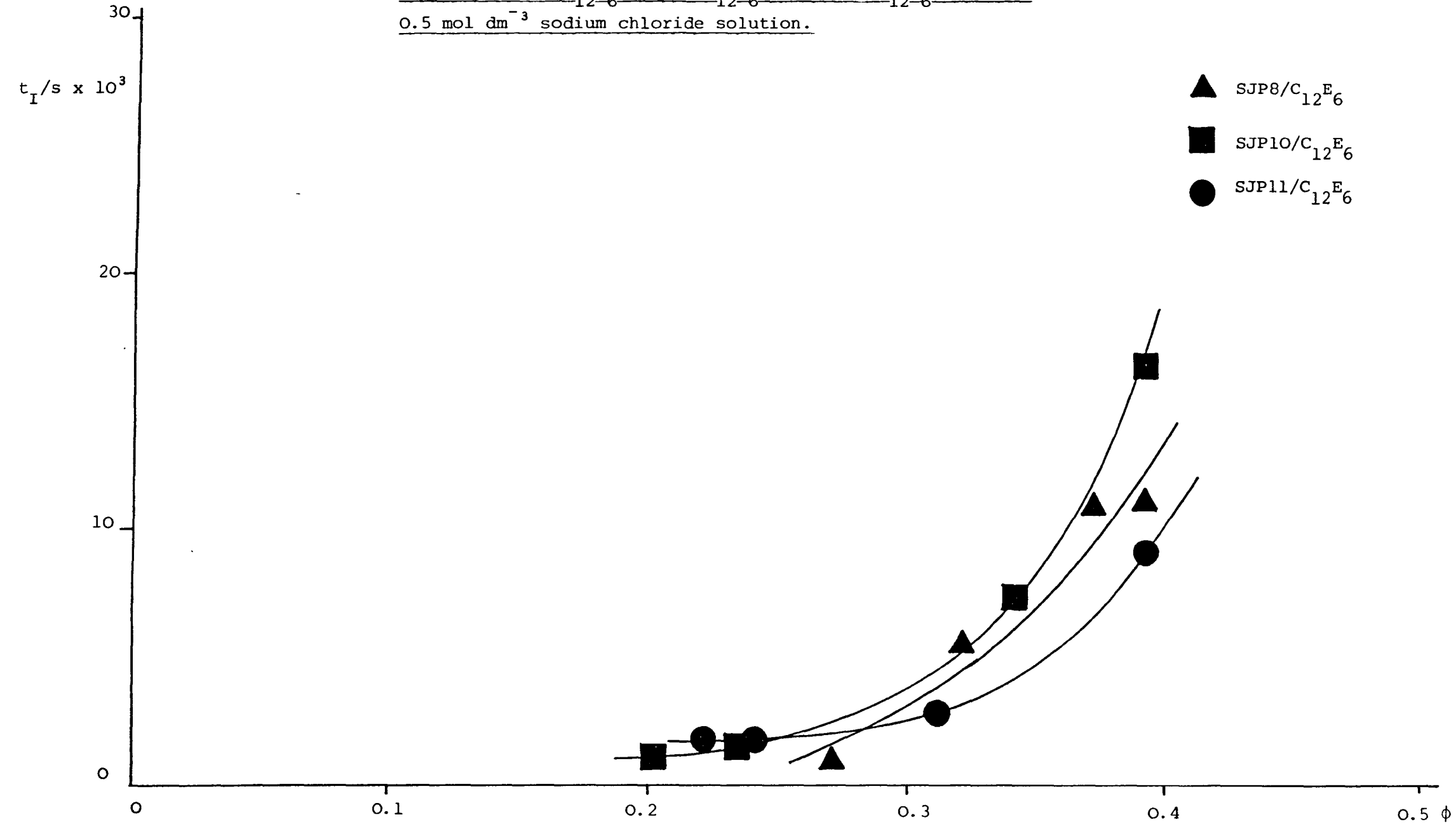

Figure 9.22.

Induction period/s versus volume fraction for the sedimentation of SJP8/$C_{12}E_6$ in 0.5 mol dm^{-3} sodium chloride solution at various gravitational accelerations.

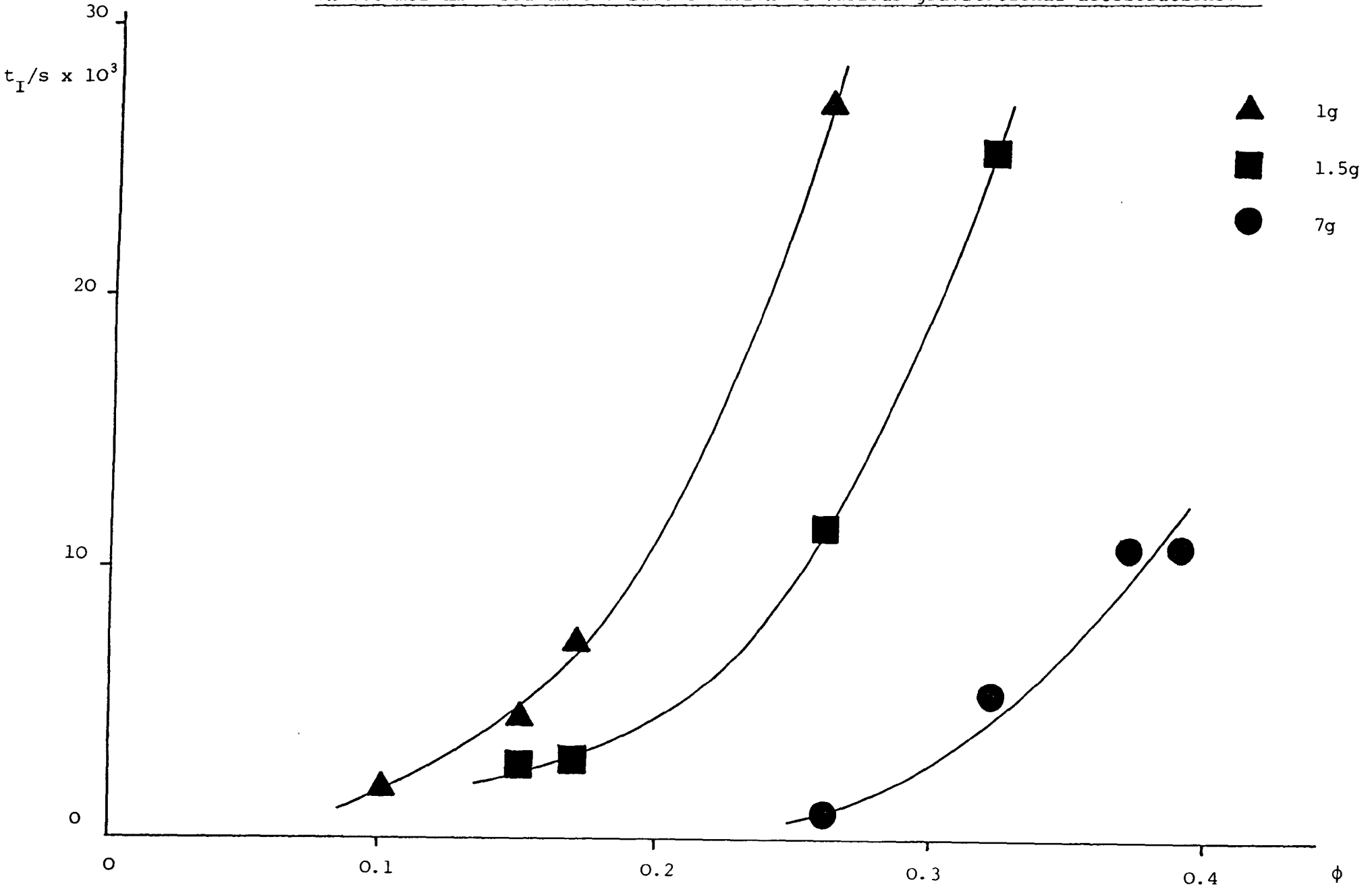

Figure 9.23.

Induction period/s versus volume fraction for the sedimentation of SJP10/$C_{12}E_6$ in 0.5 mol dm^{-3} sodium chloride solution at various gravitational accelerations.

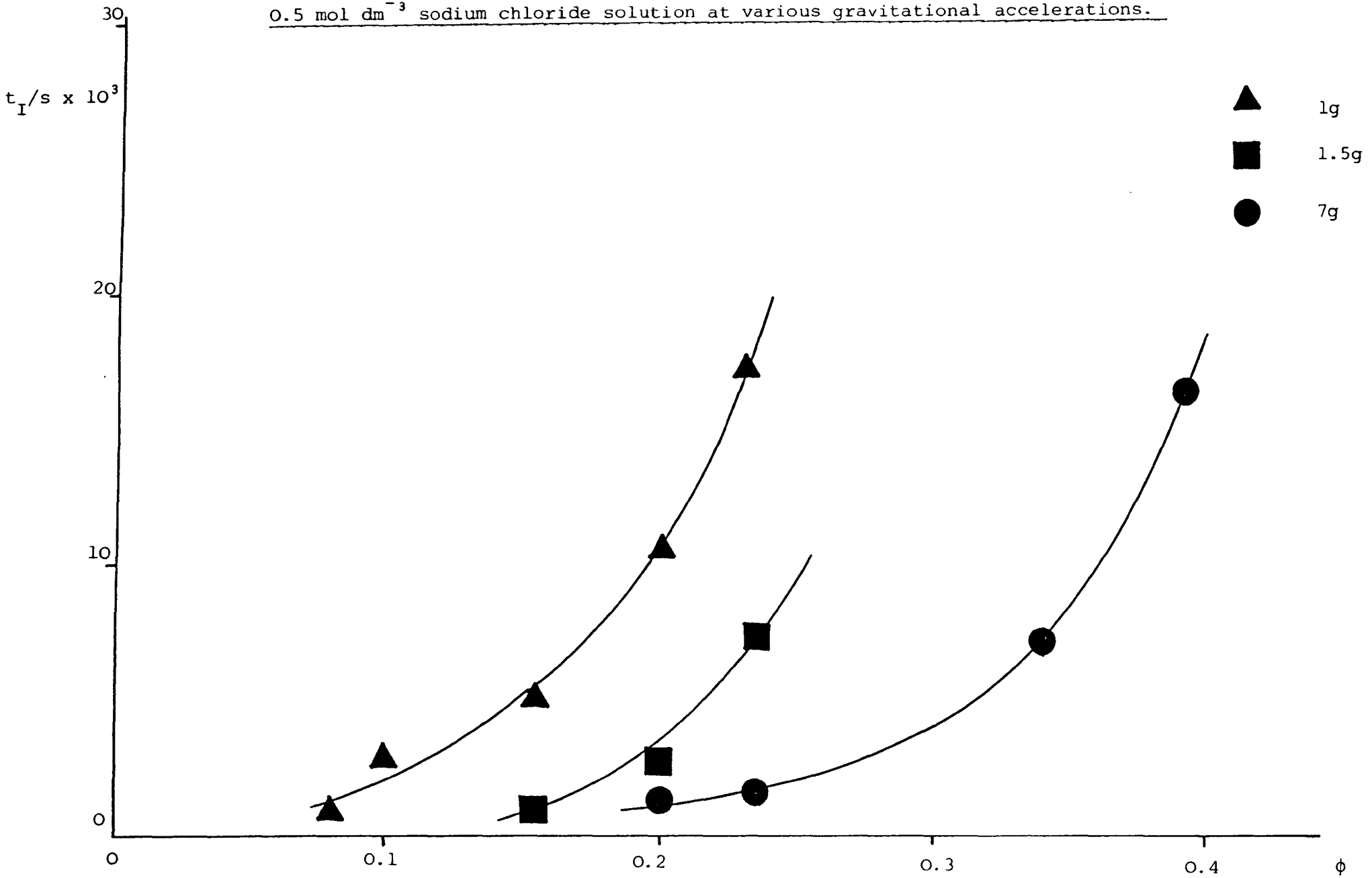

Figure 9.24.

Induction period/s versus volume fraction for the sedimentation of SJP11/$C_{12}E_6$ in 0.5 mol dm^{-3} sodium chloride solution at various gravitational accelerations.

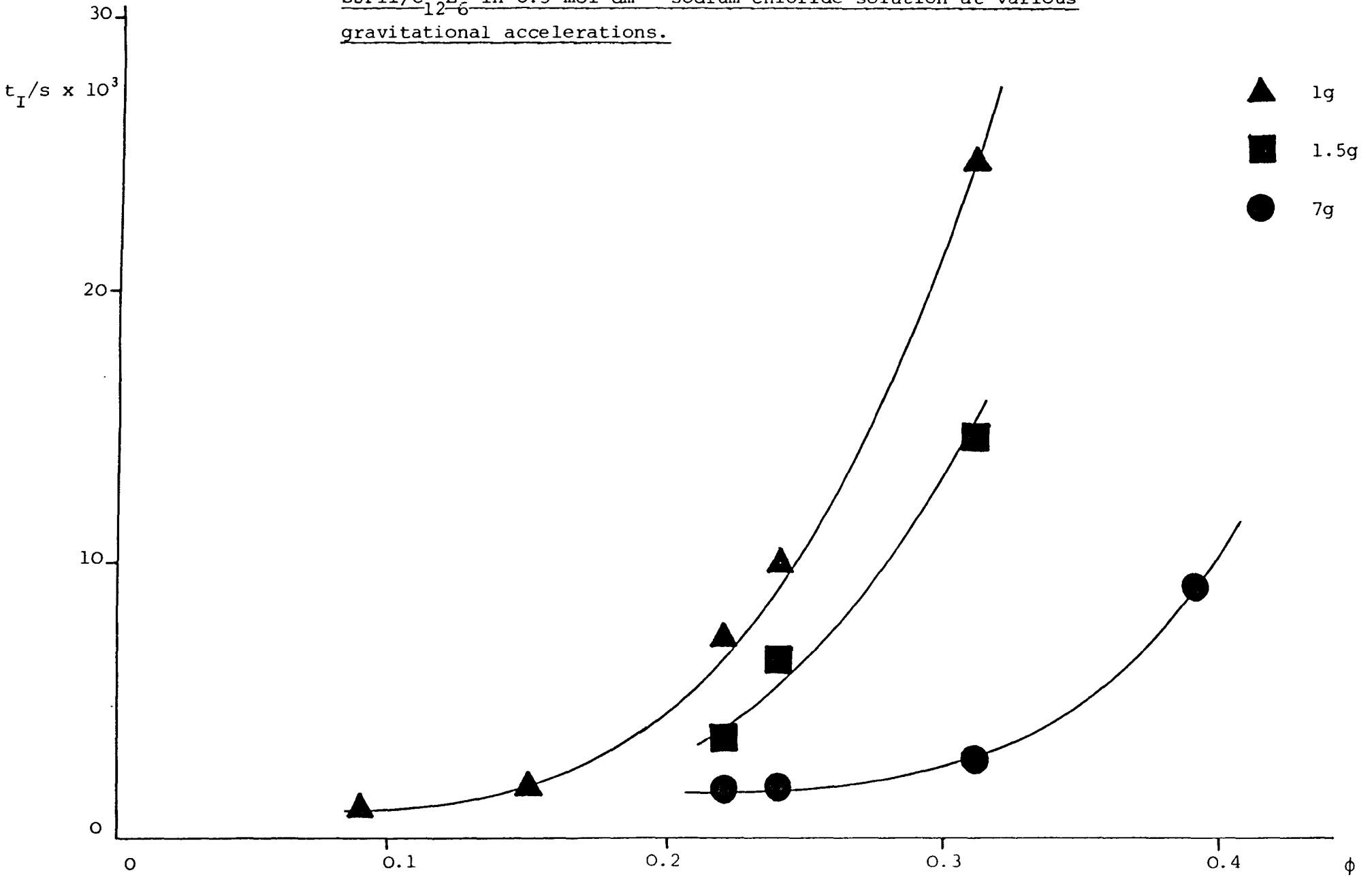

becomes more closely packed and the rate of channel formation decreases, thus increasing the induction period. Once the channels have formed rapid sedimentation follows. This qualitative picture explains the experimentally obtained results well. It also explains the absence of an induction period at low volume fractions where no continuous network was formed of sufficient packing so as to hamper upward liquid flow.

It was also noted that the induction periods for the SJP10/$C_{12}E_6$ case were significantly higher than the induction periods for the SJP8/$C_{12}E_6$ and SJP11/$C_{12}E_6$ systems at all gravitational accelerations. The SJP10 latex was intermediate in size and therefore this effect cannot be attributed to particle size, but possibly to the electrical properties of the surface. In (8.3) the electrophoretic mobility measurements indicated a slightly higher zeta potential for the SJP10/$C_{12}E_6$ system in 0.5 mol dm^{-3} sodium chloride solution (10.2 mV) than for the SJP8/$C_{12}E_6$ and SJP11/$C_{12}E_6$ systems (9.7 mV). The Stern potential, closely related to the zeta potential, plays a significant role in the particle interaction forces and hence in the strength of aggregation. The Stern potential is used in the determination of the repulsive interaction potential acting between a pair of particles, see equations (3.7) and (3.9), the higher the Stern potential the greater the repulsive force. A system with a high repulsive potential would be less strongly aggregated than one with a lower repulsive potential. This may explain the longer time for the network to form and hence the longer induction times exhibited by the latex with the highest surface charge although this is by no means clear.

The sedimentation rates for the three systems at various gravitational accelerations, 1g, 1.5g and 7g were plotted as a function of volume fraction for the three systems. These are presented in Figures 9.25 - 9.27 for SJP8/$C_{12}E_6$, SJP10/$C_{12}E_6$ and SJP11/$C_{12}E_6$ respectively. Figures 9.28 -

Figure 9.25.

Sedimentation rate/ms^{-1} versus volume fraction for SJP8/$C_{12}E_6$ in 0.5 mol dm^{-3} sodium chloride solution at various gravitational accelerations.

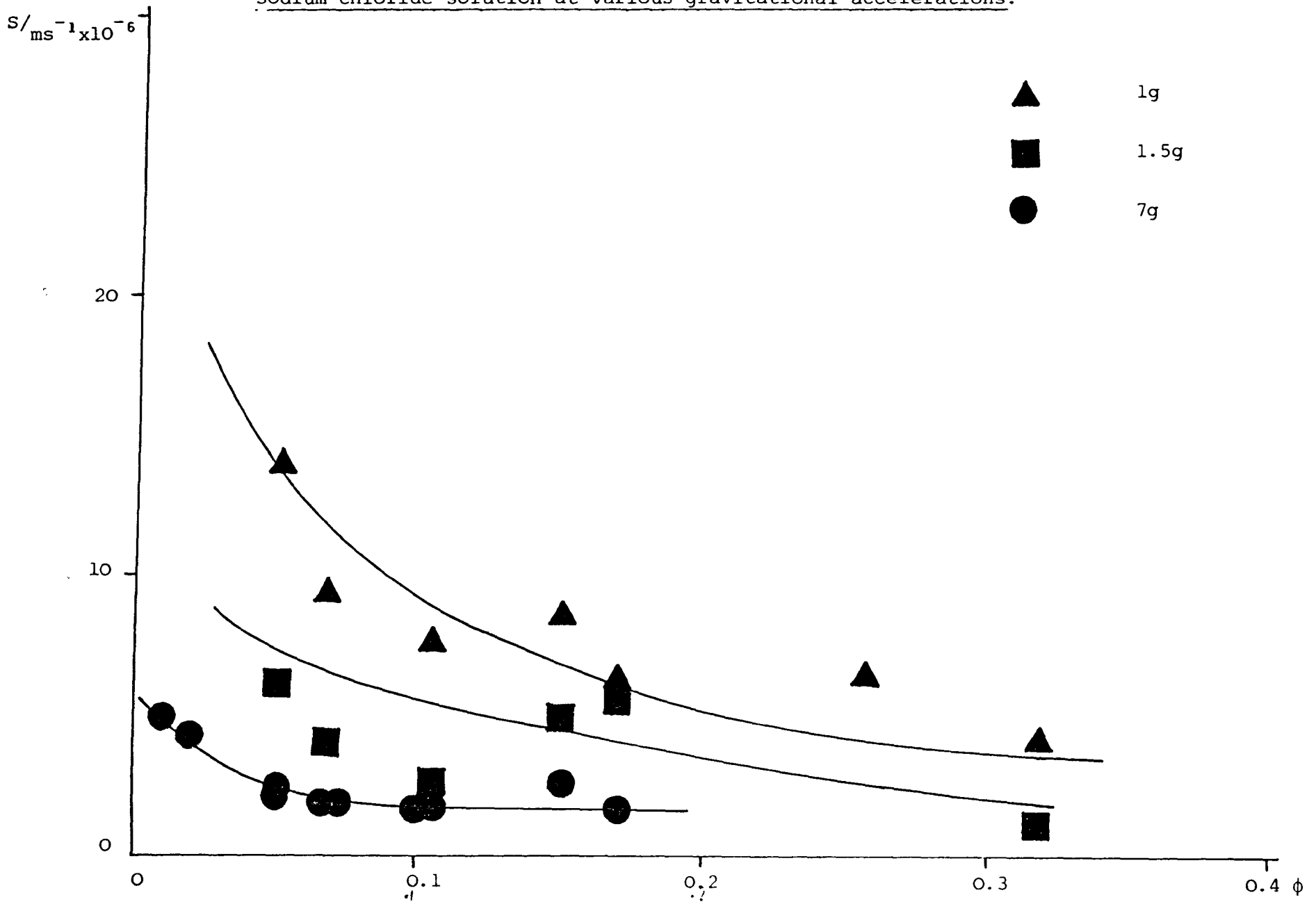

Figure 9.26

Sedimentation rate/ms^{-1} versus volume fraction for SJP10/$C_{12}E_6$ in 0.5 mol dm^{-3} sodium chloride solution at various gravitational accelerations.

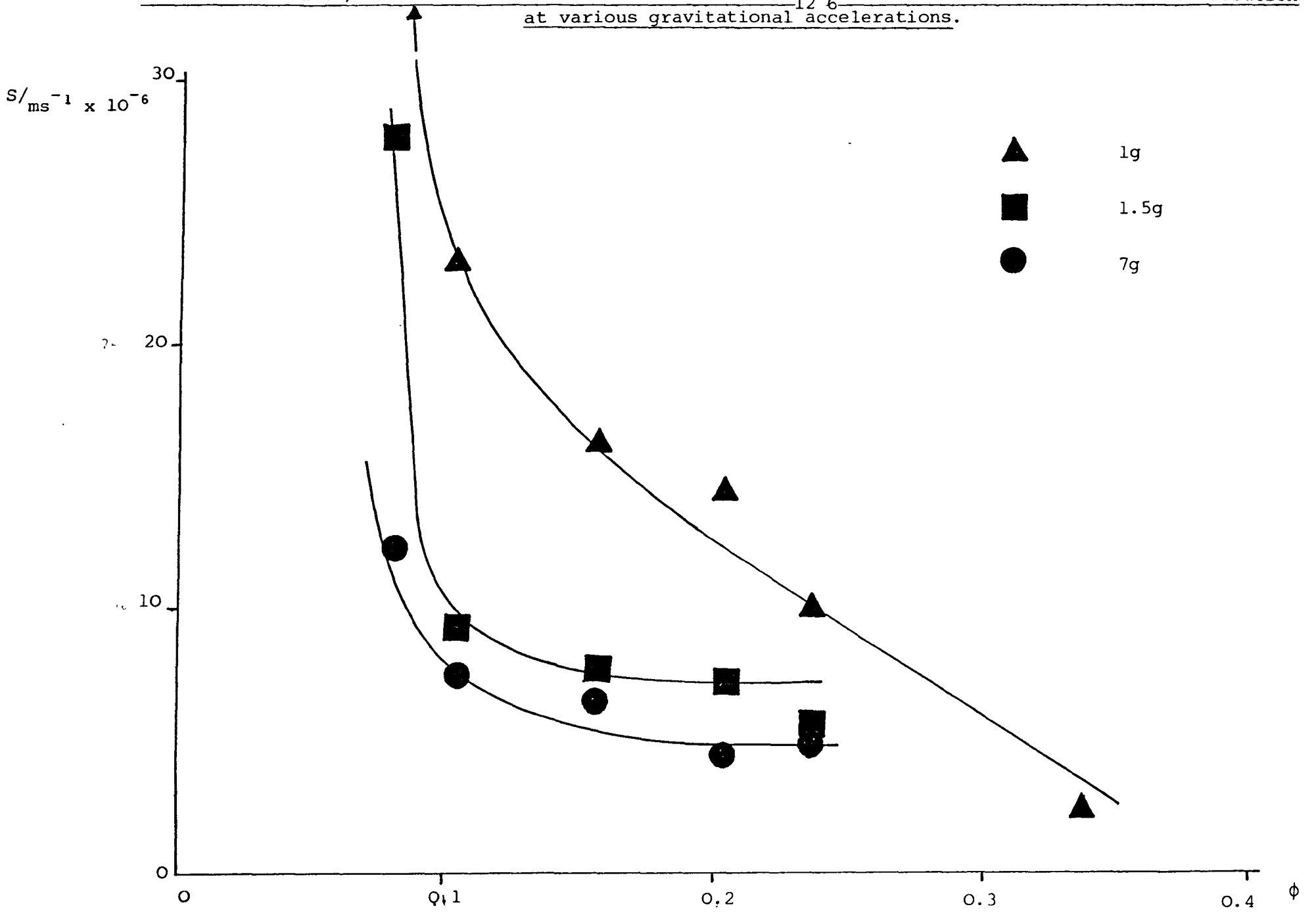

Figure 9.27.

Sedimentation rate/ms^{-1} versus volume fraction for SJP11/$C_{12}E_6$ in 0.5 mol dm^{-3} sodium chloride solution at various gravitational accelerations.

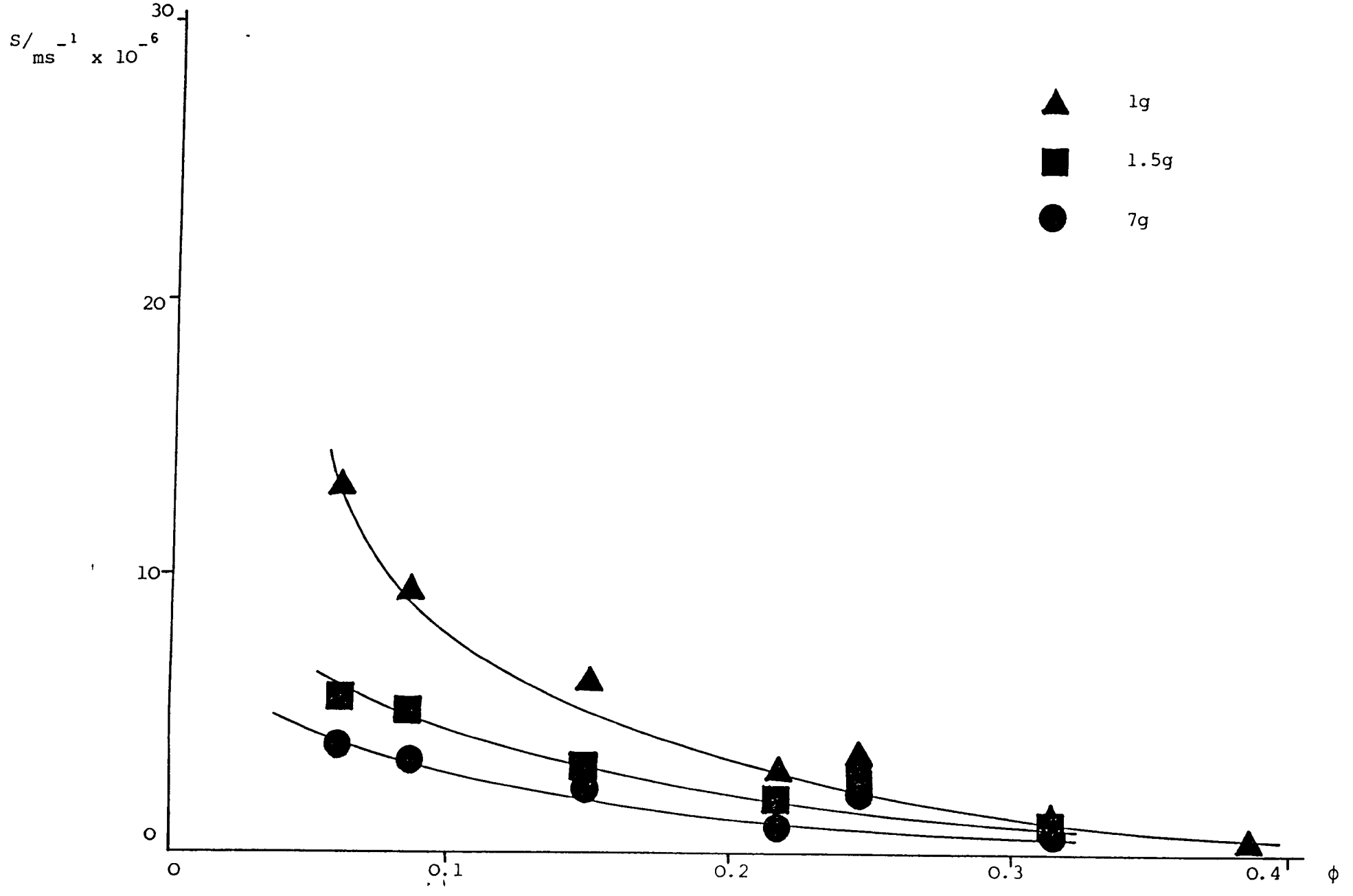

Figure 9.28.

Sedimentation rate/ms^{-1} versus volume fraction at 1g for SJP8/$C_{12}E_6$, SJP10/$C_{12}E_6$ and SJP11/$C_{12}E_6$, all in 0.5 mol dm^{-3} sodium chloride solution.

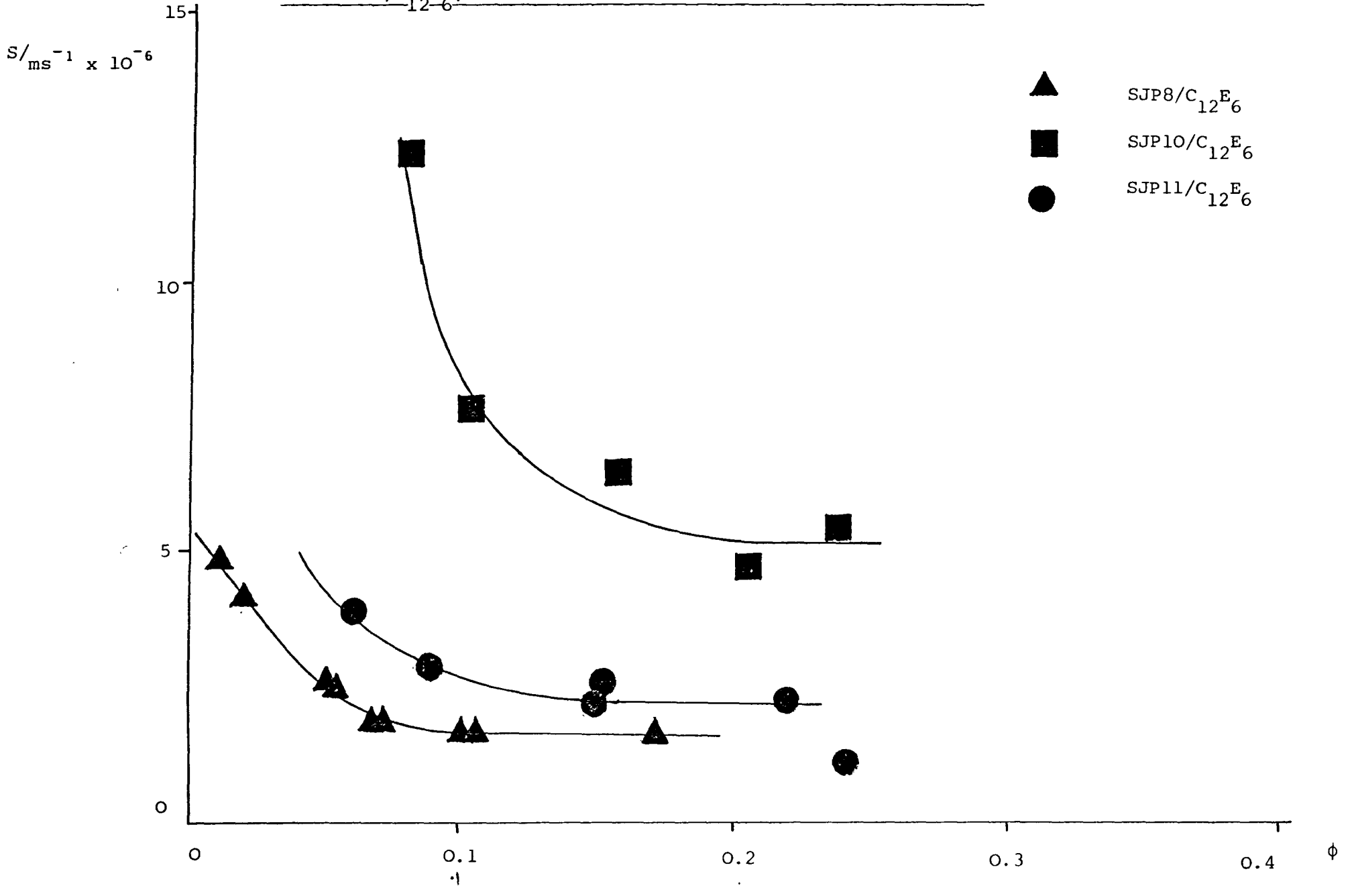

Figure 9.29

Sedimentation rate/ms^{-1} versus volume fraction at 1.5g for SJP8/$C_{12}E_6$–SJP10/$C_{12}E_6$ and SJP11/$C_{12}E_6$, all in 0.5 mol dm^{-3} sodium chloride solution.

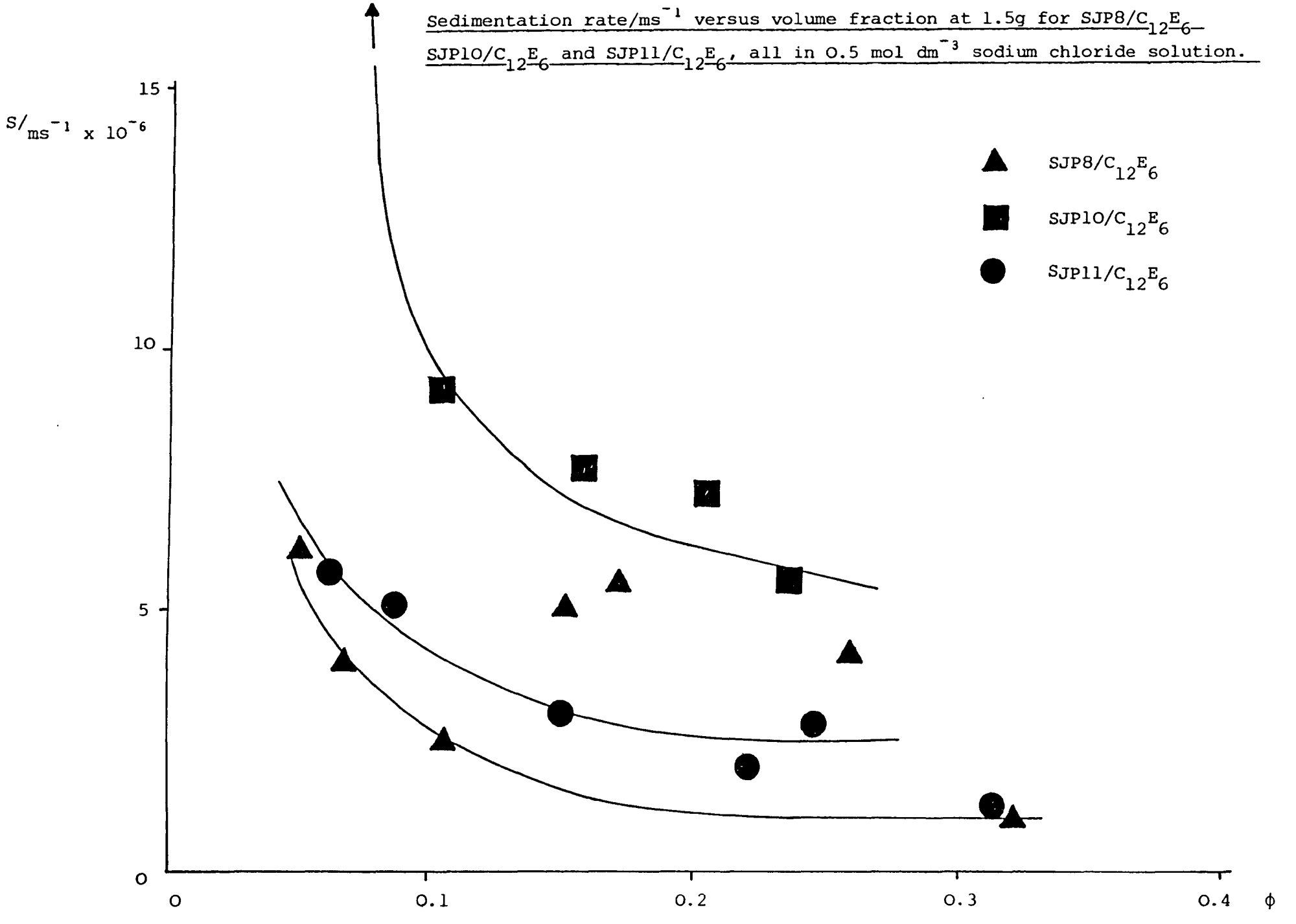

Figure 9.30.

Sedimentation rate/ms^{-1} versus volume fraction at 7 g for $SJP8/C_{12}E_6$, $SJP10/C_{12}E_6$ and $SJP11/C_{12}E_6$, all in 0.5 mol dm^{-3} sodium chloride solution.

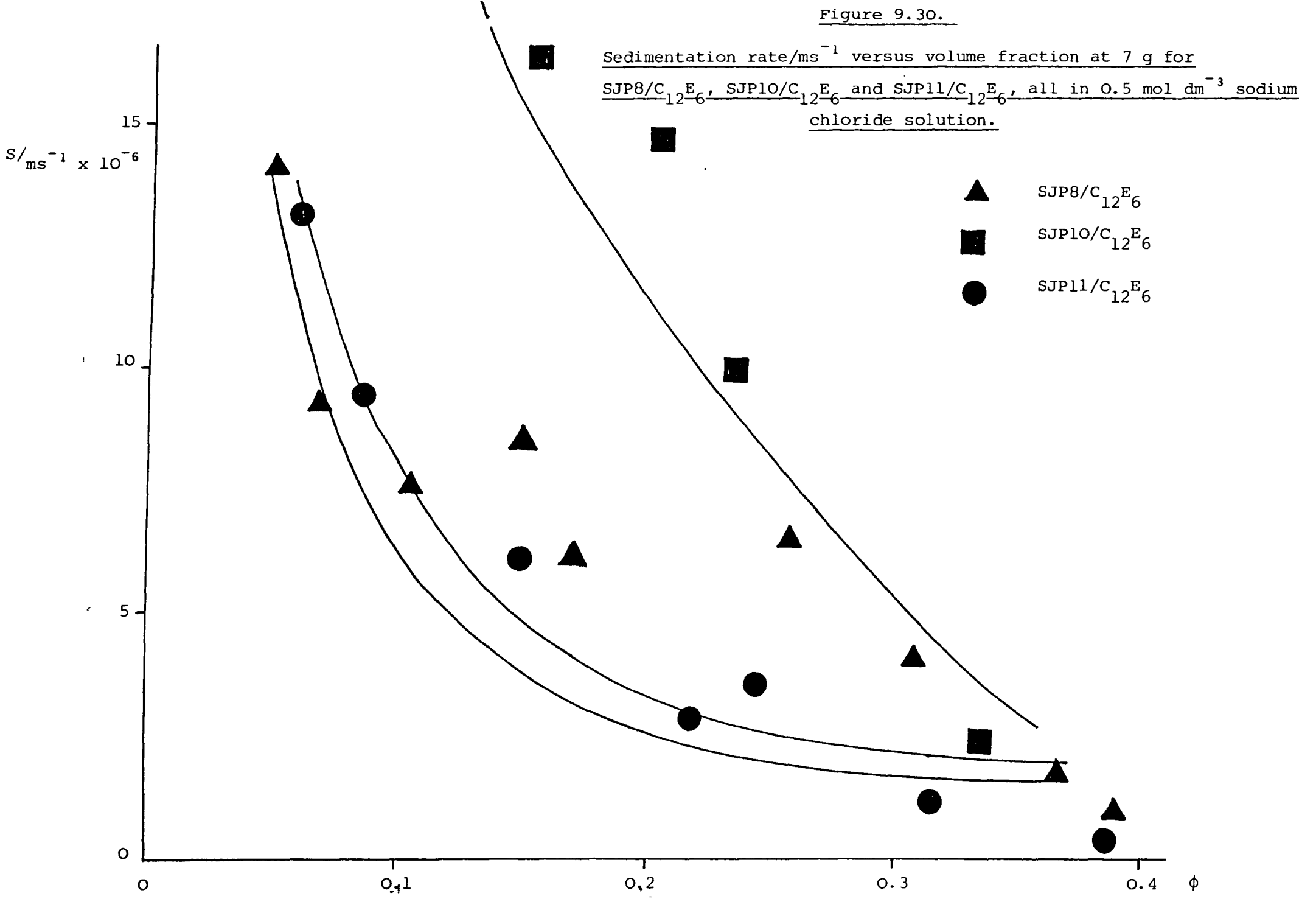

9.30 show the plots for the different systems at 1g, 1.5g and 7g. As expected the sedimentation rate for a given system increased with increased gravitational acceleration.

It was also noted that the sedimentation rates for the SJP10/$C_{12}E_6$ systems were significantly faster than the SJP8/$C_{12}E_6$ and SJP11/$C_{12}E_6$ systems. Explanation of this and the higher induction periods exhibited by the SJP10/$C_{12}E_6$ system is difficult. Higher repulsive forces and subsequently weaker aggregation in the system does not explain the rapid settling rates. Rapid sedimentation may be as a result of larger or denser flocs. At present the situation is not clear and is still to be resolved.

Many theoretical approaches to the study of the sedimentation behaviour of particulate systems are concerned with the dilute limit where multiparticle interactions may be ignored. Work by Buscall et al [128], however, has extended a theoretical treatment to a wide range of particle volume fractions, described by equation (6.32):

$$\frac{S}{S_o} = \left(1 - \frac{\phi}{\phi_m}\right)^{k_s \phi_m}$$

The above equation was fitted to experimental data for the SJP8/$C_{12}E_6$ system for two values of the maximum packing fraction, 0.62 and the effective maximum packing fraction described earlier, 0.4. The sedimentation rate at infinite dilution was taken as the extrapolated value of 5.38×10^{-6} ms^{-1}. Values calculated for k_s in the two cases were 13.7 and 13.3 respectively as opposed to the value of 5.4 obtained by Buscall et al. The equation was therefore unsensitive for the system and the fit of the data gave no insight as to the packing fraction. The theoretical curve and the experimental points are presented in Figure 9.31. A reasonable fit was obtained for the low value fraction data, but not for the more concentrated systems although the

Figure 9.31.

Relative sedimentation rate versus volume fraction for SJP8/$C_{12}E_6$ in 0.5 mol dm^{-3} sodium chloride solution. Drawn line calculated using equation (6.32) taking $\phi_m = 0.62$ and $k_s = 13.7$, and taking $\phi_m = 0.4$ and $k_s = 13.3$. $S_o = 5.38 \times 10^{-6} ms^{-1}$

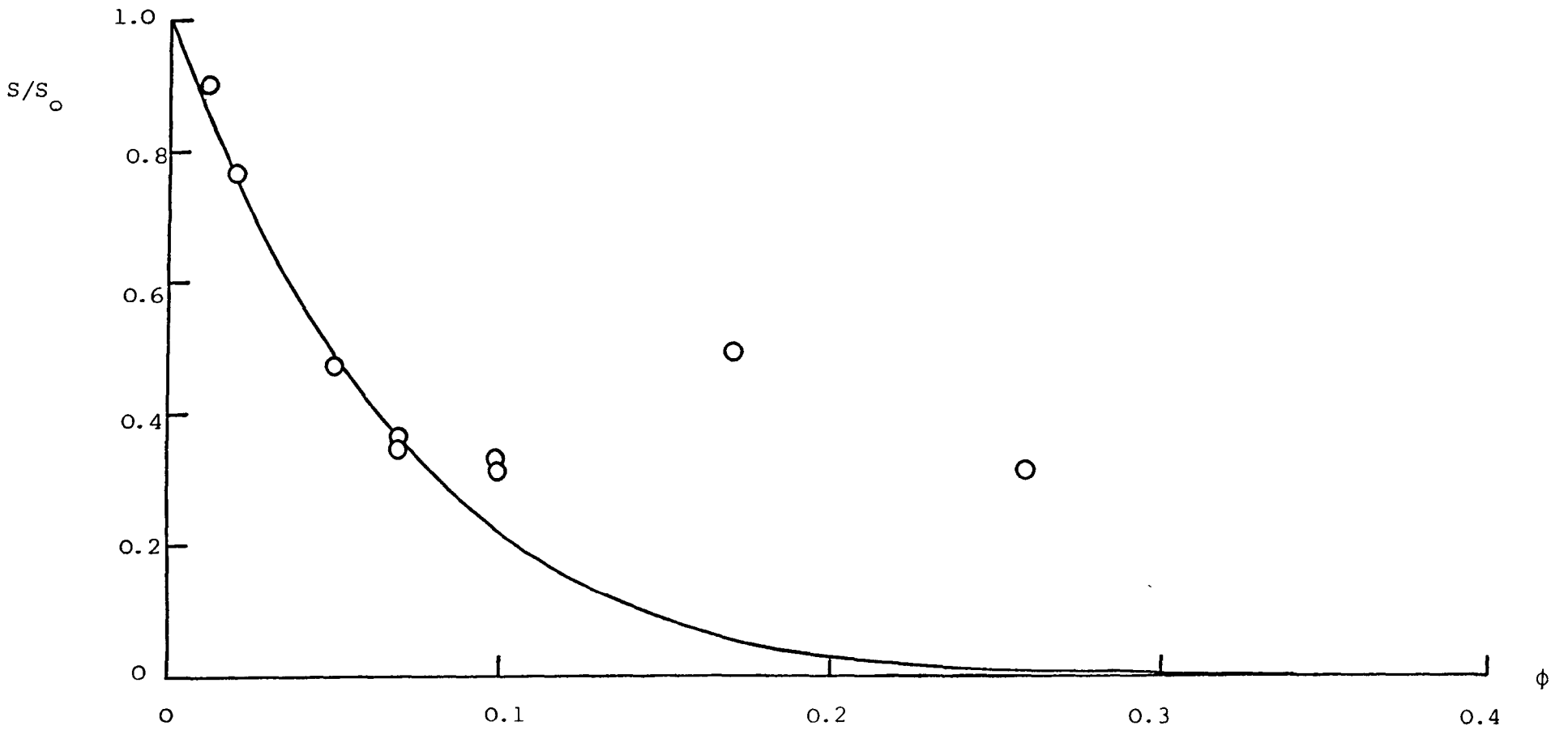

sedimentation rate data at high concentrations for this system did not follow the trends expected and found with the other systems.

Chapter Ten

Pulse Shearometry

Chapter Ten. Pulse Shearometry.

10.1. Introduction.

Pulse shearometry is a dynamic testing method of determining the wave rigidity modulus, $\tilde{G}$, of a system. The technique consists of initiating a sinusoidal shear wave through the system under investigation, density ρ^*, and measuringits propagation velocity, u. The wave rigidity modulus may be calculated from equation (2.48):

$$\tilde{G} = \rho^* u^2$$

At sufficiently high frequencies the wave rigidity modulus approximates to the high frequency limit of the shear modulus, $G(\infty)$, and hence by use of high frequency wave propagation this property may be evaluated. The Rank Pulse Shearometer, used in this work, was operated at a shear wave frequency of 1200 $rads^{-1}$, sufficiently high for the determination of the high frequency shear modulus.

The bulk of the wave rigidity modulus determinations were carried out on the weakly flocculated latex systems described in Chapter Seven, polystyrene latices SJP8 (particle diameter 0.97 μm), SJP10 (particle diameter 1.41 μm) and SJP11 (particle diameter 1.92 μm), all coated with a monolayer of $C_{12}E_6$ in 0.5 mol dm^{-3} sodium chloride solution. A volume fraction range of ϕ = 0.25 - 0.6 was investigated for the three systems.

10.2. Instrumentation.

The Rank Pulse Shearometer, supplied by Rank Brothers, Bottisham, Cambridge, was used in this work, for the determination of high frequency limit of the shear moduli.[13,10] The pulse shearometer cell, illustrated in Figure 10.1,[10] was a development of the design of van Olphen,[197] and consisted of two parallel metal discs mounted in a cylindrical glass

Figure 10.1

The Pulse Shearometer

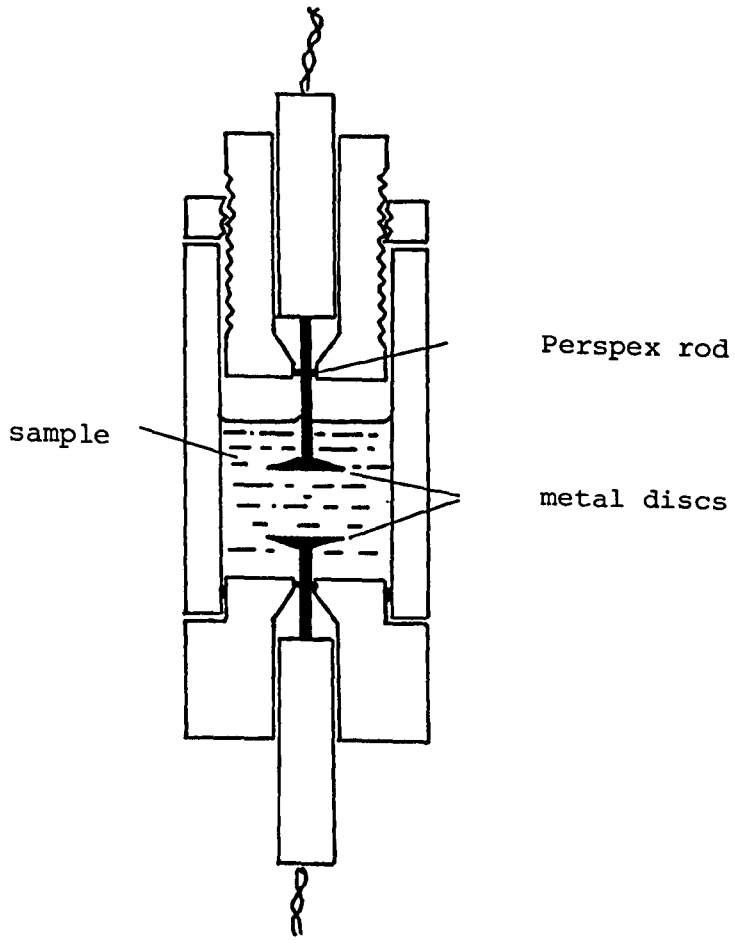

sample chamber. One disc was mounted in the top of the chamber, consisting of a close-fitting cylinder to minimise evaporation which could be raised or lowered by means of a screw to vary the disc separation, d_p. Each disc, of diameter 2.5 cm, was connected, via a perspex rod, to a piezo-electric crystal of the type used in audio pick-up cartridges. These water soluble lithium chloride crystals were isolated from the chamber by means of a silicone rubber seal which also served to hold the disc in place. The seals were under tension to ensure intimate contact between the crystal and the perspex rod while still allowing free movement of the disc.

The lower disc was chosen to be the transmitter and the upper the receiver. A single pulse was applied to the transmitter crystal which produced a rotational displacement of the transmitter disc of $< 10^{-4}$ radians. A BBC/Acorn microcomputer received the signals and analysed the data. The receiver crystal response to the propagated pulse could be displaced on the monitor as a voltage/time graph which consisted of a linear portion followed by a damped sine wave. The initiation of the pulse corresponded to the start of the trace and the arrival of the pulse at the upper disc was indicated by the appearance of the sine wave. The length of the trace to the first peak corresponded to the propagation time, t_p, which was determined automatically by the computer.

Hence the propagation velocity, u, was determined from the following expression:

$$u = \frac{d_p}{t_p} \qquad (10.1)$$

and subsequently the high frequency shear modulus from the wave rigidity modulus:

$$\tilde{G} \simeq G(\infty) = \rho^* u^2$$

In order to achieve higher accuracy a series of results was taken, as a function of disc separation, and the gradient of the plot of propagation distance versus propagation time was used to evaluate the propagation velocity and subsequently the wave rigidity modulus.

10.3. Experimental.

The disc separation was initially set to zero in order to prevent the discs from touching during the experiment and hence from damaging the crystals. An empty cell was used and the top section was lowered slowly until the discs just touched, showed by a large amplitude wave upon pulsing; the position was marked by a locking screw.

About 50 cm^3 of sample was placed in the shearometer cell so that both discs were immersed and so that there was sufficient space above the sample for the discs to be brought into close proximity without the upper cylinder compressing the sample.

To investigate the thixotropic nature of the sample a fixed disc separation was set, the sensitivity and gain adjusted to suitable levels and measurements of the shear modulus as a function of time, t_{as}, taken. The system was shaken (in the cell) and zero time set; measurements of propagation time were then taken every 30 seconds as the system relaxed.

To determine the wave rigidity modulus determinations were made of the propagation velocity as a function of increasing disc separation and the results analysed by the BBC microcomputer. To take account of the thixotropic nature of the systems two sets of data were determined, the first with the propagation velocity evaluated one minute after shearing the system, i.e. adjusting the disc separation, and the second with the velocity determined ten minutes after shearing of the system. The measurements taken one minute after disc separation adjustment were repeated for decreasing disc separation.

The systems were well shaken before each set of measurements to prevent sedimentation effects.

10.4. Results.

The thixotropic behaviour of the three systems under investigation, SJP8/$C_{12}E_6$, SJP10/$C_{12}E_6$ and SJP11/$C_{12}E_6$ all in 0.5 mol dm^{-3} sodium chloride solution was found to be similar. The thixotropic behaviour of the SJP11/$C_{12}E_6$ system is presented in the form of a plot of high frequency shear modulus versus time after shearing of the system in Figure 10.2. The value of the shear modulus rose rapidly initially and then achieved an approximately constant value. In all cases, after 10 minutes the value was constant within experimental error. This time scale was also considered suitable for measurements as within 10 minutes sedimentation effects could be neglected.

For all the SJP8/$C_{12}E_6$, SJP10/$C_{12}E_6$ and SJP11/$C_{12}E_6$ systems investigated, in the volume fraction range ϕ = 0.25 - 0.6 good straight lines were obtained from the plots of propagation distance versus propagation time enabling accurate evaluations of propagation velocities and hence shear moduli. Figure 10.3 shows a typical propagation distance versus propagation time plot. The densities of the systems were calculated from the density of polystyrene, 1055 kgm^{-3}, and that of the continuous phase, taken to be 1000 kgm^{-3}. The results obtained for the propagation velocities, the densities determined and the high frequency limit shear moduli obtained for all the systems measured both 1 minute and 10 minutes after system shearing are presented in Tables 10.1 - 10.6.

10.5. Discussion.

Plots were constructed of the high frequency limit shear modulus versus the volume fraction for the three different systems, SJP8/$C_{12}E_6$,

Figure 10.2.

Thixotropic behaviour of SJP11/$C_{12}E_6$ in 0.5 mol dm^{-3} sodium chloride solution

High frequency shear modulus/Nm^{-2} versus time after shearing of the system/min.

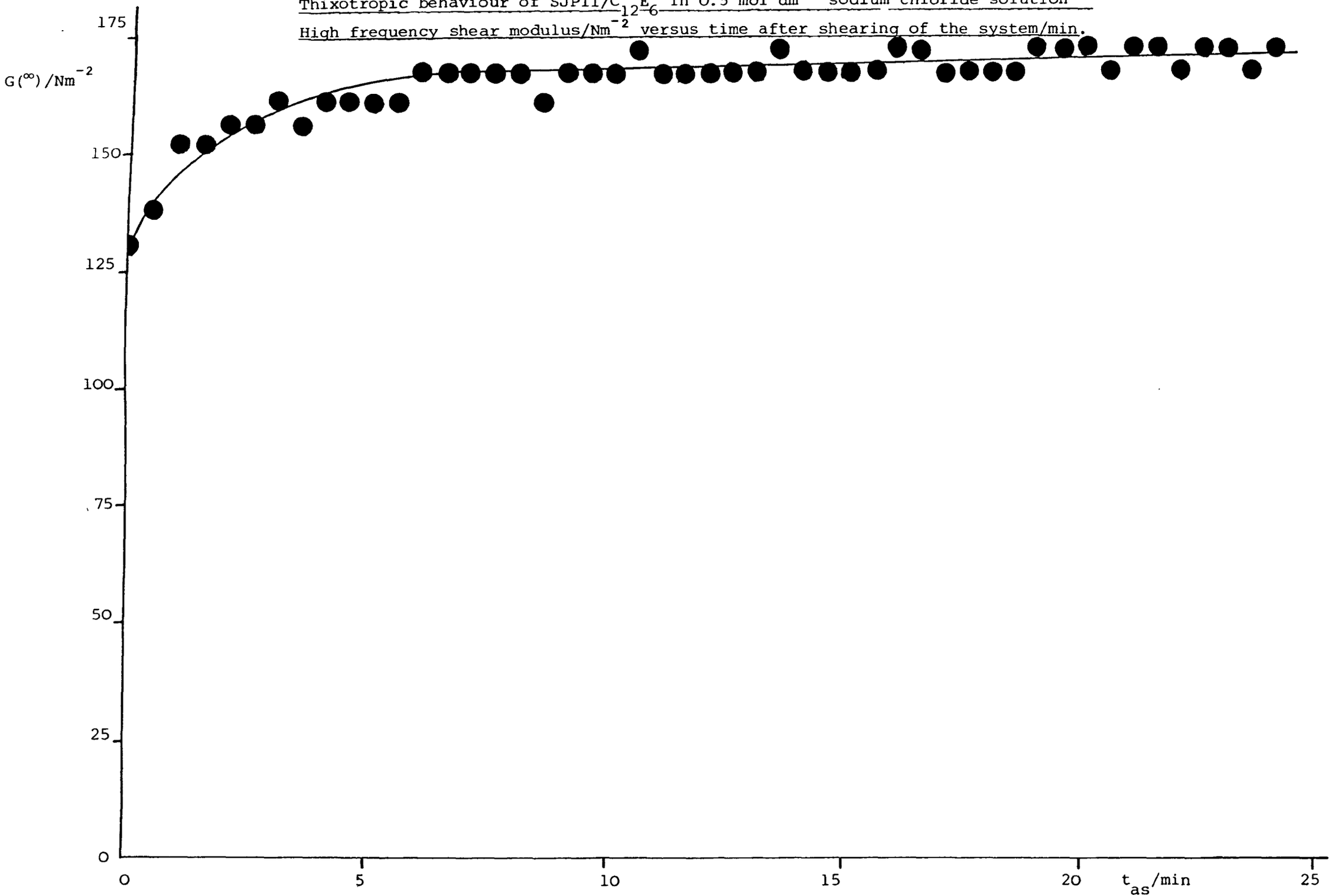

Figure 10.3.

Propagation distance/m versus propagation time/s for polystyrene latex SJP8/$C_{12}E_6$ in 0.5 mol dm^{-3} sodium chloride solution at ϕ = 0.56. Reading taken 1 minute after shearing system.

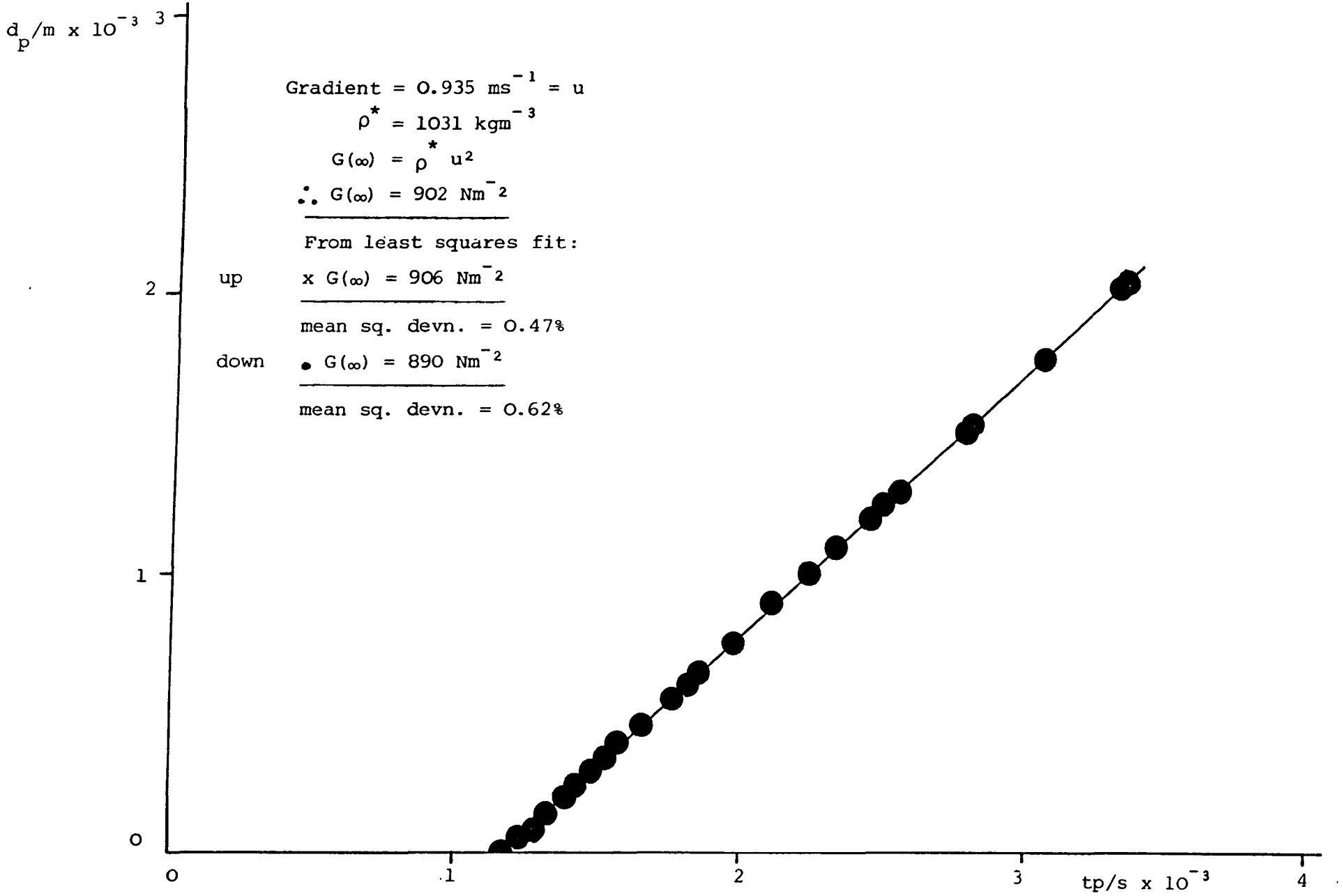

Table 10.1.

Propagation velocities/ms^{-1}, densities/kgm^{-3} and high frequency limit shear moduli/Nm^{-2} calculated from least squares fit for polystyrene latex SJP8/$C_{12}E_6$ in 0.5 mol dm^{-3} sodium chloride solution at various volume fractions, 1 minute after shearing.

ϕ	ρ^*/kgm^{-3}	u/ms^{-1}	$G(\infty)/Nm^{-2}$
0.27	1015	0.29, 0.28	84, 79
0.31	1017	0.37, 0.36	143, 132
0.315	1017	0.30, 0.34, 0.28	93, 120, 79
0.32	1017	0.40	160
0.34	1019	0.34, 0.34	116, 119
0.36	1019	0.38, 0.39	150, 155
0.38	1020	0.40, 0.39	163, 154
0.39	1021	0.47, 0.45	222, 203
0.40	1022	0.51, 0.51, 0.52	268, 261, 278
0.41	1022	0.51, 0.51	263, 271
0.45	1024	0.61, 0.61	386, 384
0.47	1026	0.65, 0.65, 0.63	432, 437, 409
0.48	1026	0.66, 0.66	450, 446
0.50	1027	0.71, 0.72	518, 530
0.54	1029	0.84, 0.83	720, 706
0.56	1031	0.94, 0.93	906, 890
0.61	1033	1.22, 1.22, 1.17	1540, 1542, 1424

Table 10.2.

Propagation velocities/ms^{-1}, densities/kgm^{-3} and high frequency limit shear moduli/Nm^{-2} calculated from least squares fit for polystyrene latex SJP8/$C_{12}E_6$ in 0.5 mol dm^{-3} sodium chloride solution at various volume fractions, 10 minutes after shearing.

ϕ	ρ^*/kgm^{-3}	u/ms^{-1}	$G(\infty)/Nm^{-2}$
0.31	1017	0.35	128
0.315	1017	0.29	84
0.32	1017	0.41	172
0.34	1019	0.37	137
0.36	1019	0.33	111
0.38	1020	0.40	164
0.39	1021	0.43	192
0.40	1022	0.54	303
0.41	1022	0.51	267
0.47	1026	0.67	460
0.48	1026	0.72	528
0.50	1027	0.76	588
0.54	1029	0.87	783
0.56	1031	0.95	926
0.61	1033	1.25	1613

Table 10.3.

Propagation velocities/ms^{-1}, densities/kgm^{-3} and high frequency limit shear moduli/Nm^{-2} calculated from least squares fit for polystyrene latex SJTP10/$C_{12}E_6$ in 0.5 mol dm^{-3} sodium chloride solution at various volume fractions, 1 minute after shearing.

ϕ	ρ^*/kgm^{-3}	u/ms^{-1}	$G(\infty)/Nm^{-2}$
0.34	1018	0.40, 0.39, 0.38	166, 157, 149
0.39	1021	0.42, 0.48, 0.50	184, 233, 256
0.42	1023	0.59, 0.61	355, 377
0.48	1026	0.62, 0.65, 0.62	400, 429, 398
0.49	1027	0.71, 0.73	524, 541
0.51	1028	0.80, 0.78	654, 630
0.52	1029	0.82	684

Table 10.4.

Propagation velocities/ms^{-1}, densities/kgm^{-3} and high frequency limit shear moduli/Nm^{-2} calculated from least squares fit for polystyrene latex SJP10/$C_{12}E_6$ in 0.5 mol dm^{-3} sodium chloride solution at various volume fractions, 10 minutes after shearing.

ϕ	ρ^*/kgm^{-3}	u/ms^{-1}	$G(\infty)/Nm^{-2}$
0.34	1018	0.33	111
0.39	1021	0.52	280
0.42	1023	0.62	393
0.48	1026	0.59	363
0.49	1027	0.77	605
0.51	1028	0.85	741
0.52	1029	0.86	756

Table 10.5.

Propagation velocities/ms^{-1}, densities/kgm^{-3} and high frequency limit shear moduli/Nm^{-2} calculated from least squares fit for polystyrene latex SJP11/$C_{12}E_6$ in 0.5 mol dm^{-3} sodium chloride solution at various volume fractions, 1 minute after shearing.

ϕ	ρ^*/kgm^{-3}	u/ms^{-1}	$G(\infty)/Nm^{-2}$
0.31	1017	0.24, 0.25	61, 64
0.39	1021	0.39, 0.40	158, 160
0.47	1026	0.58	347
0.51	1028	0.72, 0.73, 0.72	540, 549, 536
0.54	1029	0.76	600
0.55	1030	0.84	730

Table 10.6.

Propagation velocities/ms^{-1}, densities/kgm^{-3} and high frequency limit shear moduli/Nm^{-2} calculated from least squares fit for polystyrene latex SJP11/$C_{12}E_6$ in 0.5 mol dm^{-3} sodium chloride solution at various volume fractions, 10 minutes after shearing.

ϕ	ρ^*/kgm^{-3}	u/ms^{-1}	$G(\infty)/Nm^{-2}$
0.31	1017	0.24	59
0.39	1021	0.40	162
0.47	1026	0.62	394
0.51	1028	0.80	654
0.54	1029	0.84	723
0.55	1030	0.92	863

SJP10/$C_{12}E_6$ and SJP11/$C_{12}E_6$. These are presented in Figures 10.4 to 10.6 and compared in Figures 10.7 and 10.8. Below a volume fraction of approximately 0.3 with all the systems, insufficient response was obtained from the shearometer to enable the determination of the shear modulus. At these low concentrations there was little elasticity in the systems. As the concentrations increased an increasing elastic response was observed as the particles became more closely packed and a network was formed enabling propagation of the shear wave.

It was noted that the SJP10/$C_{12}E_6$ system, intermediate in particle size, exhibited higher shear modulus values at a given volume fraction than the other two systems.

Buscall et al[111] have developed a theoretical expression to predict the high frequency shear modulus from a knowledge of the inter-particle interaction potential for systems in which the repulsive forces are dominant and their expression is given in equation (5.53):

$$G_\infty^{th} = \frac{\alpha^{\dagger *}}{\hat{R}} \frac{d^2 V_T}{d\hat{R}^2}$$

where $$\alpha^{\dagger *} = \frac{3}{32} \phi_m n$$

$$\hat{R} = 2a \left(\frac{\phi_m}{\phi} \right)^{1/3}$$

It was decided to assess the validity of this approach for weakly flocculated systems. At the minimum of the potential energy well, assuming steric repulsion (but neglecting electrostatic effects) and van der Waals attraction, there are only attractive forces acting which may be described by Hamaker's equation, equation (3.13). Thus equation (5.53) becomes:

Figure 10.4.

High frequency limit shear modulus/Nm^{-2} versus volume fraction for polystyrene latex SJP8/$C_{12}E_6$ in 0.5 mol dm^{-3} sodium chloride solution.

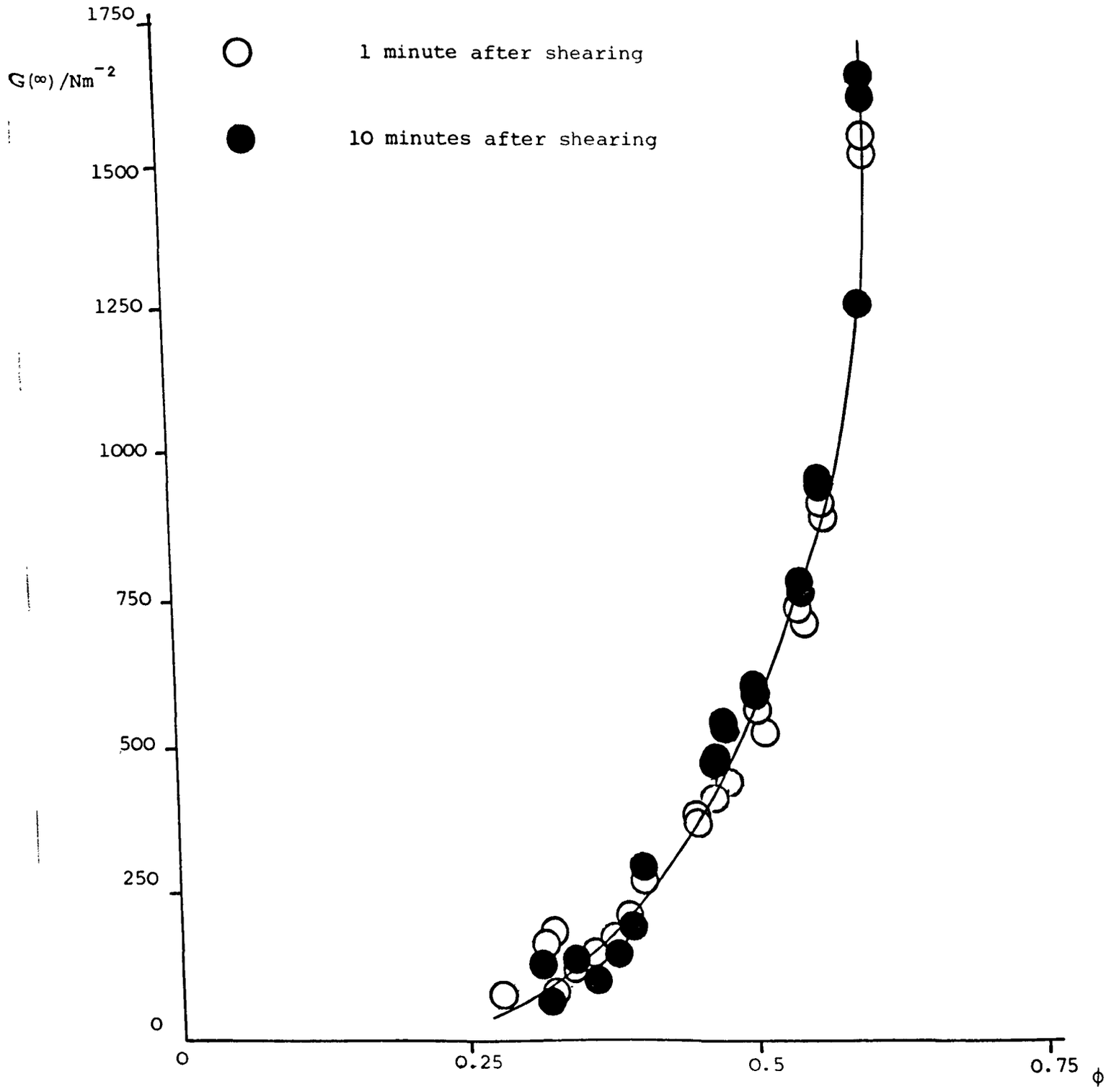

Figure 10.5.

High frequency limit shear modulus/Nm^{-2} versus volume fraction for polystyrene latex SJP10/$C_{12}E_6$ in 0.5 mol dm^{-3} sodium chloride solution.

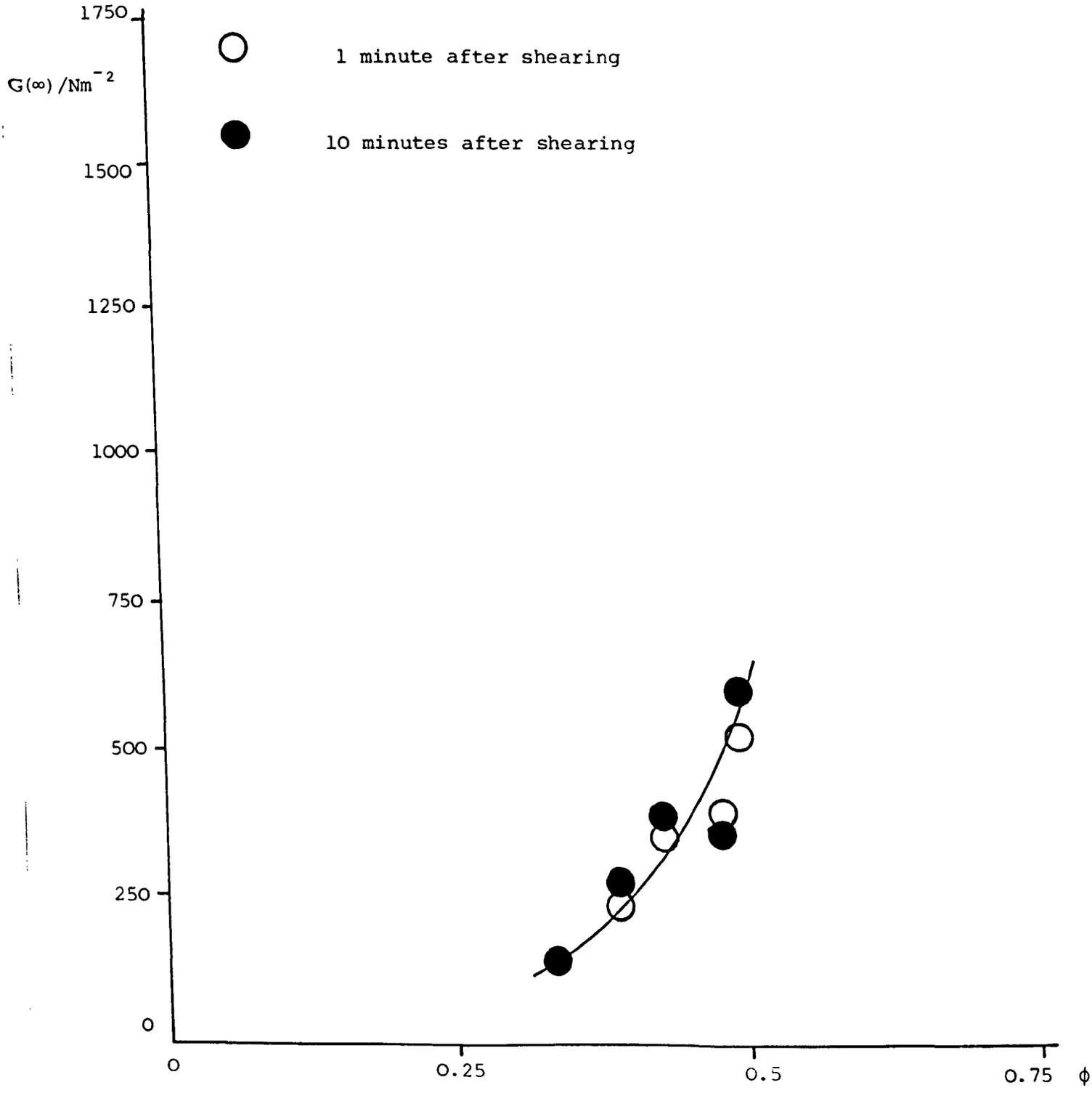

Figure 10.6.

High frequency limit shear modulus/Nm^{-2} versus volume fraction for polystyrene latex SJP11/$C_{12}E_6$ in 0.5 mol dm^{-3} sodium chloride solution.

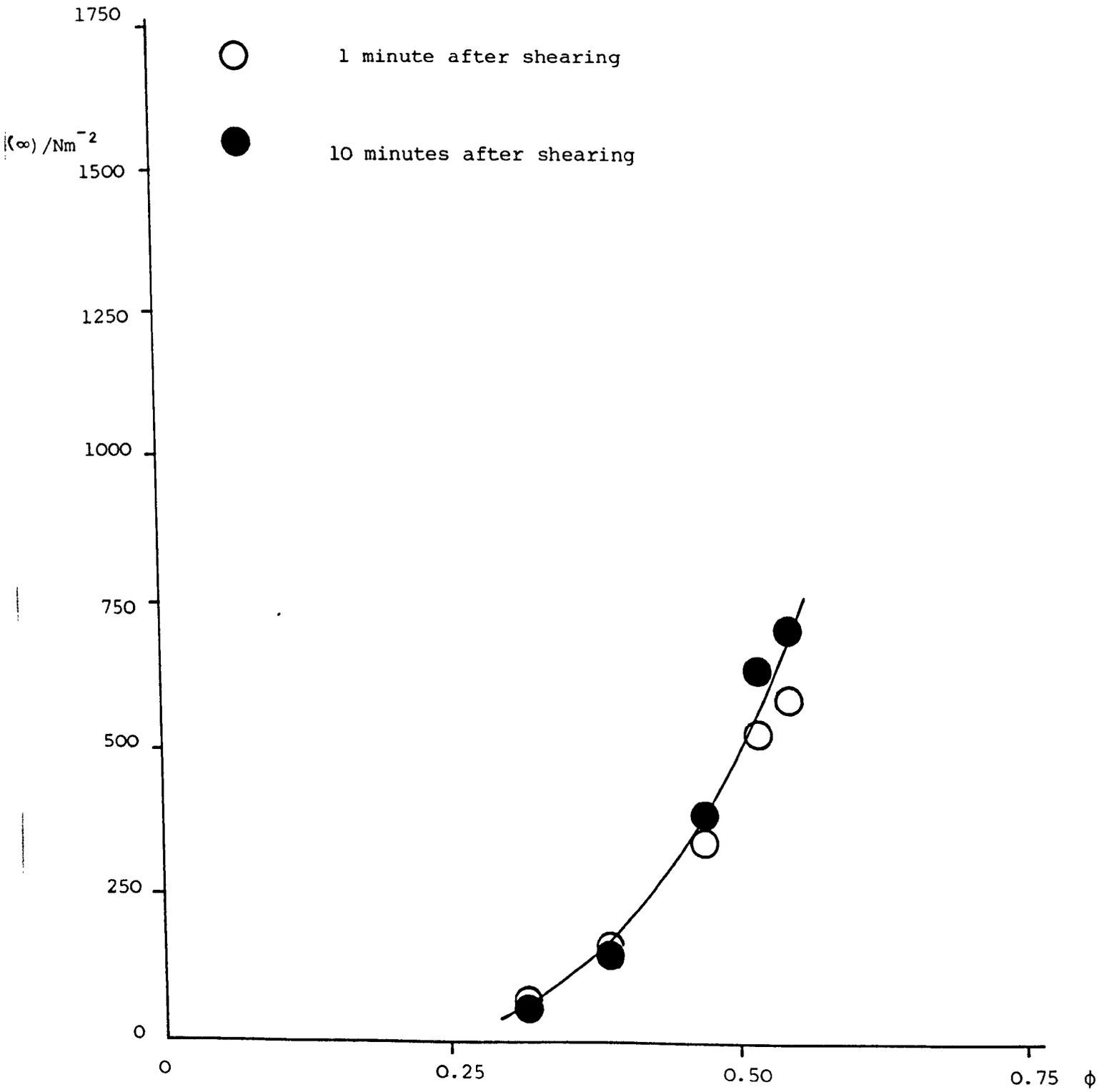

Figure 10.7.

High frequency limit shear modulus/Nm^{-2} versus volume fraction for polystyrene latex systems SJP8/$C_{12}E_6$, SJP10/$C_{12}E_6$ and SJP11/$C_{12}E_6$ all in 0.5 mol dm^{-3} sodium chloride solution. Readings taken 1 minute after shearing of system.

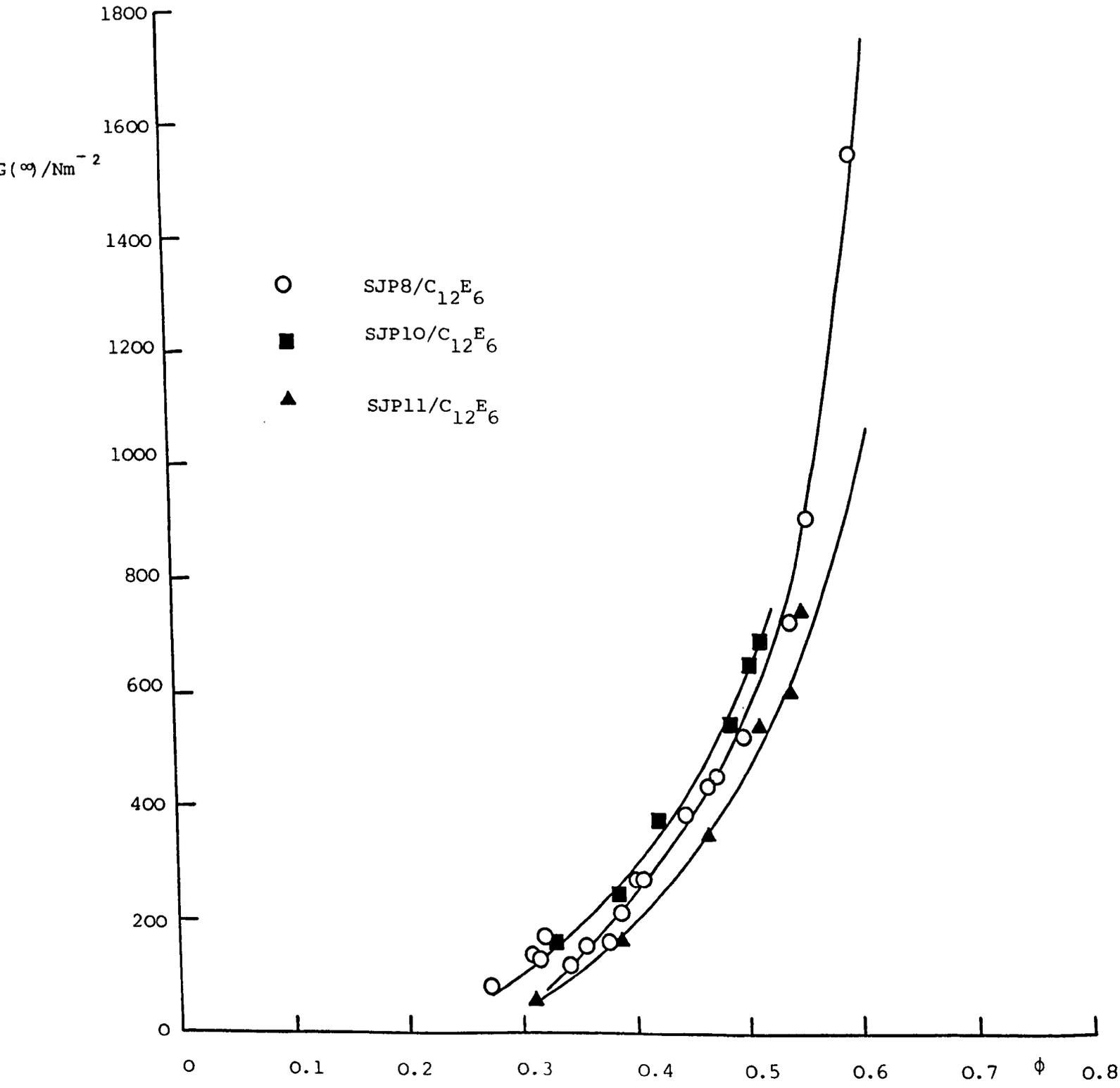

Figure 10.8.

High frequency limit shear modulus/Nm^{-2} versus volume fraction for polystyrene latex systems SJP8/$C_{12}E_6$, SJP10/$C_{12}E_6$ and SJP11/$C_{12}E_6$, all in 0.5 mol dm^{-3} sodium chloride solution. Readings taken 10 minutes after shearing of system.

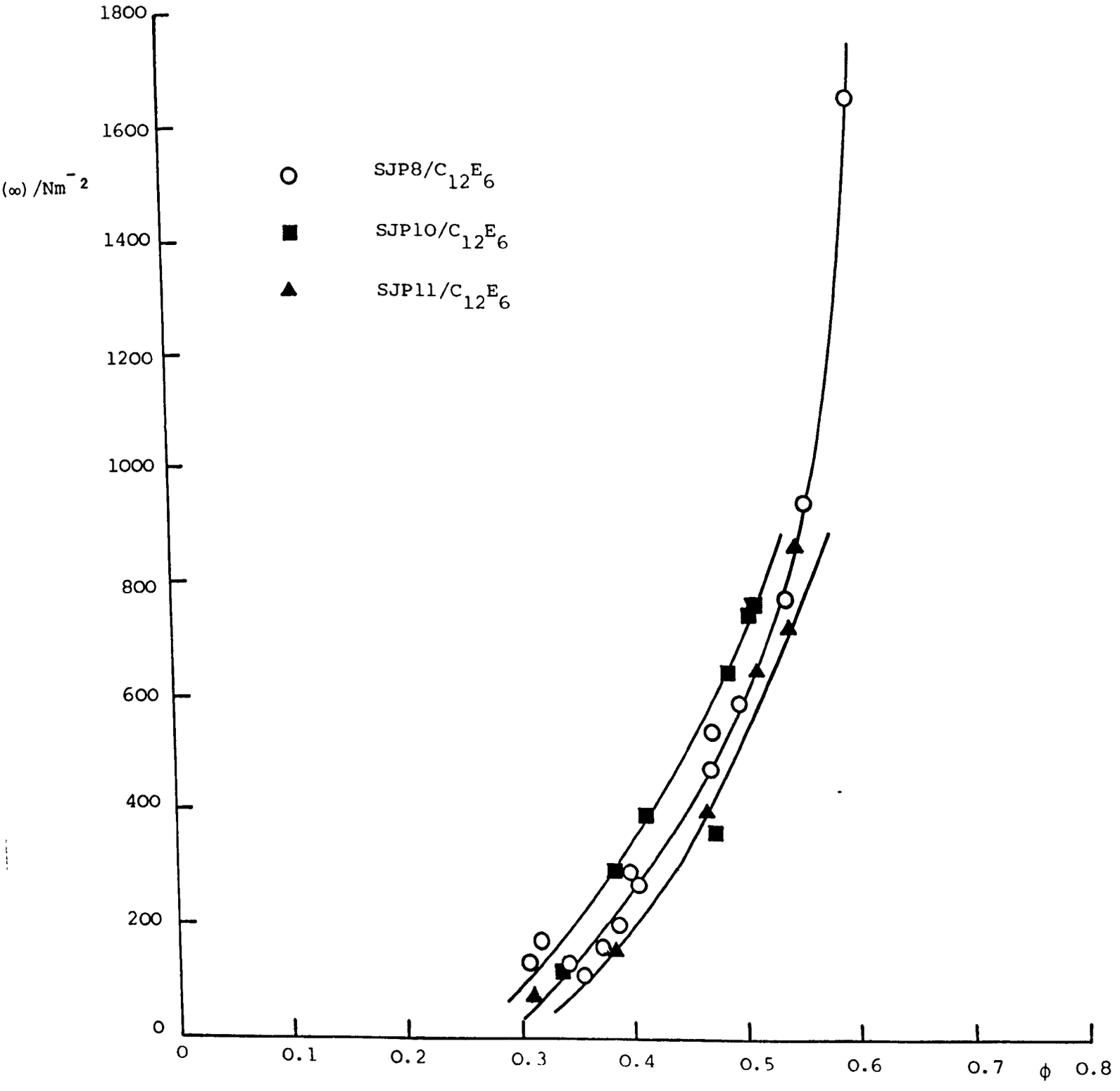

$$G_{\infty}^{th} = \frac{\alpha^{\dagger *}}{\hat{R}} \frac{d^2 V_A}{d\hat{R}^2}$$

$$= \frac{\alpha^{\dagger *}}{\hat{R}} \cdot \frac{-A}{24a^2} \left[\frac{3(x^2 + 2x) + 4}{(x^2 + 2x)^3} + \frac{3}{(x + 1)^4} - \frac{6(x^2 + 2x) + 4}{(x^2 + 2x)^2 (x + 1)^2} \right]$$

where $x = \frac{H_o}{2a}$

Vold[198] determined a relationship between the mean number of particle contacts, i.e. the coordination number, and the volume fraction of a system from computer simulation results; Figure 10.9 shows these results figuratively. From this plot coordination numbers were obtained for the range of volume fractions under consideration and values for $\alpha^{\dagger *}$ computed.

Using equation (5.53) values were calculated for the theoretical shear modulus, as a function of volume fraction, for the three systems SJP8/$C_{12}E_6$, SJP10/$C_{12}E_6$ and SJP11/$C_{12}E_6$. The theoretical results, compared with experimentally obtained results, are presented in Figures 10.10 - 10.12. The maximum packing fraction was taken to be 0.62 i.e. random packing, and the Hamaker constant 9×10^{-21}J.[199,200]

The order of magnitude of the calculated shear moduli was found to be in agreement with the values experimentally obtained but the shapes of the shear modulus versus volume fraction curves were found to be dissimilar, the experimental curves being substantially steeper. The theoretical model of Buscall[111] was based upon a colloidly stable system with a dominant repulsive potential whereas the systems under investigation in this work were weakly flocculated with an attractive potential. The static lattice model used successfully by Buscall for well dispersed colloidal dispersions was therefore clearly unsuitable for the flocculated systems under consideration here. In order to obtain a good fit, the coordination

Figure 10.9.

Mean number of particle contacts versus volume fraction as calculated by Vold[198] from computer simulation results.

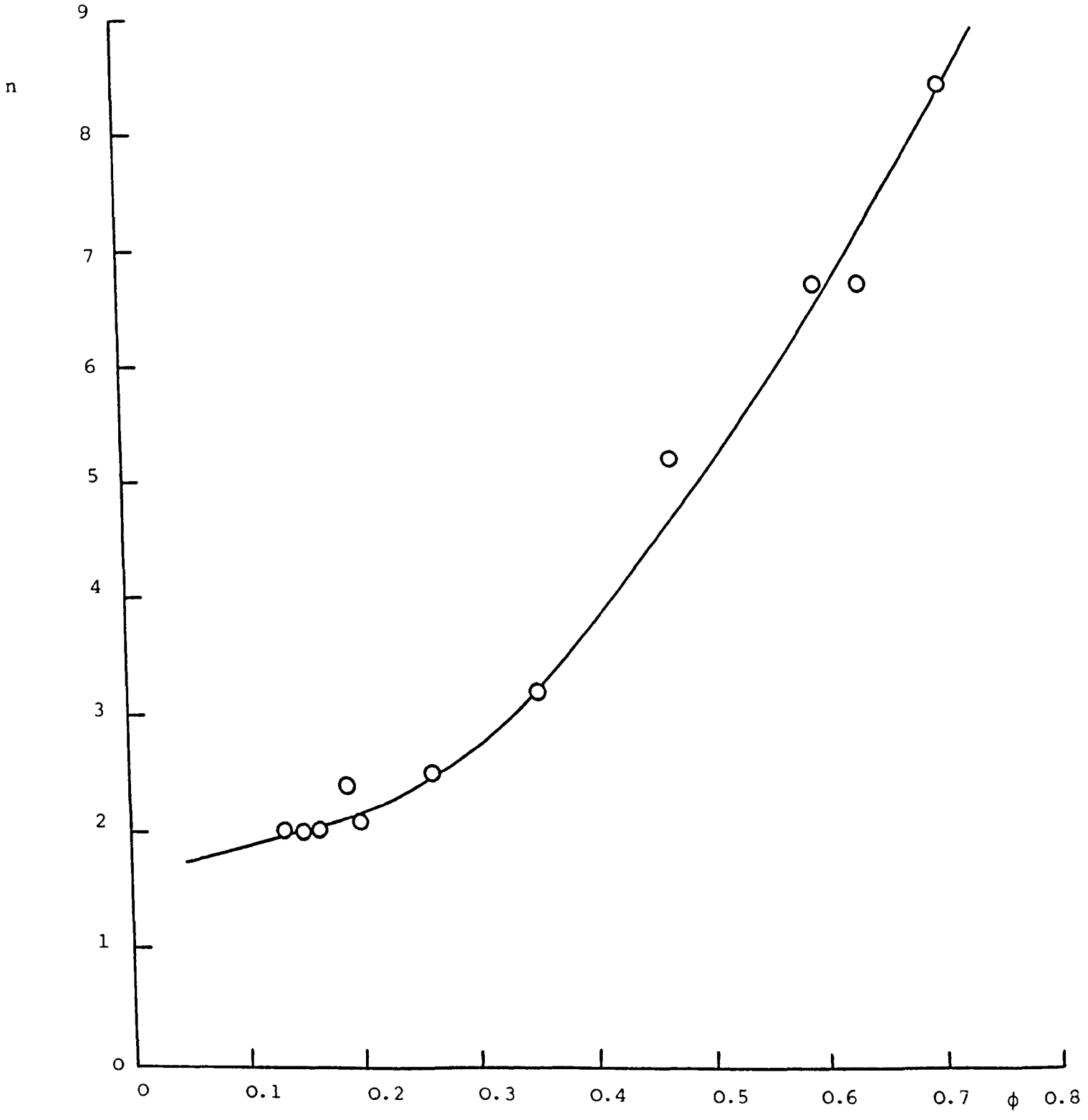

Figure 10.10.

High frequency limit shear modulus versus volume fraction for SJP8/$C_{12}E_6$ in 0.5 mol dm^{-3} sodium chloride solution. Theoretical line calculated from the equation of Buscall et al[111] with the coordination numbers calculated from Vold's computer simulation results.[198]

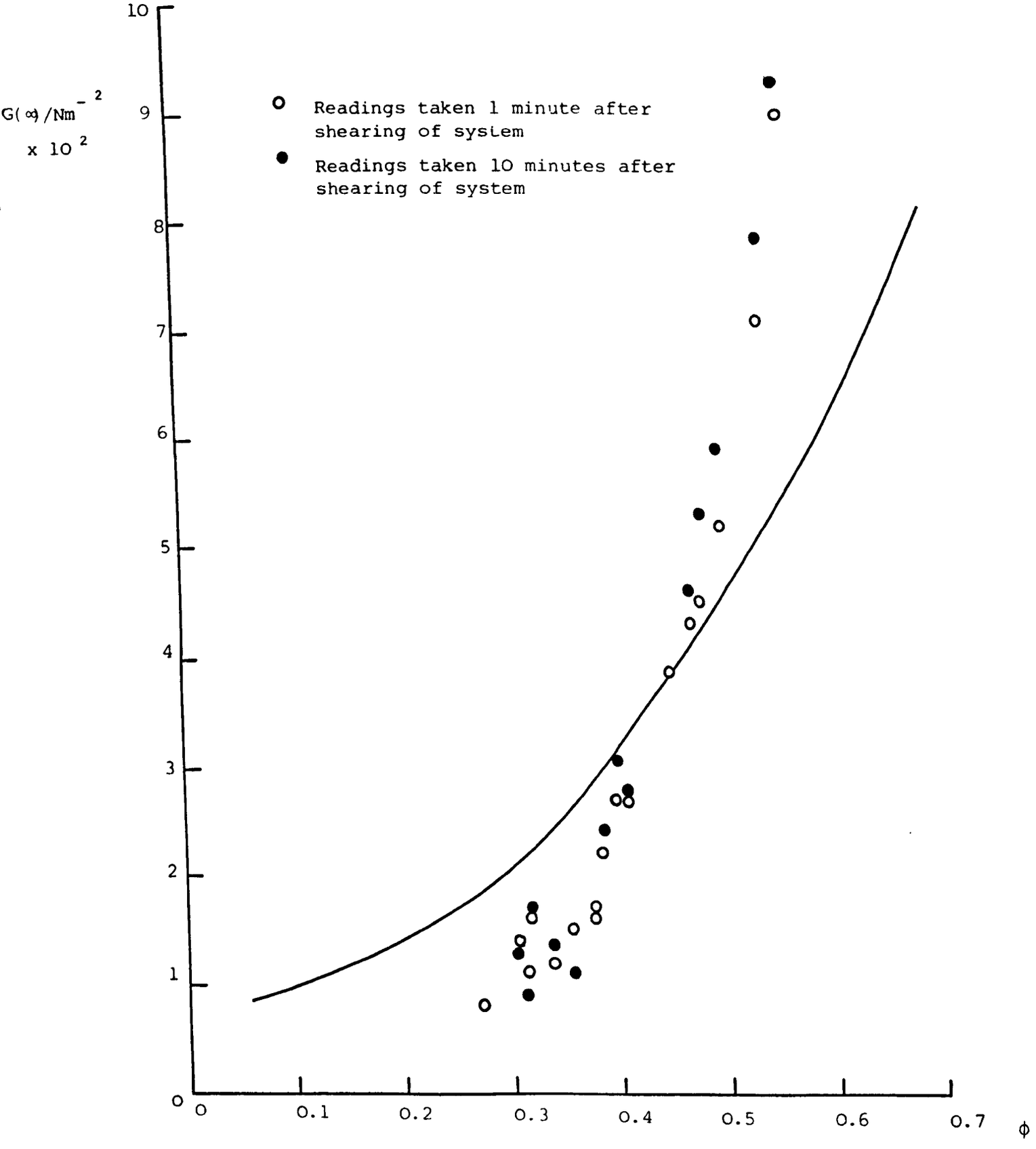

Figure 10.11.

High frequency limit shear modulus versus volume fraction for SJP10/$C_{12}E_6$ in 0.5 mol dm^{-3} sodium chloride solution. Theoretical line calculated from the equation of Buscall et al[111] with the coordination numbers calculated from Vold's computer simulation results.[198]

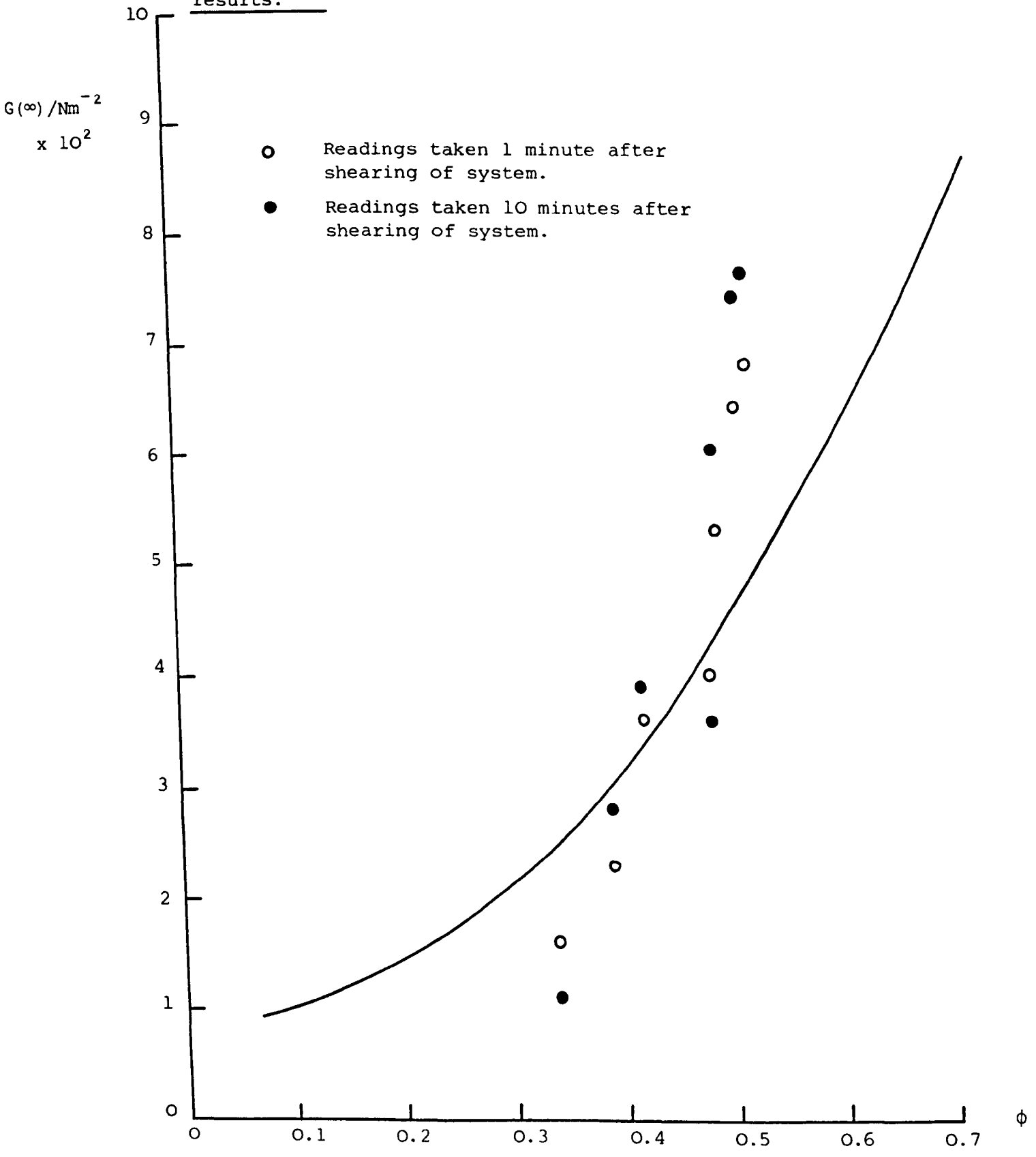

Figure 10.12.

High frequency limit shear modulus versus volume fraction for SJP11/$C_{12}E_6$ in 0.5 mol dm^{-3} sodium chloride solution. Theoretical line calculated from the equation of Buscall et al[111] with the coordination numbers calculated from Vold's computer simulation results.[198]

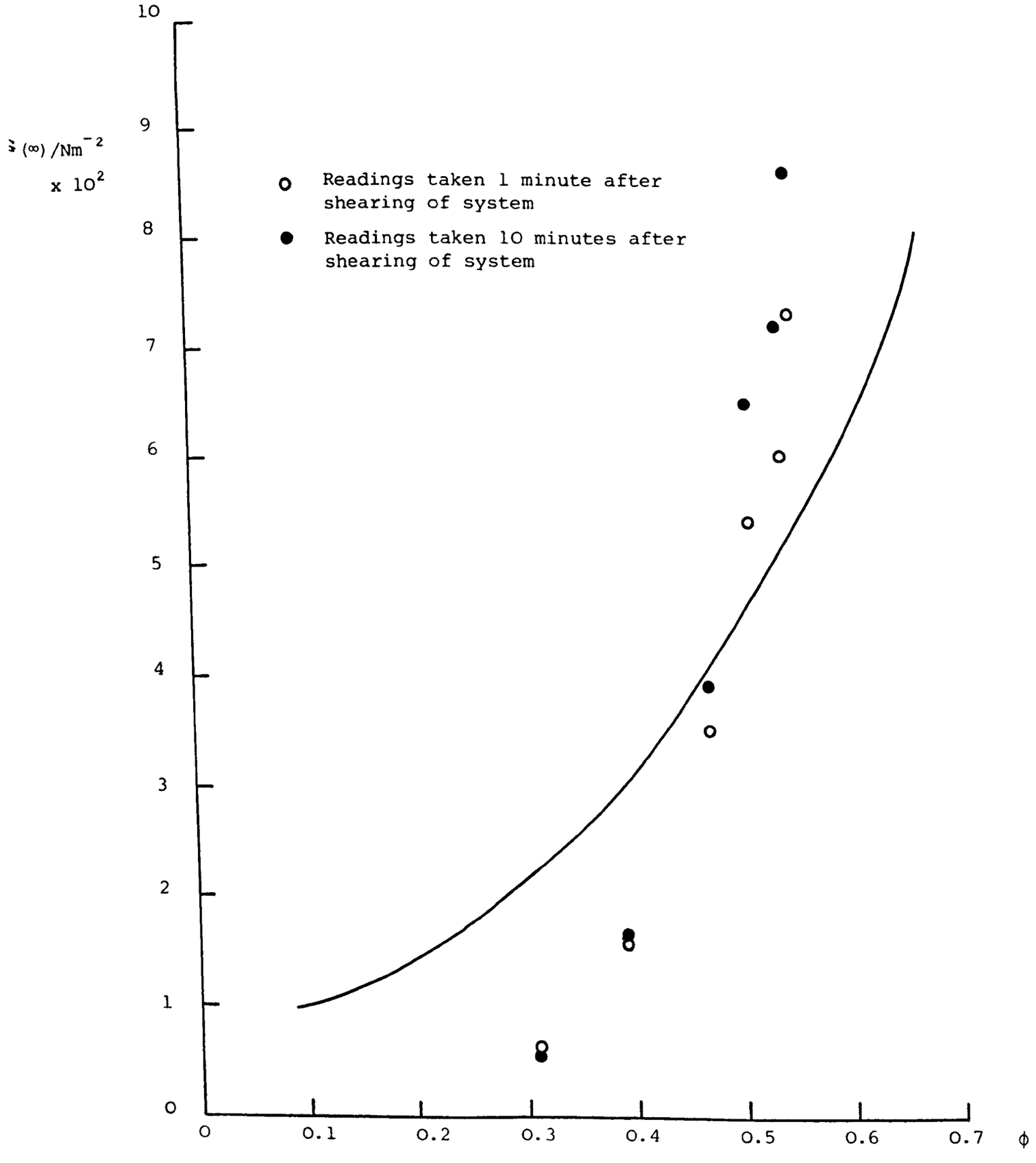

number would have to be a more rapidly increasing function of volume fraction than was indicated by Vold.[198] Vold's data was calculated for strongly flocculated systems where particles were assumed to stick on contact. In this work with more mobile weakly flocculated systems a different dependence of coordination number on volume fraction was required. Inclusion of an electrostatic repulsive term would alter the magnitude of the calculated data but not the slope of the shear modulus versus volume fraction plot.

Chapter Eleven

Continuous Shear Viscometry

Chapter Eleven. Continuous Shear Viscometry.

11.1. Introduction.

Viscosity measurements were performed using a continuous shear viscometry technique. A Deer PDR 81 Rheometer was used which had a concentric cylinder geometry as described in (2.2) and utilised a rotational mode to measure the flow properties of a system over a wide range of shear stress and shear rates.

The system studied under the application of a continuous shear stress was polystyrene latex SJP8 (particle diameter 0.94 μm) coated with a monolayer of $C_{12}E_6$ in 0.5 mol dm^{-3} sodium chloride solution. A volume fraction range of 0.2 - 0.6 was investigated.

The results obtained will be discussed briefly in (11.6) with a more detailed consideration of the systems microstructure discussed in Chapter Twelve.

11.2. The Deer Rheometer - Instrumentation.

The instrument used was a Deer PDR81 rheometer, schematically illustrated in Figure 11.1,[201] fitted with double concentric cylinder platens machined from Perspex.

The sample cell consisted of an annular slot in a solid perspex cylinder ca.50 mm in length and 50 mm in diameter, and the shear stress applied by means of a hollow Perspex cylinder lowered into the slot, with gaps on either side close to 1.5 mm.[10] The precise widths of the inner and outer gaps were scaled to give the same mean shear rate in each gap. Within each gap the shear rate varied by ca. 5%. The hollow cylinder was mounted on a spindle rotated on a low friction air

Figure 11.1.

The Deer Rheometer

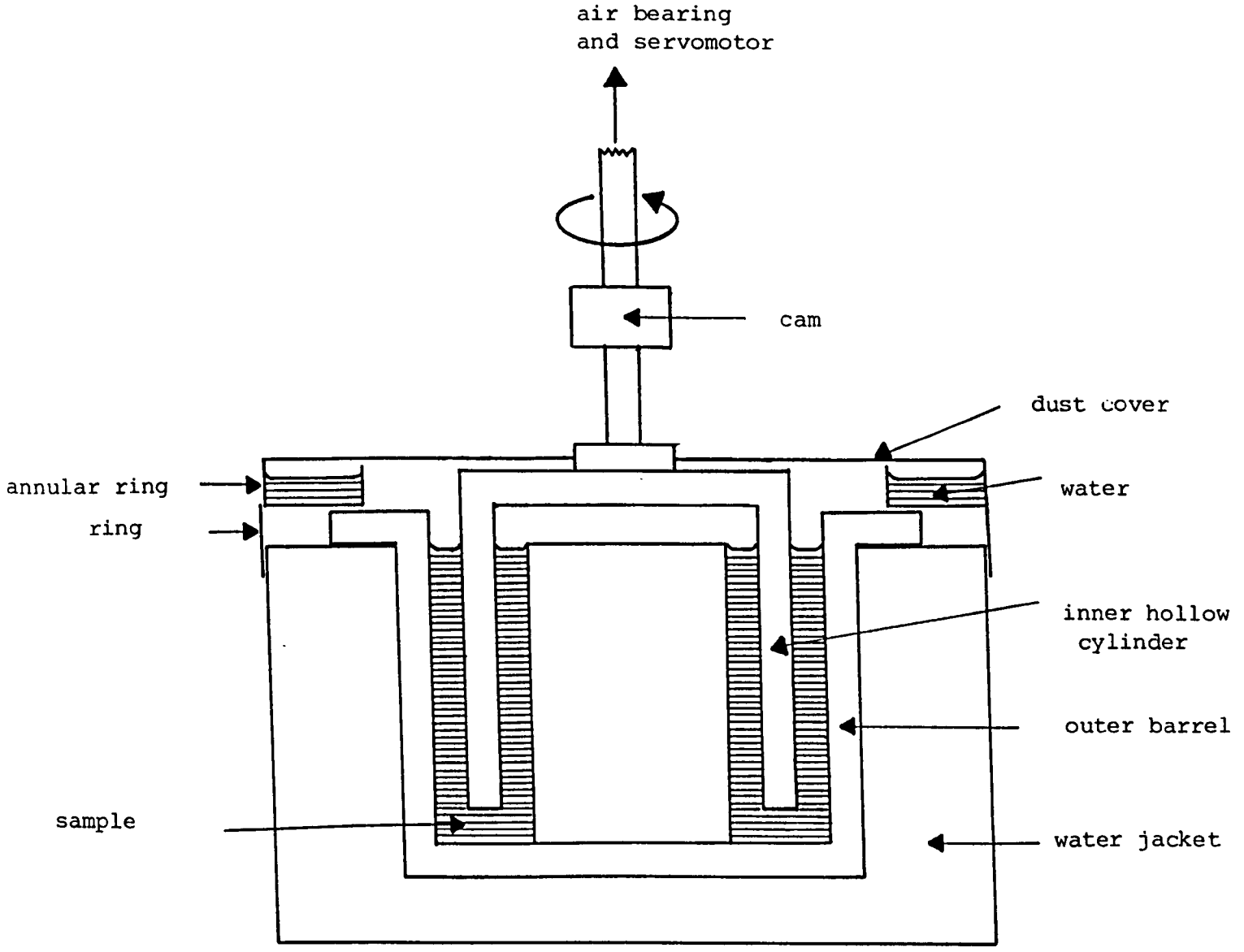

bearing and the air bearing supplied with clean air at a pressure of 55 p.s.i. through a series of filters and a pressure reducing value.[201] A servo-motor rotor was mounted on top of the spindle which enabled the rheometer to provide a constant torque, regardless of the spindle rotation rate.

The solid Perspex cylinder containing the sample was surrounded by a thermostatted water jacket maintained at a constant temperature of 25 ± 0.1°C. To prevent evaporation of the sample an annular trough containing distilled water was placed on top of the barrel; this served to maintain a constant humidity above the surface of the sample. After the hollow cylinder was lowered into the sample the trough was covered by two semi-circular plates to prevent sample evaporation and draughts. The separation between the lower edge of the inner cylinder and the interior base was set at 3 mm by means of a micrometer and an electrical indicator.

Variation of the applied torque was achieved by two helipots covering the ranges of 0 - 1 gcm and 0 - 10 gcm and push buttons enabled application and removal of the torque. The torque was converted to the shear stress by means of a calibration constant described in (11.3).

Angular velocities at high rates of rotation (> 0.1 $rads^{-1}$) were measured directly from a meter on the console. The velocities were converted from an oscillating electrical signal generated by a tachometer disc and a photoelectric cell on the rheometer.

In order to measure angular velocities at low shear rates the 'creep mode' of measurement was utilised.[202] For this, the control console was connected to a variable sensitivity displacement- time chart recorder. Angular velocities were then recorded as a function of the position of a double-headed cam located on the spindle near the base of the driving unit. The angular velocities were determined from the gradient of the linear portion of the curve.

By using an instrument constant, described in (11.3), which included the barrel and cylinder dimensions, the angular velocities were converted to shear rates.

11.3. Calibration of the instrument.

Two calibration constants had to be determined for the Deer rheometer, one to convert the angular velocity, ω, to the shear rate, $\dot{\gamma}$, and the other to convert the torque, T^*, to the shear stress, τ.

The shear rate may be given by:

$$\dot{\gamma} = \frac{r_c \omega}{\delta^1} = \alpha_D \omega \qquad (11.1)$$

where r_c = radius of cylinder

δ^1 = distance between cylinder and barrel walls

ω = angular velocity of the cylinder

α_D = calibration constant.

The calibration constant for the cell used in this work was 15.41.

The shear stress may be given by

$$\tau = \beta_D T^* \qquad (11.2)$$

The calibration constant, β_D, was determined using 40% w/w and 60% w/w sucrose solutions of known viscosity.[203] In both cases the angular velocity, and hence the shear rate, was measured as a function of applied torque and plots made of torque versus shear rate. The gradient of the stress versus shear rate plot was the viscosity of the solutions, η, see (2.1). The viscosity of both 40% w/w and 60% w/w sucrose solution at 25°C has been accurately determined to be

5.206×10^{-3} Nsm^{-2} and 4.402×10^{-2} Nsm^{-2} respectively.[203]

The calibration constants determined for the two solutions were 0.34 and 0.33, in very good agreement. The value taken throughout the work was 0.335.

Therefore:

$$\dot{\gamma} = 15.41\ \omega \qquad (11.3)$$

$$\tau = 0.335\ T^{*} \qquad (11.4)$$

In order for the creep mode of measurement to be used for determining the viscosity at low shear rates, the control console of the rheometer was connected to a Bryans Southern Instrument chart recorder, model number 28000. This had to be calibrated in terms of the vertical deflection; the horizontal deflection was the time, already calibrated from the known velocity of the operation of the chart recorder.

The chart recorder was set at a sensitivity of 25V and a torque applied to the Deer rheometer so that a sawtooth output was obtained on the recorder. The full scale deflection was measured and found to be 11.95 cm. Stiles[202] has calculated that full scale deflection of the peaks obtained on this recorder at 25V was equivalent to 0.662 π radians. Hence 1 cm vertical deflection was taken to be 0.0554 π radians.

11.4. Experimental.

The Deer rheometer cell was allowed to attain temperature equilibrium before the measurements commenced; approximately an hour was allowed for this purpose. The bias on the air bearing was also reset daily; the cylinder was lowered into the empty barrel and the cam freed to allow cylinder rotation. The bias was then adjusted until no angular

velocity showed on the meter or on the chart recorder, a slight torque in one direction was countered by an electrically applied torque in the other.

The system under investigation was then added to the annular slot in the barrel, the cylinder carefully lowered into position, the perspex covers added and the sample left for thirty minutes for temperature equilibration. A sample volume of 30 cm^3 was used, this was sufficient to fill the annular slot after the inner cylinder was lowered with a slight overspill onto the top of the inner barrel to ensure that the annular slot was exactly full in each measurement. This was important as the angular velocity achieved as the result of an applied torque is dependent upon the amount of system resisting the rotation. Likewise it was important to ensure that the inner cylinder was lowered to the same depth for every measurement.

A stress, in the form of a torque, was then applied to the inner cylinder and the resultant shear rate (angular velocity) measured either from the chart recorder or directly off the meter. The stress was gradually increased and the shear rate determined as a function of shear stress. The torque was increased from low values to high values rather than decreased as high torques caused a disruption in the system which would affect the low stress creep measurements. The applied torque range was 0.0001 to 10 g.cm (3.35×10^{-5} to 3.35 Nm^{-2}), the angular velocity range 0 - 20 $rads^{-1}$ (0 - 308 s^{-1}).

11.5. Results.

The results, for each SJP8/$C_{12}E_6$/NaCl system measured, were plotted as shear stress as a function of shear rate, with the gradient of the linear section of the curves corresponding to the coefficient of

viscosity, η, of the system. The plots obtained all showed pseudo-plastic behaviour, as described in (2.2) and hence Bingham yield stress values, τ_B, were obtained for each system. At high shear stresses a sudden increase in viscosity was observed, the shear rate at which this occurred, $\dot{\gamma}_{critical}$, was also noted. Figures 11.2 and 11.3 show typical shear stress versus shear rate curves for the system under investigation. Table 11.1 presents values for the viscosity, the Bingham yield stress, the critical shear rate and the critical shear stress, all at the different volume fractions considered.

11.6. Discussion.

The results were plotted in the form of the rheograms described in (2.2) as $\log_{10}$ viscosity versus $\log_{10}$ shear stress. Typical rheograms are presented in Figures 11.4 and 11.5 for the system at two volume fractions. The shape obtained for the rheograms is that described in (2.2) with the four distinct regions illustrated in Figure 2.13. Plateau values for the viscosity were obtained at low and high shear corresponding to the zero shear viscosity, $\eta(0)$, and the high shear limiting viscosity, $\eta(\infty)$. The values obtained for these are presented in Table 11.2 for the system at all the volume fractions investigated. The values for $\eta(0)$ were measured using the Creep mode and required a very sensitive response from the instrument. Some scatter may be observed in the data at the very low shear stresses due to working at the limit of apparatus. The best plateaus were drawn through the points and the $\eta(0)$ values taken from these. The values for $\eta(\infty)$ were taken to be the minimum viscosity measured. At high volume fractions the torque range of the rheometer was insufficient to detect this and values for $\eta(\infty)$ were extrapolated values. It must be noted that due to the shear thickening response at high shear stresses the limiting value for $\eta(\infty)$ may not have been attained.

Figure 11.2.

Shear stress/Nm^{-2} versus shear rate/s^{-1} for polystyrene latex SJP8/$C_{12}E_6$ in 0.5 mol dm^{-3} sodium chloride solution at ϕ = 0.34 at 25°C.

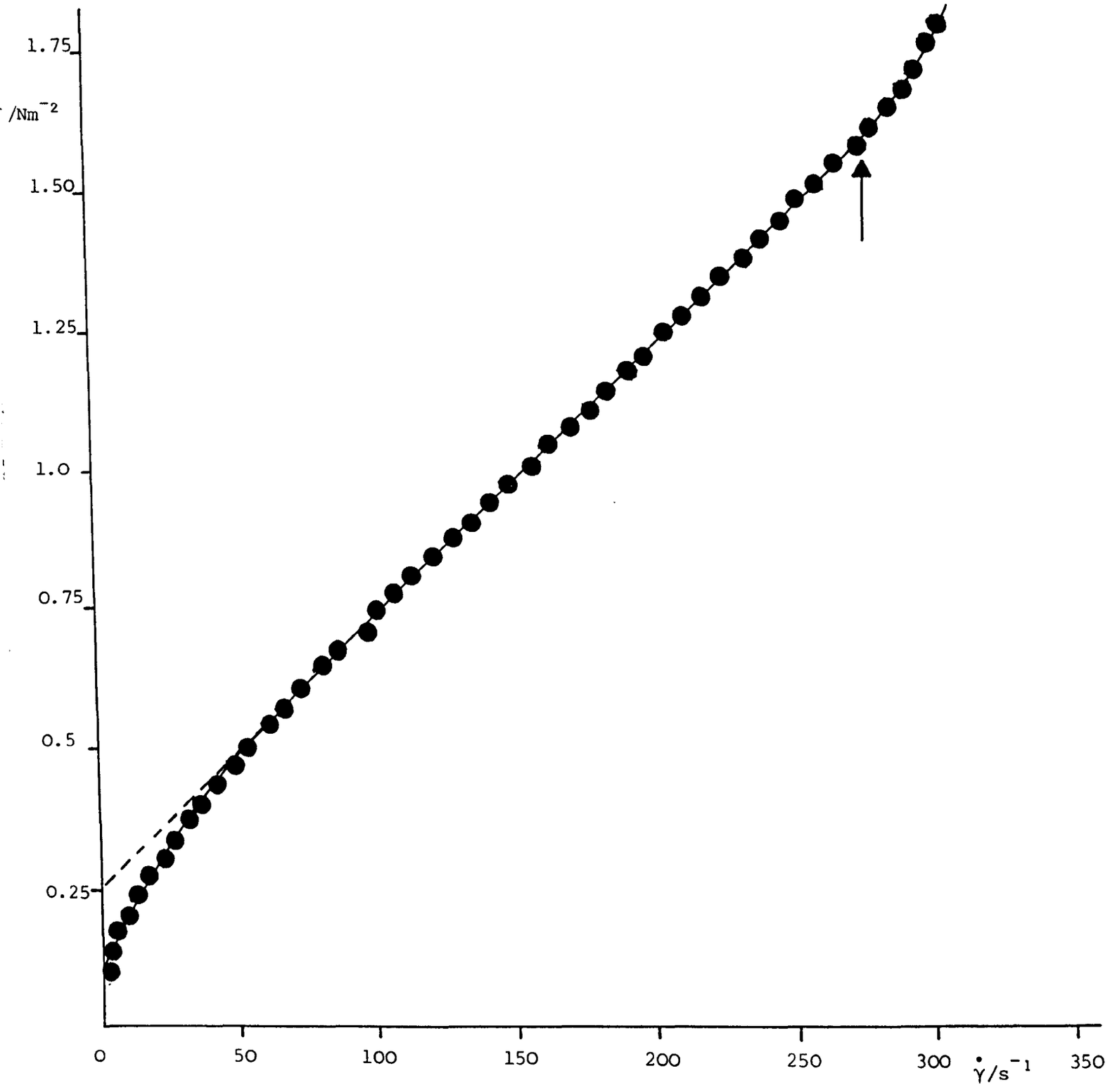

Figure 11.3.

Shear stress/Nm^{-2} versus shear rate/s^{-1} for polystyrene latex SJP8/$C_{12}E_6$ in 0.5 mol dm^{-3} sodium chloride solution at ϕ = 0.56 at 25°C.

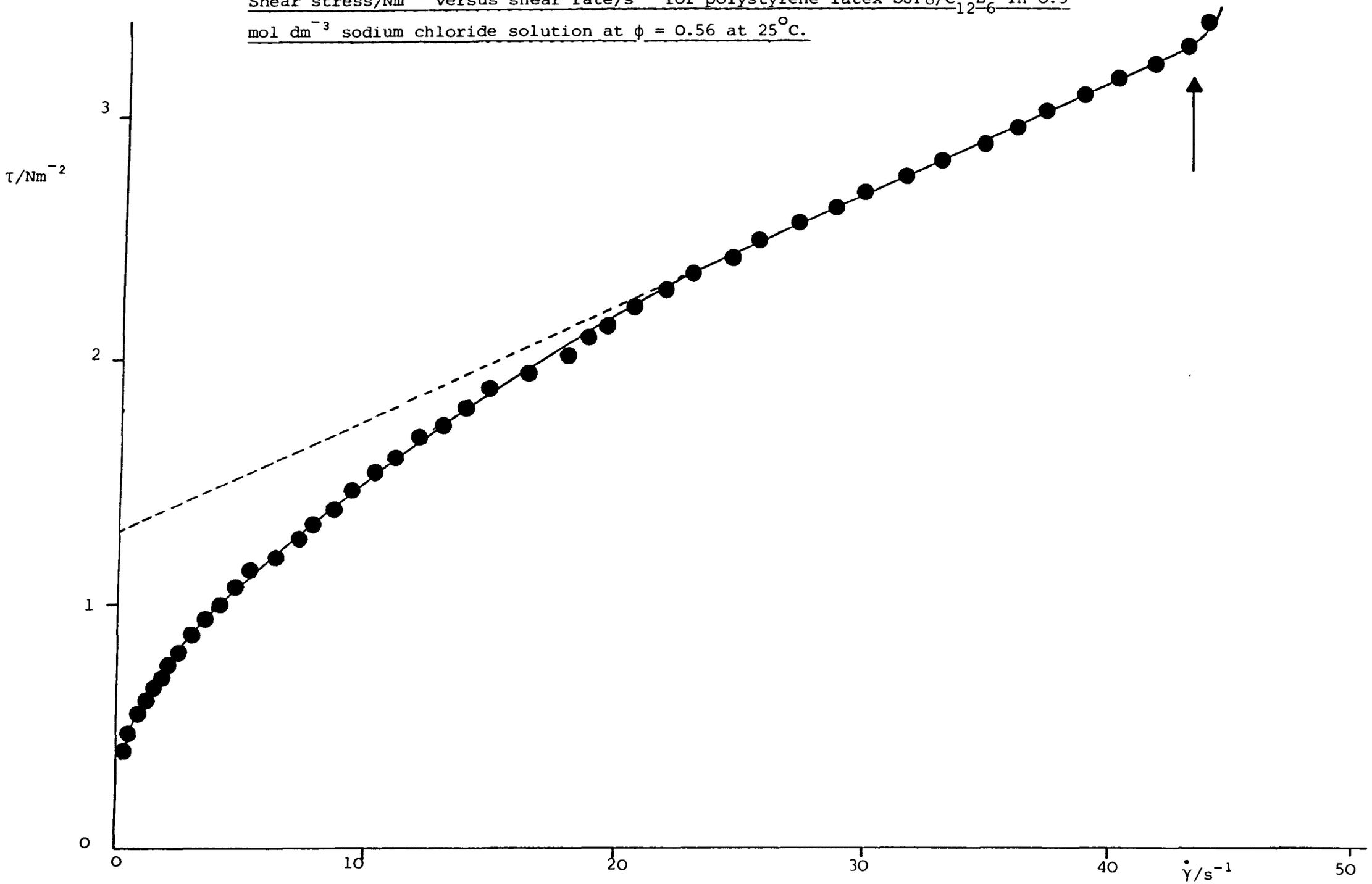

Table 11.1.

Viscosities/Nsm^{-2}, Bingham yield stresses/Nm^{-2} and shear rates/s^{-1} and shear stresses/Nm^{-2} at the onset of unsteady flow for polystyrene latex SJP8/$C_{12}E_6$ in 0.5 mol dm^{-3} sodium chloride solution at 25°C at various volume fractions.

ϕ	η/Nsm^{-2}	τ_B/Nm^{-2}	$\gamma_{critical}/s^{-1}$	$\tau_{critical}/Nm^{-2}$
0.21	2.73×10^{-3}	0.05	143	0.44
0.23	2.54×10^{-3}	0.08	155	0.49
0.25	3.13×10^{-3}	0.14	207	0.79
0.27	3.85×10^{-3}	0.15	240	1.06
0.31	3.90×10^{-3}	0.21	220	1.09
0.315	3.70×10^{-3}	0.21	228	1.07
0.32	4.22×10^{-3}	0.23	286	1.46
0.34	4.78×10^{-3}	0.26	296	1.70
0.36	4.71×10^{-3}	0.29	300	1.74
0.38	6.04×10^{-3}	0.30	-	-
0.39	6.25×10^{-3}	0.36	-	-
0.40	7.25×10^{-3}	0.33	-	-
0.41	7.42×10^{-3}	0.36	-	-
0.45	9.62×10^{-3}	0.42	-	-
0.47	0.012	0.53	-	-
0.48	0.013	0.52	-	-
0.50	0.021	0.74	-	-
0.54	0.036	0.83	-	-
0.56	0.046	1.31	-	-

Figure 11.4.

$\log_{10}$ viscosity/Nsm^{-2} versus $\log_{10}$ shear stress/Nm^{-2} for polystyrene latex SJP8/$C_{12}E_6$ in 0.5 mol dm^{-3} sodium chloride solution, ϕ = 0.21 at 25°C.

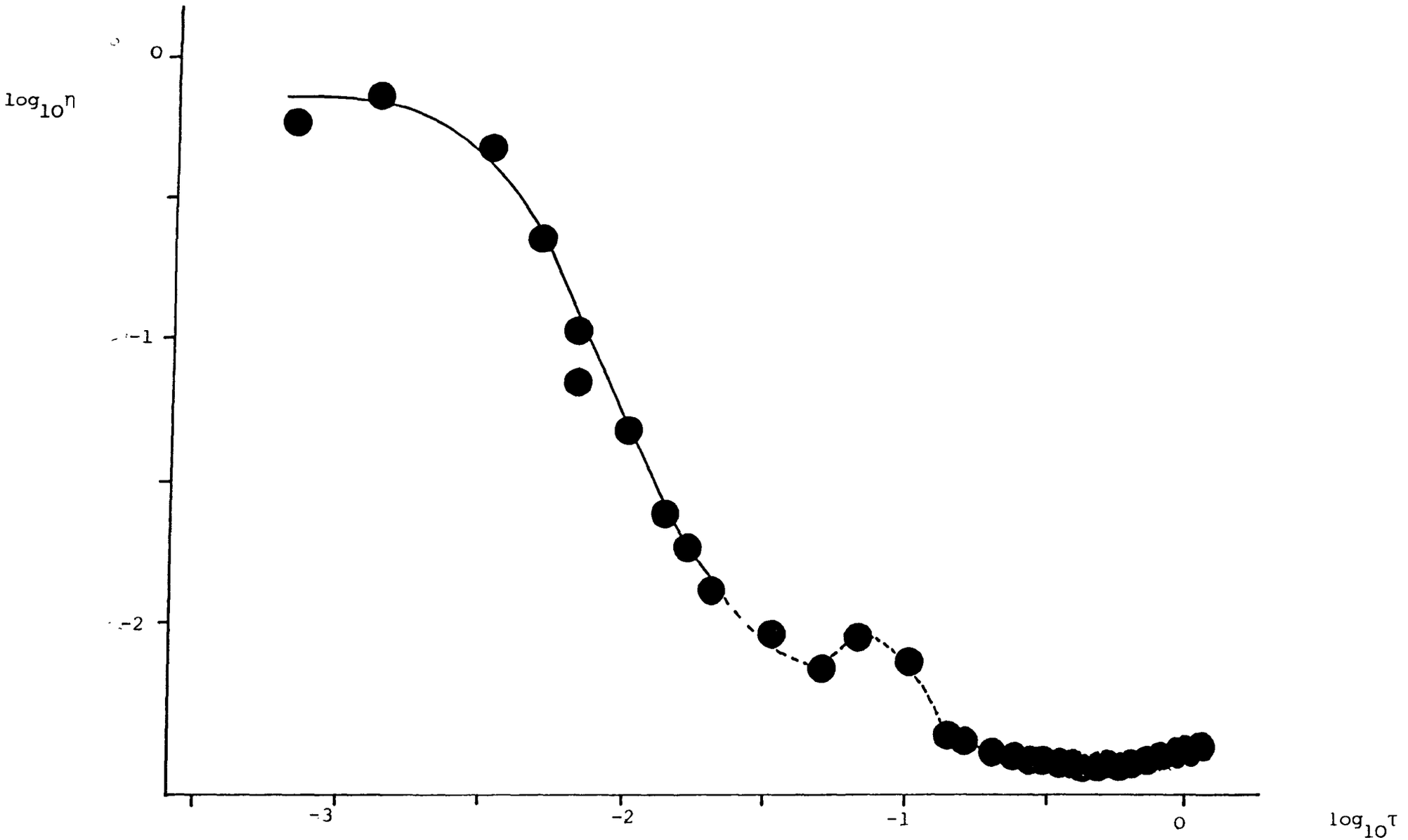

Figure II.5.

$\log_{10}$ viscosity/Nsm^{-2} versus $\log_{10}$ shear stress/Nm^{-2} for polystyrene latex SJP8/$C_{12}E_6$ in 0.5 mol dm^{-3} sodium chloride solution, ϕ = 0.36 at 25°C.

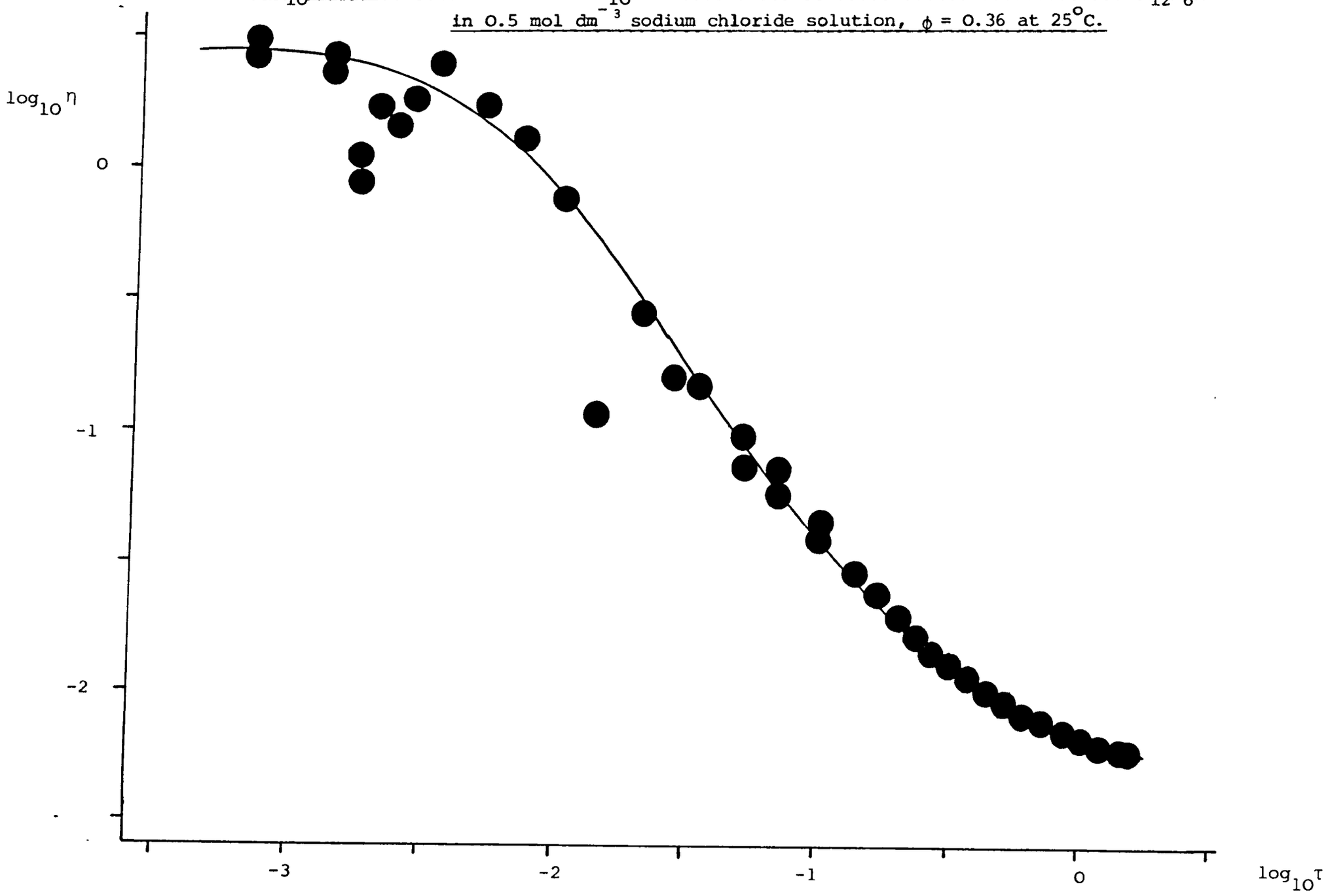

Table 11.2.

Zero shear limiting viscosities/Nsm^{-2} and high shear limiting viscosities, Nsm^{-2} for polystyrene latex SJP8/$C_{12}E_6$ in 0.5 mol dm^{-3} sodium chloride solution at 25°C at various volume fractions.

ϕ	$\eta(0)/Nsm^{-2}$	$\log_{10}\eta(0)$	$\eta(\infty)/Nsm^{-2}$	$\log_{10}\eta(\infty)$	
0.21	0.78	-0.11	3.02×10^{-3}	- 2.52	
0.23	0.83	-0.08	3.09×10^{-3}	- 2.51	
0.25	1.00	0	3.80×10^{-3}	- 2.42	
0.27	1.58	0.2	4.68×10^{-3}	- 2.33	
0.31	1.29	0.11	4.79×10^{-3}	- 2.32	
0.315	1.86	0.27	4.68×10^{-3}	- 2.33	
0.32	2.51	0.4	5.01×10^{-3}	- 2.30	
0.34	-	-	5.50×10^{-3}	- 2.26	
0.36	2.75	0.44	5.89×10^{-3}	- 2.23	
0.38	2.63	0.42	7.08×10^{-3}	- 2.15	
0.39	3.16	0.5	7.59×10^{-3}	- 2.12	
0.40	7.94	0.9	8.51×10^{-3}	- 2.07	
0.41	6.31	0.8	8.91×10^{-3}	- 2.05	
0.45	13.80	1.14	0.011	- 1.94	
0.47	14.13	1.15	0.015	- 1.83	
0.48	19.95	1.30	0.014	- 1.84	*
0.50	36.31	1.56	0.022	- 1.66	*
0.54	95.50	1.98	0.038	- 1.42	*
0.56	446.68	2.65	0.071	- 1.15	*

* extrapolated values.

The viscosity values obtained at low shear stresses were considerably higher than the viscosities measured at high shear. At low shear the slow relaxation of the applied stress, i.e. the high viscosity values, were a function of the restricted diffusive motion of the particles caused by the attractive colloidal interaction forces as described in (5.5).

At higher stresses marked shear thinning occurred which may be attributed to the transition from a three dimensional to a two dimensional microstructure as described by Hoffman,[109] see (5.5). Shear thinning occurred as the applied stresses became sufficiently high to alter the systems microstructure and the extent of shear thinning may be taken as an indication of the strength of the interparticle interactions. An unusual feature of the data was a step that occurred in this shear thinning region. It occurred consistently at each volume fraction studied though at different stress levels. It was thought that this might indicate some form of structural rearrangement within the system though the precise nature of this is unclear. This effect has been previously noted.[204]

At higher stresses still the hydrodynamic forces became much greater than the colloidal forces and hence controlled the structure. This was seen from the low value of $\eta(\infty)$ which was indicative of single particles being the flow unit. It was possible that a 'layered' flow occurred as was observed by Hoffman[109] with other latex systems and described in (5.5).

As the shear stress was further increased a shear thickening response was observed in the lower volume fraction systems. The range of the Deer rheometer was insufficiently high to detect such a response in the higher volume fraction systems but it was assumed to occur beyond the range of the instrument. The values obtained for the shear stress at

the onset of shear thickening were plotted as a function of volume fraction and presented in Figure 11.6. A straight line was obtained. The Reynolds number is characteristic of a particular measuring element and is the dimensionless ratio of inertial to viscous forces, i.e. it is proportional to $\dot{\gamma}^2_{crit}/\tau_{crit}$. A plot was constructed of $\dot{\gamma}^2_{crit}/\tau_{crit}$ versus volume fraction and a horizontal line was obtained as illustrated in Figure 11.7. This was evidence that the shear thickening behaviour observed was due to turbulence as a result of eddies and vortices forming at a critical viscosity for the geometry and dimensions of the Deers measuring cell and not due to some other effect.

Creep compliance measurements were performed at low shear stresses and the response of the systems on the removal of the applied stress was indicative of viscoelastic behaviour, as described in (2.2). Most of the energy was found to be lost as a result of an irreversible deformation and a viscous flow. A little energy was stored showing that the systems had some elasticity.

Buscall and McGowan[2], working with polystyrene latex flocculated with a cellulosic adsorbate, plotted their viscosity data in normalised form, i.e. in rheograms of normalised viscosity, η_{norm}, versus $\log_{10}$ shear stress. Values for the normalised viscosity were determined from:

$$\eta_{norm} = \frac{\eta(\tau) - \eta(\infty)}{\eta(0) - \eta(\infty)} \qquad (11.5)$$

where $\eta(\tau)$ is the viscosity at any stress. They found that their normalised viscosity data could be fitted to one curve at volume fractions below 0.36 and that at higher volume fractions the lower Newtonian region moved out to higher stresses.

The viscosity data obtained in this work was normalised using equation (11.5) and a typical normalised data plot is presented in

Figure II.6.

Shear stress at the onset of shear thickening/Nm^{-2} versus volume fraction for polystyrene latex SJP8/$C_{12}E_6$ in 0.5 mol dm^{-3} sodium chloride solution at 25°C.

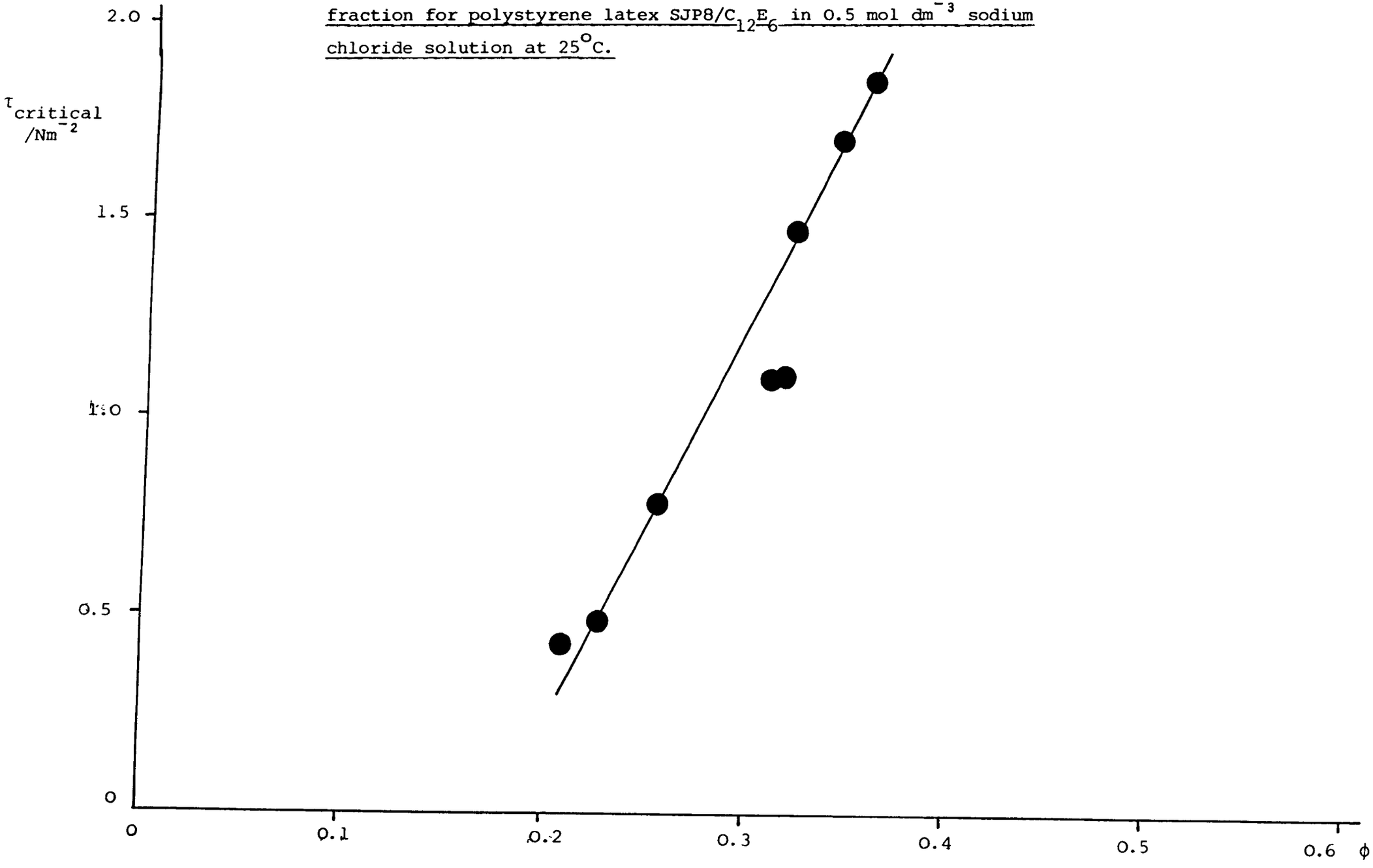

Figure 11.7.

Reynolds Number at the onset of unsteady flow versus volume fraction.

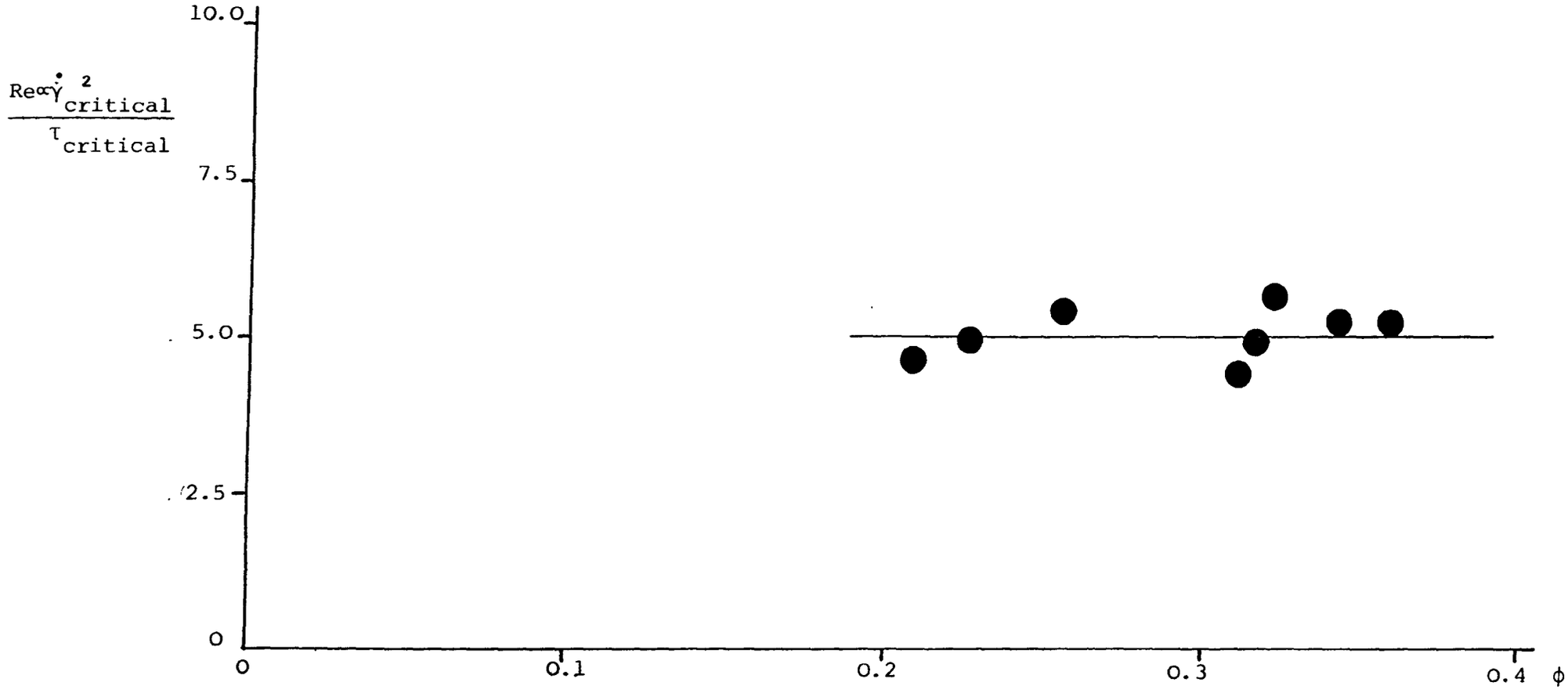

Figure 11.8. From such a plot it was possible to determine values for the stress at the onset of shear thinning, τ^*; the values obtained for the system under investigation at a range of volume fractions are presented in Table 11.3. To see if the same result was obtained as that of Buscall and McGowan all the data obtained for the system at different concentrations was plotted together in Figure 11.9. From this it can be seen that below a volume fraction of approximately 0.4 all the data grouped together in one zone. The fit obtained here to one curve was not as good as that of Buscall but a similar trend was observed. At higher volume fractions the viscosity data shifted to higher stress values as found by Buscall.

The values obtained for the viscosity, the Bingham yield stress, the zero shear rate viscosity, $\log_{10}$ zero shear rate viscosity, the high shear rate limiting viscosity, $\log_{10}$ high shear rate limiting viscosity and the shear stress at the onset of shear thinning were also considered as a function of volume fraction. The plots obtained are presented in Figures 11.10 to 11.16. It can be seen from all the plots that at a volume fraction of approximately 0.4 - 0.5 all the properties experienced a sudden change in trend, and all the gradients increased dramatically. Clearly at a volume fraction of approximately 0.4 - 0.5 a large change in the microstructure occurred. This will be considered more fully in Chapter Twelve.

Krieger and Dougherty[82] have developed an expression to describe the volume fraction dependence of the viscosity of a particulate dispersion and this is given by equation (5.13):

$$\eta_r = \left(1 - \frac{\phi}{\phi_m}\right)^{-[\eta]\phi_m}$$

For a hard sphere system the intrinsic viscosity has the value of 2.5

Figure 11.8.

Normalised viscosity versus $\log_{10}$ shear stress/Nm^{-2} for polystyrene latex SJP8/$C_{12}E_6$ in 0.5 mol dm^{-3} sodium chloride solution, ϕ = 0.36 at 25°C.

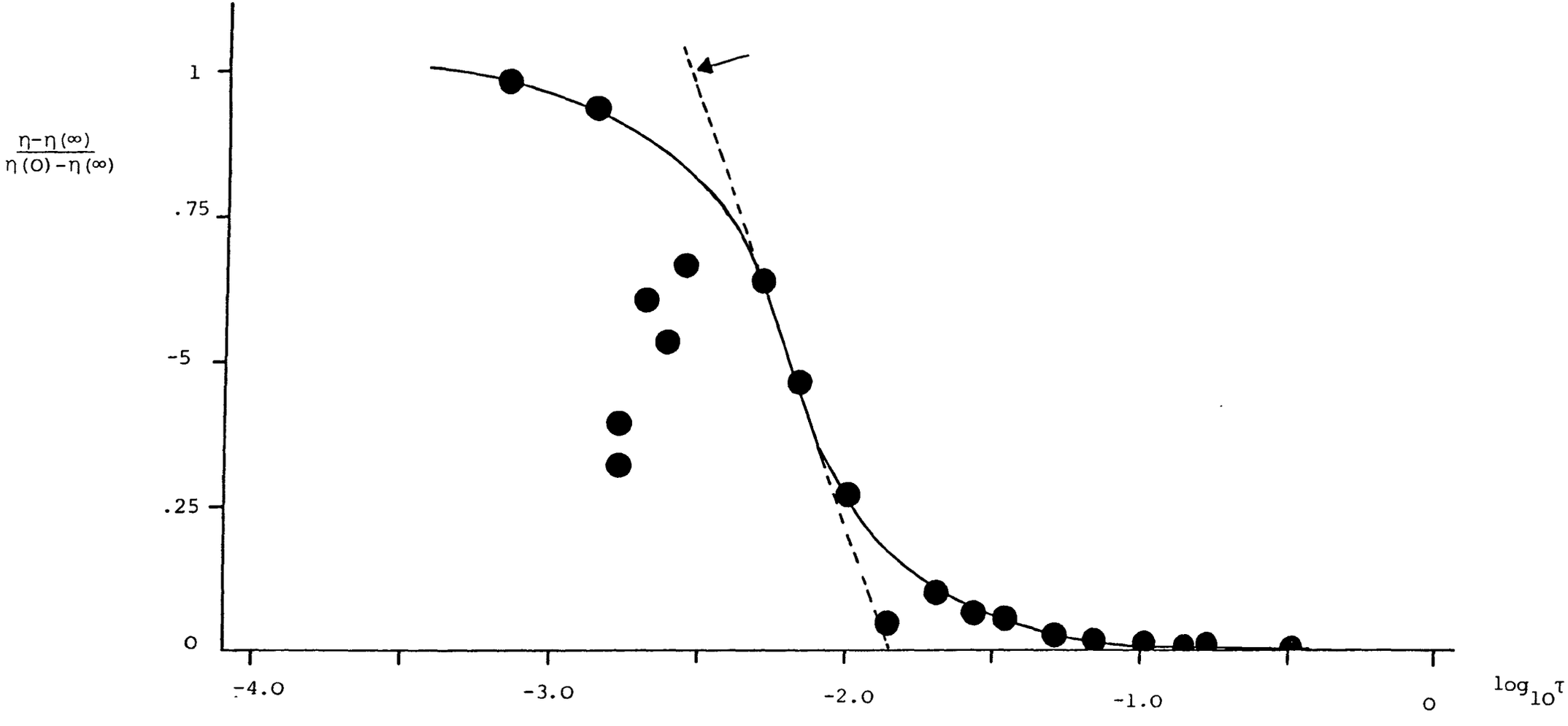

Table 11.3.

Shear stress at the onset of shear thinning/Nm^{-2} for polystyrene latex SJP8/$C_{12}E_6$ in 0.5 mol dm^{-3} sodium chloride solution at 25°C at various volume fractions.

ϕ	τ^*/Nm^{-2}
0.21	1.68×10^{-3}
0.23	4.90×10^{-3}
0.25	3.69×10^{-3}
0.31	2.75×10^{-3}
0.315	2.40×10^{-3}
0.32	1.62×10^{3}
0.36	2.75×10^{-3}
0.38	2.00×10^{-3}
0.40	3.16×10^{-3}
0.47	5.41×10^{-3}
0.56	0.033

Figure 11.9.

Normalised viscosity versus $\log_{10}$ shear stress/Nm^{-2} for polystyrene latex SJP8/$C_{12}E_6$ in 0.5 mol dm^{-3} sodium chloride solution at 25°C at various volume fractions.

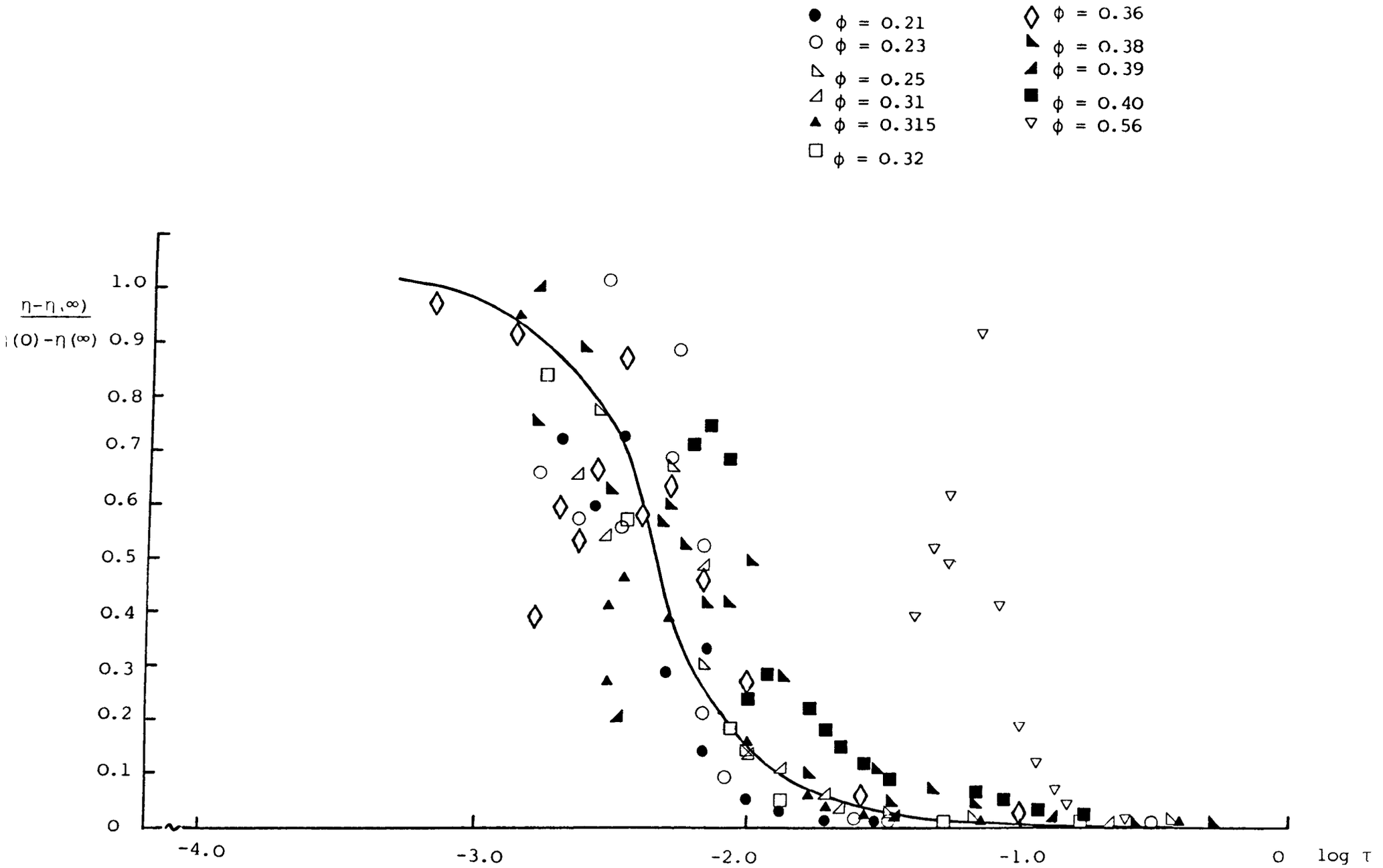

Figure 11.10.

Viscosity/Nm^{-2} versus volume fraction for polystyrene latex SJP8/$C_{12}E_6$ in 0.5 mol dm^{-3} sodium chloride solution at 25°C.

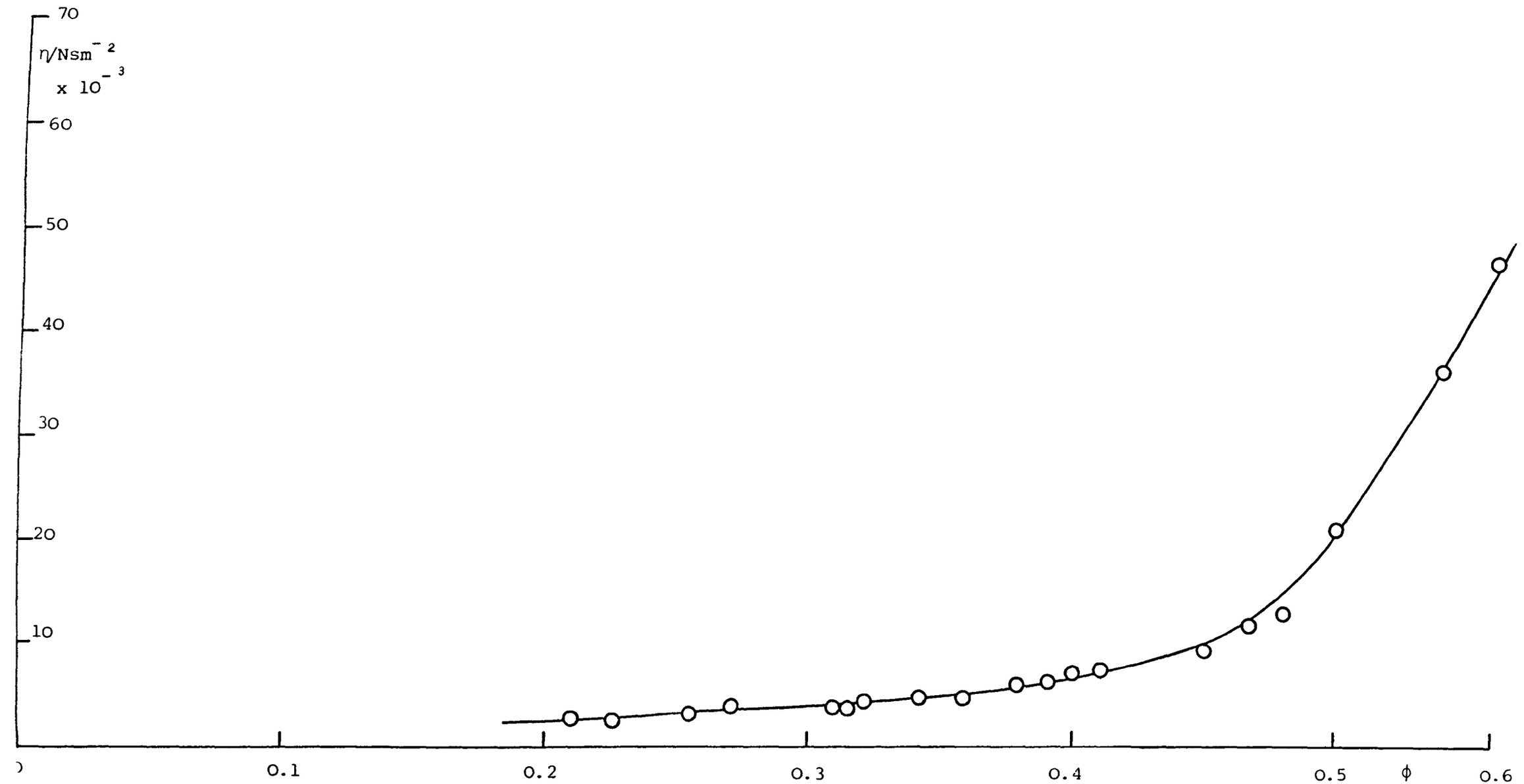

Figure 11.11.

Bingham yield stress/Nm^{-2} versus volume fraction for polystyrene latex SJP8/$C_{12}E_6$ in 0.5 mol dm^{-3} sodium chloride solution at 25°C.

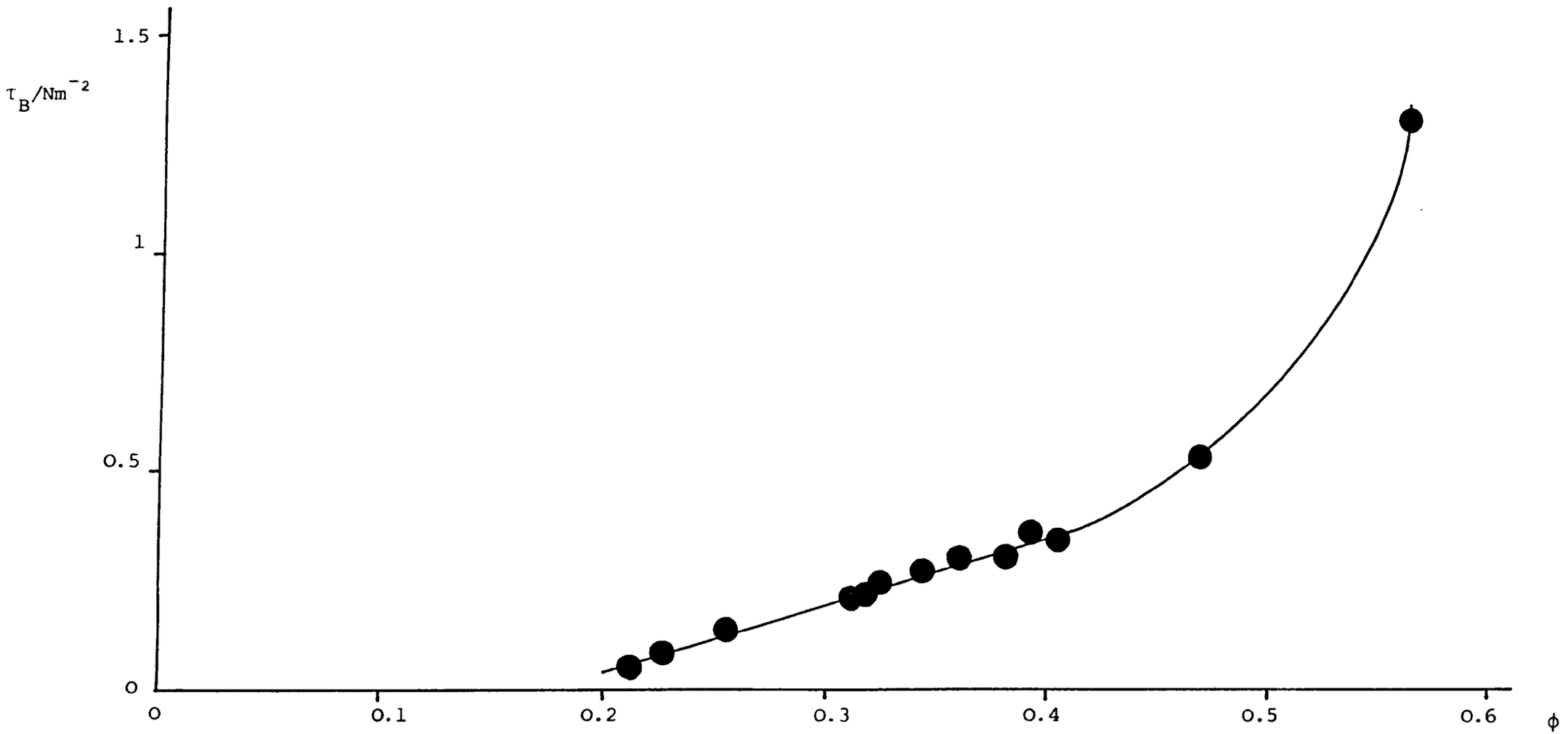

Figure 11.12.

Zero shear rate viscosity/Nsm^{-2} versus volume fraction for polystyrene latex SJP8/$C_{12}E_6$ in 0.5 mol dm^{-3} sodium chloride solution at 25°C.

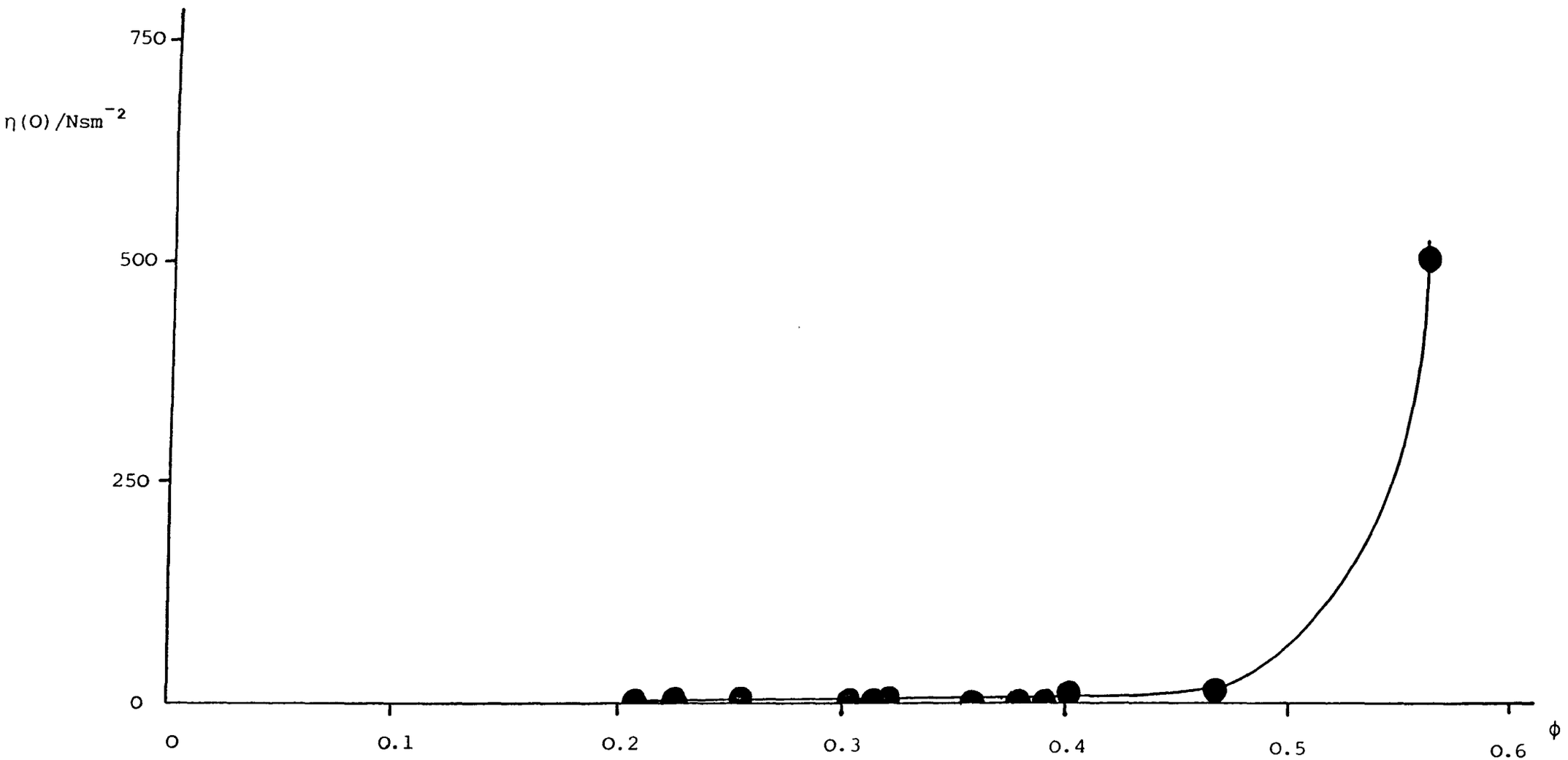

Figure 11.13.

Log_{10} zero shear viscosity/Nsm^{-2} versus volume fraction for polystyrene latex SJP8/$C_{12}E_6$ in 0.5 mol dm^{-3} sodium chloride solution at 25°C.

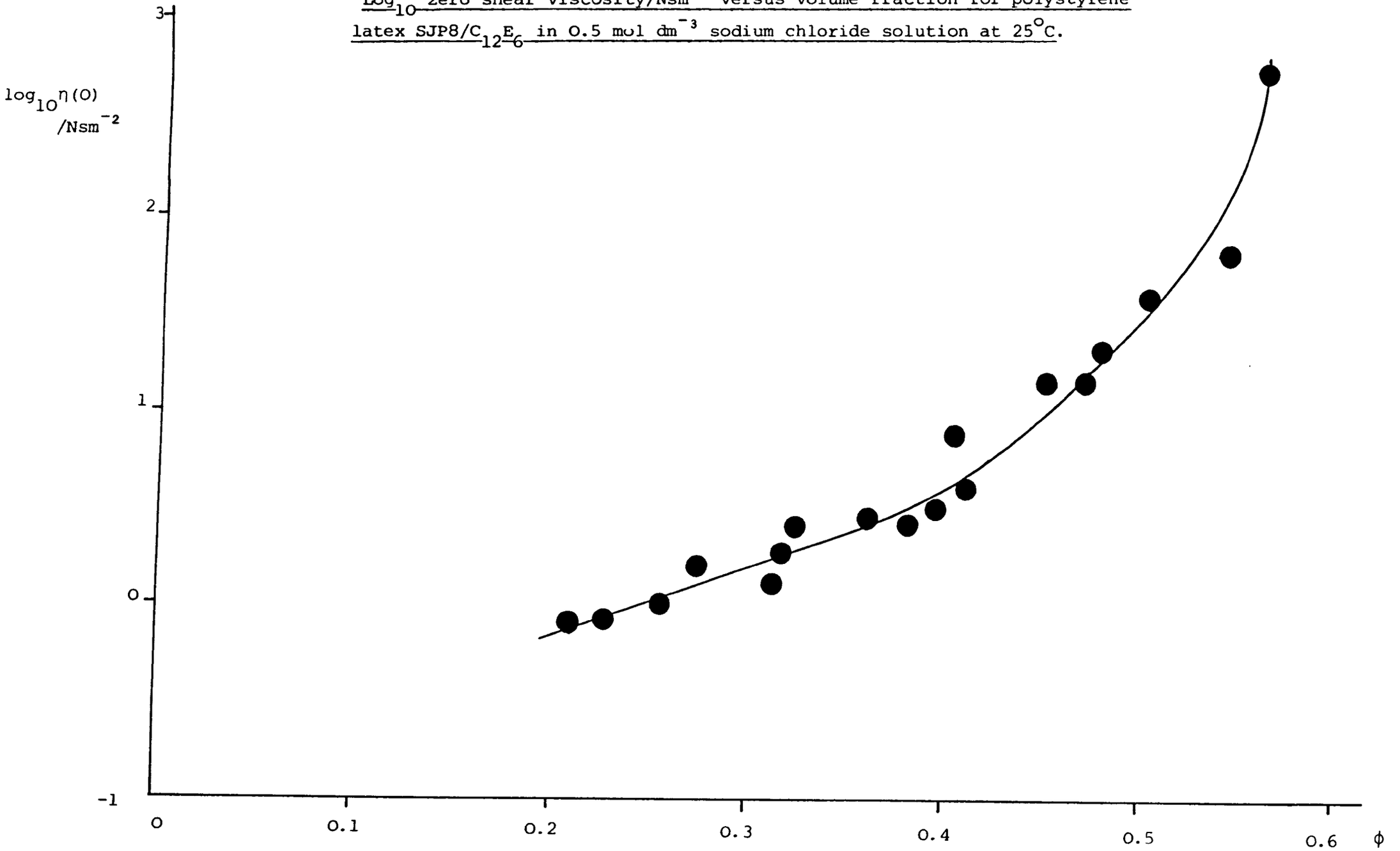

Figure 11.14.

High shear limiting viscosity/Nsm^{-2} versus volume fraction for polystyrene latex SJP8/$C_{12}E_6$ in 0.5 mol dm^{-3} sodium chloride solution at 25°C.

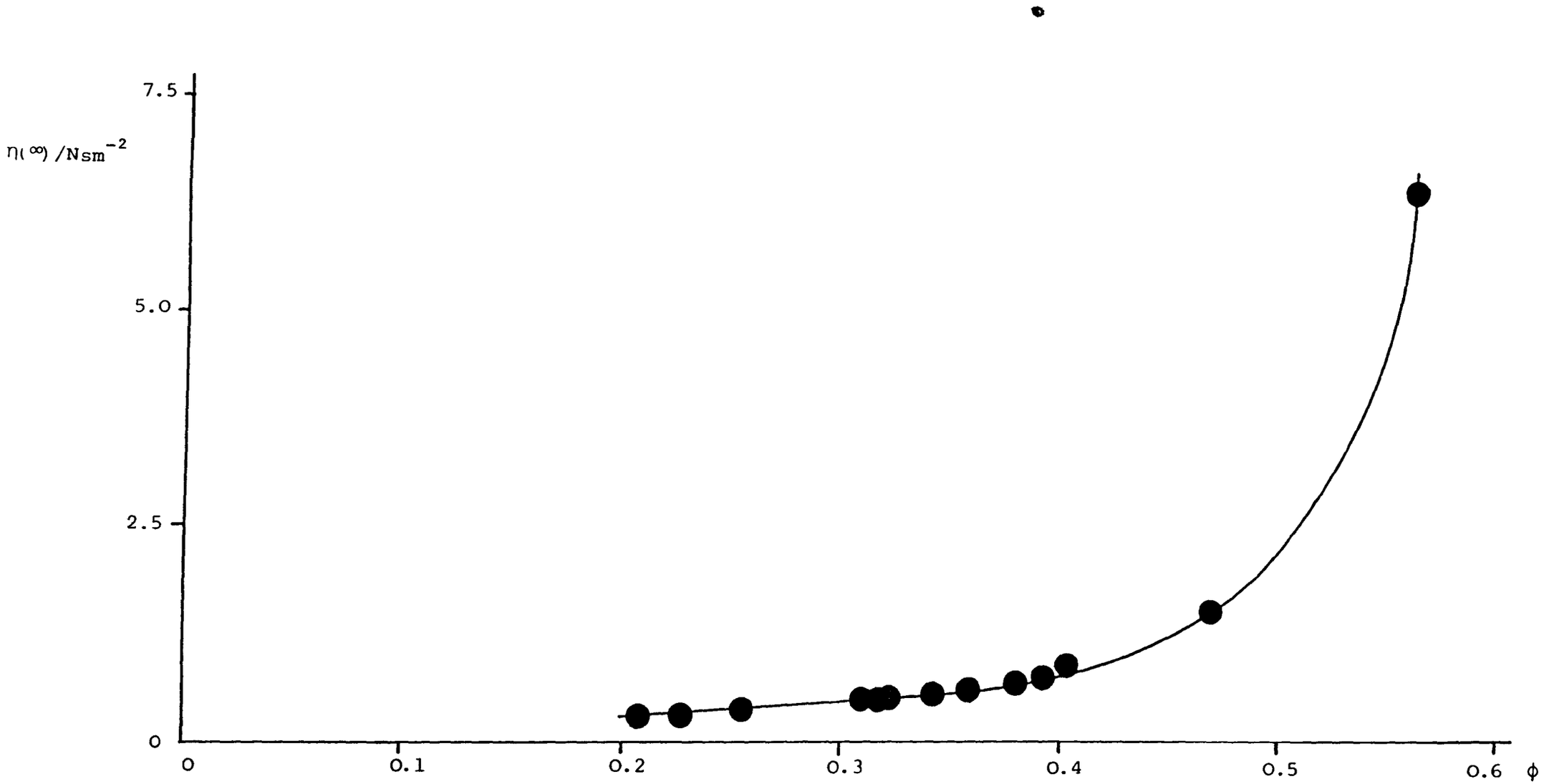

Figure 11.15.

Log_{10} high shear limiting viscosity/Nsm^{-2} versus volume fraction for polystyrene latex SJP8/$C_{12}E_6$ in 0.5 mol dm^{-3} sodium chloride solution at 25°C.

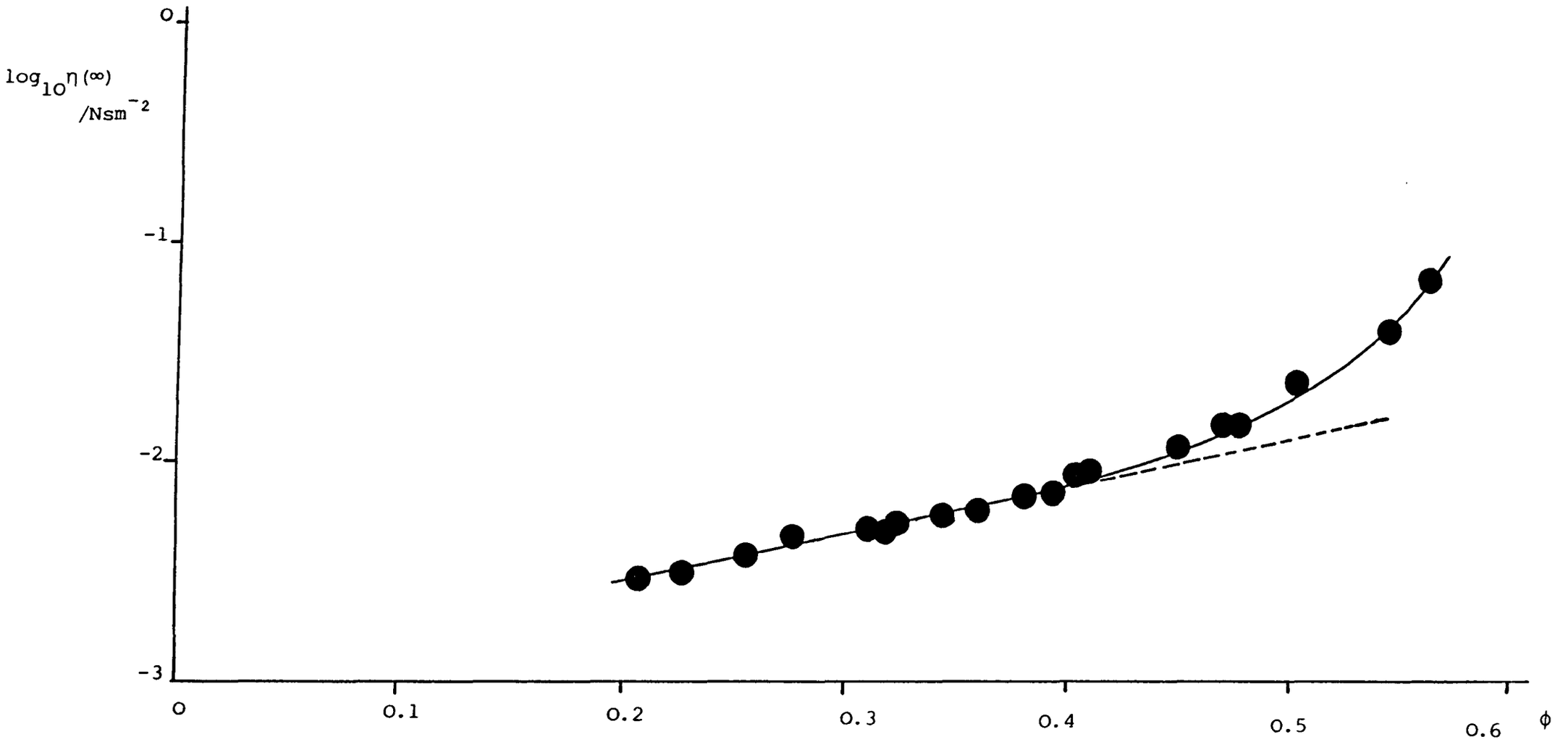

Figure 11.16.

Stress at the onset of shear thinning/Nm^{-2} versus volume fraction for polystyrene latex SJP8/$C_{12}E_6$ in 0.5 mol dm^{-3} sodium chloride solution at 25°C.

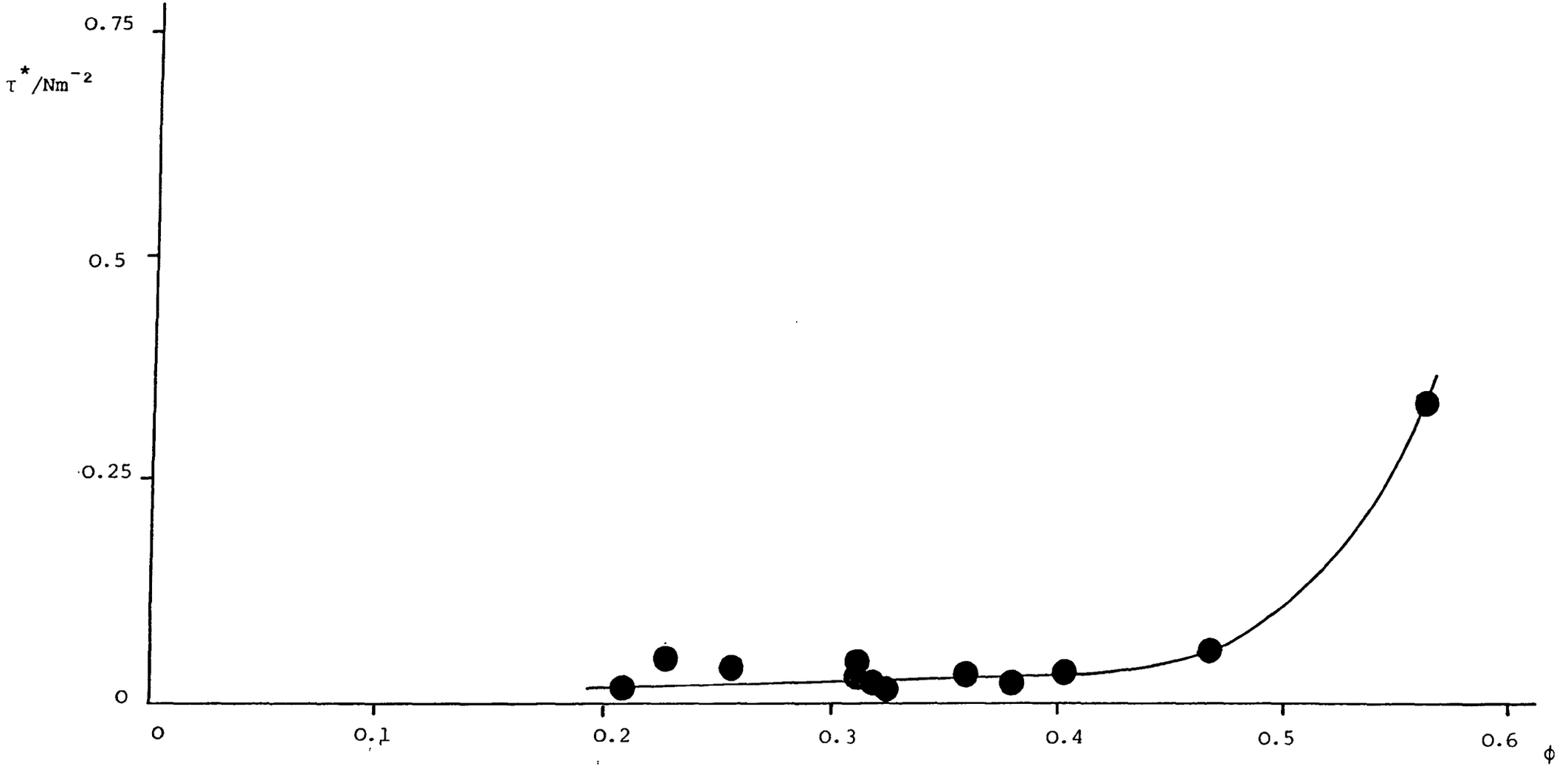

as calculated by Einstein. The maximum packing fraction was taken to be 0.62, the value for a randomly packed system and the value experimentally obtained for the systems used in this work under applicatiion of an applied stress as explained in (9.4). Figure 11.17 shows the calculated relative viscosity plotted as a function of volume function using this equation together with the points obtained experimentally. The high shear values of viscosity gave a reasonable fit to the equation for hard spheres, evidence of single particle units at high shear. The fact that the experimental values were slightly high may be attributed to the fact that the limiting value for $\eta_r(\infty)$ may not have been reached due to the onset of turbulent flow. The zero shear viscosity values do not fit Krieger's predictions at all and this is probably due to the flocculation process. Clearly an attractive perturbation to the hard sphere interaction is required under Creep conditions.

Figure 11.17.

Log_{10} Relative viscosity versus volume fraction for polystyrene latex SJP8/$C_{12}E_6$ in 0.5 mol dm^{-3} sodium chloride solution - calculated from Krieger's equation[82] for Hard Spheres.

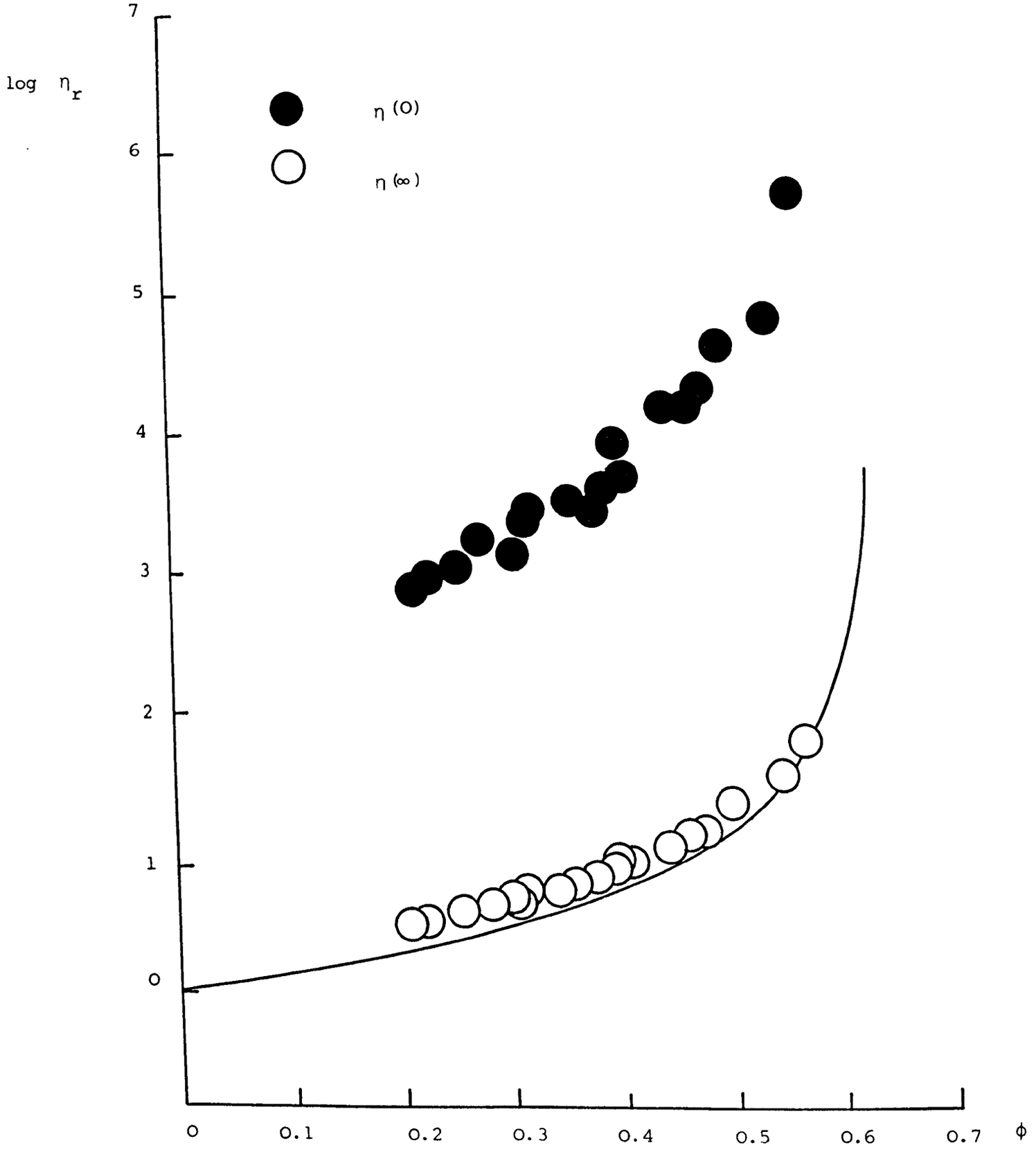

Chapter Twelve

Discussion

Chapter Twelve Discussion

The statistical mechanical description of condensed phases has been based upon molecular liquids such as liquid argon. The extension of these models to colloidal dispersions should strictly consider not only the particles but also the molecular nature of the dispersion medium. However, due to the large difference in the size of the units it is satisfactory to treat the suspension medium as a continuum.

Long, Osmond and Vincent,[194] while working on the equilibrium aspects of weakly flocculated systems of polystyrene latices coated with $C_{12}E_6$ in barium chloride solution, have pointed out the analogy between weakly flocculated systems and the liquid/gas equilibrium. They postulated the existence of a critical particle concentration below which no flocculation occurred and above which singlet particles were in equilibrium with aggregates and found experimental evidence for this from light scattering and electron microscopy studies. This is similar to the behaviour of gas, as the concentration is increased a condensed phase is formed which is in equilibrium with the vapour phase.

Pair Potentials.

The similarity between weakly flocculated systems and the condensed phase can be compared further by examining the forms of the pair interaction potentials. The pair potential of liquid argon is taken to be the Lennard-Jones 6,12 potential. The pair potential for the systems used in this piece of work were calculated from the summation of the attractive and repulsive energies described in Chapter Three and discussed in (3.6), given by equation (3.32):

$$V_T = V_A + V_R + V_S$$

where V_A is given by equation (3.13):

$$V_A = -\frac{A}{12}\left(-\frac{1}{x^2+2x} + \frac{1}{x^2+2x+1} + 2\ln\frac{x^2+2x}{x^2+2x+1}\right)$$

with $x = \frac{H_o}{2\alpha}$

V_R is given by equation (3.8):

$$V_R = 2\pi\varepsilon_r\varepsilon_o a\psi_d^2 \ln\left\{1 + \exp(-\kappa(H_o-2\delta))\right\}$$

and V_S is given by equation (3.29):

$$V_S = \frac{4\pi c_s{}^2 kT}{3v_1\rho_s{}^2}(\Psi^* - \chi)^*\left(\delta - \frac{H_o}{2}\right)^2\left(3\alpha+2\delta+\frac{H_o}{2}\right)$$

The electrostatic repulsion was taken to start at the surface of the adsorbed layer which may be considered to be rigid. The surface active agent layer was assumed to have a negligible effect on the attractive potential.

The energy profiles for V_A and V_S are presented in Figure 12.1 for the SJP8/$C_{12}E_6$ system in 0.5 mol dm^{-3} sodium chloride solution. It was noted that the steric energy of repulsion was virtually vertical at $H_o = 2\delta$ and hence to a good approximation the steric interaction was approximated by a hard sphere interaction at the dimensions of the adsorbed layer.

The potential energy profiles, calculated for the three systems SJP8/$C_{12}E_6$, SJP10/$C_{12}E_6$ and SJP11/$C_{12}E_6$ in 0.5 mol dm^{-3} sodium chloride solution, are presented in Figure 12.2. A potential energy minimum was obtained in each case at a particle surface-surface separation of 9.8×10^{-9} m and the total interaction attractive until the adsorbed layers of the particles came into contact. The potential energy wells were shallow: 7.4 kT for the SJP8/$C_{12}E_6$ case, 11.18 kT for the SJP10/$C_{12}E_6$ system and 15.57 kT for the SJP11/$C_{12}E_6$ case.

Figure 12.1.

van der Waals&steric energy profiles for the system SJP8/$C_{12}E_6$ in 0.5 mol dm^{-3} sodium chloride solution.

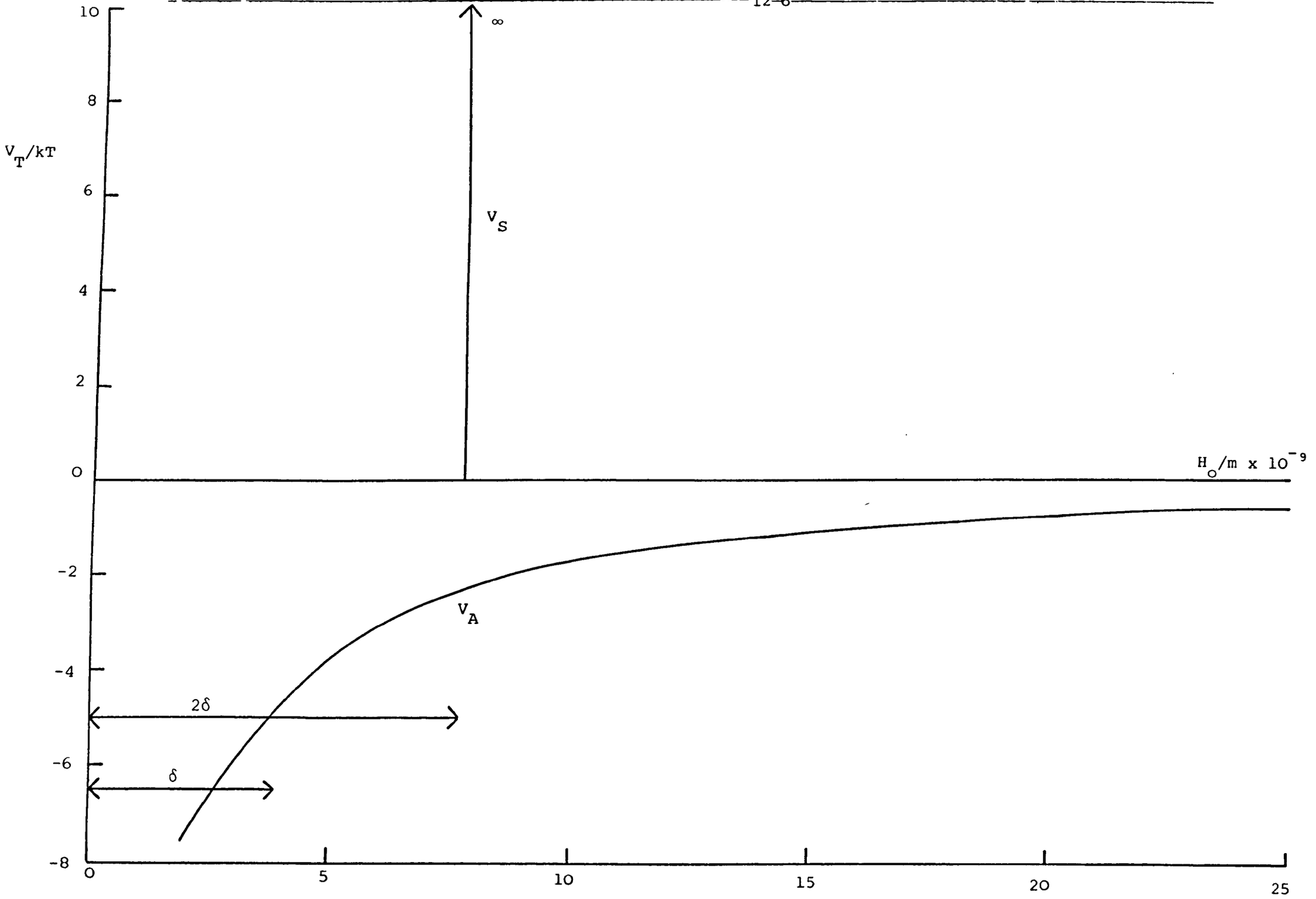

Figure 12.2.

Potential energy profiles for latices SJP8 (diameter 9.74 x 10^{-7} m), SJP10 (diameter 1.411 x 10^{-6} m) and SJP11 (diameter 1.916 x 10^{-6} m) all with full coverage of $C_{12}E_6$ (adsorbed layer thickness 3.85 x 10^{-9} m) in 5 x 10^{-1} mol dm^{-3} NaCl.

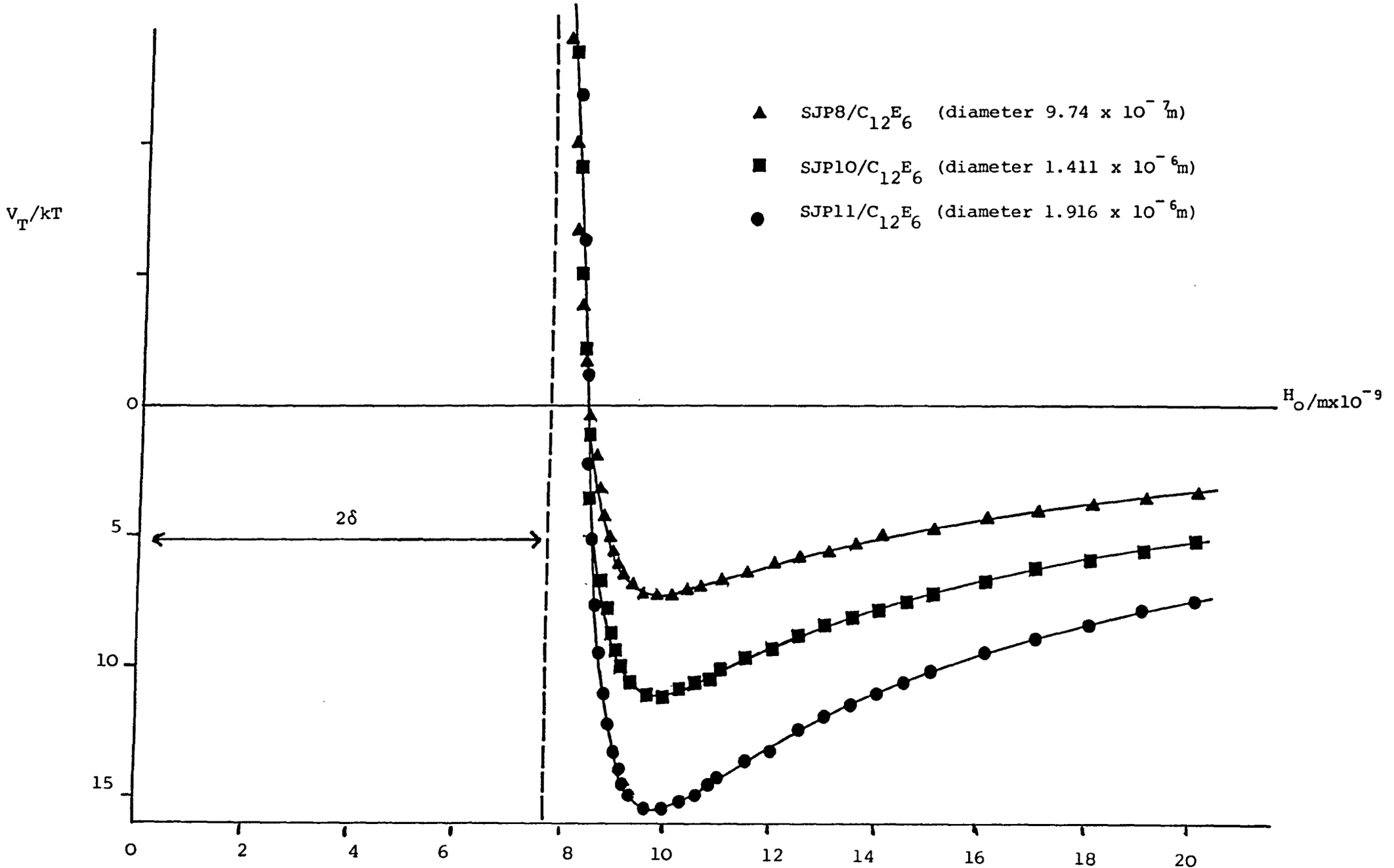

Aggregated systems are indicative of attractive interaction potentials. Evidence from rapid sedimentation at a critically high electrolyte concentration, i.e. at critically high electrostatic repulsion damping, see (7.6) and Chapter Nine, substantiates this theory as does the actual observation of flocs from freeze etch and optical microscopy techniques. Shallow potential minima are characteristic of weakly flocculated systems. Weakly flocculated systems, with particles occupying a shallow energy minimum, require only a small amount of input energy to overcome the attractive energy and allow the particles to be redispersed. This was also observed in this work with the sedimented systems being readily redispersed on shaking. Evidence from optical microscopy, see (8.5), showed that a slight agitation of the flocculated system caused complete break up of the flocs. Also, marked shear thinning was observed in the viscous behaviour, indicative of a three dimensional flocculated network structure at zero shear being broken up with the application of shear. The reasonable agreement of the high shear viscosity data with Krieger's model, see (11.6), is indicative that for these systems at high shear stresses, the viscous forces dominate the colloidal forces.

Hence the calculated potential energy profiles were considered to be consistent with the experimentally observed physical behaviour. It can be observed from Figure 12.2 that the forms of the pair potential curves for the systems under consideration are of a similar form to the Lennard-Jones 6,12 potential. Hence a similar type of behaviour may be expected from colloidal systems and molecular liquids.

Microstructure.

The radial distribution function, g(r), is a statistical description of the structure of an assembly of atoms or particles, see (4.2). A

hard sphere radial distribution function was initially considered as the repulsion obtained was assumed to be hard sphere to a first approximation. The hard sphere radial distribution function for system SJP8/$C_{12}E_6$ was calculated using the program of Henderson,[60] described in (4.3) and is presented in Figure 12.3. A theoretical description of the systems structure was then related to a theoretical model for an experimentally determined physical property and the model tested.

Physical Properties.

Zwanzig and Mountain,[79] and more recently Zukoski,[80] have derived models for the description of the high frequency limit of the shear modulus, see (4.5), which may be expressed by equation (4.31):

$$G(\infty) = \rho kT + \frac{2\pi\rho^2}{15} \int_0^\infty g(r) \frac{d}{dr} \left[r^4 \frac{dV(r)}{dr} \right] dr$$

The theoretical high frequency limit of the shear modulus was calculated from equation (4.31) using the hard sphere model for the radial distribution function and the model described above for the pair potential.

A plot was constructed of the theoretical $G(\infty)$ versus the volume fraction and compared against the experimentally obtained points, see (10.4), for the systems SJP8/$C_{12}E_6$, SJP10/$C_{12}E_6$ and SJP11/$C_{12}E_6$ all in 0.5 mol dm^{-3} sodium chloride solution. These plots are presented in Figures 12.4 - 12.6. It can be seen that the shape of the theoretically predicted curves were in good agreement with the shapes of the experimentally obtained curves in all cases but that the experimental points were consistently higher than those predicted. This suggested that the model used to describe the structure required some modification.

A Barker-Henderson perturbed hard sphere model was used as a more realistic description of the pair potential in order to calculate the pair distribution function. A hard sphere reference pair distribution function

Figure 12.3.

Hard sphere radial distribution function calculated for system SJp8/$C_{12}E_6$ from the program of Henderson.[60]

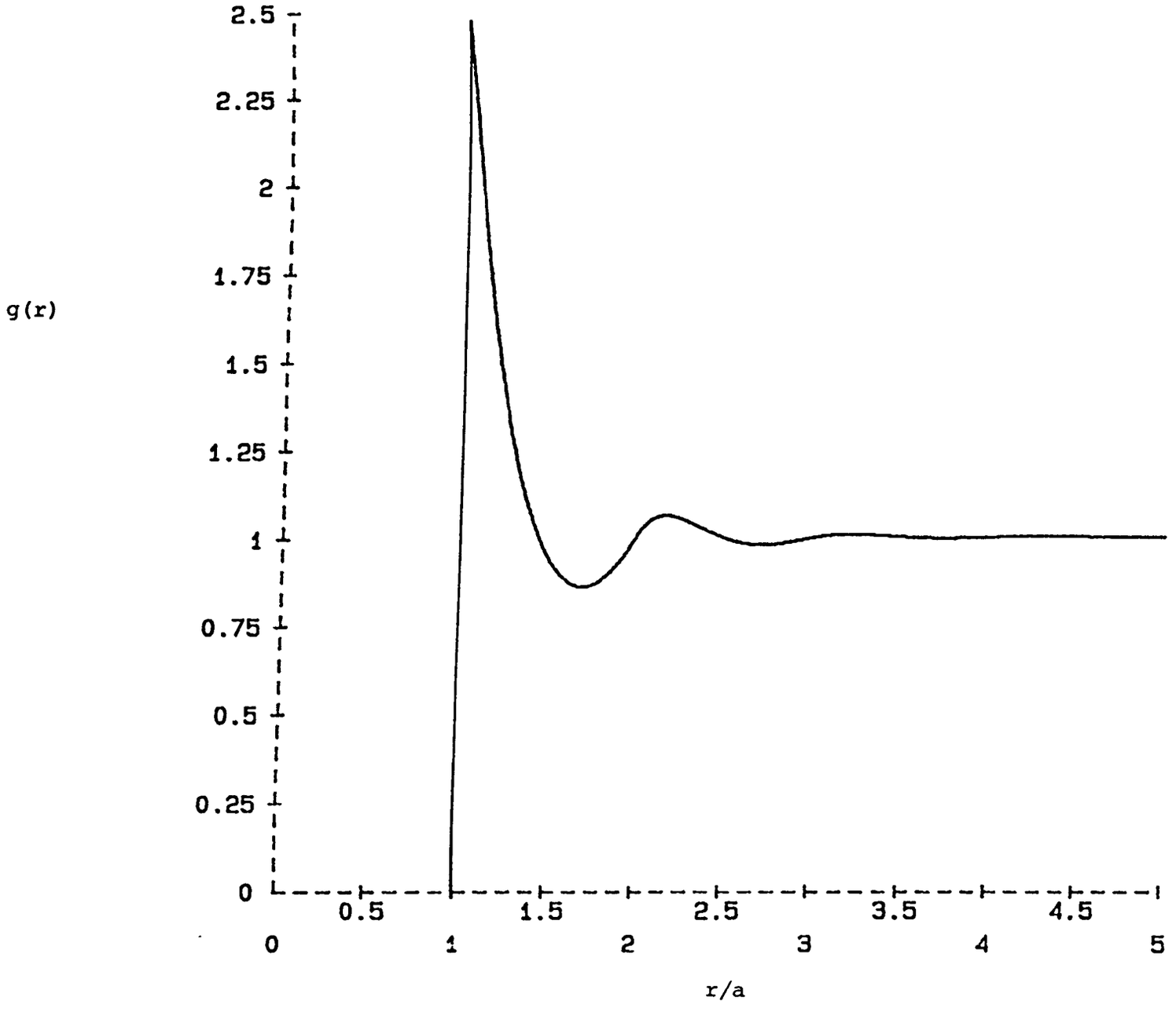

Figure 12.4.

High frequency limit of the shear modulus/Nm^{-2} versus volume fraction for SJP8/$C_{12}E_6$ in 0.5 mol dm^{-3} sodium chloride solution. Full line calculated from equation (4.31) Points: experimental.

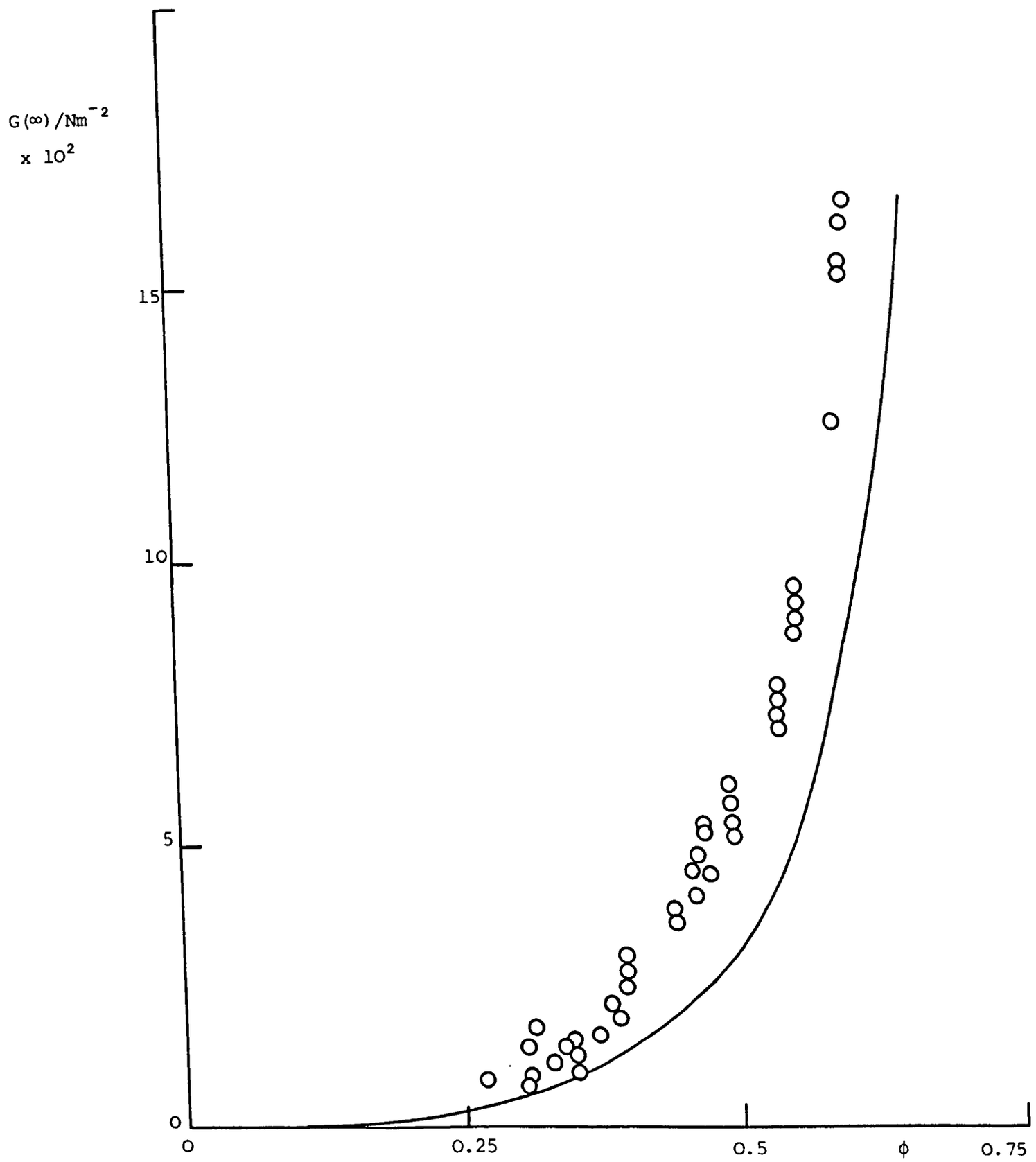

Figure 12.5.

High frequency limit of the shear modulus/Nm^{-2} versus volume fraction for SJPlO/$C_{12}E_6$ in 0.5 mol dm^{-3} sodium chloride solution. Full line: calculated from equation (4.31). Points: experimental.

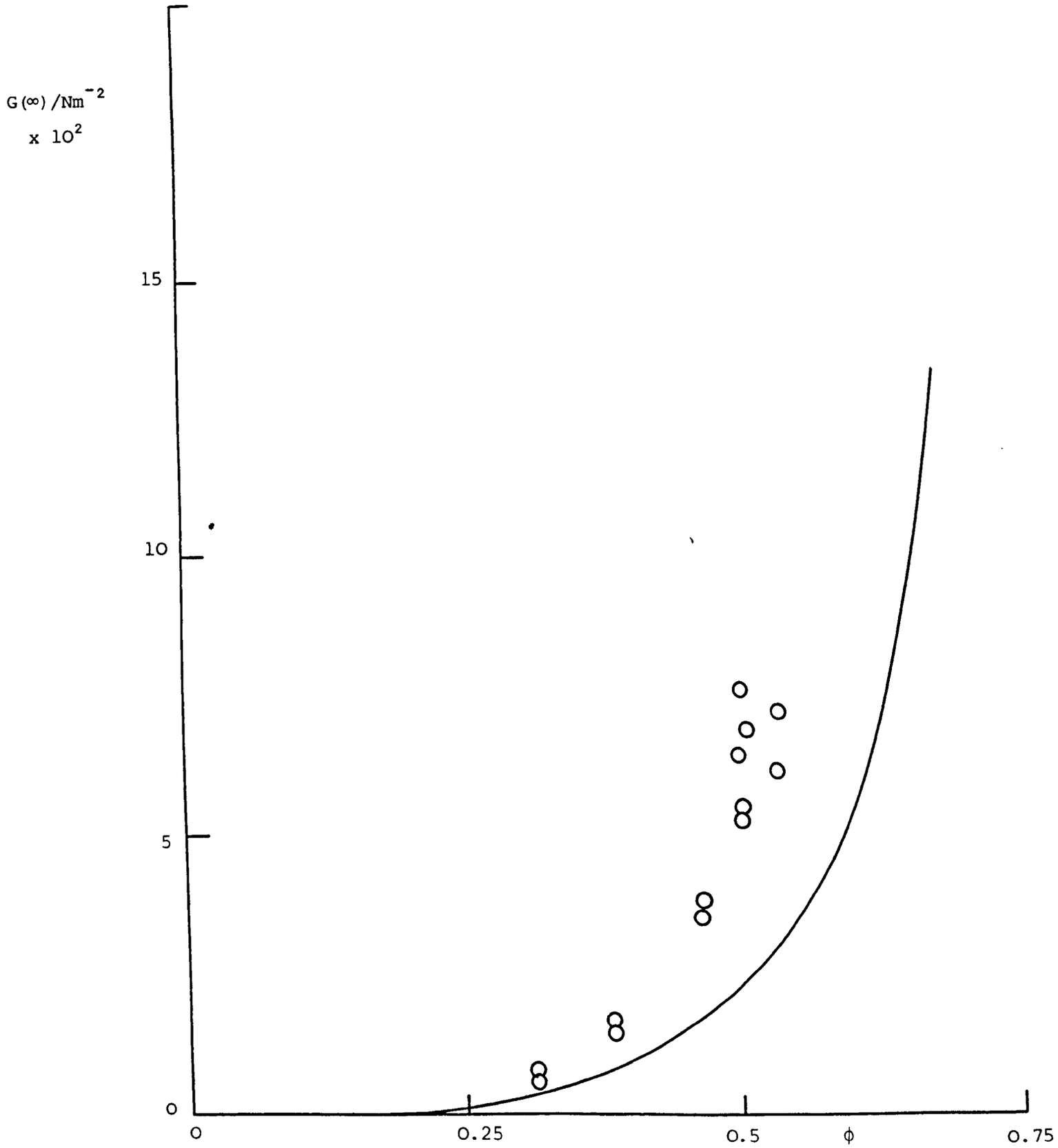

Figure 12.6.

High frequency limit of the shear modulus/Nm^{-2} versus volume fraction for SJP11/$C_{12}E_6$ in 0.5 mol dm^{-3} sodium chloride solution. Full line: calculated from equation (4.31). Points: experimental

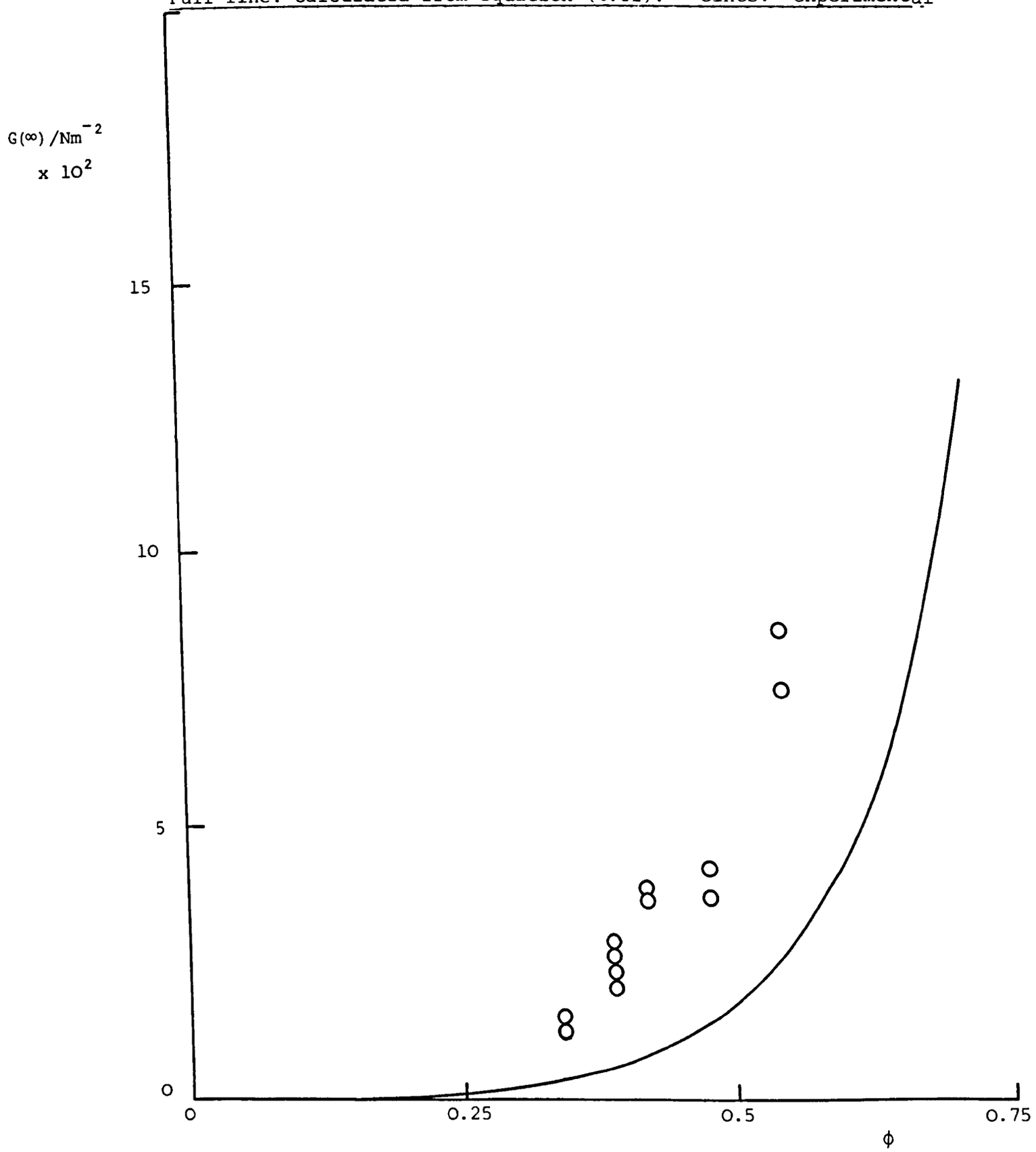

was used with the semi-empirical corrections of Verlet and Weis applied to the Percus-Yevick solution.[205,206] The expression for the high frequency limit shear modulus using this analysis is written:[205,206]

$$\hat{G}(\infty) = \frac{3\phi}{4\pi} - \frac{6\phi^2}{5\pi}\left[\left(\frac{dg_p(\hat{r})}{d\hat{r}}\right)\hat{r} = 2a_{HS}\right] + \frac{3\phi^2}{40\pi}\int_0^\infty \left\{ g_o(\hat{r})\left[3\hat{r}^3\frac{dV}{d\hat{r}} + \hat{r}^4\frac{d^4V}{d\hat{r}}\right]\right\} d\hat{r} \qquad (12.1)$$

where $\hat{G}(\infty)$ is the dimensionless high frequency modulus given by:

$$\hat{G}(\infty) = \frac{G(\infty)a^3}{kT} \qquad (12.2)$$

$\hat{r}$ is the particle centre-centre separation scaled on the Barker-Henderson effective hard sphere radius, a_{HS}, see (4.1), $g_p(\hat{r})$ is the perturbed radial distribution function and $g_o(\hat{r})$ the hard sphere reference radial distribution function, see (4.4), $V(\hat{r})$ is the dimensionless pair interaction potential given by:[205]

$$V(\hat{r}) = V_A(\hat{r}) + V_R(\hat{r}) \qquad (12.3)$$

The predicted elastic modulus values were tested for their sensitivity towards various parameters and it was found that, for these weakly flocculated systems, $G(\infty)$ was dominated by short range repulsive interactions. The predicted values for the shear modulus were only weakly dependent upon the parameters affecting the attractive potential as shown in Tables 12.1 and 12.2, in which are presented the sensitivity analysis of the model to the Hamaker constant and the adsorbed layer thickness respectively. However, as shown in Figures 12.7 to 12.11, the high frequency modulus was very sensitive to the highly screened electrostatic interaction. Variations of the zeta potential produced a marked effect on the predicted elastic modulus values.

Two models were tested, based on constant charge electrostatic repulsion and constant potential electrostatic repulsion. From Figures 12.7 to 12.11 it can be seen that the pair interactions based on constant charge electrostatic repulsion predicted much larger $G(\infty)$ values

Table 12.1.

Values for the high frequency limit shear modulus/Nm^{-2} calculated for polystyrene latex SJP8/$C_{12}E_6$ in 0.5 mol dm^{-3} sodium chloride solution at various volume fractions to test the sensitivity of the theoretical model to the Hamaker constant. Interaction based on constant surface potential.

ϕ \ A/J	4.5×10^{-21}	9×10^{-21}	18×10^{-21}	80×10^{-21}
0.25	46.2	45.9	41.6	32.0
0.35	1.33×10^2	1.32×10^2	1.25×10^2	99.5
0.45	3.45×10^2	3.38×10^2	3.44×10^2	2.65×10^2
0.55	8.80×10^2	8.38×10^2	8.36×10^2	6.90×10^2
0.60	1.44×10^3	1.37×10^3	1.35×10^2	1.13×10^3

Table 12.2.

Values for the high frequency limit shear modulus/Nm^{-2} calculated for polystyrene latex SJP8/$C_{12}E_6$ in 0.5 mol dm^{-3} sodium chloride solution at various volume fractions to test the sensitivity of the theoretical model to the Hamaker constant. Interaction based on constant surface potential.

ϕ \ δ/nm	1.0	3.85	9.0
0.25	25.5	45.9	47.1
0.35	79.1	1.32×10^2	1.36×10^2
0.45	2.11×10^2	3.38×10^2	3.50×10^2
0.55	5.45×10^2	8.38×10^2	8.94×10^2
0.60	8.94×10^2	1.37×10^3	1.46×10^3

Figure 12.7.

Wave rigidity modulus/Nm^{-2} versus volume fraction for polystyrene latex SJP8/$C_{12}E_6$ in 0.5 mol dm^{-3} sodium chloride solution. Points were experimentally determined. Curves were calculated assuming constant surface potential electrostatic interactions.

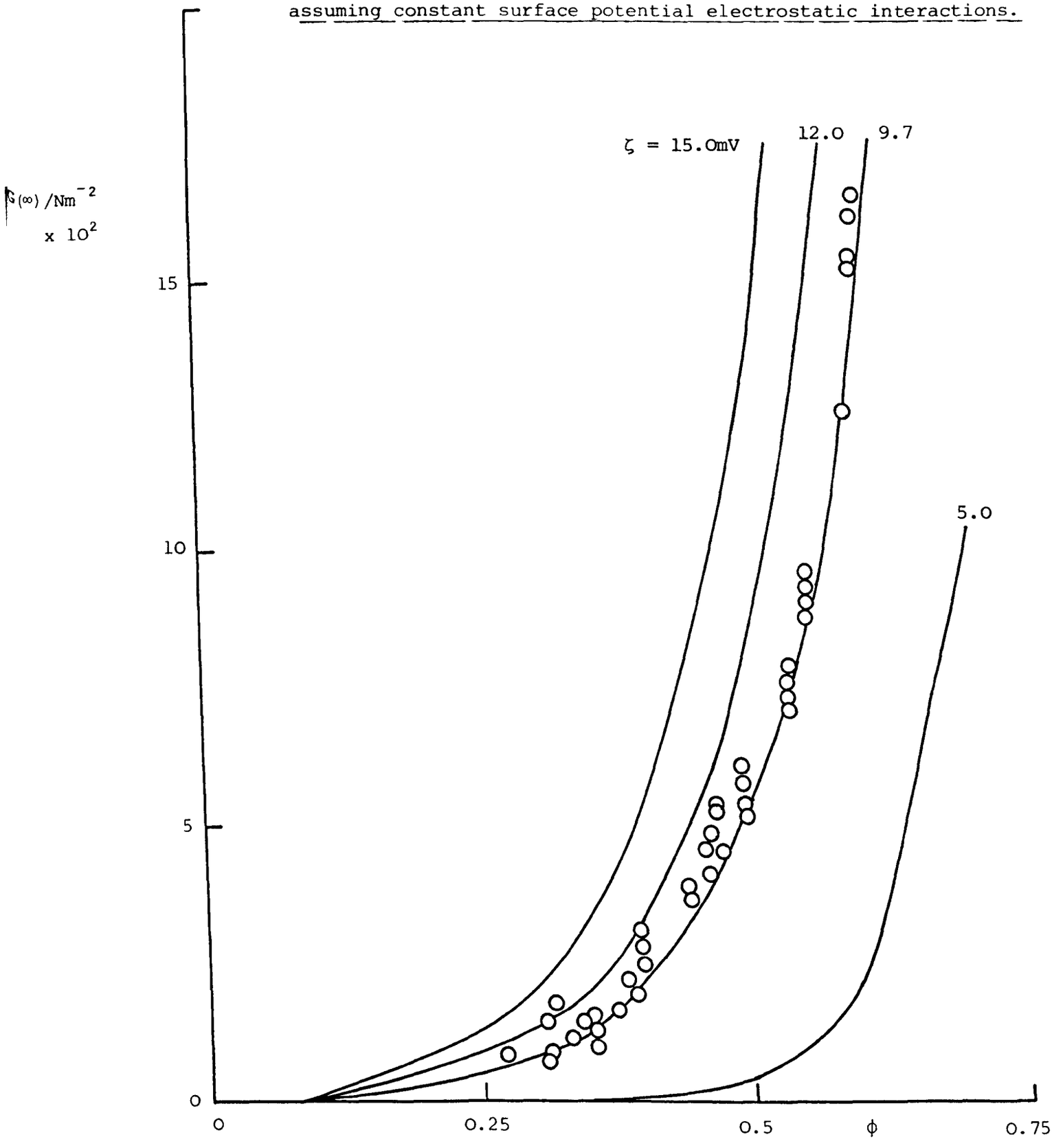

Figure 12.8.

Wave rigidity modulus/Nm^{-2} versus volume fraction for polystyrene SJP10/$C_{12}E_6$ in 0.5 mol dm^{-3} sodium chloride solution. Points were experimentally determined. Curves were calculated assuming constant surface potential electrostatic interactions.

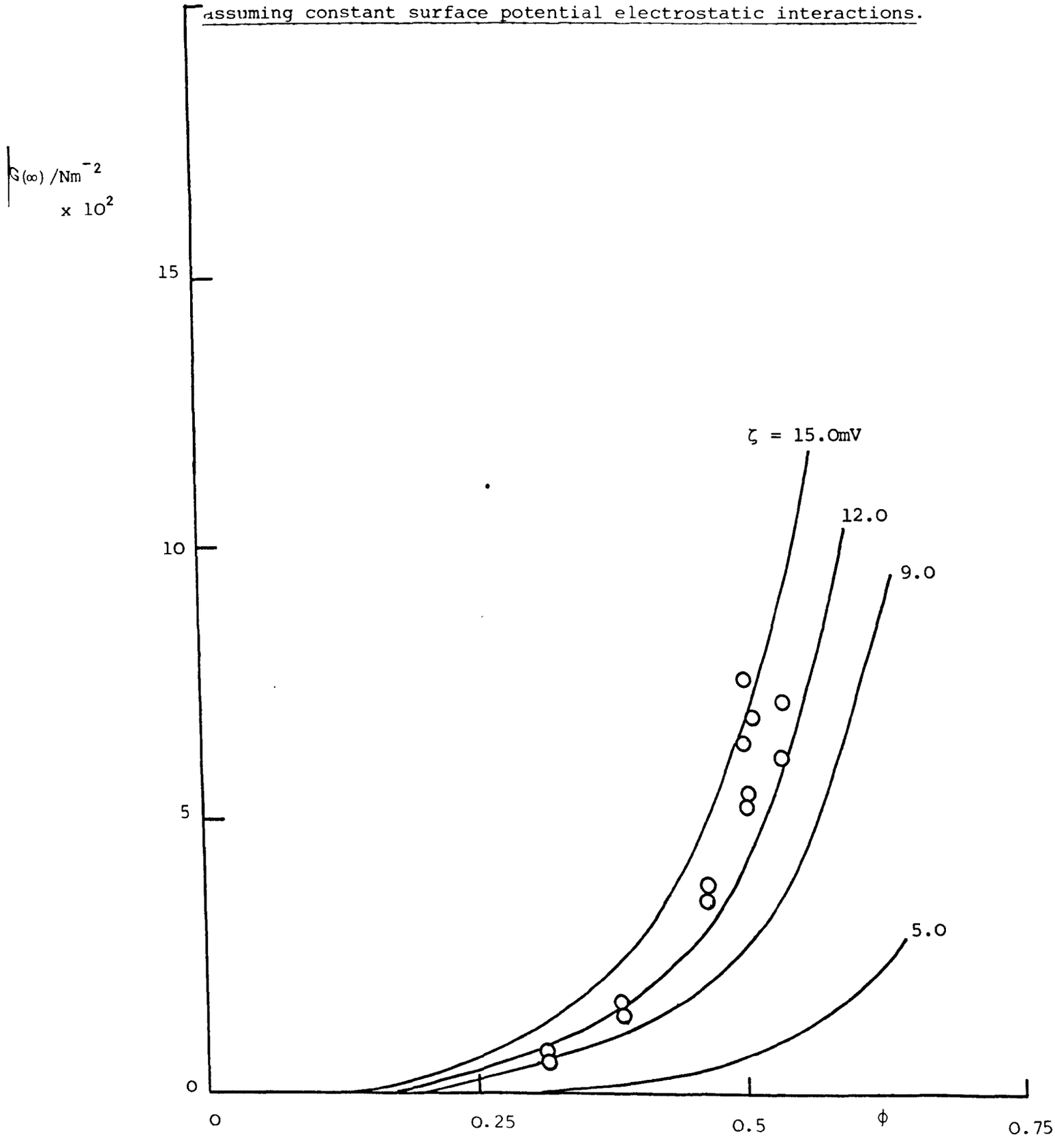

Figure 12.9.

Wave rigidity modulus/Nm^{-2} versus volume fraction for polystyrene latex SJP11/$C_{12}E_6$ in 0.5 mol dm^{-3} sodium chloride solution. Points were experimentally determined. Curves were calculated assuming constant surface potential electrostatic interactions

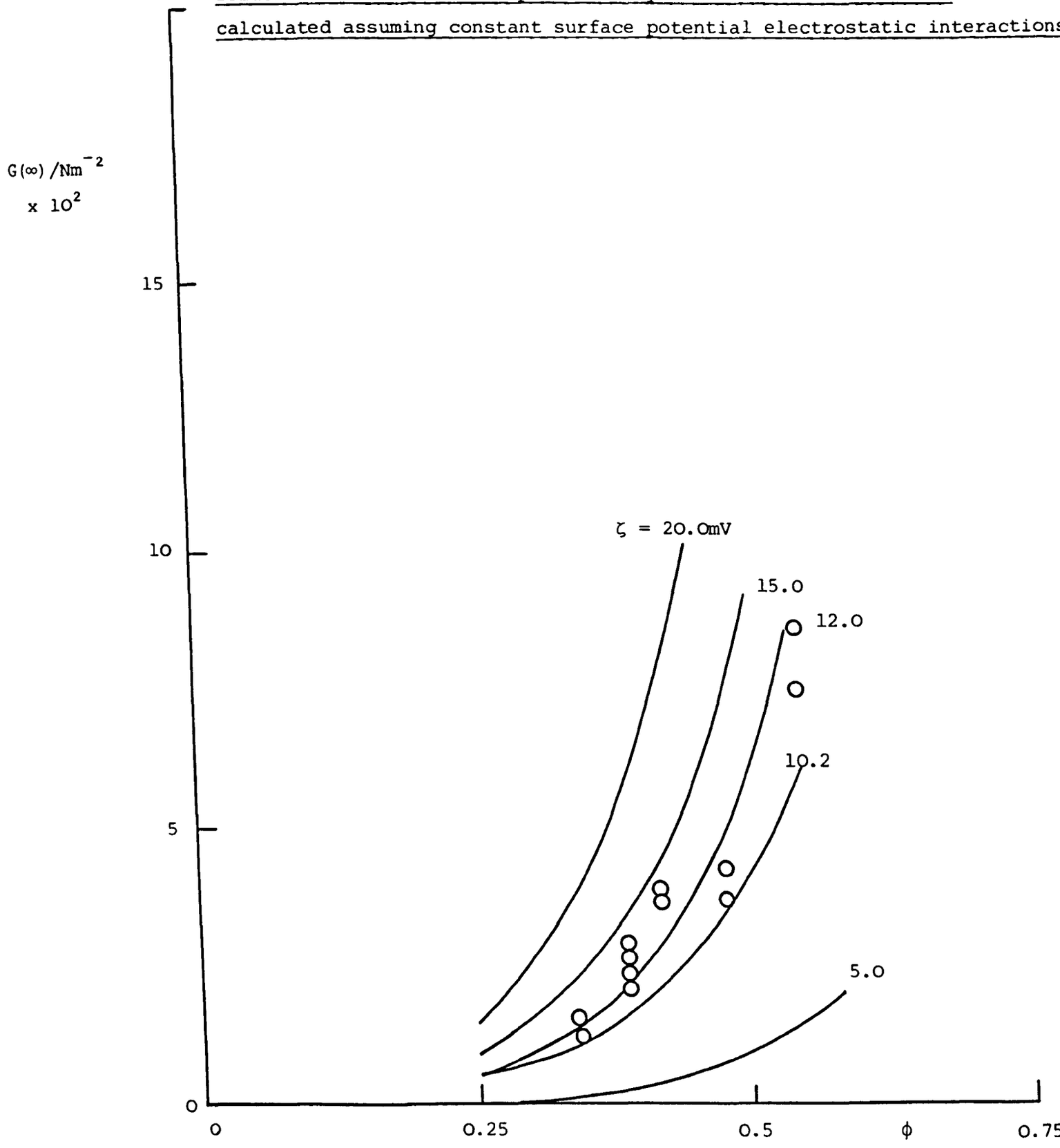

Figure 12.10.

Wave rigidity modulus/Nm^{-2} versus volume fraction for polystyrene latex SJP8/$C_{12}E_6$ in 0.5 mol dm^{-3} sodium chloride solution. Points were experimentally determined. Curves were calculated assuming constant surface charge electrostatic interactions.

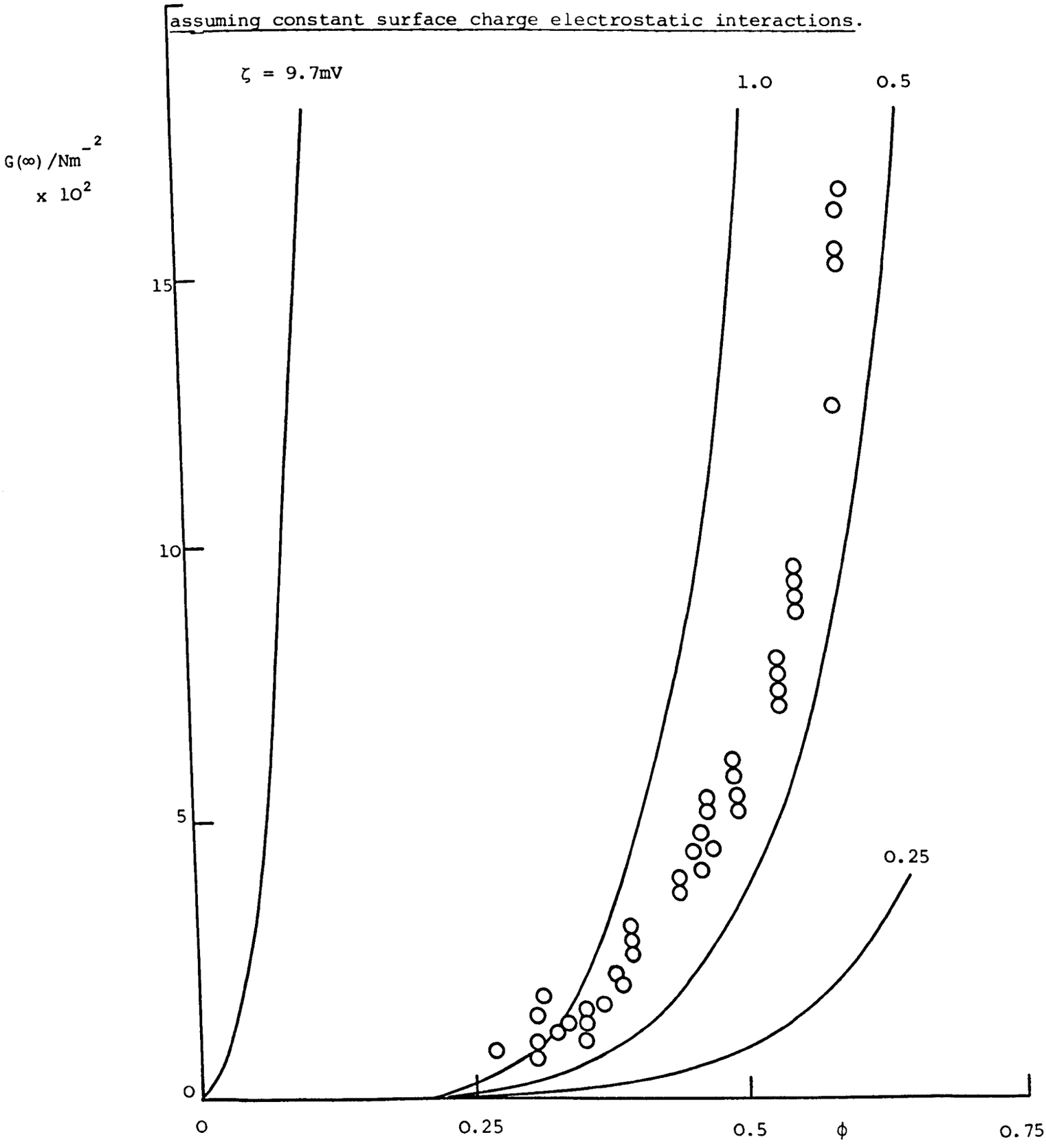

Figure 12.11.

Wave rigidity modulus/Nm^{-2} versus volume fraction for polystyrene latex SJP10/$C_{12}E_6$ in 0.5 mol dm^{-3} sodium chloride solution. Points were experimentally determined. Curves were calculated assuming constant surface charge electrostatic interactions.

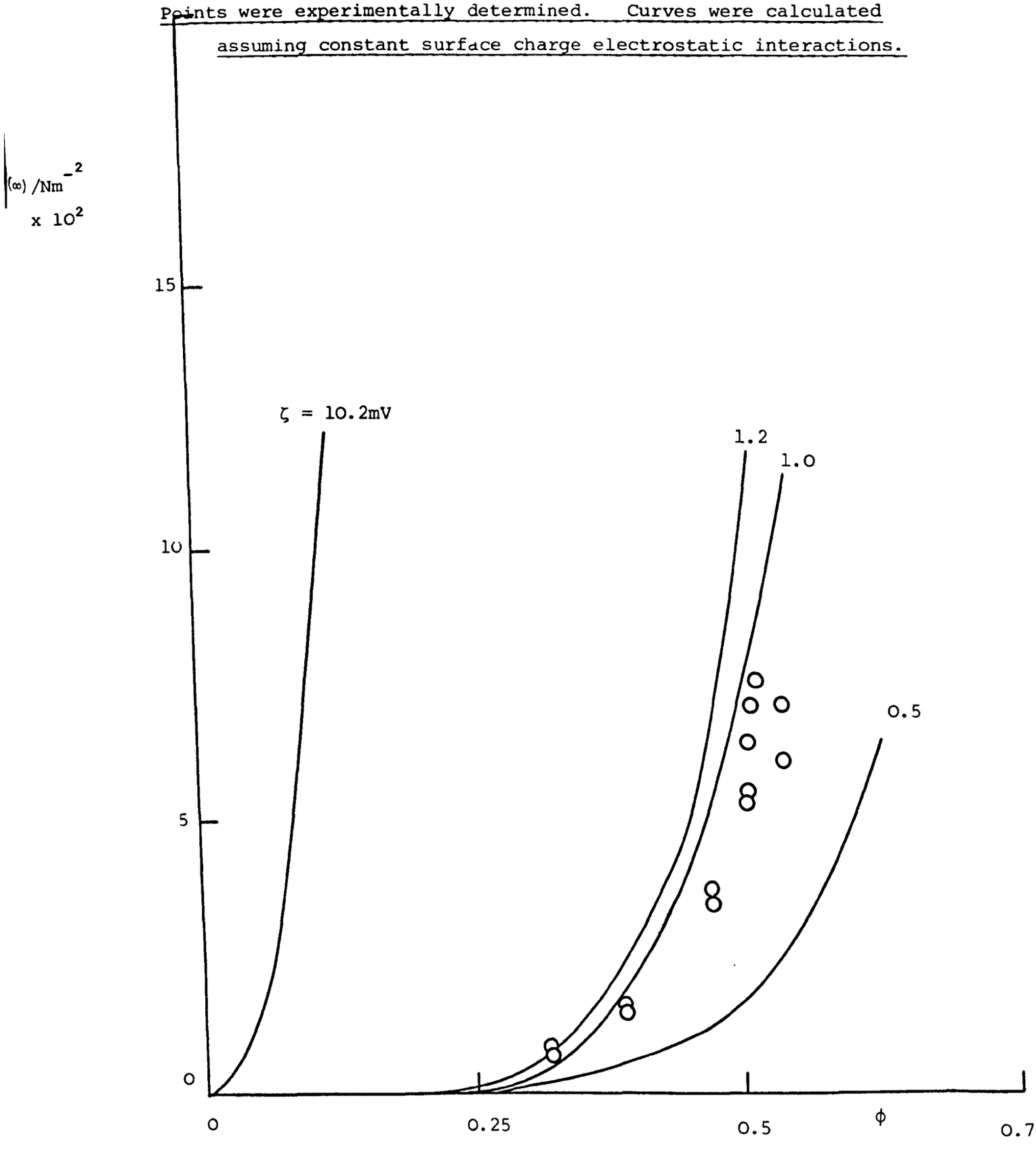

than those predicted at constant potential. This was a consequence of the singular nature of the repulsive term in the constant charge case as the separation goes to zero.

The experimentally obtained values for the high frequency elastic modulus are presented in Figures 12.7 to 12.11 with the theoretically predicted curves to enable a comparison. Over a wide range of parametric values only electrostatic interactions significantly affected the comparison between the model and the experimental results. This was despite the low surface potentials and extremely high κa values.

It can be seen from Figures 12.7 to 12.11 that the particle interactions calculated with constant surface charge significantly overpredicted the observed values of $G(\infty)$ whereas particle interactions with constant surface potential provided a very good model for the elastic properties of weakly flocculated suspensions. Zeta potentials required to bring the model and the data into excellent agreement were within 3 - 4 mV of the values measured electrophoretically. Excellent agreement was obtained in the SJP8/$C_{12}E_6$ case, where there was the most comprehensive experimental data, at exactly the zeta potential experimentally determined.

The elastic properties of weakly aggregated suspensions thus provide a very sensitive method of testing for short range repulsive interactions. The results obtained indicate that electrostatic repulsion is adequate to predict $G(\infty)$.

Work on molecularly smooth mica has provided evidence for the existence of hydration forces at high salt concentrations. No evidence was found in this work for the presence of hydration forces, as had they been present one would expect an under-estimation of the theoretical shear modulus which was not found. The reason for this may be due to the relatively softer nature of the nonionic surface active agent surface compared with that of mica.

Another physical property that may be experimentally determined and theoretically predicted using a similar model to that for the high frequency shear modulus ie utilising both the radial distribution function and the pair interaction potential, is the zero shear rate viscosity, $\eta(0)$. There are three contributions to the viscosity, as outlined in (4.6), these being kinetic, hydrodynamic and potential. For a colloidal sol the kinetic contribution is negligible due to the particle size dependence and hence to a good approximation the viscosity may be calculated from the sum of the hydrodynamic and viscous components. The hydrodynamic contribution is greatest at high shear stress and may be calculated from the Krieger equation, equation (4.51):

$$\eta_H = \eta_o \left(1 - \frac{\phi}{\phi_m} \right)^{-2.5\phi_m}$$

An expression has been developed by Kirkwood et al[83] and Eisenschitz et al[84] and described by Croxton[64] to describe the potential component of the viscosity given by equation (4.54):

$$\eta_v = \frac{2\pi\rho^2}{15} \beta \int_0^\infty \frac{dV(r)}{dr} g(r) u(r) r^3 dr$$

where β is a two-body friction constant with units of time and $u(r)$ is the radial distortion function, described in (4.6) and given by equation (4.55):

$$\frac{d^2u(r)}{dr^2} + \left(\frac{2}{r} - \frac{1}{kT} \frac{dV}{dr} \right) \frac{du(r)}{dr} - \frac{6}{r^2} = - \frac{m\beta\dot{\gamma}}{(kT)^2} \frac{dV}{dr} r$$

If the relaxation time of the system is faster than the flow of the system then relatively little distortion will occur. The ratio of the rate of diffusion of a system to the characteristic time for flow is characterised by the Deborah number which may be expressed:

$$De = \frac{a^2/D}{1/\dot{\gamma}} \qquad (12.4)$$

where D is the diffusion coefficient given by the Stokes Einstein equation to be:

$$D = \frac{kt}{6\pi\eta a} \qquad (12.5)$$

Hence the Deborah number is:

$$De = \frac{6\pi\eta a^3 \dot{\gamma}}{kT} \qquad (12.6)$$

At zero shear stresses the shear rate is zero and hence the Deborah number is zero. A low Deborah number indicates that the relaxation of a system is rapid in comparison with the flow and that it may be assumed that no distortion of the microstructure occurs. Hence the radial distortion function was equated to unity at zero shear stress

$$\text{i.e. } \tau \to 0 \qquad \int g(r)u(r) \to \int g(r)$$

This simplified the solution of equation (4.54) which at zero shear stress reduces to:

$$\eta(0) = \frac{2\pi\rho^2}{15} \beta \int_0^\infty \frac{dV(r)}{dr} g(r) r^3 dr \qquad (12.7)$$

For evaluation of the theoretical zero shear viscosity it was necessary to evaluate the frictional term, β. This was taken to be equal to the characteristic diffusion time for a sphere given by the Einstein Smoluchowski relation to be:

$$\beta = \frac{a^2}{D(\phi)} \qquad (12.8)$$

where $D(\phi)$ is the self diffusion coefficient in the concentrated dispersion. It is not possible to calculate this directly but it is possible to calculate the low volume fraction limit of the diffusion coefficient, the free diffusion coefficient, $D(0)$, from the Stokes Einstein equation.

$$\text{As } \phi \to 0 \qquad D(\phi) \to D(0)$$

$$\text{and} \qquad \beta = \frac{6\pi\eta a^3}{kT} \qquad (12.9)$$

It is clear from this discussion that β is a function of volume fraction of a concentrated dispersion. Klein and Hess[207] have determined the effect of volume fraction on the normalised self diffusion coefficient for small polystyrene spheres where the interactions were dominated by repulsive forces and found a sharp decrease at low volume fractions plateauing to a value of 0.5.

A theoretical curve was calculated from equation (12.7), with evaluation of β from (12.9), for the zero shear viscosity as a function of volume fraction for SJP8/$C_{12}E_6$ in 0.5 mol dm^{-3} sodium chloride solution.[208] This is presented in Figure 12.12. A hard sphere potential was assumed for the radial distribution function and the model for the pair interaction potential was the same as that used for the theoretical shear modulus. The theroetical values for the relative zero shear viscosity are compared with the values experimentally obtained in Table 12.3 and the agreement seen to be poor. The reason for this was thought to be partly due to the use of the hard sphere radial distribution function; a better correlation between theoretical and experimental values would be expected using the Barker-Henderson perturbed hard sphere model for g(r). The main reason for the discrepancy was considered to be due to the calculation of β. The diffusion coefficient of the system in concentrated form from independent predictions is required, for example a statistical mechanical model for diffusion of the system analogous to that of Klein and Hess[207] for small particles where the repulsion dominates would be ideal. Instead an estimate was made of the diffusion coefficient ratio required from the experimental data. The ratios of the self diffusion coefficient to the free diffusion coefficient required to bring the theoretical values into agreement with the experimental results were calculated and the values tabulated in Table 12.3 and plotted

Figure 12.12.

Theoretical zero shear viscosity/Nsm^{-2} versus volume fraction for polystyrene latex SJP8/$C_{12}E_6$ in 0.5 mol dm^{-3} sodium chloride solution calculated from equation (12.7), assuming a hard sphere potential.

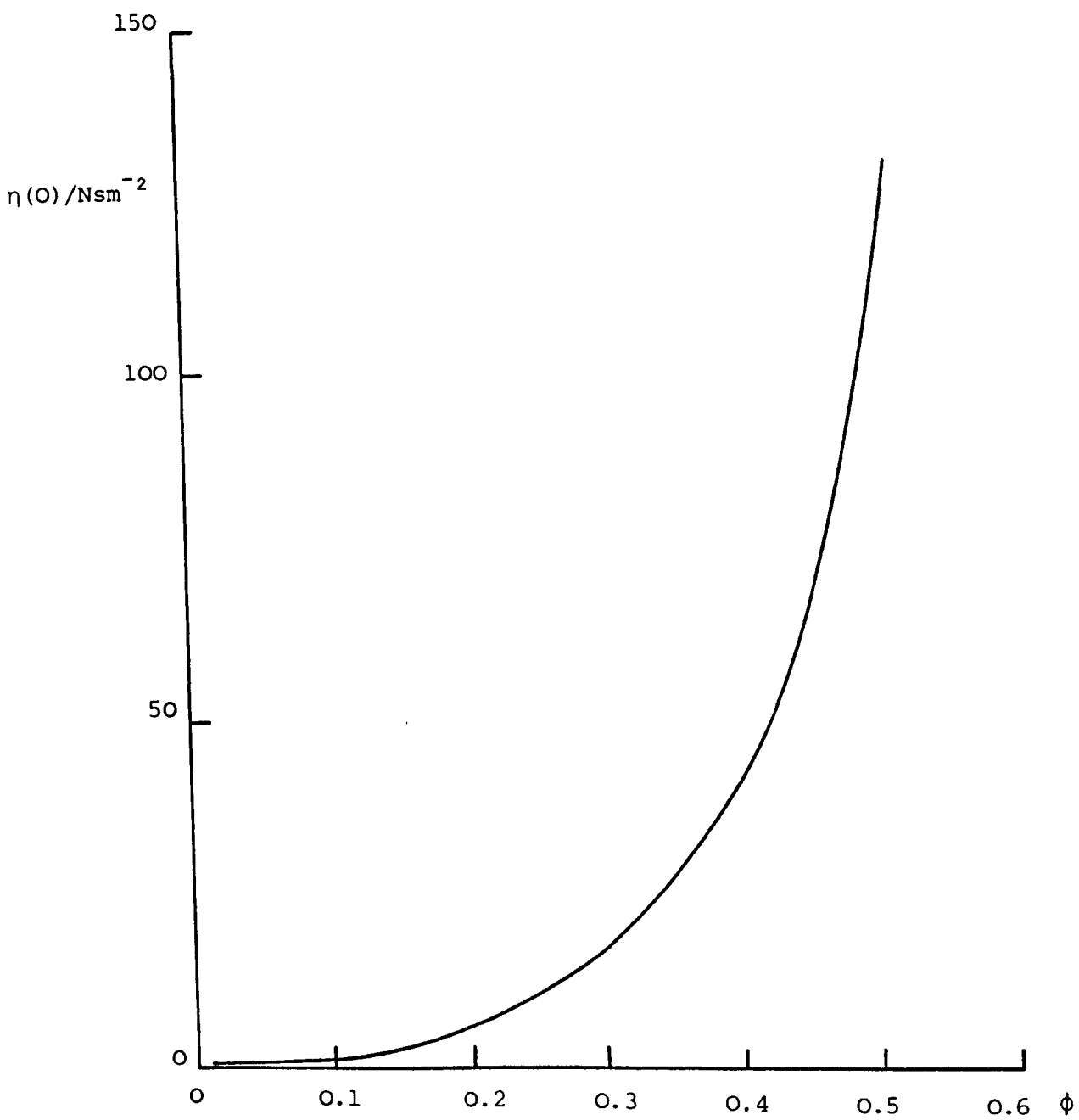

Table 12.3.

Theoretical and experimental values obtained for the relative zero shear rate viscosity and the ratio of the two quantities, equivalent to the ratio of the self and free diffusion coefficients for system SJP8/$C_{12}E_6$ in 0.5 mol dm^{-3} sodium chloride solution.

ϕ	$\eta_r(0)^{th}$	$\eta_r(0)^{exp}$	$\frac{\eta_r(0)^{th}}{\eta_{r(0)}^{exp}} \equiv \frac{D(\phi)}{D(0)}$
0.22	7.2	178	0.040
0.25	10.0	1123	8.90×10^{-3}
0.27	12.1	1780	6.80×10^{-3}
0.31	18.0	1447	0.012
0.315	19.2	2044	9.39×10^{-3}
0.32	20.5	2821	$7.27 \times 10^{-}$
0.38	38.5	2887	0.013
0.39	42.0	3551	0.01
0.40	45.0	8519	5.28×10^{-3}
0.41	49.5	4471	0.011
0.45	72.0	15502	4.64×10^{-3}
0.47	88.0	15864	5.55×10^{-3}
0.48	95.5	22408	4.26×10^{-3}
0.50	114.2	40777	2.80×10^{-3}

as a function of volume fraction in Figure 12.13. The $D(\phi)/D(0)$ values decreased with increased volume fraction to a value of approximately 0.01 and then approached zero at a volume fraction of 0.62 where the system was close packed.

Solution of equation (4.55) for the radial distortion function would enable theoretical calculations of the viscosities at high shear stress.

Some interesting qualitative observations were made during this work. In Chapter Nine, when comparing the sedimentation behaviour of the three latex systems it was noted that the latex intermediate in size, latex SJP10, appeared to have stronger interactions than the other two. The reasons for this are not yet clear. In Chapter Eleven it was noted that the shear modulus values obtained for SJP10/$C_{12}E_6$ as a function of volume fraction were higher than the values obtained for the smaller and larger latex systems. This indicated a more rigid structure and possibly stronger flocculation, in keeping with observations made for the faster sedimentation rates. It is evidence against the effect being due to surface charge effects as high charges cause high repulsions and hence weaker aggregation.

In Chapter Ten a change in viscous properties was noted for the system under investigation at a suspension volume fraction of approximately 0.4 - 0.45. This was in agreement with the value obtained for the volume fraction of the sediment rapidly formed by the settling particles, described in Chapter Nine. The reason for this can be attributed to maximum packing of the flocs achieved at a volume fraction of 0.4 - 0.45. Under the application of an external force a higher volume fraction was obtained of 0.62, the maximum packing fraction for randomly packed individual spheres as the floc structure was destroyed.

Figure 12.13.

Ratio of self and free diffusion coefficients, calculated from zero shear viscosity data, as a function of volume fraction.

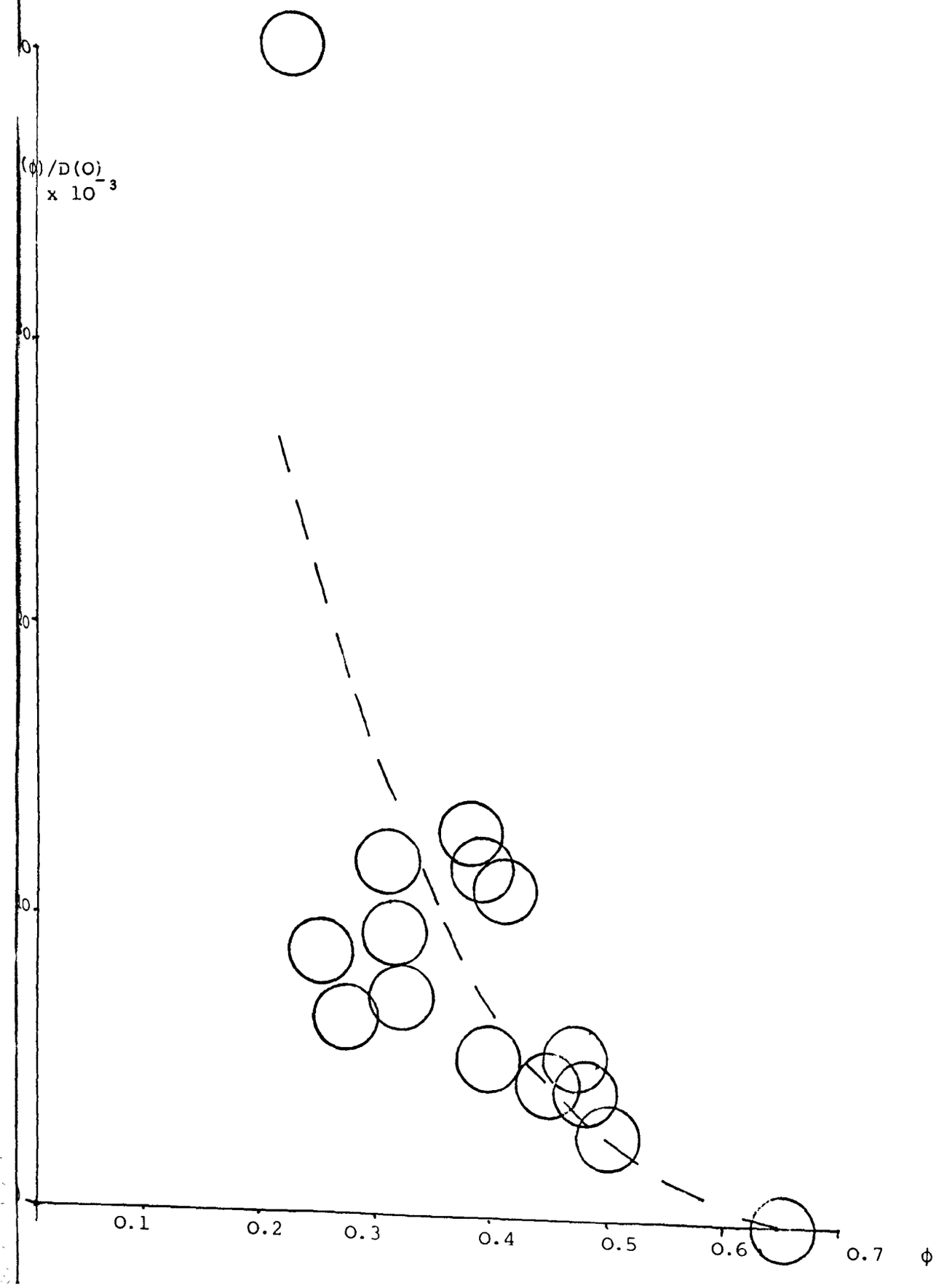

Appendix I.

Calculation of quantities of reactants needed to grow a seed latex to a required size.

Have seed latex diameter x, volume fraction a

Require resultant latex diameter y, volume fraction b

Total reaction volume required v

Growth factor $z = \frac{y^3}{x^3}$

Volume of seed latex particles necessary

$$= \frac{\text{volume of resultant latex particles required}}{\text{growth factor}}$$

$$= \frac{v \times b}{z}$$

Volume of seed latex necessary

$$= \frac{v \times b}{z \times a}$$

Glossary

a	radius of spherical particle
a_{HS}	hard sphere radius
$a^{\dagger}$	amplitude
c_{eqm}	equilibrium concentration
$c(r)$	direct correlation function
c^{*}	concentration of material in adsorbed layer
$\hat{c}$	surface active agent concentration
d_{BH}	Barker-Henderson diameter
d_{E}	effective diameter
d_{o}	point on interaction potential where exp (-V(r)/kT) becomes negligible
d_{p}	propagation distance
d_{s}	distance from particle surface to Stern plane
d^{*}	particle surface-surface separation (electroviscous effects)
d_{o}^{*}	minimum particle surface-surface separation (electroviscous effects)
e	fundamental unit charge
f_{c}	dimensionless collective friction coefficient
g	acceleration due to the earth's gravitational field
$g(r)$	radial distribution function
$g_{o}(r)$	reference component of radial distribution function
$g_{1}(r)$	first order perturbation correction of radial distribution function
h	Planck's constant
$h(r)$	total correlation function
h'	any height (sedimentation)
$h^{\dagger}$	solvation factor
h^{*}	any point below sediment boundary
h_{o}^{*}	initial height of sedimenting system
h_{e}^{*}	equilibrium height of sedimenting system
k	Boltzmann's constant
k_{o}	conductivity of dispersion

k_1, k_2 etc. viscosity coefficients etc.

k_s sedimentation coefficient

$k^\dagger$ coefficient (Cross equation)

$k^* = \alpha^{\dagger *} \phi_m$ (theoretical sedimentation rate, Buscall etal)

l electrode separation (electrophoresis)

l_{cc} outer cylinder height (couette viscometer)

m particle mass

m_L mass of adsorbent particles in sample

n coordination number

n_o number of cations or anions per unit volume

n_{eqm} equilibrium number of moles of adsorbate in sample

n_i initial number of moles of adsorbate in sample

$\hat{n}$ number of carbon atoms in alkyl chain

p pressure

$p(r)$ probability function

r particle centre-centre separation

r_c cylinder radius

r_{cc} arbitrary radius (couette viscometer)

r_{cp} arbitrary radius (cone and plate viscometer)

r_{min} value of r at minimum of potential well

r^* distance between atoms

$\hat{r}$ rescaled particle centre-centre separation

s_o fluid velocity due to an isolated sphere

s^* particle displacement (theoretical shear modulus calculation)

t time

t_{as} time after shearing of system

t_e experimental time

t_I induction period

t_M Maxwell relaxation time

t_p propagation time

t_r stress relaxation time

u wave propagation velocity

$u(r)$ radial distortion function

u^* fluid velocity

v volume

v_1 molecular volume of dispersion

$\bar{v}_1$ molar volume of solvent

v_m molar volume of solvent

v_{ov} overlap volume

v^* velocity

$x = H_o/2a$ (pair potential calculations)

x_o critical damping length

$x^\dagger$ distance from a planar surface

χ number of ethylene oxide units in a polyoxyethylene chain

$y(r)$ indirect correlation function

z ionic valency

A Hamaker constant

$A^\dagger_{ij}$ hydrodynamic coefficient

A^* Helmholtz free energy

A^*_o Helmholtz free energy of reference system

A^*_1, A^*_2 perturbation corrections to Helmholtz free energy

A^*_c cross sectional area of channel (electrophoresis)

A^*_{cc} cylinder area (couette viscometer)

A^*_L specific surface area of adsorbent particles

A^*_s area occupied by one molecule at the surface

A^*_{xy} projected area of particle pair in xy plane

$\hat{A}$ acceleration in units of g

B_2 second virial coefficient

$B^\dagger_{ij}$ Hydrodynamic coefficient

D diffusion coefficient

$D(O)$ free diffusion coefficient

$D(\phi)$ self diffusion coefficient

De Deborah number

D^* final latex particle diameter

E	applied potential (electrophoresis)
E_1	primary electroviscous factor
F	force
F_i	interparticle force
F_G	gravitational force
F_V	viscous force of sedimenting sphere
G	shear modulus
$G(\infty)$	high frequency limit of shear modulus
G_∞^{th}	theoretical high frequency limit of shear modulus
G'	elastic or storage modulus
G''	loss modulus
G^*	complex modulus
$\tilde{G}$	wave rigidity modulus
$H(r)$	hydrodynamic function
H_o	particle surface-surface separation
$H_o^\dagger$	surface-surface separation of planes
I	current
$[I]$	total ionic concentration of aqueous plase (latex preparation)
$J(t)$	Creep compliance
K	bulk modulus/compression modulus
$K(\infty)$	high frequency limit of bulk modulus/compression modulus
K^*	network modulus
$K^{*'}$	approximate network modulus
L	particle centre-centre separation (electroviscous effects)
L_o	minimum particle centre-centre separation (electroviscous effects)
$[M]$	monomer concentration in aqueous phase (latex preparation)
N_A	Avogadro's number
N_p	number of particles
P	dynamic pressure of fluid
P_E	excess osmotic pressure due to double layer overlap
P_{EX}	excess pressure
$[P]$	initiator concentration in aqueous phase (latex preparation)

$\bar{P}_{EX}$	mean excess pressure
$\bar{P}'_{EX}$	approximate mean excess pressure
R	Universal gas constant
R_{cc}	cylinder radius (couette viscometer)
R_{cp}	cone and plate radius (cone and plate viscometer)
Re	Reynolds number
Re_{cc}	Reynolds number (couette viscometer)
$Re_{cc\ crit}$	Reynolds number at the onset of unsteady flow (couette viscometer)
R_1	distance between rotor centre and bottom of centrifuge tube
R^*	distance between rotor centre and top of sediment
$\hat{R}$	particle separation in ordered array
S	sedimentation rate
S(Q)	structure factor
S_o	sedimentation rate of particle at infinite dilution
S_1	sedimentation rate at 1g
T	absolute temperature
T_{cc}	torque (couette viscometer)
T_{cp}	torque (cone and plate viscometer)
T^*	torque
U_E	electrophoretic mobility
V	potential energy
$V_o(r)$	unperturbed reference potential
V_A	potential energy of attraction
V_A^D	potential energy of attraction, Debye
V_A^K	potential energy of attraction, Keeson
V_{A_L}	potential energy of attraction, London
V_B	Born repulsion
V_{HS}	hard sphere potential
V_{ij}	pair potential
$V_p(r)$	perturbed component of potential
V_k	potential energy of repulsion

V_s	potential energy of steric repulsion
$\underline{V}$	parameter used to overcome non-convergent integrals
$W(r_{12})$	modifying potential function
$Z\ (\kappa a)$	Booths function
Z_{cp}	cone and plate separation
α	particle radius
α_D	calibration constant for Deer rheometer ($\Rightarrow$ shear rate)
$\alpha^{\dagger}$	sedimentation term
$\alpha^{\dagger\dagger}$	empirical constant used in sedimentation
$\alpha^{\dagger *}$	term used in theoretical shear modulus calculation (Buscall etal)
α^{*}	atomic polarisability
$\alpha^{*\dagger}$	Booths dimensionless group (electroviscous effects)
α^{**}	scaling coefficient (sedimentation)
$\hat{\alpha}_{cp}$	cone angle (cone and plate viscometer)
β	two body coefficient of friction
β_D	calibration constant for Deer rheometer ($\Rightarrow$ stress)
β^{*}	sedimentation coefficient
γ	strain
$\dot{\gamma}$	shear rate, rate of strain
$\dot{\gamma}_{critical}$	critical shear rate at the onset of unsteady flow
$\dot{\gamma}_r$	reduced shear rate
$\hat{\gamma}$	surface tension
δ	thickness of adsorbed layer
δ^1	distance between cylinder and barrel walls (Deer rheometer)
$\delta^{\dagger}$	phase lag
$\left(\frac{\partial \rho}{\partial p}\right)$	osmotic compressibility
ε_o	permittivity of free space
ε_r	relative permittivity of medium
ζ	electrokinetic potential, zeta potential

η viscosity

$\eta(0)$ zero shear rate viscosity

$\eta(\infty)$ high shear rate limiting viscosity

η_o viscosity of medium

η_H hydrodynamic contribution to viscosity

η_K kinetic contribution to viscosity

$\eta_{norm} = \frac{\eta-\eta(\infty)}{\eta(0)-\eta(\infty)}$ normalised viscosity

η_{pl} plastic viscosity

$\eta_r = \eta/\eta_o$ relative viscosity

η_v potential contribution to viscosity

$[\eta]$ intrinsic viscosity

η' dynamic viscosity

$\hat{\theta}$ angular coordinate (theoretical shear modulus calculation, Buscall etal)

κ Debye-Hückel reciprocal length

λ_o specific conductivity of continuous phase

λ_p polydispersity factor

μ dipole moment

$\Delta\mu_E$ excess chemical potential of system

ν Hertzian frequency

ν_o frequency of electronic fluctuation

π_E excess osmotic pressure

ρ particle number density

$\rho(r)$ density distribution function

ρ_o macroscopic number density

$\Delta\rho$ density difference between disperse and continuous phases

$\rho^\dagger$ fluid density

ρ^* density

ρ_o^* density of medium

ρ_p^* density of particle

ρ^{**} density of stabilising species

σ particle diameter

$\sigma^{\dagger}$	surface charge density
$\sigma_1^{\dagger}$	surface charge density of Stern layer
τ	shear stress
τ_B	Bingham yield stress
$\tau_{critical}$	stress at onset of unsteady flow
$\dot{\tau}$	time differential of stress
τ^*	stress at the onset of shear thinning
ϕ	volume fraction
ϕ_o	initial volume fraction
ϕ_E	effective volume fraction
ϕ_{HS}	hard sphere volume fraction
ϕ_m	maximum packing fraction
ϕ_p	packing density of adsorbed layer
ϕ'	effective volume fraction due to the presence of adsorbed layer
$\bar{\phi}$	mean volume fraction in sediment
$\bar{\phi}'$	approximate mean volume fraction in sediment
χ_r	isothermal compressibility
χ^*	dimensionless enthalpy parameter
ψ	electrostatic potential
ψ_o	electrostatic potential at the surface
ψ_d	Stern potential
ψ^*	dimensionless entropy parameter
ω	angular frequency
ω_r	angular velocity of rotor
$\tilde{\omega}$	driving frequency
Γ	surface excess concentration
Δ	adsorbed layer surface-surface separation
Λ	wavelength of propagation wave
Ξ	potential energy minimum
Φ	specific adsorption potential

$\hat{\Phi}$ angular coordinate (theoretical shear modulus calculation, Buscall et al)

$\Psi(r_{12})$ potential of mean force

Ω_{cc} angular rotation (couette viscometer)

Ω_{cp} angular rotation (cone and plate viscometer)

References

1. R. Buscall. Colloids & Surfaces 5, 269 (1982)

2. R. Buscall & I.J. McGowan. Faraday Discuss. Chem. Soc., 76, 277 (1983)

3. R. Buscall. Third National Conference on Rheology, Melbourne, May 16-17, (1983)

4. M. Reiner & G.W. Scott Blair. 'Rheology. Theory and Applications'. Ed. F.R. Eirich. Volume 4. Academic Press, (1967)

5. J.W. Goodwin. Lecture course V. M.Sc. Surface Chemistry and Colloids. Bristol University (1981-82)

6. J.W. Goodwin. Technologically Important Aspects of Interface Science. Part 2. Concentrated Suspensions. Imperial College of Science and Technology, (1984)

7. J.W. Goodwin. 'Surfactants'. Ed. Th. F. Tadros. Academic Press, (1984)

8. M. Reiner. 'Rheology Theory and Applications'. Ed. F.R. Eirich. Volume 1. Academic Press (1967)

9. J.W. Goodwin. 'Science and Technology of Polymer Colloids. Characterisation, Stabilisation and Application Properties'. Volume II. Ed. G.W. Poehlein, R.H. Ottewill & J.W. Goodwin. Martinus Nijhoff (1983)

10. R. Buscall, J.W. Goodwin, M.W. Hawkins & R.H. Ottewill. J. Chem.Soc. Faraday Trans.I., 78, 2873 (1982)

11. J.D. Ferry. 'Viscoelastic Properties of Polymers'. Third Edition. Wiley. (1980)

12. J.W. Goodwin & R.W. Smith. Discuss. Faraday Soc. 57, 126 (1974)

13. J.W. Goodwin & A.M. Khider. 'Colloid and Interface Science' Volume IV. Ed. M. Kerker. Academic Press (1976)

14. D.J. Shaw 'Introduction to Colloid and Surface Chemistry' Third Edition. Butterworth. (1980)

15. E.J.W. Verwey & J. Th. G. Overbeek.'Theory of the Stability of Lyophobic Colloids'. Elsevier (1948)

16. J. Th. G. Overbeek. 'Colloidal Dispersions'. Ed. J.W. Goodwin. R.S.C. (1982)

17. Spring School in Colloid Science. Bristol University (1977)

18. G. Gouy. J. Physique. 9, 457 (1910)

19. G. Gouy. Ann. Physique, 7, 129 (1917)

20. D.L. Chapman. Phil. Mag. 25, 475 (1913)

21. P. Debye & E. Hückel. Physik Z, 24, 185 (1923)

22. P. Debye. Physik Z, 25, 93 (1924)

23. J. Lyklema. 'Colloidal Dispersions'. Ed. J.W. Goodwin. R.S.C. (1982)

24. K.J. Mysels 'Introduction to Colloid Chemistry'. Interscience (1959)

25. A.W. Adamson. 'Physical Chemistry of Surfaces'. Third Edition (1976)

26. O. Stern. Z. Elektrochem. 30, 508 (1924)

27. I. Langmuir. J. Chem. Phys. 6, 873 (1938)

28. B. Derjaguin. Trans. Faraday Soc. 36, 203 (1940)

29. H. Reerink & J. Th. G. Overbeek. Discuss. Faraday Soc. 18, 74 (1954)

30. W.H. Keesom. Proc. Acad. Sci. Amsterdam 18, 633 (1915)

31. W.H. Keesom. Proc. Acad. Sci. Amsterdam 23, 939 (1920)

32. P. Debye. Physik Z, 21, 178 (1920)

33. P. Debye. Physik Z, 22, 302 (1921)

34. F. London Z. Physik. Chem. 63, 245 (1930)

35. R.H. Ottewill. Lecture course III. M.Sc. Surface Chemistry and Colloids. Bristol University (1981-82)

36. J. Visser. Adv. Coll.Int.Sci. 3, 331 (1972)

37. J. H. de Boer. Trans. Faraday Soc. 32, 10 (1936)

38. H.C. Hamaker. Rec. Trav. Chim. 55, 1015 (1936)

39. H.C. Hamaker. Rec. Trav. Chim. 56, 3 (1937)

40. H.C. Hamaker. Rec. Trav. Chim. 56, 727 (1937)

41. H.C. Hamaker. Physica 4, 1058 (1937)

42. E.M. Lifshitz. Dokl. Akad. Nauk. SSSR 97, 643 (1954)

43. E.M. Lifshitz. Zhur. Eksp. Teoret Fiz. 29, 94 (1955)

44. H.B.G. Casimir & D. Polder. Physic. Rev. 73, 360 (1948)

45. J.H. Schenkel & J.A. Kitchener. Trans. Faraday Soc. 56, 161 (1960)

46. D. Tabor & R.H.S. Winterton. Proc. Roy. Soc.A. 312, 435 (1969)

47. B.V. Derjaguin & L. Landau. Acta Physicochim USSR 14, 633 (1941)

48. T. Sato & R. Ruch.'Stabilization of Colloidal Dispersions by Polymer Adsorption'. Marcel Dekker (1980)

49. Th. F. Tadros. Adv. Coll. Int. Sci. 12, 141 (1980)

50. D.H. Napper.'Polymeric Stabilization of Colloidal Dispersions' Academic Press (1983)

51. D.H. Napper. Lecture Course VI M.Sc. Surface Chemistry and Colloids, Bristol University (1981-82)

52. E.W. Fischer. Kolloid Z. 160, 120 (1958)

53. I. Marković. Ph.D. Bristol University (1984)

54. R.H. Ottewill & T. Walker. Kolloid Z. 227, 108 (1968)

55. R.H. Ottewill & T. Walker. J.Chem.Soc. Faraday Trans. I. 70, 917 (1974)

56. A. Doroszkowski & R. Lambourne. J. Polymer Sci., 34, 253 (1971)

57. M.J. Vold. J. Colloid Sci. 16, 1 (1961)

58. D.W.J. Osmond, B. Vincent & F.A. Waite. J. Coll. Int. Sci. 42, 262 (1973)

59. R.H. Ottewill.'Colloidal Dispersions' Ed J.W. Goodwin R.S.C. (1981)

60. D.A.McQuarrie.'Statistical Mechanics' Harper & Row (1976)

61. J.E.Lennard-Jones & A.F. Devonshire Proc. Roy. Soc. A 163, 53 (1937)

62. J.E.Lennard-Jones & A.F. Devonshire Proc. Roy. Soc. A 165, 1 (1938)

63. R.H. Ottewill. 'Science and Technology of Polymer Colloids. Characterisation, Stabilisation and Application Properties' Volume II. Ed. G.W. Poehlein, R.H. Ottewill and J.W.Goodwin. Martinus Nijhoff (1983)

64. C.A. Croxton.'Introduction to Liquid State Physics'. Wiley. (1975)

65. J.A. Barker & D. Henderson. Mol. Phys. 21, 187 (1971)

66. L.S. Ornstein & F. Zernicke. Proc. Sci. Amsterdam 17, 793 (1914)

67. M.S. Werthein. Phys. Rev. letters 10, E501 (1963)

68. G.J. Throop & R.J. Bearman. J. Chem. Phys. 42, 2408 (1965)

69. L. Verlet & J. Weis. Phys. Rev. 5A, 939 (1972)

70. R.W. Zwanzig. J. Chem. Phys. 22, 1420 (1954)

71. J.A. Barker & D. Henderson. J. Chem. Phys. 47, 4717 (1967)

72. C.A. Castillo, R. Rajagopalan, C.S. Hirtzel. Rev. Chem. Eng. (in press)

73. J.D. Weeks, D. Chandler & H.C. Anderson. J. Chem. Phys. 54, 5237 (1971)

74. N.F. Carnahan & K.E. Starling. J.Chem. Phys. 51, 635 (1969)

75. H.S. Green. Proc. Intern. Congr. Rheol. 1st Holland 1948, 1-12 (1949)

76. H.S. Green. 'The Molecular Theory of Fluids' North Holland Publishing Company, Amsterdam (1952)

77. K.F. Herzfeld. J. Chem. Phys. 28, 595 (1958)

78. M.S. Green. J. Chem. Phys. 22, 398 (1954)

79. R. Zwanzig & R.D. Mountain. J. Chem. Phys. 43, 4464 (1965)

80. C.F. Zukoski. Bristol University (1984)

81. R.B.Bird, W.E. Stewart & E.N.Lightfoot. 'Transport Phenomena'. Wiley (1960)

82. I.M. Krieger. Adv. Coll. Int. Sci. 3, 111 (1972)

83. J.G. Kirkwood, F.P. Buff, M.S. Green. J. Chem. Phys. 17, 988 (1949)

84. R. Eisenschitz & M.J. Wilford. Proc. Phys. Soc. 80, 1078 (1962)

85. J.W. Goodwin. Specialist Periodical Reports. Colloid Science Volume 2. Eyre and Spottiswoode (1975)

86. A. Einstein. Ann. Physik. 19, 289 (1906)

87. A. Einstein. Ann. Physik. 34, 591 (1911)

88. G.K. Batchelor & J.T. Green. J. Fluid Mech. 56, 375 (1972)

89. G.K. Batchelor & J.T. Green. J. Fluid Mech. 56. 401 (1972)

90. M. Mooney. J. Coll. Sci. 6, 162 (1951)

91. M.E. Woods & I.M. Krieger. J. Coll. Int. Sci. 34, 91 (1970)

92. R.C. Ball & P. Richmond. Phys. Chem. Liq. 9, 99 (1980)

92a. C.R. Wildemuth & M.C. Williams. Rheol. Acta 23, 627 (1984)

93. J.W. Goodwin. 'Colloidal Dispersions'. Ed. J.W. Goodwin Royal Society of Chemistry (1982)

94. N.A. Frankel & A. Acrivos. Chem. Eng. Sci. 22, 847 (1967)

95. N.L. Ackerman & H.T. Shen. A.I.Ch.E.J. 25, 327 (1979)

96. A.L. Graham. Rheology Research Centre Report No.62. Univ.Wisconsin (1980)

97. M.M. Cross. J.Coll. Int. Sci. 33, 30 (1970)

98. R. Pätzold. Rheol. Acta 19, 322 (1980)

99. G.K. Batchelor. J. Fluid Mech. 41, 545 (1970)

100. G.K. Batchelor. Ann. Rev. Fluid Mech. 6, 227 (1974)

101. G.K. Batchelor. J. Fluid Mech. 83, 97 (1977)

102. F. Booth. Proc. Roy. Soc. A205, 533 (1950)

103. I.G. Watterson & L.R. White. J. Chem. Soc. Faraday Trans.2. 77, 1115 (1981)

104. W.B. Russel. J. Fluid Mech. 85, 673 (1978)

105. D.A. Lever. J. Fluid Mech. 92, 421 (1979)

106. W.B. Russel. J. Fluid Mech. 85, 209 (1978)

107. W.B. Russel. J. Rheol. 24, 287 (1980)

108. I.M. Krieger & T.J. Dougherty. Trans. Soc. Rheol. 3, 137 (1959)

109. R.L. Hoffman 'Science and Technology of Polymer Colloids, Characterisation, Stabilisation and Application Properties'. Volume II. Ed. G.W. Poehlein, R.H. Ottewill & J.W. Goodwin. Martinus Nijhoff (1983)

110. S.J. Willey & C.W. Macosko. J. Rheol. 22, 525 (1978)

111. R. Buscall, J.W. Goodwin, M.W. Hawkins & R.H. Ottewill. J. Chem. Soc. Faraday Trans. 1. 78, 2889 (1982)

112. L. Barclay, A. Harrington & R.H. Ottewill. Kolloid Z. 250, 655 (1972)

113. A.S. Michaels & J.C. Bolger. Ind. Engng. Chem. Fund. 1, 24 (1962)

114. M.J. Pearse. Warren Spring Laboratory, Department of Industry (1977)

115. A.S. Michaels & C.S. Lin. Ind. Engng. Chem. 46, 1239 (1954)

116. J. Happel & H. Brenner. 'Low Reynolds Number Hydrodynamics'. Prentice-Hall (1965)

117. G.K. Batchelor. J. Fluid Mech. 52, 245 (1972)

118. J.M. Burgers. Proc. Acad. Sci. Amsterdam.
44, 1045 (1942) 44, 1177 (1942)
45, 9 (1942) 45, 126 (1942)

119. C.W. Pyun & M. Fixman. J. Chem. Phys. 41, 937 (1964)

120. C.C. Reed & J.L. Anderson 'Colloid and Interface Science' Vol. IV. Ed. M. Kerker. Academic Press (1976)

121. C.C. Reed & J.L. Anderson. A.I.Ch.E.J. 26, 816 (1980)

122. G.K. Batchelor. J. Fluid Mech. 119, 379 (1982)

123. G.K. Batchelor, J. Fluid Mech.

124. E. Dickinson & R. Parker. J. Coll. Int. Sci. 97, 220 (1984)

125. A.D. Maude & R.L. Whitmore. Brit. J. Appl. Phys. 9, 477 (1958)

126. P.Y. Cheng & H.K. Schachman. J. Polym. Sci. 16, 19 (1955)

127. J.F. Richardson & W.N. Zaki. Trans. Inst. Chem. Engrs. 32, 35 (1954)

128. R. Buscall, J.W. Goodwin, R.H. Ottewill and Th. F. Tadros. J. Coll. Int. Sci. 85, 78 (1982)

129. S.J. Partridge. M. Sc. Bristol University (1982)

130. A.B. Glendinning & W.B. Russel. J. Coll. Int. Sci. 89, 124 (1982)

131. R.W. O'Brien. J. Fluid Mech. 91, 17. (1979)

132. E. Dickinson. CISG/RSC Meeting. (December 1984)

133. Th. F. Tadros. Adv. Coll. Int. Sci. 12, 141 (1980)

134. G.F. Kynch. Trans. Faraday Soc. 48, 166 (1952)

135. F.A. Bovey, I.M. Kolthoff, A.I. Medalia & E.J. Meehan 'Emulsion Polymerisation'. Interscience (1955)

136. V.I. Eliseeva, S.S. Ivanchev, S.I. Kuchanov & A.V. Lebedev 'Emulsion Polymerisation and its Applications in Industry'. Plenum Publishing (1981)

137. D.C. Blackley. 'Emulsion Polymerisation. Theory and Practice'. Applied Science Publishers (1975)

138. J.W. Vanderhoff, H.J. van den Hul, R.J.M. Tausk & J. Th. G. Overbeek. 'Clean Surfaces: Their Preparation and Characterization for Interfacial Studies'. Ed. G. Goldfinger. Marcel Dekker (1970)

139. R.E. Wachtel & V.K. La Mer. J. Colloid Sci. 17, 531 (1962)

140. R.H. Ottewill & J.N. Shaw, Kolloid Z. 215, 161 (1967)

141. J. Hearn, R.H. Ottewill & J.N. Shaw. Br. Polym. J. 2, 116 (1970)

142. A. Kotera, K. Furusawa & Y. Takeda. Kolloid Z. 239, 677 (1970)

143. J.W. Goodwin, J. Hearn, C.C. Ho & R.H. Ottewill. Br. Polym. J. 5, 347 (1973)

144. J.W. Goodwin, J. Hearn, C.C. Ho & R.H. Ottewill. Colloid & Polymer Sci. 252, 464 (1974)

145. A.M. Homola, M. Inoue,A.A. Robertson. J. Appl. Polym. Sci. 19, 3077 (1975)

146. R. Pelton. Ph.D. Thesis, Bristol University (1976)

147. Y. Chung-Li, J.W. Goodwin & R.H. Ottewill. Progr. Coll. & Polym. Sci. 60, 163 (1976)

148. J.W. Goodwin, R.H. Ottewill, R. Pelton, G. Vianello & D.E. Yates. Brit. Polym. J. 10, 173 (1978)

149. J.W. Goodwin, R.H. Ottewill & R. Pelton. Colloid & Polymer Sci. 257, 61 (1979)

150. R. Buscall. 'Science and Technology of Polymer Colloids. Characterisation, Stabilisation and Application Properties'. Volume II. Ed. G.W. Poehlein, R.H. Ottewill & J.W. Goodwin. Martinus Nijhoff (1983)

151. J.W. Vanderhoff. 'Science and Technology of Polymer Colloids. Characterisation, Stabilisation and Application Properties'. Volume II. Ed. G.W. Poehlein, R.H. Ottewill & J.W. Goodwin. Martinus Nijhoff (1983)

152. W.D. Harkins. J. Chem. Phys. 13, 381 (1945)

153. W.D. Harkins. J. Chem. Phys. 14, 47 (1946)

154. W.D. Harkins. J. Am. Chem. Soc. 69, 1428 (1947)

155. A.I. Yurzhenko & M. Kolechkova. Dokl. Akad. Nauk SSSR 47. 354 (1945)

156. W.V. Smith & R.H. Ewart. J. Chem. Phys. 16, 592 (1948)

157. J.N. Shaw. J. Polmer Sci. C27, 237 (1969)

158. P. Bolt & J.W. Goodwin. Unpublished work. Bristol University.

159. I. Johnson & V.K. La Mer. J. Am. Chem. Soc. 69, 1184 (1947)

160. P.A. Hiltner & I.M. Krieger. J. Phys. Chem. 73 2386 (1969)

161. S. Hachisu, Y. Kohayashi & A. Kose. J. Coll. Int. Sci. 42, 342 (1973)

162. J.S. Clunie, J.F. Goodman & P.C. Symons. Trans. Faraday Soc. 65, 287 (1969)

163. J.S. Clunie & B.T Ingram. 'Adsorption from Solution at the Solid/ Liquid Interface'. Ed. G.D. Parfitt & C.H. Rochester. Academic Press (1983)

164. C.H. Giles, D. Smith & A. Huitson. J. Coll. Int. Sci. 47, 755 (1974)

165. C.H. Giles, T.H. MacEwan, S.N. Nakhwa & D. Smith. J. Chem. Soc. 3973 (1960)

166. T. Sato & R. Ruch. 'Stabilization of Colloidal Dispersions by Polymer Adsorption'. Marcel Dekker (1980)

167. R.J. Newton. Ph.D. Bristol University (1984)

168. W.D. Harkins & H.F. Jordan. J. Am.Chem. Soc. 52, 1751 (1930)

169. S.J. Burkitt. M.Sc. Bristol University (1981)

170. J.M. Corkill, J.F. Goodman & S.P. Harrold. Trans. Faraday Soc. 60, 202 (1964)

171. D.B. Hough. Ph.D. Bristol University (1973)

172. H. Lange. Kolloid Z. 201, 131 (1965)

173. J.M. Corkill, J.F. Goodman & J.R. Tate. Trans. Faraday Soc. 62, 979 (1966)

174. T. Walker. Ph.D. Bristol University (1966)

175. L.M. Barclay & R.H. Ottewill. Special Disc. Faraday Soc. 1, 138 (1970)

176. L.M. Barclay. Ph.D. Bristol University (1970)

177. J.M. Corkill, J.F. Goodman & R.H. Ottewill. Trans. Faraday Soc. 57. 1627 (1961)

178. J.G. Stark & H.G. Wallace. 'Chemistry Data Book'. SI Edition Murray (1976)

179. J.M. Corkill, J.F. Goodman, D.R. Haisman & S.P. Harrold. Trans. Faraday Soc. 57, 821 (1961)

180. D.J. Shaw. 'Electrophoresis'. Academic Press (1969)

181. E. Hückel. Physik Z. 25, 204 (1924)

182. M. von Smoluchowski. 'Handbuch der Elektrizitat und des Magnetismus'. 2, 366 (1914)

183. D.C. Henry. Proc. Roy. Soc. A. 133, 106 (1931)

184. J. Th. G. Overbeek. Kolloid Beih. 54, 287 (1943)

185. F. Booth. Proc. Roy. Soc. A. 203, 514 (1950)

186. P.H. Wiersema, A.L. Loeb & J. Th. G. Overbeek. J. Coll. Int. Sci. 22, 78 (1966)

186a. R.W. O'Brien & L.R. White. J. Chem. Soc. Faraday II 1607 (1978)

187. R.H. Ottewill & J.N. Shaw. J. Electroanal. Chem. 37, 133 (1972)

188. J. Levine, M. Levine, K.A. Sharp & D.E. Brooks. Biophys. J. 42, 127 (1983)

189. R.M. Tennent. 'Science Data Book' Oliver and Boyd (1971)

190. C.R.C. 'Handbook of Chemistry and Physics' 49th Edition Ed. R.C. Weast. Chemical Rubber Company (1968)

191. R.F. Stewart & D. Sutton. Chemistry & Industry. 10, 373 (1984)

192. R.F. Stewart & D. Sutton. 'Solid Liquid Separation'. Ed. J. Gregory Ellis Horwood (1984)

193. P.F. Luckham, B. Vineent, J. McMahon & Th. F. Tadros. Colloids and Surfaces. 6, 83 (1983)

194. J.A. Long, D.W.J. Osmond & B. Vinvent. J. Coll. Int. Sci. 42, 545 (1973)

195. R.M. Cornell, J.W. Goodwin & R.H. Ottewill. J. Coll. Int. Sci. 71, 254 (1979)

196. A. Kose & S. Hachisu. J. Coll. Int. Sci. 55, 487 (1976)

197. H. van Olphen. Clays & Clay Min. 4, 204 (1956)

198. M.J. Vold. J. Phys. Chem. 64, 1616 (1960)

199. J. Visser. Adv. Coll. Int. Sci. 3, 331 (1972)

200. D.B.Hough & L.R. White. Adv. Coll. Int. Sci. 14, 3 (1980)

201. L. Marshall.B.Sc. Bristol University (1984)

202. J.A. Stiles. B. Sc. Bristol University (1979)

203. International Critical Tables of Numerical Data, Physics, Chemistry and Technology. McGraw-Hill (1933)

204. J. Shankey. Private communications. ICI Corporate Bioscience and Colloid Laboratory.

205. C.F. Zukoski, R.W. Hughes, J.W. Goodwin, S.J.Partridge.
Poster presented at Annandal. June (1985)

206. C.F. Zukoski. Private communications.

207. R. Klein and W. Hess. Faraday Discuss. Chem. Soc. 76, 137 (1983)

208. R.W. Hughes. Private communications.